Annual reports on NMR Spectroscopy

Volume 61

AP

List of Contributors

Laetitia Beguin, *Laboratoire de RMN en milieu orienté, Université Paris-Sud 11, ICMMO, UMR CNRS 8182, Bat. 410, 91405 Orsay Cedex, France*

Qun Chen, *Physics Department and Shanghai Key Laboratory for Functional Magnetic Resonance Imaging, East China Normal University, Shanghai 200062, P.R. China*

Rubén H. Contreras, *Department of Physics, University of Buenos Aires, and CONICET Ciudad Universitaria, Pab. 1, (C1428EHA) Buenos Aires, Argentina*

Jacques Courtieu, *Laboratoire de RMN en milieu orienté, Université Paris-Sud 11, ICMMO, UMR CNRS 8182, Bat. 410, 91405 Orsay Cedex, France*

Cornelius Faber, *Department of Experimental Physics 5, University of Würzburg, 97074 Würzburg, Germany*

Jonathan Farjon, *Laboratoire de RMN en milieu orienté, Université Paris-Sud 11, ICMMO, UMR CNRS 8182, Bat. 410, 91405 Orsay Cedex, France*

Petrik Galvosas, *Faculty of Physics and Earth Sciences, University of Leipzig, Linnestrasse 5, 04103 Leipzig, Germany*

Leonid B. Krivdin, *A. E. Favorsky Irkutsk Institute of Chemistry, Siberian Branch of the Russian Academy of Sciences, 1 Favorsky Street, 664033 Irkutsk, Russia*

Hiromichi Kurosu, *Department of Human Life and Environment, Nara Women's University, Kitauoya-Nishimachi, Nara 630-8506, Japan*

Denis Merlet, *Laboratoire de RMN en milieu orienté, Université Paris-Sud 11, ICMMO, UMR CNRS 8182, Bat. 410, 91405 Orsay Cedex, France*

Frank Stallmach, *Faculty of Physics and Earth Sciences, University of Leipzig, Linnestrasse 5, 04103 Leipzig, Germany*

Latifa Ziani, *Laboratoire de RMN en milieu orienté, Université Paris-Sud 11, ICMMO, UMR CNRS 8182, Bat. 410, 91405 Orsay Cedex, France*

Preface

Volume 61 of Annual Reports on NMR consists of a collection of five reviews pointing to the importance of NMR studies in many areas of scientific research. It begins with an account of Resolution Enhancement in *in vivo* NMR Spectroscopy by C. Faber; this is followed by a discussion of Spin Echo NMR Diffusion Studies from F. Stallmach and P. Galvosas; Recent Advances in Theoretical Calculations of Indirect Spin–Spin Coupling Constants are covered by L. B. Krivdin and R. H. Contreras; Q. Chen and H. Kurosu review Solid-State NMR Studies on Semicrystalline Polymers; finally J. Farjon, L. Ziani, L. Beguin, D. Merlet and J. Courtieu report on Selective NMR Excitations in Chiral Analysis.

It is my pleasure to express my gratitude to all of these authors for their timely and interesting accounts of the recent research developments in the diverse areas of NMR involvement covered in this volume. My thanks also go to the production staff at Elsevier for their assistance in the regular production of volumes of Annual Reports on NMR.

Royal Society of Chemistry
Burlington House
Piccadilly
London, UK

G. A. WEBB
October 2006

Resolution Enhancement in *In Vivo* NMR Spectroscopy

CORNELIUS FABER

Department of Experimental Physics 5, University of Würzburg, 97074 Würzburg, Germany

In vivo NMR spectroscopy requires adequate spectral, spatial, and temporal resolution. Current methodology provides numerous efficient methods to optimize all three kinds of resolution. The achievable spatial and temporal resolution mainly depend on the experimental setup including the object that is studied, the magnetic field strength, and the hardware used for signal detection. Spectral resolution is a much more sensitive parameter. While the maximum resolution is also limited by the experimental setup, small and apparently unimportant influences can dramatically deteriorate spectral resolution. This chapter shortly reviews current methodology and limits in spatial and temporal resolution in in vivo NMR spectroscopy. Dipolar fields causing inhomogeneity of the magnetic field, which often leads to severe line broadening, are discussed as major nuisance to spectral resolution. Several methods to avoid or refocus line broadening are discussed. Shimming and susceptibility matching are methods that reduce field inhomogeneities in the sample. Two-dimensional spectroscopy can provide resolution of frequency differences that are smaller than the actual line widths. Two techniques are discussed that use physical mechanisms to actively refocus line broadening. Magic angle spinning averages out dipolar interactions, while distant dipolar field (DDF) spectroscopy,

also termed intermolecular zero-quantum coherence (iZQC) spectroscopy, uses the local nature of the DDF to locally refocus magnetization. The origin of the DDF is discussed in detail and a pictorial explanation of signal refocusing is given. Current DDF spectroscopy methods and their in vivo applications are summarized.

1. INTRODUCTION

In vivo NMR spectroscopy (MRS) has the same fundamental objective as any high-resolution NMR experiment: resolving spectral patterns, which are the main source of information that can be obtained. Chemical shift, fine structure, and peak intensities constitute a 'fingerprint' of every molecule, allowing for its identification and for quantification in multicomponent samples, including living organisms. Multiplicity patterns and integrated peak areas yield information on molecular structure. Chemical-shift values provide structural information and its variations over time indicate reaction kinetics. For small molecules in solution, analysis of chemical shift and fine structure of every atomic nucleus is often no problem in a modern high-resolution spectrometer. Even in large molecules such as proteins the full spectroscopic information is accessible. There, severe overlap of resonance lines is avoided by the analysis of multidimensional experiments using hydrogen, carbon, and nitrogen nuclei to achieve sufficient dispersion of chemical shifts. First prerequisite for every high-resolution NMR experiment is to have extremely homogeneous magnetic fields inside the probe. For molecules in solution in susceptibility-matched glass tubes, this precondition can be achieved efficiently with elaborate shim units, which are part of every modern NMR spectrometer. However, if the sample itself is not homogeneous, as for instance in emulsions, resins, specimens of tissue or rock, or in living organisms, resolution may be heavily compromised. For the application to living organisms many efficient remedies for different aspects of this problem have been demonstrated over the last decades. *In vivo* NMR spectroscopy has become a highly developed and valuable tool in medical diagnostics and biomedical research with animal models for numerous diseases.[1–4] MRS provides unique advantages compared to other diagnostic techniques. It allows collecting data from tissue inside the living organism. The penetration depth MR can '*look inside the body*' is virtually unlimited; an advantage only afforded by nuclear medicine techniques PET and SPECT. These, however, require application of marker substrates that are radioactive. Other techniques, such as fluorescent imaging have strongly limited penetration depth and also require application of marker substances. MRS combines the advantages of being absolutely noninvasive, providing unlimited penetration depth, and not requiring marker substances.

In principle, MRS can detect any isotope with a nonzero nuclear spin. Practical limitations are, of course, given by their abundance in the organism. Therefore, the most relevant nuclei that are observed by *in vivo* MRS are ^{1}H, ^{13}C, and ^{31}P. Two other nuclei involved in metabolic events have been omitted here. ^{17}O and ^{23}Na are often detected by MR spectroscopic methods, yielding important physiological information. ^{17}O-labeled water content, produced from inhaled ^{17}O gas, allows for

quantification of oxygen use in the organism.[5] ^{23}Na is the naturally abundant sodium isotope and its concentration is indicative for the function of the cellular sodium potassium pump. Strong increase in the detected sodium concentration can be related to a breakdown of the pump and is therefore a marker for tissue viability.[6,7] However, total signal intensities of both ^{17}O and ^{23}Na are normally quantified and related to physiological function. Although measured with spectroscopic techniques no further spectral information is exploited, making such investigations more imaging than spectroscopy.

^{1}H is part of almost every metabolically relevant molecule. Its high gyromagnetic ratio makes *in vivo* metabolite detection at concentration below 1 mM possible.[2] Information on many important neurotransmitters and carbohydrate metabolites, for example N-acetyl aspartate (NAA), creatine (Cr), choline (Cho), lactate, glutamine/glutamate (Glx), glucose, myo-inositol (mI), γ-amino butyric acid (GABA), aspartate (Asp), and taurine (Tau) can be provided by ^{1}H MRS. Fig. 1 shows an exemplary spectrum obtained at a magnetic field strength of 17.6 T from a 5–mm voxel in the rat brain *in vivo*. A number of metabolites are detectable and can be quantified from spectra of such quality.

^{13}C MRS has the advantage of large chemical-shift dispersion resulting in very good spectral resolution. The smaller gyromagnetic ratio and the low natural abundance of the ^{13}C isotope (1.1%) hamper detection of metabolites not present at high concentrations. If patients or animals are infused or fed with ^{13}C-labeled substrates, for instance glucose, turnover rates of metabolic reactions can be determined.[8,9]

Phosphorous MRS provides good spectral dispersion and the lower gyromagnetic ratio is compensated by the high natural abundance of ^{31}P. High-energy
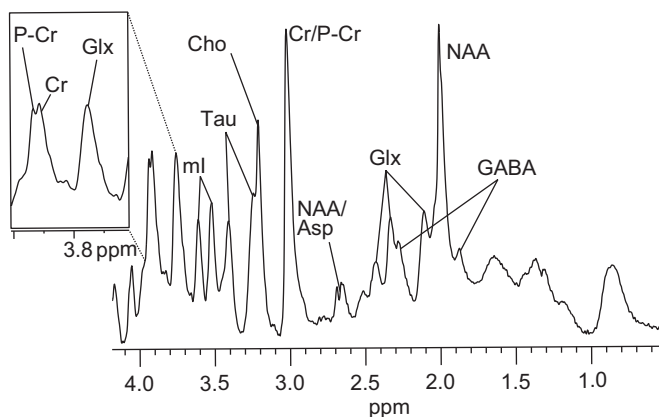

Fig. 1.   *In vivo* ^{1}H single voxel MRS from the rat brain at 17.6 T (spectrum courtesy of Thomas Neuberger). *In vivo* ^{1}H spectrum from a (5 mm)^{3} voxel positioned in the center of the brain of a female Fisher rat. The resonances were assigned according to Ref. 12 and referenced relative to the residual water signal, which was set to 4.7 ppm. Prior to acquisition shimming of an (8 mm)^{3} voxel was performed using FASTMAP. There were 128 averages collected in 9 min scan time. A number of metabolite resonances were observed with narrow line widths, resolving the Cr and P–Cr lines at 3.9 ppm.

phosphate metabolites such as ATP and phosphocreatine are directly observable. Intracellular pH and intracellular magnesium concentration can be determined, making ^{31}P MRS a valuable tool for the study of numerous diseases.[9,10] Independent of the observed nucleus, if a distinct spectral line is resolved, quantification or relative intensities can be directly linked to biochemical, metabolic, or physiological events.[1] Deviations from normal values can be used as indicators for pathologies and thus for detection and characterization of diseases. Kinetics of metabolic or biochemical reactions can be studied, if spectra are acquired in a temporally resolved manner.

In vivo MRS is particularly powerful for applications in large organs without pronounced intrinsic structure. Traditionally it is used for investigations of the brain. Numerous studies have demonstrated that unique information on tumors, damage after hypoxia, or a number of neurodegenerative diseases can be obtained.[2–4] Localized ^{1}H NMR spectra from the mouse brain have been used to obtain cerebral metabolite profiles of different mouse strains.[11] A study at a magnetic field strength of 9.4 T measured 18 different metabolites in the rat brain, composing a neurochemical profile.[12] Recently, quantification of Vitamin C, as 19th metabolite, was accomplished in a similar setup.[13] Proton MRS has also been applied successfully for investigations of the spinal cord, despite the problems imposed by its smaller size and strong respiratory and cardiac motion.[14–17] In cardiovascular research MRS methodology is highly developed for investigation of related diseases. Proton spectra have been recorded from isolated hearts of different organisms including mice,[18] rats,[19] and rabbits.[20] *In vivo* ^{1}H MRS has been performed successfully in dogs,[21] humans,[22] and mice[23,24] Efficient shimming procedures and effective gating strategies were crucial to avoid artifacts imposed by cardiac and respiratory motion, blood flow, and differences in magnetic susceptibility in the nearby lung.[22,25] Fig. 2 exemplifies the spectral quality that can be achieved in the mouse heart, if *state-of-the-art* methods for motion compensation and shimming are applied. Major cardiac metabolites were observed and could be quantified (Fig. 2a). Metabolic dysfunctions, as for example in genetically modified mice, can be detected (Fig. 2b). Further applications of MRS to skeletal muscle, the liver, or other organs have been reported. However, intrinsically inhomogeneous regions are problematic and compromise the diagnostic potential. Objects such as the lung, leaves of green plants, or tissue near air interfaces or near metallic implants are inaccessible with MRS.

This chapter gives an overview of the requirements to obtain spatially and spectrally resolved MR spectra from living organisms. Since the physical and experimental conditions influencing resolution of a spectrum are similar for different nuclei, the focus will be on ^{1}H MRS. Most of the considerations are also valid for any other nucleus. Concrete solutions, however, may not always be compatible. The following sections start with a classification into spatial, temporal, and spectral resolution. Basic conditions encountered in *in vivo* MRS and requirements to obtain spatially and temporally resolved spectra are discussed. Conventional methodology is reviewed shortly. The focus of this chapter is on spectral resolution. Magnetic field inhomogeneities as major source of line broadening are explored.
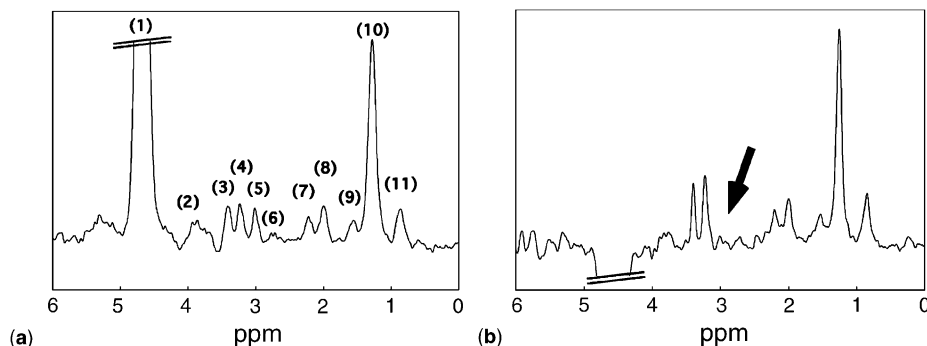
Fig. 2. *In vivo* cardiac ^{1}H single voxel MRS in mice at 11.75 T (from Ref. 24 with permission). (a) ^{1}H spectrum from a 2 μl voxel positioned in the interventricular septum of a wild type mouse *in vivo*. The resonances were assigned according to Ref. 19 and referenced relative to the residual water signal (peak (1)), which was set to 4.7 ppm; (2) (P)Cr–CH$_2$, 3.88 ppm; (3) taurine, 3.38 ppm; (4) carnitine, 3.21 ppm; (5) (P)Cr–CH$_3$, 2.99 ppm; (6) unassigned, 2.72 ppm; (7) glycerides (CH), 2.20 ppm; (8) unassigned, 2.0 ppm; (9) glycerides (CH), 1.55 ppm; (10) glycerides (–CH$_2$)n, 1.26 ppm; (11) glycerides terminal methyl, 0.85 ppm. (b) Spectrum from a guanidinoacetate *N*-methyltransferase deficient mouse (GAMT−/−), where no creatine was detectable (black arrow). Both spectra consisted of 512 averages and were scaled equally.

Subsequently, several techniques to reduce line broadening are discussed. Spectroscopic techniques using the distant dipolar field (DDF) are treated in detail, explaining the underlying mechanisms and reviewing current applications.

2. RESOLUTION IN *IN VIVO* MRS

In vivo MRS requires a more differentiated definition of resolution than is the case for high-resolution NMR, where the term 'resolution' clearly refers to spectral resolution. There, the samples are usually isotropic and duration of the measurement is irrelevant, unless slow kinetic processes are directly observed. *In vivo*, spectral resolution is only one aspect, besides temporal and spatial resolution. Measurement time is strictly limited by the time a subject can tolerate inside the magnet, an animal can be kept under anesthesia, or in extreme cases a plant needs to grow out of the probe. This defines a time scale during which any experiment has to be completed. More important for experimental considerations, if metabolic processes are studied, their time scale defines the temporal resolution required.

Spatial resolution is the aspect of resolution that is most particular to *in vivo* MRS. Metabolic information, obtainable from the spectrum, is desired from only one or a limited number of well-defined regions in the organism under investigation. Most studies focus on one organ requiring localization strategies that limit the detected signal to the region of interest. Furthermore, information on the local

distribution of metabolites is often desired. Therefore, the signal has to be acquired in a spatially resolved manner. The higher the spatial resolution, the more detailed differentiation of distinct types of tissue, such as healthy and diseased, can be accomplished.

3. SPATIAL RESOLUTION

In order to provide detailed physiological information, *in vivo* MR spectroscopy must be able to assign measured signals to well-defined regions in the organism. To this end the signal has to be localized in the organism with sufficiently high spatial resolution. A very simple method to achieve localization is to exploit the sensitivity profile of the rf-resonator used for signal detection. A surface coil placed on the skin near the region of interest or small implanted coils provide coarse localization, which may be sufficient for specific problems. Better-defined localization can be performed following two different principles: the spectroscopic imaging approach or the single/multiple voxel approach.

3.1. Spectroscopic imaging

Spectroscopic imaging or chemical-shift imaging (CSI) achieves localization by phase encoding the signal along all spatial dimensions.[26,27]Fig. 3a shows the pulse sequence of a possible simple implementation of a three-dimensional (3D) spatial, 1D spectroscopic CSI experiment. Immediately after the excitation pulse with flip angle α, magnetization is phase encoded by three simultaneously applied orthogonal gradient pulses. Immediately after the gradients have been switched off the signal is acquired as FID. Alternative implementations use an additional 180° refocusing pulse and record the signal as spin echo after an echo time TE. The pulse sequence has to be repeated $N_x \times N_y \times N_z$ times with alternating gradients to yield a spatial resolution with N_x, N_y, and N_z data points along the x, y, and z direction, respectively. For high spatial resolution a large number of repetitions are required, resulting in long acquisition times, which is the major drawback of CSI. Its major advantage is the inherently high signal-to-noise ratio (SNR), which is achieved because the whole sample, or a large voxel, is excited. The final data set is composed of $N_x \times N_y \times N_z$ localized spectra. The experiment can be significantly accelerated when the excitation pulse is applied slice selectively (Fig. 3b). Then, only $N_x \times N_y$ phase-encoding steps are required, leading to a rigorous reduction of measurement time. Concomitantly, SNR is reduced because only spins in a slab are excited and contribute to the detected signal. Fig. 3c shows an example of a 2D spatial CSI acquired from the head of a mouse. The data was acquired without water suppression, as shown in Fig. 3b. A matrix of 22 by 22 1D spectra was obtained. Observation of a water line correlates with signal in a gradient echo reference image. Narrow line widths are observed in the center of the brain, and broader lines toward the edges, reflecting the field homogeneity in the mouse. To provide
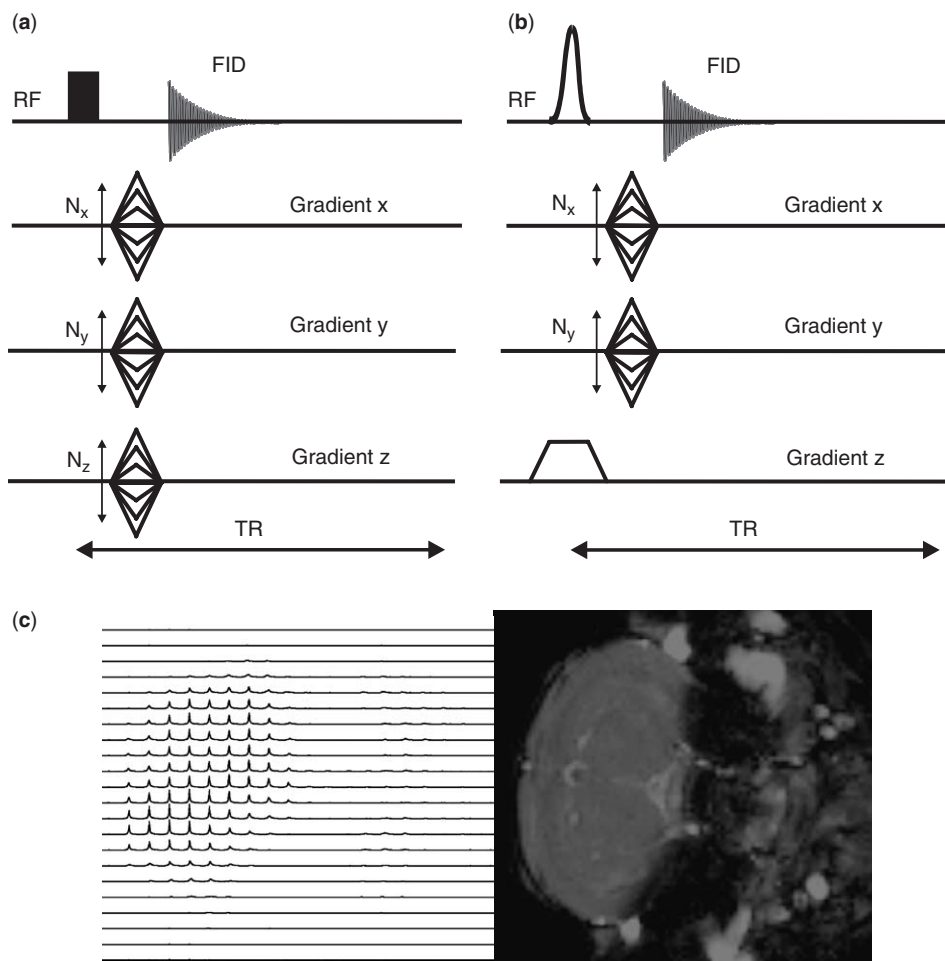
Fig. 3.   Chemical-shift imaging (CSI). (a) Pulse sequence for a 3D spatial, 1D spectroscopic CSI experiment. Black bar indicates excitation rf-pulse of flip angle α. Triangles indicate gradient pulses. After the repetition time TR the sequence is repeated $N_x \times N_y \times N_z$ times, stepping through different gradient amplitudes. (b) Pulse sequence for a 2D spatial, 1D spectroscopic CSI experiment. The excitation rf-pulse of flip angle α is applied with a defined frequency bandwidth under a slice selection gradient (trapezoid). Only $N_x \times N_y$ repetitions are required. (c) CSI data set from the head of a mouse *in vivo*. 22 by 22 spectra (without water suppression) show the spatial distribution corresponding to a gradient echo image (right hand side).

meaningful metabolic information, CSI must be performed in combination with water suppression. Narrow lines in the central brain can be suppressed efficiently. For strongly broadened lines, suppression is problematic limiting the suitability of CSI near surfaces with pronounced differences in magnetic susceptibility. Spatial resolution that can be achieved with CSI is mainly limited by experimental time

constraints. Doubling spatial resolution in one dimension requires doubling the number of phase encoding steps. Recording a 2D CSI with 32 by 32 encoding steps and a repetition time of 1 s already requires 17 min. Increasing the resolution to 64 by 64 spectra requires more than 1 h. CSI is generally not suitable to reach very high spatial resolutions *in vivo*.

3.2. Single/multi voxel localization

The second strategy to achieve localization of the acquired signal produces spectra only from one or a small number of distinct voxels. Signal from outside the selected region(s) is either eliminated by subtraction in difference spectra[28] or by dephasing under gradient pulses. Gradient dephasing is either done prior to excitation (outer volume suppression) or incorporated into excitation and refocusing (voxel localization). The most popular implementations of voxel localization are PRESS,[29] STEAM,[30] and LASER.[31] All follow the same fundamental principle: three consecutive rf-pulses (or combinations of rf-pulses) under orthogonal gradients each excite or refocus spins only in a distinct slice. Fig. 4 exemplifies this scheme for the PRESS sequence. A 90° pulse excites spins only in a slab along the z-direction. The first 180° pulse refocuses spins only in a slab along the y-axis. At this time point all spins outside a stick along the x-axis are dephased. The final 180° pulse refocuses only a slab along x, creating the desired voxel (gray). Spatial resolution that can be achieved with voxel localization techniques has one major limitation. SNR in a localized spectrum scales with the size of the voxel, limiting its minimum size. High spatial resolution can be realized if the experimental setup provides high SNR, which may be the case at high magnetic field strengths or with small rf-resonators. Using a microcoil probe at 14.1 T localized spectra of single neurons could be recorded.[32] More recently, subcellular localization was accomplished in *Xenopus laevis* oocytes. Spectra from $(180\,\mu m)^3$ voxels provided separate information from the nucleus, the vegetal and the animal hemisphere of oocytes.[33]

4. TEMPORAL RESOLUTION

Direct observation of dynamic metabolic processes requires data acquisition with sufficient temporal resolution. A localized 1D NMR spectrum with adequate spectral resolution can be recorded in a few tenths of one second. This time frame determines the lower limit of kinetics that can be directly followed with MRS. *In vivo*, however, localized spectra recorded in a single scan are only in seldom cases of useful quality.[34] Extensive averaging is required for small voxels prolongating measurement times. From a practical point of view, temporal resolution is limited by the number of averages required to obtain a spectrum with satisfying SNR. In order to increase temporal resolution in voxel localized MRS one must optimize SNR efficiency. In most experiments T_2 relaxation is the major source of signal loss during a localization sequence. Minimizing the echo time, or generally the duration
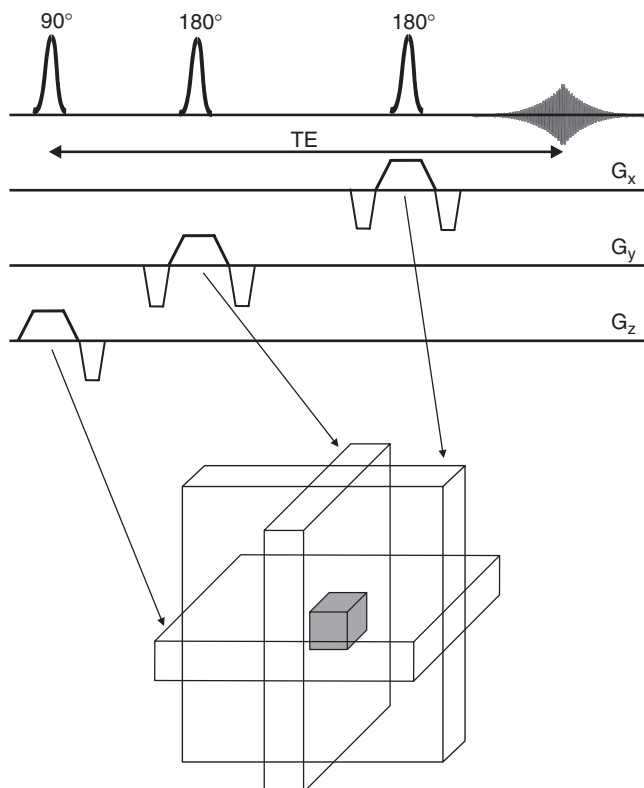
Fig. 4. Principle of PRESS localization. Signal is excited with a selective $90°$ pulse and refocused twice by two consecutive $180°$ pulses. Each pulse is applied under a slice selection gradient. The first pulse excites a slice along the z-direction, the second pulse refocuses a stick in the x-direction, and the third pulse finally refocuses signal only in the desired voxel (gray box).

of localization, reduces relaxation losses and thereby increases SNR. Localization using the STEAM sequence has been reported with an ultra-short echo time of $1\,\mathrm{ms}$.[35] A possibility to actively increase SNR is to perform an experiment at higher B_0. Numerous publications have pointed out the benefits of higher magnetic field strengths (see for example Refs. 36–40). In most *in vivo* measurements SNR scales linearly with B_0. Required scan time scales with the square of the desired SNR. Doubling the field strength can provide four times better temporal resolution in voxel localized MRS. Obviously, NMR spectrometers are not equipped with a '*field strength button*' to turn up B_0, but when planning a kinetic study the aspect of magnetic field strength is worth consideration. Reducing measurement times and thus allowing for significantly better temporal resolution is the major benefit of higher magnetic fields.

The above considerations are not valid for 2D spectra or CSI experiments. Both require numerous repetitions, which act as intrinsic averaging and make data

acquisition without further averaging possible. Minimum scan time is determined by the number of repetitions needed to achieve the desired spectral or spatial resolution in the 2D spectrum or the CSI experiment, respectively. For spectroscopic imaging a number of techniques to accelerate data acquisition have been proposed. Most of these strategies either use multiecho readout, reduced k-space sampling, or combine spectroscopic imaging with fast imaging sequences such as BURST, EPI, or FLASH. Reviews of these methods can be found in Chapter 6 of Ref. 2, under the aspect of usefulness for fMRI in Ref. 41, or comparing the efficiency of different methods in Ref. 42. More recent developments include the implementation of a steady-state free precession CSI experiment[43] or the combination of CSI with parallel imaging techniques.[44,45] Despite substantial acceleration that is reached with fast spectroscopic imaging, the method is not suitable for directly studying fast metabolic kinetics or physiological responses. Spectroscopic imaging is more suitable for events on a minute to hour time scale.

5. SPECTRAL RESOLUTION

Living organisms are inherently inhomogeneous and, at least if more complex than a single cell, mostly consist of regions with different magnetic susceptibility. Strong susceptibility gradients are for example found at air–tissue boundaries or interfaces between muscle and bone. These give rise to spatially varying resonance frequencies leading to often severe line broadening, which renders analysis of *in vivo* spectra difficult. Observed line widths *in vivo* normally exceed the natural line widths and are, besides chemical exchange processes, dominated by magnetic field variations over the volume of interest. In the following discussion, we will completely neglect chemical exchange and focus on field variations as a sole source of line broadening.

The observed line shape in a spectrum depends on field distortions over the volume of interest. A number of methods to calculate field inhomogeneities due to spatial variations of magnetic susceptibility have been reported. Two efficient methods are described, for example, in Refs. 46, 47. In order to calculate the line width in a spectrum, local resonance frequencies have to be integrated over the field variations. The line shape can be described by the probability.[48]

$$p(\omega) = \frac{1}{V} \int_V d^3\vec{r}\, \delta(\omega - \omega(\vec{r})) \tag{1}$$

We assume that all relevant contributions to ω come from dipolar magnetic fields B^{dip} and, with the gyromagnetic ratio γ, are given by

$$\omega(\vec{r}) = \gamma B_z^{\mathrm{dip}}(\vec{r}) \tag{2}$$

Transverse components of B^{dip} do not influence the resonance frequency in a first-order approximation and can thus be neglected. Dipolar fields originate from all interfaces with susceptibility differences in the observed tissue, resulting in a complex distribution (see, for example, Refs. 46, 47 and References therein). For the treatment in this chapter, a very simple example will be sufficient. The simplest case

for a source of a dipolar field is a spherical inclusion with radius R and susceptibility χ_1 in a homogeneous sample of susceptibility χ_0. In a magnetic field B_0 (along the z-axis) the z-component of the additional field is given by

$$B_z^{dip}(\vec{r}) = \frac{\chi_0 - \chi_1}{3}\left(\frac{R}{r}\right)^3 B_0(3\cos^2\theta - 1) \tag{3}$$

where θ is the angle between $\vec{r}$ and the z-axis. Fig. 5 graphs Eq. (3). A nuclear spin at position $\vec{r}$ experiences either an increased or a decreased magnetic field, depending on θ. Between $0°$ and $54.7°$, and $125.3°$ and $180°$, B^{dip} is positive and increases the local resonance frequency. Between $54.7°$ and $125.3°$ the local resonance frequency is decreased by a negative B^{dip}. At the magic angle of $54.7°$ (and $125.3°$) the dipolar field vanishes. The line width observed in presence of such a spherical inclusion is obtained after integrating over all spins in the voxel.[49] Most theoretical treatments use spherical voxels, for which Eq. (1) can be solved.[48,50] Corresponding lines obtained for a dipole field described by Eq. (3) have a typical '*dipolar*' shape and depend on the volume fraction η that is occupied by the inclusion (Fig. 6). For a spherical inclusion in a spherical voxel η is given by the two radii $\eta = (R_{inclusion}/R_{voxel})^3$. If the inclusion occupies 1% of the voxel, the line is severely broadened
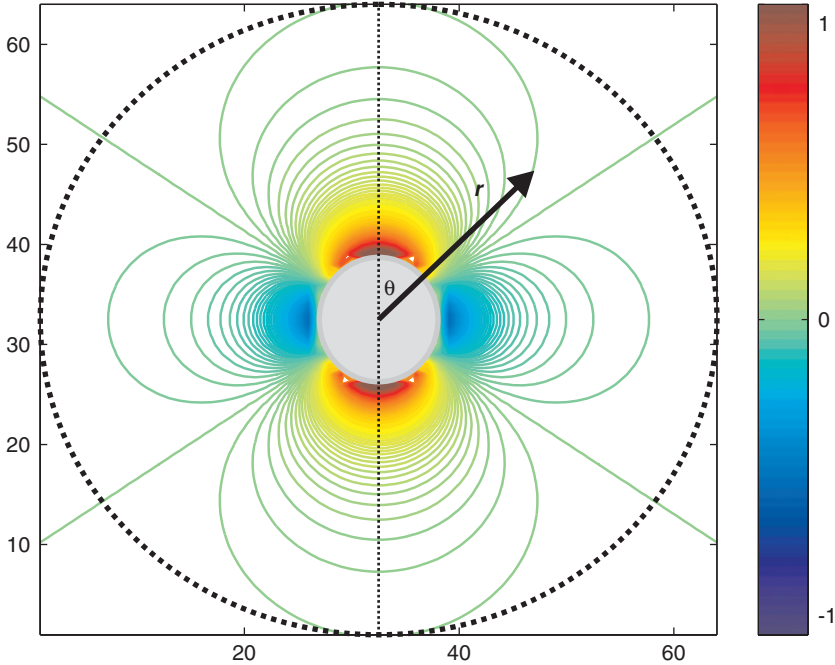

Fig. 5. Dipolar field originating from a spherical inclusion with different magnetic susceptibility. Contour plot of the field in the central z–y plane of a 64^3 matrix calculated according to Eq. (3). Maximum field was set to 1. A nuclear spin at position r (arrow) experiences a dipolar field that depends on the angle θ. Dashed circle indicates the border of a cubic voxel often used for theoretical analyses.
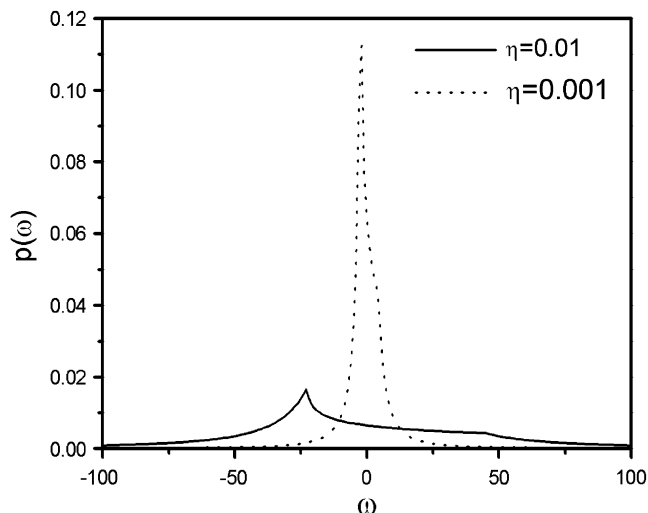
Fig. 6. Frequency distribution in presence of a dipolar field. $p(\omega)$ was calculated according to Eq. (1) in a spherical voxel around a spherical inclusion with susceptibility difference $\Delta\chi$. Parameter were chosen to reflect an air bubble of 0.5 mm diameter in water ($\Delta\chi = 9$ ppm) at 17.6 T. The line width depends on the volume fraction $\eta = (R_{inclusion}/R_{voxel})^3$ occupied by the inclusion.

while for $\eta = 10^{-3}$ only a few Hertz width at half-maximum are obtained (Fig. 6). The actual situation in the experiment is better described by a cubic than by a spherical voxel. This increases the number of contributing spins that are close to the magic angle and, therefore, experience only small frequency shifts. Fig. 7 compares line shapes calculated for cubic (b) and spherical voxels (a) with a 1–mm diameter air inclusion at 17.6 T. In the cubic voxel the line shape is different, with the maximum near zero frequency shift. As for the spherical voxel, line widths decrease in cubic voxels when increasing the voxel size (Fig. 7b). The consequence for the presence of numerous inhomogeneities in one voxel is quite intuitive. The line width increases with the perturber density.

In living tissue sources of susceptibility differences are manifold. Although these mostly do not originate from spherical structures, the effects on the line shape are similar. Spins close to tissue interfaces contribute strongly to inhomogeneous line broadening. Thus, a straightforward method to reduce spectral line widths is to avoid susceptibility differences by reducing the size of the volume of interest. This is illustrated schematically for an arbitrary 1D frequency distribution in Fig. 8. For simplicity only two equally abundant spin species, I (red) and S (black), were considered here. The central panel shows large variations of the effective magnetic field for each spin species along an arbitrary direction, which is chosen as z here. The difference between the two species is given by the chemical shifts and is constant at all positions because both experience nearly identical dipolar fields. In Fig. 8 a value of 1 a.u. was chosen, which can be 1 kHz in a real experiment at high magnetic field. On top of the central panel the frequency distributions observable in
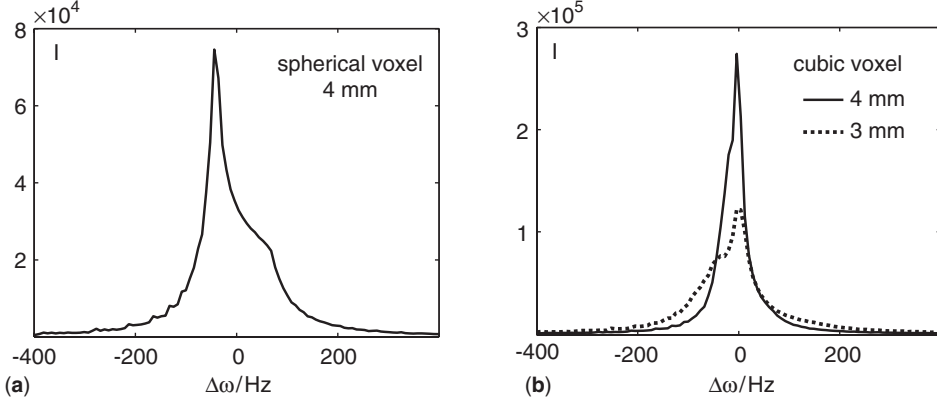
Fig. 7. Line shapes in spherical and cubic voxels. Distribution of frequencies in a $(128)^3$ matrix $\Delta\omega(x,y,z)$ (Eqs. (2) and (3)), representing a 3 or 4 mm voxel. $\Delta\omega$ originates from a spherical inclusion of 1 mm diameter at the origin ($\Delta\chi = 9$ ppm, $B_0 = 17.6$ T). (a) Distribution in a spherical voxel. Only $\Delta\omega(x,y,z)$ for 0.5 mm $<$ sqrt($x^2+y^2+z^2$) < 2 mm is plotted. Apparent peaks in the slope of the distribution are due to digitization. Line shape and width corresponds to the curves in Fig. 6. (b) Distribution in a cubic voxel with a diameter of 3 mm (dashed line) and 4 mm (solid line). Only $\Delta\omega(x,y,z)$ for 0.5 mm $<$ sqrt($x^2+y^2+z^2$ is plotted. Owing to more spins with small frequency shifts line width are different with the maximum near $\Delta\omega(x,y,z) = 0$. For a constant size of the inclusion, the line narrows for a larger voxel.
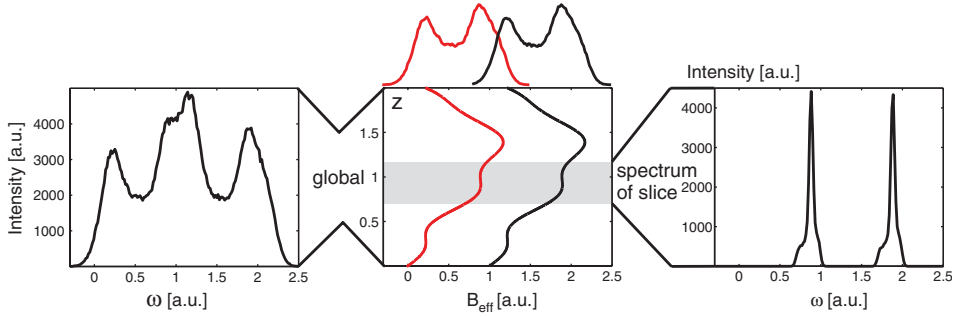

Fig. 8. Resolution enhancement by spatial localization, schematically. Two spin species I (red) and S (black) experience a magnetic field that varies along the z-direction. The effective magnetic field B_{eff} for each spin is given by the chemical shift and the varying field (central panel). For each spin species a strongly distorted line would be detected (top of central panel). The global spectrum reflects the B_{eff} distribution of both spins (left panel). A spectrum localized to the gray slice shows two distinct lines at their respective resonance frequencies $\omega = \gamma B$, with $\gamma = 1$ for clarity (right panel). Residual inhomogeneous line broadening results from the field variation at the edge of the slice.

an NMR experiment are shown for each spin species separately. In the global spectrum, shown in the left panel, both lines overlap and it is not evident that two distinct species are present. All spectroscopic information is lost due to the strongly varying magnetic field. If the volume from which signal is detected is reduced to a

slice with only small field variations (gray area in the central panel), two well-resolved lines are observed (right panel). However, owing to remaining field variation at the edges of the slice both lines are still inhomogeneously broadened.

This simplified example perfectly reflects the situation *in vivo*. When a spectrum is acquired from a large volume containing different anatomical structures, a wide range of frequencies is sampled and one single broad line without any spectroscopic features is obtained. Fig. 9a shows an example of a spectrum obtained from a mouse head without any localization. A dominant water line and weak lipid lines
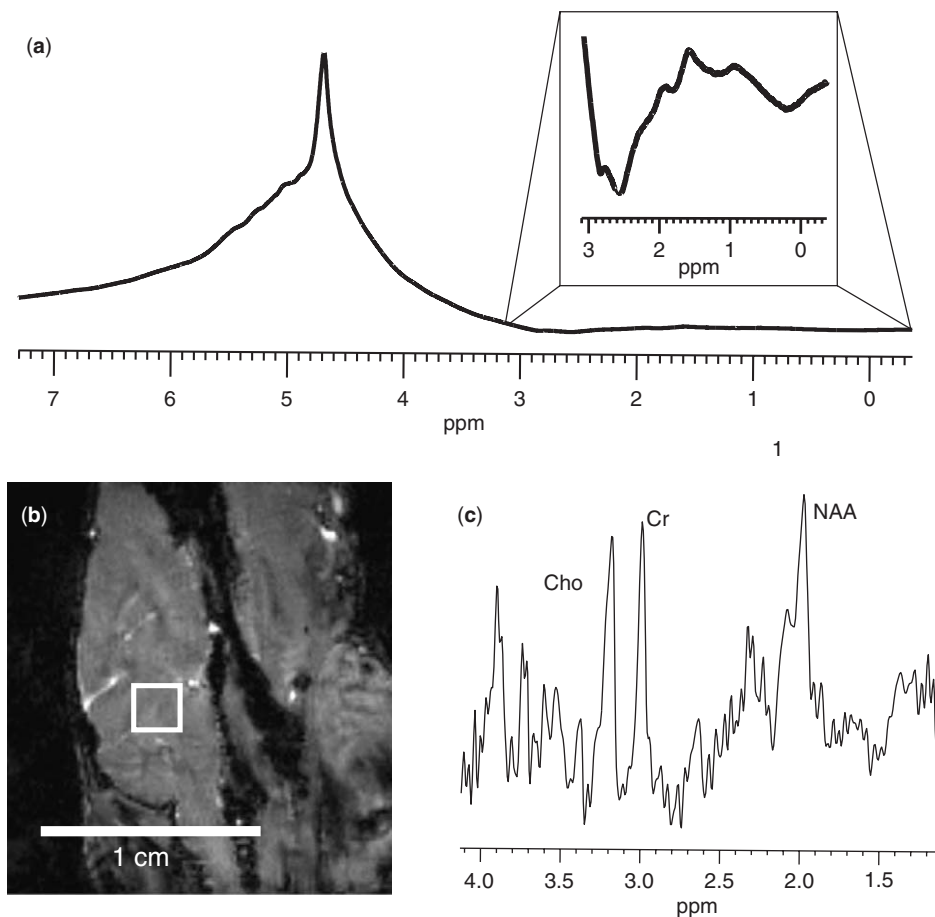

Fig. 9. Resolution enhancement by spatial localization, experimentally. *In vivo* MRS of the mouse brain at 17.6 T. (a) Global 1D spectrum of a C57Bl6 mouse. The head was positioned in the center of a 38 mm resonator. Shimming of a $(4.5\,mm)^3$ voxel was done with FASTMAP. (b) Gradient echo image of the mouse brain showing the position of the voxel for PRESS localization. (c) 1D spectrum localized to the (2 mm) voxel shown in (b) with the PRESS sequence (TE = 15 ms). VAPOR water suppression[35] was used, 1,024 averages were collected in 17 min. Major brain metabolites were observed.

(inset) were observed, both strongly broadened. The line width prohibited successful water suppression, which is the prerequisite for resolving metabolic information under the dominant water signal. In principle, metabolic information can be obtained without water suppression if the dynamic range of the digitizer in the spectrometer is sufficient to resolve metabolite resonance under the 10^4 times more intense water signal.[51] However, a second requirement for MRS without water suppression is a sufficiently narrow line width to avoid direct overlap of resonance lines. This is clearly not fulfilled under the conditions given here. Fig. 9c shows a localized spectrum acquired with the PRESS sequence from the same mouse in the same setup as the global spectrum (Fig. 9a). When the spectrum was localized to a 2 mm cubic volume inside the brain, large susceptibility gradients were avoided and the line width of the water resonance decreased significantly. Water suppression could be performed successfully with the VAPOR sequence and the major brain metabolites Cho, Cr, and NAA were observed in the spectrum.

Reducing the voxel size is the most fundamental method to obtain resolved spectra and forms the basis of every localized *in vivo* MRS experiment. Although it is very efficient, there is a strict limitation to this method. As pointed out above, SNR decreases with the voxel size. If resolved spectra cannot be obtained from millimeter-sized voxels (in small animal experiments), further reduction requires intolerably long measurement times. Independent of the voxel size, it is a precondition to have a homogeneous region in the tissue from which the spectrum is obtained. For objects with intrinsic microscopic inhomogeneities, localization to small voxels will not produce resolved spectra. Even if sufficiently large homogeneous regions are present in the object, stray fields from adjacent structures may spoil the spectrum. The next section will discuss shimming to make magnetic fields homogeneous and obtain resolved spectra. The following sections will discuss further techniques to enhance spectral resolution in the case shimming is no longer efficient.

5.1. Shimming

To obtain well-resolved spectra, as for example shown in Figs. 1 and 2, it is one fundamental precondition to compensate magnetic-field variations over the volume of interest. Although magnetic fields are normally homogeneous inside an empty magnet, positioning the sample (subject, animal) in the magnet inevitably leads to field distortions. Both the sample itself and the probe give rise to local dipolar fields. Prior to the measurement these local fields must be compensated. In order to achieve a homogeneous magnetic field under the given experimental constraints, NMR spectrometers are equipped with efficient shim systems. For correction the magnetic field is described by the expansion in spherical harmonics (see for example Ref. 52). Shim systems are constructed to be capable of producing each harmonic separately. Thus, each harmonic can be superimposed onto the actual field in the sample with deliberate sign and amplitude, eliminating unwanted distortions. Shim coils are usually grouped into first-order (or linear) shims X, Y, and, Z,

second-order (or quadratic) shims $Z,^2$ ZX, ZY, $2XY$, $X^2–Y^2$, and higher-order shims. A general problem arises from imperfections of the shim coils. The generated correction fields are not perfectly orthogonal and, therefore, not exactly described by spatial harmonics. Corrections to one harmonic influence other orders making shimming a complicated and often cumbersome task. In high-resolution NMR or with micro coils, global shimming is performed, homogenizing the field over the whole sample volume. *In vivo*, or generally with structured samples, strong local field variations are present and cannot be corrected globally. Therefore, shimming is often done locally on a volume selected with a single-shot voxel localization sequence. Distant from the isocenter of the spectrometer, localized shimming is significantly complicated by lower-order terms created by corrections to the quadratic shims.[53] Therefore, maximizing the integral of the FID as criterion for field homogeneity requires considerable experience or efficient optimization procedures for automatic shimming[54] and, still, often leads into local minima.

An alternative strategy for automatic shimming is to determine the magnetic field distribution over the volume of interest and then apply the required corrections. Such field maps can be obtained from acquired spectroscopic images[55,56] or phase difference images.[57,58] In particular, spectroscopic imaging is very time-consuming and, thus, not appropriate for generating field maps under strict time constraints normally given for *in vivo* experiments. Calculation of a field map is dramatically accelerated when only 1D projections of the magnetic field are used.[59] One of the most widely used methods, dubbed Fast Automatic Shimming Technique by Mapping Along Projections (FASTMAP), employs 1D projections along six directions to adjust all first- and second-order shims.[60] Several improvements, modifications, or extensions to higher orders have been proposed in the recent years.[61–63] A more detailed discussion of shimming for *in vivo* MRS can be found for example in Chapter 9 of Ref. 2.

Problems with shimming occur especially at high magnetic fields. Local dipolar fields, which are the major source of line broadening *in vivo*, scale with the strength of the external main magnetic field B_0 (see Eq. (3)). *In vivo*, shim systems developed for lower B_0 are often not capable of creating sufficiently strong correction fields required at higher B_0. Although algorithms like FASTMAP calculate adequate corrections, shim currents may not be appropriate to produce homogeneous fields. Inside homogeneous organs, such as the brain, this problem is less pronounced. Field distortions originate from large structures adjacent to the brain and can be corrected when shimming to a voxel inside the brain. At 7 T a line width of 5.5 Hz has been reported for the Cr/PCr line in the monkey brain,[64] at 9.4 T a water line width of down to 11 Hz in the mouse brain has been reported,[39] and at 11.7 T the Cr and PCr lines have been resolved in the rat brain.[40] These line widths are likely to be dominated by microscopic dipolar fields or other line-broadening mechanisms inaccessible with shimming.

In intrinsically structured organs the situation is different. On a millimeter scale improvements in shim device technology may lead to further advances in localized MRS. However, as soon as the structures have submillimeter dimensions, distortions can no longer be corrected by shimming. Many samples and organs cannot be

made accessible to MRS by shimming alone. Different methods for resolution enhancement have to be applied.

5.2. Higher magnetic field strength

In high-resolution NMR spectroscopy there is an ongoing trend toward higher B_0. Besides better SNR, higher fields provide enhanced resolution in the spectra. Spectral dispersion of resonance lines is constant in ppm and increases in Hz with the main magnetic field. High-resolution spectrometers guarantee nearly constant line widths that are independent of B_0. Thus, spectra acquired at higher field strength benefit from better frequency dispersion while line widths do not change. *In vivo*, the ultimate line width is determined by microscopic dipolar fields and has been shown to be tissue-specific with considerable regional variations.[64] The influence of these microscopic fields grows with B_0 (see Eq. (3)) spoiling at least part of the gain in resolution. In the brain, microscopic fields are often negligible and the achievable line width is limited by influences that act on a larger scale. These can be compensated by elaborate shimming (see above). Several convincing examples of enhanced resolution at higher magnetic field have been presented.[36,37,39] Although this has been challenged,[65] MRS in the brain clearly gains in both sensitivity and resolution at higher magnetic fields. However, in other less homogeneous types of tissue the stronger local dipolar fields compensate the better spectral dispersion, and higher B_0 alone does not result in resolution enhancement.

5.3. Two-dimensional spectroscopy

To spread the spectrum into a second dimension is an experimental strategy to increase spectral resolution. Lines can be separated even if their line widths exceed their chemical-shift difference. The idea of two-dimensional (2D) spectroscopy was first formulated by Jeneer[66] and experimentally shown by Ernst and co-workers.[67] Since these seminal works NMR spectroscopy has been extended to the third and higher dimensions and a stunning variety of experiments have been developed as the foundation of modern high-resolution NMR. These techniques are, in particular, helpful for the investigation of large molecules with numerous resonance lines. However, long acquisition times are the consequence of higher dimensionality and prohibit application to living organisms. *In vivo*, only a small number of resonances are of interest and the main problem is line broadening due to inhomogeneities of the magnetic field. Resonance overlap that occurs *in vivo* can mostly be resolved with 2D experiments. The feasibility of 2D MRS in living organisms has first been demonstrated without particular localization. The sensitivity profile of the rf-resonator was used to limit the detected signal to a, more or less, well-defined anatomic region. Double-quantum coherence-transfer spectra were acquired with a solenoidal coil wrapped around a transplanted tumor,[68] COSY spectra of the rabbit liver were acquired with a saddle coil,[69] and COSY spectra of the rat brain with a

surface coil.[70] Fig. 10 gives an example from one of the early *in vivo* applications. In the 1D spectrum no distinct lines of the lipid resonances were resolved. The spectrum showed only two strongly broadened peaks. In the COSY spectrum correlation peaks were resolved and could be assigned to specific chemical bonds, allowing for identification of distinct fatty acids.

After the value of 2D MRS for studying dynamic metabolic processes had been recognized,[71] numerous voxel localization techniques have been combined with COSY and other experiments. For a comprehensive description of these methods and a detailed discussion of 2D MRS *in vivo* the reader is referred to the review by
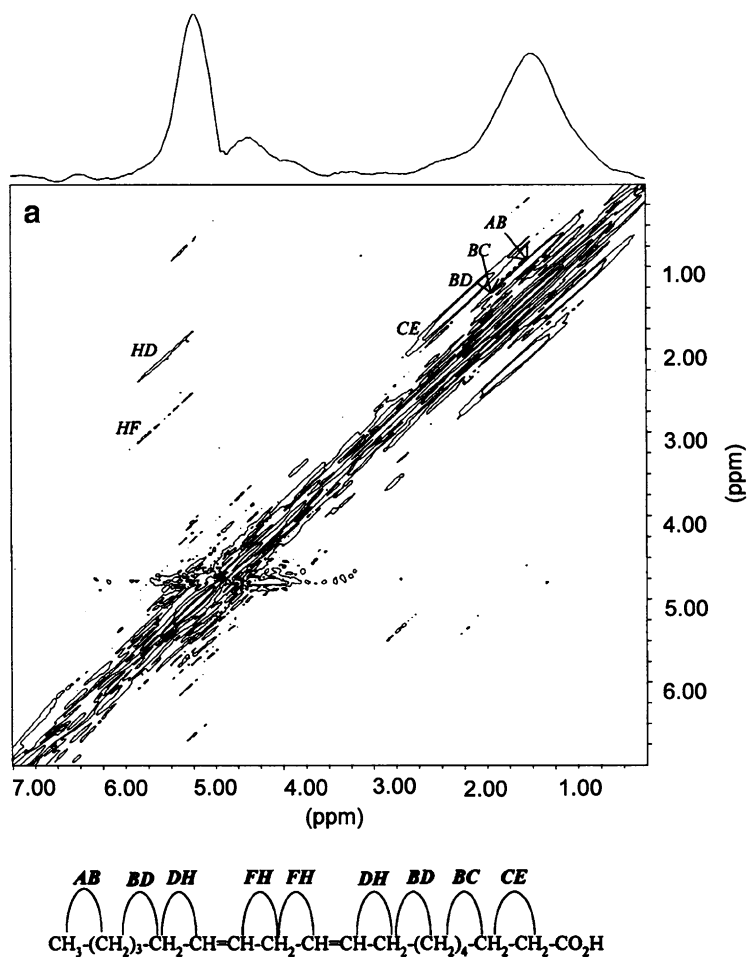
Fig. 10. *In vivo* resolution enhancement by 2D spectroscopy (from Ref. 72 with permission). *In vivo* ^{1}H MRS of the hind leg of C57Bl10 mice. The 1D spectrum does not provide any useful spectroscopic information. In the 2D COSY spectrum specific linolenic acid like correlations (HD) were observed.

Meric *et al.*[72] Voxel localization has made spectroscopic information available from any deliberately chosen region inside the organism but, as in the case of 1D experiments, spatial resolution is limited by decreasing sensitivity in smaller voxels. A major breakthrough was the successful implementation of CSI with two spectroscopic dimensions, partly overcoming the sensitivity problem. This technique termed correlation peak imaging (CPI) was first applied to perform plant histochemistry[73,74] and later to the rat brain.[75,76] However, even more than with normal CSI, measurement times become enormous because a four-dimensional (two spectroscopic and two spatial) experiment is performed. Fast acquisition schemes for CPI have been proposed[76,77] but measurement times are still long for routine *in vivo* applications.

A potent method to spread a spectrum in the second dimension is heteronuclear spectral editing. Either magnetization is transferred directly onto a heteronucleus and frequency-encoded there, or scalar coupling to a heteronucleus is exploited to modulate magnetization. However, this chapter will not discuss these techniques. Examples and discussions of different techniques are, for example, found in Refs. 2, 4, 72.

5.4. Susceptibility matching

One potential strategy to avoid line broadening is to reduce differences in magnetic susceptibility, a common method used for NMR spectroscopy with microcoils.[78] These are usually immersed in fluorocarbons or other liquids that have a susceptibility value close to the wire material. Dipolar fields originating from the susceptibility difference are minimized (in analogy to Eq. (3)), strongly reducing obtainable line widths. For *in vivo* experiments, the idea is to surround the tissue of interest with a liquid of similar susceptibility. The first experimental *in vivo* implementation has been reported for the study of perfused carcinoma and tumor cell. Reduced line widths were observed from a sample in an immersion chamber surrounding NMR tube and resonator.[79] For the study of isolated and perfused organs this susceptibility matching is intrinsically exploited by the setup of having buffer around the organ. *In vivo*, susceptibility matching is more difficult to achieve. However, an experimental *in vivo* setup immersing xenograft tumors in a water bath has been reported.[80] Generally, immersing animals or patients in susceptibility matching liquids is problematic. While this method may be feasible for xenograft tumors on the thigh of nude mice, it is not suitable for investigations of the brain. More appropriate are plasticine or dough matching tissue susceptibility, which can be used in studies with nude mice (personal communication, Gerd Melkus, University of Würzburg). However, matching susceptibility differences inside the body remain problematic in animals and patients.

In plants matching of intrinsic susceptibility differences can be done. Green leaves are mostly composed of air inclusions because ventilation is essential for photosynthesis. Numerous air–cell interfaces give rise to ample dipolar fields, leading to severe line broadening. Fig. 11a shows an example of a 1D spectrum obtained at 11.75 T from a harvested leaf of an *Arabidopsis thaliana* plant. Only an extremely
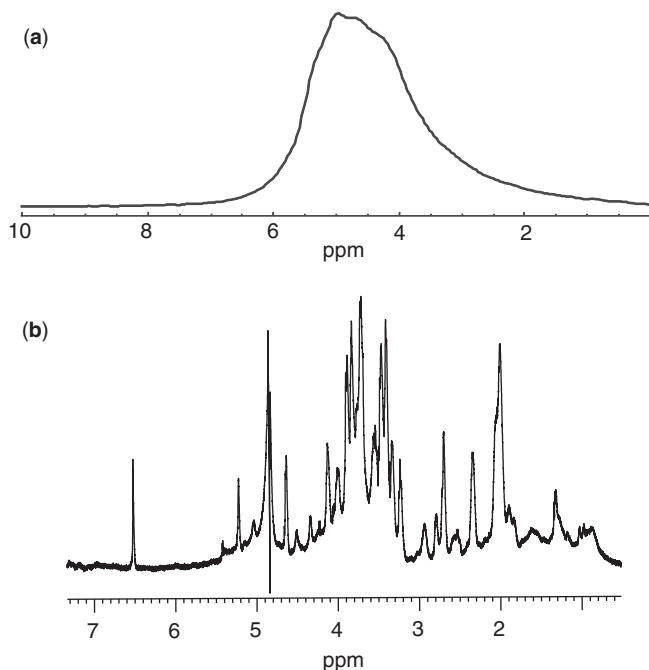
Fig. 11. Resolution enhancement by susceptibility matching in harvested *Arabidopsis thaliana* leaves. (a) ^{1}H spectrum of the untreated leaf acquired at 11.75 T. One strongly broadened water line was observed. (b) ^{1}H spectrum of the intact leaf filled with D_2O. Several resonances of sugars and amino acids were observed. For data acquisition with a 600–MHz high-resolution spectrometer, the leaf was placed in a 5 mm NMR tube; 80 averages were collected.

broadened water resonance is observed, making water suppression an impossible task. No metabolic information can be obtained from this spectrum. After the leaf had been immersed in D_2O and repeatedly exposed to low pressure (20 mbar), air-filled voids were flooded with D_2O. The leaf could be (extremely) carefully rolled up, inserted into a 5 mm NMR tube, and investigated in a high-resolution NMR spectrometer. Fig. 11b shows a corresponding spectrum obtained at 14.1 T. Line width between 10 and 20 Hz were observed, making efficient water suppression by presaturation possible. A number of well-defined resonance lines were observed, which could be attributed to several sugars, amino acids, and other metabolites. Although investigation of a harvested plant is not an *in vivo* experiment, this technique provides a unique possibility of obtaining a metabolic profile of green leaves.

5.5. MAS

Recently the concept of magic angle spinning has been applied to mice *in vivo*.[81,82] In solid-state spectroscopy, spinning the whole sample at kHz frequencies around

an axis that is tilted at the magic angle (54.7°) with respect to the main magnetic field, is a common technique to remove the effects of dipolar couplings.[83] In contrast to liquid-state NMR short-range dipolar interactions are not averaged to zero by diffusion of the molecules and give rise to line widths of hundreds of Hertz. Dipolar interaction between two spins I and S at the positions $\vec{r}_1$ and $\vec{r}_2$, respectively, is given by the Hamiltonian:

$$H = \frac{4\pi}{\mu_0} \frac{\gamma_I \gamma_S \hbar}{|\vec{r}_1 - \vec{r}_2|^3} \frac{3\cos^2\theta - 1}{2} \left(3S_z I_z - \hat{I}\hat{S}\right) \tag{4}$$

θ is the angle between $|\vec{r}_1 - \vec{r}_2|$ and the main magnetic field. Averaging over θ makes the interaction disappear since the integral over the second Legendre polynomial is zero.

In vivo, signal is obtained from spins in the liquid state and line broadening mainly results from field variations due to spatial differences in magnetic susceptibility. If these originate from microscopic sources with isotropic distribution, also in the liquid state, magic angle spinning is capable to reduce line broadening[84–87] and allows for investigation of cell cultures, organs, or mice *in vivo*. Obviously, kHz spinning rates are not suitable for mice and even individual cells are damaged.[85] Application of the pulse sequence PHORMAT (phase corrected magic angle turning) allowed for reduction of spinning rates down to 1 Hz.[87] *In vivo* MAS spectra of mice have been recorded with the localized magic angle turning (LOCMAT) sequence with spinning rates of 4 Hz.[82] LOCMAT provides a voxel-localized 2D spectrum. Fig. 12 shows an example of an *in vivo* spectrum obtained from a $(8\,\text{mm})^3$ voxel in the liver of a mouse (a). In the 2D spectrum, along the directly detected dimension (F2 in Fig. 12b) resonance lines are strongly broadened, as would be observed in the stationary mouse. The corresponding projection does not reveal distinct resonance lines (Fig. 12c). Along the F1 dimension, line broadening is removed by MAS and the projection (Fig. 12d) displays a spectrum with a number of well-resolved lines.

These results demonstrate that MAS is a very promising technique to enhance resolution in *in vivo* MRS. The effect of spinning forces on animal disease model, especially those that received surgery, remains to be investigated.

5.6. Resolution enhancement using the DDF

A completely different approach to resolution enhancement is the use of the DDF to locally refocus magnetization and thus decrease line widths in the spectra. The occurrence of multiple spin echoes as direct manifestations of the DDF were observed for the first time in solid ^{3}He at very low temperature.[88] Later similar observations were made in liquid He[89] and in water at room temperature.[90,91] Warren and co-workers observed additional cross peaks in 2D NMR spectra and developed experiments that exploit the DDF to create spectral patterns.[92,93] The prototype of experiments that exploit the DDF to enhance spectral resolution is the
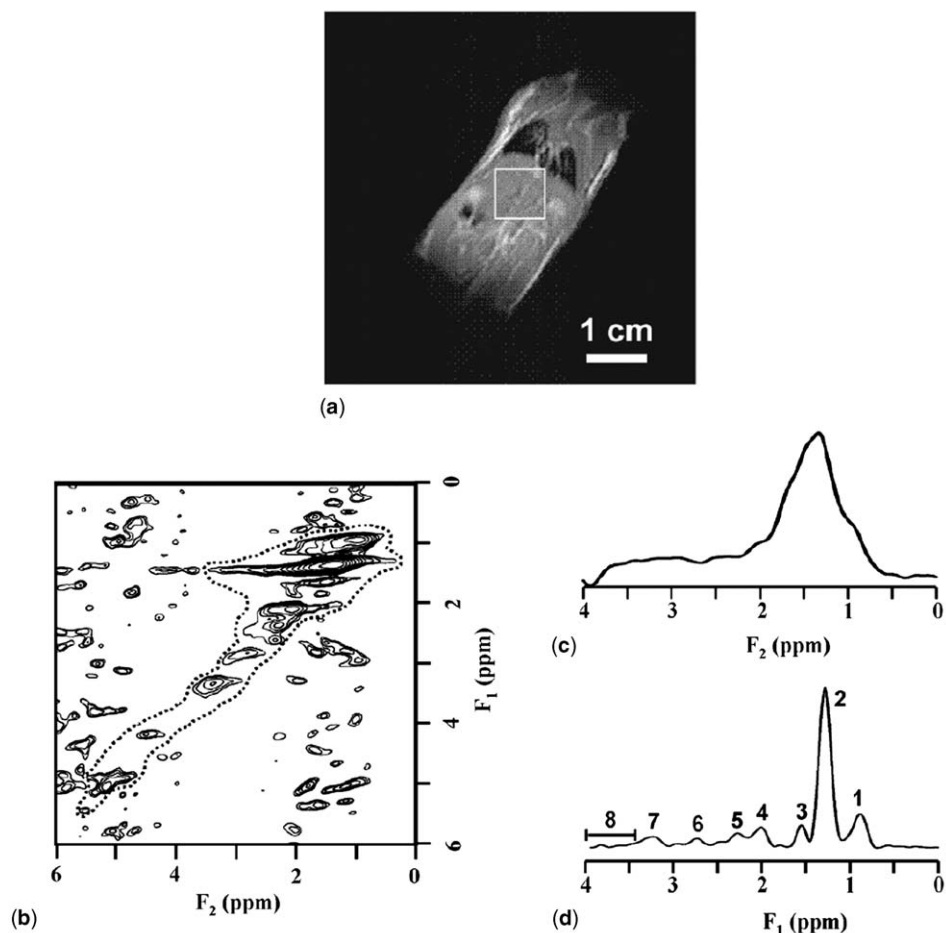
Fig. 12. *In vivo* resolution enhancement by MAS (from Ref. 82 with permission). (a): 85 MHz *in vivo* ^{1}H MR coronal image of the stationary mouse. ((b)–(d)): 85–MHz *in vivo* ^{1}H, 4–Hz LOCMAT spectra of the $8 \times 8 \times 8\, mm^3$ VOI in the liver depicted in image (a). b: 2D spectrum. c: Anisotropic projection. d: Isotropic spectrum. e: Anisotropic spectrum corresponding to the methylene line 2. Resonance assignments: (1) lipids CH_3 terminal; (2) lipids $-CH_2-CH_2-CH_2-$; (3) lipids CH_2CH_2CO; (4) lipids $CH\_CH-CH_2-CH_2$; (5) lipids $-CH_2-CH_2-COO$; (6) lipids $CH\_CH-CH_2-CH\_CH$; (7) choline, betaine methyl; and (8) glucose and glycogen (3.4–3.8 ppm).

HOMOGeneity Enhanced by Intermolecular Zero-quantum Echo Detection (HOMOGENIZED) sequence.[94] The underlying idea is schematically depicted in Fig. 13. We consider again two equally abundant spins I and S that experience the same 1D field profile as in Fig. 8. In the microscopic vicinity, the frequency difference between I and S is not influenced by the field profile, but dominated by the chemical-shift difference $\Delta\omega$ (left panel). DDF experiments are designed to exploit a
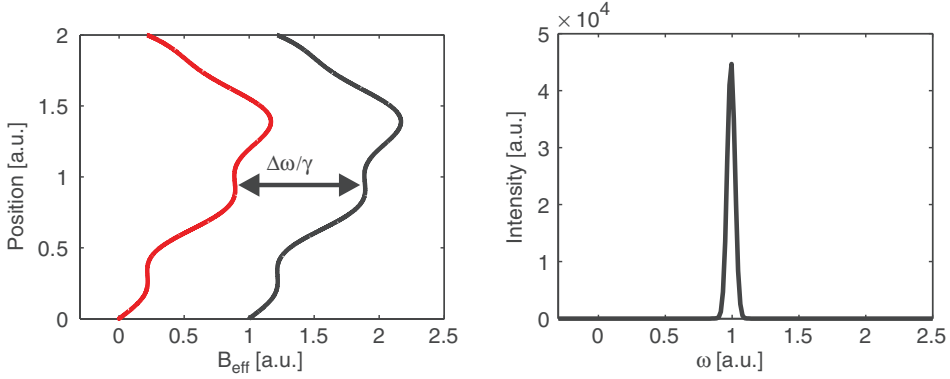
Fig. 13. Resolution enhancement using the DDF, schematically. Two spin species I (red) and S (black) experience a spatially varying magnetic field (left panel). DDF experiments exploit a local net-interaction that depends on $\Delta\omega$. Since $\Delta\omega$ is constant throughout the sample, a narrow line at $\Delta\omega$ in the indirect dimension of a 2D experiment is obtained. The 1D projection along the indirect dimension shows a sharp line (right panel).

local net-interaction between I and S spins. This interaction only depends on $\Delta\omega$ and produces a sharp line in the indirect dimension of a 2D spectrum (projection shown in the right panel). How this can be achieved will be discussed in the following sections.

5.6.1. *Origin of the DDF*

The DDF, also termed "demagnetizing field", describes the magnetic field originating from the sample magnetization (spin polarization). It has long been omitted in the treatment of liquid-state NMR, mainly because of its small amplitude. The common conception is that intermolecular dipolar interactions can be neglected in liquid-state NMR except for a few special cases, for example the NOE. For short distances diffusion leads to spatial averaging of Eq. (4) and defines a lower distance limit for which dipolar interactions have to be considered (Fig. 14a). For larger distances between interacting spins, diffusion only insignificantly alters θ and thus does not make the interaction disappear (Fig. 14b). In high-resolution NMR, samples are normally isotropic and integrating Eq. (4) over all spins in the samples leads to pairwise cancellation of the contributions to the interaction, which is consequently averaged out by isotropy.

The field due to a single dipole $\vec{\mu}$ is given by:

$$\vec{B}^{\text{dip}}(\vec{r}) = \frac{\mu_0}{4\pi}\left(\frac{\vec{\mu}}{r^3} - 3\frac{(\vec{\mu}\cdot\vec{r})\cdot\vec{r}}{r^5}\right) \tag{5}$$

Since under most experimental situations the condition

$$B_0 \gg \frac{\mu_0}{4\pi}\left(\frac{|\vec{\mu}|}{r^3}\right) \tag{6}$$
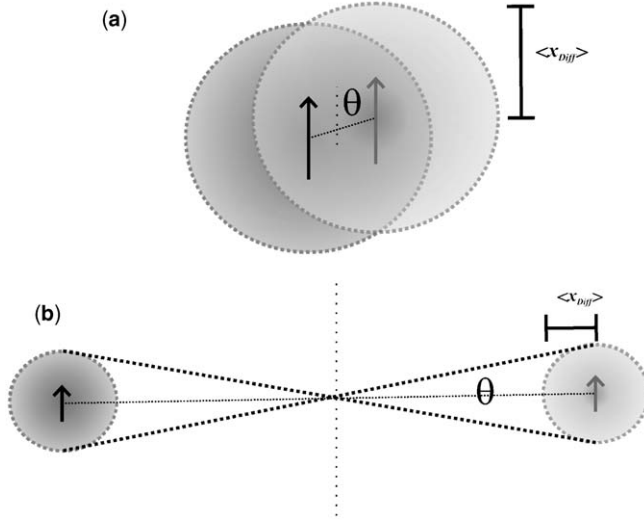
Fig. 14. The impact of diffusion on long-range and short-range dipolar interactions. During the experiment every spin diffuses in a sphere with a radius given by the mean diffusion displacement $\langle x_{\text{Diff}} \rangle$. Dipolar interaction of two spins (arrows) is given by Eq. (4) and depends on θ. (a) For two spins that are separated by less than $\langle x_{\text{Diff}} \rangle$, θ samples all values between $0°$ and $180°$. Consequently, dipolar interaction is averaged out by diffusion. (b) For two spins that are separated by more than $\langle x_{\text{Diff}} \rangle$, θ varies only insignificantly. Dipolar interaction is not averaged out by diffusion. *Note:* (b) is scaled down with respect to (a), $\langle x_{\text{Diff}} \rangle$ is identical in both.

is fulfilled, only the secular part of Eq. (5) contributes to the dipolar field. Precession around B_0 averages out all other components. B^{dip} can be written as

$$\vec{B}^{\text{dip}}(\vec{r}) = \frac{\mu_0}{4\pi} \left(\frac{3\cos^2\theta - 1}{2r^3} \right) (3\mu_z \hat{z} - \vec{\mu}) \tag{7}$$

Recalling that the sum of all dipoles in the sample results in the macroscopic magnetization vector $\vec{M}$,[95] the DDF present in the sample can be written as

$$\vec{B}_{\text{DDF}}(\vec{r}) = \frac{\mu_0}{4\pi} \int d^3r' \frac{1 - 3\cos^2\theta}{2|\vec{r} - \vec{r}'|^3} \left[3M_z(\vec{r}')\hat{z} - \vec{M}(\vec{r}') \right] \tag{8}$$

For an isotropic spherical sample the integral vanishes and there is no DDF. For cylindrical sample geometries, for example, NMR tubes, the DDF has very small, often negligible, values. Edzes calculated and measured frequency shifts of 1 Hz for a cylindrical water sample at 400 MHz.[96] If $\vec{M}$ is a function of $\vec{r}$, the DDF is a nonlocal function and calculation requires integration over the whole sample, which generally is not simple. The situation simplifies considerably when Eq. (8) is

Fourier transformed[47,88]

$$\vec{B}_{\text{DDF}}(\vec{k}) = \frac{1}{3}\mu_0 \frac{3(\hat{k}\cdot\hat{z})^2 - 1}{2}\left[3M_z(\vec{k})\hat{z} - \vec{M}(\vec{k})\right] \tag{9}$$

In Fourier space the DDF is a local function and simply obtained from multiplication of the magnetization term with a spatial weighting function. If, further, M is a 1D function in real space, only Fourier components along direction $\hat{s}$ are relevant. The DDF will be one dimensional in real space.[88]

$$\vec{B}_{\text{DDF}}(s) = \frac{1}{3}\mu_0 \frac{3(\hat{s}\cdot\hat{z})^2 - 1}{2}\left[3M_z(s)\hat{z} - \vec{M}(s)\right] \tag{10}$$

At a magnetic field strength of 17.6 T the z-component of the DDF has a value of 0.44 μT. Spins precess with a frequency of 19 Hz in the DDF. The reciprocal of this (53 ms for pure water at 17.6 T) is defined as the dipolar time constant, also called demagnetizing time

$$\tau_d = \frac{1}{\gamma\mu_0 M_0}. \tag{11}$$

The precondition of the DDF being a 1D function can be realized by application of magnetic field gradients of strength G and duration T. These modulate the transverse magnetization with a spatial frequency $k_m = \gamma GT$. A 90° rf-pulse transforms the modulated magnetization into M_z giving rise to a DDF modulated with $\cos(k_m s)$. The local nature of the DDF can be made plausible with the help of Fig. 15. To calculate the DDF for a general form of $\vec{M}$, the integral in Eq. (8) has to be solved. $\vec{M}$ at every position $\vec{r}'$ contributes to the DDF at position $\vec{r}$, indicated in Fig. 15a. For isotropic $\vec{M}$ there are always two contributions that cancel out pairwise. Fig. 15b shows the situation when $\vec{M}$ is modulated in one dimension, as indicated by the sine curve. Owing to the r^{-3} dependence of dipolar interaction, close to a spin at position s the modulation leads to strong spatial variations that impede a pairwise cancellation over the first modulation period (gray region in the middle of the cylinder). Further distant from position s, the interaction is dominated by the modulation and for every positive contribution in the upper half (white region) a negative one is found in the lower half (black region).

A rigorous treatment summing over all interactions between the spins in the sample has been given for the COSY Revamped with Asymmetric Z-gradient Echo Detection (CRAZED) experiment.[93] For a modulation $\hat{s}\|\hat{z}$ the signal originating from the action of the DDF can be calculated according to

$$S \propto \left|\sum_{j=1}^{N} \frac{3\cos^2\theta_j - 1}{r_j^3}\cos(k_m s_j)\right| \tag{12}$$
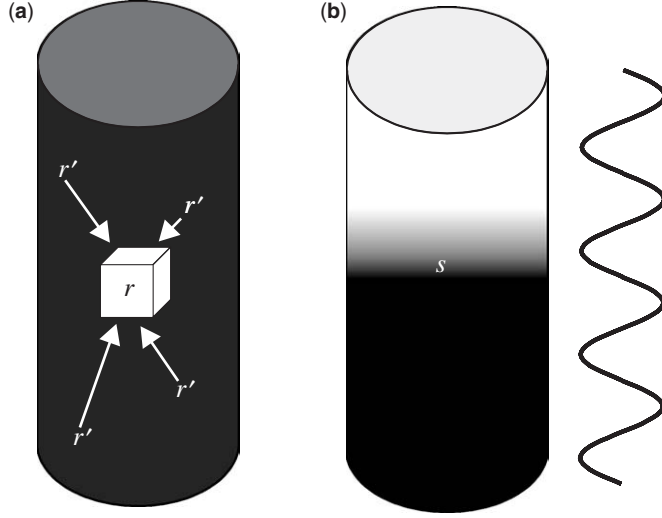
Fig. 15. Local nature of the DDF. (a) In general, $\vec{M}$ at position $\vec{r}$ depends on $\vec{M}$ at all other positions $\vec{r'}$ in a sample (cylinder). To calculate $\vec{M}$ Eq. (8) must be integrated over the sample volume. (b) For a 1D sine modulation of $\vec{M}$ along direction s, the magnetization becomes a local function. Only contributions from roughly the first modulation period contribute significantly to the value of $\vec{M}$ (gray region around s). Contributions from larger distances cancel out pairwise. For every positive contribution (white region) there is a corresponding negative one (black region).

where N is the number of spins in the sample and the sum is calculated for a spin at the origin. If the sample dimensions are large and all variations of the spin density can be neglected, compared to the cosine modulation the sum can be replaced by an integral over the sample volume

$$S \propto \left| \int_v \frac{3\cos^2\theta - 1}{r^3} \cos(k_m s)(r^2 \sin\theta) dr d\theta d\varphi \right| \tag{13}$$

The solution of this integral for $k_m = 100 \, \text{mm}^{-1}$ is shown in Fig. 16. Largest contribution to the signal comes from within a spherical shell between roughly $1/k_m$ and $5/k_m$. For larger distances the contribution quickly vanishes. The minimum of the curve is close to (not at) a distance commonly defined as the correlation distance

$$d_c = \frac{\pi}{k_m} \tag{14}$$

It is a common misconception that the DDF produces signal from one sharply defined distance d_c. As shown in Fig. 16 it is a range of distances from which the signal originates.

However, signal detected with DDF experiments is generated locally, which has been demonstrated experimentally[97–100] and was used to create a new kind of contrast in MRI.[101–105] A method dubbed SOlvent-LOcalized (SOLO) NMR explicitly creates the DDF only in regions with distinct chemical shift of the solvent and thus
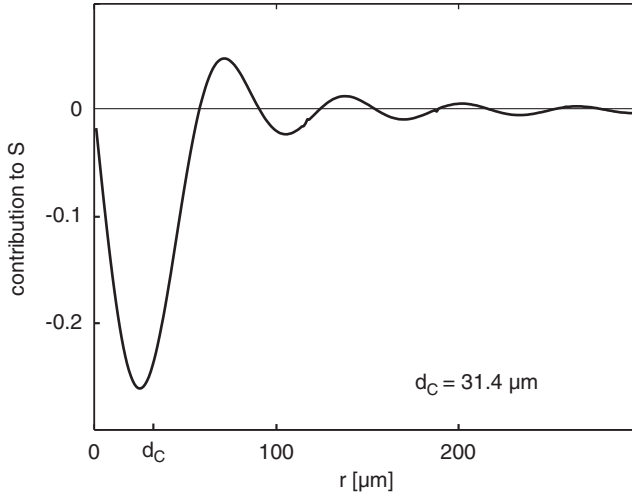
Fig. 16.   Distance dependence of signal contributions from dipolar interactions. The graph shows the solution of Eq. (13) for the center of an infinite sample for $k_m = 100/mm$. Main contribution is obtained from spins with a distance close to d_c. For larger distances the contribution drops to zero. Therefore, the assumption of an infinite sample is valid to a good approximation.

achieves separation of substances in different compartments.[106] The local nature of the DDF explains how the concept depicted in Fig. 13 can be realized. d_c is an experimental parameter that can be chosen as small as ten micrometer (for smaller values, diffusion averages out the modulation). Signal generated from within such small distances is not influenced by long-range field inhomogeneities in the sample and sharp lines can be obtained. This was demonstrated experimentally for homogeneous samples in deshimmed magnetic fields,[94,107,108] in a temporally unstable field of a strongly drifting 1 GHz magnet,[109] and *in vivo*.[110,111] Fig. 17 shows a HOMOGENIZED spectrum of a grape obtained in a strongly deshimmed magnetic field. Along the directly detected dimension peaks are severely broadened. No spectral information can be obtained from the 1D projection. Along the indirect dimension lines are sharp, resulting in a well-resolved 1D projection.

It is important to point out that all of the considerations above rely on the precondition of a 1D modulation of the magnetization. If $\vec{M}$ varies significantly on the length scale of the imposed modulation, calculation of the DDF becomes more complicated. To my knowledge there are no general analytical solutions for signal evolution in DDF experiments. Several studies have addressed the issue of varying magnetization for MRI applications and calculated signal evolution numerically.[112–117]

5.6.2. *Signal formation under the DDF*

In order to understand how signal is generated in DDF experiments, we consider a simple sequence consisting of two rf-pulses with flip angles $90°$ and β, respectively,

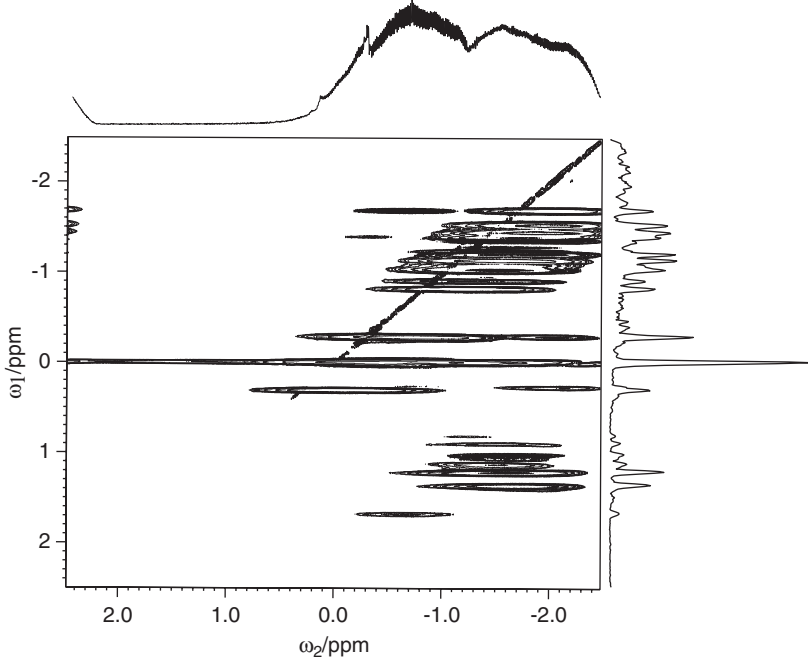**Fig. 17.** Resolution enhancement using the DDF, experimentally. HOMGENIZED spectrum ($\beta = 45°$) of a deshimmed grape acquired at 17.6 T. Along ω_2 lines were severely broadened. Along ω_1 sharp lines were observed. In the 2D spectrum, peaks were aligned along a shifted diagonal parallel to the residual COSY signal.

separated by a delay t_1 during which the magnetization is modulated along by a gradient pulse (correlation gradient, CG) of strength G and duration T (Fig. 18). Evolution of the magnetization is described by the Bloch equations including the contribution of the DDF.

For the moment, we consider only one spin species and neglect relaxation, diffusion, and radiation damping. In the rotating frame, evolution of the magnetization is given by:

$$\frac{d\vec{M}(\vec{r}, t)}{dt} = \gamma \vec{M}(\vec{r}, t) \times [\vec{B}_{DDF}(\vec{r}, t) + \gamma GsT + \Delta\omega t] \tag{15}$$

where $\Delta\omega$ is the frequency offset in the rotating frame. The longitudinal and transverse magnetization directly after the second pulse is

$$\begin{aligned} M_z(0) &= -M_0 \sin\beta \cos(\gamma GTs + \Delta\omega t_1), \\ M^+(0) &= M_0[\cos\beta \cos(\gamma GTs + \Delta\omega t_1) + i \sin(\gamma GTs + \Delta\omega t_1)] \end{aligned} \tag{16}$$

For a sufficiently strong gradient no signal is detected at this time because the total magnetization is zero when integrated over s (Fig. 18). The CG has wound M^+ onto a helix along $\hat{s}$ with a period of $2d_c$ as defined by Eq. (14). d_c represents the distance
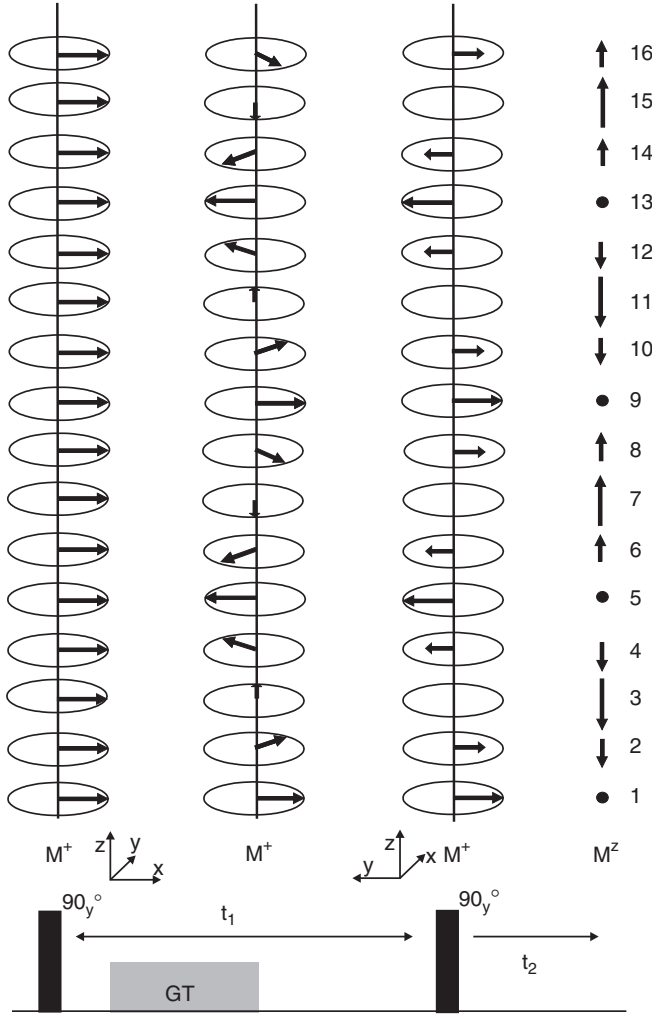
Fig. 18. Pictorial description of DDF experiments for one spin species. The first 90° pulse excites x-magnetization (first stack), which is dephased during t_1 (second stack). The second pulse transforms M_x into M_z (third and fourth stack, respectively; note rotated reference frame). M_y remains in the transverse plane. Positions are numbered for explanations in the text.

at which M^+ is dephased by 180°. Part of M^+ is rotated into M_z by the second rf-pulse and gives rise to the DDF that is described by Eq. (10) if the condition of a 1D modulation along $\hat{s}$ is fulfilled. Both M^+ and M_z are modulated with the same spatial frequency. Due to its local nature the DDF also varies with the same spatial frequency. For $\hat{s}\|\hat{z}$ the effective DDF in Eq. (15) is

$$\vec{B}_{\text{DDF}}(s) = \mu_0 M_z(s)\hat{z} = -\mu_0 M_0 \sin \beta \cos (\gamma G T s + \Delta\omega t_1)\hat{z} \tag{17}$$

Before we solve Eq. (15) analytically, a pictorial explanation will be given of how signal is created by the DDF. First we will discuss the experiment depicted in Fig. 18 with a second pulse $\beta = 90°$, which produces no detectable signal if only one spin species is present. According to Eq. (17) the amplitude of M_z also represents the DDF. M^+ experiences locally different magnetic fields and thus precesses with different frequencies in the rotating frame.[118] Over one modulation period there are always two M^+ vectors that cancel pairwise. These are, for example, vectors at positions 2 and 4, or 6 and 8 in Fig. 18 (right). In each pair both vectors experience the same DDF and therefore rotate in the same direction. Their phase difference of 180° will remain constant and they will cancel out for all future times. After application of the pulse sequence shown in Fig. 18 with two 90° pulses, no DDF signal will be created in a sample containing one spin species only. However, if the second pulse is applied with a flip angle $\beta \neq 90°$ the DDF will refocus part of M^+ and signal will be detected. This has been analyzed theoretically in detail[94,119] but is difficult to depict.

The analytical solution of Eq. (15) shows this behavior. During the interval t_2 following the second pulse, M^+ evolves under the influence of B_{DDF}, so that

$$
\begin{aligned}
M_z(t_2) &= M_z(0), \\
M^+(t_2) &= M^+(0)\, e^{i\Delta\omega t_2}\, e^{-i\gamma\mu_0 M_0 t_2\, \sin\beta\, \cos(\gamma GTs + \Delta\omega t_1)}.
\end{aligned} \tag{18}
$$

The second exponential in M^+ is a complicated function, which can be simplified by expanding it in Bessel functions J_m using the Jacobi–Anger expansion

$$
e^{i\xi\cos\varphi} = \sum_{m=-\infty}^{\infty} i^m J_m(\xi) e^{im\varphi} \tag{19}
$$

Noting that Eq. (16) can be written as

$$
M^+(0) = \frac{1}{2} M_0 [(\cos\beta + 1)e^{i(\gamma GTs + \Delta\omega t_1)} + (\cos\beta - 1)e^{-i(\gamma GTs + \Delta\omega t_1)}]
$$

it follows

$$
\begin{aligned}
M^+(t_2) = &\left\{ \frac{1}{2} M_0\, e^{i\Delta\omega t_2} \left[(\cos\beta + 1)\, e^{i(\gamma GTs + \Delta\omega t_1)} + (\cos\beta - 1)\, e^{-i(\gamma GTs + \Delta\omega t_1)} \right] \right\} \\
&\times \sum_{m=-\infty}^{\infty} i^m J_m\left(-\sin\beta\, \frac{t_2}{\tau_d} \right) e^{im(\gamma GTs + \Delta\omega t_1)}
\end{aligned} \tag{20}
$$

All terms with a phase factor $e^{in(\gamma GTs)}$ with $n \neq 0$ are effectively cancelled out by spatial averaging. Only for values of $m = -1$ and $m = 1$ in the sum, the phase factor is eliminated in the first and the second term in brackets, respectively. The detectable signal can thus be written

$$
M^+(t_2) = \frac{1}{2} M_0\, e^{i\Delta\omega t_2} \left[(\cos\beta + 1)i^{-1} J_{-1}\left(-\sin\beta\, \frac{t_2}{\tau_d} \right) + (\cos\beta - 1)iJ_1\left(-\sin\beta\, \frac{t_2}{\tau_d} \right) \right] \tag{21}
$$

and with $J_1(\xi) = -J_{-1}(\xi)$

$$M^+(t_2) = iM_0 e^{i\Delta\omega t_2} \cos\beta \, J_1\left(-\sin\beta \frac{t_2}{\tau_d}\right) \tag{22}$$

For a flip angle $\beta = 90°$ the signal vanishes, as has been seen in Fig. 18. For other flip angles there is a residual x-component of the magnetization, which is refocused by the action of the DDF. Maximum signal is obtained for $\beta = 45°$.[94,119,120] Detectable signal builds up with a time constant τ_d according to a first-order Bessel function and can be detected as a non-linear spin echo. It is noted here that similar consideration apply for stimulated echos that have been dubbed NOn-linear Stimulated Echos (NOSE).[121–123]

In order to give a pictorial description of how signal is created by the DDF we consider a sample with two spin species I and S. To simplify the situation, we assume that the second pulse is applied frequency selectively with $\beta = 90°$ acting only on the I spins. Fig. 19 illustrates the pulse sequence and the magnetization vectors. Up to the second pulse both spin species behave identically (different Larmor precession has been neglected). The second pulse transforms part of M^{I+} into M_z^I. M^{S+} remains unaffected. For the I spins the above considerations for the one spin case are valid. No signal will be created. The effective DDF experienced by the S spins comes from M_z^I and is given by Refs. 119,124–126.

$$\vec{B}_{DDF}^S(s) = \mu_0 \frac{2}{3} M_z^I(s)\hat{z} = -\mu_0 \frac{2}{3} M_0^I \cos(\gamma GTs + \Delta\omega_I t_1)\hat{z} \tag{23}$$

In contrast to M^{I+}, M^{S+} also has x-components and therefore two spins that cancel out pairwise come from different position. In Fig. 19 these are, for example, positions 2 and 6, or 3 and 7, or 4 and 8. In each pair the spins experience a DDF of opposite sign and will therefore rotate in opposite directions. Part of the magnetization eventually refocuses. For example the vectors at position 2 and 3 will precess clockwise, while vectors at 7 and 8 will precess counter-clockwise. Due to the varying amplitude of the DDF these four vectors eventually refocus along the y-axis, forming the nonlinear spin echo.

The solution of Eq. (15) is similar to the one spin case. M^I and M^S have to be treated separately. The DDF is given by Eqs. (17) and (23) for the I and the S spins, respectively. The transverse magnetization at the beginning of t_2 is unchanged for the I spins

$$M^{I+}(t_2) = M_0[\cos\beta \cos(\gamma GTs + \Delta\omega_I t_1) + i \sin(\gamma GTs + \Delta\omega_I t_1)] \, e^{i\Delta\omega_I t_2} \, e^{-i\gamma B_{DDF}^I} \tag{24}$$

and for the S spins

$$M^{S+}(t_2) = M_0^S e^{i(\gamma GTs + \Delta\omega_S t_1)} e^{i\Delta\omega_S t_2} e^{-i\gamma B_{DDF}^S} \tag{25}$$

The last exponential can again be expanded into Bessel functions and after spatial averaging the only remaining contribution is

$$M^+(t_2) = iM_0^S e^{i\Delta\omega_S t_2} e^{i(\Delta\omega_S - \Delta\omega_I)t_1} J_1\left(-\frac{2}{3}\frac{t_2}{\tau_{dI}}\right) \tag{26}$$
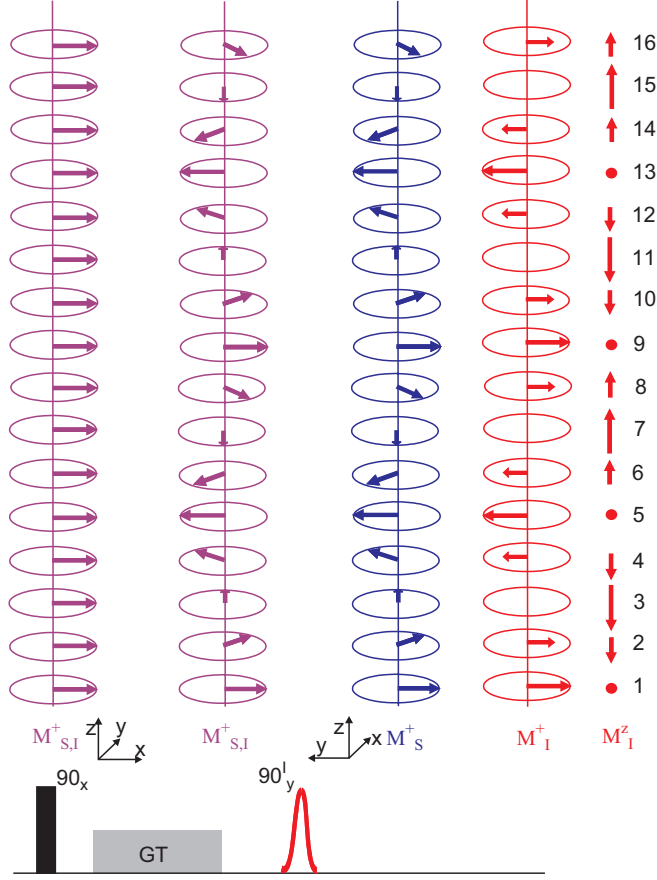
Fig. 19. Pictorial description of DDF experiments for two spin species. The first 90° pulse excites x-magnetization of both species, I (red) and S (blue) (first stack, purple for both species), which is dephased during t_1 (second stack). The second pulse transforms M_x^I into M_z^I (fifth stack, note rotated reference frame). M_y^I (fourth stack) and M^{S+} (third stack) remain in the transverse plane. Positions are numbered for explanations in the text.

where

$$\tau_{dI} = \frac{1}{\gamma \mu_0 M_0^I}$$

Again, detectable signal builds up with a time constant τ_{dI} according to a first-order Bessel function. Eq. (26) has important experimental implications. If a 2D experiment is performed incrementing t_1 and detecting the signal during t_2, a spectrum is obtained with one cross peak at $(\Delta\omega_S - \Delta\omega_I, \Delta\omega_S)$. Signal is created by refocusing through the action of the DDF, which is a local process. Along the indirectly detected dimension the signal is therefore not broadened by long-range field inhomogeneities.

Eq. (15) can also be solved analytically for application of the pulse sequence depicted in Fig. 18 on a two-spin system.[119] Solution is a little more involved and
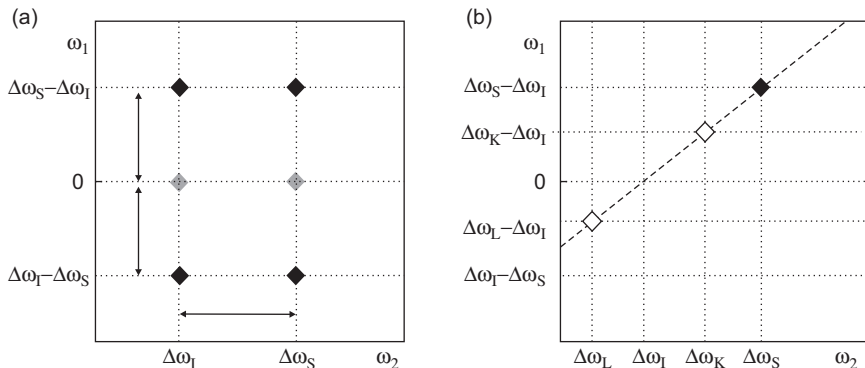
Fig. 20. Spectral patterns in DDF experiments. (a) In the HOMOGENIZED spectrum of a two-component sample (spin species I and S with resonance frequencies $\Delta\omega_I$ and $\Delta\omega_S$, respectively), six peaks (diamonds) are detected at $\Delta\omega_I$ and $\Delta\omega_S$ along ω_2 and at zero and both difference frequencies along ω_1. The relative peak intensities depend on the flip angle β. For $\beta = 90°$ no peaks are detected at $\omega_1 = 0$ (gray diamonds). (b) With a second pulse selectively acting on the solvent spins (I), only one peak (full diamond) with increased intensity (see text) is observed. For dilute multicomponent samples with a dominant solvent spin species, all solute peaks are aligned along a diagonal (empty diamonds).

shows that in a 2D spectrum six or four peaks are detected for $\beta \neq 90°$ or $\beta = 90°$, respectively (Fig. 20a). *In vivo*, water provides one dominant spin species. In most experiments it is sufficient to consider only the DDF contributed by the water spins. Metabolite resonances are, therefore, observed along ω_1 at their difference frequencies to the water resonance (positive and negative), forming two diagonals. Proper choice of β (for example, $\beta = 45°$) can enhance one of the diagonals[119] (see Fig. 17). To avoid overlap with residual COSY signal, the water resonance is often detected slightly off resonance (see Fig. 17).

5.6.3. *DDF experiments*

Experimental implementations of DDF experiments use an additional 180° pulse following the second rf-pulse. Since τ_{dI} is of the order of 100 ms (53 ms for pure water at 17.6 T, 100 ms at 9.4 T) signal is normally acquired as spin echo, allowing the signal to build up while minimizing T_2^* relaxation. The pulse sequence shown in Fig. 18 with $\beta = 45°$ and an additional 180° pulse is the original HOMOGENIZED sequence.[94] The sequence shown in Fig. 19 is the basic element of the SEL-HOMOGENIZED class of experiments.[108,127] These have several advantages compared to the original experiment:

1. $\beta = 90°$ maximizes the DDF, which leads to a faster signal build up than with other flip angles. Relaxation losses can be minimized.
2. Only one peak is detected in the spectrum of a two-component system. For more complex samples this makes the spectra easier to analyze.

3. The intensity of the cross peak at $\Delta\omega_S - \Delta\omega_I$ is doubled compared to an experiment with a nonselective pulse $\beta = 90°$.
4. $\beta = 90°$ avoids signal from like spins which acts as an intrinsic water suppression.

To understand advantages 2–4 a different theoretical description is more suitable. This will be discussed in the following section.

5.6.4. *The quantum mechanical description*

The analytical solution of the Bloch equation using classical electro-dynamics and magnetization vectors is adequate to describe simple experiments, as was the case above. Further, it is very useful in providing a physical explanation of the local nature of this phenomenon and also provides equations to quantitatively describe the outcome of experiments. However, as soon as the experimental situation becomes a little more complex, analytical solutions may become difficult and one gets easily lost in collecting phase factors (see Eq. (20)). Warren first noted that the product operator formalism commonly used in protein NMR is also valid for experiments exploiting the DDF.[93] It was shown that dipolar interactions given by Eq. (4) have to be considered explicitly if the isotropy in the sample is broken, for example by application of a magnetic field gradient.[128,129] Dipolar couplings create significant signal contributions from second-order terms in the density matrix[130]

$$\sigma_0 \approx 1 - \frac{\hbar\omega}{kT}\sum_i^N I_{zi} + \frac{1}{2}\left(\frac{\hbar\omega}{kT}\right)^2 \sum_{i,j}^N I_{zi}I_{zj} + \cdots, \qquad (27)$$

which are normally neglected by the high temperature approximation. These higher-order terms correspond to multiple-quantum coherences, which explains the commonly used acronyms iZQC, iDQC, and iMQC for intermolecular zero-, double-, and multiple-quantum coherence, respectively. The quantum description has caused some controversy in the literature,[118,131–135] but in the meanwhile it is generally acknowledged that it also provides an appropriate description of the underlying physics.[136] The formalism has been used to describe iDQC[93] and iZQC[94] experiments, to describe heteronuclear iMQC,[137] to investigate the boundary between liquidlike and solidlike behavior in NMR[138] and to investigate different coherence orders.[139–145] There are two tutorial reviews explaining the basic principles.[146,147]

Although the quantum description does not allow for quantitative analysis of experiments, it is extremely powerful and simple to apply for predicting cross peaks in 2D experiments. The basic idea is that all first-order terms in the density matrix are averaged out by the CG or an unmatched pair of CGs and only iZQCs or other iMQC survive, respectively. Applying the conventions for following evolution of product operators,[148] the experiment shown in Fig. 18 can be analyzed as follows. Interaction between like spin gives rise to peaks at $\omega_1 = 0$ in the indirect dimension and is described by the operators I^+I^- and S^+S^-. Interaction between I and S gives rise to peaks at $\Delta\omega_I - \Delta\omega_S$ and $\Delta\omega_I - \Delta\omega_S$ in the indirect dimension described by

the operators S^+I^- and S^-I^+, respectively.

$$I^+I^- \equiv (I_xI_x + iI_yI_x - iI_xI_y + I_yI_y) \xrightarrow{(\pi/2)_y} 2(I_zI_z + I_yI_y) = \text{unobservable} \quad (28)$$

$$S^+I^- \equiv (S_xI_x + iS_yI_x - iS_xI_y + S_yI_y) \xrightarrow{(\pi/2)_y^{I,S}} 2(S_zI_y - S_yI_z)$$
$$\xrightarrow{\text{dipolar coupling}} i(I_x - S_x) \equiv \tfrac{i}{2}\big[(I^+ + I^-) - (S^+ + S^-)\big] \quad (29)$$

$$S^-I^+ \equiv (S_xI_x - iS_yI_x + iS_xI_y + S_yI_y) \xrightarrow{(\pi/2)_y^{I,S}} -2(S_zI_y - S_yI_z)$$
$$\xrightarrow{\text{dipolar coupling}} -i(I_x - S_x) \equiv -\tfrac{i}{2}\big[(I^+ + I^-) - (S^+ + S^-)\big] \quad (30)$$

Unobservable terms have been omitted in Eqs. (29) and (30). This simple analysis shows, without longish calculations, that only four peaks will be detected at the frequencies indicated in Fig. 20.

For the SEL-HOMOGENIZED class of experiments (Fig. 19) the calculation for like spins is identical and for unlike spins

$$S^+I^- \equiv (S_xI_x + iS_yI_x - iS_xI_y + S_yI_y)$$
$$\xrightarrow{(\pi/2)_y^{I}} 2(iS_xI_z - S_yI_z) \xrightarrow{\text{dipolar coupling}} (S_y - iS_x) \equiv -iS^+ \quad (31)$$

$$S^-I^+ \equiv (S_xI_x - iS_yI_x + iS_xI_y + S_yI_y) \xrightarrow{(\pi/2)_y^{I}} 2(iS_xI_z + S_yI_z) \xrightarrow{\text{dipolar coupling}} (S_y + iS_x)$$
$$\equiv iS^- \quad (32)$$

Again unobservable terms have been omitted. Signal is only detected at $\omega_2 = \Delta\omega_S$, explaining the mechanism of the intrinsic water suppression. If quadrature detection is used, only Eq. (31) results in observable signal, as indicated in (Fig. 20b). Finally, the factor 1/2 present in Eqs. (29) and (30) is not obtained in Eqs. (31) and (32), explaining the doubled intensity in experiments with selective pulses.

5.6.5. *Signal evolution in the real experiment*

For the *in vivo* application of DDF experiments several other mechanisms influencing the signal have to be considered. These are relaxation, diffusion, J-coupling, and radiation damping. Radiation damping is an important issue in high-resolution NMR and can, also in MRI, be used to create turbulent spin dynamics. In joint action with the DDF it may lead to unwanted effects[149–159] which, on the other hand, can be exploited to enhance image contrast.[117] However, in most *in vivo* MRS applications radiation damping can be neglected because large rf-resonators with moderate Q-values are used. Scalar coupling can be incorporated in the quantum description or treated by computer simulations.[160–165] In HOMOGENIZED spectra scalar coupling leads to additional correlation peaks similar to those observed in COSY.

Relaxation and diffusion are more difficult to handle. Transverse relaxation reduces the amount of M^+ that can be refocused, similar to conventional spin-echo experiments. Longitudinal relaxation dissipates M_z and therefore reduces the DDF,

attenuating the refocusing process. Diffusion causes a blurring of the imposed modulation and thus causes signal evolution to deviate from Eq. (26) at long evolution times.[166,167] In the classical formalism, both can be included in the Bloch Eq. (15). However, a general solution has not been presented so far. For a one-component system diffusion has been treated neglecting relaxation,[120] or making simplifying assumptions.[168–170] The quantitative effects of relaxation on the DDF signal have been explored theoretically and experimentally.[171,172] Under the approximation that diffusion and dipolar effects are independent from each other and act on different time scales (usually diffusion is assumed to act on a millisecond time scale while the DDF acts on a time scale of seconds) a solution has been presented that is valid under most experimental conditions.[133,166,173] Recently it was shown that diffusion constant and T_2 can be determined simultaneously with DDF experiments.[174]

For two-component systems there is no general solution available.[175,176] Approximate solutions are possible, if the DDF is dominated by only one component, as is the case in highly dilute samples or for experiments of the SEL-HOMOGENIZED class.[177–179] In vivo, water spins are the dominant component determining the DDF. Mutual interactions (apart from scalar coupling) between metabolite spin species can be neglected. Therefore, every not J-coupled metabolite resonance can be described by a two-component model. If relaxation is considered but diffusion and radiation damping neglected, signal evolution is described in analogy to Eq. (26) by

$$M^{S+} = iM_0^S \exp(i\Delta\omega_S t_2) \exp(i(\Delta\omega_S - \Delta\omega_I)t_1) \exp\left(-\frac{t_1 + t_2}{T_2^S}\right) J_1(\Lambda_I) \qquad (33)$$

with

$$\Lambda_I = -\frac{2}{3}\sin\beta \exp\left(-\frac{t_1}{T_2^I}\right)\left[1 - \exp\left(-\frac{t_2}{T_1^I}\right)\right]\frac{T_1}{\tau_{dI}} \qquad (34)$$

where $T_{1,2}^{I,S}$ are longitudinal and transverse relaxation times of spins I and S, respectively. Fig. 21 graphs Eq. (33) for T_2 values for the S spins of 250 ms (solid curve) and 150 ms (dashed curve). Signal builds up quickly and reaches a maximum near T_2 before magnetization decays. Without relaxation up to 58% of M_0 can be refocused by DDF experiments. In vivo at high magnetic fields, magnetization decays due to T_2 relaxation before the maximum is reached and only about 20%–30% of M_0 are refocused. Shorter T_2 has an even more dramatic effect on the amount of magnetization that is refocused. The parameters used in Fig. 21 reflect values in an in vivo experiment in a small animal at 17.6 T, demonstrating that significant signal can be produced. Signal evolution is first dominated by a steep rise given by the strength of the DDF that depends on $1/\tau_{dI}$ and thus on M_0^I. For short t_2 the Bessel function can be approximated by $J_1(\xi) \approx (\xi/2)$ making the detectable signal depend on the product $M_0^I M_0^S$. Higher magnetic fields cause a faster rise, explaining why DDF experiments benefit more from higher B_0 than conventional MRS. However, higher B_0 often means shorter T_2 which reduces the detectable signal. Further attenuation of the DDF is caused by solvent T_1 relaxation during t_2 and solvent T_2 relaxation during t_1. T_1 increases with higher B_0 partly compensating losses caused by shorter
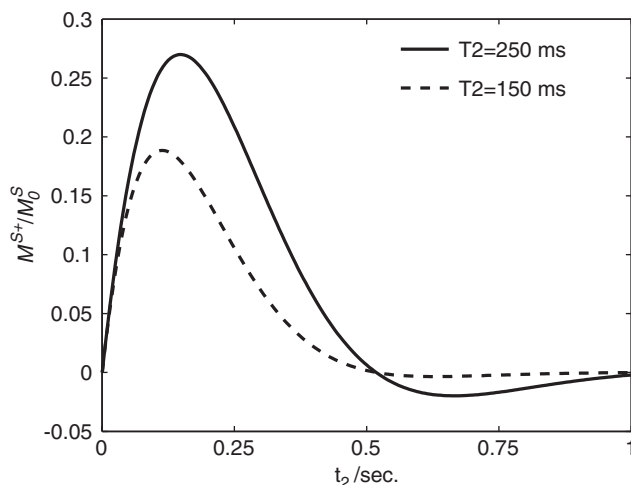
Fig. 21. Signal build-up in the SEL-HOMOGENIZED experiment. Observable signal M^{S+} as fraction of M_0^S according to Eq. (33). Parameters were chosen to simulate *in vivo* conditions at 17.6 T. $t_1 = 5$ ms, $\tau_{DI} = 65$ ms, $\beta = 90°$, $T_1^I = 1.5$ s, $T_2^I = 25$ ms, $T_2^S = 250$ ms (solid line), $T_2^S = 150$ ms (dashed line). The amount of signal that is refocused depends strongly on T_2^S.

T_2. For most applications DDF spectroscopy strongly benefits from high magnetic fields.

5.6.6. *Solvent suppression and localization*

Further requirements for *in vivo* application of DDF techniques are efficient water suppression and signal localization. Making use of a selective second pulse alone does not provide sufficient suppression of the water signal.[127] Methods that can be applied to improve suppression must not influence the DDF because this would also suppress signal build-up. Therefore, presaturation of the solvent signal or selective excitation of the metabolites is not possible. Both result in the elimination of transverse solvent magnetization prior to the second pulse. No DDF will be created and, consequently, no signal will be refocused. A suitable method to suppress residual solvent signal is selective refocusing prior to acquisition, which provides very efficient suppression if applied repeatedly.[108,127]

In order to localize the DDF signal, three schemes are possible (Fig. 22). The first *in vivo* localization of DDF spectra was achieved with the schemes of Fig. 22a and b. However, in that study only water signal was analyzed and no further spectral information extracted.[180] Localization prior to the DDF sequence (Fig. 22a) or incorporation into the DDF sequence (Fig. 22b), for example, by three slice selective 180°-pulses during t_1 relies on spoiling magnetization in unwanted regions. Since both strategies spoil prior to the second pulse that creates the DDF, part of the spoiled magnetization will be refocused by the DDF and localization will be not very efficient.[181] Best localization can be achieved if volume selection is performed
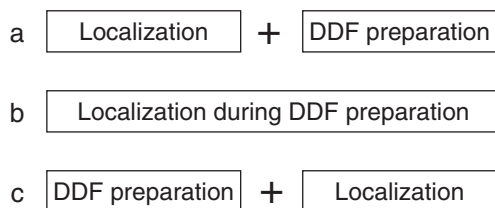
a	Localization	+	DDF preparation

b	Localization during DDF preparation

c	DDF preparation	+	Localization

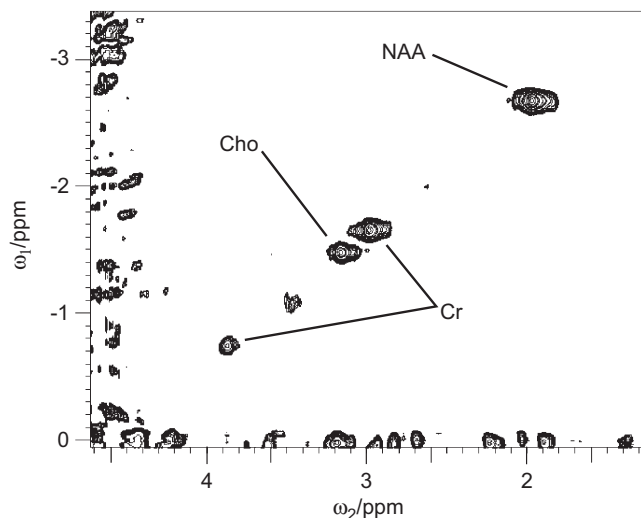**Fig. 22.**   Possible localization schemes for DDF spectroscopy experiments.

Fig. 23.   Localized *in vivo* SEL-HOMOGENIZED spectrum from the rat brain. Three major brain metabolites NAA, Cho, and Cr were observed with well-resolved lines. The spectrum was acquired at 17.6 T with a surface coil. Localization to an $(8\,mm)^3$ voxel was achieved with a sequence following the scheme depicted in (Fig. 22c); a selective HOMOGENIZED sequence was followed by a LASER localization combined with solvent suppression.[181] Further parameters were: TR = 5 s, TE = 180 ms, 128 t_1-increments, CG = 10 G ms cm^{-1}, 2 averages.

immediately prior to acquisition with a PRESS or LASER scheme.[181–183] Fig. 23 shows a localized DDF spectrum obtained with selective DDF excitation and LASER localization prior to acquisition.

5.6.7. *Improved DDF sequences*

Similar to the HOMOGENIZED-like experiments, DDF signal can also be created with a pair of gradients flanking the second pulse. The gradients act as a double-quantum filter and thus produce iDCQ spectra. Methods detecting iDQC signal have been dubbed IDEAL (Intermolecular Dipolar interaction Enhanced All Lines) and also produce narrow lines in inhomogeneous fields due to the local nature of the

DDF.[107] IDEAL is also a 2D experiment and for solvent suppression similar considerations apply as for HOMOGENIZED. Improved versions called IDEAL-II and IDEAL-III have been presented.[184,185] Both require a smaller number of t_1-increments and thus allow for faster data acquisition which is often an important issue *in vivo*. IDEAL-II furthermore enhances splitting due to scalar coupling and thus might be suitable for determining coupling constants *in vivo*.

A different approach to accelerate data acquisition has been presented as ultrafast iZQC spectroscopy.[111] Similar to the Frydman-approach in conventional NMR spectroscopy[186] different portions of the magnetization experience different t_1-intervals. Following one excitation a number of t_1 steps are acquired, significantly accelerating the experiment. In contrast to the Frydman-method, different portions of the magnetization are not separated spatially but excited separately with a small flip angle pulses. The drawback of ultrafast iZQC spectroscopy is that the often sparse SNR is further reduced by dividing the magnetization in several portions. It still remains to be shown that the increased acquisition speed makes up for the reduced signal.

5.6.8. *Where are the limits?*

In vivo application of DDF spectroscopy has been demonstrated in rodent brains,[110,181] worms,[111] and xenograft tumors in nude mice.[181] While the rodent brain can be considered as homogeneous, tumors with necrotic regions and worms produce considerable field distortions. DDF spectroscopy has proven to be capable of coping with this degree of inhomogeneities. Theoretical description as given by Eq. (33) only holds if Eq. (10) is valid, which implies a 1D modulation of the magnetic field. The intrinsic field distortions in the organisms derogate this precondition to some extent. Therefore, theoretical analysis is not fully valid. To which extent signal deviates or which exact degree of inhomogeneities makes DDF spectroscopy impossible has not been analyzed in sufficient detail to date. However, several cases can be deduced from the data available.

1. Field distortions occur with similar spatial frequency and intensity as the imposed modulation: The above theoretical analysis is not valid. Signal evolution will be dominated by the exact form of perturbations. DDF spectroscopy is likely not to produce useful results.
2. Field distortions are distributed over the volume of interest, but small in amplitude compared to the imposed modulation: This may be close to the situation in worms. DDF spectroscopy can be expected to produce results close to the theoretical predictions.
3. Distortions of large amplitude are spatially separated by several d_c: Close to the perturbers field distortions dominate and no DDF signal is refocused. In between the perturbers, homogeneous regions are large enough to fulfill the condition of a 1D modulation. DDF signal is refocused in these regions. This is illustrated in Fig. 24 for the example of a rat brain. Without localization a spectrum from the brain is obtained. Inside the brain the DDF refocuses magnetization of the metabolite spins. Outside the brain the DDF is spoiled by field distortions. A further example of a gel phantom is shown in Fig. 25.
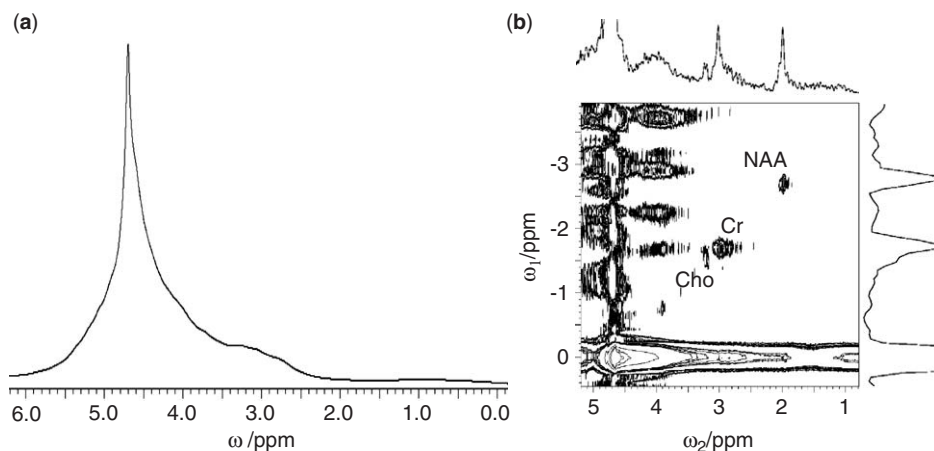
Fig. 24. Signal refocusing in large homogeneous tissue regions: intrinsic localization and solvent suppression in the HOMOGENIZED experiment. (a) Global 17.6 T *in vivo* 1D spectrum of the head of a female Fisher rat positioned in the center of a 38–mm rf-resonator. Only the strongly broadened water line was observed. (b) Global HOMOGENIZED spectrum without water suppression. The local nature of the DDF refocuses signal only in homogeneous regions, which are mainly inside the brain. Thus, a resolved spectrum of brain metabolites was obtained. In ω_2 the residual water signal was set to 4.7 ppm. For the 1D projections, the spectrum was summed over the upper right quarter excluding residual water signal. Only 64 t_1 increments were acquired resulting in broad lines observed along ω_1. For further experimental details, see Ref. 110.
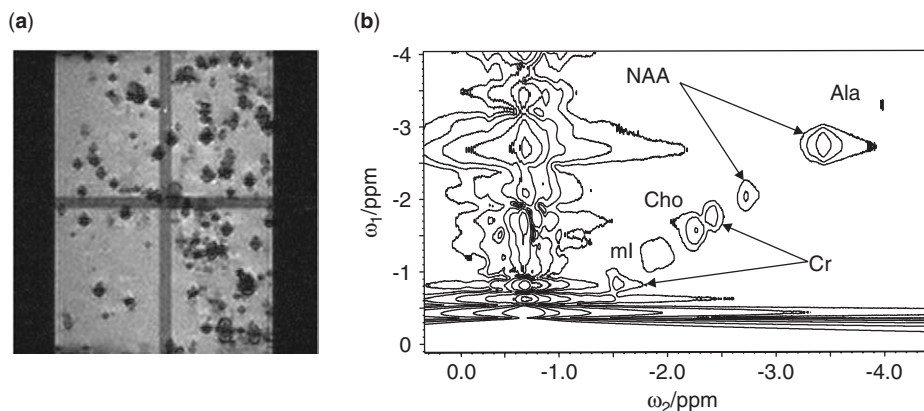
Fig. 25. Signal refocusing with numerous strong field distortions. (a) Gradient echo image of the gel phantom with air bubbles. Major brain metabolites were contained at their typical *in vivo* concentrations:[187] 10 mM NAA, 2.5 mM Cho, 10 mM Cr, 15 mM glutamate, 8 mM inositol, 1.4 mM alanine, 2 mM GABA, and 1.4 mM Asp. (b) HOMOGENIZED spectrum without water suppression. Five metabolites were observed in the spectrum. Homogeneous regions between the air bubbles were sufficiently large to allow refocusing through the DDF.

Air bubbles in the phantom cause strong field distortion. These are at suffi-
cient distance to leave homogeneous regions in which the DDF refocuses
metabolite signal.

In order to allow for a general classification of objects regarding their field ho-
mogeneity and their suitability for DDF spectroscopy, further numerical and ex-
perimental studies are required. DDF spectroscopy has great potential, in
particular, for metabolite quantification from whole organs or tumors. Recently
it could be shown that DDF spectra can be acquired from significantly larger voxels
than PRESS spectra in xenograft tumors. The larger volume compensated the lower
signal intensity and produced superior SNR per time compared to PRESS.[181]

6. CONCLUSION

Spatial, temporal, and spectral resolution are the prerequisites for successful *in vivo*
MRS. Spatial resolution is achieved by voxel localization techniques or CSI, al-
lowing for spatial resolution of centimeters in humans, millimeters in small animals,
and down to 180 µm in single cells. Temporal resolution is strongly dependent on
the overall experimental setup but normally not the critical parameter in questions
addressed with MRS. Spectral resolution is pivotal for obtaining metabolic infor-
mation. For conventional MRS techniques extremely homogeneous magnetic fields
in the volume of interest are required. These can be realized efficiently in homo-
geneous volumes with localized shimming routines. If the voxel is subject to field
distortions, field homogeneity remains poor and different strategies to obtain re-
solved spectra have to be applied. Susceptibility matching allows for reducing field
distortions in special applications. If undistorted fields are not possible, 2D spectra
may provide resolution of smaller frequency intervals than the line widths in the
spectra. Finally, dipolar interactions can be used to enhance spectral resolution.
MAS actively averages out angle dependencies of line broadening mechanism and
thus can produce resolved spectra. DDF spectroscopy uses local refocusing of
magnetization to avoid line broadening due to field distortions. The feasibility of
MAS and DDF spectroscopy *in vivo* has been proven. With whole tumor char-
acterization a potential application has been demonstrated for DDF techniques.
Fast DDF methods and novel pulse sequences promise to extend the range of
applications in the future.

ACKNOWLEDGEMENTS

REFERENCES

1. R. Kreis, Quantitative localized H-1 MR spectroscopy for clinical use, *Prog. Nucl. Magn. Reson. Spectrosc.*, 1997, **31**, 155–195.
2. R. A. de Graaf, *In Vivo NMR Spectroscopy*, John Wiley and Sons Ltd., Chichester, 1998.
3. B. Ross and S. Bluml, Magnetic resonance spectroscopy of the human brain, *Anatomical Record*, 2001, **265**, 54–84.
4. W. Chen and X. H. Zhu, Dynamic study of cerebral bioenergetics and brain function using *in vivo* multinuclear MRS approaches, *Concepts Magn. Reson. Part A*, 2005, **27A**, 84–121.
5. X. H. Zhu, N. Y. Zhang, Y. Zhang, X. L. Zhang, K. Ugurbil and W. Chen, *In vivo* O-17 NMR approaches for brain study at high field, *NMR Biomed.*, 2005, **18**, 83–103.
6. H. J. Berendse and H. T. Edzes, Observation and general interpretation of sodium magnetic-resonance in biological-material, *Ann. NY Acad. Sci.*, 1973, **204**, 459–485.
7. S. K. Hilal, A. A. Maudsley, H. E. Simon, W. H. Perman, J. Bonn, M. E. Mawad, A. J. Silver, S. R. Ganti, P. Sane and I. C. Chien, *In vivo* NMR imaging of tissue sodium in the intact cat before and after acute cerebral stroke, *Am J. Neuroradiol.*, 1983, **4**, 245–249.
8. N. Beckmann, I. Turkalj, J. Seelig and U. Keller, C-13 NMR for the assessment of human brain glucose-metabolism *in vivo*, *Biochemistry*, 1991, **30**, 6362–6366.
9. R. G. Shulman, T. R. Brown, K. Ugurbil, S. Ogawa, S. M. Cohen and J. A. D. Hollander, Cellular applications of P-31 and C-13 nuclear magnetic-resonance, *Science*, 1979, **205**, 160–166.
10. J. J. H. Ackerman, T. H. Grove, G. G. Wong, D. G. Gadian and G. K. Radda, Mapping of metabolites in whole animals by P-31 NMR using surface coils, *Nature*, 1980, **283**, 167–170.
11. A. Schwarcz, O. Natt, T. Watanabe, S. Boretius, J. Frahm and T. Michaelis, Localized proton MRS of cerebral metabolite profiles in different mouse strains, *Magn. Reson. Med.*, 2003, **49**, 822–827.
12. J. Pfeuffer, I. Tkac, S. W. Provencher and R. Gruetter, Toward an *in vivo* neurochemical profile: Quantification of 18 metabolites in short-echo-time H-1 NMR spectra of the rat brain, *J. Magn. Reson.*, 1999, **141**, 104–120.
13. M. Terpstra, I. Tkac, R. L. Rao and R. Gruetter, Quantification of vitamin C in the rat brain *in vivo* using short echo-time H-1 MRS, *Magn. Reson. Med.*, 2006, **55**, 979–983.
14. B. Gomez-Anson, D. G. MacManus, G. J. M. Parker, C. A. Davie, G. J. Barker, I. F. Moseley, W. I. McDonald and D. H. Miller, *In vivo* H-1-magnetic resonance spectroscopy of the spinal cord in humans, *Neuroradiology*, 2000, **42**, 515–517.
15. F. J. Cooke, A. M. Blamire, D. N. Manners, P. Styles and B. Rajagopalan, Quantitative proton magnetic resonance spectroscopy of the cervical spinal cord, *Magn. Reson. Med.*, 2004, **51**, 1122–1128.
16. A. T. K. Kendi, F. U. Tan, M. Kendi, S. Huvaj and S. Tellioglu, MR spectroscopy of cervical spinal cord in patients with multiple sclerosis, *Neuroradiology*, 2004, **46**, 764–769.
17. Y. G. Kim, G. H. Choi, D. H. Kim, Y. D. Kim, Y. K. Kang and J. K. Kim, *In vivo* proton magnetic resonance spectroscopy of human spinal mass lesions, *J. Spinal Disorders Techn.*, 2004, **17**, 405–411.
18. U. Flogel, M. W. Merx, A. Godecke, U. K. M. Decking and J. Schrader, Myoglobin: A scavenger of bioactive NO, *Proc. Natil. Acad. Sci. USA*, 2001, **98**, 735–740.
19. K. Ugurbil, M. Petein, R. Maidan, S. Michurski, J. N. Cohn and A. H. From, High-resolution proton NMR-studies of perfused rat hearts, *FEBS Lett.*, 1984, **167**, 73–78.

20. M. Yamamoto, J. D. Lee, H. Shimizu, N. Kawasaki, A. Hara, Y. Ishii and T. Nakamura, Evaluation of postischemic myocardial-metabolism by H-1-magnetic resonance spectroscopy in the rabbit heart, *Jpn. Circ. J.-English Edition*, 1994, **58**, 707–712.

21. P. A. Bottomley and R. G. Weiss, Noninvasive localized MR quantification of creatine kinase metabolites in normal and infarcted canine myocardium, *Radiology*, 2001, **219**, 411–418.

22. J. Felblinger, B. Jung, J. Slotboom, C. Boesch and R. Kreis, Methods and reproducibility of cardiac/respiratory double-triggered H-1-MR spectroscopy of the human heart, *Magn. Reson. Med.*, 1999, **42**, 903–910.

23. J. E. Schneider, D. J. Tyler, M. ten Hove, A. E. Sang, P. J. Cassidy, A. Fischer, J. Wallis, L. M. Sebag-Montefiore, H. Watkins, D. Isbrandt, K. Clarke and S. Neubauer, *In vivo* cardiac H-1-MRS in the mouse, *Magn. Reson. Med.*, 2004, **52**, 1029–1035.

24. J. E. Schneider and S. Neubauer, Experimental cardiovascular MR in small animals, In: *Modern Magnetic Resonance*, G. A. Webb, ed., Springer Verlag, Berlin, 2005.

25. P. J. Cassidy, J. E. Schneider, S. M. Grieve, C. Lygate, S. Neubauer and K. Clarke, Assessment of motion gating strategies for mouse magnetic resonance at high magnetic fields, *J. Magn. Reson. Imag.*, 2004, **19**, 229–237.

26. A. A. Maudsley, S. K. Hilal, W. H. Perman and H. E. Simon, Spatially resolved high-resolution spectroscopy by 4-dimensional NMR, *J. Magn. Reson.*, 1983, **51**, 147–152.

27. T. R. Brown, B. M. Kincaid and K. Ugurbil, NMR chemical-shift imaging in 3 dimensions, *Proc. Natl. Acad. Sci. USA-Biological Sciences*, 1982, **79**, 3523–3526.

28. R. J. Ordidge, A. Connelly and J. A. B. Lohman, Image-selected *in vivo* spectroscopy (Isis) – a new technique for spatially selective NMR-Spectroscopy, *J. Magn. Reson.*, 1986, **66**, 283–294.

29. P. A. Bottomley, Spatial localization in NMR-spectroscopy *in vivo*, *Ann. NY Acad. Sci.*, 1987, **508**, 333–348.

30. J. Frahm, K. D. Merboldt and W. Hanicke, Localized proton spectroscopy using stimulated echoes, *J. Magn. Reson.*, 1987, **72**, 502–508.

31. M. Garwood and L. DelaBarre, The return of the frequency sweep: Designing adiabatic pulses for contemporary NMR, *J. Magn. Reson.*, 2001, **153**, 155–177.

32. S. C. Grant, N. R. Aiken, H. D. Plant, S. Gibbs, T. H. Mareci, A. G. Webb and S. J. Blackband, NMR spectroscopy of single neurons, *Magn. Reson. Med.*, 2000, **44**, 19–22.

33. S. C. Lee, J. H. Cho, D. Mietchen, Y. S. Kim, K. S. Hong, C. Lee, D. M. Kang, K. D. Park, B. S. Choi and C. Cheong, Subcellular *in vivo* H-1 MR spectroscopy of *Xenopus laevis* oocytes, *Biophys. J.*, 2006, **90**, 1797–1803.

34. W. Chen, G. Adriany, X. H. Zhu, R. Gruetter and K. Ugurbil, Detecting natural abundance carbon signal of NAA metabolite within 12-cm(3) localized volume of human brain using H-1-{C-13} NMR spectroscopy, *Magn. Reson. Med.*, 1998, **40**, 180–184.

35. I. Tkac, Z. Starcuk, I. Y. Choi and R. Gruetter, *In vivo* H-1 NMR spectroscopy of rat brain at 1 ms echo time, *Magn. Reson. Med.*, 1999, **41**, 649–656.

36. R. Gruetter, S. A. Weisdorf, V. Rajanayagan, M. Terpstra, H. Merkle, C. L. Truwit, M. Garwood, S. L. Nyberg and K. Ugurbil, Resolution improvements in *in vivo* H-1 NMR spectra with increased magnetic field strength, *J. Magn. Reson.*, 1998, **135**, 260–264.

37. I. Tkac, P. Andersen, G. Adriany, H. Merkle, K. Ugurbil and R. Gruetter, *In vivo* H-1 NMR spectroscopy of the human brain at 7 T, *Magn. Reson. Med.*, 2001, **46**, 451–456.

38. K. Ugurbil, G. Adriany, P. Andersen, W. Chen, M. Garwood, R. Gruetter, P. G. Henry, S. G. Kim, H. Lieu, I. Tkac, T. Vaughan, P. F. Van de Moortele, E. Yacoub and X. H. Zhu, Ultrahigh field magnetic resonance imaging and spectroscopy, *Magn. Reson. Imaging*, 2003, **21**, 1263–1281.

39. I. Tkac, P. G. Henry, P. Andersen, C. D. Keene, W. C. Low and R. Gruetter, Highly resolved *in vivo* H-1 NMR spectroscopy of the mouse brain at 9.4 T, *Magn. Reson. Med.*, 2004, **52**, 478–484.

40. S. Xu, J. H. Yang, C. Q. Ll, W. J. Zhu and J. Shen, Metabolic alterations in focally activated primary somatosensory cortex of alpha-chloralose-anesthetized rats measured by H-1 MRS at 11.7 T, *Neuroimage*, 2005, **28**, 401–409.

41. R. V. Mulkern, N. K. Chen, K. Oshio, L. P. Panych, F. J. Rybicki and G. Gambarota, Fast spectroscopic imaging strategies for potential applications in fMRI, *Magn. Reson. Imaging*, 2004, **22**, 1395–1405.

42. R. Pohmann, M. von Kienlin and A. Haase, Theoretical evaluation and comparison of fast chemical shift imaging methods, *J. Magn. Reson.*, 1997, **129**, 145–160.

43. W. Dreher, C. Geppert, M. Althaus and D. Leibfritz, Fast proton spectroscopic imaging using steady-state free precession methods, *Magn. Reson. Med.*, 2003, **50**, 453–460.

44. U. Dydak, M. Weiger, K. P. Pruessmann, D. Meier and P. Boesiger, Sensitivity-encoded spectroscopic imaging, *Magn. Reson. Med.*, 2001, **46**, 713–722.

45. U. Dydak, K. P. Pruessmann, M. Weiger, J. Tsao, D. Meier and P. Boesiger, Parallel spectroscopic imaging with spin-echo trains, *Magn. Reson. Med.*, 2003, **50**, 196–200.

46. R. Salomir, B. D. De Senneville and C. T. W. Moonen, A fast calculation method for magnetic field inhomogeneity due to an arbitrary distribution of bulk susceptibility, *Concep. Magn. Reson. Part B-Magn. Reson. Eng.*, 2003, **19B**, 26–34.

47. J. P. Marques and R. Bowtell, Application of a Fourier-based method for rapid calculation of field inhomogeneity due to spatial variation of magnetic susceptibility, *Concep. Magn. Reson. Part B-Magn. Reson. Eng.*, 2005, **25B**, 65–78.

48. Y. C. N. Cheng, E. M. Haacke and Y. J. Yu, An exact form for the magnetic field density of states for a dipole, *Magn. Reson. Imaging*, 2001, **19**, 1017–1023.

49. D. A. Yablonskiy and E. M. Haacke, Theory of NMR signal behavior in magnetically inhomogeneous tissues – the static dephasing regime, *Magn. Reson. Med.*, 1994, **32**, 749–763.

50. C. H. Ziener, W. R. Bauer and P. M. Jakob, Frequency distribution and signal formation around a vessel, *Magn. Reson. Mater. Phys. Biol. Med.*, 2005, **18**, 225–230.

51. D. B. Clayton, M. A. Elliott and R. E. Lenkinski, *In vivo* proton spectroscopy without solvent suppression, *Concep. Magn Reson.*, 2001, **13**, 260–275.

52. G. N. Chmurny and D. I. Hoult, The ancient and honourable art of shimming, *Concep. Magn. Reson.*, 1990, **2**, 131–149.

53. D. I. Hoult, Shimming on spatially localized signals, *J. Magn. Reson.*, 1987, **73**, 174–177.

54. D. Holz, D. Jensen, R. Proksa, M. Tochtrop and W. Vollmann, Automatic shimming for localized spectroscopy, *Med. Phys.*, 1988, **15**, 898–903.

55. J. Wilkins and S. Miller, The use of adaptive algorithms for obtaining optimal electrical shimming in magnetic-resonance imaging (MRI), *IEEE Trans. Biomed. Eng.*, 1989, **36**, 202–210.

56. J. Tropp, K. A. Derby, C. Hawryszko, S. Sugiura and H. Yamagata, Automated shimming of B_0 for spectroscopic imaging, *J. Magn. Reson.*, 1989, **85**, 244–254.

57. E. Schneider and G. Glover, Rapid *in vivo* proton shimming, *Magn. Reson. Med.*, 1991, **18**, 335–347.

58. P. Webb and A. Macovski, Rapid, fully-automatic, arbitrary-volume *in vivo* shimming, *Magn. Reson. Med.*, 1991, **20**, 113–122.

59. R. Gruetter and C. Boesch, Fast, noniterative shimming of spatially localized signals – in vivo analysis of the magnetic-field along axes, *J. Magn. Reson.*, 1992, **96**, 323–334.

60. R. Gruetter, Automatic, localized *in vivo* adjustment of all 1st-order and 2nd-order shim coils, *Magn. Reson. Med.*, 1993, **29**, 804–811.

61. J. Shen, R. E. Rycyna and D. L. Rothman, Improvements on an *in vivo* automatic shimming method (FASTERMAP), *Magn. Reson. Med.*, 1997, **38**, 834–839.

62. L. M. Klassen and R. S. Menon, Robust automated shimming technique using arbitrary mapping acquisition parameters (RASTAMAP), *Magn. Reson. Med.*, 2004, **51**, 881–887.

63. Z. G. Chen, S. S. Li, J. H. Yang, D. Letizia and J. Shen, Measurement and automatic correction of high-order B-0 inhomogeneity in the rat brain at 11.7 Tesla, *Magn. Reson. Imaging*, 2004, **22**, 835–842.

64. C. Juchem, H. Merkle, F. Schick, N. K. Logothetis and J. Pfeuffer, Region and volume dependencies in spectral line width assessed by H-1 2D MR chemical shift imaging in the monkey brain at 7 T, *Magn. Reson. Imaging*, 2004, **22**, 1373–1383.

65. T. Michaelis, Low-field vs. high-field proton MRS of mouse brain *in vivo*, *Magn. Reson. Med.*, 2005, **54**, 1046–1047.

66. J. Jeener, *Ampere International Summer School*, Basko Polje, Yugoslavia, 1971.

67. W. P. Aue, E. Bartholdi and R. R. Ernst, 2-dimensional spectroscopy – application to nuclear magnetic-resonance, *J. Chem. Phys.*, 1976, **64**, 2229–2246.

68. C. H. Sotak, D. M. Freeman and R. E. Hurd, The unequivocal determination of *in vivo* lactic-acid using two-dimensional double-quantum coherence-transfer spectroscopy, *J. Magn. Reson.*, 1988, **78**, 355–361.

69. B. A. Berkowitz, S. D. Wolff and R. S. Balaban, Detection of metabolites *in vivo* using 2D proton homonuclear correlated spectroscopy, *J. Magn. Reson.*, 1988, **79**, 547–553.

70. B. Barrere, M. Peres, B. Gillet, S. Mergui, J. C. Beloeil and J. Seylaz, 2D Cosy H-1-NMR – a new tool for studying *in situ* brain metabolism in the living animal, *FEBS Lett.*, 1990, **264**, 198–202.

71. B. A. Berkowitz and R. S. Balaban, Two-dimensional nuclear magnetic-resonance studies of enzyme-kinetics and metabolites *in vivo*, *Methods Enzymol.*, 1989, **176**, 330–341.

72. P. Meric, G. Autret, B. T. Doan, B. Gillet, C. Sebrie and J. C. Beloeil, *In vivo* 2D magnetic resonance spectroscopy of small animals, *Magn. Reson. Mater. Phys. Biol. Med.*, 2004, **17**, 317–338.

73. A. Metzler, M. Izquierdo, A. Ziegler, W. Kockenberger, E. Komor, M. Vonkienlin, A. Haase and M. Decorps, Plant histochemistry by correlation peak imaging, *Proc. Natl. Acad. Sci. USA*, 1995, **92**, 11912–11915.

74. A. Ziegler, A. Metzler, W. Kockenberger, M. Izquierdo, E. Komor, A. Haase, M. Decorps and M. VonKienlin, Correlation-peak imaging, *J. Magn. Reson. Series B*, 1996, **112**, 141–150.

75. M. von Kienlin, A. Ziegler, Y. Le Fur, C. Rubin, M. Decorps and C. Remy, 2D-spatial/2D-spectral spectroscopic imaging of intracerebral gliomas in rat brain, *Magn. Reson Med.*, 2000, **43**, 211–219.

76. D. Mayer, W. Dreher and D. Leibfritz, Fast echo planar based correlation-peak imaging: Demonstration on the rat brain *in vivo*, *Magn. Reson. Med.*, 2000, **44**, 23–28.

77. D. Mayer, W. Dreher and D. Leibfritz, Fast U-FLARE-based correlation-peak imaging with complete effective homonuclear decoupling, *Magn. Reson. Med.*, 2003, **49**, 810–816.

78. D. L. Olson, T. L. Peck, A. G. Webb, R. L. Magin and J. V. Sweedler, High-resolution microcoil H-1-NMR for mass-limited, nanoliter-volume samples, *Science*, 1995, **270**, 1967–1970.

79. D. Ballon, U. Mahmood, A. Jakubowski and J. A. Koutcher, Resolution enhanced NMR-spectroscopy in biological-systems via magnetic-susceptibility matched sample immersion chambers, *Magn. Reson. Med.*, 1993, **30**, 754–758.

80. J. P. Dyke, K. L. Zakian, W. M. Spees, C. Matei, Y. C. Chen, M. L. Mao, D. C. Shungu and J. A. Koutcher, Metabolic response of the CWR22 prostate tumor xenograft after 20 Gy of radiation studied by H-1 spectroscopic imaging, *Clin. Cancer Res.*, 2003, **9**, 4529–4536.

81. R. A. Wind, J. Z. Hu and D. N. Rommereim, High-resolution H-1 NMR spectroscopy in a live mouse subjected to 1.5 Hz magic angle spinning, *Magn. Reson. Med.*, 2003, **50**, 1113–1119.

82. R. A. Wind, J. Z. Hu and P. D. Majors, Localized *in vivo* isotropic–anisotropic correlation H-1 NMR spectroscopy using ultraslow magic angle spinning, *Magn. Reson. Med.*, 2006, **55**, 41–49.

83. E. R. Andrew, A. Bradbury and R. G. Eades, Removal of dipolar broadening of nuclear magnetic resonance spectra of solids by specimen rotation, *Nature*, 1959, **183**, 1802–1803.

84. A. N. Garroway, Magic-angle sample spinning of liquids, *J. Magn. Reson.*, 1982, **49**, 168–171.

85. P. Weybright, K. Millis, N. Campbell, D. G. Cory and S. Singer, Gradient, high-resolution, magic angle spinning H-1 nuclear magnetic resonance spectroscopy of intact cells, *Magn. Reson. Med.*, 1998, **39**, 337–345.

86. R. A. Wind, J. Z. Hu and D. N. Rommereim, High-resolution H-1 NMR spectroscopy in organs and tissues using slow magic angle spinning, *Magn. Reson. Med.*, 2001, **46**, 213–218.

87. J. Z. Hu, D. N. Rommereim and R. A. Wind, High-resolution H-1 NMR spectroscopy in rat liver using magic angle turning at a 1 Hz spinning rate, *Magn. Reson. Med.*, 2002, **47**, 829–836.

88. G. Deville, M. Bernier and J. M. Delrieux, NMR multiple echoes observed in solid He-3, *Phys. Rev. B*, 1979, **19**, 5666–5688.

89. D. Einzel, G. Eska, Y. Hirayoshi, T. Kopp and P. Wolfle, Multiple spin echoes in a normal Fermi-liquid, *Phys. Rev. Lett.*, 1984, **53**, 2312–2315.

90. R. Bowtell, R. M. Bowley and P. Glover, Multiple spin echoes in liquids in a high magnetic-field, *J. Magn. Reson.*, 1990, **88**, 643–651.

91. R. P. O. Jones, G. A. Morris and J. C. Waterton, Multiple spin echoes in a high-resolution spectrometer, *J. Magn. Reson.*, 1992, **98**, 115–122.
92. Q. H. He, W. Richter, S. Vathyam and W. S. Warren, Intermolecular multiple-quantum coherences and cross correlations in solution nuclear-magnetic-resonance, *J. Chem. Phys.*, 1993, **98**, 6779–6800.
93. W. S. Warren, W. Richter, A. H. Andreotti and B. T. Farmer, Generation of impossible cross-peaks between bulk water and biomolecules in solution NMR, *Science*, 1993, **262**, 2005–2009.
94. S. Vathyam, S. Lee and W. S. Warren, Homogeneous NMR spectra in inhomogeneous fields, *Science*, 1996, **272**, 92–96.
95. A. Vlassenbroek, J. Jeener and P. Broekaert, Macroscopic and microscopic fields in high-resolution liquid NMR, *J. Magn. Reson. Series A*, 1996, **118**, 234–246.
96. H. T. Edzes, The nuclear magnetization as the origin of transient changes in the magnetic-field in pulsed NMR experiments, *J. Magn. Reson.*, 1990, **86**, 293–303.
97. W. Richter, S. H. Lee, W. S. Warren and Q. H. He, Imaging with intermolecular multiple-quantum coherences in solution nuclear-magnetic-resonance, *Science*, 1995, **267**, 654–657.
98. R. Bowtell and P. Robyr, Structural investigations with the dipolar demagnetizing field in solution NMR, *Phys. Rev. Lett.*, 1996, **76**, 4971–4974.
99. P. Robyr and R. Bowtell, Nuclear magnetic resonance microscopy in liquids using the dipolar field, *J. Chem. Phys.*, 1997, **106**, 467–476.
100. R. Bowtell, S. Gutteridge and C. Ramanathan, Imaging the long-range dipolar field in structured liquid state samples, *J. Magn. Reson.*, 2001, **150**, 147–155.
101. W. S. Warren, S. Ahn, M. Mescher, M. Garwood, K. Ugurbil, W. Richter, R. R. Rizi, J. Hopkins and J. S. Leigh, MR imaging contrast enhancement based on intermolecular zero quantum coherences, *Science*, 1998, **281**, 247–251.
102. R. R. Rizi, S. Ahn, D. C. Alsop, G-S. Roe, M. Mescher, W. Richter, M. D. Schnall, J. S. Leigh and W. S. Warren, Intermolecular zero-quantum coherence imaging of the human brain, *Magn. Reson. Med.*, 2000, **43**, 627–632.
103. L. S. Bouchard, R. R. Rizi and W. S. Warren, Magnetization structure contrast based on inter-molecular multiple-quantum coherences, *Magn. Reson. Medicine*, 2002, **48**, 973–979.
104. T. Hou, Z. Chen, D. W. Hwang, J. H. Zhong and L. P. Hwang, Intermolecular double-quantum coherence MR microimaging of pig tail with unique image contrast, *Magn. Reson. Imaging*, 2004, **22**, 543–550.
105. J. H. Zhong, Z. Chen and E. Kwok, *In vivo* intermolecular double-quantum imaging on a clinical 1.5 T MR scanner,, *Magn. Reson. Med.*, 2000, **43**, 335–341.
106. C. Faber, Solvent-localized NMR spectroscopy using the distant dipolar field: A method for NMR separations with a single gradient, *J. Magn. Reson.*, 2005, **176**, 120–124.
107. Z. Chen, Z. W. Chen and J. H. Zhong, High-resolution NMR spectra in inhomogeneous fields via IDEAL (intermolecular dipolar-interaction enhanced all lines) method, *J. Am. Chem. Soc.*, 2004, **126**, 446–447.
108. Z. Chen, T. Hou, Z. W. Chen, D. W. Hwang and L. P. Hwang, Selective intermolecular zero-quantum coherence in high-resolution NMR under inhomogeneous fields, *Chem. Phys. Lett.*, 2004, **386**, 200–205.
109. Y. Y. Lin, S. Ahn, N. Murali, W. Brey, C. R. Bowers and W. S. Warren, High-resolution, > 1 GHz NMR in unstable magnetic fields, *Phys. Rev. Lett.*, 2000, **85**, 3732–3735.
110. C. Faber, E. Pracht and A. Haase, Resolution enhancement in *in vivo* NMR spectroscopy: De-tection of intermolecular zero-quantum coherences, *J. Magn. Reson.*, 2003, **161**, 265–274.
111. G. Galiana, R. T. Branca and W. S. Warren, Ultrafast intermolecular zero quantum spectroscopy, *J. Am. Chem. Soc.*, 2005, **127**, 17574–17575.
112. T. Enss, S. Ahn and W. S. Warren, Visualizing the dipolar field in solution NMR and MR imaging: Three-dimensional structure simulations, *Chem. Phys. Lett.*, 1999, **305**, 101–108.
113. S. Garrett-Roe and W. S. Warren, Numerical studies of intermolecular multiple quantum coher-ences: High-resolution NMR in inhomogeneous fields and contrast enhancement in MRI, *J. Magn. Reson.*, 2000, **146**, 1–13.

114. L. S. Bouchard, F. W. Wehrli, C. L. Chin and W. S. Warren, Structural anisotropy and internal magnetic fields in trabecular bone: Coupling solution and solid dipolar interactions, *J. Magn. Reson.*, 2005, **176**, 27–36.
115. L. S. Bouchard and W. S. Warren, Multiple-quantum vector field imaging by magnetic resonance, *J. Magn. Reson.*, 2005, **177**, 9–21.
116. C. Faber, C. Heil, B. Zahneisen, D. Z. Balla and R. Bowtell, Sensitivity to local dipole fields in the CRAZED experiment: An approach to bright spot MRI, *J. Magn. Reson.*, 2006, **182**, 315–324.
117. S. Datta, S. Y. Huang and Y. Y. Lin, Contrast enhancement by feedback fields in magnetic resonance imaging, *J. Phys. Chem.*, 2006, **110**, 22071–22078.
118. M. H. Levitt, Demagnetization field effects in two-dimensional solution NMR, *Concepts Magn. Reson.*, 1996, **8**, 77–103.
119. S. Ahn, N. Lisitza and W. S. Warren, Intermolecular zero-quantum coherences of multi-component spin systems in solution NMR, *J. Magn. Reson.*, 1998, **133**, 266–272.
120. P. Robyr and R. Bowtell, Measuring diffusion in liquids with a single gradient pulse, *J. Magn. Reson. Series A*, 1996, **121**, 206–208.
121. I. Ardelean, S. Stapf, D. E. Demco and R. Kimmich, The nonlinear stimulated echo, *J. Magn. Reson.*, 1997, **124**, 506–508.
122. I. Ardelean, R. Kimmich, S. Stapf and D. E. Demco, Multiple nonlinear stimulated echoes, *J. Magn. Reson.*, 1997, **127**, 217–224.
123. I. Ardelean, R. Kimmich, S. Stapf and D. E. Demco, The nonlinear stimulated echo in the presence of inequivalent spins, *J. Magn. Reson.*, 1998, **132**, 138–143.
124. A. S. Bedford, R. Bowtell and R. M. Bowley, Multiple spin echoes in multicomponent liquids, *J. Magn. Reson.*, 1991, **93**, 516–532.
125. R. Bowtell, Indirect detection via the dipolar demagnetizing field, *J. Magn. Reson.*, 1992, **100**, 1–17.
126. W. S. Warren, S. Lee, W. Richter and S. Vathyam, Correcting the classical dipolar demagnetizing field in solution NMR, *Chem. Phys. Lett.*, 1995, **247**, 207–214.
127. D. Balla and C. Faber, Solvent suppression in liquid state NMR with selective intermolecular zero-quantum coherences, *Chem. Phys. Lett.*, 2004, **393**, 464–469.
128. S. Lee, W. Richter, S. Vathyam and W. S. Warren, Quantum treatment of the effects of dipole–dipole interactions in liquid nuclear magnetic resonance, *J. Chem. Phys.*, 1996, **105**, 874–900.
129. J. Jeener, A. Vlassenbroek and P. Broekaert, Unified derivation of the dipolar field and relaxation terms in the Bloch–Redfield equations of liquid NMR, *J. Chem. Phys.*, 1995, **103**, 1309–1332.
130. E. D. Minot, P. T. Callaghan and N. Kaplan, Multiple echoes, multiple quantum coherence, and the dipolar field: Demonstrating the significance of higher order terms in the equilibrium density matrix, *J. Magn. Reson.*, 1999, **140**, 200–205.
131. G. J. Bowden, T. Heseltine and M. J. Prandolini, Double-quantum and cross-correlation peaks in Cosy NMR-spectra, *Chem. Phys. Lett.*, 1995, **233**, 639–643.
132. R. Kimmich and I. Ardelean, Intermolecular multiple-quantum coherence transfer echoes and multiple echoes in nuclear magnetic resonance, *J. Chem. Phys.*, 1999, **110**, 3708–3713.
133. I. Ardelean and R. Kimmich, Diffusion measurements with the pulsed gradient nonlinear spin echo method, *J. Chem. Phys.*, 2000, **112**, 5275–5280.
134. J. Jeener, Comment on "diffusion measurements with the pulsed gradient nonlinear spin echo method," [*J. Chem. Phys.*, 2000, **112**, 5275], *J. Chem. Phys.*, 2002, **116**, 1204–1205.
135. I. Ardelean and R. Kimmich, Response to "Comment on diffusion measurements with the pulsed gradient nonlinear spin echo method" [*J. Chem. Phys.*, 2002, **116**, 1204], *J. Chem. Phys.*, 2002, **116**, 1206–1206.
136. J. Jeener, Equivalence between the "classical" and the "Warren" approaches for the effects of long range dipolar couplings in liquid nuclear magnetic resonance, *J. Chem. Phys.*, 2000, **112**, 5091–5094.
137. P. R. Bachiller, S. Ahn and W. S. Warren, Detection of intermolecular heteronuclear multiple-quantum coherences in solution NMR, *J. Magn. Reson. Series A*, 1996, **122**, 94–99.
138. W. S. Warren and S. Ahn, The boundary between liquidlike and solidlike behavior in magnetic resonance, *J. Chem. Phys.*, 1998, **108**, 1313–1325.

139. S. Ahn and W. S. Warren, Effects of intermolecular dipolar couplings in solution NMR in separated time intervals: The competition for coherence transfer pathways, *Chem. Phys. Lett.*, 1998, **291**, 121–129.

140. H. M. Zhang, N. Lizitsa, R. G. Bryant and W. S. Warren, Experimental characterization of intermolecular multiple-quantum coherence pumping efficiency in solution NMR, *J. Magn. Reson.*, 2001, **148**, 200–208.

141. W. S. Warren, S. Y. Huang, S. Ahn and Y. Y. Lin, Understanding third-order dipolar effects in solution nuclear magnetic resonance: Hahn echo decays and intermolecular triple-quantum coherences, *J. Chem. Phys.*, 2002, **116**, 2075–2084.

142. C. L. Chin, X. P. Tang, L. S. Bouchard, P. K. Saha, W. S. Warren and F. W. Wehrli, Isolating quantum coherences in structural imaging using intermolecular double-quantum coherence MRI, *J. Magn. Reson.*, 2003, **165**, 309–314.

143. X. P. Tang, H. Ong, K. Shannon and W. S. Warren, Simultaneous acquisition of multiple orders of intermolecular multiple-quantum coherence images, *Magn. Reson. Imaging*, 2003, **21**, 1141–1149.

144. K. L. Shannon, R. T. Branca, G. Galiana, S. Cenzano, L. S. Bouchard, W. Soboyejo and W. S. Warren, Simultaneous acquisition of multiple orders of intermolecular multiple-quantum coherence images *in vivo*, *Magn. Reson. Imaging*, 2004, **22**, 1407–1412.

145. Z. Chen, Z. W. Chen, D. W. Hwang, J. H. Zhong and L. P. Hwang, Separation and characterization of different signals from intermolecular three-spin orders in solution NMR, *J. Magn. Reson.*, 2004, **171**, 244–252.

146. W. Richter and W. S. Warren, Intermolecular multiple quantum coherences in liquids, *Concepts Magn. Resonance*, 2000, **12**, 396–409.

147. R. T. Branca, S. Capuani and B. Maraviglia, About the crazed sequence, *Concepts Magn. Reson. Part A*, 2004, **21A**, 22–36.

148. F. van de Ven, *Multidimansional NMR in liquids: Basic principles and experimental methods*, VCH Publishers, Inc., New York, 1995.

149. D. L. Mattiello, W. S. Warren, L. Mueller and B. T. Farmer, Minimizing the water resonance in biological NMR: Characterization and suppression of intermolecular dipolar interactions by multiple-axis gradients, *J. Am. Chem. Soc.*, 1996, **118**, 3253–3261.

150. A. Vlassenbroek, J. Jeener and P. Broekaert, Radiation damping in high-resolution liquid NMR – a simulation study, *J. Chem. Phys.*, 1995, **103**, 5886–5897.

151. Y. Y. Lin, N. Lisitza, S. D. Ahn and W. S. Warren, Resurrection of crushed magnetization and chaotic dynamics in solution NMR spectroscopy, *Science*, 2000, **290**, 118–121.

152. S. Y. Huang, Y. Y. Lin, N. Lisitza and W. S. Warren, Signal interferences from turbulent spin dynamics in solution nuclear magnetic resonance spectroscopy, *J. Chem. Phys.*, 2002, **116**, 10325–10337.

153. S. Y. Huang, J. D. Walls, Y. Wang, W. S. Warren and Y. Y. Lin, Signal irreproducibility in high-field solution magnetic resonance experiments caused by spin turbulence, *J. Chem. Phys.*, 2004, **121**, 6105–6109.

154. S. Y. Huang, C. Anklin, J. D. Walls and Y. Y. Lin, Sizable concentration-dependent frequency shifts in solution NMR using sensitive probes, *J. Am. Chem. Soc.*, 2004, **126**, 15936–15937.

155. S. Datta, S. Y. Huang and Y. Y. Lin, The transient dynamics leading to spin turbulence in high-field solution magnetic resonance: A numerical study, *J. Chem. Phys.*, 2006, **124**.

156. J. D. Walls, F. K. H. Phoa and Y. Y. Lin, Spin dynamics at very high spin polarization, *Phys. Rev. B*, 2004, **70**, 1–8.

157. J. D. Walls and Y. Y. Lin, Constants of motion in NMR spectroscopy, *Solid State Nuclear Magnetic Resonance*, 2006, **29**, 22–29.

158. B. W. Zheng, Z. Chen, S. H. Cai, J. H. Zhong and C. H. Ye, Theoretical formalism and experimental verification of line shapes of NMR intermolecular multiple-quantum coherence spectra, *J. Chem. Phys.*, 2005, **123**.

159. P. Broekaert, A. Vlassenbroek, J. Jeener, G. Lippens and J. M. Wieruszeski, Observation and selective suppression of the dipolar-field effects in 2D NMR in liquids in homogeneous fields, *J. Magn. Reson. Series A*, 1996, **120**, 97–104.

160. S. Ahn, W. S. Warren and S. Lee, Quantum treatment of intermolecular multiple-quantum coherences with intramolecular J coupling in solution NMR, *J. Magn. Reson.*, 1997, **128**, 114–129.

161. S. Ahn, S. Lee and W. S. Warren, The competition between intramolecular J couplings, radiation damping, and intermolecular dipolar couplings in two-dimensional solution nuclear magnetic resonance, *Molec. Phys.*, 1998, **95**, 769–785.

162. C. B. Cai, Z. Chen, S. H. Cai, L. P. Hwang and J. H. Zhong, Finite difference simulation of diffusion behaviors under inter- and intra-molecular multiple-quantum coherences in liquid NMR, *Chem. Phys. Lett.*, 2005, **407**, 438–443.

163. C. B. Cai, Z. Chen, S. H. Cai and J. H. Zhong, A simulation algorithm based on Bloch equations and product operator matrix: application to dipolar and scalar couplings, *J. Magn. Reson.*, 2005, **172**, 242–253.

164. X. Q. Zhu, C. B. Cai, Z. Chen and J. H. Zhong, Multiplet patterns due to co-existing intermolecular dipolar and intramolecular scalar couplings in liquid nuclear magnetic resonance, *Chin. Phys.*, 2005, **14**, 516–523.

165. X. Q. Zhu, Z. Chen, S. H. Cai and J. H. Zhong, Selection of intra- or inter-molecular multiple-quantum coherences in NMR of highly polarized solution, *Physica B-Condens. Matter*, 2005, **362**, 286–294.

166. C. Ramanathan and R. Bowtell, Dynamics of the nuclear magnetic resonance COSY-revamped by asymmetric z-gradients (CRAZED) experiment, *J. Chem. Phys.*, 2001, **114**, 10854–10859.

167. J. P. Marques, S. Grant, S. Blackband and R. W. Bowtell, Intermolecular multiple quantum coherences at high magnetic field: The nonlinear regime, *J. Chem. Phys.*, 2005, **123**.

168. I. Ardelean and R. Kimmich, Diffusion measurements using the nonlinear stimulated echo, *J. Magn. Reson.*, 2000, **143**, 101–105.

169. Z. Chen and J. H. Zhong, Unconventional diffusion behaviors of intermolecular multiple-quantum coherences in nuclear magnetic resonance, *J. Chem. Phys.*, 2001, **114**, 5642–5653.

170. J. H. Zhong, Z. Chen, E. Kwok and S. Kennedy, Enhanced sensitivity to molecular diffusion with intermolecular double-quantum coherences: Implications and potential applications, *Magn. Reson. Imaging*, 2001, **19**, 33–39.

171. Z. Chen, Z. W. Chen and J. H. Zhong, Quantitative study of longitudinal relaxation related to intermolecular dipolar interactions in solution NMR, *Chem. Phys. Lett.*, 2001, **333**, 126–132.

172. J. H. Zhong, Z. Chen, S. K. Zheng and S. D. Kennedy, Theoretical and experimental characterization of NMR transverse relaxation process related to intermolecular dipolar interactions, *Chem. Phys. Lett.*, 2001, **350**, 260–268.

173. J. Jeener, Macroscopic molecular diffusion in liquid NMR, *revisited, Concep. Magn. Reson.*, 2002, **14**, 79–88.

174. W. Barros, J. C. Gore and D. F. Gochberg, Simultaneous measurement of D and T-2 using the distant dipolar field, *J. Magn. Reson.*, 2006, **178**, 166–169.

175. M. Engelsberg and W. Barros, Distant-dipole field in liquids and diffusion: A perturbative approach, *J. Chem. Phys.*, 2005, **122**.

176. M. Engelsberg, W. Barros and F. Hallwass, Intermolecular double-quantum coherences in two-dimensional spectra of binary mixtures in solution. The role of diffusion, *J. Chem. Phys.*, 2004, **120**, 10659–10665.

177. I. Ardelean, E. Kossel and R. Kimmich, Attenuation of homo- and heteronuclear multiple spin echoes by diffusion, *J. Chem. Phys.*, 2001, **114**, 8520–8529.

178. Z. Chen, G. X. Lin and J. H. Zhong, Diffusion of intermolecular zero- and double-quantum coherences in two-component spin systems, *Chem. Phys. Lett.*, 2001, **333**, 96–102.

179. Z. Chen, Z. W. Chen and J. H. Zhong, Quantitative characterization of intermolecular dipolar interactions of two-component systems in solution nuclear magnetic resonance, *J. Chem. Phys.*, 2001, **115**, 10769–10779.

180. A. Bifone, G. S. Payne and M. O. Leach, *In vivo* multiple spin echoes, *J. Magn. Reson.*, 1998, **135**, 30–36.

181. D. Z. Balla, G. Melkus and C. Faber, Spatially localized intermolecular zero-quantum coherence spectroscopy for in vivo applications, *Magn. Reson. Med.*, 2006, **56**, 745–753.

182. M. Mescher, W. Richter, L. DelaBarre, M. Garwood and W. S. Warren, In *Proc. Intl. Soc. Mag. Reson. Med.*, 2000, **8**, 600.

183. B. Boulat, P. T. Narasimhan and R. E. Jacobs, In *ENC*, Asilomar, CA, 2006.

184. Z. Chen, Z. Chen and J. Zhong, In *Proc. Intl. Soc. Mag. Reson. Med.*, 2004, pp 2300, Kyoto, Japan.

185. Z. Chen, S. Cai, Z. Chen and J. Zhong, *Biomedical magnetic resonance imaging and spectroscopy at very high fields*, University of Würzburg, Würzburg, Germany, 2006, p. 32.

186. L. Frydman, T. Scherf and A. Lupulescu, The acquisition of multidimensional NMR spectra within a single scan, *Proc. Natl. Acad. Sci. USA*, 2002, **99**, 15858–15862.

187. V. Govindaraju, K. Young and A. A. Maudsley, Proton NMR chemical shifts and coupling constants for brain metabolites, *NMR Biomed.*, 2000, **13**, 129–153.

Spin Echo NMR Diffusion Studies

FRANK STALLMACH AND PETRIK GALVOSAS

Faculty of Physics and Earth Sciences, University of Leipzig, Linnestrasse 5, 04103 Leipzig, Germany

The basic principles of NMR diffusion studies and a generalized approach to calculate NMR spin echo attenuation due to diffusion in the presence of gradients of the polarizing magnetic field are presented. By means of this generalized approach, PFG NMR sequences for diffusion studies, including those using alternating pulsed field gradients (APFG) and modern techniques for advanced cross-term suppression by magic pulsed field gradient (MPFG) ratios, are reviewed. Gradient systems and experimental procedures for the generation of high-intensity pulsed field gradients are discussed and recent examples of their successful application in diffusion studies with porous materials are given.

1. INTRODUCTION

Already in the first spin echo NMR experiments, which were introduced just a few years after the experimental discovery of the nuclear magnetic resonance (NMR) phenomenon,[1,2] Hahn[3] realized that the self-diffusion of the molecules carrying the nuclear spins under investigation reduces the intensities of the observed NMR signals. He also noticed that this effect depends on the homogeneity of the polarizing magnetic field and estimated the field gradient of his magnet using the known self-diffusion coefficient. Hahn actually proposed to apply these new spin echo techniques for studies of "relative values of the self-diffusion coefficient D, a quantity which is very difficult to measure by ordinary methods".[3] Thus, this paper must actually be considered as the birth certificate of NMR diffusometry.

The invention of the CPMG method[4,5] and the idea to generate gradients of the magnetic field by an electrical current flowing through suitable arrangements of wires in the vicinity of the investigated sample by Carr and Purcell[5] allowed to decouple relaxation- and diffusion-based attenuations of the spin echo NMR signals. These ideas facilitated the early constant field gradient NMR diffusometry.[6–8] Furthermore, they stimulated the development of the first gradient coils for NMR applications as well as of the methodology to control the gradients during the spin echo experiments.[9,10] The gradient coil technology opened the door for two major developments in NMR, which both rely on the ability to suddenly switch gradients of the polarizing magnetic field (so-called pulsed field gradients: PFG) on and off. Stejskal and Tanner proposed to employ a pair of pulsed field gradients in the spin echo[11] and later stimulated echo[12] NMR pulse sequences, which decisively improved the early constant field gradient NMR diffusion studies. In the NMR tomography (MRT), simultaneously developed by Lauterbur[13] and Mansfield *et al.*[14] these pulsed field gradients are used to measure spatial distribution of the resonant nuclei.

Diffusion studies or diffusion-related problems form an important fraction of all published NMR and MRT investigations. Roughly estimated, their relative amount steadily increased from about 10% of the annually published NMR and MRT papers in 1989 to 20% in 2005 (see Fig. 1). This development was and still is promoted by new ideas in adapting the basic principles of NMR diffusometry to scientifically and technologically interesting diffusion problems as well as by the improved commercial availability of the necessary hardware including gradient coils, suitable power sources and interfaces to the conventional NMR spectrometer hardware and software.

Among these later developments, the introduction of alternating pulsed field gradients with equal,[17,18] variable,[19] and even magic[20,21] amplitude ratios may be considered as one of the key inventions. By applying the formalism of the generalized PFG NMR sequence,[21] we reconsider the corresponding pulse sequences in Section 3. Additionally, the generation and application of pulsed field gradients of high intensities[22–26] substantially improved the experimental and instrumental basis
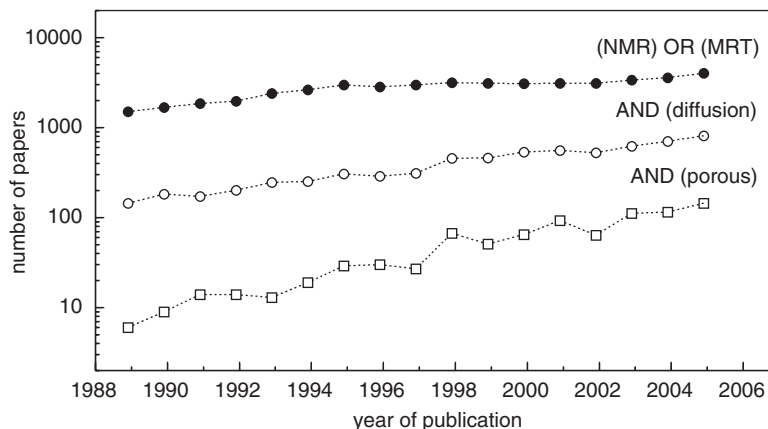
Fig. 1. Annual number of scientific papers published in die field of NMR or MRT (●) dealing with diffusion phenomena (○) in porous materials (□). Results of an online search in the "Abstract, Title, Keywords" field of the "Journals" database of *ScienceDirect* (Elsevier B.V., NL).[15] [*Source:* Adapted from Ref. 16.]

for the NMR diffusometry. Section 4 reviews such innovative hardware solutions, as well as procedures and routines necessary for a safe utilization of high-intensity pulsed field gradients. From the applications point of view, the propagator presentation,[27] the short-diffusion time approximation[28] and the use of regularized inverse Laplace transformations[29–31] enhanced and facilitated, respectively, the analysis, and thus the interpretation of PFG NMR data. Based on combinations of different pulse sequences, these concepts even produced new methods such as, the diffusion-ordered spectroscopy,[32–34] time-correlated diffusion and flow studies[35,36] and diffusion–relaxation correlations,[29,30,37,38] not known until very recently. The present state-of-the-art of these new correlation methods and of high-intensity pulsed field gradient applications in studying transport processes will be summarized in Section 5, where, however, we restrict our discussion to examples from porous materials.

With the exemption of the introduction to basic principles of PFG NMR diffusion studies (Section 2), which especially the newcomer in the field of NMR diffusometry may find useful, the above selection covers areas, which had not yet been subject of a reconsideration in a review. However, we shall note that there are a number of textbooks and review articles covering the variety of pulsed field gradient methods in NMR spectroscopy and tomography, as well as the peculiarities of their applications to diffusion problems in different systems. The books of Callaghan,[39] Kärger and Ruthven,[40] Kimmich,[41] Blümich,[42] Berger and Braun,[43] Heitjans and Kärger,[44] Stapf and Han[45] as well as the review articles of Price,[46–49] Stallmach and Kärger *et al.*,[50–52] Watson,[53] Johnson,[32] Cobas,[34] Brand *et al.*,[33] and Ardelean and Kimmich[54] are just a few examples, where the reader may find

comprehensive representations of the PFG NMR diffusometry in the respective fields of application.

2. FUNDAMENTALS OF PULSED FIELD GRADIENT NMR DIFFUSION STUDIES

2.1. Principles of diffusion studies

2.1.1. *Diffusion equation*

In a system, which consists of mobile components initially distributed inhomogeneously in space, the random motion of the individual particles of each component will lead to a successive decay of the associated concentration differences (see Fig. 2). This process is called transport diffusion and described by the diffusion equation (see e.g., 40, 44, and 55). The diffusion equation (also known as Fick's second law) is a partial differential equation for the concentration $c(r, t)$ with the coefficient of transport diffusion D_t as the characteristic parameter.

Under equilibrium conditions, the particles (molecules) undergo thermal (Brownian) motion, which means that they change their positions with time even without the presence of concentration gradients. This process is called self-diffusion. Self-diffusion processes may be described by a diffusion equation in a similar way as in
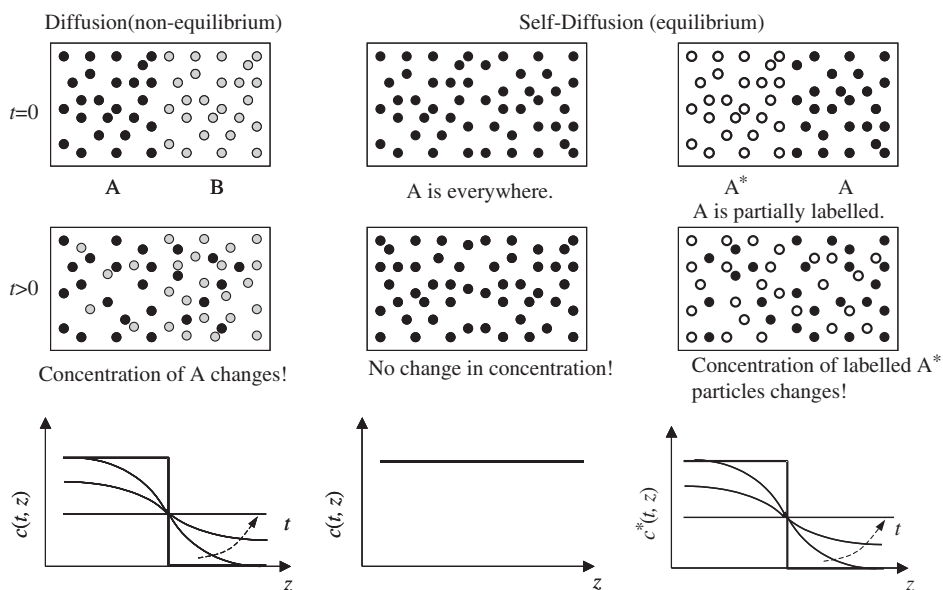
Fig. 2. Observation of concentration changes due to random motion of particles under macroscopic nonequilibrium (diffusion) and equilibrium (self-diffusion) conditions. The diffusion equation describes such changes theoretically and defines the coefficients of transport diffusion (D_t) and of self-diffusion (D), respectively.

the case of transport diffusion, if one considers the motion of labeled particles in an environment of unlabeled but otherwise completely identical particles:

$$\frac{\partial c^*(\boldsymbol{r}, t)}{\partial t} = D\boldsymbol{\nabla}^2 c^*(\boldsymbol{r}, t) \tag{1}$$

c^* denotes the concentration of the labeled particles. In order to ensure that the labeling does not affect the self-diffusion coefficient D, the label of the particles must not affect the mobility of the particles and the interaction between them. Thus, experimental techniques for measurements of the self-diffusion coefficients require (1) the introduction of a spatially dependent initial concentration $c_0^*(\boldsymbol{r})_{t=0}$ of labeled particles, and similar to transport diffusion studies, (2) the measurement of the concentration changes $c^*(\boldsymbol{r}, t)$, (3) the solution of the diffusion equation and (4) the fit of this solution to the experimentally observed concentrations with D as adjustable parameter.

The initial condition for the solution of the diffusion equation (Eq. (1)) is given by the initial concentration of the labeled particles $c_0^*(\boldsymbol{r})_{t=0}$. The necessary boundary condition is written as:

$$0 = D\,\boldsymbol{n}\,\boldsymbol{\nabla}\,c^* + \rho c^*|_s, \tag{2}$$

were $\boldsymbol{\nabla}c^*$ denotes the particle flux due to self-diffusion, which is modified at the interfaces S between different regions in the considered system. The parameter ρ accounts for properties of the interface, where the particles may be absorbed (or passed through) and reflected, respectively.

Many of the different experimental techniques for diffusion studies are just distinguished from each other by the methods of how the time and space dependent concentrations c and c^*, respectively, are measured, and – in case of self-diffusion – which kind of labels are used. For example, for self-diffusion studies by tracer-exchange methods molecules may be labeled using different isotopes of atoms in the diffusing molecules. The resulting space and time-dependent changes in isotope concentration may be detected gravimetrically or – in the case of radio active isotopes – by measuring the associated changes in radiation intensity.[40,44] If NMR active isotopes are used, changes in the spatial distribution of the NMR signal intensity may be monitored.[41,42] Small fluorofors, such as rhodamine attached to macromolecules represent another, very sensitive marker for molecule positions and concentrations. They are detected by optical techniques. For example, by using confocal laser-scanning microscopy, three-dimensional (3D) concentration maps of such fluorescence markers may be measured with spatial resolution on a micrometer (μm) scale.[56]

In the following sections, we will show that by using pulsed magnetic field gradients in NMR a very special type of label is employed. It is distinguished from the previously mentioned labels by the fact that its generation as well as the detection of its motion are just two successive parts of an NMR pulse sequence. These parts are usually called the encoding and decoding periods of the pulse sequence. The label itself is the spatially dependent phase of the macroscopic magnetization of the observed NMR active nuclei. It survives only during the time scale of longitudinal

(T_1) relaxation, but may be repeatedly generated during each successive scan of the NMR experiment. However, theory and mathematics of the diffusion equation, which are summarized in this and the following sections, apply to it in the same manner as for the more conventional labels mentioned above. Moreover, one of the major advantages of PFG NMR is that important characteristic parameters of the self-diffusion process, such as the averaged (effective) diffusion coefficient and the mean square displacement may be derived directly from the experimental data not requiring the knowledge of the solution of the diffusion equation.

2.1.2. Propagator and mean square displacement

The general concept, how the diffusion equation is solved, may be found in standard textbooks on partial differential equations (e.g., 44, 57). Here, we just present the concept of the so-called propagator and its relations to the self-diffusion coefficient and the mean square displacement, which proved to be very useful to understand the principles of the PFG NMR technique.

The *propagator* $P(r_2, r_1, t)$ is defined as the (conditional) probability density to find a diffusing particle, which started at $t = 0$ in position r_1, after time t in the volume element dr at position r_2. It is obtained by solving the diffusion equation (Eq. (1)) with respect to the appropriate boundary condition (Eq. (2)) for a point source of the initial concentration $c_0^* = P(r_2, r_1, t = 0) = \delta(r_2 - r_1)$. Thus, it is equivalent to the so-called fundamental solution of the diffusion equation (e.g., 57) and describes, how labeled particles initially concentrated at one point (r_1) move (= propagate) due to self-diffusion in space.

It is easily to recognize that the solution of the diffusion equation for any other initial condition of labeled diffusing particles ($p_0(r_1)$) is given by the superposition of this initial condition with the propagator. It is calculated by multiplying the propagator with the initial condition $p_0(r_1)$ and integrating over all starting positions r_1

$$\bar{P}(r, t) = \int_V P(r_1 + r, r_1, t) p_0(r_1) \ dr_1, \tag{3}$$

where the vector r_2 is replaced by the vector of particle displacement $r = r_2 - r_1$. $\bar{P}(r, t)$ represents the propagator, averaged over all starting positions. Therefore, it is called the *averaged propagator*.[27] It depends only on the particle displacement and denotes the probability density that an arbitrary selected particle is displaced by the distance r during time t. The averaged propagator plays a central role in the interpretation of PFG NMR diffusion studies. As we shall see in Section 2.3, PFG NMR measures the Fourier transform of this averaged propagator.

As an example, particle displacements due to random thermal motion in a homogeneous, infinitely extended 3D volume are normally distributed. Thus, the averaged propagator is given by the 3D Gaussian function. A 1D representation of it is plotted in Fig. 3.

$$\bar{P}(r, t) = \frac{1}{\sqrt{(4\pi D t)^3}} \ \exp\left(-\frac{(r(t))^2}{4Dt} \right) \tag{4}$$
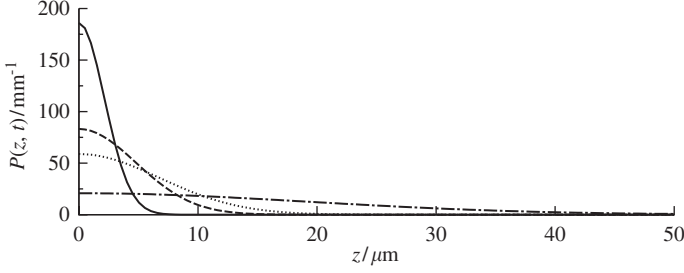
Fig. 3. Gaussian-shaped propagator $P(z, t)$ for a fluid with a self-diffusion coefficient of $D = 2.3 \times 10^{-9} \, \text{m}^2 \, \text{s}^{-1}$ (e.g., liquid water at 298 K). The particle displacement $z_2 - z_1$ during time t is denoted by z. The plot was calculated using Eq. (4) for one spatial dimension with times t equal to 1 ms (—), 5 ms (- - -), 20 ms ($\cdot \; \cdot \; \cdot$) and 80 ms ($\cdot - \cdot - \cdot$) typically used in NMR diffusion studies.

The *mean square displacement* $\langle r^2(t) \rangle$ of the particles is an important parameter, which quantifies the diffusion process. It is given by the second moment of the averaged propagator:

$$\langle r^2(t) \rangle = \int_V \bar{P}(\mathbf{r}, t) r^2 \; \mathrm{d}\mathbf{r} \tag{5}$$

For the above-considered example of diffusion in a homogeneous, infinitely extended 3D volume, the calculation of the second moment using the averaged propagator given in Eq. (4) yields the well-known Einstein relation:

$$\langle r^2(t) \rangle = 6Dt, \tag{6}$$

which may be considered as an alternative definition of the self-diffusion coefficient.

2.2. The three time intervals of a PFG NMR experiment

In order to rationalize the principle of pulsed field gradient NMR technique to measure self-diffusion coefficients, we need to introduce the (1D) density $m(z, t)$ of the macroscopic magnetization $M(t)$ of the observed NMR active nuclei. At any time t, the macroscopic magnetization is obtained by integrating over the magnetization density $M(t) = \int m(z, t) \, \mathrm{d}z$. In a free induction decay (FID) (see Fig. 4) and spin echo NMR experiment, respectively, one observes the magnetization after it was flipped by an appropriate rf pulse into the plane perpendicular to the direction of the homogeneous polarizing magnetic field B_0. Due to its precision with the Larmor frequency $\omega_0 = \gamma B_0$, $M(t)$ induces a voltage into the NMR receiver coil. If this voltage is recorded with a phase-sensitive receiver tuned to the frequency $f_0 = \omega_0/(2\pi)$, it samples the magnetization in the rotating frame of reference. Without any field gradients, $M(t)$ would decay due to transverse (T_2) relaxation. This decay of the transverse magnetization of $M(t)$ is indicated in the simplified PFG
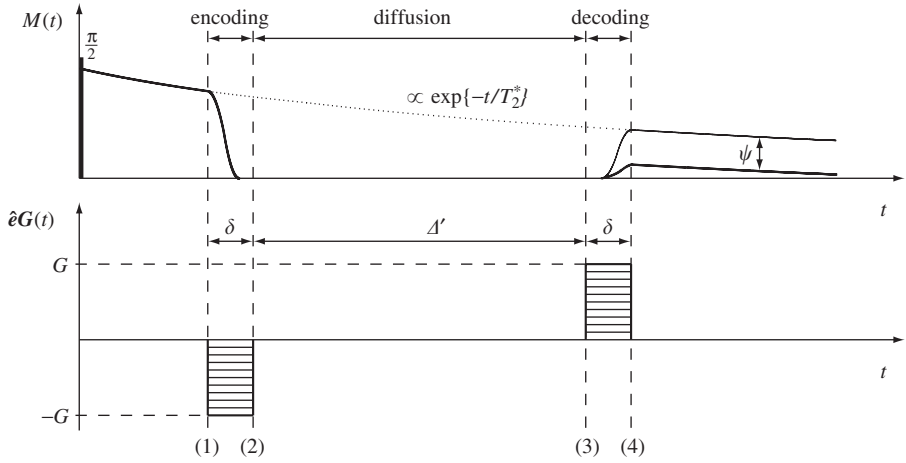
Fig. 4. FID pulse sequence with a schematic representation of the evolution of the NMR signal $M(t)$ without (dotted line) and with (solid lines) magnetic field gradient pulses $-G$ and $+G$.
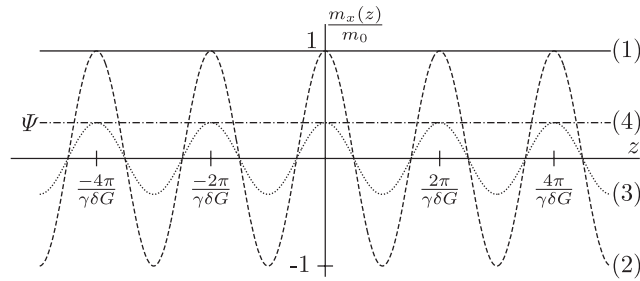

Fig. 5. Evolution of the x-component of the magnetization density in the rotating frame of reference under the influence of pulsed field gradients. The numbers on the curves refer to the times indicated in the simplified PFG NMR experiment drawn in Fig. 4.

NMR experiment in Fig. 4. For simplicity, however, it will be neglected in the following considerations.

2.2.1. *Phase encoding – the labeling process*

Let us consider the evolution of the magnetization density $m(z, t)$ in the rotating frame of reference (RFR) under the influence of the pulsed field gradients ($G(t)$) pointing in z-direction. Fig. 5 illustrates this evolution by drawing the x-component of $m(z, t)$ for the four instances of time indicated in Fig. 4. Just after the $\pi/2$ rf pulse, $m(z, t)$ is assumed to be homogeneously distributed in space with only a component in the x-direction of the RFR. This situation is shown by the straight line (1) in Fig. 5.

During a gradient pulse, the Larmor frequency $\omega(z, t)$ depends on the z-coordinate. In the RFR, a space-dependent offset frequency $\Delta\omega(z, t)$ results;

$$\Delta\omega(z, t) = \omega_0 - \omega(z, t) = -\gamma G(t)z, \tag{7}$$

which rotates $m(z, t)$ out of its original direction parallel to x. The phase φ of this rotation depends linearly on the z coordinate and increases with the intensity and duration of the gradient pulse

$$\varphi(z, t) = \int_0^t \Delta\omega(z, t')\,\mathrm{d}t' = -\gamma \int_0^t G(t')\,\mathrm{d}t'\ z. \tag{8}$$

At the end of the first gradient pulse (label (2) in Figs. 4 and 5), the accumulated phase is equal to $\gamma G\delta z$ and the magnetization density is twisted like a helix with the thread period of $l_G = 2\pi/(\gamma G\delta)^{-1}$ in z-direction. Using the complex notation for the x- and y-components of $m(z, t)$, this may be written as:

$$m(z) = m_x + \mathrm{i}m_y = m_0[\cos(\gamma G\delta z) + \mathrm{i}\sin(\gamma G\delta z)] = m_0 \exp\{\mathrm{i}\gamma G\delta z\}. \tag{9}$$

The x-component of this magnetization helix, which is plotted in Fig. 5, is a spatial cosine modulation of the original constant magnetization density. It is this spatially modulated magnetization density of the observed nuclear spins, which represents the label utilized in PFG NMR self-diffusion studies. Generally, it is generated by the first field gradient pulse in the PFG NMR sequence. In PFG NMR sequences consisting of more than two pulsed gradients, the total labeling process may be split into more than one pulsed gradient at the beginning of the sequence. Such advanced sequences are discussed in Section 3.2. The labeling part of PFG NMR sequences is often referred to as the *position encoding* period. The phase labeling introduced here is not only used for NMR diffusion studies, but represents also one of the basics of NMR imaging where it is usually called *phase encoding* (see, e.g., Refs. 39 and 42).

2.2.2. *Diffusion of the magnetization*

Since the magnetization is generated by the nuclear spins, which are hosted by atoms bounded to diffusing molecules, it represents a measure for the concentration of these molecules. More importantly, the molecular diffusion determines the further evolution of the space-dependent magnetization density in time. Thus, after a field gradient pulse labelled the molecules by a magnetization phase, the diffusion equation (Eq. (1)) represents the equation of motion for the space-dependent magnetization density with Eq. (9) as the corresponding initial condition.

In the following paragraphs, the solution of the diffusion equation will be deviated for this problem. Here, we will briefly depict what happens to the magnetization density after the phase encoding: The molecules, which are the carriers of the magnetization phase, change positions due to diffusion. This process smears out the original spatial phase distribution. It is a general property of sine and cosine shaped initial distributions as given in Eq. (9) that diffusion just reduces their amplitudes but does not change their spatial periods. Thus, the diffusion process continuously attenuates the amplitude of the magnetization density

until the second gradient pulse of opposite sign deletes the phase label (see Section 2.2.3) and, thus, refocuses the magnetization density in x-direction. The magnetization density immediately prior and after the second gradient pulse of the simplified PFG NMR sequence (Fig. 4) is also drawn in Fig. 5. Only after the second gradient pulse, a macroscopic magnetization and the corresponding NMR signal arises. However, it is attenuated due to diffusion by the factor Ψ as indicated in Figs. 4 and 5.

In order to find the NMR signal attenuation factor Ψ, we need to calculate the space and time dependence of the local magnetization during the time $\Delta = \Delta' + \delta$, which for $\Delta' \gg \delta$ is mainly determined by the distance between the two pulsed field gradients. This is achieved by solving the diffusion equation with the initial condition given by Eq. (9). According to Section 2.1.2, we just need to convolute the (1D) propagator $P(z_2, z_1, \Delta)$ with this initial condition given in Eq. (9).

$$m(G\delta, \Delta, z_2) = \int P(z_2, z_1, \Delta) m_0 \, e^{i\gamma\delta G z_1} \, dz_1 \qquad (10)$$

In a homogeneous infinitely extended region, m_0 is constant and the propagator $P(z_2, z_1, \Delta)$ is a Gaussian function. Thus, Eq. (10) may be written as:

$$m(G\delta, \Delta, z_2) = \frac{m_0}{\sqrt{4\pi D\Delta}} \int \exp\left[-\frac{(z_2 - z_1)^2}{4D\Delta}\right] e^{i\gamma\delta G z_1} \, dz_1. \qquad (11)$$

With the substitutions $z_1 - z_2 = z$ and $dz_1 = dz$ it follows

$$m(G\delta, \Delta, z_2) = \frac{m_0 e^{i\gamma\delta G z_2}}{\sqrt{4\pi D\Delta}} \int \exp\left[-\frac{z^2}{4D\Delta}\right] e^{i\gamma\delta G z} \, dz. \qquad (12)$$

The integral represents the Fourier transform of a Gaussian function with respect to the displacement z. It yields a decaying function $\Psi(G\delta, \Delta)$, which is exponential in $(\gamma\delta G)^2$. It does not effect the spatial period of the phase oscillation. Thus, Eq. (12) may be written as:

$$m(G\delta, \Delta, z_2) = \Psi(G\delta, \Delta) m_0 e^{i\gamma\delta G z_2} \qquad (13a)$$

$$\Psi(G\delta, \Delta) = \exp\{-(\gamma\delta G)^2 D\Delta\} \qquad (13b)$$

The factor Ψ represents the attenuation factor of the amplitude of the magnetization density due to self-diffusion as plotted in Figs. 4 and 5. The spatial period of its oscillations remains unchanged as seen from the factor $e^{i\gamma\delta G z_2}$. Due to this spatially oscillating magnetization density, there is no macroscopic magnetization and thus, no NMR signal observable.

2.2.3. Magnetization decoding – The NMR signal attenuation

The second field gradient pulse of amplitude $+G'$ superimposes an additional phase to the local magnetization in the same way as the first one (see Eq. (8)). At the end of this gradient pulse, the magnetization density is given by

$$m(G\delta, \Delta, z_2) = \Psi(G\delta, \Delta) m_0 \, e^{i\gamma\delta(G-G')z_2}. \qquad (14)$$

The NMR signal $M(G\delta, \Delta)$, which is obtained by integration of the magnetization density over the z-coordinate is calculated by:

$$M(G\delta, \Delta) = \Psi(G\delta, \Delta) \quad \int m_0 \, e^{i\gamma\delta(G-G')z_2} \, dz_2. \tag{15}$$

Only, if the amplitudes of both field gradients are the same ($G-G' = 0$) as drawn in Fig. 4, the space-dependent phase of the magnetization disappears and the NMR signal is refocused to its maximum possible amplitude. With $M_0 = \int m_0 dz$ and introducing the generalized gradient value b, summarizing all pulsed field gradient parameters which may be changed in the pulse sequence, one obtains in z-direction:

$$M(b) = \Psi(b)M_0 \tag{16a}$$

$$\Psi(b) = \exp\{-bD\} \quad \text{with} \quad b = (\gamma G\delta)^2\Delta. \tag{16b}$$

The attenuation factor Ψ, derived in Eq. (13) remains unchanged and damps the signal. Thus, Eq. (16) represents the NMR signal attenuation due to diffusion in the presence of pulsed magnetic field gradients. It is this signal attenuation, which is analyzed in PFG NMR to study self-diffusion processes. If one plots the logarithm of the NMR signal intensity as function of the generalized gradient parameter b, the slope of the decay curve yields the self-diffusion coefficient D.

It shall be mentioned here that already slightly different amplitudes or widths of the two pulsed field gradients yield additional losses in the NMR signal intensity. If we denote such differences with $d(G\delta) = G\delta - G'\delta'$,[58,59] Eq. (15) must be written as:

$$M(\tilde{G}\delta, \Delta) = \Psi(G\delta, \Delta) \quad \int m_0 \, e^{i\gamma d(G\delta)z} \, dz. \tag{17}$$

The integral is the Fourier transform of the amplitude of the magnetization density with respect to the field gradient parameter $\gamma \, d(G\delta)$ and represents the loss in NMR signal intensity due to mismatched pulsed field gradients. The physical reason for the loss in NMR signal intensity is the remaining phase label and, thus, the incomplete refocusing of the magnetization. This loss of PFG NMR signal due to mismatched field gradient pulses represents a major source for erroneously determined self-diffusion coefficients. Therefore, care should be taken to detect and compensate possible mismatches during the experiment. Such techniques are indispensable for NMR diffusion studies using high-intensity pulsed field gradients. They are reviewed in Section 4.

2.3. General relations for the PFG NMR signal attenuation

2.3.1. *The Fourier relationship with the averaged propagator*

The exponential attenuation of the NMR signal with increasing generalized gradient parameter b derived above (Eqs. (13) and (16)) holds for self-diffusion in an infinitely extended homogeneous medium, where the propagator is a Gaussian function. In general, the propagator may deviate from being a Gaussian function

with the consequence that the NMR signal will not decay exponentially with increasing b. However, already the existence of a 1D displacement probability density, which is nothing else than the averaged propagator as defined by Eq. (3), is sufficient to derive the signal attenuation in the PFG NMR experiment quite generally.

Due to self-diffusion during the time Δ between the pulsed field gradients, the molecules carrying the magnetization phase via the nuclear spins are displaced by the distance $z = z_2 - z_1$. According to Eq. (8), the net magnetization phase of a spin after the second pulsed gradient depends on its z-positions during the two pulsed gradients and, thus, on the molecular displacements in gradient direction.

$$\varphi = \gamma G \delta (z_2 - z_1) = \gamma G \delta z \tag{18}$$

The contribution of each nuclear spin to the total NMR signal is proportional to the phase factor $e^{i\varphi}$. The total signal is obtained by summing over all spins. This may be achieved by integrating the phase factor over all possible displacements in the sample. However, since the net phase depends on the displacement z, one needs to weight each phase factor by the probability density for the displacement. It is the averaged propagator $\bar{P}(z, \Delta)$ in gradient direction, which represents this probability density. Thus, the NMR signal attenuation is obtained by:

$$\Psi(G\delta, \Delta) = \frac{M(G\delta, \Delta)}{M_0} = \int \bar{P}(z, \Delta)\, e^{i\gamma G \delta z} \; dz. \tag{19}$$

This equation may be considered as the Fourier transform of the averaged propagator with respect to the displacement z. Thus, by Fourier inversion of Eq. (19) the averaged propagator may be directly deduced from the spin echo attenuation observed experimentally:

$$\bar{P}(z, \Delta) = \frac{1}{2\pi} \int \Psi(G\delta, \Delta)\, e^{-i\gamma G \delta z} \; d(\gamma G \delta) \tag{20}$$

The pair of Eqs. (19) and (20) represents the key advantage of the PFG NMR method for diffusion studies. The spin echo attenuation and the averaged propagator are Fourier conjugates, which connect data obtained in a straightforward experiment to theoretical descriptions of diffusion processes based on the diffusion equation (Eq. (1)). For self-diffusion in an infinitely extended homogenous region, it may easily be proofed that Eq. (19) yields the decaying exponential function derived in Eq. (16b).

2.3.2. *Model-free methods of data analysis*

In most PFG NMR experiments, the NMR signal attenuation is measured at a fixed diffusion time (Δ) as function of the pulsed field gradient width (δ) and amplitude (G), respectively (see Fig. 4 and Section 3.2). Due to the Fourier relationship between the signal attenuation and the averaged propagator, the actually observed pattern of Ψ depends on the system studied. Thus, a detailed analysis of the experimentally observed PFG NMR data will require an approach, which is optimized for the investigated system. Examples for such optimized approaches are

presented in Section 5. However, important key parameters characterizing the diffusion process may be obtained by using straightforward methods of data analysis not requiring any additional information than the measured PFG NMR signal attenuation. These model-free methods will be summarized here.

2.3.2.1. Single-exponential decay.   If the ln Ψ-vs.-b plots are linear, their slopes yield – according to Eq. (16) – the self-diffusion coefficient D. If these plots for different Δ do not collapse on one line, the self-diffusion coefficient depends on the observation time $(D = D(\Delta))$ and the time-dependence of the mean square displacement may be calculated via Einstein's relation (Eq. (6)).

Non single-exponential decays may have multiple origins such as a multi-component, anisotropic and restricted self-diffusion, respectively. Examples for detailed analysis in such cases are presented in Section 5. Regardless of the actual reason for the observed non single-exponential decay, which – due to the Fourier relationship – is equivalent to a non-Gaussian averaged propagator (see Eqs. (19) and (20)), the following three approaches for data analysis are always correct.

2.3.2.2. Propagator presentation.   By Fourier inversion of the experimentally observed PFG NMR signal attenuation, the averaged propagator $\bar{P}(z, \Delta)$ may be calculated (see Eq. (20)). Since $\bar{P}(z, \Delta)$ is the solution of the diffusion equation, it contains the maximum information available from PFG NMR. This approach requires good signal-to-noise data, acquisition of many data points and an attenuation of the signal by far more than one order of magnitude. It represents the basics of the method of dynamic NMR microscopy,[60] structural imaging[61] and of advanced methods in studying displacement correlations.[35,36,62] The propagator presentation of PFG NMR studies was introduced by Kärger *et al.*[27] and applied for the interpretation of diffusion measurements of hydrocarbons in microporous zeolites.

2.3.2.3. Moments of the averaged propagator.   Using the series expansion of the exponential term in Eq. (19), the attenuation of the NMR signal may be written as:

$$\Psi(G\delta, \Delta) = \int \bar{P}(z, \Delta)\, \mathrm{d}z + \sum_{n=1}^{\infty} \frac{(\mathrm{i}\gamma G\delta)^n}{n!} \int z^n \bar{P}(z, \Delta)\, \mathrm{d}z \qquad (21)$$

Due to the definition of the averaged propagator as displacement probability density, the first integral is equal to unity. The sum represents the higher moments $(n \geq 1)$ of the averaged propagator. Thus, the shape of the NMR signal attenuation is determined by the moments of the averaged propagator, describing the particle displacement in the investigated sample.

For pure self-diffusion, the averaged propagator is an even function (displacements by $+z$ and $-z$ are equally probable). Thus, all odd moments $(n = 2k + 1$ with $k \in N)$ in Eq. (21) become zero and the NMR signal attenuation is a real function given by the Fourier cosine transform of the averaged propagator and its even

moments, respectively.

$$\Psi(G\delta, \Delta) = 1 + \sum_{k=1}^{\infty} \frac{(-1)^k (\gamma G\delta)^{2k}}{(2k)!} \int z^{2k} \bar{P}(z, \Delta)\, dz \qquad (22)$$

In principle, the moments of the averaged propagator may be determined by fitting the observed NMR signal attenuation to a polynomial in $(\gamma g\delta)^2$. However, to our knowledge this approach was not yet being used for moments with $k > 1$. For $k = 1$ it is extensively used in PFG NMR data analysis and known as small gradient pulse approximation (see below).

If any kind of coherent motion such as, e.g., flow due to a pressure gradient, transport diffusion due to a concentration gradient and shaking of the sample due to mechanical instabilities, respectively, changes the centre of mass of the observed molecules during the time between the pulsed field gradients, the odd terms of the sum in Eq. (21) do not vanish yielding a non-zero imaginary part of the NMR signal attenuation. Such an imaginary part of $\Psi(g\delta, \Delta)$ means nothing else than a frequency independent (zero-order) phase shift of the NMR signal. Thus, a zero-order phase shift of the observed signal during a PFG NMR experiment, which depends on the pulsed gradient intensity and width, respectively, is an unambiguous indication for a coherent motion. It may – in principle – be used to characterize this motion by the odd moments of the propagator (compare also small gradient pulse approximation).

A superposition of a coherent and a diffusive motion (e.g., flow and flow-induced dispersion or flow- and self-diffusion) results in $\Psi(g\delta, \Delta,)$ being a complex function with non-zero real and imaginary parts. In this case, Fourier inversion of $\Psi(G\delta, \Delta)$ as discussed above is the preferred way of data analysis and may be used to separate both types of motion.[39,60,62]

2.3.2.4. Small gradient pulse approximation.   For small pulsed field gradients, all terms with $n > 2$ in the series expansion of the NMR signal attenuation given in Eq. (21) may be neglected yielding:

$$\Psi_s(G\delta, \Delta) = 1 + i\gamma G\delta \int z(\Delta)\bar{P}(z, \Delta)\, dz - \frac{(\gamma G\delta)^2}{2} \int z^2(\Delta)\bar{P}(z, \Delta)\, dz$$

$$= 1 + i\gamma G\delta \langle z(\Delta) \rangle - \frac{(\gamma G\delta)^2}{2} \langle z^2(\Delta) \rangle. \qquad (23)$$

The first integral is the first moment of the averaged propagator. It defines the mean displacement $\langle z(\Delta) \rangle$, which is zero for pure self-diffusion and non-zero only for a coherent motion changing the centre of mass of the observed molecules. Thus, the imaginary part of $\Psi_s(G\delta, \Delta)$, i.e., the phase shift of the observed PFG NMR signal may be analyzed to characterize this motion by the mean displacement and the velocity v of the centre of mass of the molecules, respectively.

$$\frac{d\, \mathfrak{I}(\Psi_s(G\delta, \Delta))}{d(\gamma G\delta)} = \langle z(\Delta) \rangle = \Delta v \qquad (24)$$

The second integral in Eq. (23) represents the second moment of the averaged propagator, which is the mean square displacement $\langle z^2(\varDelta) \rangle$ in gradient direction. Thus, the mean square displacement may always be obtained by just analyzing the initial slope of the real part of the PFG NMR signal attenuation.

$$-\frac{\mathrm{d}\,\Re(\varPsi_s(G\delta,\varDelta))}{\mathrm{d}(\gamma G\delta)^2} = \frac{\langle z^2(\varDelta) \rangle}{2} = \varDelta\,D_{\mathrm{eff}}(\varDelta) \tag{25}$$

In close analogy to the Einstein relation (Eq. (6)), the second part of Eq. (25) defines the effective self-diffusion coefficient $D_{\mathrm{eff}}(\varDelta)$, which may be calculated from the initial slope and used to characterize the investigated system.

2.3.3. Narrowgradient pulse approximate

The derivations for the PFG NMR signal attenuation presented in Sections 2.2, 2.3.1 and 2.3.2 do not take into account the self-diffusion during the time intervals δ, where the pulsed field gradients are applied. Thus, the relations derived are correct for infinitely small gradient pulses ($\delta \to 0$). As can be seen in Eq. (8), the phase φ, which determines the spatial period of the local magnetization, depends on the time integral over the gradient pulse $G(t)$. Thus, in principle one may fulfill the requirement of infinitely small gradient pulses for a given spatial period of the magnetization density by a corresponding increase of the amplitude of the pulsed gradient, keeping the time integral over $G(t)$ constant. However, there are experimental and technical limitations for the maximum amplitude and minimum width of the pulsed field gradients, which require a finite value for δ. As long, as one can ensure that $\delta \ll \varDelta$, the considerations in Sections 2.2 and 2.3 hold in good approximation. In PFG NMR, the simplification $\delta \ll \varDelta$ is called *narrow gradient pulse approximation*.

Generally, the pulsed field gradients are generated by short electrical current pulses flowing through a gradient coil, having an ohmic resistance R and an inductance L. Thus, rectangular shaped gradient pulses as drawn in Fig. 4 would require infinitely high-output voltages of the current source, driving the gradient current. In practice, the maximum output voltage is limited, which leads to finite rise and fall times of the gradient pulse. Thus, the gradient pulse will deviate from a rectangular shape. However, as long as the narrow gradient pulse approximation is applicable, the above-derived relations for the NMR signal attenuation remain unchanged if one replaces the pulsed gradient amplitude G by an effective one defined by:

$$G_{\mathrm{eff}} = \frac{1}{\delta}\int_\delta G(t)\,\mathrm{d}t. \tag{26}$$

If the narrow gradient pulse approximation is not applicable, because δ is in the same order of magnitude than $\varDelta$, or the encoding and decoding periods of the pulse sequence are split into more than one interval (as for the pulse sequences discussed in the next section), the self-diffusion during these intervals and the shape of the gradient pulses must be taken into account in the analysis of the observed spin echo

attenuation. The Bloch–Torrey equation presents the theoretical background for such considerations. It will be discussed in Section 2.4.2.

2.4. Spin echo PFG NMR

The simplified PFG NMR sequence (Fig. 4) with two pulsed gradients of opposite polarity for phase encoding and magnetization decoding, respectively, has the disadvantage that the observed NMR signal is the FID. Therefore, the accessible diffusion time Δ is limited by the relaxation time T_2^*, describing the decay of the transverse magnetization in inhomogeneous polarizing magnetic fields B_0. Since B_0 fields used in NMR are never perfectly homogeneous, T_2^* of the FID is always smaller than the transverse relaxation time in a homogeneous magnetic field T_2. The reason is the successive dephasing of the magnetization due to spatially inhomogeneous distribution of Larmor frequencies. By using suitable rf pulse sequences, the dephased magnetization may be refocused to a spin echo NMR signal even at times large compared to the T_2^* relaxation time. Because the observation of spin echoes allows to extend the diffusion times beyond T_2^*, most PFG NMR diffusion studies are performed using such spin echo rf sequences. Generally, the necessary phase encoding and magnetization decoding magnetic field gradients are applied prior to and after the refocusing rf pulse, respectively.

2.4.1. *Effective magnetic field gradient pulses*

The refocusing rf pulses, which are π pulses in the primary spin echo sequence and the CPMG sequence, invert the effect of the field gradients on the accumulated magnetization phase. In the concept of the effective magnetic field gradients introduced by Karlicek and Lowe,[17] this is taken into account by inverting the sign of all magnetic field gradients prior to the considered refocusing π rf-pulse. Starting from the time of the spin echo maximum (t_e), this method is applied successively for each refocusing π rf-pulse yielding the effective magnetic field gradients.

In order to compare different PFG NMR pulse sequences with respect to their signal attenuation properties, it is necessary to define the direction of the field gradients. Throughout this paper, the directions of pulsed and constant field gradients are defined by particular gradients, which will be designated in the individual pulse sequences. In the laboratory frame of reference (LFR), these selected gradients determine the direction of unit vectors. In the pulse sequence diagrams drawn, all the gradients (including the effective ones) are displayed as scalar products with their respective unit vector. Using these unit vectors, the signs and directions of the respective (pulsed and constant) effective gradients necessary for the calculation of the NMR signal attenuation may be determined consistently.

For example, in the primary spin echo sequence with two pulsed gradients of equal polarity $\mathbf{G}(t)$ in the LFR (see Fig. 6), which was the first PFG NMR experiment proposed for diffusion studies,[11] the second pulsed gradient is chosen to
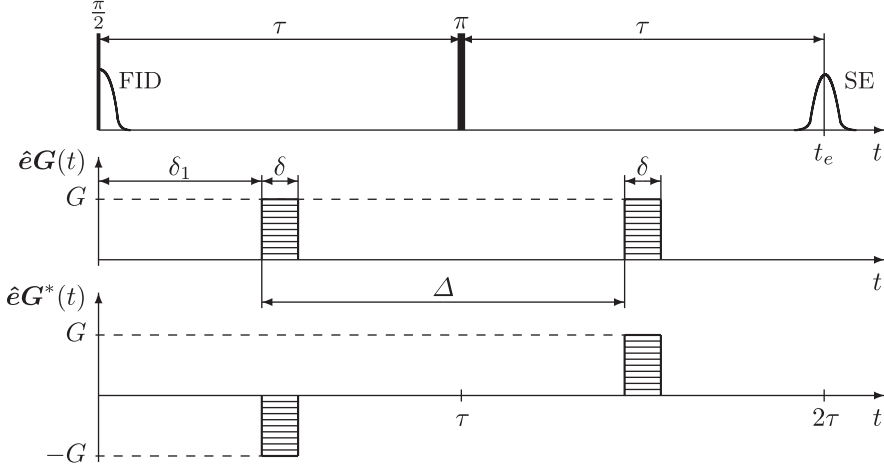
Fig. 6. Primary spin echo sequence with two pulsed magnetic field gradients $G(t)$ and the corresponding effective gradients $G^*(t)$. The π rf-pulse inverts the first gradient pulse. $\hat{e}$ represents the unit vector in direction of the second pulsed magnetic field gradient.

determine the direction of the unit vector $\hat{e}$. Thus, the time dependence of the pulsed gradient $G(t)$ may be drawn unambiguously by $\hat{e}G(t)$. The transformation into the effective gradients $G^*(t)$ is given by:

$$G(t) \rightarrow G^*(t) = \begin{cases} -G(t) & \text{for} \quad t \leq \tau \\ G(t) & \text{for} \quad \tau \leq t \end{cases} \tag{27}$$

and illustrated in Fig. 6 by the time dependence of $\hat{e}G^*(t)$. The effective gradients consist of a phase encoding gradient and a magnetization decoding gradient of opposite signs. Their pattern corresponds to the pulsed gradients in the simplified PFG NMR sequence (Fig. 4) used to derive the basic relations for the NMR signal attenuation $\Psi(G\delta, \Delta)$ in Sections 2.2–2.3.3. Thus, these relations also describe the attenuation of the spin echo NMR signal amplitude (spin echo attenuation) due to diffusion. Therefore, it is also denoted by the factor Ψ.

2.4.2. Bloch–Torrey equation

If – for any of the reason discussed in Section 2.3.3 – the narrow gradient pulse approximation is not applicable, the spin echo attenuation due to diffusion may be calculated by the Bloch–Torrey equation. It represent the equation of motion for the three components of the local magnetization $M^l(r, t)$ under the influence of the magnetic field B (including the effects of rf pulses and magnetic field gradients), transverse (T_2) and longitudinal (T_1) relaxation as well as self-diffusion (D)

$$\frac{\partial M^l(r, t)}{\partial t} = \gamma M^l \times B - \frac{M_x^l e_x + M_y^l e_y}{T_2} - \frac{M_z^l - M_0^l}{T_1} e_z + D\nabla^2 M^l. \tag{28}$$

Eq. (28) combines the Bloch equations for the macroscopic magnetization[1] with the diffusion equation (Eq. (1)). By integrating the local magnetization $M^l(r, t)$ over the sample volume, one obtains the time-dependent magnetization $M(t)$. Their x- and y- components are proportional to the observable NMR signal. In Eq. (28), M_0^l denotes the local equilibrium magnetization for a homogeneous polarizing magnetic field B_0 pointing in z-direction ($B_0 = (0, 0, B_0)$).

Due to the magnetic field gradients $G(t)$, the magnetic field B depends on time and space. With the generally accepted approximation that off-resonance magnetic field components perpendicular to B_0 may be neglected in the evaluation of Eq. (28),[63] the magnetic field gradients modulate only the z-component of $B(r, t)$

$$B_z(r, t) = B_0 + rG(t) \tag{29}$$

and Eq. (28) may be solved by a separation of variables ansatz (for details see, e.g., Refs. 17 and 64). This ansatz leads to a differential equation for the spin echo attenuation given by:

$$\frac{d\Psi(t)}{dt} = -\Psi(t)\, D\left[\gamma \int_0^t dt'\, G^*(t')\right]^2 \tag{30}$$

with the so-called double integral as the solution

$$\Psi(t) = \exp\left\{-D\gamma^2 \int_0^t dt'\left[\int_0^{t'} dt''\, G^*(t'')\right]^2\right\}. \tag{31}$$

Eq. (31) depends only on the self-diffusion coefficient D and the time integrals over the effective magnetic field gradients $G^*(t)$. The appearance of the effective gradients, as defined in the previous section, ensures that the inverting action of refocusing rf pulses is taken into account in the spin echo attenuation. Thus, the total spin echo amplitude, which is observed at the echo time (t_e) is given by:

$$M(t_e) = \Psi(t_e)R(t_e)M_0, \tag{32}$$

where M_0 represents the initial magnetization and $R(t_e)$, which depends on the actual rf pulse sequence used, denotes the signal decay due to transverse and longitudinal relaxation.

The application of the double integral (Eq. (31)) to the pulsed gradients in the primary spin echo sequence drawn in Fig. 6 yields:

$$\Psi(t_e) = \exp\left\{-D\gamma^2\delta^2\left(\Delta - \frac{1}{3}\delta\right)G^2\right\}, \tag{33}$$

where G^2 denotes the square of the pulsed field gradient amplitude as already known from Eq. (16). The term $\frac{1}{3}\delta$ represents the correction due to diffusion during the pulsed field gradients.

Eq. (33) describes only the correct spin echo attenuation due to diffusion, if the spin echo is refocused to its maximum possible amplitude. This requires that the spatially dependent phase shift caused by the phase encoding field gradients is totally compensated by the magnetization decoding gradients at the echo time t_e.

In terms of the effective field gradients this condition may be written as:

$$\int_0^{t_e} \boldsymbol{G}^*(t)\, \mathrm{d}t = 0. \tag{34}$$

2.4.3. *Constant magnetic field gradients*

In principle, constant magnetic field gradients $\boldsymbol{g}$ have the same influence on the diffusion-based spin echo attenuation as pulsed field gradients. Applying the double integral (Eq. (31)) to the primary spin echo with a constant magnetic field gradient instead of a pulsed field gradient yields:

$$\Psi(t_e) = \exp\left\{ -\frac{2}{3} D\gamma^2 \tau^3 \boldsymbol{g}^2 \right\} \quad \text{with} \quad \boldsymbol{g}^*(t) = \begin{cases} -\boldsymbol{g} & \text{for} \quad t \leq \tau \\ \boldsymbol{g} & \text{for} \quad \tau \leq t \end{cases} \tag{35}$$

where $\boldsymbol{g}^*(t)$ denotes transformation of the constant field gradient into the corresponding effective gradient.

As mentioned in the introduction, constant gradient NMR diffusion studies (see Refs. 3 and 6–8) were performed long before the invention of the PFG NMR technique by Stejskal and Tanner.[11] The CPMG sequence[4,5] was actually invented to reduce the diffusion influence in relaxation studies. This is achieved by using short τ values and simultaneously increasing the time scale of observation of the transverse magnetization decay by successively applying refocusing π rf pulses at the time τ after each recorded spin echo maximum. Each of the π rf pulses leads to a sign inversion of the preceding effective (constant) gradient and the diffusion attenuation of the nth spin echo amplitude, which arises in the CPMG echo train at the time $t_e = 2\tau n$, is given by:

$$\Psi(t_e) = \exp\left\{ -\frac{1}{3} D(\gamma \boldsymbol{g}\tau)^2 t_e \right\}. \tag{36}$$

Constant gradient diffusion studies have the disadvantage that the magnetic field gradient is on during the rf pulses and the signal detection, which, e.g., limits the excited sample volume and, thus, the signal-to-noise ratio due to finite transmitter bandwidth as well as leads to the loss of spectral information in the detected signal. Nevertheless, nowadays the strongest gradients used for NMR diffusion studies are those, generated permanently in the fringe field of the homogeneous main NMR magnet[65] or even in specially gradient-maximized super-conducting magnets.[66] Additionally, modern inside-out NMR instruments, such as down-hole logging tools[67,68] and the NMR Mouse,[69] which have an inhomogeneous polarizing magnetic field, employ τ-dependent spin echo measurements to study diffusion processes.[70,71]

2.4.4. *Coupling between pulsed and background field gradients*

In many PFG NMR experiments, the pulsed field gradients used for the diffusion studies lead to the desired spin echo attenuation. However, so-called background field gradients may often be present as well. Sometimes, constant background field

gradients are applied intentionally. In other cases, e.g., where the polarizing magnetic field is inhomogeneous by design or where it is disturbed due to internal susceptibility contrasts in the investigated sample, background field gradients are inevitable and may be considered to have properties of a constant field gradient. Regardless of its origin, if background magnetic field gradients are present, they will interfere with the phase encoding and the magnetization decoding of the PFG NMR experiment and, thus, lead to an alteration of the pattern of the spin echo attenuation.

The simultaneous presence of constant background field gradients $\boldsymbol{g}$ and pulsed field gradients $\boldsymbol{G}(t)$ may be accounted for by replacing $\boldsymbol{G}^*(t)$ in the double integral (Eq. (31)) by the sum of both effective gradients $\boldsymbol{G}^*(t) + \boldsymbol{g}^*(t)$. As a consequence, the double integral and, thus, the spin echo attenuation disintegrates in three terms.[21,64]

$$\Psi(t) = \exp\{-D\gamma^2[A_p(t) + A_c(t) + A_b(t)]\} \tag{37}$$

with

$$A_p(t) = \int_0^t \mathrm{d}t' \left[\int_0^{t'} \boldsymbol{G}^*(t'') \, \mathrm{d}t''\right]^2, \tag{37a}$$

$$A_c(t) = 2\int_0^t \mathrm{d}t' \int_0^{t'} \boldsymbol{G}^*(t'') \, \mathrm{d}t'' \int_0^{t'} \boldsymbol{g}^*(t'') \, \mathrm{d}t'' \tag{37b}$$

and

$$A_b(t) = \int_0^t \mathrm{d}t' \left[\int_0^{t'} \boldsymbol{g}^*(t'') \, \mathrm{d}t''\right]^2, \tag{37c}$$

where $A_{p(\text{ulse})}$ and $A_{b(\text{ackground})}$ depend only on the pulsed field gradient and the constant background field gradient, respectively, and $A_{c(\text{ross})}$ denotes the *cross term* between both gradients.

Generally, the term A_p is known, since the time dependence of the pulsed field gradients represents the quantity, which is varied during PFG NMR experiment to measure the spin echo attenuation. The resulting part of the spin echo attenuation will depend on the square of the pulsed gradient amplitude. A_p represents the central quantity in PFG NMR in order to determine diffusion coefficients. In some literature, this term is denoted as b-value, ($b \equiv \gamma^2 A_p$, compare also Eq. (16)). We will use this abbreviation whenever suitable and, especially, on the abscissa of spin echo attenuation plots.

In principle, the pure background gradient term A_b has the same properties as A_p and may easily be incorporated into the analysis of the spin echo attenuation. Even if the background gradient is not known, A_b represents just an additional global attenuation term. It reduces the total signal amplitude in much the same way as the relaxation term $R(t_e)$, but it does not change with changing the pulsed field gradients. Thus, the term A_b does not alter the analysis of the experimentally observed spin echo attenuation.

In contrast, the cross term A_c depends on both the pulsed and the background field gradients. Thus, it changes its value by changing the pulsed field gradients resulting in a deviation of the spin echo attenuation from the pure quadratic dependence on $\boldsymbol{G}$. Thus, in general, the cross term A_c must be taken into account in analyzing the PFG NMR spin echo attenuation. If this is not possible, since the background gradient is not known, one needs to perform PFG NMR experiments, which reduce the influence of this cross term or even suppress it completely. Such background gradient suppression is possible by using NMR spin echo sequences with APFG NMR. They will be discussed in the Section 3, using the approach of Eq. (37).

2.4.5. *Spin echo pulse sequence according to Stejskal and Tanner*

In order to illustrate the application of Eq. (37), we consider again the primary spin echo (SE) NMR sequence, now with pulsed gradients $\boldsymbol{G}(t)$ and a constant background gradient $\boldsymbol{g}$ as drawn in Fig. 7. Their transformations into the effective gradients were already discussed and are given by Eqs. (27) and (35), respectively. The three terms of the spin echo attenuation calculated by using Eq. (37) are:

$$A_p(t_e) = \delta^2 \left(\Delta - \frac{1}{3}\delta \right) \boldsymbol{G}^2, \tag{38a}$$

$$A_c(t_e) = \delta \left[2\tau^2 - \frac{2}{3}\delta^2 - (\delta_1^2 + \delta_2^2) - \delta(\delta_1 + \delta_2) \right] \boldsymbol{G}\boldsymbol{g} \tag{38b}$$

and

$$A_b(t_e) = \frac{2}{3}\tau^3 \boldsymbol{g}^2, \tag{38c}$$

which are consistent with the result given in the original publication of Stejskal and Tanner.[11] The pulsed gradient term A_p and the background gradient term A_b are
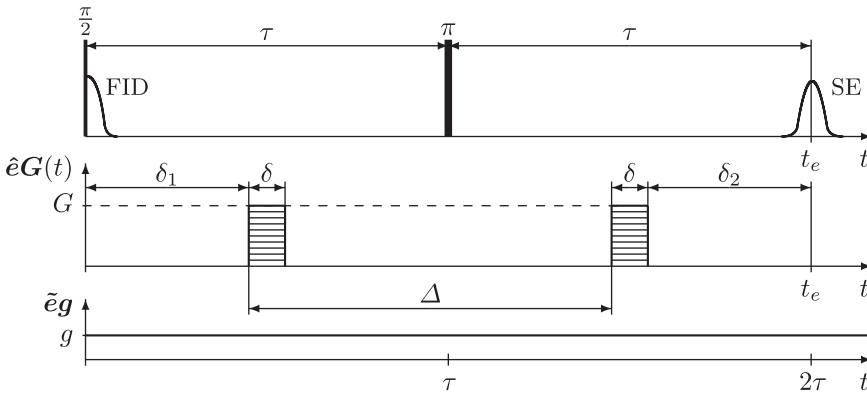
Fig. 7. Primary spin echo sequence with pulsed field gradients $\boldsymbol{G}(t)$ and a constant (background) field gradient $\boldsymbol{g}$. $\hat{\boldsymbol{e}}$ and $\tilde{\boldsymbol{e}}$, respectively, denote the unit vectors in the directions of both gradients during the second τ interval in the LFR.

already known from Eqs. (33) and (35), respectively. The cross term A_c, representing the coupling between both gradients, depends on the scalar product $\boldsymbol{Gg}$ and the time parameters of the pulse sequence. It has its maximum if both gradients act in parallel and disappears if they are perpendicular to each other.

By generally evaluating the ratio $A_c(t_e)/A_p(t_e)$, one can show that the cross term is always proportional to (see Ref. 64):

$$A_c(t_e) \propto \cos(\alpha) \frac{g\tau}{G\delta} A_p(t_e), \tag{39}$$

where α denotes the angle between the background and the pulsed field gradients. Thus, the cross term may only be neglected in the evaluation of the spin echo attenuation measured with the Stejskal and Tanner PFG NMR sequence, if the condition $g\tau \ll G\delta$ is fulfilled or background and pulsed gradients are perpendicular to each other.

2.4.6. *Stimulated spin echo pulse sequence according to Tanner*

In systems where the longitudinal (T_1) relaxation time exceeds the transverse (T_2) relaxation time, it may be of advantage to observe a stimulated spin echo. It is generated by three successive $\pi/2$ rf pulses as drawn in the top of Fig. 8. The second $\pi/2$ rf pulse flips the transverse magnetization into the longitudinal direction, where it decays with the longitudinal (T_1) relaxation time. After the so-called z-storage interval $\varDelta'$, the magnetization is recalled into the transverse plane by the third $\pi/2$ rf pulse, where it forms the stimulated spin echo (STE). A magnetization phase label introduced by the field gradients in the *preparation* interval prior the second $\pi/2$ rf pulse is preserved during the z-storage interval and refocused after the third $\pi/2$ rf pulse during the *read* interval (Fig. 8). For equal spin echo times t_e and in the
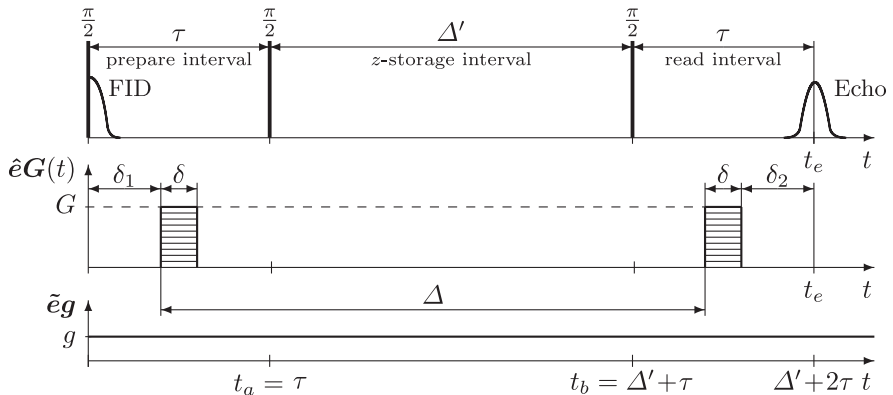
Fig. 8. Simulated spin echo sequence with pulsed field gradients $\boldsymbol{G}(t)$ and a constant (background) field gradient $\boldsymbol{g}$. $\hat{\boldsymbol{e}}$ and $\tilde{\boldsymbol{e}}$, respectively, denote the unit vectors in the directions of the pulsed and the constant background field gradients during the second τ interval in the LFR.

absence of any gradients, this sequence offers a gain in observable NMR signal intensity with respect to the primary SE sequence, if (see Ref. 72)

$$\ln 2 \le \Delta' \left(\frac{1}{T_2} - \frac{1}{T_1} \right). \tag{40}$$

For pulse sequence with a z-storage interval, there are two options for the formation of a STE.[18] The first option requires that the integrals over the effective gradients during the preparation interval ($I_p(t)$)

$$I_p(t) = \int_0^t [\boldsymbol{G}^*(t') + \boldsymbol{g}^*(t')]\, \mathrm{d}t' \tag{41}$$

and during the read interval ($I_r(t)$)

$$I_r(t) = \int_{t_b}^t [\boldsymbol{G}^*(t') + \boldsymbol{g}^*(t')]\, \mathrm{d}t' \tag{42}$$

fulfill the equation (condition I)

$$0 = I_p(t_a) - I_r(t_e), \tag{43}$$

where $\boldsymbol{G}^*(t)$ and $\boldsymbol{g}^*(t)$ denote the time dependence of all effective pulsed and background gradients of the stimulated spin echo PFG NMR sequence, respectively. However, a STE may arise also, if (condition II)

$$0 = I_p(t_a) + I_r(t_e) \tag{44}$$

is fulfilled. Condition II corresponds to the condition for the formation of a spin echo considered in Eq. (34) and applies only for STE-like sequences with additional refocusing π rf pulses. However, as Cotts *et al.*[18] showed, the cancellation of unwanted cross terms in the spin echo attenuation of STE-like PFG NMR sequences – if possible at all – is only to realize for condition I. Additionally, since – to our knowledge – all applications of STE PFG NMR sequences are based on condition I, we will restrict all our further considerations to this case.

Since the physical situation for the magnetization, which is flipped by the first and the third $\pi/2$ rf pulses from the z-direction into the transverse plane, is the same, the relations between the signs of the effective and the corresponding laboratory gradients in the read and the preparation intervals must be the same. Consequently, only condition I ensures that a STE occurs. This is formally accounted for by an additional sign inversion of the effective gradients acting during the read interval before they are used to calculate the spin echo attenuation by Eq. (37). With these rules, the pulsed, cross and background gradient terms of the STE PFG NMR sequence according to Tanner are found to be[12]

$$A_p(t_e) = \delta^2 \left(\Delta - \frac{1}{3}\delta \right) \boldsymbol{G}^2, \tag{45a}$$

$$A_c(t_e) = \delta \left[2\tau(\varDelta' + \tau) - \frac{2}{3}\delta^2 - (\delta_1^2 + \delta_2^2) - \delta(\delta_1 + \delta_2) \right] \boldsymbol{Gg} \qquad (45b)$$

and

$$A_b(t_e) = \tau^2 \left(\varDelta' + \frac{2}{3}\tau \right) \boldsymbol{g}^2, \qquad (45c)$$

which are consistent with the corresponding equations in the original publication.

Due to the same pattern of the pulsed gradients, the pulsed gradient terms A_p of the SE (Eq. (38)) and the STE (Eq. (45)) NMR diffusion experiment are equal. Comparing the background (A_b) and cross (A_c) terms of both sequences shows that they coincide for $\varDelta' = 0$. The cross term of the STE PFG NMR experiment exhibits a similar linear dependence on the pulsed gradients as found for the SE PFG NMR experiment. If the z-storage time $\varDelta'$ dominates the diffusion time $\varDelta$, which is usually the case in STE PFG NMR experiments, the cross term may also be estimated by Eq. (39). Thus, also in the stimulated spin echo NMR diffusion experiment with two pulsed gradients of equal polarity, disturbing influences of an unknown background gradient may only be excluded, if the condition $g\tau \ll G\delta$ is fulfilled.

3. REVIEW OF PFG NMR PULSE SEQUENCES

Until the pioneering idea of Karlicek and Lowe,[17] who first applied APFG in conjunction with the π rf pulses in a CPMG sequence, and its extension by Cotts *et al.*[18] who combined the STE sequence with such APFG, only the SE and the STE with unipolar pulsed or even constant field gradients as discussed in Sections 2.4.5 and 2.4.6 were used for PFG NMR diffusion studies. Obviously, the degree of freedom to change parameters in a NMR diffusion experiment increases if APFG are applied. This led to a number of new APFG NMR pulse sequences proposed for diffusion studies. Most of these sequences have in common that their phase encoding period as well as their magnetization decoding period consist of more than one pulsed field gradient. Generally, due to the increased number of adjustable parameters in the APFG NMR pulse sequence, the spin echo attenuations are more complex than considered so far. Nevertheless, the concept to understand these different sequences is based on the Bloch–Torrey equation (Eq. (28)), the resulting double integral for the spin echo attenuation (Eq. (31)) and the general decomposition of this spin echo attenuation into the pulsed, background and cross terms (Eq. (37)) introduced in Section 2.4.

In this section, we will discuss the most frequently used PFG NMR sequences with respect to their spin echo attenuation properties. In order to be able to do this consistently, we will first introduce a generalized PFG NMR sequence and give the spin echo attenuation for it. After a brief discussion of APFG NMR sequences, which are based on the CPMG experiment,[4] we show how the result of the generalized PFG NMR sequence may be used to derive the spin echo attenuations of STE APFG NMR sequences. All equations presented in the corresponding sections

were calculated with the symbolic calculus program Maple IV.5 (students edition) and cross-checked against known results. Based on our results, we critically review some of the corresponding relations reported in the literature. Finally, we utilize the generalized PFG NMR sequence to introduce the concept of MPFG ratios, recently proposed for advanced cross-term suppression and introduce a joint formalism for the spin echo attenuation equation of two- and four-pulse PFG NMR sequences.

3.1. The generalized PFG NMR sequence

The generalized PFG NMR sequence as drawn in Fig. 9 is developed on the basis of the 13-interval condition I sequence of Cotts *et al.*[18] It consists of the same rf pulse scheme like the standard 13-interval sequence with refocusing π rf pulses in the preparation and read intervals and a z-storage interval (Δ') between the second and third $\pi/2$ rf pulses.

In contrast to the original 13-interval condition I sequence, the first and the last pulsed field gradients of the generalized PFG NMR sequence, which will be denoted as F gradients, may have different amplitudes than the second and third pulsed field gradients, which will be denoted as G gradients. Such unequal pulsed field gradients were first proposed by Sørland *et al.*[73] who applied them to suppress unwanted coherence pathways in spin echo NMR diffusion studies.
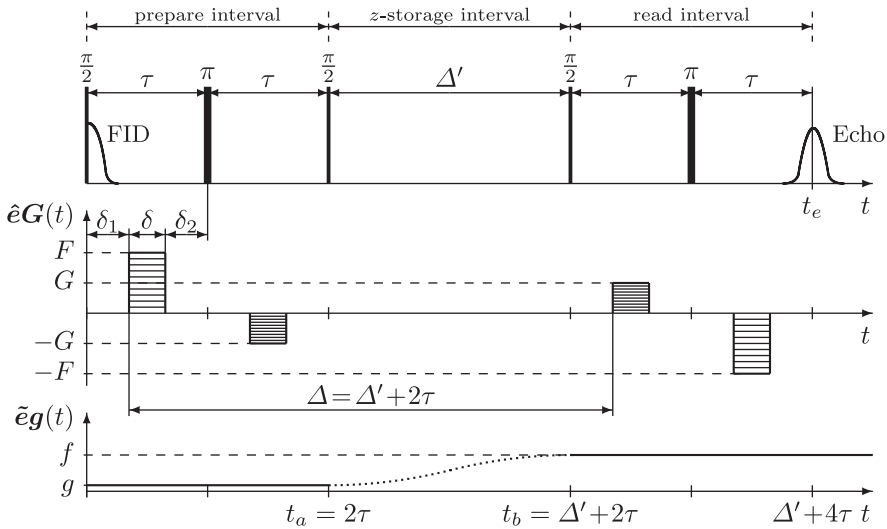
Fig. 9. Generalized PFG NMR sequence with pairs of unequal pulsed gradients $G(t)$ with amplitude F and G, respectively, and different background gradients $g(t)$ during the preparation (g) and read (f) interval. The positions and lengths of the pulsed gradients are equal in each τ interval, $\hat{e}$ and $\tilde{e}$ denote the unit vectors in direction of the third pulsed gradient and the first background gradient in the LFR, respectively. [*Source:* Adapted from Ref. 64.]

Additionally, a background gradient is taken into account. In generalization of the usual assumption of a constant background gradient during the whole time of the pulse sequence, a background gradient is considered, which may change its value from g during the preparation interval to f during the read interval. Such variable background gradients may account for diffusion processes in heterogeneous (e.g., porous) media, where the molecules move into locations with different local background gradients during a long z-storage interval but experience different constant background gradients during the generally short preparation and read intervals.

When transforming the laboratory gradients of the generalized PFG NMR sequence into the effective gradients one has to obey the following rules: (1) The signs of the effective and laboratory gradients acting immediately prior to the observed spin echo should be equal. This is the convention proposed by Karlicek and Lowe[17] and also applied by Cotts *et al.*[18] (2) The π rf pulse in the read interval inverts the signs of the gradients acting during the τ interval immediately prior to it. (3) Due to the same physical situation for the magnetization after the $\pi/2$ rf pulses (compare Section 2.4.6), the relations between the signs of laboratory and corresponding effective gradients acting during the first τ interval of the preparation interval must be the same as during the first τ interval of the read interval. (4) The sign relation between laboratory and corresponding effective gradients acting during the first τ interval (found by rule 3) must be inverted again in order to find the sign relation for the gradients acting during the (second) τ interval after the refocusing π rf pulse of the preparation interval. For illustration of these rules, the reader is referred to Fig. 11, where the laboratory and effective gradients of the original 13-interval condition I sequence are drawn.

In order to account for condition I in the calculation of the spin echo attenuation for the generalized PFG NMR sequence using Eq. (37), the signs of the determined effective gradients in the read interval must be inverted additionally [compare 18]. With these rules, the three terms of the spin echo attenuation of the generalized PFG NMR sequence are found to be

$$A_p(t_e) = \delta^2 \left[(\Delta' + \tau)(\boldsymbol{G} - \boldsymbol{F})^2 + 2\tau \boldsymbol{F}^2 - \frac{1}{3}\delta(\boldsymbol{G}^2 + \boldsymbol{F}^2) \right], \tag{46a}$$

$$A_c(t_e) = \delta \left\{ \left[\left(\delta_1^2 + \delta_1\delta + \frac{1}{3}\delta^2 \right)(\boldsymbol{G} + \boldsymbol{F}) - 2\tau^2 \boldsymbol{F} \right](\boldsymbol{f} - \boldsymbol{g}) \right.$$
$$\left. + \tau(\delta_1 - \delta_2)(\boldsymbol{G}\boldsymbol{g} - \boldsymbol{F}\boldsymbol{f}) \right\} \tag{46b}$$

and

$$A_b(t_e) = \frac{2}{3}\tau^3(\boldsymbol{f}^2 + \boldsymbol{g}^2). \tag{46c}$$

This result was first published in Ref. 64. In the following sections it will be used to derive the corresponding relations for some known APFG NMR sequences.

3.2. APFG NMR sequences based on the CPMG experiment

If there is no z-storage interval between the phase encoding and magnetization decoding pulsed field gradients, a spin echo NMR signal may only arise due to the phase inversion properties of π rf pulses in the pulse sequence. In such pulse sequences, which are similar to the CPMG sequence,[4] the definition of the effective gradients and the condition for the formation of the spin echo (Eq. (34)) has to follow the rules proposed by Karlicek and Lowe.[17] These rules were introduced in this paper in Sections 2.4.1 and 2.4.2 and already applied to calculate the three terms of the spin echo attenuation of the original Stejskal and Tanner SE PFG NMR sequence (see Eq. (38)). This SE NMR diffusion experiment may be considered as the simplest CPMG-like PFG NMR sequences, since it consists only of one refocusing π rf pulse.

3.2.1. *Pulse sequence according to Karlicek and Lowe*

The APFG NMR sequences proposed by Karlicek and Lowe[17] consist of a CPMG sequence with $n = 4m+1$ ($m = 1, 2, 3, \ldots$) refocusing π rf pulses and an even number of $n-1$ pulsed gradients in the 2τ intervals between the π rf pulses. The $(n-1)/2$ successive pulsed gradients of the first (phase encoding) and second (magnetization decoding) series have an alternating polarity in the LFR. However, the last gradient of the phase encoding series and the first gradient of the magnetization decoding series have the same polarity. Thus, the effective pulsed gradients of the phase encoding and magnetization decoding series, respectively, have equal but opposite signs, which fulfills the spin echo condition (Eq. (34)). For $m = 1$, this sequence is drawn in Fig. 10.
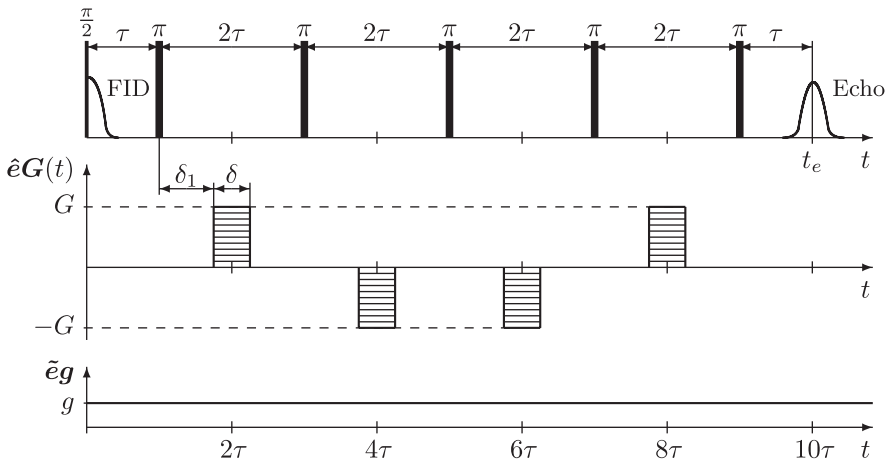
Fig. 10. Pulse sequence according to Karlicek and Lowe[17] with pulsed gradients $G(t)$ and a constant background gradient g. $\hat{e}$ and $\tilde{e}$ are the unit vectors in direction of the first pulsed gradient and the background gradient in the LFR, respectively.

For the special case of $m = 1$, the Karlicek and Lowe sequence consists of four pulsed field gradients. The three terms of the spin echo attenuation, which are found by evaluation of Eq. (37) using the above-described effective gradients, are ($m = 1$)

$$A_p(t_e) = \delta^2 \left(12\tau - \frac{2}{3}\delta \right) \boldsymbol{G}^2, \tag{47a}$$

$$A_c(t_e) = 0 \tag{47b}$$

and

$$A_b(t_e) = \frac{10}{3}\tau^3 \boldsymbol{g}^2. \tag{47c}$$

This result is consistent with the original paper by Karlicek and Lowe.[17] The advantage of this sequence is that a constant background gradient does not lead to a cross term with the pulsed gradients. However, the long time until the observation of the spin echo ($t_e = 10\tau$ for m = 1) restricts the application of this sequence to systems, where the transverse relaxation time in a homogeneous magnetic field is comparable with or larger than the echo time ($T_2 \gtrsim t_e$). Furthermore, strong background gradients may lead to an additional NMR signal attenuation due to the large background gradient term A_b. Additionally, the long phase encoding and magnetization decoding pulsed gradient series do not allow one to appoint a well-defined diffusion time for the Karlicek and Lowe sequence, which, however, is often necessary for the interpretation of diffusion studies in heterogeneous systems.[16,27,28,50,74]

3.2.2. *11-interval pulse sequence according to Sørland et al.*

If in the generalized PFG NMR sequence (Fig. 9) the *z*-storage interval is set to $\Delta' = 0$ and the second and the third $\pi/2$ rf pulses are ignored, one obtains the 11-interval sequence with unequal F and G gradients, as proposed by Sørland et al.[19] It is a CPMG-like sequence since it consists only of two refocusing π rf pulses, which are responsible for the formation of a spin echo. The 11-interval sequence is the shortest pulse sequence for cancelation of the cross term by using alternating pulsed field gradients. It can be up to 20% shorter as compared to the pulse sequence proposed by Karlicek and Lowe[17] assuming the same time pattern of the pulsed field gradients. This might be important for samples with a critical short T_2. Using Eq. (37), the three terms of the spin echo attenuation of this sequence are found to be:

$$A_p(t_e) = \delta^2 \left[\tau(\boldsymbol{G} - \boldsymbol{F})^2 + 2\tau\boldsymbol{F}^2 - \frac{1}{3}\delta(\boldsymbol{G}^2 + \boldsymbol{F}^2) \right], \tag{48a}$$

$$A_c(t_e) = \delta\tau(\delta_1 - \delta_2)(\boldsymbol{G} - \boldsymbol{F})\boldsymbol{g} \tag{48b}$$

and

$$A_b(t_e) = \frac{4}{3}\tau^3 \boldsymbol{g}^2. \tag{48c}$$

Eq. (48) does not confirm the result for the 11-interval sequence reported in Eq. (4) of Sørland *et al.*[19] The results for the spin echo attenuation reported by Sørland *et al.* are equivocal* and show – for the special case of equal F and G gradients ($F = -G$ here and $x = 0$ in Ref. 19) – the wrong sign of the cross term. Most likely, the reason is an inconsistency in the definitions of the effective pulsed and background gradients in Ref. 19.

Nevertheless, our Eq. (48) confirms the cancellation of the cross term for $\delta_1 = \delta_2$, as found by Sørland *et al.*[19] However, compared to the Karlicek and Lowe sequence, this condition for cross-term cancellation represents a loss in variability to choose the positions of the pulsed field gradients. Additionally, at equal echo times t_e, the pure background gradient term of the 11-interval sequence is by the factor of 6.25 larger than that of the Karlicek and Lowe sequence, which – in the case of strong background gradients and high self-diffusion coefficients – represents an additional, unwanted loss in NMR signal intensity.

3.3. APFG NMR sequences based on the stimulated spin echo

3.3.1. *13-interval pulse sequence according to Cotts et al.*

If the F and G pulsed field gradients have equal amplitudes but opposite polarities in the LFR and the background gradient does not change during the whole time, the generalized 13-interval PFG NMR sequence (Fig. 9) simplifies to the 13-interval sequence according to Cotts *et al.*[18] In Eq. (46), this is simply accounted for by setting $F = -G$ and $f = g$, which leads to:

$$A_p(t_e) = (2\delta)^2 \left[\Delta' + \frac{3}{2}\tau - \frac{1}{6}\delta \right] G^2, \tag{49a}$$

$$A_c(t_e) = 2\delta\tau(\delta_1 - \delta_2)Gg \tag{49b}$$

and

$$A_b(t_e) = \frac{4}{3}\tau^3 g^2. \tag{49c}$$

Compared to the stimulated spin echo sequence with two unipolar pulsed field gradients (see Section 2.4.6), the advantage of this 13-interval APFG NMR sequence is that the cross term as well as the background gradient term do not depend on the z-storage interval. For $\delta_1 = \delta_2$ the cross term even cancels completely and the spin echo attenuation due to diffusion is solely controlled by the pulsed field gradients. Thus, unknown background gradients do not interfere with the spin echo attenuation, if they are constant during the pulse sequence and the pulsed gradients are centered in the τ intervals ($\delta_1 = \delta_2$ in Fig. 9).

---

*Obviously, Sørland *et al.* define the quantity x as gradient current (Eq. (4) in Ref. 19) or gradient itself (Eq. (5) in Ref. 19).
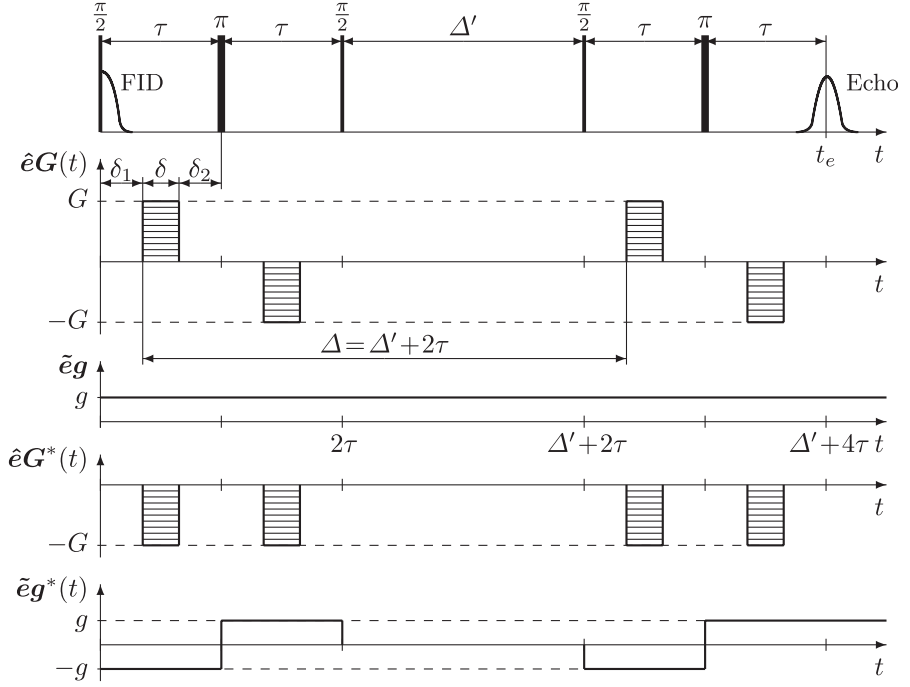
Fig. 11.   13-interval PFG NMR sequence proposed by Cotts *et al.*[18] with pulsed gradients $G(t)$ according to condition I and a constant background gradient g. The positions and lengths of the pulsed gradients are equal in each τ interval. The effective gradients $G^*(t)$ and $g^*(t)$ are also drawn, $\hat{e}$ and $\tilde{e}$ are the unit vectors in direction of the third pulsed and the background gradient in the LFR, respectively.

For illustration, the pulsed and background gradients in the LFR as well as the corresponding effective gradients are drawn in Fig. 11. The background and cross terms in Eq. (49) are reduced and even canceled, respectively, because the magnetization phase label introduced by the background gradient during the preparation and read intervals are refocused by the π rf pulses. In contrast, for successive pulsed field gradients of opposite polarity, the phase label increases due to the π rf pulse. Thus, the phase encoding and magnetization decoding periods are split into two time intervals, which lead to the more complex pulsed gradient term in the spin echo attenuation (Eq. (49a)) than known from the SE and STE sequences with two unipolar-pulsed field gradients.

3.3.2. *9-interval pulse sequence according to Cotts et al.*

If no F pulsed field gradients are applied and the background gradient does not change during the whole time of the pulse sequence, the generalized 13-interval PFG NMR sequence simplifies to the 9-interval sequence according to Cotts *et al.*[18]

In Eq. (46), this is accounted for by setting $\boldsymbol{F} = 0$ and $\boldsymbol{f} = \boldsymbol{g}$, which leads to

$$A_p(t_e) = \delta^2 \left[\Delta' + \tau - \frac{1}{3} \delta \right] \boldsymbol{G}^2, \tag{50a}$$

$$A_c(t_e) = \delta\tau(\delta_1 - \delta_2)\boldsymbol{G}\boldsymbol{g} \tag{50b}$$

and the same background gradient term $A_b(t_e)$ as given in Eq. (49c). Due to the missing F pulsed gradients, the pulsed and the cross term of the 9-interval sequence are reduced as compared to the 13-interval sequence (Eq. (49)). If one defines the diffusion time Δ as $\Delta' + \tau$, then the pulsed gradient term coincides with the corresponding terms of the SE and the STE PFG sequences (Eqs. (38a) and (45a)). However, in contrast to the SE and STE sequences with unipolar-pulsed gradients, the 9-interval sequence allows to cancel disturbing influences of constant unknown background gradients by centering the alternating G gradients in the τ intervals ($\delta_1 = \delta_2$ in Eq. (50b)).

3.3.3. *13-interval pulse sequence according to Sørland et al.*

Sørland *et al.*[73] proposed unequal pulsed field gradients in the 13-interval sequence in order to suppress unwanted coherences in the formation of the spin echo attenuation. Thus, the F and G gradients have in fact the different amplitudes of the generalized PFG NMR sequence drawn in Fig. 9. However, Sørland *et al.* assumed a constant background gradient, which is accounted for in Eq. (46) by setting $\boldsymbol{f} = \boldsymbol{g}$. This leads to

$$A_p(t_e) = \delta^2 \left[(\Delta' + \tau)(\boldsymbol{G} - \boldsymbol{F})^2 + 2\tau\boldsymbol{F}^2 - \frac{1}{3}\delta(\boldsymbol{G}^2 + \boldsymbol{F}^2) \right], \tag{51a}$$

$$A_c(t_e) = \delta\tau(\delta_1 - \delta_2)(\boldsymbol{G} - \boldsymbol{F})\boldsymbol{g} \tag{51b}$$

and a background gradient term as already given in Eq. (49c). The pulsed gradient term corresponds to Eq. (46a). As for all related 13-interval sequences, the cross term cancels, if the G and F pulsed gradients are centered in their τ intervals ($\delta_1 = \delta_2$) allowing effective suppression of disturbing influences of unknown background gradients in the spin echo attenuation as long as they are the same during the preparation and read intervals.[**]

3.3.4. *13-interval sequence with variable background gradients*

The behavior of the cross term of the spin echo attenuation in the case of background gradients, which change during the z-storage interval, was first discussed by Seeland *et al.*[75] They calculated the cross term for the 13-interval sequence with four

---

[**]It shall be mentioned here that the factor δ^2 in the relations for the cross and background gradient terms of the spin echo attenuation given in Eq. (3) of the original paper by Sørland *et al.*[73] is too much and that the reported sign of the cross term is wrong. This becomes obvious, if – as it was done by Sørland *et al.* – the pulsed gradients are inserted in our Eq. (51b) as effective gradients with $\boldsymbol{G} = -\boldsymbol{G}^*$ and $\boldsymbol{F} = \boldsymbol{F}^*$, respectively.

pulsed field gradients of equal amplitude under the simplified assumption that the background gradient changes its sign during the z-storage interval. They found a remaining cross term of

$$A_c(t_e) = -4\delta\tau^2 \boldsymbol{g}\boldsymbol{G} \tag{52}$$

even thought the pulsed gradients were centered in the τ intervals. This result is confirmed by the generalized PFG NMR sequence, if one sets $\boldsymbol{F} = -\boldsymbol{G}$ and $\boldsymbol{f} = -\boldsymbol{g}$.

Seeland et al.[75] also discussed the re-introduction of the cross term in the case of unequal pulsed field gradients. However, the equation (3) in Ref. 75 cannot be verified by our approach of the generalized PFG NMR sequence. Most likely, the reason is an inconsistency in the definition of the effective pulsed and background gradients in Ref. 75. The correct equation for F and G pulsed gradients of different amplitudes and a background gradient $\boldsymbol{g}$, which changes its sign during the z-storage interval, follows from Eq. (46b) and is given by:

$$A_c(t_e) = -\delta\left\{2\left[\left(\delta_1^2 + \delta_1\delta + \frac{1}{3}\delta^2\right)(\boldsymbol{G} + \boldsymbol{F}) - 2\tau^2\boldsymbol{F}\right]\boldsymbol{g} - \tau(\delta_1 - \delta_2)(\boldsymbol{G} + \boldsymbol{F})\boldsymbol{g}\right\}. \tag{53a}$$

Recently proposed experimental approaches to suppress cross terms with variable background gradients by magic pulsed field gradient ratios will be discussed in the next section.

3.4. Cross-term suppression by magic pulsed field gradient ratios

Within a period of roughly one year during 2003/2004, two independent groups extended the original ideas for cancellation of the cross term between the pulsed and background field gradients by APFG NMR sequences to the case, where the background gradient changes during the z-storage interval.[20,21,64,76] The published approaches differ with respect to the pattern of the alternating pulsed field gradients applied. However, their common feature is that the complete cancellation of the cross term with variable background gradients generally requires two conditions. In the case of 13-interval like APFG sequences, the first condition determines the timing of the pulsed field gradients in the τ intervals. The second condition regards the sign and intensity ratio between the succeeding F and G pulsed field gradients. This second condition represents the key result for all these advanced approaches for background gradient suppression, which – more precisely – should actually be called advanced approaches to cross-term suppression as we do throughout this review. These distinct and well-defined ratios between the F and G pulsed field gradients were named as magic pulsed field gradient (MPFG) ratios[21] and pulse sequences, which obey these conditions for advanced cross-term suppression, are called MPFG NMR sequences. Later, Sun et al.[77] introduced the abbreviation MAGR (magic asymmetric gradient ratio) for gradient schemes, which also allow cross-term cancellation. We would like to point out that the MAGR ratios are just the inverse of the MPFG ratios, which we use here.

In the following we will derive the MPFG ratio and the corresponding spin echo attenuation term for the generalized PFG NMR sequence drawn in Fig. 9. We also present the interrelated MPFG ratios approach proposed by Galvosas et al.[21] and the symmetric pulsed field gradient approach by Sun et al.,[20] and show that for pulsed field gradients centered in the τ interval the results are consistent with the MPFG ratio and spin echo attenuation of the generalized PFG NMR sequence. For the corresponding results obtained with the 13-interval sequence with trapezoidal and sine shaped pulsed field gradients,[77] we refer the reader to the original paper and Section 3.5, where we outline an approach to determine spin echo attenuation equations for arbitrary shaped pulsed field gradients.

3.4.1. The MPFG ratio for the generalized PFG NMR sequence

As demonstrated by the two examples in Section 3.3.4, the cross term in the 13-interval PFG NMR sequence does not cancel if the background gradient changes its value during the z-storage interval Δ'. If the pulsed field gradients are centered in the τ intervals, which represents the sufficient condition for cancellation of the cross term with constant background gradients, the remaining cross term for background gradients changing from g to f during Δ' is given by:

$$A'_c(t_e) = \frac{\delta}{12}[(\delta^2 - 21\tau^2)\boldsymbol{F} + (\delta^2 + 3\tau^2)\boldsymbol{G}](\boldsymbol{f} - \boldsymbol{g}). \tag{54}$$

Eq. (54) follows from Eq. (46b) for the generalized PFG NMR sequence (Fig. 9) by choosing $\delta_1 = \delta_2 = \frac{1}{2}(\tau - \delta)$. Thus, centering the pulsed field gradients suppresses the cross term but does not cancel it completely if $\boldsymbol{f} \neq \boldsymbol{g}$. However, the remaining cross term may be zeroed, if the F and G gradients of the generalized PFG NMR sequence additionally obey the magic pulsed field gradient (MPFG) ratio.[20,21,64,76]

$$\eta \equiv \frac{\boldsymbol{G}}{\boldsymbol{F}} = \frac{G}{F} = \frac{8}{1 + \frac{1}{3}\left(\frac{\delta}{\tau}\right)^2} - 1. \tag{55}$$

There are three very interesting aspects of this condition necessary to cancel the cross term with variable background gradients. (1) The MPFG ratio $\eta = G/\boldsymbol{F}$ depends only on the two time intervals δ and τ. Since the duration of a pulsed field gradient (δ) cannot exceed the duration of the τ interval ($0 \leq \delta \leq \tau$), it follows for the MPFG ratio $5 \leq \eta \leq 7$. Experimentally, such a MPFG ratio can easily be realized for the amplitudes of the F and G gradients. (2) Since the MPFG ratio is always positive, the $\boldsymbol{F}$ and $\boldsymbol{G}$ vectors must always have the same direction in the LFR. Thus, the F and G pulsed field gradients in the 13-interval sequence must obey the pattern given in Fig. 12. For example, if one starts the experiment with a small F gradient of positive sign as drawn in Fig. 12, it must be followed by a larger G gradient of positive sign. The condition I requires for the read interval a negative sign of the large G gradient followed by a small F gradient of negative sign. (3) These equal signs of the F and G gradients separated by a π rf pulse result in opposite signs for the corresponding effective gradients. Consequently, the pulsed
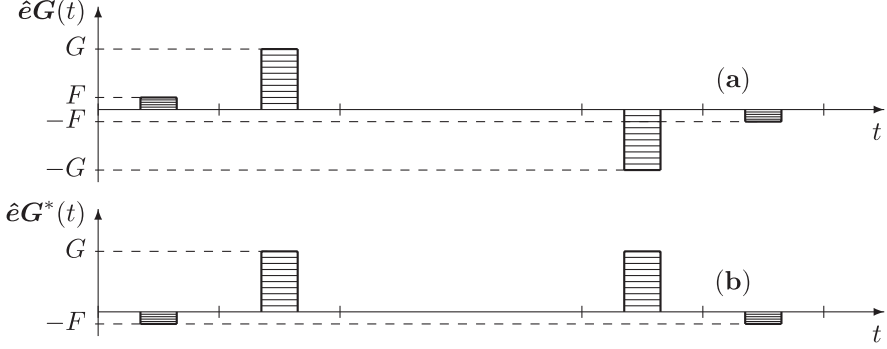
Fig. 12. Pulsed field gradients $\boldsymbol{G}(t)$ in the LFR (**a**) and the corresponding effective gradients $\boldsymbol{G}^*(t)$. (**b**) for the generalized PFG NMR sequence (Fig. 9) obeying the magic pulsed field gradient ratios for cross-term cancellation in the case of variable background gradients. The signs and amplitudes of the F and G gradients correspond to the requirements of Eq. (55). [*Source:* Adapted from Ref. 64.]

gradient term of the spin echo attenuation is reduced. If the MPFG ratio (Eq. (55)) is obeyed, one obtains from Eq. (46a)

$$A_p(t_e) = (\delta \boldsymbol{G})^2 \left\{ (\varDelta' + \tau) \left[1 - \frac{1}{\eta} \right]^2 + 2\tau \left(\frac{1}{\eta} \right)^2 - \frac{1}{3} \delta \left[1 + \left(\frac{1}{\eta} \right)^2 \right] \right\}. \tag{56}$$

Depending on the experimentally chosen δ/τ ratio, which determines the necessary MPFG ratio by Eq. (55), the A_p term of the MPFG 13-interval sequence (Eq. (56)) amounts to only 20% – 25% of the value found for the original 13-interval sequence according to Cotts *et al.* (compare Eq. (49a)). This means that equal maximum pulsed field gradient amplitudes lead to a smaller spin echo attenuation in the case of the MPFG 13-interval sequence and, thus, to a reduced sensitivity for the measurement of small self-diffusion coefficients. However, the MPFG 13-interval sequence offers the advantage of canceling the cross terms with background gradients, which change during the z-storage time. Based on the timing diagram of the generalized PFG NMR sequence, this advanced cross-term suppression requires one, only to center the pulsed field gradients in the τ intervals and to obey the intensity and sign relations of the F and G gradients given by the MPFG ratio (Eq. (55)).

3.4.2. *Interrelated MPFG ratios approach*

Galvosas *et al.*[21] proposed a generalized 13-interval sequence for cancellation of background gradients changing during the z-storage interval, which consists of F and G pulsed gradients and timing parameters as the generalized PFG sequence (Fig. 9) used here. However, the two F gradients in Ref. 21 are allowed to have different amplitudes in the preparation (F^p) and read (F^r) intervals. In order to fulfill the condition I, this requires different amplitudes for the two G gradients (G^p and G^r). The authors calculated the pulsed, cross and background gradient terms

for their sequence, and showed that the cross term separates in two parts depending on the background gradients acting during the preparation (g) and read (f) intervals, respectively. Consequently, there are separate MPFG ratios for the pulsed gradients acting during the read (η^p) and preparation (η^p) interval[21]

$$\eta^p \equiv \frac{G^p}{F^p} = \frac{2\tau^2 - a}{a + \tau(\delta_2 - \delta_1)} \tag{57a}$$

$$\eta^r \equiv \frac{G^r}{F^r} = \frac{2\tau^2 - \tau(\delta_2 - \delta_1)}{a} - 1 \tag{57b}$$

with

$$a = \delta_1^2 + \delta_1\delta + \frac{1}{3}\delta^2,$$

which also depend only on the time parameters of the pulse sequence.[†] These MPFG ratios have similar properties than the single MPFG ratio discussed in the previous section. For pulsed field gradients centered in the τ intervals, both MPFG ratios of Eq. (57) coincide and even agree with Eq. (55).

The advantage of the generalized 13-interval sequence with two MPFG ratios for cancellation of variable background gradients is that it does not require to center the four pulsed field gradients in the τ intervals. Thus, disturbing influences of eddy currents during the spin echo observation may be reduced, if the pulsed field gradients follow immediately their preceding rf pulses.

3.4.3. *Symmetric pulsed field gradient approach*

By proposing a modified 13-interval sequence, in which – in contrast to the most frequently definitions of the time intervals[11,12,17,18,73] – the F and G pulsed field gradients of different amplitudes are placed symmetrically to the refocusing π rf pulses, Sun et al.[20] were able to cancel the cross term with background gradients, which change during the z-storage interval, using a single MPFG ratio. The required ratio is given by[§,20,21]

$$\eta^s \equiv \frac{G}{F} = \frac{2\tau^2}{a} - 1, \tag{58}$$

where a is defined as in Eq. (57). Eq. (58) is equivalent to Eq. (21) in the original paper of Sun et al.[20] if one substitutes $\tau = \delta_1 + \delta + \delta_2$. Again, by centering the pulsed field gradients in the τ intervals, Eq. (58) transfers into Eq. (55), which demonstrates the consistency between all the slightly different approaches for advanced cross-term suppression.

[†]Note that the signs of the MPFG ratios in Eq. (57) are opposite to that in Eqs. (7a) and (7b) of Ref. 21. This is because in Ref. 21 all gradients enter into the presented equations as effective gradients, while, in this paper, we consistently use the gradients in the LFR.

[§]Note that the sign of the MPFG ratio in Eq. (58) is opposite to that in Eq. (16) of Ref. 21. This is because in Ref. 21 all gradients enter into the presented equations as effective gradients, while, in this paper, we consistently use the gradients in the LFR.

The symmetric pulsed field gradient approach for the 13-interval sequence of Sun *et al.* has the advantage that – due to the single MPFG ratio – it is easier to set up experimentally than the generalized 13-interval sequence as suggested by Galvosas *et al.*, where, if the pulsed field gradients are not centered in the τ intervals, four different pulsed field gradient amplitudes must be applied.

So far, most applications of 13-interval MPFG sequences for advanced cross-term suppression – even in model system – used pulsed field gradients centered in the τ intervals. For this case, all approaches presented in this review yield coinciding results with respect to the required MPFG ratio and the spin echo attenuation due to the pulsed field gradients. The corresponding equations are presented in Section 3.4.1. For the spin echo attenuation equations due to pulsed field gradients, which are not centered in the τ intervals, we refer the reader to Ref. 21 in which the corresponding results of Sun *et al.*[20] were recalculated because of a misprint (as stated in Ref. 77) in the original article.

3.5. Generalizations

3.5.1. *Joint formalism for two- and four-pulse PFG NMR sequences*

All PFG NMR sequences for diffusion studies, which we considered so far, consist of one or two pairs of pulsed field gradients. For the calculation of the spin echo attenuation by Eq. (37), only the effective gradients and the respective spin echo condition need to be known. Due to the small number of maximal four pulsed field gradients, the effective gradient patterns of such two- and four-pulse PFG NMR sequences are expected to be similar. They are distinguished only by the time parameters and sign relations between the pulsed field gradients.

Consequently, it is possible to find a joint formalism, including the pulsed gradient terms for the considered four-pulse PFG NMR sequences. This joint formalism is based on the pulsed gradient term (Eq. (46a)) of the generalized PFG NMR sequence drawn in Fig. 9. Written as the logarithm of the spin echo attenuation, this equation reads as follows:[64,73]

$$\ln \Psi = -\gamma^2 D \delta^2 \left[(\Delta' + \tau)(\boldsymbol{G} - \boldsymbol{F})^2 + 2\tau \boldsymbol{F}^2 - \frac{1}{3}\delta(\boldsymbol{G}^2 + \boldsymbol{F}^2) \right]. \tag{59}$$

Using the substitutions given in Table 1, Eq. (59) transforms into the known equations for the spin echo attenuations of the corresponding pulse sequences.

With the substitution $\Delta' = 0$, Eq. (59) includes the spin echo attenuations of CPMG-like PFG NMR sequences (see first three lines in the top part of Table 1). The STE sequences do not require a substitution for Δ' in Eq. (59), since they really consist of a z-storage interval. For the two-pulse PFG NMR experiments, such as the 9-interval sequences, one needs to set $\boldsymbol{F} = 0$. The proposed joint formalism even allows one to reproduce the spin echo attenuation for the SE,[11] the STE,[12] the Karlicek and Lowe[17] and the 17-interval[18] PFG NMR sequences by just redefining the τ interval.

Table 1.   Substitutions of time and gradient parameters

PFG NMR sequence	Ref.	$\Delta' =$	$\tau =$	$\boldsymbol{F} =$	See Eq.
SE (primary spin echo)	[11]	0	Δ	0	(38a)
Karlicek and Lowe ($m = 1$)	[17]	0	2τ	$-\boldsymbol{G}$	(47a)
11-Interval	[19]	0			(48a)
STE (stimulated spin echo)	[12]		$\Delta - \Delta'$	0	(45a)
9-Interval	[18]			0	(50a)
13-Interval Cotts	[18]			$-\boldsymbol{G}$	(49a)
17-Interval Cotts	[18]		$\frac{10}{3}\tau$	$-\boldsymbol{G}$	see ref.
13-Interval Sørland	[73]				(51a)
13-Interval MPFG ($\delta_1 = \delta_2$)	[20,21]			$\boldsymbol{G}/\eta$	(56)

Note: Substitutions of time and gradient parameters in Eqn. (59) to obtain the spin echo attenuation equations due to pulsed field gradients for the listed PFG NMR sequences. The substitutions of τ by Δ and $\Delta - \Delta'$ required for the SE and STE PFG NMR sequences respectively, account for possible shifts of the unipolar pulse field gradients in the preparation and read (τ) intervals. η denotes the magic pulsed field gradient ratio necessary for advanced cross-term suppression (Eq. (55)).

However, we shall note again that it is the similarity of the effective pulsed gradient pattern of all these two- and four-pulse PFG NMR sequences, which allows the formal generalization of the spin echo attenuation by Eq. (59) and Table 1. It holds only for the pulsed gradient term and not for the background and cross terms. From the experimental point of view, the later restriction, however, does not confine the principle advantages of this joint formalism, since – if the background gradient is not known – one should always apply APFG NMR or even MPFG NMR sequences with optimized settings of the time and gradient parameters, which allow to cancel the cross term.

The principal advantage of this joint formalism is the opportunity to develop a generalized approach for automated data analysis, where a single equation (Eq. (59)) and a lock-up table for time and gradient parameters are sufficient to describe experimental data obtained by a whole family of PFG NMR pulse sequences. Additionally, the generalized description is of educational use since it shows that the pulsed gradient term of the double integral (Eq. (31)) has a common solution for four-pulse PFG NMR diffusion experiments and, thus, all the different sequences are closely related to each other.

3.5.2. *Arbitrary pulsed field gradient shapes*

So far, the pulsed field gradients were always assumed to have perfect rectangular shape, i.e., the time dependence of the pulsed field gradients $\boldsymbol{G}(t)$ was determined by $\boldsymbol{F}$ and $\boldsymbol{G}$, respectively, which did not exhibit amplitude variations during the δ intervals. For all times outside the δ intervals, $\boldsymbol{G}(t)$ was equal to zero. However, due to limited output voltage of the current source, experimentally generated pulsed field gradients have always finite rise and fall times (see Section 4.2.4). Sometimes, gradient pulses of different than rectangular shape are applied intentionally in order to reduce disturbing influences of eddy currents or pulsed gradient mismatches.[25,74,77,78]

If the pulsed gradient shape is not known precisely, the correct determination of self-diffusion coefficients requires the comparison of the experimentally observed spin echo attenuation with that of a reference sample of known diffusivity, which was measured under identical experimental conditions.[79] However, a more convenient approach is the direct calculation of the b-value as function of the experimental parameters. This requires (1) the knowledge of the *gradient shape*, which represents the time-dependence of the pulsed field gradients during the time interval δ, and (2) a solution of the double integral (Eq. (31)) with this gradient shape. If one assumes for the generalized PFG NMR sequence (Fig. 9) that the two pulsed field gradients of the F pair have the same shape and the two pulsed gradients of the G pair have the same shape, which, however may be different from the shape of the F pair (which still allows different amplitudes between the F and G gradient pairs), one may solve Eq. (37a) and obtain – after a long calculation – a general equation for the pulsed gradient term:[64]

$$A_p(t_e) = (\Delta' + \tau)\left[\int_0^\delta \mathrm{d}t\, \boldsymbol{G}(t' + \tau + \delta_1) - \int_0^\delta \mathrm{d}t\, \boldsymbol{G}(t' + \delta_1)\right]^2 + 2\tau\left[\int_0^\delta \mathrm{d}t\, \boldsymbol{G}(t' + \delta_1)\right]^2$$
$$+ 2\left\{\int_0^\delta \mathrm{d}t\left[\int_0^t \mathrm{d}t'\, \boldsymbol{G}(t' + \delta_1)\right]^2 - \int_0^\delta \mathrm{d}t\, \boldsymbol{G}(t' + \delta_1)\int_0^\delta \mathrm{d}t \int_0^t \mathrm{d}t'\, \boldsymbol{G}(t' + \delta_1)\right.$$
$$+ \int_0^\delta \mathrm{d}t\left[\int_0^t \mathrm{d}t'\, \boldsymbol{G}(t' + \tau + \delta_1)\right]^2$$
$$\left. - \int_0^\delta \mathrm{d}t\, \boldsymbol{G}(t' + \tau + \delta_1)\int_0^\delta \mathrm{d}t \int_0^t \mathrm{d}t'\, \boldsymbol{G}(t' + \tau + \delta_1)\right\}, \qquad (60)$$

where the shapes of the F and the G pulsed field gradients during their respective δ intervals are denoted by $\boldsymbol{G}(t' + \delta_1)$ and $\boldsymbol{G}(t' + \tau + \delta_1)$, respectively. The advantage of Eq. (60) is that the integrals are evaluated only during the δ intervals. Thus, it is integrated over the shape of the G and F gradients. If these shapes are known, the spin echo attenuation may be calculated straightforwardly.

As a consistency check, the reader may prove on its own that for F and G pulsed field gradients of rectangular shape, i.e., $\boldsymbol{G}(t' + \delta_1) = \boldsymbol{F}$ and $\boldsymbol{G}(t' + \tau + \delta_1) = \boldsymbol{G}$, Eq. (60) reproduces Eq. (46a)) of the generalized PFG NMR sequence. For the 13-interval sequence consisting of unequal F and G pulsed field gradients of half-sine shape, which was recently proposed,[77] the required pulsed field gradient shape functions $\boldsymbol{G}(t)$ are:

$$\left.\begin{array}{c}\boldsymbol{G}(t + \delta_1) = \boldsymbol{F}\sin\frac{\pi t}{\delta} \\ \boldsymbol{G}(t + \tau + \delta_1) = \boldsymbol{G}\sin\frac{\pi t}{\delta}\end{array}\right\} \quad \text{for } 0 \le t \le \delta. \qquad (61)$$

Inserting Eq. (61) into Eq. (60), one easily calculates the pulsed gradient term;

$$A_p(t_e) = \frac{\delta^2}{\pi^2}[(\Delta' + \tau)(2\boldsymbol{G} - 2\boldsymbol{F})^2 + 2\tau(2\boldsymbol{F})^2 - \delta(\boldsymbol{G}^2 + \boldsymbol{F}^2)], \qquad (62)$$

which is consistent with the equation published in Ref. 64. Moreover, if the formal replacements of Table 1 are applied to Eq. (62), one obtains for four half-sine shaped pulsed field gradients of equal amplitude the result published by Latour et al. and Fordham et al.[80,81] and for the SE sequence ($\Delta' = 0$, $\tau = \Delta$ and $\boldsymbol{F} = 0$) with two such pulsed field gradients the equation:

$$A_p(t_e) = \frac{(\boldsymbol{G}\delta)^2}{\pi^2}(4\Delta - \delta). \tag{63}$$

Eq. (63) agrees with the results published by Gross and Kosfeld[82] and later by Price.[48] Thus, arbitrary pulsed field gradient shapes – even if they are known only numerically – may be handled quite effectively by calculating the pulsed gradient term using Eq. (60) and the substitutions of Table 1.

3.6. Diffusion-edited pulse sequences

Kimmich[41] classified the vast and still increasing amount of NMR pulse sequences according to their main purpose into three basic methods. The NMR diffusometry (NMRD) measures molecular motions as described in the previous sections. With the NMR relaxometry (NMRR), relaxation processes of the spin system are investigated. The NMR tomography (or magnetic resonance imaging: MRI) studies spatial distributions of the nuclear spins.[42,83] Additionally, there is the conventional NMR spectroscopy (NMRS), which measures one- and multi-dimensional frequency distributions.[43,84] These methods may be combined mutually by merging their respective pulse sequences. Combinations with the NMR diffusometry lead to so-called diffusion-edited or diffusion-encoded NMR pulse sequences. Their common feature is that they contain pairs of magnetic field gradients for encoding of translational motions.

For the design of a diffusion-edited NMR pulse sequence, one starts with a known NMR diffusion experiment (see previous sections) and substitutes the exciting rf-pulse and the spin echo detection, respectively, by a NMRS, NMRR or MRI pulse sequence or a part of it. Thus, the acquired NMR signal contains all the information encoded by the respective NMRS, NMRR and MRI sequence as well as information on the diffusion of the observed molecules. Examples for this approach are all diffusion-weighted pulse sequences, where – according to the self-diffusion of the observed molecules – the NMR signal is attenuated by a PFG NMR sequence prior to it is detected or further encoded by spectroscopy, relaxometry and tomography methods, respectively.

The combination of a PFG NMR sequence with NMR spectroscopy leads to the family of so-called DOSY (diffusion-ordered spectroscopy) methods.[32] In its simplest realization, the NMR spectrum is obtained by Fourier transformation of the decaying half of the spin echo.[85,86] Each line in the spectrum (chemical shift δ_i) is attenuated by $\Psi_i = \exp(-bD_i)$, where $b = \gamma^2 A_p$ depends on the PFG NMR pulse sequence selected and D_i represents the self-diffusion coefficient of the molecules

giving rise to the observed chemical shift. If the chemical shift dependent signal attenuations are analyzed by an inverse Laplace transformation, it adds a diffusion dimension to the frequency dimensions of the conventional spectroscopy. The correlation of these dimensions often simplifies the identification of different components in complex mixtures.

In order to improve the spectral resolutions of the DOSY methods, one may combine them with pulse sequences, which improve or suppress the sensitivity of the NMR spectra to certain features. For example, Otto et al.[87,88] suppressed the residual magnetization of homonuclear J coupled spins in a 13-interval PFG NMR DOSY experiment by replacing its exciting $\pi/2$ rf pulse with a primary spin echo sequence, in which the inter echo time t_{ie} is set to $t_{ie} = J/2$. Additionally, the authors showed that unwanted broad background signals in ^1H NMR spectra may be canceled by using a sufficiently long CPMG sequence prior to the diffusion encoding.[87] The 13-interval PFG NMR DOSY experiments with a selective TOCSY and zero-quantum filtering proposed by Bradley et al.[89] serve the same purpose of suppressing background signals, and thus, improving the spectral resolution. For detailed reviews on DOSY and related methods, we refer the reader to Refs. 32, 33.

Many of the modern NMRD applications (including DOSY experiments) use shaped, APFG and an additional z-storage interval between the PFG NMR section of the pulse sequence and the signal acquisition,[78,90–92]), which prevent disturbing influences of slowly decaying eddy currents on the NMR signal formation and detection. However, the additional z-storage interval leads to an enhanced T_1 weighting of the NMR signal intensity, which might complicate the quantitative analysis of NMR spectra.

If the investigated system is composed of components with different longitudinal and transverse relaxation times, respectively, PFG NMR diffusion studies may suffer by relaxation time weighting of the observed NMR signal. By adding relaxation delays prior to the SE and STE PFG NMR sequence, Heink et al.[93] developed pulse sequences, which allow one to investigate the influence of the T_2 or T_1 relaxation time weighting on the observed PFG NMR spin echo attenuation. This principle was later adapted by Johansson et al.[94] to compensate for variable relaxation time weightings in NMR diffusion studies using constant field gradients. It is also used to compensate for the variable T_1 weighting encountered in stimulated spin echo NMR diffusion sequences, if the diffusion time and, thus, the duration of the z-storage interval is changed.[95]

If the longitudinal relaxation times of the components in an investigated system are clearly different, one may apply an inverting π rf pulse at $t = T_{1i} \ln 2$ prior the exciting $\pi/2$ rf pulse of the PFG NMR sequence.[96–98] According to the principle of the the inversion recovery experiment, this cancels the NMR signals with the relaxation times T_{1i}, while all other signals are just reduced in their amplitude. Alternatively, NMR signal contributions with long T_1 relaxation times, can be suppressed by a saturation recovery sequence prior the PFG NMR diffusion encoding.[99]

These few examples show that by carefully selecting experimental parameters in diffusion-edited pulse sequences, one is able to simplify data analysis of NMR

spectra or of PFG NMR spin echo attenuations. However, these diffusion-edited pulse sequences may be adapted for direct evaluation of these disturbing influences and even for correlating them with the self-diffusion measurements. Examples are relaxation–relaxation correlations (RRCOSY),[30] diffusion–relaxation correlations (DRCOSY),[29,37] diffusion–diffusion correlations (DDCOSY)[100] and diffusion–diffusion exchange (DEXSY)[100] and even relaxation–diffusion–chemical shift correlations.[101,102] All these methods combine two or more NMR pulse sequences into one single experiment and change the corresponding experimental parameters independently. Thus, the NMR signal is acquired in a multidimensional dataset. For instance, by means of pulsed field gradients with a successively increased gradient amplitude, one can encode the diffusion in the first part of the pulse sequence. In the second part of the experiment one may change independently a delay time to accomplish relaxation weighting of the NMR signal or apply again field gradients of variable amplitudes in a second PFG subsequence, which leads to a double PFG NMR sequence.[103] The reader may find a more exhaustive discussion of the different possibilities to combine individual subsequences in Ref. 100 as well as the name conventions for the correlation methods used in this paragraph. The multidimensional data set is subsequently analyzed by multidimensional inverse Laplace transformation[29–31,100] in order to obtain the various correlations or exchange diagrams, respectively. Alternatively, the diffusion-encoded dimensions may also be analyzed by Fourier inversion, which yields information on the displacement probability distributions (the propagator) as already pointed out in Section 2.3.2 (see, e.g., Refs. 27, 35, 36, and 61).

4. GENERATION AND APPLICATION OF HIGH-INTENSITY PULSED FIELD GRADIENTS

The study of slow molecular transport processes with PFG NMR requires the application of intense magnetic field gradient pulses as one can see easily from Eq. (16b). Only if $Db_{max} \gtrsim 1$, where b_{max} corresponds to the highest gradient pulse applied, the achieved echo attenuation is suitable for a reliable data processing and subsequent extraction of diffusion related parameters such as mean square displacements or diffusion coefficients. In general, a larger b value can be obtained by increasing either the pulse amplitude G, the pulse duration δ and/or the diffusion time Δ. However, if the mobile molecules under study exhibit a small T_2 as, e.g., observed in micro- and mesoporous media,[50,104] viscous polymers[23,24,105] or metal hydrates,[106,107] one wants to keep the time, when the magnetization stays in the x–y plane, as short as possible. In such cases, the extension of δ is, therefore, limited. The additional restriction $\delta_{max} \leq \Delta \lesssim T_1$ applies to systems, where NMR diffusion studies at short observation times Δ need to be performed, because the transverse relaxation time T_1 is short or the time-dependence of the self-diffusion coefficient at short diffusion times[28,108] shall be studied. Because of such limitations, it is often indispensable to increase the pulsed field gradient amplitude G instead.

In this section, we focus on gradient systems and experimental procedures for generation and successful application of high-intensity pulsed field gradients. We would like to point out that the automated mismatch correction (Section 4.2.2), the optimum shape of the pulsed field gradients (Section 4.2.4), which is described here for the first time in an English-speaking journal, and the triggering of the pulse sequence to the main phase of the lab power supply (Section 4.2.5) are not only useful experimental procedures for applications of high-intensity pulsed field gradients, but rather apply for all PFG NMR studies, where one wants to exploit the power of the expensive NMR gradient hardware systems to the nominal limits given by the manufacturers.

4.1. Gradient probe and amplifier design

Pulsed magnetic field gradients are generated by directing short pulses of electric currents through suitably arranged coil systems. Stable and reproducible current pulses need to be generated by suitable current sources. Possible origins of instabilities in the current pulses, their detection and options for their compensation are discussed in Section 4.2. Furthermore, high mechanical stability of both the coils[22] and the sample[109] are indispensable prerequisites for faultless diffusion measurements and are mainly an issue of PFG NMR probe design. Here, we review those gradient probe, coil and amplifier concepts designed for high-intensity pulsed field gradient applications.

All NMR spectrometers can be equipped with an interface, which allows to control the timing, the shape and the intensity of the pulsed field gradients via the pulse programmer. The desired pulse shapes and intensities are generated as a low-power analog output signal in a DAC, which drives a suitable high-power current source. Depending on the output current of the power supply and the current-to-gradient conversion factor of the gradient coil system, the achieved maximum pulsed gradient intensities are often in the order of $1\,T\,m^{-1}$.[17,110,111] This value is strong enough for most imaging applications, sufficient for diffusion studies on fluids with not too high viscosity, but not strong enough for measuring small diffusion coefficients in substances with short T_2 relaxation times.[24,25,50]

Modern commercial systems as, e.g., described in Refs. 25 and 111 are designed to generate pulsed field gradients of up to a few $10\,T\,m^{-1}$. However, as pointed out in Ref. 25, care must be taken when pushing these systems up to their nominal limits. Today, the highest nominal gradient values of commercial diffusion probes are rated to be $38\,T\,m^{-1}$ at $80\,A$[112] and $30\,T\,m^{-1}$ at $50\,A$[113,114] gradient current, respectively. The latter system was used by one of us successfully with gradient intensities of up to $9.12\,T\,m^{-1}$ [111]. Only a few groups report successful diffusion studies with pulsed field gradients larger than $10\,T\,m^{-1}$. They are often based on home-built power supplies and/or specially designed gradient coils.

In 1990, Dippel et al.[115] modified a home-built PFG spectrometer, which was originally described in Ref. 116 to be capable of generating magnetic field gradient

pulses of up to $50 \, \text{T} \, \text{m}^{-1}$. It was successfully used with field gradient pulses of up to $35 \, \text{T} \, \text{m}^{-1}$ [117]. The system was later re-equipped with a water/air-cooled actively shielded anti-Helmholtz gradient coil (10 mm sample diameter) and a specially designed gradient current power supply, which consists of a directly binary coded current source (DBCCS).[26,118] The DBCCS works like a conventional DAC with, however, a direct high current output. Current pulses of up to ± 120 A with a maximum duration of 9 ms can be adjusted in steps of ± 1.875 A corresponding to a 6 bit resolution. This system is used in routine measurements with unipolar-pulsed field gradients of up to $25 \, \text{T} \, \text{m}^{-1}$ (see, e.g., Refs. 119 and 120 and references therein). Successful measurements with APFG of the same amplitude were also reported.[106,107]

In 1993, Heink et al.[22] described a PFG NMR spectrometer, in which pulsed field gradients of up to $25 \, \text{T} \, \text{m}^{-1}$ were generated and later used over several years in routine measurements (see, e.g., Refs. 22, 44, and 50 and references therein). Originally, the power supply of this gradient system[22] was a highly stabilized and adjustable voltage source providing the necessary current pulses of up to 70 A by discharging as many sets of capacitors as field gradient pulses were required. The gradient probe, developed for this system and later also used by Galvosas et al.[26] consists of an air-cooled, actively shielded anti-Helmholtz coil of 16.5 mm inner diameter suitable for NMR tubes of 7.5 mm diameter. Its support material is VESP-EL® (DuPont), which ensures sufficient high mechanical and thermal stability. For illustration, a photograph of the top part of this NMR probe and a drawing of the gradient coil system are provided in Fig. 13. An evacuated glass dewar (not drawn in Fig. 13) is placed in the space between the NMR sample and the gradient coil. It protects the gradient coil from thermal stresses and reduces temperature gradients across the NMR sample, when controlling the sample temperatures by a stream of nitrogen and air, respectively. This PFG NMR probe design allows diffusion measurements in a temperature range of 130 K $\lesssim T \lesssim$ 480 K.

Skirda and Valiullin reported NMR diffusion studies with pulsed field gradients of up to 103 and $200 \, \text{T} \, \text{m}^{-1}$ on porous media and polymers, respectively (see, e.g., Refs. 23 and 121 and references therein). The gradient pulses are generated by an air-cooled Anti-Helmholz gradient coil, in which titanium is used as support material. Together with the home-built high current source, pulsed field gradients as short as about 20 μs may be applied. The system is designed for NMR sample tubes of about 7 mm diameter and diffusion measurements in a temperature range of 220 K $\lesssim T \lesssim$ 480 K.[122]

Callaghan et al.[24] introduced a system, which is capable of generating $40 \, \text{T} \, \text{m}^{-1}$ gradient pulses, and actually reported successful diffusion studies with field gradient pulses of up to $25 \, \text{T} \, \text{m}^{-1}$. This gradient system consists of a quadrupolar array of wires potted in epoxy. It is suitable for NMR samples of up to 3 mm diameter and driven by a commercial power supply (Bruker, Germany) providing current pulses of up to 40 A.

In 2001, Galvosas et al.[26] described an NMR system utilizing magnetic field gradient pulses of up to $\pm 35 \, \text{T} \, \text{m}^{-1}$ in routine measurements. The gradient probe is
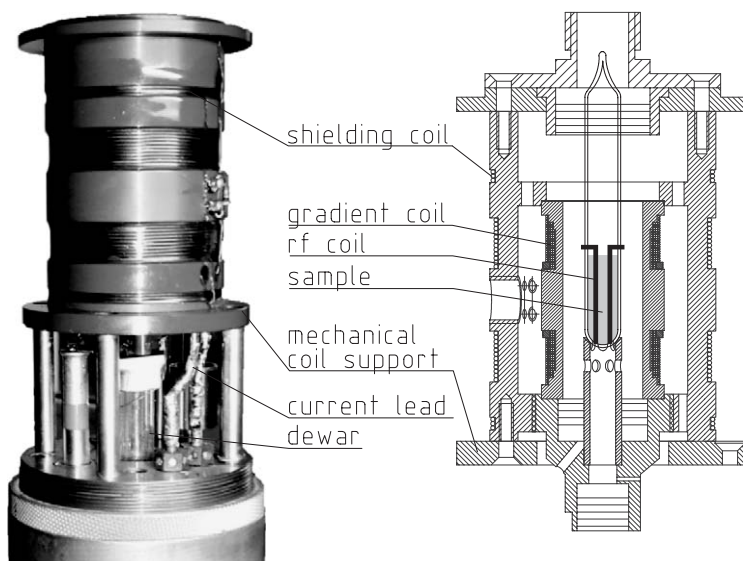
Fig. 13.   Top part of the PFG NMR probe originally developed by Heink *et al.*[22] and also used by Galvosas *et al.*[26] On the photograph (left), the shielding coil as well as the two leads to the gradient coil system are visible. The right-hand side figure represents the drawing of the cross-section through the gradient and shielding coil and indicates sample and rf coil positions. The dewars are omitted for clarity.
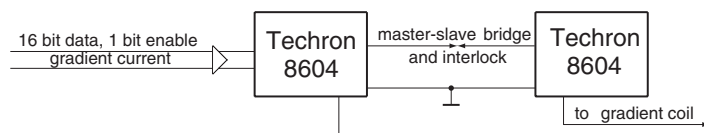
Fig. 14.   PSPPC gradient current power supply as used by Galvosas *et al.*[26] Two commercial gradient amplifiers Techron 8604 are connected in a push–pull configuration.[123] The master (left) is controlled by a digital interface. The slave (right) inverts the output signal of the master. This doubles the voltage across the gradient coil, which is connected in series to the output terminals of the two amplifiers.

the same as described in Ref. 22 (see discussion above and Fig. 13). The current source is based on two commercially available TECHRON 8606 power supplies (Crown Int. Inc., USA). By connecting these power supplies in the so-called push–pull configuration (PSPPC)[123] (see Fig. 14), voltages across the gradient coil of up to ± 300 V and currents of up to ± 100 A can be generated. This leads to the above-mentioned pulsed field gradient amplitudes of up to ± 35 T m^{-1} This gradient system serves as the reference system for the further discussions of the various experimental aspects and possible problems, which one might encounter, while using high-intensity pulsed field gradients.

4.2. Detecting and controlling gradient current instabilities

4.2.1. *Influence and classification of gradient instabilities*

All the considerations in Sections 2 and 3 assume perfectly, often rectangular, shaped field gradient pulses of known and adjustable amplitude. In contrast, in a real NMR experiment, the short current pulses $i(t)$, which determine the shapes $G(t)$ of the field gradient pulses ($G(t) \propto i(t)$), are subjected to instabilities, which may give rise to experimental uncertainties of $i(t)$ and, thus, $G(t)$. During the phase labeling and the magnetization decoding time periods of the PFG NMR sequence, these uncertainties act directly on the observable macroscopic magnetization. In principle, since these uncertainties are small, their influence on the desired diffusion-based spin echo attenuation $\Psi(b)$ is negligible. However, via the spin echo conditions (Eqs. (34) and (43)), they directly affect the formation of the spin echo after the last field gradient pulse, causing instabilities and losses of intensities of the observed spin echo, which may be mis-interpreted as diffusion-based spin echo attenuations (see, e.g., Refs. 25, 26, 58, 59, 72, 104, and 124).

In order to prevent that even small uncertainties of the driving currents pulses influence the formation of the spin echo via the resulting uncertainties of the field gradients, any difference between the areas of the phase labeling and magnetization decoding pulsed field gradients, which we denoted as d($G\delta$) in Eq. (17), must obey the condition[58,59]

$$\mathrm{d}(G\delta) \ll \frac{\pi}{\gamma l}. \tag{64}$$

The quantity l denotes the length of the NMR sample in direction of the APFG . For example, for $l = 1\,\mathrm{cm}$ and $\delta = 1$ ms, which are typical parameters for PFG NMR experiments, differences between the amplitudes of the phase labeling and magnetization decoding pulsed field gradients must be much smaller than $\mathrm{d}\,G \ll 1 \times 10^{-3}\;\mathrm{Tm^{-1}}$! It is remarkable that this high accuracy does not depend on the actual pulsed field gradient intensity. Thus, it applies in the same way for conventional small and specially designed high-pulsed field gradient applications.

Any failure to obey the accuracy requirement according to Eq. (64) leads to an incomplete refocusing of the phase label of the magnetization (compare Fig. 5 and Eq. (17)) and, thus, to artifacts in the diffusion measurements.[25,104,124] Under certain conditions, these artifacts even lead to oscillations of the observed spin echo attenuations,[25] which, however, must clearly be distinguished from the true diffraction pattern observed in the structural NMR imaging approach developed by Callaghan *et al.*[61] Hence, experimental procedures have to be applied, which limit uncertainties of the electrical current pulses generating the field gradient pulses to the required accuracy, which record possible violations of these requirements and which compensate or correct for them if necessary.

The experimental uncertainties of the gradient current pulses may be divided into two classes. First, if the uncertainties are caused by the running NMR sequence itself and are reproducible from scan to scan, they are often correlated to one of the

experimental gradient parameters (G, δ, Δ). For example, eddy currents induced by switching the field gradients may affect the magnetic field at the position of the sample and, hence, the formation of the NMR spin echo. Their influence increases with increasing G but can be reduced using actively shielded gradient coils and APFG pulse sequences.[91] Furthermore, if the gradient coil or/and the gradient current source heats up due to heavy load, the electric resistivity of the gradient coil circuit changes. Consequently, the gradient currents of successive gradient pulses differ, if they are generated by a constant voltage source. Using constant current sources as power supplies, long repetition delays between successive scans and equilibrating gradient pulses[125] prior to the actual measurements may reduce such errors. The signature of these and all other correlated pulsed field gradient uncertainties is that they are reproducible. Due to this property, one is able to design procedures to correct or even compensate for them. Some of these correlated current uncertainties cause reproducible mismatches of the pulsed field gradients $d(G\delta)$. Procedures to compensate such mismatches are described, e.g., in Refs. 26, 58, 59. They are reviewed in the Sections 4.2.2 and 4.2.3.

The second class of uncertainties are uncorrelated to the values of the gradient parameters and cause stochastic fluctuations of the gradient current and, thus, of the mismatch value $d(G\delta)$ from scan to scan. It is indispensable to identify and eliminate the origins of such uncorrelated uncertainties of the gradient currents or to suppress their influence as much as possible. One source of such uncertainties is the gradient amplifier overload, when the gradient current is controlled by not suitable pulsed gradient shape functions.[126] This issue is discussed in detail in Section. 4.2.4. Another source of uncorrelated errors is the hum of the lab power supply, which is almost impossible to remove. However, its influence on the NMR experiment can be transformed into a correlated uncertainty and than be compensated[26] as it will be shown in Section 4.2.5.

4.2.2. *Compensating mismatched pulsed field gradients*

The most sensitive, most appropriate and, in fact, often the only possible approach to detect mismatched field gradient pulses is the observation of the spin echo in the time domain with an additional small read gradient during the preparation and signal acquisition periods. This read gradient must have a non-zero component parallel to the applied pulsed field gradients, which — regardless of the system studied — may always be generated by the same gradient coil system as used for the pulsed field gradients $G(t)$.

If g denotes the sum of all constant (external and internal) field gradients and the additionally applied small read gradient g_r, a mismatch of the field gradient pulses of $d(G\delta)$ causes the echo conditions (Eqs. (34) and (43)) to be fulfilled to a different instant in time. This leads to a shift of the spin echo maximum by[59,104,127]

$$\Delta t = -\frac{d(G\delta)g}{g^2},$$ (65)

where Δt is the displacement of the spin echo maximum from its nominal position t_e, which would be observed without any mismatch.

The occurrence of the shifted spin echo means that the spatial magnetization phase due to the mismatch has a minimum at $t = t_e + \Delta t$. As long as the observed spin echo shift due to the mismatched field gradient pulses is small compared to the characteristic time of the decay envelop of the spin echo in the time domain ($\Delta t \ll T_2^*$), the arising spin echo amplitude allows one to determine the desired diffusion-based spin echo attenuation even without correction of the mismatched pulsed field gradients.[72]

Another approach is to use the spin echo shift to detect a mismatch and correct for it by adjusting the amplitude or width of one of the pulsed field gradients until the observed spin echo arises at the nominal position t_e.[59,104,127] If the gradient amplifier is an analog controlled device, the mismatch can be corrected easily by adjusting one of the gradient amplitudes.[128] For digitally controlled gradient current amplifiers, especially when the amplifier generates ultra-high-intensity pulsed field gradients, this is not always an option since the digital resolution might not be small enough to achieve the necessary accuracy (see Eq. (64) and Ref. 26).

The presence of the additional external read gradient is not necessary during the whole time of the NMR experiment. It is sufficient, if it is applied during the spin echo acquisition and – in order to satisfy the spin echo condition (Eq. (34)) – during a second period prior the acquisition. The main advantages of this PGSE-MASSEY called sequence,[124] which is illustrated in Fig. 15, are that the influence of the read gradient on the diffusion-based spin echo attenuation, the power dissipation in the gradient coil and, hence, the thermal load on the gradient circuit are reduced. This concept can easily be adapted to other (A)PFG NMR pulse sequences.[26,129]

Fig. 15. PGSE-MASSEY pulse sequence[124] with a read gradient g_r, which is terminated at t^* to circumvent interactions with the π rf pulse. A possible mismatch is depicted at the second gradient pulse, $\hat{e}$ denotes the unit vector in direction of the second pulsed gradient and is also valid for the read gradient since both are generated by the same gradient coil. t_c is used to correct for a mismatch while Δt denotes the time between the nominal spin echo position (dotted line) and the shifted echo (solid line). See text for details.

Additionally, if the signal accumulation is performed after Fourier transformation of the spin echo in the in the frequency domain, this sequence allows one even to correct to some extent for pulsed gradient mismatches, which randomly fluctuate from scan to scan (for details see Ref. 124).

4.2.3. Automated mismatch correction

The key ideas of the PGSE-MASSEY sequence[124] were later adapted for a procedure, which automatically detects and corrects for correlated mismatches of the pulsed field gradients by changing the interval over which the read gradient is applied.[26] This procedure was originally described for the 13-interval PFG NMR sequence[26] and proved to be sufficiently sensitive to be applied for high-intensity pulsed field gradients in the reference gradient system described in Section 4.1 (Figs. 13 and 14). In the following, we outline its basic principles using the pulse sequence depict in Fig. 15.

If there is a pulsed field gradient mismatch $d(\boldsymbol{G}\delta)$, which is represented by the black bars at the second gradient pulse in Fig. 15, the presence of the read gradient $\boldsymbol{g}_r$ ensures that the echo condition according to Eq. (34) can still be satisfied. Initially, the correction period of the read gradient (t_c in Fig. 15) is set to zero and the spin echo occurs at the shifted time $2\tau + \Delta t$, where

$$\Delta t = -\frac{d(\boldsymbol{G}\delta)}{\boldsymbol{g}_r} \tag{66}$$

denotes the time shift due to the mismatched pulsed gradients and assumes that there exists; no other gradient than the additional read gradient.[¶]

In the second step, the time shift is measured. Especially for low signal-to-noise ratios, this is achieved conveniently by convoluting the spin echo signals observed with and without any pulsed field gradients. Assuming, that the signal with pulsed field gradients is simply attenuated by the factor $\Psi(b)$ and shifted by Δt due to mismatched pulsed field gradients, this convolution is given by:

$$A(t') = \Psi(b) \int_{-\infty}^{\infty} M_{xy}(b = 0, \ t - t') M_{xy}(b = 0, t + \Delta t) \ dt. \tag{67}$$

The integral in Eq. (67) represents the autocorrelation function of the NMR signal in the original position with that shifted by mismatched pulsed filed gradients. Its maximum occurs at time $t'_{max} = -\Delta t$. Hence, the shift of the spin echo in the time domain is simply determined by the position of the maximum of the auto correlation function given in Eq. (67).

The advantage of this convolution compared to the direct observation of the spin echo shift is easily rationalized, if one considers the general property of the convolution that uncorrelated signals (noise) do not contribute to the convolution

---

[¶]The sign of Eq. (66) is opposite as compared to the corresponding equation in Ref. 26. The difference is caused by the fact that the pulse sequence considered in Ref. 26 satisfies condition I (see Eq. (43)). In this chapter, the pulse sequence satisfies condition II instead (see Eq. (44)). The same applies later again to Eq. (68).
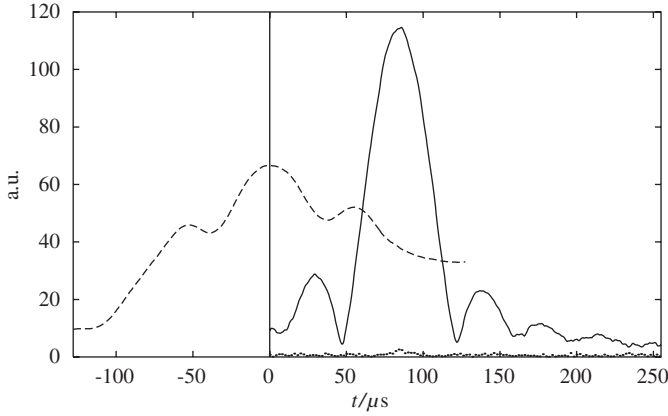
Fig. 16.   Example for the determination of spin echo positions by the autocorrelation function approach described in the text: ^{19}F NMR spin echo signal envelope of CF$_4$ adsorbed in NaX zeolite without (—) and with pulsed field gradients ($\cdots$) recorded in the presence of a read gradient of 53 mT m^{-1}. $t = 0$ is the start of the acquisition window of the spin echo signal. The convolution (- - -) is a smooth function although the signal with pulsed field gradients switched on ($\cdots$) is strongly attenuated and noisy. The maximum of the convolution appears at $t = 0$, which means that no pulsed field gradient mismatch occurred in this case. [*Source:* Adapted from Ref. 64.]

function. Thus, the position of a maximum in a convolution is determined more accurately than the maximum of the corresponding original noise-containing signal. This is demonstrated in Fig. 16, where the ^{19}F NMR time domain spin echo signal of CF$_4$ adsorbed in NaX zeolite was acquired without and with pulsed field gradients.[64] The spin echo under the influence of the gradients is strongly attenuated (signal-to-noise ratio of about two). Nevertheless, the result of the convolution is a smooth function, which allows one to determine the position of the maximum of the auto correlation function. In the presented example, the maximum of the autocorrelation function appears at $t = 0$, which means that no time shift and, thus, no mismatch occurred. This is hardly to see in the original attenuated signal.

Subsequent to the precise determination of the spin echo shift, it is easy to correct for a possible mismatch by changing the correction time t_c of the read gradient in such a way that the echo condition is satisfied at the time 2τ ($\Delta t = 0$). It is easy to rationalize from the principle of gradient echoes[41,42] that the required correction time t_c must correspond to the inverse time shift observed due to the mismatched pulsed field gradients. Thus, t_c is given by:

$$t_c = -\Delta t = t'_{max} \tag{68}$$

and simply determined by calculating the time t'_{max}, which represents the position of the maximum of the autocorrelation function (Eq. (67)).

Thus, in a second run of the PFG NMR pulse sequence, which is only necessary, if one observes $t'_{max} \neq 0$, the correction time of the read gradient is set to $t_c = t'_{max}$. This ensures that the spin echo is observed at the nominal position. Hence, the

spatially dependent magnetization phase due to mismatched pulsed field gradients is deleted by the read gradient acting during the correction time t_c and the spin echo intensity is solely reduced by the desired diffusion-based spin echo attenuation $\Psi(b)$.

The complete procedure can be performed automatically by the spectrometer control software. It requires a macro or script, which successively starts the PFG NMR pulse sequence with $t_c = 0$, saves the time domain spin echo NMR signals acquired without and with pulsed field gradients, convolutes both signals and calculates the position t'_{max} of the maximum of the convolution. If a mismatch occurred, which corresponds to the result $t'_{max} \neq 0$, it sets $t_c = t'_{max}$ and starts the sequence without any change of the pulsed field gradient settings again.

For measurements, which are not compatible with a read gradient during the spin echo detection (e.g., DOSY methods, phase encoded MRI, etc.), the final pulse sequence is performed without the read gradient acting during data acquisition but with the small part of it during the time interval t_c. Possible negative values for the mismatch correction time t_c, which are determined by the convolution approach described above, are accounted for by reversing the sign of the read gradient acting during t_c in the final run.[26,130]

4.2.4. *The optimum shape of the gradient pulse*

Generally, a time-dependent pulsed field gradient $G(t)$ is proportional to the electrical current $i(t)$ flowing through the gradient coil. The current $i(t)$ is generated and controlled via a gradient current source, which is usually a (high) power (operational) amplifier driven in a current controlled mode. This is internally realized via a feedback loop adjusting the output current $i(t)$ proportional to an input voltage $u(t)$. The so-called setpoint function $u(t)$ carries the desired time pattern of the gradient pulse. The gradient current $i(t)$ and $u(t)$ are connected via:

$$i(t) = vu(t), \tag{69}$$

where v is a constant conversion factor of the current source. However, care must be taken if sudden changes of the current through the coil are required since $di(t)/dt$ is limited by the gradient coil inductance L. It is easily realized via

$$u_L(t) = L\frac{di(t)}{dt} + R_L i(t), \tag{70}$$

that $(di(t)/dt) \rightarrow \infty$ requires $u_L \rightarrow \infty$, which means nothing else than an infinite high voltage across the gradient coil. This is of course impossible for real gradient current sources. The maximum voltage across the coil is always limited by the DC power supply of the gradient current source U_B. Thus, if one requires a sudden change of the gradient current, which corresponds to a setpoint function (step function)

$$u(t) = \begin{cases} 0 & \text{for} \quad t < 0 \\ I/v & \text{else,} \end{cases} \tag{71}$$

the output current $i(t)$ cannot follow instantaneously. Instead, when at $t = 0$ the current is switched on, it will first undergo an exponential growth controlled by the coil time constant $\tau_L = L/R_L$

$$i(t) = \begin{cases} 0 & \text{for} \quad t < 0 \\ \frac{U_B}{R_L}\left[1 - e^{-(t/\tau_L)}\right] & \text{for} \quad 0 \leq t \leq t_L, \\ I & \text{for} \quad t_L \leq t \end{cases} \tag{72}$$

and settle to the required current I only after a finite time $t_L = \tau_L \ln \frac{U_B}{U_B - IR_L}$. The current slew rate is given by:

$$\frac{\mathrm{d}i(t)}{\mathrm{d}t} = \frac{U_B}{L}e^{-(t/\tau_L)} = k_i\, e^{-(t/\tau_L)} \quad \text{for} \quad 0 \leq t \leq t_L, \tag{73}$$

where k_i denotes the initial slope of the current representing the limit for a given U_B and L. Inserting Eq. (72) into Eq. (70) leads to:

$$u_L(t) = \begin{cases} 0 & \text{for} \quad t < 0 \\ U_B & \text{for} \quad 0 \leq t \leq t_L, \\ IR_L & \text{for} \quad t_L \leq t. \end{cases} \tag{74}$$

Thus, for the time $0 \leq t \leq t_L$, the voltage across the coil is equal to U_B which means an overload of the gradient current source. During this time, error currents caused by the ripple, hum and noise of the DC power supply add unsuppressed by the feedback loop to the gradient current, causing random mismatches. Therefore, it is necessary to avoid overloads and to keep the voltage across the coil always smaller but as close as possible to U_B, which corresponds to the condition:

$$u_L(t) \lesssim U_B \tag{75}$$

Shaping the gradient and hence choosing a setpoint function different from the step function in Eq. (71) can help to prevent such amplifier overloads. Sinoidal and trapezoidal shaped gradient pulses were proposed and often applied for this purpose.[25,77,80,131] However, it is easy to recognize that a common drawback for all of those functions is a loss of gradient intensity given by the time integral $\int_0^\delta G(t)\,\mathrm{d}t$ with respect to the limits of the gradient width and amplitude. Therefore, in general, the best choice for the shape of the rising edge of a setpoint function is a pattern similar to $i(t)$ in Eq. (72).[126] The falling edge must be shaped accordingly (see Ref. 126), leading to a complete gradient pulse

$$u(t) = \begin{cases} \frac{U_B}{v\,R_L}\left[1 - e^{-(t/\tau_S)}\right] & \text{for} \quad 0 \leq t \leq t_S \\ I/v & \text{for} \quad t_S \leq t \leq t'_S \\ \frac{U_B}{v\,R_L}\left[e^{(\delta - t)/\tau_S} - 1\right] & \text{for} \quad t'_S \leq t \leq \delta \\ 0 & \text{else,} \end{cases} \tag{76}$$

where τ_S is a time constant to be defined. The transitions between the exponentially shaped edges of the pulse and the desired constant current I are defined by $t_S = \tau_s \ln \frac{U_B}{U_B - IR_L}$ and $t'_S = \delta - \tau_S \ln (U_B + IR_L)/(U_B)$, respectively.[64,126]

For a rising edge as given by the first line in Eq. (76), the voltage across the coil is obtained via Eqs. (70) and (69)

$$U_B \frac{\tau_L}{\tau_S} \leq u_L(t) < U_B \quad \text{for} \quad 0 \leq t \leq t_S. \tag{77}$$

The voltage across the coil $u_L(t)$ is always smaller than U_B as long τ_s is larger compared to the coil time constant τ_L. While $\tau_S > \tau_L$ is a necessary condition for τ_S in order to ensure that the gradient current source will never be overloaded, it is possible to choose τ_S similar to τ_L. This choice of τ_S exploits the gradient current source to its maximum while in the meantime maintaining a stable feedback loop preventing any amplifier overload.

Such an exponential shape (Eq. (76)) is convenient to use since all parameters are well known for the given gradient system (v, U_B, R_L and τ_L) and well controlled by the NMR experiment (τ_S, I), respectively. Furthermore, the gradient shape is given by an analytical expression and precisely reproduced by the gradient current source (see Ref. 126), which makes the processing of the NMR data more reliable and easier.

It is important to recognize that the rising and falling edges of the optimum shaped field gradient pulses do not change their shapes and slopes, when choosing different maximum currents I as usually done in a PFG NMR experiment, in which the gradient amplitude is increased step by step. Only the transition times, to and from the current plateau t_S and t'_S, change. Fig. 17 illustrates this for field gradient pulses with a nominal length of $\delta = 150$ μs generated in the reference gradient system (see Fig. 13 and 14, $\tau_L = 165$ μs, $\tau_S = 200$ μs and $U_B = \pm 300$ V). The currents in the three distinct plateau regions correspond to pulsed field gradient amplitudes of 24, 15, and 5 T m^{-1}, respectively. It is evident from Fig. 17 that the
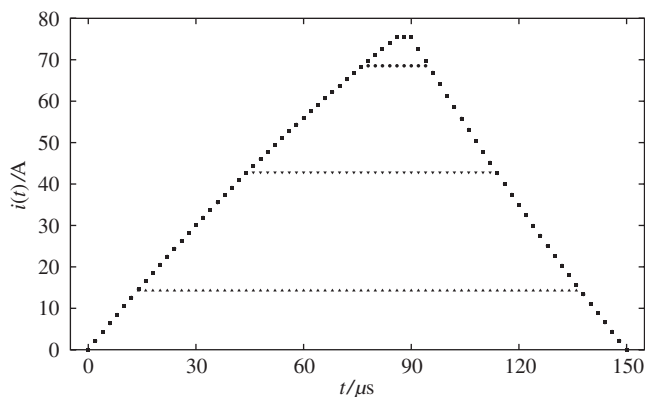
Fig. 17. The optimum shape of the field gradient pulse determined for the reference gradient system described in Section 4.1 and a gradient current $i(t)$ with a nominal length of $\delta = 150$ μs. The limit for the gradient current for this length is 75.5 A (■). Smaller gradient currents of 68.6 A (●), 42.9 A (▼), and 14.3 A (▲) are depicted as well. The current is set to a new value every 2 μs using Eq. (76) and Eq. (69). [*Source:* Adapted from Ref. 126.]

gradient pulse cannot be generated by a simple scaling of a unique gradient shape by a factor. Instead, the gradient current is set every 2 μs (corresponding to the points in Fig. 17) and guided up and down until the desired current value I is reached. It is also clear from Fig. 17 that for short gradient current pulses the maximum output current is given by the interception of the rising and falling edges of the pulse. For the example in Fig. 17, the peak value of the gradient current is 75.5 A corresponding to a pulsed field gradient of 26. 4 T m^{-1}.

Since the shape of the gradient current pulse is determined by an analytical expression given by Eq. (76), it is possible to calculate directly the pulsed gradient term $A_p(t_e)$ using Eq. (60). The result is:

$$A_p(t_e) = \left\{ (\Delta' + \tau)\{S_G[f_1(I_G) + \delta I_G] - S_F[f_1(I_F) + \delta I_F]\}^2. \right.$$
$$\left. + 2\tau[f_1(I_F) + \delta I_F]^2 + f_2(I_F) - \frac{1}{3}\delta^3 I_F^2 + f_2(I_G) - \frac{1}{3}\delta^3 I_G^2 \right\} \ c^2, \quad (78)$$

where S_G and S_F represent the signs of the gradient currents I_G and I_F used to generate the G and F gradients of the generalized PFG NMR sequence (Fig. 9), respectively. c is the current-to-gradient conversion ratio and f_1 and f_2 denote the shape factors for the exponential shape. They describe the deviation from the rectangular shape. For $\tau_S = 0$ and $I \ll I_0$ these factors disappear and Eq. (78) transforms into the spin echo attenuation given in Eq. (59). The f_1 and f_2 functions are rather complex (see Ref. 64) and are given here for completeness:

$$f_1(I, I_0, \tau_S) = \tau_S \left(I_0 \ln \frac{I_0^2}{I_0^2 - I^2} - I \ln \frac{I_0 + I}{I_0 - I} \right) \quad (79)$$

and

$$f_2(I, I_0, \tau_S, \delta) = \tau_S^3 \left\{ 4I_0 I - (I_0^2 - I^2) \ln \frac{I_0 + I}{I_0 - I} \left[\frac{1}{3} \left(\ln \frac{I_0 + I}{I_0 - I} \right)^2 + 2 \right] \right\}$$
$$+ \tau_S^2 \delta \left\{ I_0 I \left[\left(\ln \frac{I_0}{I_0 - I} \right)^2 - \left(\ln \frac{I_0}{I_0 + I} \right)^2 \right] - I^2 \left[2 + \left(\ln \frac{I_0 + I}{I_0 - I} \right)^2 \right] \right.$$
$$+ \left. I_0^2 \left[\left(\ln \frac{I_0 + I}{I_0 - I} \right)^2 - \left(\ln \frac{I_0}{I_0 - I} \right)^2 - \left(\ln \frac{I_0}{I_0 + I} \right)^2 \right] \right\}$$
$$- \delta^2 I \ f_1(I, I_0, \tau_S). \quad (80)$$

Regardless of the somehow long mathematical expression the advantage is obvious: A setpoint function (gradient shape) given by Eq. (76) in conjunction with an analytical expression for the calculation of the pulsed field gradient term $A_p(t_e)$ of the spin echo attenuation given by Eq. (78) serves both, the maximum exploitation of the gradient current source and a reliable processing of the acquired PFG NMR data.[126]

4.2.5. *Synchronization of the pulse sequence to the lab power supply*

Since the observation time of PFG NMR experiments is typically in the range of (1 … 1000) ms error values influencing the gradient current in a frequency range of (1 … 1000) Hz may cause a mismatch of the gradient pulses. As reported in[26] the hum of the mains power supply falls into this range. Therefore, it is a prominent source for small mismatches of the gradient pulses. Naturally, this will cause random (uncorrelated) instabilities of the spin echo in the time domain since there is no correlation between the mains frequency and the repetition rate of the NMR experiment. In fact, it was shown in Ref. 26 that in non-synchronized PFG NMR experiments with a small read gradient for mismatch detection, random shifts of the spin echo position occurred from scan to scan, which are caused by slight differences of the gradient (current) amplitudes due to the hum of the power supply (see Fig. 2 in Ref. 26). However, triggering the pulse sequence to the phase of the mains power supply reduced this random shift of the spin echo hugely. Even at the maximum possible pulsed field gradient amplitudes, there was no random shift of the spin echo observed. Only, reproducible shifts occurred, which increased with increasing pulsed gradient value. These reproducible spin echo shifts could be attributed to reproducible pulsed field gradient mismatches, which could easily be corrected by the automated procedure, described in Section 4.2.2.

If the synchronization of the NMR pulse sequence to the lab mains phase is not feasible due to limitations of the NMR apparatus or the pulse sequences used, one can blank the gradient current amplifier and unblank it only during the duration of the field gradient pulses.[111] While this reduces the influence of the hum of the gradient amplifier it makes it impossible to generate read gradients by the same system. Additionally, one can choose the observation time Δ in the PFG NMR diffusion experiment as a multiple of the mains period. Hence, superimposed hum caused by the DC power supply of the gradient current source adds to the pulsed field gradients in the prepare and read interval in equal measures.[111]

Only the synchronization of the pulse sequence to the mains of the lab power supply and the optimum shaped pulsed field gradients (Section 4.2.4) in connection with the automated routine for mismatch detection and correction (Section 4.2.3) enables routine use of high-intensity pulsed field gradients for NMR diffusion studies in the author's lab (see.[51,52]) Specific examples from porous materials will be given in the next sections. In the very first diffusion studies with these procedures, the reference gradient system was exploited to its maximum pulsed field gradient amplitude capabilities of $\pm 35\,\mathrm{T\,m^{-1}}$ using dry glycerol ($D = 1.36 \times 10^{-12}\,\mathrm{m^2\,s^{-1}}$) as a suitable test sample for proving exponential spin echo decays (see Fig. 4 in Ref. 26). Subsequently, temperature-dependent diffusion studies with a viscous dibloc copolymer PEE-PDMS (molar weight $10\,\mathrm{kg\,mol^{-1}}$) showed that self-diffusion coefficients down to $(3.0 \pm 0.1) \times 10^{-15}\,\mathrm{m^2\,s^{-1}}$ are measurable with good accuracy.[26] The spin echo attenuation plots for these studies are provided in Fig. 18. They exhibit linear decays on the semi-logarithmic presentation, which allow reliable determination of such small self-diffusion coefficients.
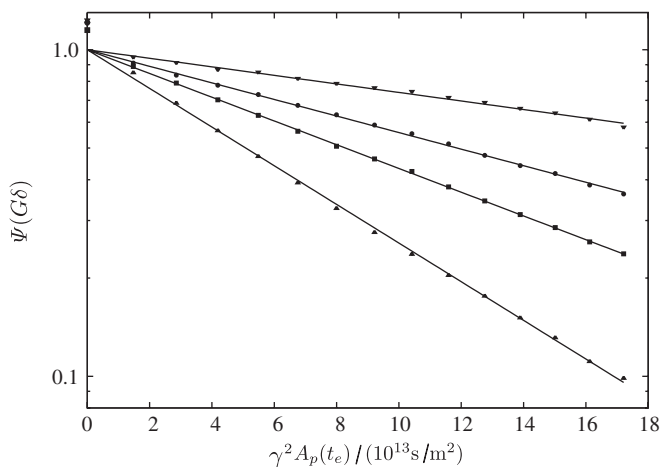
Fig. 18. Spin echo attenuation versus gradient intensity for PEE-PDMS at different temperatures (with increasing slope at 285.5 K, 296.5 K, 304 K, and 310 K, respectively). The measurements were performed using the 13-interval sequence with equal pulsed field gradient intensities F and G (see Section 3.3.1 and Fig. 11) with $\Delta = 500$ ms, $\delta = 1$ ms, $\tau = 2.5$ ms and $G_{max} = \pm 35$ T m^{-1}. [*Source:* Adapted from Ref. 26 with permission from Elsevier.]

5. RECENT PFG NMR DIFFUSION STUDIES ON POROUS MATERIALS

According to the classical definition, a porous material consists of a solid matrix, in which microscopically small void spaces, the so-called pores, are embedded.[132] The central property that fluids may be stored inside and transported through the pore space makes porous materials interesting and indispensable for a number of applications (see, e.g., Refs. 16, 40, 45, 53, and 132). Owing to the small size of the pores, pore and matrix space form a large internal interface. Its geometric and chemical properties determine to a large extent the interaction between the matrix and the pore fluids and, thus, macroscopic properties of the porous material.

The diffusion of the pore fluids to the internal pore matrix interface mediates these fluid/matrix interactions to the majority of the pore fluid molecules. For example, it is the precondition for the enhanced longitudinal and transverse relaxation rates, often observed in NMR studies with fluids in porous materials,[133,134] and utilized to derive pore structure parameters like surface-to-volume ratios or pore sizes.[133–135] On the other hand, the solid matrix volume is not accessible for any mass transport process of the pore fluid and, thus, enlarges the diffusion pathway between distant points inside the pore space. Hence, geometric properties of the pore/matrix interface have direct influence on the diffusion coefficients of the pore fluids.

Since PFG NMR allows non-destructive investigations of diffusion processes, it represents a well-suited tool to explore both fluid/matrix interactions as well as

geometric properties of the pore space of the porous material. Generally, it depends on the length scale of the observed diffusion process compared to the typical pore size of the porous material, which kind of information one may obtain from such investigations. The following sections provide typical examples for PFG NMR diffusion studies of fluids in different types of porous materials and highlight strategies for data interpretation.

5.1. Nanoporous materials

In nanoporous materials (pore radius $R_p \lesssim 25\,\text{nm}^{\|}$), PFG NMR diffusion studies are only able to provide information on transport process over length scales, which exceeds the typical pore dimensions. This has two main reasons: First, even with the highest pulsed field gradient amplitudes generated, the spatial period of the magnetization phase (compare Fig. 5 and Eq. (9)) remains large compared to the pore radius R_p. This is expressed by the relation $(2\pi)/(n\gamma\delta G) \gg R_p$, where n denotes the number of position encoding pulsed field gradients applied in the pulse sequence. Second, increasing the number n of pulsed field gradients or their width δ would decrease the spatial period of the magnetization phase towards the pore radius but leads at the same time to an increase of diffusion time, since $\Delta > n\delta$. The shortest possible diffusion times may be realized in SE PFG NMR experiments and are in the order of 1 ms. During that time, the root mean square displacements of liquid-like pore fluids clearly exceed the value of 1 µm (compare Fig. 3), which is by orders of magnitude larger than the pore radius R_p. Thus, if PFG NMR allows the investigation of self-diffusion processes in such materials, they are representative for averaged fluid/matrix interaction but, generally, do not allow one to deduce quantitative information on the pore size of the nanopores. Nevertheless, especially for new types of nanoporous materials, which are designed with optimized pore structures for application in gas storage, separation, filtration and catalysis, respectively, PFG NMR provides often the first experimental data on diffusion processes inside the pore system and allows one to draw conclusions on the pore architecture.

5.1.1. Anisotropic diffusion in MCM-41

In mesoporous materials of MCM-41 type,[136] which consist of hexagonally arranged cylindrical pores ($R_p \simeq 3\,\text{nm}$) in an amorphous SiO_2 matrix, PFG NMR studies clearly showed that the self-diffusion of n-hexadecane[137,138] as well as of water[139] is anisotropic and best described by an axisymmetrical diffusion tensor. In such cases, the spin echo attenuation is given by:[39]

$$\Psi(b) = \frac{1}{2}\int_0^\pi \text{e}^{-b(D_{\text{par}}\,\cos^2\Theta + D_{\text{perp}}\,\sin^2\Theta)}\sin\Theta\ \text{d}\Theta, \tag{81}$$

$^{\|}$This upper limit of pore radii includes both micro- and meso-porous materials according to the IUPAC classification.
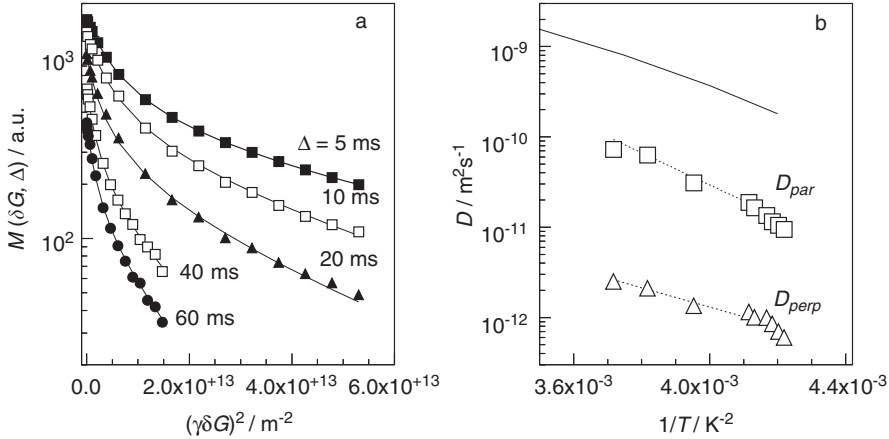
Fig. 19. PFG NMR studies of water self-diffusion in MCM-41[139a,139b]: (a) Examples for the fits of the model of an axisymmetrical diffusion tensor (Eq. (81)) to the experimentally observed signal intensities ($M(G\delta, \Delta)$) for five different diffusion times at $T = 263$ K. (b) Dependence of the parallel ($\square$) and perpendicular ($\triangle$) components of the diffusion tensor on the inverse temperature. For comparison, the full line represents the self-diffusion coefficients of super-cooled bulk liquid water. [*Source:* Redrawn from Ref. 139b with permission from Springer-Verlag.]

where $b = \gamma^2 A_p$ is the pulsed gradient parameter according to the pulse sequence used (see Section 3) and D_{par} and D_{perp} denote the two elements of the axi-symmetrical diffusion tensor representing the diffusion parallel and perpendicular to the pore orientation, respectively. The integral over $\sin \Theta \, d\Theta$, which represents the powder average over all orientations of the hexagonally arranged pores with respect to the field gradient direction, occurs since the measurements are generally performed in beds of randomly oriented MCM-41 particles. The deviation from a single-exponential spin echo attenuation clearly observed in these materials and described by Eq. (81) results from the orientation distribution of the MCM-41 particles and, thus, may be considered as an apparent multi-component self-diffusion.[137–139] Especially in the studies with water as pore fluid,[139] which were performed below the freezing point of bulk water in order to exclude any diffusion of interparticle water between the individual MCM-41 particles, it was shown that the deviation from a single-exponential spin echo attenuation are well represented by the axisymmetrical diffusion tensor model (see Eq. (81) and Fig. 19). The consistent occurrence of parallel and smaller (but non-zero) perpendicular tensor components ($D_{par} > D_{perp} > 0$ in Eq. (81)) for different measurement conditions (Fig. 19) confirms the preferred diffusion in axial pore direction. However, the non-zero components of D_{perp} require that the pore channel walls are partially permeable or that the channels are slightly bent over the length scale of the observed diffusion process.[139] This conclusion from PFG NMR diffusion studies provides important insight into the pore architecture of such mesoporous materials, which is not available from diffraction data.

In other PFG NMR diffusion studies with MCM-41, a diffusion anisotropy was not found because the diffusional exchange between adjacent domains of hexagonally oriented pores was not excluded and the typical diffusion length during the PFG NMR experiments exceeded this domain size.[138,140–142] In all these cases, the reported diffusion coefficients are rather representative for the diffusion between the domains and, thus, do not provide direct information on the mesopore architecture (see, e.g., Refs. 138 and 142 and references therein).

5.1.2. *Intracrystalline diffusion in metal-organic frameworks*

Metal-organic framework (MOF) coordination polymers represent the newest family of crystalline nanoporous materials.[143,144] They are especially interesting for chemical engineering applications, since by changing organic linkers between the metal coordination centers, one is able to design a variety of related materials with different pore sizes or chemical properties of the matrix. The most prominent MOF materials are Zn-MOF-5 ($R_p \simeq 0.7$ nm,[145]) and Cu-BTC ($R_p \simeq 0.4$ nm[146]).

Until very recently, only theoretically determined diffusion coefficients of guest molecules in such metal-organic frameworks were available.[147,148] PFG NMR provided the very first experimental diffusion data for MOF's.[149,150] They include temperature dependencies and activation energies of diffusion as well as tracer-exchange rates of methane and ethane in MOF-5.[150] Additionally, *n*-hexane and benzene self-diffusion in MOF-5 was studied at room temperature.[149,150] The results show that *n*-hexane and benzene exhibit self-diffusion coefficients in the micropores in the order of a few 10^{-9} m^{2}s^{-1} which are similar to the corresponding values in the bulk liquids and which confirm the data obtained by MD-simulations.[148,151] However, the PFG NMR studies revealed non-exponential spin echo attenuations for *n*-hexane and benzene, which were independent of observation time (see Fig. (1) in Ref. 150). This is a clear indication for a multi-component diffusion, which is not influenced by the exchange between the gas phase surrounding the MOF-5 crystals. By solid state MAS NMR it was demonstrated that a part of the micropores of the MOF-5 contained residual diethylformamide (DEF) solvent from the MOF-5 synthesis, which could not be removed by sample activation. Thus, the current explanation for the multi-component diffusion behavior experimentally observed for *n*-hexane and benzene is that in parts of the MOF-5 crystals the DEF solvents blocked the micropores and reduced the mobility of the adsorbed molecules (for more details see Ref. 150).

Compared to MOF-5, the self-diffusion coefficient of *n*-hexane in the Cu-BTC structure is two orders of magnitude smaller. At room temperature one obtains a value of $(1.1 \pm 0.2) \times 10^{-11}$ m^{2}s^{-1} [149] Fig. 20 represents a series of spin echo attenuations measured with the 13-interval PFG NMR sequence at variable temperatures and the Arrhenius plot of the obtained self-diffusion coefficients. Due to the Cu^{2+}-ions, which act as coordination center in the Cu-BTC framefork, the longitudinal and transverse relaxation times of the *n*-hexane adsorbed in the micropores are small, which allow only the application of short diffusion times of 5 ms and 10 ms, respectively, and short pulsed field gradients of $\delta = 300$ µs. Thus, in
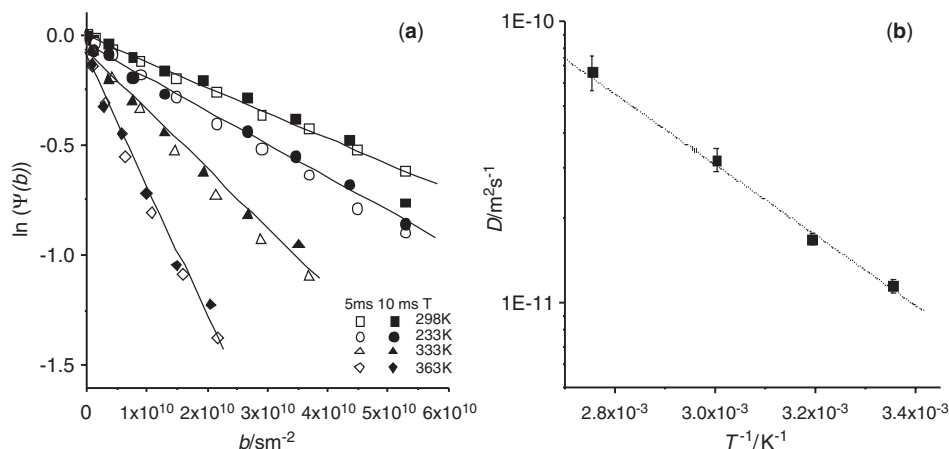
Fig. 20. PFG NMR studies of intracrystalline self-diffusion of *n*-hexane in Cu-BTC: (a) Spin echo attenuations plots for diffusion times of 5 and 10 ms at different temperatures. The slopes and, thus, the self-diffusion coefficients increase with increasing temperatures, (b) Arrhenius presentation of the temperature dependence of the self-diffusion coefficients. [*Source:* Adapted from Ref. 149].

order to achieve a sufficient spin echo attenuation, pulsed field gradients of up to $G = \pm 25\,T\ m^{-1}$ were necessary. The obtained spin echo attenuations are independent of the diffusion time and sufficiently well described by a single-exponential decay (see Fig. 20). They exhibit an increasing slope with increasing temperature. The temperature dependence of the intracrystalline self-diffusion coefficient is plotted in Fig. 20. The corresponding activation energy for self-diffusion of *n*-hexane in Cu-BTC was found to be $E_A = (24 \pm 2)\,kJ\ mol^{-1}$.[149]

5.1.3. *Internal and external diffusion barriers in zeolites*

Similar intracrystalline self-diffusion studies in microporous zeolites have a long history and are an example how non-destructive PFG NMR diffusion studies enlarged the picture of scientists and engineers on transport processes in porous materials.[40,50,104] Furthermore, techniques originally developed for the interpretation of PFG NMR diffusion studies in beds of zeolite crystals like the propagator concept[27,40] and the fast NMR tracer exchange method[40,152] proved to be useful for a number of other materials, where internal or external interfaces alter diffusion processes.

On the other hand, by applying the new techniques for generation of high-intensity alternating pulsed field gradients, the experimental insight into diffusion processes in zeolites improved remarkably over the past years.[51,52] Prominent examples are the experimental verification and theoretical treatment of single-file diffusion in ALPO$_4$-5 zeolites, in which molecules adsorbed in narrow 1D micropores are not able to pass each other,[153,154] and the detection of internal transport

resistances in large MFI-type zeolites,[154–156] which proved the heterogeneous morphology of apparently perfectly shaped zeolite crystals.

The application of the short-time approximation of Mitra *et al.*[28] which allows one to extract surface-to-volume ratios (S_V) from effective self-diffusion coefficients (D_{eff}), to zeolites systems enabled the investigation of the influence of the external crystal boundaries on the intracrystalline diffusion of adsorbed molecules. In the first of these studies, which was performed with the 13-interval sequence with unequal F and G pulsed field gradients using ethane as probe molecule in H-ZSM-5 zeolites, the apparent crystal raduis calculated via the surface-to-volume ratio ($\hat{R}_c = 3/S_V$) from the initial slope of the time dependence of the relative effective self-diffusion coefficients ($D_{eff}(\Delta)/D_0$) was about a factor of three smaller than the radius of the zeolite crystals (R_c) determined by microscopy.[157] However, by including the terms, which represent the second order in molecular displacement ($D_0\Delta$), the short-time approximation transforms into the equations:[28,158]

$$\frac{D_{eff}(\Delta)}{D_0} = 1 - \frac{4}{3\sqrt{\pi}} \frac{1}{\hat{R}_c} \sqrt{D_0\Delta} - \frac{1}{2\hat{R}_c^2} D_0\Delta + \cdots \tag{82}$$

for reflecting boundaries and

$$\frac{D_{eff}(\Delta)}{D_0} = 1 - \frac{2}{3\sqrt{\pi}} \frac{1}{\hat{R}_c} \sqrt{D_0\Delta} - \frac{1}{\hat{R}_c^2} D_0\Delta + \cdots \tag{83}$$

for absorbing boundaries, respectively. PFG NMR studies with large NaX crystals showed that for *n*-hexane (*n*-C_6H_{14}, measured by ^1H NMR at 298 K) the spin echo attenuations are single-exponential and that the obtained effective intracrystalline diffusion coefficients obey Eq. (82).[158] Thus, on the time scale of the PFG NMR experiment, the external boundary of the NaX crystal represents an impermeable diffusion barrier for the adsorbed *n*-C_6H_{14} molecules. In the same crystals, tetrafluoromethane (CF_4, measured by ^{19}F NMR at 203 K) shows a distinct multiexponential spin echo attenuation, which evidences a partial exchange of the CF_4 molecules with the gas phase surrounding the zeolite crystals. Thus, the external crystal boundary is permeable for CF_4 molecules. Since the relative amount of exchanging molecules depends on the diffusion time, mean intracrystalline life times may be determined from the spin echo attenuations using the so-called NMR tracer desorption technique.[40,152] Moreover, the effective self-diffusion coefficients of the part of the CF_4 molecules, which did not exchange with the gas phase, follow the time dependence given by Eq. (83) for absorbing boundary conditions. The crystal sizes, determined by the PFG NMR-based approaches using Eqs. (82) and (83) as well as those measured by optical microscopy agree very well with each other. These studies confirmed that the effective intracrystalline self-diffusion coefficients measured by PFG NMR exhibit different time dependencies for the case of permeable and impermeable zeolite crystal boundaries and proved the applicability of the short-time approximation to diffusion processes in these cases.[158]

Diffusion studies in zeolites will remain a challenging task for PFG NMR in the future. However, the interests will shift to diffusion studies involving more than one
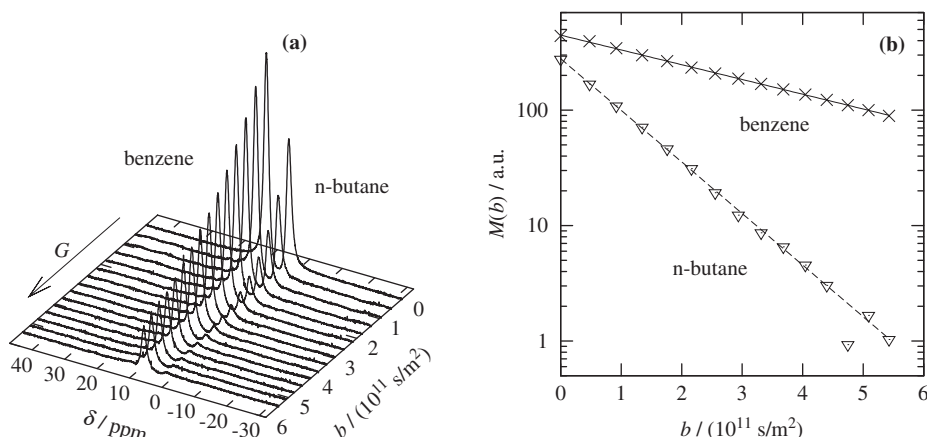
Fig. 21. FT PFG NMR diffusion measurements for benzene and *n*-butane in zeolite NaX using the 13-interval PFG NMR sequence with pulsed field gradient of up to $\pm 20\,T\,m^{-1}$. (a) NMR spectra as function of applied pulsed gradient amplitude *G*. (b) Spin echo attenuation plot for each individual species. Their slopes correspond to diffusion coefficients of $(1.03 \pm 0.04) \times 10^{-11}\,m^2\,s^{-1}$ and $(2.94 \pm 0.10) \times 10^{-12}\,m^2\,s^{-1}$ for *n*-butane and benzene, respectively. [*Source:* Adapted from Ref. 130 with permission from Elsevier.]

mobile chemical component. Thus, DOSY methods or at least FT PFG NMR methods suitable for high intensity pulsed field gradients are desirable. As an example, Fig. 21 represents the spin echo attanuations for benzene and *n*-butane adsorbed simultaneously in NaX zeolites. The measurements were performed with the automated correction procedure for mismatched pulsed field gradients described in Section 4.2.3 and utilized pulsed field gradients of up to $\pm 20\,T\,m^{-1}$ in the 13-interval PFG NMR sequence.[130]

Due to the inherently small mobility of adsorbed molecules and the strong fluid/matrix interactions, NMR lines of adsorbed species in nanoporous materials are generally broad (see Fig. 21). Thus, soild-state NMR methods to increase the spectral resolution combined with sufficiently large pulsed field gradients are of high interest for such studies. First results of magic angle spinning (MAS) PFG NMR studies in nanoporous materials were recently reported for water/lipid mixtures in cylindrical aluminum oxide tubes[92] and adsorbents in zeolite NaX and silicalite-1, respectively.[78,159,160] In the later studies, a mixture consisting of four adsorbed species in NaX zeolites[78] and a technically important iso/*n*-butane mixture in silicalite-1[159,160] were successfully investigated.

5.2. Materials with interconnected macropores

According to the IUPAC classification, pores with a radius of $R_p > 25\,nm$ are macropores. Due to the larger pore size, fluid/matrix interaction in macroporous materials are smaller than in nanoporous materials. This leads to larger transverse

relaxation times of the pore fluids, which makes NMR studies easier. Generally, if a material contains a substantial amount of interconnected macropores, its transport properties are governed by this macropore system. However, compared to the examples of crystalline nanoporous materials given above, macropores exhibit often a non-regular geometry and a chemical heterogeneous pore/matrix interface. The following sections provide examples for PFG NMR studies, which are aimed to characterize macropore systems and which are substantially influenced by the macropores, respectively.

5.2.1. *Formulated nanoporous materials and catalysts*

For technical applications in adsorption, separation, filtration and catalysis, respectively, nanoporous materials, which are often produced as small particles of a few micrometer size, are formulated to millimeter-sized objects such as, e.g., pellets and tablets. In this process, a secondary macro or transport pore system is created, which surrounds the nanoporous material and which has to ensure the accessibility of the active nanoporous materials inside the formulated particles. The same situation applies for those formulated catalysts, which consist of finely dispersed catalytic active compounds deposited on the pore/matrix interface of chemically inert support materials, such as, certain metal oxides, ceramics, or glasses.

For the characterization of transport properties of such formulated materials, PFG NMR studies are well suited. Depending on the size of the corresponding macro or transport pores as well as on the state of the pore fluid used to explore these pores, information on the pore structure and the type of the diffusion process, respectively, may be deduced.

Water in porous Al_2O_3 and SiO_2 catalyst support pellets[161] and cyclo-octane in formulated catalysts with MFI zeolites as active nanoporos phase[16,50] showed effective self-diffusion coefficients, which are reduced by a factor of about 1.6 of up to 4.4 as compared to corresponding value in the bulk liquid. This reduction is caused by the tortuous pathway, which the molecules have to overcome in the transport pores in order to be displaced over the length scales of a few micrometers, typically measured by PFG NMR (see Figs. 3 and 5). If these diffusion lengths are much larger than the typical radius characterizing the internal structure of the pellets, PFG NMR measures an effective self-diffusion coefficient D_{eff}, which is independent of diffusion time.[50] However, compared to the bulk liquid self-diffusion coefficient D_0, D_{eff} will be reduced by the so-called tortuosity factor of the transport pore system[50,161]

$$D_{eff} = \frac{D_0}{\tau_t}. \tag{84}$$

The tortuosity factor τ_t may be considered as a pore structure parameter.[132] It plays an important role in optimizing transport diffusion processes for engineering applications of porous materials. By using liquids, which are inert to the pore/matrix interface and which saturate the transport pores of the formulated particles,

this tortuosity factor may be measured by PFG NMR. Besides the above-mentioned examples,[50,161] this approach was applied to characterize commercial Pt/Re-Al$_2$O$_3$ naphtha reforming catalysts[162] and Mo/Co-Al$_2$O$_3$ hydro-processing catalysts.[163] These studies used liquid *n*-alkanes as probe molecules. It was shown that the tortuosity measured by PFG NMR increases with increasing coke deposition in the catalysts[162,163] and that reforming the catalysts by removing the coke deposits regenerates the originally smaller tortuosities.[162] Additionally, it was reported that the tortuosity increases with increasing size of the probe molecules,[163] which indicates that larger molecules may experience stronger restrictions on their diffusion pathway through the transport pores.

The valuable information obtained from PFG NMR studies with formulated catalysts is not limited to the tortuosity factor. For the above-mentioned formulated MFI-based zeolite catalysts,[50,164,165] also a correlation between the tortuosity, determined with water as probe liquid, and catalytic properties (activity and selectively) were found.[16] For a fluid cracking catalysts (FCC) with small faujasite zeolites as active phase, the oil-to-gasoline conversion ratio and the coke yield correlate well with the long-range diffusion coefficients of *n*-octane through the pellets.[166,167] For ZrO-based dehydration catalysts, PFG NMR studies with adsorbed *n*-propane and propene[168] showed that the transition from the Knudsen to the gas-diffusion mechanism controls the temperature dependence of the self-diffusion in the transport pore system. This observation allows one to develop an analytical model for extrapolating the measured temperature dependence to reaction conditions.[168] It is similar to the recently proposed long-range diffusion model proposed for the description of self-diffusion through beds of zeolite crystals[169] and FCC catalysts.[166,167] However, it uses the independently measured pore size of the transport pore system as input parameter and, thus, does not require the assumption of different tortuosity factors for the gas and Knudsen regime as in Ref. 169.

5.2.2. *Mineral-based construction materials*

Mineral-based construction materials, such as bricks, mortar and concretes consist of heterogeneous pore systems and pore/matrix interfaces, which are formed by physical mixing of the respective raw materials and successive chemical conversions during firing and hydration, respectively. NMR diffusion and relaxation studies of pore fluids in such materials were reported in order to characterize the pore system,[170,171] to investigate moisture and salt transport,[172,173] to follow changes in the pore system due to successive hydration[174,175] or crack formation[176,177] and to characterize diffusion of microscopically small liquid waste inclusions,[178] respectively.

A constant gradient STE NMR technique was applied to measure diffusion in water-saturated fired clay bricks.[179] Due to the substantial iron content, these materials have strong internal field gradients and very short T_2 relaxation times. Nevertheless, at long *z* storage times in the STE sequence, the NMR spin echo signal

decay is controlled by the long-range diffusion in the externally applied constant gradient.[179] This allowed the determination of the effective self-diffusion coefficient of water in the fired clay brick and, thus, the evaluation of the tortuosity of the pore space using Eq. (84).

For hydrating white[174,175] and blast furnace slag[180] cement pastes, it was shown that changes in the transverse relaxation times of the water in the hydrating cement paste are accompanied by a corresponding decrease in water self-diffusion. Both effects are related to the increasing formation of solid pore walls by growing hydrate crystal, such as calcium silicate hydrate phases, portlandite and ettringite, respectively. After initial hardening of the pastes and, especially, after complete hydration, diffusion measurements in cements and concretes represent a challenging task for the PFG NMR technique since the transverse relaxation times of the residual physically bound pore water as well as its diffusion coefficient are small. Generally, such studies should be performed using APFG NMR sequences since; otherwise, internal field gradients distort the results.

Already after the first day of hydration, the self-diffusion coefficients of water are smaller than about $5 \times 10^{-10}\,\mathrm{m^2\,s^{-1}}$ in the above-mentioned cement pastes.[174,175,180] They decrease further during successive hydration. For fully water-saturated white cements, a value of $D \lesssim 8 \times 10^{-11}\,\mathrm{m^2 s^{-1}}$ was reported after a few weeks of hydration.[175] The values reported in Ref. 175 correlate well with the initial water-to-cement ratio and were found to depend only slightly on diffusion time. In contrast, hydrocarbon inclusions in white cements show a strongly decreasing effective self-diffusion coefficient with increasing diffusion time following a Δ^{-1} dependence.[178] According to the Einstein relation (see Eq. (6)), this corresponds to a constant mean square displacement $\langle r^2 \rangle$ and indicates restricted diffusion in small pores. By using the relation[39,40,50]

$$D_{\mathrm{eff}}(\Delta) = \frac{R_p^2}{5\Delta} = \frac{\langle r^2 \rangle}{6\Delta}, \tag{85}$$

one may estimate the pore radius R_p from such a time-dependence of the effective self-diffusion coefficients. For the above-mentioned example, a maximum diffusion length of $4\,\mu\mathrm{m}$ was reported for n-hexanol in the hydrated sample of white cement.[178] This corresponds to a pore diameter of the hydrocarbon inclusion of about $7\,\mu\mathrm{m}$.

In bentonite-cement suspensions, which are used to construct subsurface cut-off walls in order to prevent infiltration of polluted water into aquifers, a reduction of water self-diffusion coefficients by about four orders of magnitude compared to bulk liquid water was evidenced ($D \lesssim 5 \times 10^{-13}\,\mathrm{m^2\,s^{-1}}$ at $\Delta = 10\,\mathrm{ms}$, see Refs. 181,182). By following a power law behavior ($D \propto \Delta^{-\kappa}$ with $0 < \kappa < 1$), they decrease with increasing diffusion time to a few $10^{-14}\,\mathrm{m^2\,s^{-1}}$. The self-diffusion coefficients belong to the smallest values measured by PFG NMR for water in a porous material. The small self-diffusion coefficients confirm the good barrier properties of the bentonite-cement cut-off walls although they contain up to about 80% water (by weight) in their internal structure.[182]

5.2.3. *Natural sediments*

Pores in natural sediments are formed and continuously changed during diagnese and weathering. Usually, the resulting pore spaces are heterogeneous in size and shape. The interpretation of NMR relaxation time studies of pore fluids in such materials is based on the equation:

$$\frac{1}{T_{1,2}} = \rho_{1,2} S_V \quad \propto \frac{1}{R_p},$$

(86)

which relates observed longitudinal (index 1) and transverse (index 2) relaxation times to the surface-to-volume ratio (S_V) and the pore radius (R_p), respectively. Low-field NMR relaxometry is commonly used for such studies in unconsolidated sediments and sedimentary rocks. However, the surface relaxivity parameters ($\rho_{1,\,2}$ in Eq. (86)) of these materials are often not known, which requires independent measurements of pore size or surface-to-volume ratio in order to calibrate the obtained relaxation time distributions of the pore fluid into pore size distributions. As seen from Eqs. (82), (83) and (85), such information may be obtained by PFG NMR using the time dependence of the effective self-diffusion coefficient of the pore fluids. Section 5.3 provides examples for direct combination of relaxation and diffusion studies using correlation methods. Here, we highlight time-dependent PFG NMR studies on natural sediments, which are used to deduce pore structure information.

Most sediments investigated by PFG NMR have a well-interconnected pore space, since, otherwise, it would be difficult or even impossible to introduce the pore fluids required for the NMR studies. Thus, completely restricted diffusion with a Δ^{-1} time dependence of the effective self-diffusion coefficient as predicted by Eq. (85) is usually not found. An exemption is the diffusion of an aqueous nickel nitrate solution in a dolomite rock, where the typical restricted diffusion pattern was observed and used to determine the surface relaxivity parameter of that particular rock ($\rho_2 = 6.7 \times 10^{-4}\,\mathrm{ms}^{-1}$ $R_p \lesssim 14\,\mu\mathrm{m}$, see Ref. 183 for more details).

Due to magnetic susceptibility differences between the pore and matrix space, it is a good advice to perform diffusion studies in sediments with APFG NMR sequences. For example, for a *n*-hexadecane saturated sand, the STE NMR sequence with unipolar pulsed field gradients yields spin echo attenuations, which depend on the τ interval between the first and the second rf-pulse.[184] This indicates the disturbing influences of internal field gradients in the unipolar field gradient STE PFG NMR sequence. The genuine diffusion coefficient is only obtained by the extrapolation of the apparent (τ-dependent) values to $\tau \to 0$[184] or by using the 13-interval APFG sequence.[18,184,185]

Even with APFG NMR sequences, the spin echo amplitudes in consolidated sediments such as porous sandstones and carbonate rocks do not exhibit a single-exponential decay with the gradient parameter b.[90,129,186] Depending on the type of the porous rock, the observed patterns of the spin echo attenuations were explained by models of partially restricted diffusion between randomly oriented parallel sheets and in randomly oriented tubes, respectively. The resulting spin echo attenuations

are similar to Eq. (81), where, however, the parallel (sheet model) and perpendicular (tube model) components of the diffusion tensor, respectively, are replaced by a time-dependent value proportional to R_p^2/Δ. Using these models, one obtains R_p as the equivalent sheet distance and tube radius, respectively, which may be interpreted as the pore size of the rock.[90,186]

Alternatively, also a simple two-exponential decay function was proposed to fit the observed spin echo attenuations.[129] The petrophysical interpretation of the resulting two components with different mobilities is the free diffusion in large pores and the restricted diffusion in small capillary pores. This model yielded good agreement with movable and bound fluid fractions obtained from centrifuge experiments and was found to be applicable to NMR diffusion studies at variable water saturation.[129,187]

By analyzing just the initial decay of the observed spin echo attenuations, one obtains the effective self-diffusion coefficient (see Eq. (25)). Generally, with liquids as saturating pore fluids in natural sediments, one observes effective self-diffusion coefficients, which are close to the bulk liquid diffusivity at small diffusion times and which decrease slowly with increasing diffusion time. From the initial decay of the relative effective self-diffusion coefficients $(D_{\text{eff}}(\Delta)/D_0)$, the S_V ratio may be determined using the approach proposed by Mitra *et al.*[28] which was already discussed in Section 5.1.3. So far, all interpretations of such PFG NMR studies in natural sediments utilized only the first order in mean displacement $\left(\sqrt{D_0\Delta}\right)$, which is written as:[28]

$$\frac{D_{\text{eff}}(\Delta)}{D_0} = 1 - \frac{4}{9\sqrt{\pi}} S_v \sqrt{D_0\Delta} + \cdots \tag{87}$$

for the case of reflecting boundaries (compare with Eq. (82)). When using this approach for consolidated sedimentary rocks, one has to keep in mind, that the probe for exploring the surface area are diffusing liquid molecules and surface structures with characteristic length smaller as $\sqrt{D_0\Delta}$ cannot be resolved. Additionally, the averaged pore radius has to be large as compared to $\sqrt{D_0\Delta}$ in order to fulfill the short-time approximation as precondition for the applicability of Eq. (87).[28] Refs. 90, 188–190 provide examples for measurements of the surface-to-volume ratios of different types of water-saturated sedimentary rocks by PFG NMR.

The same interpretation of the short-time dependence of the effective self-diffusion coefficients was used to investigate surface areas of grains of a glacial sand deposit.[191] The obtained data were analyzed using a fractal model, in which the obtained surface-to-volume ratios were found to scale according to a non-integer power law with the grain size.[108,192]

The long-time limit for the effective self-diffusion coefficient in sediments with a well-interconnected pore space is determined by the tortuosity of the pores (see Eq. (84)). However, with liquid probe molecules, surface relaxation often does not allow one to extend the diffusion times in a PFG NMR experiment up to such values required to observe a constant effective self-diffusion coefficient. In this case, the Padè approximation may be used to extrapolate the observed time dependence

to this limit (see, e.g., Refs. 188, 189, and 193). By using gases as probe molecules, a constant effective diffusivity is much easily obtained since gases cover much longer diffusion pathways during the time scale of the PFG NMR experiments. The decreased signal-to-noise ratio may be circumvented by using hyperpolarized gases. Examples for such tortuosity measurements of sandstones using gases provide Refs. 194–196.

Besides the Padè approximation, there are also fractal models, which were developed to exploit the whole time-dependence of the effective diffusion coefficients. The key idea of these models is that the pore structure parameter of the porous sediment obtained from the measured $D_{\text{eff}}(\Delta)$ data scales with the diffusion length $\sqrt{D_0\Delta}$ according to a non-integer power-law. By using such an approach, the fractal surface dimension of an Indiana limestone[197] was determined. Another idea incorporates the fractal scaling of the apparent surface-to-volume ratio with the diffusion length and was applied to low-porosity sandstones in order to find the long-time limit for the tortuosity determination.[190] We refer the reader to the original Refs. 190, 192, 197 in which the mathematics and data interpretation of these fractal models for diffusion studies in sediments are outlined in detail.

5.3. Diffusion–relaxation correlation maps in porous materials

Within the last five years, a set of new multidimensional NMR correlation methods have been introduced and applied to various systems such as, liquid crystals,[198,199] porous rocks[29,30,200] or porous organic materials.[99,111,201] All those investigations have in common the processing of the experimental data based on a multidimensional inverse Laplace transformation rather than a multidimensional Fourier transformation. The latter, as introduced in the 1970s, enables sophisticated chemical analysis and structural investigations, see Refs. 84 and 202 Likewise, the investigation of coherent and diffusive motion[39,60,62] is also based on a Fourier relationship as pointed out in Section 2.3.2 (see Eqs. (19) and (20)). Despite of the importance of the various Fourier transformation methods, we will confine ourselves to correlation methods using multidimensional inverse Laplace transformation for the data processing.

Song et al.[30] investigated the correlation of T_1 and T_2 for brine-saturated rocks and found a systematic deviation from $T_1 = T_2$, as expected for liquids, in dependence on the relaxation time itself. The experiment consists of a CPMG sequence, where the leading $\pi/2$ rf pulse is replaced by an inversion recovery pulse sequence. While changing the delay time for the inversion recovery (first dimension, t_1) a second dimension is sampled by recording the time dependence of the spin echo amplitudes (t_2) in the CPMG echo train. In this way, a 2D data set $M(t_1, t_2)$ is acquired, which is linked to a joint probability $p(T_1, T_2)$ via a 2D Laplace integral (see Ref. 30 for details).

$$\frac{M(t_1, t_2)}{M_0} = \int \int p(T_1, T_2)(1 - 2\,\mathrm{e}^{-t_1/T_1})\,\mathrm{e}^{-t_2/T_2}\,\mathrm{d}T_1\,\mathrm{d}T_2. \tag{88}$$

The problem and the challenge is to perform the inverse transformation of Eq. (88) in order to extract the desired 2D distribution $p(T_1, T_2)$ since the inverse Laplace transformation is numerically ill-defined and unstable to small fluctuations in the measured data set. Moreover, the direct numerical execution of a 2D inverse Laplace transformation exceeds by far the computational power of modern PC[30] and demands the use of super computers.[203] However, it is possible to rearrange the highly redundant 2D problem by just considering the most significant singular values of the two kernels in the integral equation (Eq. (88)) and to introduce suitable regularization constrains as suggested by Venkataramanan *et al.*[204] This algorithm enables the use of desktop computers for the data processing as it was done in the pioneering work of Song *et al.*[30] Here, we like to emphasize that the determination of 2D distributions, such as $p(T_1, T_2)$ consists of two steps: The first is the acquisition of a suitable data set $M(t_1, t_2)$. The second step is the subsequent processing in order to obtain the distribution. In selected cases, this might be possible by fitting a pre-defined model to the measured data. However, the inverse Laplace transformation is the natural inversion of the integral equation presented by Eq. (88). Therefore, if used in a careful way, the inverse Laplace algorithm represents the more powerful approach and does not require a model.

Compared to the relaxation–relaxation distribution given in Eq. (88), similar joint probabilities describe the correlations of diffusive motion and relaxation (diffusion–relaxation correlation) as well as of diffusive motions in different spatial directions in the case of anisotropic motions (see Eq. (81), diffusion–diffusion correlation). The different possibilities of combining appropriate PFG NMR pulse sequences were already discussed in Section 3.6 and are summarized in Refs. 100, 200. Examples of their applications to porous materials will be presented in the following paragraphs.

The first diffusion–relaxation correlation maps obtained by multidimensional inverse Laplace transformation were reported by Hürlimann *et al.*[29] for a water-saturated Indiana limestone. The correlation between the T_2 relaxation time and the averaged (effective) diffusion coefficient (DRCOSY) at different observation times Δ in a range from (0.02 … 1) s were measured. The investigations were performed in the fringe field of a 2 T super-conducting magnet providing a constant magnetic field gradient of 0.132 T m^{-1} at a ^{1}H resonance frequency of 1.764 MHz. The diffusion edited pulse sequence consists of a preceding stimulated echo sequence with variable rf distance for sampling the first dimension (using the constant field gradient for diffusion encoding) and a subsequent CPMG echo train sampling the second dimension in the time domain. The results are a 3D data set, from which the averaged diffusion coefficient $\bar{D}$ and its correlation to $T_{2\text{eff}}$ and Δ was obtained. As expected for a porous rock, $\bar{D}$ decreases with the increasing observation time due to restricted diffusion in the pore space. In addition, a strong correlation between $\bar{D}$ and $T_{2\text{eff}}$ was observed, confirming that a more pronounced restricted diffusion is linked to a faster T_2 relaxation. In the same article, the authors confirmed the result from Song *et al.*[30] for the T_1–T_2 correlation as obtained for the same Indiana limestone in a homogenous magnetic field.

In a later study, Hürlimann et al.[205] used the DRCOSY method to investigate diffusion–relaxation correlations on several sedimentary rock cores (two sandstones and two dolomites) in three different saturation conditions: First, the fully brine saturated rock cores were investigated (see top diagram in Fig. 22). A second data set was acquired after the cores had been submerged in crude oil (see middle diagram in Fig. 22). Finally the samples were immersed in brine, thus capturing the imbibition of the brine water and the replacement of the oil (see bottom diagram in Fig. 22) in the pore space. Based on the obtained diffusion–relaxation correlation
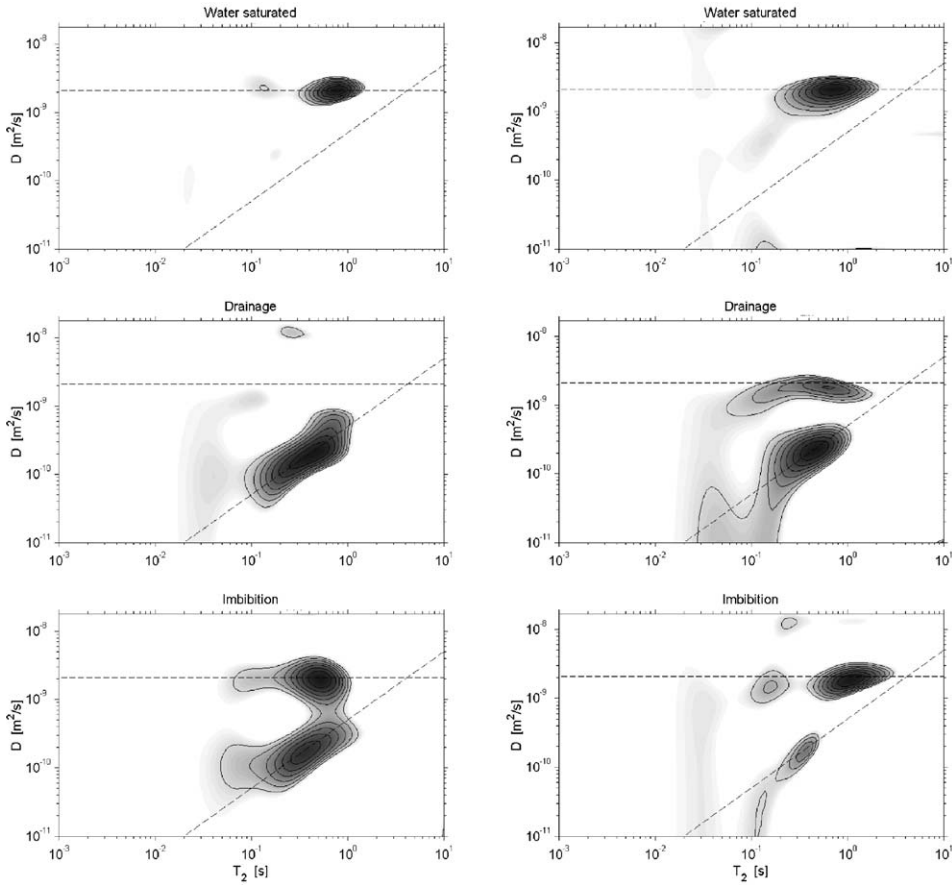
Fig. 22. Relaxation-diffusion maps for a Bentheimer sandstone (left) and a dolomite (right) from Ref. 205. The top diagrams show the fully water-saturated rocks. In the middle, the maps for the rocks after drainage with crude oils are given, while the bottom line shows the result for the samples after spontaneous (left) and forced (right) imbibition with brine. The horizontal dashed lines represent the diffusion coefficient of water whereas the sloped line indicates diffusion–relaxation correlations found for alkanes. [*Source:* Reprinted from Ref. 205 with permission from Elsevier.]

maps, it was found that water is the wetting phase (undergoing surface relaxation) and the oil is not wetting the pore/matrix interface. Additionally, characteristic differences between the sandstones and the dolomites after spontaneous imbibition of brine water were reported: While in the Bentheimer sandstone a significant amount of the oil was replaced by the water (see bottom left diagram in Fig. 22), almost no spontaneous imbibition of water was observed in the dolomite. Only after forced imbibition by centrifuging, the oil was replaced by the water (see bottom right diagram in Fig. 22).

These results presented in the diffusion–relaxation correlation maps of Fig. 22 provide detailed insight into the complex fluid/matrix interaction of oil and water in the pore structure of rocks.[205] They were obtained from the experimental DRCOSY data set by no other constrains than those given by the inverse Laplace transformation itself. The results are consistent with a previous processing of the data using much more stringent assumptions, thus, justifying the application of the 2D inverse Laplace approach (see Hürlimann et al.[205] for details). Refs. 200, 206, and 207 provide further examples for successful diffusion–relaxation correlation studies in porous rocks.

The anisotropy of liquid diffusion due to restrictions in porous hosts may also be visualized by such correlation methods. For example, Qiao et al.[201] investigated the water diffusion in tissue of chive leaves (*Allium schoenoprasum*). The leaves were chopped into cylindrical pieces with a length of about 2–5 mm leading to a random, powder-like orientation distribution of the individual pieces with no global anisotropy in the whole sample. However, a local anisotropy remained for each piece and was measured with the diffusion–diffusion correlation spectroscopy (DDCOSY) as introduced by Callaghan et al.[100] This pulse sequence consists of two successive PFG sequences with orthogonal gradients, sampling the diffusion in different directions.

As apparent from the left part of Fig. 23, the anisotropy in chive leaves can be very large with a difference in the elements of the diffusion tensor of almost two orders of magnitude. The peaks in the DDCOSY map (see Fig. 23 left) could be assigned to the different shapes and orientation of the plant cells.[201] This was possible by using the diffusion–relaxation correlation map (see Fig. 23 right) measured by the DRCOSY method and 1D PFG NMR measurements on oriented whole chive leaves. Fore instance, the peaks in the DDCOSY map (Fig. 23 left) with intensities of 0.5% and 0.6% are attributed to the xylem vessels responsible for the water uptake. However, the data analysis revealed, that the majority of the anisotropic diffusion (peaks with 14.3% and 18.7% in Fig. 23 left) has its fast component perpendicular to the plant axis and must, therefore, be attributed to the diffusion within the palisade and spongy mesophyll cells. As supported by optical micrographs, those cells are indeed radially oriented. It is this combined application of DDCOSY, DRCOSY and 1D PFG NMR measurements, which enables the unequivocal assignment of different water components to the cells sites in the tissue on a scale beyond the resolution of standard NMR microscopy.

While DDCOSY is employed in the previous example, diffusion exchange spectroscopy (DEXSY)[100] was used for the investigation of the dispersion of dextran (77
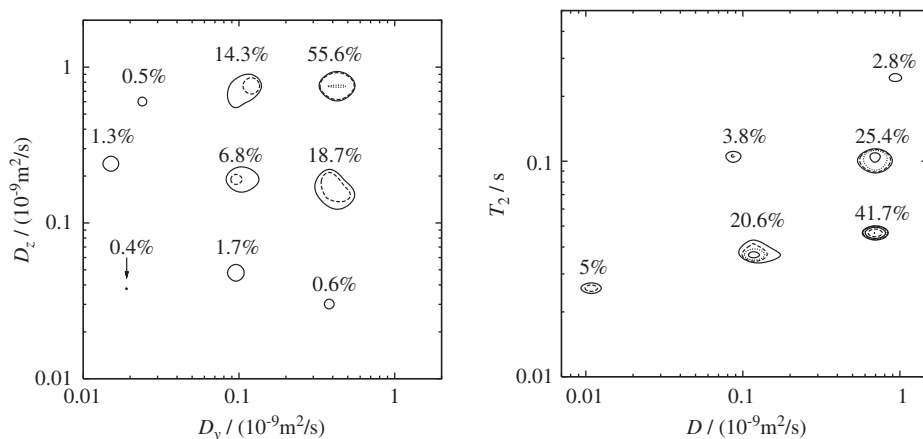
Fig. 23.   Diffusion of water in cell tissue of chopped chive leaf. The correlation between two different directions in space reveals the local anisotropy in the different sites of the cell tissue (left), which can be associated via the corresponding relaxation times and peak intensity of the diffusion–relaxation correlation (right) to cell shape and size. [*Source:* Redrawn from Ref. 201 with permission from the Biophysical Society.]
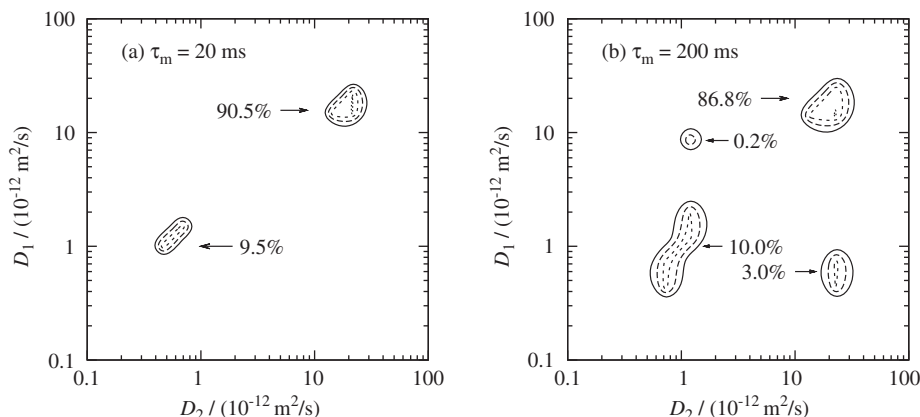
Fig. 24.   Diffusion-exchange maps for dextran diffusing through PEM hollow capsules at a mixing time of 20 ms (left) and 200 ms (right). [*Source:* Redrawn from Ref. 111 with permission from the American Institute of Physics.]

kDa) and polyelectrolyte multilayer (PEM) hollow capsules in D_2O solution.[111] The DEXSY pulse sequence consists also of two successive PFG sequences, but in contrast to DDCOSY the gradients are co-linear and separated by a mixing time t_m. This enables the observation of the diffusion coefficient before and after t_m. Diagonal peaks in the map, as shown in Fig. 24, represent molecules not changing their diffusion coefficient during t_m. In contrast, off-diagonal peaks arise from

molecules undergoing slow diffusion first and faster diffusion after t_m and vice versa. Such features are visible in Fig. 24 (left).

The dextran molecules considered in Fig. 24 represent the freely diffusing bulk solution phase of dextran and the diffusion of dextran confined in or attached to single PEM capsules. At 20 ms mixing time, there is no exchange between these two dextran species, since there are no cross peaks observed in the DEXSY map. At long mixing times of $t_m = 200$ ms, cross peaks occur and an exchange time of about 1 s can be estimated. This result confirms an earlier study on the Dextran/PEM system by Adalsteinsson *et al.*[208] using the fast NMR tracer exchange model introduced by Kärger.[152]

These few examples were selected in order to demonstrate the potential of 2D NMR methods based on inverse Laplace transformation. They allow the correlation of diffusion and relaxation of molecules in porous systems and enhance the interpretation of NMR studies in porous materials. The results are shown to be consistent with other (1D NMR) methods but have the advantage that they do not rely on pre-defined model assumptions for their interpretations. Therefore, they represent an important extension to the multidimensional NMR methodology.

ACKNOWLEDGEMENTS

REFERENCES

1. F. Bloch, Nuclear induction, *Phys. Rev.*, 1946, **70(7–8)**, 460–474.
2. E. M. Purcell, H. C. Torrey and R. V. Pound, Resonance absorption by nuclear magnetic moments in a solid, *Phys. Rev.*, 1946, **69(1–2)**, 37–38.
3. E. L. Hahn, Spin echos, *Phys. Rev.*, 1950, **80(4)**, 580–594.
4. S. Meiboom and D. Gill, Modified spin-echo method for measurement of relaxation times, *Rev. Sci. Instrum.*, 1958, **29**, 688–691.
5. H. Y. Carr and E. M. Purcell, Effects of diffusion on free precession in nuclear magnetic resonance experiments, *Phys. Rev.*, 1954, **94**, 630.
6. J. H. Simpson and H. Y. Carr, Diffusion and nuclear spin relaxation in water, *Phys. Rev.*, 1958, **111(5)**, 1201–1202.
7. D. W. McCall, D. C. Douglass and E. W. Anderson, Diffusion in liquids, *The Journal of Chemical Physics*, 1959, **31(6)**, 1555–1557.

8. D. E. Woessner, NMR spin-echo self-diffusion measurements on fluids undergoing restricted diffusion, *J. Phys. Chem.*, 1963, **67(6)**, 1365–1366.

9. D. E. Woessner, Self-diffusion measurements in liquids by the spin-echo technique, *Rev. Sci. Instrum.*, 1960, **31(10)**, 1146–1146.

10. D. W. McCall, D. C. Douglass and E. W. Anderson, Self-diffusion studies by means of nuclear magnetic resonance spin-echo techniques, *Ber. Bunsen-Ges. Phys. Chem.*, 1963, **67(3)**, 336–340.

11. E. O. Stejskal and J. E. Tanner, Spin diffusion measurements: Spin echoes in the presence of a time-dependent field gradient, *J. Chem. Phys.*, 1965, **42**, 288.

12. J. E. Tanner, Use of the stimulated echo in NMR diffusion studies, *J. Chem. Phys.*, 1970, **52**, 2523.

13. P. C. Lauterbur, Image formation by induced local interactions: Examples employing nuclear magnetic resonance, *Nature*, 1973, **242(5394)**, 190–191.

14. P. Mansfield and P. K. Grannell, "diffraction" and microscopy in solids and liquids by NMR, *Phys. Rev. B*, 1975, **12(9)**, 3618–3634.

15. Available at: http://www.sciencedirect.com, Copyright© 2006 Elsevier B.V. (last accessed: March 2006).

16. F. Stallmach, *NMR-Diffusometrie an porösen Materialien*, Universität Leipzig, 2004 (URL: http://lips.informatik.uni-Leipzig.de: 80/pub/2004-19; last accessed: December 2006).

17. R. F. Karlicek and I. J. Lowe, A modified pulsed gradient technique for measuring diffusion in the presence of large background gradients, *J. Magn. Reson.*, 1980, **37**, 75–91.

18. R. M. Cotts, M. J. R. Hoch, T. Sun and J. T. Markert, Pulsed field gradient stimulated echo methods for improved NMR diffusion measurements in heterogeneous systems, *J. Magn. Reson.*, 1989, **83(2)**, 252–266.

19. G. H. Sørland, D. Aksnes and L. Gjerdåker, A pulsed field gradient spin-echo method for diffusion measurements in the presence of internal gradients, *J. Magn. Reson.*, 1999, **137(2)**, 397–401.

20. P. Z. Sun, J. G. Seland and D. Cory, Background gradient suppression in pulsed gradient stimulated echo measurements, *J. Magn. Reson.*, 2003, **161(2)**, 168–173.

21. P. Galvosas, F. Stallmach and J. Kärger, Background gradient suppression in stimulated echo NMR diffusion studies using magic pulsed field gradient ratios, *J. Magn. Reson.*, 2004, **166(2)**, 164–173.

22. W. Heink, J. Kärger, G. Seiffert, G. Fleischer and J. Rauchfuß, PFG NMR self-diffusion measurements with large field gradients, *J. Magn. Reson. A*, 1995, **114**, 101–104.

23. V. D. Skirda, I. Y. Aslanyan, O. E. Philippova, N. S. Karybiants and A. R. Khokhlov, Investigation of translational motion of poly(ethylene glycol) macromolecules in poly(methacrylic acid) hydrogels, Macromol, *Chem. Phys*, 1999, **200**, 2152–2159.

24. P. T. Callaghan, M. E. Komlosh and M. Nyden, High magnetic field gradient PGSE NMR in the presence of a large polarizing field, *J. Magn. Reson.*, 1998, **133(1)**, 177–182.

25. W. S. Price, K. Hayamizu, H. Ide and Y. Arata, Strategies for diagnosing and alleviating artifactual attenuation associated with large gradient pulses in PGSE NMR diffusion measurements, *J. Magn. Reson.*, 1999, **139(2)**, 205–212.

26. P. Galvosas, F. Stallmach, G. Seiffert, J. Kärger, U. Kaess and G. Majer, Generation and application of ultra-high-intensity magnetic field gradient pulses for NMR spectroscopy, *J. Magn. Reson.*, 2001, **151(2)**, 260–268.

27. J. Kärger and W. Heink, The propagator representation of molecular transport in microporous crystallites, *J. Magn. Reson.*, 1983, **51**, 1–7.

28. P. P. Mitra, P. N. Sen and L. M. Schwartz, Short-time behavior of the diffusion coefficient as a geometrical probe of porous media, *Phys. Rev. B*, 1993, **47**, 8565–8574.

29. M. D. Hürlimann and L. Venkataramanan, Quantitative measurement of two-dimensional distribution functions of diffusion and relaxation in grossly inhomogeneous fields, *J. Magn. Reson.*, 2002, **157(1)**, 31–42.

30. Y. -Q. Song, L. Venkataramanan, M. D. Hürlimann, M. Flaum, P. Frulla and C. Straley, T_1–T_2 correlation spectra obtained using a fast two-dimensional laplace inversion, *J. Magn. Reson.*, 2002, **154**, 261–268.

31. I. Noda, Progress in two-dimensional (2d) correlation spectroscopy, *J. Mol. Struct.*, 2006, **799**, 2–15.

32. C. S. Johnson, Diffusion ordered nuclear magnetic resonance spectroscopy: Principles and applications, *Prog. NMR Spectr.*, 1999, **34(3–4)**, 203–256.

33. T. Brand, E. J. Cabrita and S. Berger, Intermolecular interaction as investigated by NOE and diffusion studies, *Prog. NMR Spectr.*, 2005, **46(4)**, 159–196.

34. J. C. Cobas, P. Groves, M. Martin-Pastor and A. De Capua, New applications, *processing methods and pulse sequences using diffusion NMR, Curr. Anal. Chem.*, 2005, **1(3)**, 289–305.

35. S. Stapf, NMR investigations of correlations between longitudinal and transverse displacements in flow through random structured media, *Chem. Phys.*, 2002, **284(1–2)**, 369–388.

36. A. A. Khrapitchev, S. Stapf and P. T. Callaghan, NMR visualization of displacement correlations for flow in porous media, *Phys. Rev. E*, 2002, **66(5)**, 51203.

37. P. T. Callaghan, S. Godefroy and B. N. Ryland, Diffusion-relaxation correlation in simple pore structures, *J. Magn. Reson.*, 2003, **162(2)**, 320–327.

38. Y.-Q. Song, Novel NMR techniques for porous media research, *Cem. Concr. Res.* in press, 2007.

39. P. T. Callaghan, *Principles of Nuclear Magnetic Resonance Microscopy*, Clarendon Press, Oxford, 1991.

40. J. Kärger and M. D. Ruthven, *Diffusion in Zeolites and Other Microporous Solids*, Wiley & Sons, New York, 1992.

41. R. Kimmich, *NMR Tomography, Diffusometry, Relaxometry*, Springer, Berlin, 1997.

42. B. Blümich, *NMR Imaging of Materials*, Clarendon Press, Oxford, 2000.

43. S. Berger and S. Braun, *200 and More NMR Experiments*, Wiley-VCH, Weinheim, 2004.

44. P. Heitjans and J. Kärger, eds., *Diffusion in Condensed Matter: Methods, Materials, Models*, Springer, Berlin, 2005.

45. S. Stapf and S. -I. Han, eds., *NMR Imaging in Chemical Engineering*, Wiley-VCH, Weinheim, 2006.

46. W. S. Price, Gradient NMR, *Annu. Rep. NMR Spectrosc.*, Vol. 32, Academic Press, 1996, 51–142.

47. W. S. Price, Pulsed-field gradient nuclear magnetic resonance as a tool for studying translational diffusion: Part I. basic theory, *Concepts Magn. Reson.*, 1997, **9**, 299–336.

48. W. S. Price, Pulsed-field gradient nuclear magnetic resonance as a tool for studying translational diffusion: Part II. experimental aspects, *Concepts Magn. Reson.*, 1998, **10**, 197–237.

49. W. S. Price, Protein association studied by NMR diffusometry, *Curr. Opin. Colloid Interface Sci.*, 2006, **11(1)**, 19–23.

50. F. Stallmach and J. Kärger, The potentials of pulsed field gradient NMR for investigation of porous media, *Adsorption*, 1999, **5**, 117–133.

51. J. Kärger and F. Stallmach, PFG NMR studies of anomalous diffusion, in: *Diffusion in Condensed Matter: Methods, Materials, Models*, P. Heitjans and J. Kärger, eds., Springer, Berlin, 2005, pp. 417–459.

52. J. Kärger, F. Stallmach, R. Valiullin and S. Vasenkov, Diffusion in nanoporous materials, in: *NMR Imaging in Chemical Engineering*, S. Stapf and S. -I. Han, eds., Wiley-VCH, Weinheim, 2006, pp. 231–250.

53. A. T. Watson, J. T. Hollenshead, J. Uh and G. T. P. Chang, NMR determination of porous media property distributions, *Annu. Rep. NMR Spectrosc.*, Vol. 48, Academic Press, 2002, 113–144.

54. I. Ardelean and R. Kimmich, Principles and unconventional aspects of NMR diffusometry, *Annu. Rep. NMR Spectrosc.*, Vol. 49, Academic Press, 2003, 45–115.

55. J. Crank, *The Mathematics of Diffusion*, University Press, Oxford, 1975.

56. A. Cvetkovic, A. J. J. Straathof, D. N. Hanlon, S. van der Zwaag, R. Krishna and L. A. M. van der Wielen, Quantifying anisotropic solute transport in protein crystals using 3-D laser scanning confocal microscopy visualization, *Biotechnol. Bioeng.*, 2004, **86(4)**, 389–398.

57. E. Roubine, *Mathmatics Applied to Physics*, Springer, Berlin, 1970.

58. M. I. Hrovat and C. G. Wade, NMR pulsed-gradient diffusion measurements II. Residual gradients and lineshape distortions, *J. Magn. Reson.*, 1981, **45(1)**, 67–80.

59. M. I. Hrovat and C. G. Wade, NMR pulsed-gradient diffusion measurements I. Spin-echo stability and gradient calibration, *J. Magn. Reson.*, 1981, **44(1)**, 62–75.

60. P. T. Callaghan, C. D. Eccles and Y. Xia, NMR microscopy of dynamic displacements: k-space and q-space imaging, *J. Phys. E*, 1988, **21(8)**, 820–822.

61. P. T. Callaghan, A. Coy, D. Macgowan, K. J. Packer and F. O. Zelaya, Diffraction-like effects in NMR diffusion studies of fluids in porous solids, *Nature*, 1991, **351(6326)**, 467.

62. X. Ren, S. Stapf and B. Blümich, Multiscale approach to catalyst design, in: *NMR Imaging in Chemical Engineering*, S. Stapf and S. -I. Han, eds., Wiley-VCH, Weinheim, 2006, pp. 263–284.

63. H. C. Torrey, Bloch equations with diffusion terms, *Phys. Rev.*, 1956, **104(3)**, 563–565.

64. P. Galvosas, *PFG NMR-Diffusionsuntersuchungen mit ultra-hohen gepulsten magnetischen Feldgradienten an mikroporösen Materialien*, Ph.D. thesis, Universität Leipzig, Leipzig, Germany, 2003. (URL: http://dol.dl.uni-leipzig.de/receive/UBLDissHabil_disshab_00005390; last accessed: December 2006).

65. R. Kimmich, W. Unrath, G. Schur and E. Rommel, NMR measurement of small self-diffusion coefficients in the fringe-field of superconducting magnets, *J. Magn. Reson.*, 1991, **91(1)**, 136–140.

66. I. Y. Chang, F. Fujara, B. Geil, G. Hinze, H. Sillescu and A. Tolle, New perspectives of NMR in ultrahigh static magnetic-field gradients, *J. Non. Cryst. Sol.*, 1994, **172**, 674–681.

67. R. J. S. Brown, R. Chandler, J. A. Jackson, R. L. Kleinberg, M. N. Miller, Z. Paltiel and M. G. Prammer, History of NMR well logging, *Concepts Magn. Resonance*, 2001, **13(6)**, 335–413.

68. M. Winkler, J. J. Freeman and M. Appel, The limits of fluid property correlations used in NMR well logging: An experimental study of reservoir fluids at reservoir conditions, *Petrophysics*, 2005, **46(2)**, 104–112.

69. G. Eidmann, R. Savelsberg, P. Blumler and B. Blümich, The NMR MOUSE, a mobile universal surface explorer, *J. Magn. Reson. A*, 1996, **122(1)**, 104–109.

70. G. R. Coates, H. J. Vinegar, P. N. Tutunjian and J. S. Gardner, Restrictive diffusion from uniform gradient NMR well logging, *SPE SPE*, 1993, **26472**, 575–590.

71. D. Rata, F. Casanova, J. Perlo, D. Demco and B. Blumich, Self-diffusion measurements by a mobile single-sided NMR sensor with improved magnetic field gradient, *J. Magn. Reson.*, 2006, **180(2)**, 229–235.

72. J. Kärger and W. Heink, Zur meßbarkeit von diffusionskoeffizienten mit hilfe der methode der gepulsten feldgradienten, *Exp. Tech. Phys.*, 1971, **19**, 454.

73. G. H. Sørland, B. Hafskjold and O. Herstad, A stimulated-echo method for diffusion measurements in heterogeneous media using pulsed field gradients, *J. Magn. Reson.*, 1997, **124(1)**, 172–176.

74. L. L. Latour, L. Li and C. H. Sotak, Improved PFG stimulated-echo method for the measurement of diffusion in inhomogeneous fields, *J. Magn. Reson. B*, 1993, **101(1)**, 72.

75. J. G. Seland, G. H. Sørland, K. Zick and B. Hafskjold, Diffusion measurement at long observation times in the presence of spatially variable internal magnetic field gradients, *J. Magn. Reson.*, 2000, **146**, 14.

76. P. Z. Sun, *Nuclear Magnetic Resonance Microscopy and Diffusion*, Ph.D. thesis, Massachusetts Institute of Technology, MA, 2003 (URL: http://hdl.handle.net/172.1/29996; last accessed: December 2006).

77. P. Z. Sun, S. A. Smith and J. Y. Zhou, Analysis of the magic asymmetric gradient stimulated echo sequence with shaped gradients, *J. Magn. Reson.*, 2004, **171(2)**, 324–329.

78. A. Pampel, F. Engelke, P. Galvosas, G. Krause, F. Stallmach, D. Michel and J. Kärger, Selective multi-component diffusion measurement in zeolites by pulsed field gradient NMR, *Microporous Mesoporous Mat.*, 2006, **90(1–3)**, 271–277.

79. M. Holz, S. R. Heil and A. Sacco, Temperature dependent self-diffusion coefficients of water and six selected molecular liquids for calibration in accurate ^{1}H NMR PFG-measurements, *Phys. Chem. Chem. Phys.*, 2000, **2**, 4740.

80. L. L. Latour, P. P. Mitra, R. L. Kleinberg and C. H. Sotak, Time-dependent diffusion coefficient of fluids in porous media as a probe of surface-to-volume ratio, *J. Magn. Reson. A*, 1993, **101(3)**, 342–346.

81. E. J. Fordham, P. P. Mitra and L. L. Latour, Effective diffusion times in multiple-pulse PFG diffusion measurements in porous media, *J. Magn. Reson. A*, 1996, **121(2)**, 187–192.

82. B. Gross and R. Kosfeld, Application of spin-echo method in measurement of auto-diffusion, *Messtechnik*, 1969, **77(7–8)**, 171.

83. R. Bammer, Basic principles of diffusion-weighted imaging, *Eur. J. Radiol.*, 2003, **45(3)**, 169–184.

84. R. R. Ernst, G. Bodenhausen and A. Wokaun, *Principles of Nuclear Magnetic Resonance in One and Two Dimensions*, Clarendon Press, Oxford, 1987.

85. P. Stilbs, Fourier-transform NMR pulsed-gradient spin-echo (FT-PGSE) self-diffusion measurements of solubilization equilibria in SDS solutions, *J. Colloid Interface Sci.*, 1982, **87(2)**, 385–394.

86. P. Stilbs, Fourier transform pulsed-gradient spin-echo studies of molecular diffusion, *Prog. NMR Spectr.*, 1987, **19(1)**, 1–45.

87. W. H. Otto and C. K. Larive, Improved spin-echo-edited NMR diffusion measurements, *J. Magn. Reson.*, 2001, **153(2)**, 273–276.

88. L. H. Lucas, W. H. Otto and G. K. Larive, The 2D-J-DOSY experiment: Resolving diffusion coefficients in mixtures, *J. Magn. Reson.*, 2002, **156(1)**, 138–145.

89. S. A. Bradley, K. Krishnamurthy and H. Hu, Simplifying DOSY spectra with selective tocsy edited preparation, *J. Magn. Reson.*, 2005, **172(1)**, 110–117.

90. E. J. Fordham, S. J. Gibbs and L. D. Hall, Partially restricted diffusion in a permeable sandstone–observations by stimulated echo PFG NMR, *Magn. Reson. Imaging*, 1994, **12(2)**, 279–284.

91. D. Wu, A. Chen and C. S. Johnson Jr., An improved diffusion-ordered spectroscopy experiment incorporating bipolar-gradient pulses, *J. Magn. Reson. A*, 1995, **115**, 260–264.

92. O. Wattraint and C. Sarazin, Diffusion measurements of water, ubiquinone and lipid bilayer inside a cylindrical nanoporous support: A stimulated echo pulsed-field gradient MAS-NMR investigation, *Biochim. Biophys. Acta-Biomembr.*, 2005, **1713(1)**, 65–72.

93. W. Heink, J. Kärger and H. Pfeifer, A simple pulse sequence to exclude artifacts in self-diffusion measurements by means of the NMR pulsed field gradient technique, *Z. Phys. Chem.*, 1991, **170**, 199–206.

94. D. E. Demco, A. Johansson and J. Tegenfeldt, Constant-relaxation methods for diffusion measurements in the fringe-field of superconducting magnets, *J. Magn. Reson. A*, 1994, **110(2)**, 183–193.

95. E. Fischer and R. Kimmich, Constant time steady gradient NMR diffusometry using the secondary stimulated echo, *J. Magn. Reson.*, 2004, **166(2)**, 273–279.

96. J. C. Van Den Enden, D. Waddington, H. Van Aalst, C. G. Van Kralingen and K. J. Packer, Rapid-determination of water droplet size distributions by PFG-NMR, *J. Colloid Interface Sci.*, 1990, **140(1)**, 105–113.

97. M. D. Hürlimann, Diffusion and relaxation effects in general stray field NMR experiments, *J. Magn. Reson.*, 2001, **148(2)**, 367–378.

98. A. Metais and F. Mariette, Determination of water self-diffusion coefficient in complex food products by low field H-1 PFG-NMR: Comparison between the standard spin-echo sequence and the T-1-weighted spin-echo sequence, *J. Magn. Reson.*, 2003, **165(2)**, 265–275.

99. J. G. Seland, M. Bruvold, H. Anthonsen, H. Brurok, W. Nordhoy, P. Jynge and J. Krane, Determination of water compartments in rat myocardium using combined D-T_1 and T_1-T_2 experiments, *Magn. Reson. Imaging,*, 2005, **23(2)**, 353–354.

100. P. T. Callaghan, S. Godefroy and B. N. Ryland, Use of the second dimension in PGSE NMR studies of porous media, *Magn. Reson. Imaging*, 2003, **21(3–4)**, 243–248.

101. M. D. Silva, K. G. Helmer, J. H. Lee, S. S. Han, C. S. Springer and C. H. Sotak, Deconvolution of compartmental water diffusion coefficients in yeast-cell suspensions using combined T_1 and diffusion measurements, *J. Magn. Reson.*, 2002, **156(1)**, 52–63.

102. J. G. Seland, K. E. Washburn, H. W. Anthonsen and J. Krane, Correlations between diffusion, internal magnetic field gradients and transverse relaxation in porous systems containing oil and water, *Phys. Rev. E*, 2004, **70(5)**, 051305–051310.

103. A. Jerschow and N. Müller, Suppression of convection artifacts in stimulated-echo diffusion experiments. Double-stimulated-echo experiments, *J. Magn. Reson.*, 1997, **125(2)**, 372–375.

104. J. Kärger, H. Pfeifer and W. Heink, Principles and application of self-diffusion measurements by nuclear magnetic resonance, *Adv. Magn. Reson.*, 1988, **12**, 1–89.

105. G. Fleischer and F. Fujara, NMR as a generalized incoherent scattering experiment, *NMR Basic Princ. Prog.*, 1994, **30**, 159–207.

106. G. Majer, U. Kaess and R. C. Bowman Jr., *Phys. Rev. B*, 1998, **57**, 13599–13603.

107. U. Eberle, G. Majer, A. V. Skripov and V. N. Kozhanov, NMR studies of hydrogen diffusion in the hydrogen-stabilized laves phase compound C15-HF Ti$_2$H$_x$, *J. Phys. Condens. Matter*, 2002, **14**, 153–164.

108. F. Stallmach, C. Vogt, J. Kärger, K. Helbig and F. Jakobs, Fractal geometry of surface areas of sand grains probed by pulsed field gradient NMR, *Phys. Rev. Lett.*, 2002, **88**, 105505.

109. N. K. Bär, J. Kärger, C. K. W. Schmitz and G. Seiffert, Pitfalls in PFG NMR self-diffusion measurements with powder samples, *J. Magn. Reson. A*, 1995, **113**, 278–280.

110. S. J. Gibbs, Observations of diffusive diffraction in a cylindrical pore by PFG NMR, *J. Magn. Reson.*, 1997, **124(1)**, 223–226.

111. Y. Qiao, P. Galvosas, T. Adalsteinsson, M. Schönhoff and P. T. Callaghan, Diffusion exchange NMR spectroscopic study of dextran exchange through polyelectrolyte multilayer capsules, *J. Chem. Phys.*, 2005, **122**, 214912.

112. Doty scientific, (URL: http://www.doty.com; last accessed: March 2006).

113. K. Zick, Personal communication (2006).

114. Bruker Biospin Germany, (URL: http://www.bruker-biospin.de; last accessed: March 2006).

115. T. Dippel, K. Kreuer, M. Hampele and A. Rabenau, in: *Proceedings of the 25th Congress Ampere*, M. Mehring, J. von Schütz and H. Wolf, eds., Springer-Verlag, Berlin, 1990, p. 424.

116. M. Hampele, G. Majer, R. Messer and A. Seeger, *J. Less-Common Metals*, 1991, **172**, 631–642.

117. A. Feinauer, Ph.D. thesis, Universität Stuttgart, Stuttgart, 1993.

118. U. Kaess, Kernspinresonanzuntersuchungen der wasserstoffdiffusion in metall-wasserstoff-systemen mit der methode der gepulsten feldgradienten, Ph.D. thesis, Universität Stuttgart, Stuttgart, 1998.

119. G. Majer, U. Kaess and R. Barnes, *Phys. Rev. Lett.*, 1999, **83**, 340–343.

120. U. Kaess, G. Majer, M. Stoll, D. Peterson and R. Barnes, *J. Alloys and Compounds*, 1997, **259**, 74–82.

121. R. R. Valiullin, V. D. Skirda, S. Stapf and R. Kimmich, Molecular exchange processes in partially filled porous glass as seen with NMR diffusometry, *Phys. Rev. E*, 1997, **55(3)**, 2664–2671.

122. R. R. Valiullin, Personal communication, 2006.

123. Crown International, Inc., Elkhart, Technical Manual for Gradient Amplifier 8604, 1991.

124. P. T. Callaghan, PGSE-MASSEY, a sequence for overcoming phase instability in very-high-gradient spin-echo NMR, *J. Magn. Reson.*, 1990, **88**, 493–500.

125. S. J. Gibbs and G. S. Johnson, A PFG NMR experiment for accurate diffusion and flow studies in the presence of Eddy currents, *J. Magn. Reson.*, 1991, **93(2)**, 395–402.

126. P. Galvosas, F. Stallmach and G. Seiffert, Verfahren zur Steuerung von Verstärkern mit induktiven Lasten, Deutsches Patent- und Markenamt, DE 102 16 493 A1 (April 2002).

127. F. Stallmach, J. Kärger and H. Pfeifer, ^{13}C pulsed-field-gradient NMR diffusion studies of guest molecules in zeolites, *J. Magn. Reson. A*, 1993, **102**, 270–273.

128. J. Kärger, N. -K. Bär, W. Heink, H. Pfeifer and G. Seiffert, On the use of pulsed field gradients in a high-field NMR spectrometer to study restricted diffusion in zeolites, *Z. Naturforschung*, 1995, **50a**, 186.

129. F. Stallmach and H. Thomann, Producible fluid volumes in porous media determined by pulsed field gradient nuclear magnetic resonance, United States Patent Number 5,565,775 (1996).

130. P. Galvosas, S. Gröger, F. Stallmach and J. Kärger, Monitoring low self-diffusion coefficients of mixtures adsorbed in zeolites by FT PFG NMR with ultra-high pulsed field gradients, *Magn. Reson. Imaging*, 2003, **21**, 442.

131. W. S. Price and P. W. Kuchel, Effect of nonrectangular field gradient pulses in the stejskal and tanner (diffusion) pulse sequence, *J. Magn. Reson.*, 1991, **94(1)**, 133–139.

132. F. A. L. Dullien, *Porous Media: Fluid Transport and Pore Structure*, 2nd edition, Academic Press, San Diego, CA, 1992.

133. K. R. Brownstein and C. E. Tarr, Importance of classical diffusion in NMR studies of water in biological cells, *Phys. Rev. A*, 1979, **19(6)**, 2446–2453.

134. M. H. Cohen and K. S. Mendelson, Nuclear magnetic relaxation and the internal geometry of sedimentary rocks, *J. Appl. Phys.*, 1982, **53(2)**, 1127–1135.

135. D. P. Gallegos and D. M. Smith, A NMR technique for the analysis of pore structure: Determination of continuous pore size distributions, *J. Colloid Interface Sci.*, 1988, **122(1)**, 143–153.

136. J. S. Beck, J. C. Vartuli, W. J. Roth, M. E. Leonowicz, C. T. Kresge, K. D. Schmitt, C. T. -W. Chu, D. H. Olson, E. W. Sheppard, S. B. McCullen, J. B. Higgins and J. L. Schlenker, A new family of mesoporous molecular-sieves prepared with liquid-crystal templates, *J. Am. Chem. Soc.*, 1992, **114(27)**, 10834–10843.

137. J. Kärger, C. Krause and H. Schäfer, Structure analysis of nanoporous materials by PFG NMR diffusion measurement, *Fortschr.-Ber. VDI, R.3*, 1998, **555(1)**, 104–119.

138. F. Stallmach, A. Gräser, J. Kärger, G. Krause, M. Jeschke, U. Oberhagemann and S. Spange, Pulsed field gradient NMR studies of diffusion in MCM-41 mesoporous solids, *Microporous Mesoporous Mat.*, 2001, **44–45**, 745–753.

139. (a) F. Stallmach, J. Kärger, G. Krause, M. Jeschke and U. Oberhagemann, Evidence of anisotropic self-diffusion of guest molecules in nanoporous materials of MCM-41 type, *J. Am. Chem. Soc.*, 2000, **122(38)**, 9237–9242; (b) J. Kärger, C. M. Papadakis and F. Stallmach, Structure-Mobility relations of molecular diffusion in interface systems, in: *Molecules in Interaction with Surfaces and Interfaces*, R. Haberlandt, D. Michel, A. Pöppel and R. Stannarius, eds., Springer, Heidelberg, 2004, pp. 127–162.

140. E. W. Hansen, F. Courivaud, A. Karlsson, S. Kolboe and M. Stöcker, Effect of pore dimension and pore surface hydrophobicity on the diffusion of *n*-hexane confined in mesoporous MCM-41 probed by NMR – a preliminary investigation, *Microporous Mesoporous Mat.*, 1998, **22(1–3)**, 309–320.

141. F. Courivaud, E. W. Hansen, A. Karlsson, S. Kolboe and M. Stöcker, Pulsed field gradient NMR study of the diffusion of *n*-hexane confined in hydroxylated and dehydroxylated MCM-41 of various pore diameters, *Microporous Mesoporous Mat.*, 2000, **35–36**, 327–339.

142. C. Krause, F. Stallmach, D. Hönicke, S. Spange and J. Kärger, A surprising drop of the diffusivities of benzene in a mesoporous material of type MCM-41 at medium pore filling factors, *Adsorption*, 2003, **9(3)**, 235–241.

143. M. Eddaoudi, J. Kim, N. Rosi, D. Vodak, J. Wachter, M. O'Keefe and O. M. Yaghi, Systematic design of pore size and functionality in isoreticular MOFs and their application in methane storage, *Science*, 2002, **295(5554)**, 469–472.

144. J. L. C. Rowsell and O. M. Yaghi, Metal-organic frameworks: A new class of porous materials, *Microporous Mesoporous Mat.*, 2004, **73(1–2)**, 3–14.

145. H. Li, M. Eddaoudi, M. O'Keeffe and O. M. Yaghi, Design and synthesis of an exceptionally stable and highly porous metal-organic framework, *Nature*, 1999, **402(6759)**, 276–279.

146. S. S. -Y. Chui, S. M. -F. Lo, J. P. Charmant, A. G. Orpen and I. D. Williams, A Chemically functionalizable nanoporous material [Cu$_3$(TMA)$_2$(H$_2$O)$_3$]$_n$, *Science*, 1999, **283(5405)**, 1148–1150.

147. A. I. Skoulidas and D. S. Sholl, Self-diffusion and transport diffusion of light gases in metal-organic framework materials assessed using molecular dynamics simulations, *J. Phys Chem. B*, 2005, **109(33)**, 15760–15768.

148. L. Sarkisov, T. Düren and R. Q. Snurr, Molecular modelling of adsorption in novel nanoporous metal-organic materials, *Mol. Phys.*, 2004, **102(2)**, 211–221.

149. V. Künzel, NMR-Untersuchungen zum diffusiven Stofftransport in mikroporösen metallorganischen Festkörpern (MOF), Diploma thesis, Universität Leipzig, Leipzig, Germany, 2005.

150. F. Stallmach, S. Gröger, V. Künzel, J. Kärger, O. M. Yaghi, M. Hesse and U. Müller, NMR studies on the diffusion of hydrocarbons on the metal-organic framework material MOF-5, *Angew. Chem.-Int. Edit.*, 2006, **45(13)**, 2123–2126.

151. S. Amirjalayer, M. Tafipolsky and R. Schmid, Molecular dynamics simulation of benzene diffusion in MOF-5: Importance of lattice dynamics, *Angew. Chem.-Int. Edit.*, 2006, accepted.

152. J. Kärger, NMR self-diffusion studies in heterogeneous systems, *Adv. Colloid Interface Sci.*, 1985, **23**, 129–148.

153. K. Hahn, J. Kärger and V. Kukla, Single-file diffusion observation, *Phys. Rev. Lett.*, 1996, **76**, 2762–2765.

154. S. Vasenkov and J. Kärger, Different time regimes of tracer exchange in single-file systems, *Phys. Rev. E*, 2002, **66(5)**, 52601.

155. S. Vasenkov, W. Böhlmann, P. Galvosas, O. Geier, H. Liu and J. Kärger, PFG NMR study of diffusion in MFI-type zeolites: Evidence of the existence of intracrystalline transport barriers, *J. Phys Chem. B*, 2001, **105**, 5922–5927.

156. S. Vasenkov and J. Kärger, Evidence for the existence of intracrystalline transport barriers in MFI-type zeolites: A model consistency check using MC simulations, *Microporous Mesoporous Mat.*, 2002, **55(2)**, 139–145.

157. L. Gjerdaaker, G. H. Sørland and D. W. Aksnes, Application of the short diffusion time model to diffusion measurements by NMR in microporous crystallites, *Microporous Mesoporous Mat.*, 1999, **32(3)**, 305–310.

158. O. Geier, R. Q. Snurr, F. Stallmach and J. Kärger, Boundary effects of molecular diffusion in nanoporous materials: A pulsed field gradient nuclear magnetic resonance study, *J. Chem. Phys.*, 2004, **120(1)**, 367–373.

159. A. Pampel, M. Fernandez, D. Freude and J. Kärger, New options for measuring molecular diffusion in zeolites by MAS PFG NMR, *Chem. Phys. Lett.*, 2005, **407(1–3)**, 53–57.

160. M. Fernández, J. Kärger, D. Freude, A. Pampel, J. M. van Baten and R. Krishna, Mixture diffusion in zeolites studied by MAS PFG NMR and molecular simulation, *J. Am. Chem. Soc.*, 2007, Submitted.

161. S. P. Rigby and L. F. Gladden, The use of magnetic resonance images in the simulation of diffusion in porous catalyst support pellets, *J. Catal.*, 1998, **173(2)**, 484–489.

162. X. -H. Ren, M. Bertmer, S. Stapf, D. E. Demco, B. Blümich, C. Kern and A. Jess, Deactivation and regeneration of a naphtha reforming catalyst, *Appl. Catal. A: Gen.*, 2002, **228(1–2)**, 39–52.

163. J. Wood and L. F. Gladden, Effect of coke deposition upon pore structure and self-diffusion in deactivated industrial hydroprocessing catalysts, *Appl. Catal. A: Gen.*, 2003, **249(2)**, 241–253.

164. G. H. Grosch, U. Müller and M. Hesse, Verfahren zur Herstellung eines Formkörpers, Deutsches Patent- und Markenamt, DE 198 59 561 A1, 2000.

165. U. Müller, R. Senk, W. Hader, P. Rudolf and N. Rieber, Shaped body and method for producing the same, Intern. Patent, WO/2002/085513 A2, World Intellectual Property Organization, PCT/EP2002/002278, 2002.

166. P. Kortunov, S. Vasenkov, J. Kärger, M. F. Elía, M. Perez, M. Stöcker, G. K. Papadopoulos, D. Theodorou, B. Drescher, G. McElhiney, B. Bernauer, V. Krystl, M. Kočiřík, A. Zikánová, H. Jirglová, C. Berger, R. Gläser, J. Weitkamp and E. W. Hansen, Diffusion in fluid catalytic cracking catalysts on various displacement scales and its role in catalytic performance, *Chem. Mater.*, 2005, **17(9)**, 2466–2474.

167. J. Kärger and S. Vasenkov, Quantitation of diffusion in zeolite catalysts, *Microporous Mesoporous Mat.*, 2005, **85(3)**, 195–206.

168. F. Stallmach and S. Crone, Analytical model for extrapolation of experimental NMR diffusion studies to reaction conditions for formulated catalyst particles, *Diffusion Fundamentals*, J. Kärger, F. Grinberg, P. Heitjans, eds., Leipziger Universitätsverlag GmbH, Leipzig, Germany, 2005, 474–475.

169. O. Geier, S. Vasenkov and J. Kärger, Pulsed field gradient nuclear magnetic resonance study of long-range diffusion in beds of NaX zeolite: Evidence for different apparent tortuosity factors in the knudsen and bulk regimes, *J. Chem. Phys.*, 2002, **117(5)**, 1935–1938.

170. G. Casieri, F. De Luca and P. Fantazzini, Pore-size evaluation by single-sided nuclear magnetic resonance measurements: Compensation of water self-diffusion effect on transverse relaxation, *J. Appl. Phys.*, 2005, **97(4)**, 43901.

171. A. Plassais, M. -P. Pomiès, N. Lequeux, J. -P. Korb, D. Petit, F. Barberon and B. Bresson, Microstructure evolution of hydrated cement pastes, *Phys. Rev. E*, 2005, **72(4)**, 41401.

172. L. Pel, H. Huinink, K. Kopinga, R. P. J. van Hees and O. C. G. Adan, Efflorescence pathway diagram: Understanding salt weathering, *Constr. Build. Mater.*, 2004, **18(5)**, 309–313.

173. L. Pel, H. Huinink and K. Kopinga, Salt transport and crystallization in porous building materials, *Magn. Reson. Imaging*, 2003, **21(3–4)**, 317–320.

174. N. Nestle, P. Galvosas, O. Geier, C. Zimmermann, M. Dakkouri and J. Kärger, Nuclear magnetic resonance study of diffusion and relaxation in hydrating white cement pastes of different water content, *J. Appl. Phys.*, 2001, **89**, 8061–8065.

175. K. Friedemann, F. Stallmach and J. Kärger, NMR diffusion and relaxation studies during cement hydrationa non-destructive approach for clarification of the mechanism of internal post curing of cementitious materials, *Cem. Concr. Res.*, 2006, **36(5)**, 817–826.

176. S. D. Beyea, B. J. Balcom, T. W. Bremner, R. L. Armstrong and P. E. Grattan-Bellew, Detection of drying-induced microcracking in cementitious materials with space-resolved 1H nuclear magnetic resonance relaxometry, *J. Am. Ceram. Soc.*, 2003, **86(5)**, 800–805.

177. J. J. Young, P. Szomolanyi, T. W. Bremner and B. J. Balcom, Magnetic resonance imaging of crack formation in hydrated cement paste materials, *Gem. Concr. Res.*, 2004, **34(8)**, 1459–1466.

178. N. Nestle, P. Galvosas, C. Zimmermann, F. Stallmach and J. Kärger, Direct investigation of the fate of NAPL contaminations in a hydrating cement matrix by means of magnetic resonance techniques, *Environ. Sci. Technol.*, 2004, **38**, 880–885.

179. J. Petković, H. P. Huinink, L. Pel and K. Kopinga, Diffusion in porous building materials with high internal magnetic field gradients, *J. Magn. Reson.*, 2004, **167(1)**, 97–106.

180. N. Nestle, P. Galvosas and J. Kärger, Direct measurement of water self-diffusion in hardening blast furnace slag cement pastes by means of nuclear magnetic resonance techniques, *J. Appl. Phys.*, 2001, **90**, 518–520.

181. J. Dietrich, W. Schönfelder, A. Märten, V. Klapperich and F. Stallmach, Untersuchungen zum Schadstoffrückhaltevermögen von Einphasen-Dichtwandmassen, In: *Geotechnische Aspekte im Umweltschutz 2006, Institut für Grundbau und Bodenmechanik*, J. Stahlmann, M. Rosenberg, eds., Technische Universität Braunschweig, Braunschweig, 2006, 121–142.

182. W. Schönfelder, J. Dietrich, A. Maerten, K. Kopinga and F. Stallmach, Studying diffusive water transport in bentonite-cement cut-off wall material, *Magn. Reson. Imaging*, 2007, accepted.

183. M. Lipsicas, J. R. Banavar and J. Willemsen, Surface relaxation and pore sizes in rocks – a nuclear magnetic resonance analysis, *Appl. Phys. Lett.*, 1986, **48(22)**, 1544–1546.

184. S. Vasenkov, P. Galvosas, O. Geier, N. Nestle, F. Stallmach and J. Kärger, Determination of genuine diffusivities in heterogeneous media using stimulated echo pulsed field gradient NMR, *J. Magn. Reson.*, 2001, **149(2)**, 228–233.

185. J. Kärger and F. Stallmach, NMR diffusion studies of molecules in nanoporous materials, in: *Magnetic Resonance in Colloid and Interface Science, NATO Science Series II: Mathematics, Physics and Chemistry*, J. Fraissard and O. Lapina, eds., Kluwer Academic Publishers, Dordrecht, Boston, London, 2002, pp. 57–70.

186. A. J. Lucas, S. J. Gibbs, M. Peyron, G. K. Pierens, L. D. Hall, R. C. Stewart and D. W. Phelps, Pore geometry information via pulsed field gradient NMR, *Magn. Reson. Imaging*, 1994, **12(2)**, 249–251.

187. M. Appel, F. Stallmach and H. Thomann, Irreducible fluid saturation determined by pulsed field gradient NMR, *J. Pet. Sci. Eng.*, 1998, **19(1–2)**, 45–54.

188. M. D. Hürlimann, K. G. Helmer, L. L. Latour and C. H. Sotak, Restricted diffusion in sedimentary-rocks. determination of surface-area-to-volume ratio and surface relaxivity, *J. Magn. Reson. A*, 1994, **111(2)**, 169–178.

189. G. P. Frosch, J. E. Tillich, R. Haselmeier, M. Holz and E. Althaus, Probing the pore space of geothermal reservoir sandstones by nuclear magnetic resonance, *Geothermics*, 2000, **29(6)**, 671–687.

190. H. Pape, J. E. Tillich and M. Holz, Pore geometry of sandstone derived from pulsed field gradient NMR, *J. Appl. Geophys.*, 2006, **58(3)**, 232–252.

191. C. Vogt, P. Galvosas, N. Klitzsch and F. Stallmach, Self-diffusion studies of pore fluids in unconsolidated sediments by PFG NMR, *J. Appl. Geophys.*, 2002, **50(4)**, 455–467.

192. F. Stallmach and J. Kärger, Stallmach and Kärger reply, *Phys. Rev. Lett.*, 2003, **90(3)**, 39602.

193. L. J. Zielinski and M. D. Hürlimann, Probing short length scales with restricted diffusion in a static gradient using the CPMG sequence, *J. Magn. Reson.*, 2005, **172(1)**, 161–167.

194. R. W. Mair, G. P. Wong, D. Hoffmann, M. D. Hürlimann, S. Patz, L. M. Schwartz and R. L. Walsworth, Probing porous media with gas diffusion NMR, *Phys. Rev. Lett.*, 1999, **83(16)**, 3324–3327.

195. R. Wang, T. Pavlin, M. S. Rosen, R. W. Mair, D. G. Cory and R. L. Walsworth, Xenon NMR measurements of permeability and tortuosity in reservoir rocks, *Magn. Reson. Imaging*, 2005, **23(2)**, 329–331.

196. M. Flaum, G. J. Hirasaki, C. Flaum and C. Straley, Measuring pore connectivity by pulsed field gradient diffusion editing with hydrocarbon gases, *Magn. Reson. Imaging*, 2005, **23(2)**, 337–339.

197. D. Candela and P. Wong, Using NMR to measure fractal dimensions, *Phys. Rev.Lett.*, 2003, **90(3)**, 39601.

198. P. T. Callaghan and I. Furo, Diffusion–diffusion correlation and exchange as a signature for local order and dynamics, *J. Chem. Phys.*, 2004, **120(8)**, 4032–4038.

199. P. L. Hubbard, K. M. McGrath and P. T. Callaghan, A study of anisotropic water self-diffusion and defects in the lamellar mesophase, *Langumir*, 2005, **21(10)**, 4340–4346.

200. G. Leu, E. J. Fordham, M. D. Hürlimannand and P. Frulla, Fixed and pulsed gradient diffusion methods in low-field core analysis, *Magn. Reson. Imaging*, 2005, **23(2)**, 305–309.

201. Y. Qiao, P. Galvosas and P. T. Callaghan, Diffusion correlation NMR spectroscopic study of anisotropic diffusion of water in plant tissues, *Biophys J.*, 2005, **89(4)**, 2899–2905.

202. W. P. Aue, E. Bartholdi and R. R. Ernst, Two-dimensional spectroscopy. Application to nuclear magnetic resonance, *J. Chem. Phys.*, 1976, **64(5)**, 2229–2246.

203. A. E. English, K. P. Whittall, M. L. G. Joy and R. M. Henkelman, Quantitative 2-dimensional time correlation relaxometry, *Magn. Reson. Med.*, 1991, **22(2)**, 425–434.

204. L. Venkataramanan, Y. Q. Songand and M. D. Hürlimann, Solving fredholm integrals of the first kind with tensor product structure in 2 and 2.5 dimensions, *IEEE Trans. Signal Process*, 2002, **50(5)**, 1017–1026.

205. M. D. Hürlimann, M. Flaum, L. Venkataramanan, C. Flaum, R. Freedman and G. J. Hirasaki, Diffusion–relaxation distribution functions of sedimentary rocks in different saturation states, *Magn. Reson. Imaging*, 2003, **21(3–4)**, 305–310.

206. B. Q. Sun and K. J. Dunn, Two-dimensional nuclear magnetic resonance petrophysics, *Magn. Reson. Imaging*, 2005, **23(2)**, 259–262.

207. G. H. Sørland, H. W. Anthonsen, J. G. Seland, F. Antonsen, H. C. Wideroe and J. Krane, Exploring the separate NMR responses from crude oil and water in rock cores, *Appl. Magn. Reson.*, 2004, **26(3)**, 417–425.

208. T. Adalsteinsson, W. F. Dong and M. Schönhoff, Diffusion of $77,000\,g\,mol^{-1}$ dextran in submicron polyelectrolyte capsule dispersions measured using PFG-NMR, *J. Phys Chem. B*, 2004, **108(52)**, 20056–20063.

Recent Advances in Theoretical Calculations of Indirect Spin–Spin Coupling Constants

LEONID B. KRIVDIN[1] AND RUBÉN H. CONTRERAS[2]

[1]A. E. Favorsky Irkutsk Institute of Chemistry, Siberian Branch of the Russian Academy of Sciences, 1 Favorsky Street, 664033 Irkutsk, Russia
[2]Department of Physics, University of Buenos Aires, and CONICET Ciudad Universitaria, Pab. 1 (C1428EHA) Buenos Aires, Argentina

Recent trends in theoretical calculations of indirect spin–spin coupling constants covering the period of May 2003–July 2006 are outlined with the emphasis on the currently used wavefunction- and DFT-based methods. Computational results dealing with the different spin–spin coupling constants in several representative inorganic, organic, and biomolecular species obtained within the ab initio and DFT frameworks are compiled and critically discussed to elucidate some illustrative structural trends and their practical applications.

1. INTRODUCTION

During the review period, May 2003–July 2006, a good deal of interest has been focused on theoretical calculation of nuclear magnetic resonance (NMR) indirect spin–spin coupling constants for any of several reasons. Among those are, on the one hand, experimental techniques, improving very fast and making it feasible to determine new, and sometimes, unusual couplings. On the other hand, it is the developement of more efficient and versatile codes to calculate coupling constants increasing the possibility to study larger compounds containing light as well as heavy atoms. It was the availability of the recent efficient computational codes, which stimulated many of the authors to use them as a complement to the experimental measurements. During these last three years, the methodology for calculating coupling constants continued to follow two different lines, namely, the wavefunction- and DFT-based methods. Owing to the very large computational requirements of the high-level *ab initio* calculations of coupling constants, at present, in applications involving medium to large compounds, these calculations are most frequently carried out within the DFT framework.

A number of excellent publications describing theoretical methods currently used to calculate spin–spin coupling constants could be found in the literature including reviews,[1–4] chapters of books,[5–17] or even books.[18,19] In the present review, overlap with such works will be avoided as much as possible. Emphasis will be put in critical discussion of some common problems when one is interested in getting insight into how spin–spin couplings are affected by factors such as different intra- and inter-molecular interactions, structural aspects, conformational behavior, and stereo-electronic effects together with what can be expected from the calculations obtained with the approaches currently applied in the literature. In view of the enormous

---

Abbreviations: ADF; Amsterdam density functional; AIM; Atoms in molecules; ANO; Atomic natural orbital; B3LYP; Becke three-parameter hybrid functional with the Lee–Yang–Parr functional; B3PW91; Becke–Perdew–Wang; BLYP; Becke–Lee–Yang–Parr; BSSE; Basis set superposition error; CAS; Complete active space; CC; Coupled clusters; CCSD; Coupled cluster singles and doubles; CHF; Coupled Hartree–Fock; CI; Configuration interaction; CLOPPA; Contributions from localized orbitals within the polarization propagator approach; COSY; Correlation spectroscopy; CP; Coupled perturbed; DFT; Density functional theory; DKH; Douglas–Kroll–Hess; DSO; Diamagnetic spin orbital; EOM; Equation of motion; FC; Fermi contact; FCI; Full configuration interaction; FPT; Finite perturbation theory; GGA; Generalized gradient approximation; HF; Hartree–Fock; HMBC; Heteronuclear multibond correlation; HSQC; Heteronuclear single quantum correlation; INDO; Intermediate neglect of differential overlap; IORAmm; Infinite-order regular approximation with modified metric; IPPP; Inner projections of the polarization propagator; J-OC-PSP; Decomposition of J into orbital contributions using partial spin polarization; KT; Keal–Tozer; LDA; Local density approximation; LDBS; Locally dense basis set; LMO; Localized molecular orbital; LP; Lone-pair; LPE; Lone-pair effect; MCSCF; Multiconfigurational self self-consistent field; MO; Molecular orbital; MP; Møller–Plesset; NBO; Natural bond orbital; NC; Non-contact; NMR; Nuclear magnetic resonance; NMRTWM; Nuclear magnetic resonance triplet wavefunction model; PBE; Perdew–Burke–Ernzerhof; PCM; Polarizable continuum model; PMO; Perturbed molecular orbitals; PSO; Paramagnetic spin orbital; RAS; Restricted active space; RPA; Random phase approximation; SCF; Self-consistent field; SD; Spin–dipolar; SOPPA; Second-order polarization propagator approximation; VWN; Volko–Wilk–Nusair; ZORA; Zeroth-order regular approximation; ZPV; Zero-point vibration.

amount of data on calculation and theoretical interpretation of spin–spin coupling constants that appeared during the review period, we really apologize if not all scientists working in this area will find their names in the reference list.

2. GENERAL FEATURES OF SPIN–SPIN COUPLING CONSTANTS

2.1. Theoretical background and general formalism

High-resolution NMR spectra are obtained by inducing transitions between the nuclear spin states. The nuclear Hamiltonian describing such states is given in Eq. (1)

$$H = -\frac{1}{2\pi}\sum_A \gamma_A \mathbf{I}_A (\mathbf{1} - \boldsymbol{\sigma}_A)\mathbf{B} + \sum_{A \neq B} \mathbf{I}_A (\mathbf{J}_{AB} + \mathbf{D}_{AB})\mathbf{I}_B \tag{1}$$

where $\mathbf{B}$ is the spectrometer static magnetic field, $\boldsymbol{\sigma}_A$ is the nuclear magnetic shielding second rank tensor of nucleus A, $\mathbf{D}_{AB}$ and $\mathbf{J}_{AB}$ are the direct and indirect nuclear spin–spin coupling constant second rank tensors between nuclei A and B, and $\mathbf{I}_A$ and $\mathbf{I}_B$ are the spins of magnetic nuclei A and B, respectively. The sums run over all magnetic nuclei belonging to the molecular system under study. When measurements are carried out in isotropic phase, only 1/3 of the trace of each second rank tensor is observed in the NMR spectrum. The $\mathbf{D}$ tensor is purely anisotropic, and therefore its trace is zero and has no effect on the isotropic-phase spectrum. On the other hand, $\mathbf{D}$ does not depend on the molecular electronic structure, since it depends only on the internuclear distance, $d_{A,B}$, i.e., the $\mathbf{D}$ tensor can provide interesting information on the geometry of a molecule, but it cannot provide any information on the molecular electronic structure.

In this work only the $\mathbf{J}$ tensor will be considered. This originates in magnetic nucleus–electron interactions, and, therefore, it depends on the molecular electronic structure of the compound under study. In general, very small changes in the electronic structure can produce important changes in many coupling constants. This feature makes these spectral parameters' specially suited probes to study molecular electronic structures. From a nonrelativistic point of view, Ramsey[20] described such interactions through four operators: Fermi contact, FC; Spin-Dipolar, SD; Paramagnetic Spin-Orbit, PSO; and Diamagnetic Spin-Orbit, DSO; Eqs (2a) to (2d).

$$H_{\text{FC}} = \frac{4\mu_o \hbar \mu_B}{3}\sum_A \gamma_A \sum_k \delta(\mathbf{r}_{kA})\frac{(\mathbf{S}_k \cdot \mathbf{I}_A)}{r_{kA}^3} \tag{2a}$$

$$H_{\text{SD}} = \frac{\mu_o \hbar \mu_B}{2\pi\pi}\sum_A \gamma_A \sum_k \left[\frac{3(\mathbf{S}_k \cdot \mathbf{r}_{kA})(\mathbf{I}_A \cdot \mathbf{r}_{kA})}{r_{kA}^5} - \frac{(\mathbf{S}_k \cdot \mathbf{I}_A)}{r_{kA}^3}\right] \tag{2b}$$

$$H_{\text{PSO}} = \frac{\mu_o \hbar \mu_B}{2\pi i}\sum_A \gamma_A \mathbf{I}_A \cdot \sum_k \frac{(\mathbf{r}_{kA} \times \nabla_k)}{r_{kA}^3} \tag{2c}$$

$$H_{\text{DSO}} = \frac{\mu_o^2 e\hbar\mu_B}{(4\pi)^2} \sum_{A,B} \gamma_A\gamma_B \sum_{\text{K}} \frac{[(\mathbf{I}_A \cdot \mathbf{I}_B)(\mathbf{r}_{kA} \cdot \mathbf{r}_{kB}) - (\mathbf{I}_A \cdot \mathbf{r}_{kB})(\mathbf{I}_B \cdot \mathbf{r}_{kA})]}{r_{kA}^3 r_{kB}^3} \quad (2d)$$

FC and SD are triplet operators, while the PSO is a singlet operator. Besides, the DSO term can be considered as a first-order operator since the first-order perturbation theory yields an energy term bilinear in the $\mathbf{I}_A$ and $\mathbf{I}_B$ nuclear spins, see Eq. (1), and, therefore, it is usually evaluated as an expectation value over the molecular electronic ground state, although the latter may also be expressed in a form which involves excited states.[21] Using the polarization propagator approach[22] or the linear response function methods,[23] all contributions to the coupling constants can be evaluated without explicit calculation of the involved excited states.[17]

Since indirect spin–spin coupling constants (hereafter referred to also as "coupling constants" or "spin–spin couplings" or just "couplings"), are proportional to the magnetogyric ratios of the coupling nuclei A and B; when comparing coupling constants for different isotopic species, it is usually preferred to consider the "reduced coupling constants" K_{AB} instead of J_{AB} These two couplings are connected through Eq. (3):

$$K_{AB} = 4\pi^2 \frac{J_{AB}}{h\gamma_A\gamma_B} \quad (3)$$

where h is the Planck's constant, and γ_A and γ_B are the magnetogyric ratios of the nuclei A and B, respectively.

From operators (2a)–(2d), perturbation theory yields, for isotropic phase, four terms, which make up the isotropic J_{AB} coupling constant. In anisotropic phase, a further term appears originated in the FC/SD cross-term, $\mathbf{J}_{\textbf{FC/SD}}$, but it must be emphasized that it is a tensor quantity, which is purely anisotropic since its trace is zero. Therefore, within a nonrelativistic formulation in isotropic phase, the $^nJ_{AB}$ coupling constant, where n is the number of bonds separating the coupling nuclei, can be written as:

$$^nJ_{AB} = {}^nJ_{AB}(\text{FC}) + {}^nJ_{AB}(\text{SD}) + {}^nJ_{AB}(\text{PSO}) + {}^nJ_{AB}(\text{DSO}) \quad (4)$$

Bryce and Wasylishen[24] described what could be learnt about the trends in spin–spin coupling constants from the hyperfine parameters measured in microwave and molecular beam experiments.

For the sake of simplicity, in this work, the following convention is adopted: whenever the isotopic number of a given nucleus is not explicitly shown, it will be understood that the coupling nuclei refer to the 1/2 spin isotopes with the largest natural abundances, for instance, $^nJ_{\text{CN}}$ will be understood to mean $^nJ_{^{13}\text{C}^{15}\text{N}}$. If only magnetic isotopes with spin larger than 1/2 show natural abundance, then that with the largest natural abundance will be assumed, e.g., $^nJ_{\text{ON}}$ and $^nJ_{\text{BN}}$ will be understood to mean $^nJ_{^{17}\text{O}^{15}\text{N}}$ and $^nJ_{^{11}\text{B}^{15}\text{N}}$ respectively.

It must be emphasized that the above considerations hold for compounds containing only light atoms. For compounds containing heavy nuclei, coupling constants in few cases were obtained from full relativistic calculations.[25–27] In many other cases, relativistic contributions are introduced through a perturbation

approach. In this last case, Eq. (4) does no longer hold and, for instance, cross-terms originating in singlet and triplet operators, Eqs (2a)–(2d), could yield significant contributions.

One important question deals with the relative importance of the four coupling terms in Eq. (4). It is important to remember that there is no experimental approach that could help, and so far, only theoretical approaches could answer this question. Although for many years it was assumed that the FC term was the most important, nowadays it is well established that many couplings are dominated by the non-contact contributions, as exemplified in some sections of this review.

2.2. Transmission of couplings through a hydrogen bond

Alkorta and Elguero[28] reviewed in 2003 the most important results obtained by that time from both theoretical and experimental studies of coupling constants transmitted through a hydrogen bond. A few years ago, Dingley, Cordier, and Grzesiek[29,30] published two reviews on *trans*-hydrogen-bond couplings used for the analysis of biopolymers. More recently, a review by Pecul and Sadlej[31] on *ab initio* calculations of the intermolecular nuclear spin–spin coupling constants has also appeared.

2.2.1. *Covalency*

Although the transmission of coupling constants through hydrogen bonds was known for some time,[32,33] this phenomenon took important relevance only when it was observed in nucleic acid base pairs.[34] A rather controversial matter connected with coupling constants of this type is whether their existence might be interpreted as the evidence of a certain degree of covalency of the corresponding hydrogen bond (for papers prior to 2003 dealing with this point, see Ref. 35). During this review period, this subject was thoroughly addressed by Del Bene[36] who considered five systems stabilized by the X–H–Y hydrogen bonds of different types (for Del Bene's classification of hydrogen bonds, see, for instance, Ref. 37). These systems included two hydrogen-bonded cations, $O_2H_5^+$ and $N_2H_7^+$, two neutral complexes, $(H_2O)_2$ and $FH:NH_3$, and malonaldehyde, the latter providing a case of an intramolecular hydrogen bond. Employing the MP2/6-31+G(d,p)-optimized structures, Del Bene[36] calculated the corresponding $^{2h}J_{XY}$ couplings using the EOM-CCSD approach in the CI-like approximation.[38–41] These results were compared with those obtained in related complexes having the same $X \cdots Y$ distance, but possessing no hydrogen bond. Such complexes are not stabilized by a hydrogen bond and, therefore, there is a repulsion between composite monomers. In these two different series of systems coupling constants are different, but this provides no direct evidence that the existence of intermolecular couplings is primarily related to the covalency of the hydrogen bond.

At this point it is important to recall that in general, in a hydrogen bond of the type $X–H \cdots Y$, there are three different interactions responsible for either transmitting or affecting the spin information associated with the FC term. They are as

follows: (a) the direct overlap of the electronic clouds corresponding to the molecular fragments involved in the hydrogen bond; (b) charge transfer interactions (or negative hyperconjugative interaction) of the type $LP(Y) \rightarrow \sigma^*_{X-H}$, i.e., from one of the LPs of the acceptor atom to the antibonding orbital (X–H)* involving the donor atom; and (c) electrostatic interactions. Interaction (a) defines an efficient coupling pathway through the exchange interactions in the overlap region, and it has nothing to do with any covalency. On the other hand, hyperconjugative interactions (b) are efficient for transmitting the FC term, and they define any possible covalency of the hydrogen bond. Interactions (c) do not define a coupling pathway, but they can affect coupling constants (proximity effects). In short, there can be a through-hydrogen bond transmission of couplings even if the hydrogen bond covalency is very low or even negligible.

This is also supported by Pecul's high-level *ab initio* calculations[42] of $^1J_{HeHe}$ in the van der Waals helium dimer, where she reported a calculated coupling of 1.3 Hz, i.e., a significant through-space coupling constant, although the complex is formed by van der Waals interactions providing no covalent character. It is important to note that this comment refers only to the FC transmission of spin–spin coupling and doesn't hold for the adequate rationalization of the through-hydrogen bond couplings having substantial PSO and/or DSO contributions.

Recently, Grabowski *et al.*[43] considered a formamide dimer and several related systems to study the possible covalent nature of the N–H···O hydrogen bonds. To this end, they used the Bader's theory,[44] and they obtained deeper insight into the physical nature of interactions that take place in those molecular complexes by applying the ''variation–perturbation'' approach.[45] They found that the covalent character of the hydrogen bond is manifested by a markedly increased contribution of the delocalization term relative to the electrostatic interaction energy. An unusually strong hydrogen bond with an important covalent character was reported by DuPré[46] in the molecular cage of *in*-bicyclo[4.4.4]-1-tetradecyl cation, where the covalency of the $C_b \cdots H$ hydrogen bond was studied using both the AIM and NBO methods. Coupling constants involving the bridgehead atoms were calculated at the DFT-B3LYP/6-31G(d,p)//B3LYP/6-31G(d,p) level giving $^1J_{C_aH} = 44.9$ Hz and $^1J_{C_bH} = 45.8$ Hz as compared to the experimental value of 47 Hz. These calculations also allowed to estimate the corresponding *trans*-hydrogen-bond coupling $^{2h}J_{C_aC_b} = 12.4$ Hz.
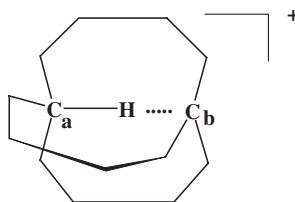
In-bicyclo[4.4.4]-1-tetradecyl cation

Somewhat connected with the controversial point about the covalent character of a hydrogen bond and couplings transmitted through it is the nature of the interaction between proximate lone pairs (LPs). It is known that the overlap between proximate LPs provides an efficient coupling pathway for the through-space transmission of the FC term of many couplings, e.g., J_{SeSe}, J_{PP}, J_{PN}, J_{FF}, J_{FP}, and J_{FN} (for details, see Ref. 47). One of such examples corresponds to the $^3J_{PP}$ coupling in the $C_2H_2(PH_2)_2$ molecule, whose through-space component was studied many years ago by applying the IPPP (Ref. 48) approach at the INDO level established an important and positive through-space contribution.[49] Recently, Malkina and Malkin[50] applied their approach, dubbed as CED (coupled energy density), to visualize coupling pathways by the real-space functions to the same molecule, $C_2H_2(PH_2)_2$, to verify that one of the important pathways for this type of couplings was a through-space component transmitted by the direct overlap of the LPs of the P atoms.

The Malkina and Malkin's CED approach[50] was recently applied by Kaupp et al.[51] to study the characteristic dependence of J_{PP} couplings of alkali metal tetraphosphane-1,4-diides to get insight into through-bond and through-space contributions. It was found that characteristic behavior of the through-space contribution to J_{PP} couplings in these compounds depends on the relative orientation of the corresponding nonbonding electron pairs, the trend predicted more than 20 years ago for J_{PP} couplings regardless the number of the formal bonds that separate the coupling nuclei.[52] It is to be noted that Hierso et al.[53] reported recently very interesting examples when J_{PP} couplings are transmitted through-space through the overlap of their nonbonding electron pairs in tetraphosphine ferrocenyl derivatives.

The nature of the interaction between proximate LPs of F atoms was addressed by Alkorta and Elguero,[54] who studied fluorine-fluorine interactions using the Bader's AIM methodology[55] in several systems with proximate LP bearing atoms, some of them constituting the traditional examples where the through-space transmission of J_{FF} couplings was observed. According to the AIM approach, for the equilibrium geometry, the existence of a bond path between two proximate atoms, where a critical point can be identified as adducing evidence that a bonding interaction between them, does exist.[55] It is important to stress that the bond critical points were found in all molecular systems studied by Alkorta and Elguero,[54] where important through-space J_{FF} couplings were determined experimentally. The interactions between the two proximate F atoms correspond in all such cases to the close-shell interactions.

Other interesting examples of the attractive interactions between proximate LP bearing atoms, divalent selenium, and halogen atoms, were reported during this review period by Iwaoka et al.[56] in three types of model compounds: $2\text{-}(CH_2X)C_6H_4SeY$, $3\text{-}(CH_2X)\text{-}2\text{-}C_{10}H_6SeY$, and $2\text{-}XC_6H_4CH_2SeY$ (Y = CN, Cl, Br, SeAr; X = F, Cl, Br). Substantial part of this interaction originates mainly in the electron delocalization interaction of the $LP(X) \rightarrow \sigma^*_{Se-Y}$ type, decreasing its strengths along the series $Se \cdots F > Se \cdots Cl > Se \cdots Br$. It is important to note that for X = F, the through-space spin–spin couplings were observed. In previous papers the same authors observed similar electron delocalization effects in the proximate

interactions of the type Se···N, Se···O, and Se···F (for the corresponding references, see Ref. 56).
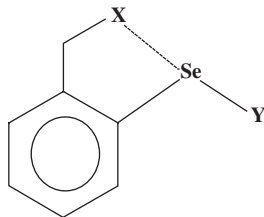
Compounds 2-$(CH_2X)C_6H_4SeY$ where Iwaoka *et al.* [56]
observed an attractive X···Se interaction.

2.2.2. *Cooperative effects*

Provasi *et al.*[57] studied the interaction energies and intra- and intermolecular couplings in the linear $(HCN)_n$ and $(HNC)_n$ complexes ($n = 1–6$). The geometry optimizations were performed at the frozen-core MP2/cc-pVTZ level, and coupling constants were calculated within the SOPPA approach using the aug-cc-pVTZ-J locally dense basis set. In both types of the chain complexes they observed cooperative effects on the interaction energies, which were also reflected in the intermolecular distances and intra- and intermolecular couplings. Although in the latter, for each monomer of both chains, noncontact terms were important, the cooperative effect was observed mainly in the FC term. It was found that the two-bond *trans*-hydrogen-bond couplings were dominated by the FC term and their signs followed the main trends discussed in Sections 2.2 and 3.3.2.

Asensio *et al.*[58] studied the cooperative effect on the hydrogen bonding in the adenine–thymine (**A.T**) and in the guanine–cytosine (**G.C**) base pairs both at the DFT and the Møller–Plesset levels. They found that the cooperative contribution to the energy of each of these complexes is similar in magnitude, but provides a more important contribution to the overall stability of the **A.T** pair, which has a lower complexation energy than the **G.C** pair.
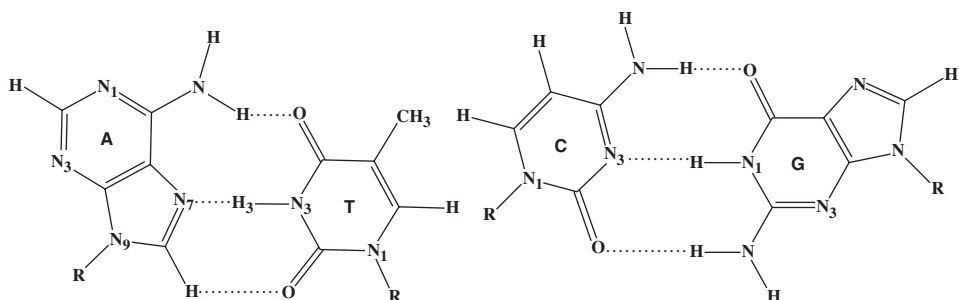
Adenine-thymine (**A.T**) and guanine-cytosine (**C.G**) hydrogen-bonded complexes

The influence of the hydrogen bond cooperative effects on the *trans*-hydrogen-bond $^{3h}J_{CN}$ couplings in proteins was studied by Salvador *et al.*[59] at the DFT-B3LYP/D95(d,p) level using a chain of eight formamide molecules as a model system. They found that the H-bonding chains must be treated differently from the isolated H-bonds, since within the chains, two effects that are absent in simple isolated H-bonds, become important, namely (i) an enhancement is observed for the coupling pathways within the chain; and (ii) moieties that are hydrogen-bond donors have more important effects on the coupling transmitted through the proximate hydrogen bond than the hydrogen bond acceptors.

However, in both cases, these effects are essential and should be taken into account when such couplings are used to study structural aspects of proteins. According to Salvador *et al.*,[59] both observations are in agreement with the data reported by Juranic *et al.*[60] It is important to recall that the relationship between the calculated $^{2h}J_{NN}$ couplings and the N⋯N distance obtained by Del Bene and Bartlett[61] using small complexes as model systems, was afterwards verified experimentally by Söntjens *et al.*[62] in ureidopyrimodinone dimers in solution. It suggests that in some cases cooperative effects on hydrogen bonds could lead to only very small changes in spin–spin coupling constants.
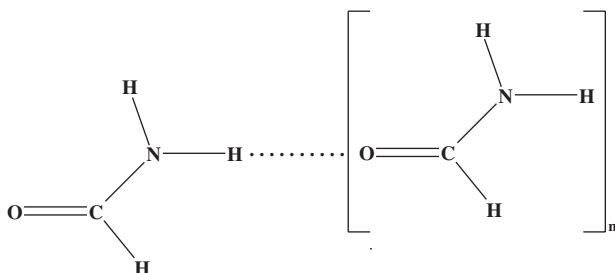
Planar formamide octamer ($n = 7$)

Tuttle *et al.*[63] emphasized that *trans*-hydrogen-bond couplings are sensitive to the extended environment of a hydrogen bond, and, for instance, in the case of a protein, several peptide groups should be included to obtain an adequate system to model *trans*-hydrogen-bond couplings. Del Bene *et al.*[64] using the EOM-CCSD method,[38–41] studied the influence of trimer formation on $^{1}J_{XH}$, $^{1h}J_{HY}$ and $^{2h}J_{XY}$ in complexes of the type AH⋯XH⋯YH$_3$, where A and X are F and Cl, and Y is N or P. Comparing calculated *trans*-hydrogen-bond couplings in the two-member complexes of the type XH⋯YH$_3$ with similar couplings in the three-member complexes, AH⋯XH⋯YH$_3$, it was observed that $^{2h}J_{XY}$ increased in the order XH⋯YH$_3$ < ClH⋯XH⋯ YH$_3$ < FH⋯XH⋯YH$_3$. This indicates, on the one hand, that the presence of the third molecule yields an increase in the proton-shared character of the X–H–Y and, on the other hand, the proton-shared character of the hydrogen bond is enhanced when increasing the proton-donating strength of AH. These calculations also showed that the presence of the third molecule practically did not affect $^{1}J_{XH}$ when the proton acceptor was PH$_3$. However, when replacing PH$_3$ with NH$_3$, $^{1}J_{XH}$ decreases following

this sequence: $XH\cdots NH_3 > ClH\cdots XH\cdots NH_3 > FH\cdots XH\cdots NH_3$, which means that this coupling decreases with the increase in the proton-shared character of the X–H–Y hydrogen bond.

2.3. Effect of hyperconjugative interactions on coupling constants

As commented briefly in the next subsection, any electron delocalization that takes place inside a molecule is an important vehicle for transmitting the spin information associated with both the FC and SD contributions to spin–spin couplings. In this way it is easy to realize that any factor affecting electron delocalization interactions should also affect notably the coupling constants involving nuclei at least in the region where they take place. Probably, the influence of the hydrogen bond co-operative effects on coupling constants originates mainly in changes of the electron delocalizations when increasing the size of a complex from a simple dimer (see Section 2.2). Since in the type of couplings considered in this subsection, the SD contribution is usually much smaller than the FC term we shall consider only the FC term, if not stipulated otherwise.

In saturated compounds, electron delocalization interactions are frequently classified as negative hyperconjugative interactions, $LP \rightarrow \sigma^*$, and σ-hyperconjugative interactions, $\sigma \rightarrow \sigma^*$. In the current literature, it is accepted that an interesting quantitative description of such interactions is that given by the natural bond orbital (NBO) method of Reed and Weinhold.[65] During the review period, several studies appeared reporting the influence of this type of interactions on coupling constants. When considering this point, it is important to make the distinction between the short-range, $^nJ_{XY}$ ($n \leq 3$), and long-range, $^nJ_{XY}$ ($n \geq 4$), couplings, where n is the number of formal bonds separating the coupling nuclei. In the former, the FC term does not require any hyperconjugative interactions to be transmitted since exchange interactions between the localized orbitals representing either bonds, LPs, or core orbitals constitute an adequate coupling pathway. However, such couplings could be either enhanced or reduced as a result of the hyperconjugative interactions. In the second case, $n \geq 4$, in saturated compounds,[66] long-range couplings, having no "through-space" component, are transmitted by the σ-hyperconjugative interactions, as discussed in the next subsection.

At this point it is important to stress that in the current literature basically there is no general agreement on the origin of couplings transmitted through-space. For instance, Barfield[67] included the rear-lobe interactions within the through-space mechanism, while in the cited work[66] such effects are rationalized as being hyperconjugative interactions. It should also be recalled that many years ago, Pople and Bothner-By[68] rationalized substituent increments of coupling constants in terms of inductive and hyperconjugative effects. Commented in this subsection are some examples where the influence of these interactions on $^nJ_{XY}$ ($n \leq 3$) couplings is important. Early papers published before this review period are reasonably covered in Refs. 35 and 47. The FC term of $^nJ_{XY}$ ($n \geq 4$) couplings (see Section 2.4), in saturated compounds, is mainly transmitted by the σ-hyperconjugative interactions,

which are notably enhanced in cyclic and polycyclic-strained compounds favoring the transmission of the FC term of *trans*-cage couplings.

Some general considerations about how hyperconjugative interactions in general are expected to affect one- and two-bond coupling constants are given in Ref. 47. Also, a few comments about how hyperconjugative interactions either *into* or *from* the coupling pathway could affect *vicinal* couplings were presented in the same review paper. Following these comments, for instance, it could be assumed that the inversion in the *cis/trans* relationship for $^3J_{C'H}$ couplings through the glycosidic bond in nucleosides reported by Munzarová and Sklenář,[69,70] originates mainly in the strong negative hyperconjugative interactions that take place within the carbonyl group, $LP(O_p) \rightarrow \sigma^*_{C-C}$.

The use of $^1J_{CH}$ couplings as conformational probes was recognized for many years. During the last few years, Kleinpeter, Pihlaja and their coworkers published a series of important papers where they continued analyzing the potential of $^1J_{CH}$ couplings to study conformations. For instance, in Ref. 71, they reported the results of CP-DFT calculations of $^1J_{CH}$ in several methyl-substituted 1,3-dioxanes, 1,3-oxathianes, and 1,3-dithianes. Their calculations were performed using the optimized geometries corresponding to the global energy minima of the preferred conformers, and in general, they found very good agreement with experimental values. Relations between $^1J_{CHeq}$ and $^1J_{CHax}$ were correctly reproduced; even the so-called "reverse Perlin effect"[72] was rightly predicted. Notario *et al.*[73] continued studying the "Perlin effect"[74] in the sulfur-containing six-membered heterocycles and reported a computational study of 1,3-dithiane sulfone where $^1J_{CH}$ couplings were calculated at the BP/IGLO-III//B3LYP/6311 + + G(2d,2p) level. Trends in the calculated $^1J_{CHax}$ and $^1J_{CHeq}$ values were compared among themselves and with the corresponding couplings in other sulfur six-membered heterocycles, and their differences were rationalized in terms of the stereoelectronic effects calculated within the NBO method.

During the review period Juaristi and colleagues[75] continued studying how much stereoelectronic effects are pronounced in the values of $^1J_{CH}$. In a subsequent paper[76] some of these authors and other coworkers arrived at the conclusion that the behavior of the $^1J_{CH}$ coupling in the OCH moiety is not due to the electron delocalizations of the type $LP(O) \rightarrow \sigma^*_{C-H}$ (negative hyperconjugative interactions, according to Reed and Schleyer[77]), but mainly due to a polarization effect, which somewhat contradicts with the results reported previously by some of these authors. However, this is not supported by the recent paper by Maiti *et al.*,[78] where it was shown that in several complexes of hexafluoroisopropanol-amine the $^1J_{CH}$ coupling correlates with the hydrogen bond strength, changing by *ca.* -0.2 Hz when the enthalpy of the hydrogen bond increases by *ca.* 1 kJ mol^{-1}. This trend was rationalized as originating in the increase of the $\sigma_{O-H} \rightarrow \sigma^*_{C-H}$ hyperconjugative interaction when increasing the hydrogen bond strength, i.e., an effect similar to that taking place due to the $LP(O) \rightarrow \sigma^*_{C-H}$ negative hyperconjugative interaction. A more general study of how negative hyperconjugative interactions as well as the σ- and π-hyperconjugative interactions affect $^1J_{CH}$ couplings was published recently.[79] It is based on a qualitative theoretical model that allows to predict how $^1J_{C_{sp3}H}$

couplings would be affected by the hyperconjugative interactions involving either the σ_{C-H} bond or any of the other three bonds containing the same C_{sp3} atom.

This can be rationalized based on the methodology of the Contributions from Localized Orbitals within the Polarization Propagator Approach (CLOPPA),[80] assuming that the FC contribution to $^1J_{C_{sp3}H}$ couplings can be dissected into the occupied i,j and vacant a,b localized molecular orbital (LMO) contributions, Eq. (5):

$$^1J_{CH}^{FC} = \sum_{ia,jb} {}^1J_{ia,jb}^{FC}(CH) \tag{5}$$

where

$$^1J_{ia,jb}^{FC}(CH) = W_{ia,jb}[U_{ia,C}U_{jb,H} + U_{ia,H}U_{jb,C}] \tag{6}$$

and $U_{ia,C}$,$(U_{jb,H})$ are the "perturbators", i.e., the matrix elements of the FC operator between the occupied $i(j)$ and vacant $a(b)$ LMOs evaluated at the C(H) site of the coupling nuclei, giving a measure of the strength of the $i \to a$ $(j \to b)$ virtual excitation due to the FC operator; $W_{ia,jb}$ are the polarization propagator matrix elements corresponding to the response of the electronic molecular system to the presence of the FC electron-nucleus interaction connecting two virtual excitations, $i \to a$ and $j \to b$. These matrix elements decrease while increasing the $\varepsilon_{i \to a}$ and $\varepsilon_{j \to b}$ energy gaps between these occupied and vacant LMOs involved in each virtual excitation. This indicates that any hyperconjugative interaction involving either the occupied i, j or the vacant a, b LMOs should affect the corresponding $^1J_{ia,jb}^{FC}(CH)$ term. According to the CLOPPA formalism, the sum in Eq. (5) is largely dominated by the two types of principal terms giving rise to the coupling "bond contribution" and "other bond contribution":

(1) $i = j$ corresponds to the occupied LMO localized on the σ_{C-H} bond involving the coupling nuclei, and $a = b$ corresponds to the vacant LMO localized on that σ_{C-H} bond. The corresponding term in Eq. (5) is dubbed "bond contribution", J^b;

(2) either i or j corresponds to the occupied LMO on the σ_{C-H} bond containing the coupling nuclei, and j or i corresponds to the occupied LMO on other σ_{C-X} bond involving the C coupling nucleus; and $a = b$ correspond to the localized vacant MO placed at that σ_{C-H} bond containing the coupling nuclei. The corresponding term in Eq. (5) is dubbed "other bond contribution," J^{ob}.

However, it should be stressed that this term involves also the σ_{C-H} bond and antibond containing the coupling nuclei. In $^1J_{CH}$ couplings the J^b contribution is positive while the J^{ob} are negative, having the former a notable larger absolute value than the latter. Approximately, it can be written as:

$$^1J_{CH} \sim J^b + J^{ob}(1) + J^{ob}(2) + J^{ob}(3) \tag{7a}$$

or as

$$^1J_{CH} \sim |J^b| - |J^{ob(1)}| - |J^{ob(2)}| - |J^{ob(3)}|. \tag{7b}$$

Since this is only a qualitative description, it will be easy to identify how hyperconjugative interactions affect the J^b and J^{ob} contributions. Indeed, polarization propagator matrix elements in Eq. (6) decrease whenever there is an interaction increasing the energy gap between the i or j bonds and the a or b antibonds.

Hyperconjugative interactions that increase the energy gap (decreases the corresponding $^1J_{CH}$ coupling) in J^b are (i) those transferring charge into the antibonding orbital, σ^*_{C-H}, where σ_{C-H} bond contains the coupling nuclei; (ii) those transferring charge from the σ_{C-H} bond containing the coupling nuclei to any of the nearby antibonding orbitals. It should be noted that, according to Maiti et al.[78] (*vide supra*), interactions that increase the relevant energy gap when increasing the hydrogen bond strength correspond to the type (i). It is noteworthy that the hydrogen bond strengthens whenever the $LP_{Acceptor} \rightarrow \sigma^*_{Donor}$ interaction increases.

There are two more types of hyperconjugative interactions that increase the energy gaps (decreasing the absolute values of J^{ob}s): (iii) those transferring charge from the bonding orbital that corresponds to "other bond"; and (iv) the same as those quoted above for the J^b contribution, i.e., (i) and (ii). However, the effects of the interactions (iv) on J^{ob}s can be neglected at the qualitative level, since in absolute value $|J^{ob}| << |J^b|$.

Among other interesting examples of the manifestation of the interactions (iii) is the increasing of the $^1J_{C_3H_3}$ couplings in 1-X-bicyclo[1.1.1]pentanes with increasing the electron acceptor character of the $\sigma^*_{C_1-X}$ antibond,[79] as follows from the experimental values of $^1J_{C_3H_3} = 167.8$ Hz for X = H, and $^1J_{C_3H_3} = 181.2$ for X = F. The electron acceptor character of the corresponding $\sigma^*_{C_1-X}$ antibond can be estimated from the sum of the occupancies of the three bonds (each playing the role of "other bond") $\Sigma\sigma_{C_{2,4,5}C_3} = -111$ for X=H, and $\Sigma\sigma_{C_{2,4,5}C_3} = -156$ for X=F, expressed in 10^{-3} units, considering in both cases the difference between the actual occupancy given by the NBO method and that of an ideal bond, i.e., 2.000.

1-X-bicyclo[1.1.1]pentane
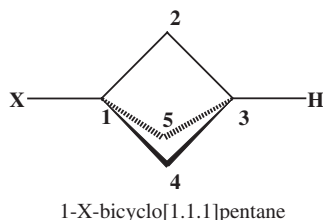
The latter assertions about the energy gaps affected by the hyperconjugative interactions can be easily understood through the diagram shown in Fig. 1. Indeed, if the occupied i orbital undergoes a hyperconjugative interaction of the type $i \rightarrow BD^*$, then according to the simple PMO theory, the energy gap between these two orbitals changes from $\varepsilon(a,i)$ to $\varepsilon(a,i')$. This change can affect significantly the energy gap for the virtual transition $i \rightarrow a$. It is important to note here that the a antibonding orbital is not affected by the $i \rightarrow BD^*$ hyperconjugative interaction.

The qualitative trends commented above for $^1J_{C_{sp3}H}$ can be easily extended upon $^1J_{C_{sp3},C_{sp3}}$ couplings involving, for instance, the $\sigma_{C_1-C_2}$ bond; the main difference is
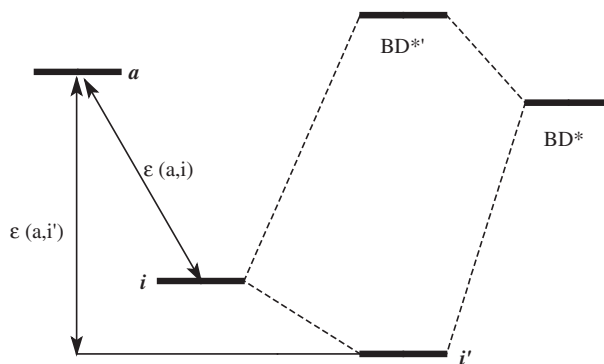
Fig. 1. Hyperconjugative interactions according to the simple PMO theory.

that there are now six "other bond contributions," three associated with C_1 and three associated with C_2. Accordingly, Eqs. (7a) and (7b) should be modified to include the "other bond contributions" corresponding to C_2.

Recently, Wrackmeyer and Tok[81] observed a small $^1J_{C_1C_2}$ coupling in boraadamantane, which is assumed to be a consequence of the strong hyperconjugative interaction involving the $\sigma_{C_2-C_3}$ bond and the electron-deficient B atom. The experimental value is $^1J_{C_2C_3} = 19.5$ Hz, while the DFT-B3LYP[82,83] calculated value with the 6–311 + G(d,p) basis set is 17.6 Hz. Indeed, these values are dramatically small, as compared to the experimental and calculated magnitudes of $^1J_{C_3C_4}$ in boraadamantane, 32.6 Hz and 31.9 Hz, respectively, or the $^1J_{CC}$ coupling in adamantane, 32.3 Hz (see Section 4.2.3).

Boraadamantane
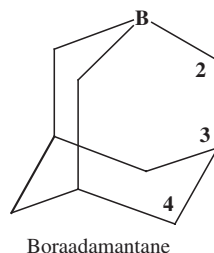
In nitrogen heteroaromatic compounds the LP(N) nonbonding electron pair plays a role similar to that described in Section 4.2.4 for $^1J_{CC}$ in azomethines. In particular, in pyrimidine derivatives substituent effects on $^1J_{CC}$ couplings can be affected by the orientations of the ring nitrogen LPs.[84]

It is evident from Eq. (6) that a given $^1J_{CH}$ coupling can also be affected through the "perturbator" terms. Electrostatic interactions, like those described in Section 3.3.5, should affect such terms, and this is one of the main reasons why some authors could have some difficulties in distinguishing between the "energy gap" and the "perturbator" effects on $^1J_{CH}$ couplings since many times both effects operate simultaneously.

Although electrostatic and hyperconjugative interactions in many cases are intertwined, i.e., electrostatic interactions sometimes can either inhibit or enhance hyperconjugative interactions; cases are known where the latter are very weak but the former are significant. The converse is less known yet, although the "agostic" interactions seem to provide some interesting examples when the electrostatic effects are notably less important than those affecting hyperconjugative interactions in organic compounds. The nature of agostic interactions was discussed for many years, and recently Scherer and McGrady[85] developed a revised bonding concept to rationalize them. Their main idea is that an agostic interaction is a phenomenon driven by the electron delocalization that causes a global bonding redistribution within the metal–alkyl fragment producing geometrical distortions and significant changes in force constants. Consequently, agostic interactions would arise mainly from the delocalization of the M–C bond over the metal–alkyl moiety. This means that agostic interactions do not proceed through the presence of the three-center-two-electron interactions between the metal atom and C–H bonds. Therefore, the notable reduction of $^1J_{CH}$ couplings observed for bonds participating in an agostic interaction should proceed mainly through the hyperconjugative interactions and not through a direct metal–C–H bond interaction. A similar behavior of spin–spin couplings could be elucidated from the recently reported results on the DFT-all-electron-ZORA-calculated $^1J_{SiH}$ couplings in $HSiCl_3$, $(CO)_4Fe(H)(SiCl_3)$, $MeCp(CO)_2MnHSiCl_3$, and $MeCp(CO)(PMe_3)MnHSiCl_3$ systems.[86]

Recently, the CP-DFT-B3PW91 calculations of $^1J_{CH}$ couplings were carried out in several systems, and this parameter was considered as an additional tool to characterize the α-agostic interaction. This is the case, for instance, of quasi-tetrahedral alkylidyne–alkylidene rhenium complexes $Re(CR)(CHR)(X)(Y)$ (R = alkyl; X = Y = alkyl; Y = siloxy; X = Y = alkoxy). Calculated $^1J_{CH}$ couplings in the *syn*-isomers are lower than those in *anti*-isomers in agreement with the observed experimental trend.[87] Solans-Monfort and Eisenstein[88] performed DFT-calculations of $^1J_{CH}$ couplings (using the Autschbach's approach[89]) on two sets of complexes, one is a pseudotetrahedral series where the agostic interaction is weak, and it was observed only in one of the two isomers. The other one is a pseudo-octahedral cyclopentadienyl tantalum alkylidene series, where the alkylidene C–H α-agostic interaction is strong. They found that calculated $^1J_{CH}$ couplings reproduce the experimental trends either for weak or strong α-C–H agostic interactions in d^o metal alkylidene complexes (Re, Mo, Ta).

In contrast to $^1J_{CH}$ couplings, the effect of the hyperconjugative interactions upon *geminal* and *vicinal* coupling constants was studied in much less detail. Experimental $^2J_{HH}$ couplings are known to cover a range from about -24 to $+43$ Hz[90] and, although their actual values are known to depend on several factors[68,91] like, for instance, the electronegativity of the atom placed α to the CH_2 moiety, one of them is undoubtedly the existence of the hyperconjugative interactions involving the coupling pathway. Recently, it was shown[47] that hyperconjugative interactions *from* the coupling pathway yield negative increase in the $^2J_{HH}$ coupling, whereas hyperconjugative interactions *into* the coupling pathway yield a positive increase. The first case is exemplified by the $^2J_{HH}$ coupling corresponding to the CH_2 moiety

placed α to an sp^2 carbon atom, like that in the $C=C$ double bond in propene, while the second case is dramatically pronounced in the very large and positive $^2J_{HH} = +43\,Hz$ in formaldehyde.

Propene   Formaldehyde
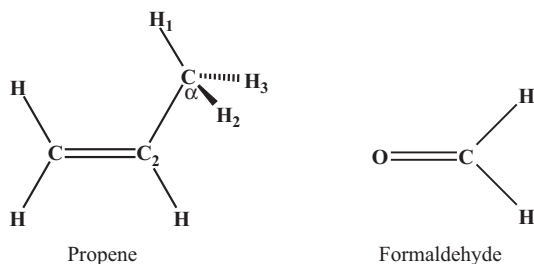
The latter case is typical of *geminal* couplings through a carbonyl group that were described in detail by Hansen.[92] These couplings are very large and positive provided the magnetogyric ratios of both coupling nuclei are of the same sign, and are by far dominated by the FC term. The main effect defining such unusual couplings is commonly accepted to originate in the very strong negative hyperconjugative interactions of the type $LP(O_p) \rightarrow \sigma^*_{C-H}$, where $LP(O_p)$ is the in-plane oxygen LP of purely p-character. Therefore, like long-range couplings transmitted through a saturated molecular fragment (see Section 2.4), *geminal* couplings through a carbonyl carbon atom can be considered to be ones mainly transmitted by the hyperconjugative interactions taking place *within* the coupling pathway.

Recently,[93] the proton NMR spectra of 2-methylthiirane and 2-methyloxirane were studied both theoretically and experimentally to investigate, mainly, the negative hyperconjugative interactions effects on $^2J_{HH}$ and $^3J_{HH}$ couplings. Some of these theoretical and experimental couplings are displayed in Table 1, and in general, their agreement is very good. Calculated values include the four coupling contributions, although the trends observed in this table originate mainly in the FC term. In the same table calculated values for methylcyclopropane are also included although experimental values are not known except for just a few values predicted by Elleman and Manatt.[94] It follows that $^2J_{HH}$ is more negative for $X = CH_2$

Table 1. Comparison of ring J_{HH} couplings (in Hz) in 2-methylthiirane (**1**), 2-methyloxirane (**2**), and 2-methylcyclopropane (**3**)

$^nJ_{H_iH_j}$		(**1**)	(**2**)	(**3**)[a]
$^2J_{H_1H_2}$	Exp.	−1.07	5.11	−3.0
	Calc.	−0.81	5.65	−5.20
$^3J_{H_1H_3}$	Exp.	5.72	2.71	5.0
	Calc.	5.77	2.03	5.07
$^3J_{H_2H_3}$	Exp.	6.34	4.27	8.5
	Calc.	7.34	4.12	9.28

[a]Predicted values of the two- and three-bond J_{HH} couplings taken from Ref. 94.

(methylcyclopropane, calculated value -5.20 Hz), which is notably more positive than in other less strained compounds, where $^2J_{HH}$ couplings are close to -12 Hz.[35]
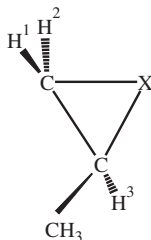
2-Methylcyclopropane (X = CH$_2$); 2-methyloxirane (X = O); 2-methylthiirane (X = S).

Since the influence of the hyperconjugative interactions on $^2J_{HH}$ couplings originates in the FC term, it can be expected that similar effects will be observed for the couplings involving other isotopic species provided they are dominated by the FC contribution. This is the case, for instance, of $^2J_{CH}$ couplings in pyridine where $^2J_{C_2H_3} = +3.12$ Hz and $^2J_{C_3H_2} = +8.47$ Hz.[95] For both couplings, the strong LP(N)$\rightarrow\sigma^*_{C_2-C_3}$ negative hyperconjugative interaction is operating, and this seems to be the main reason why both couplings are positive.[96] On the other hand, the marked difference between those two originates mainly in the following facts: (i) there is also a rather strong LP(N)$\rightarrow\sigma^*_{C_2-H_2}$ interaction, which increases only $^2J_{C_3H_2}$; (ii) the $\sigma^*_{N_1-C_2}$ antibond is notably better electron acceptor than the σ^*_{C3-C4} antibond. For this reason, the $\sigma_{C_3-H_3}\rightarrow\sigma^*_{N_1-C_2}$ interaction is stronger than the $\sigma_{C_2-H_2}\rightarrow\sigma^*_{C_3-C_4}$ one. These last two interactions correspond to a negative increase in the $^2J_{C_2H_3}$ and $^2J_{C_3H_2}$ couplings, respectively.

Pyridine
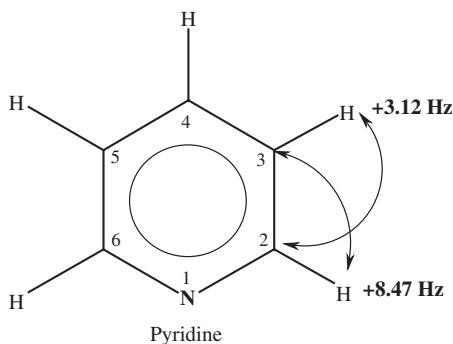
Table 1 shows the calculated and measured $^3J_{HH}$ couplings in the three-membered rings of 2-methylcyclopropane, 2-methyloxirane, and 2-methylthiirane. The corresponding negative hyperconjugative interactions calculated within the NBO method were presented by Tormena *et al.*[93] These results seem to indicate that the influence of hyperconjugative interactions on $^3J_{HH}$ couplings is more complicated than the trends observed for $^2J_{HH}$ couplings. Although there is an evidence[97] that hyperconjugative interactions within the coupling pathway tend to increase *vicinal* couplings, the situation seems to be quite different when bonds or antibonds

belonging to the coupling pathway interact with antibonds or bonds which are external in respect to that coupling pathway.

2.4. Transmission of the Fermi contact term

It is well known that in saturated compounds involving only light nuclei like H, C, and N, coupling constants are largely dominated by the FC term. For this reason, the knowledge of how this interaction is transmitted through the molecular electronic system is particularly important. During the last few years, this topic was discussed in the literature based on different approaches.[98] Thus, Castillo *et al.*[99] correlated J_{FF} coupling constants in aromatic compounds with the delocalization index from Kohn and Sham orbitals given by the Bader's Atoms In Molecules approach (AIM).[44]

It is now known[100] that the FC term is transmitted by the "Fermi hole,"[101] which is an indication that electron delocalization interactions favor the FC transmission of long-range couplings. As a matter of fact, this mechanism was known for a long time. Thus, in conjugating systems the FC term can be transmitted through the π-electronic system,[52] while in aromatic compounds, like toluene, it is transmitted mainly through the π-electronic system due to the hyperconjugative interactions of the types $\sigma_{C-H} \rightarrow \pi^*$ and $\pi \rightarrow \sigma^*_{C-H}$.[102] This is also true for the couplings involving other types of isotopes in the side-chain but having similar coupling pathways.[103]

In saturated compounds, the transmission of the FC term of the long-range couplings could not be adequately rationalized for a long time, as evenly addressed by Gakh *et al.*[104] Indeed, it was shown recently[66] that in this type of compounds usually the transmission of the FC term of the long-range couplings mainly takes place through the electron delocalization due to the σ-hyperconjugative interactions. It is known that these types of interactions are strongly enhanced for the C–C bonds belonging to strained cyclic and polycyclic hydrocarbons where such bonds are very good donors while their antibonding orbitals are very poor electron acceptors for the hyperconjugative interactions.[105] On these grounds, it was rationalized[66] that the notable difference between the experimental values of $^4J_{F_1C_4} = 13.54\,\text{Hz}$[106] in 1-F-cubane and $^4J_{F_1C_4} = 3.3\,\text{Hz}$[107] in 1-F-bicyclo[2.2.2]octane was quite expected:

$^4J_{C_4F} = 13.54\,\text{Hz}$ $^4J_{C_4F} = 3.3\,\text{Hz}$
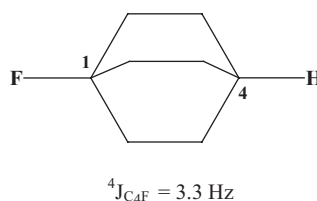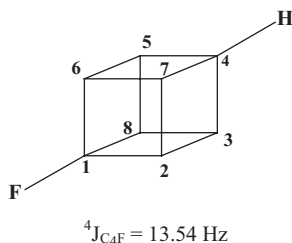
This dramatic difference of *ca.* 10 Hz originates in two different factors, namely (i) the larger strain of the cubane substrate in comparison with that of the bicyclo[2.2.2]octane moiety; and (ii) the larger amount of favorable σ-hyperconjugative

interactions in 1-F-cubane as compared to that in 1-F-bicyclo[2.2.2]octane. The latter is schematically illustrated below where the cage-bonds involved in the relevant hyperconjugative interactions with the $(C_1–X)^*$ and $(C_4–Y)^*$ antibonds for transmitting the FC interaction between F_1 and C_4 are highlighted. In this way, it is obvious that in 1-F-cubane, there are six equivalent pathways while in 1-F-bicyclo[2.2.2]octane there are only three equivalent pathways:
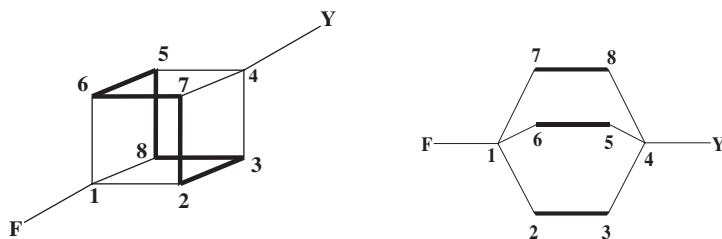
The bonds involved in important σ-hyperconjugative interactions that define

the coupling pathways of the FC term of $^4J_{C_4F}$ couplings (Y = H) are highlighted.

The suggestion made above concerning the ability of a strained cage compound for transmitting the FC contribution of long-range couplings was studied recently, considering the $^4J_{C_\alpha H_3}$ couplings in several members of the bicyclo[1.1.1]pentane series (Y = H) with the X substituent bearing a ^{13}C atom in the α-position to the bridgehead carbon atom, C_1.
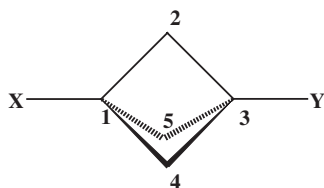
1-X-3-Y-bicyclo[1.1.1]pentanes

The four-bond $^4J_{C_\alpha H_3}$ couplings were measured and calculated at the CP-DFT-B3LYP/EPR-III level of theory in five representative members of this series with X = CH_3, CH_2OH, $COCH_3$, CO_2H, and CN and Y = H.[108] It is important to note that, although there are three similar pathways connecting the coupling nuclei, none of them corresponds to a W configuration that is efficient for transmitting the FC interaction through a four-bond pathway. Table 2 compiles the calculated and experimental couplings of this type that show a fairly good agreement. Also, the related $^4J_{C_\alpha F}$ couplings measured in 1-X,3-F-bicyclo[1.1.1]pentanes[109] are given in the fourth column of the same table. Comparison of the four-bond couplings, $^4J_{C_\alpha H_3}$ (Y = H) and $^4J_{C_\alpha F}$ (Y = F) shows that the FC term is transmitted much more effectively in the latter case.

A similar different efficiency relating the corresponding experimental four-bond couplings is observed in compounds with X = Y = H, $^4J_{HH}$ = 18 Hz;[110] X = CH_3

Table 2.   Comparison between theoretical and experimental $^4J_{C_2H_3}$ (in Hz) in 1-X-bicyclo [1.1.1]pentanes

X	Total[a]	Exp.[a]	Exp.[b]
	Y = H	Y = H	Y = F
CH$_3$	11.6	11.7	25.1
CH$_2$OH	11.6	11.5	27.40
COCH$_3$	11.9	11.3	29.20
CO$_2$H	14.0	14.0	36.70
CN	15.3	16.5	37.81

[a]Taken from Ref. 108.
[b]The respective experimental $^4J_{C\alpha,F}$ couplings in 1-X-3-F-bicyclo[1.1.1]pentanes are also shown, taken from Ref. 109.

and Y = H, $^4J_{CH} = 11.7$ Hz;[109] X = F and Y = H, $^4J_{FH} = 69.71$ Hz.[111] To get a better understanding of the efficiencies of the related moieties for transmitting the *trans*-cage coupling, these three coupling constants should be multiplied by the corresponding magnetogyric ratios, namely $\gamma_H/\gamma_H = 1$, $\gamma_H/\gamma_C = 3.9761$, and $\gamma_H/\gamma_F = 1.0624$, which gives 18, 46.5, and 74.1 Hz, respectively. This indicates that the efficiency of the bicyclo[1.1.1]pentane moiety to transmit the FC term of the *trans*-cage couplings increases markedly through the series H < C < F.

In the current literature, there are several excellent examples showing that strained polycyclic compounds are very efficient for transmitting the FC term of the *trans*-cage couplings. One of them relating to the long-range spin–spin coupling, $^7J_{FF} = 2.8$ Hz,[112] in difluorodiadamantane is illustrated below where the bonds participating in the σ-hyperconjugative interactions and defining the FC transmission of this long-range coupling are highlighted:
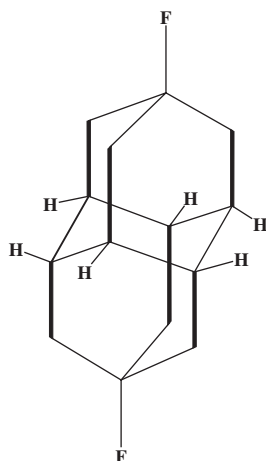
difluorodiadamantane

Also, the difference of $^5J_{SnSn} = 120\,Hz$ in 1,4-di-$(Sn(CH_3)_3)_2$-bicyclo[2.2.2] octane[113] and $^4J_{SnSn} = 1{,}611\,Hz$ in 1,3-di-$(Sn(CH_3)_3)_2$-bicyclo[1.1.1]pentane[114] can be rationalized on similar grounds. It is important to recall that the transmission mechanism of the FC term is essentially the same as that for the SD term, although, of course, for the same compounds the efficiencies of their transmissions could be very different. Recently, Provasi *et al.*[115] calculated long-range $^nJ_{FF}$ couplings in some conjugating 1,n-difluoropolyenes, and 1,n-difluoropolyynes and found noticeable couplings even for $n = 7$, 9, or 11. Interestingly, such couplings showed substantial NC contributions, in some of them the SD term being the dominant one. On the other hand, in a saturated substrate, like for instance, in 1-n-difluoroalkanes, for $n = 7$, the calculated total $^7J_{FF}$ coupling amounts to only 0.76 Hz with comparable contributions (in absolute value) from the four Ramsey terms. Therefore, these results highlight the important role played by the electron delocalizations in conjugated systems in transmitting not only the FC but also the SD term.

2.5. Signs of coupling constants

In most cases of experimental measurements of coupling constants only their absolute values are determined in spite of the fact that a number of special NMR techniques exist providing experimental determination of their relative signs. Very early in the evolution of NMR spectroscopy there were attempts to determine the origin of these signs. Thus, the Dirac Vector Model,[116] was one of the first examples. However, it is now known that in many instances this model yields a wrong sign, like, for instance, the well-known case of the positive reduced *geminal* couplings.

When considering the sign of a coupling constant it is important to recall that couplings measured in isotropic phase are made up from four contributions, FC, PSO, SD, and DSO. In cases dominated by the FC term, obviously the sign of the total coupling coincides with that of the FC term. However, now it is well known that in many cases (see below for some examples), noncontact terms may be dominant. Only the sign of the DSO term is known to follow a rather simple rule, i.e., if the space spanned by the molecular electronic system is partitioned into two parts by means of a sphere with a diameter equal to the distance between both coupling nuclei, then electrons inside that sphere yield a negative contribution while electrons outside that sphere yield a positive contribution to J^{DSO}.[117,118] Obviously, the signs of couplings dominated by the DSO term are determined by this trend (see Section 3.2.2). For many types of couplings the magnitude of the DSO term is similar but of opposite sign to the corresponding PSO term; however, this is by no means a general trend and in many couplings any of them can be dominant; indeed, there are cases where the PSO and DSO terms are of the same sign. It is also important to note that the PSO and the SD terms are notably affected by the presence of a π-electronic system. Some interesting examples of the through-space $^{TS}J_{HH}$ coupling dominated by the spin–orbital terms were calculated by Cibulski *et al.*[119] at the DFT-B3LYP/Huz-IIsu2 level of theory for the inner protons in porphyrin and porphycene. In this last paper, the observed trends of $^1J_{NH}$ couplings (which are dominated by the FC term) are also discussed.

Del Bene and Elguero[120] presented a new model to analyze the FC sign of a coupling constant, which was dubbed as NMRTWM (the Nuclear Magnetic Resonance Triplet Wave-Function model). Briefly, this model provides insight into the dependence of the sign of the FC term on the nodal properties of wave functions for excited triplet states that contribute to the coupling constant and the resulting alignment of nuclear magnetic moments. The wave function for the excited triplet states which contribute to the coupling constant behave in a regular manner, giving the sign of each contribution determined by the nodal character of the excited-state wave function and the response of the nuclei to the phases of this function. Thus, the sign of the total FC term is determined from the competition of positive and negative contributions from various states. Afterwards, the NMRTWM approach was applied to analyze the signs of different coupling constants in some interesting cases. It should be noted that, according to the Dirac Vector Model, *geminal*-reduced couplings should be negative, although, as pointed out above, this rule is often violated.

The NMRTWM model perfectly described the sign of the reduced $^{2h}K_{XY}$ couplings transmitted through X–H–Y hydrogen bonds.[121] In the long series of papers published by Del Bene and Elguero (see also Section 3.1), it was determined that *geminal* couplings through the hydrogen bonds of the types N–H–N, O–H–O, O–H–N, C–H–O, C–H–N, C–H–F, F–H–O, and F–H–N are by far dominated by the FC term. Thus, it was determined[121] that (with only one exception) such *geminal*-reduced couplings are positive, i.e., their signs are not in agreement with the Dirac model. However, they are in agreement with those predicted by the NMRTWM, being determined by the excited triplet states, contributing to the coupling constant under study, that have an odd number of nodes intersecting the X–Y axis. The NMRTWM method was also applied to analyze the sign of $^{1h}J_{YH}$ couplings relating to the hydrogen bonds of the type X–H···Y, where Y = N, O, and F.[122]

Del Bene *et al.*[123] studied, using the EOM-CCSD approach, $^{1}J_{XY}$ couplings in 18 compounds of the type H_mX–BYH_n with X and Y = C, N, and P. In their set of compounds, they included the X and Y combinations involving single, double, and triple X–Y bonds with the total $^{1}J_{XY}$ ranging from –250 to + 200 Hz. In most cases, the sign of calculated couplings are the same as those of the corresponding FC term. In approximately half of the 18 compounds studied, the signs of $^{1}J_{XY}$ couplings were not correctly reproduced by the Dirac Vector Model. The NMRTWM model was also applied to analyze the signs of the corresponding reduced-FC terms in this series.[123] For X and/or Y corresponding to the LP bearing atoms, they discussed the influence of the nonbonding electron pairs on the nodal properties of the wave functions for the excited triple states of the compounds under study.
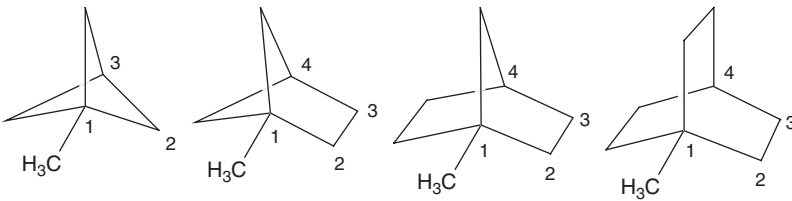
2.6. Multipath additivity

Basically, a general caveat to the interpretation of spin–spin couplings in (poly)cyclic compounds lies in the multipath coupling mechanism that is often unjustifiably ignored by many authors. According to this concept, spin–spin coupling constants in such systems are transmitted via two or more physically quasi-independent

coupling pathways. However, the decomposition of the total coupling constant into individual coupling paths is far from being straightforward and still remains a challenge. The obvious drawback of the early empirical multipath coupling treatments was the assumption that spin–spin coupling is transmitted only via chemical bonds, i.e., contains only through-bond contributions. According to the principles of the multipath coupling mechanism, each coupling route contributes additively to the total value of spin–spin coupling while deviations from additivity are expected when mutual electronic perturbations of the coupling paths and/or significant through-space interactions come into play.
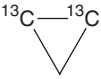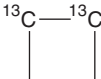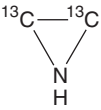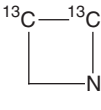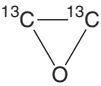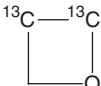
Apart from the pure empirical[124] and semiempirical[125,126] additivity principles, the very first and the most straightforward theoretical approach to account for the multipath coupling mechanism in cyclic molecules was gained by Contreras and coworkers[127,128] based on the general Inner Projections of the Polarization Propagator (IPPP)[129] formalism. As an example, it was used to account for the multipath contributions in bicycloalkanes (Table 3).[127,128] The RPA-IPPP approach was further developed by Contreras and coworkers[130] into the CLOPPA[80] (for some details of CLOPPA formalism, see Section 2.3), which enabled to decompose total values of J into contributions of chemical bonds, LPs, or molecular fragments presented by a set of LMOs. The results of such decomposition of J_{CC} couplings into individual molecular contributions in small heterocycles (together with parent cyclopropane and cyclobutane) are presented in Table 4.[131] Generally, this approach provided for the first time the reliable explanation of the additivity and nonadditivity of the multipath-coupling constants as arising from the different multipath through-bond and through-space coupling contributions.

Table 3. Two- and three-bond path contributions (in Hz) to the FC term of J_{CC} couplings in bicycloalkanes calculated at the RPA-IPPP-INDO level[a]

Contribution				
I,j	1,3	1,4	1,4	1,4
Two-bond	0.30	−0.05	−2.03	
Three-bond		7.29	4.92	3.27
T-S	−10.54	−8.22	−3.88	−0.64
Addit. sum	−9.40	−1.03	3.93	9.17
Non-addit.	−15.35	−2.48	−1.3	4.15
Total	−24.75	−3.51	2.63	13.32
Exp.	(−)25.15	(−) 4.48	7.38	13.21

[a]Calculated values are taken from Refs. 127 and 128 (for references to experimental values, see references cited therein).

Table 4. Contributions of individual molecular fragments (in Hz) to the FC term of J_{CC} couplings in small heterocycles calculated at the CLOPPA-INDO level[a]
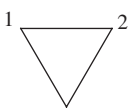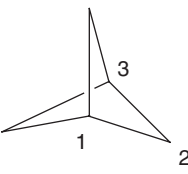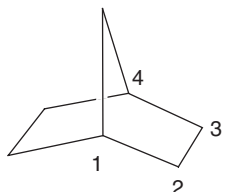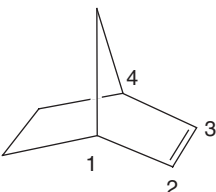
Compound	Molecular fragment	Contribution	Compound	Molecular fragment	Contribution
^{13}C—^{13}C (▽)	C–H (2)[b]	−0.1	^{13}C—^{13}C (□)	C–H (4)[b]	−0.6
	C–C–C	−7.3		C–C–C–C	+5.4
	C–CH$_2$–C[c]	−7.4		C–CH$_2$–CH$_2$–C[c]	+4.8
	C–C	+20.7		C–C	+30.4
^{13}C—^{13}C (N, H)	LP	+0.1	^{13}C—^{13}C (NH)	LP	−0.1
	N–H	0.0		N–H	−0.3
	C–N–C	−8.8		C–H (2)	−0.3
	C–NH–C[c]	−8.7		C–C–N-C	+4.4
	C–C	+29.2		C–CH$_2$–NH–C[c]	+3.7
				C–C	+31.5
^{13}C—^{13}C (O)	LP (2)[b]	+0.1	^{13}C—^{13}C (O)	LP (2)[b]	−0.5
	C–O–C	−8.5		C–H (2)[a]	−0.4
	C–O–C[c]	−8.4		C–C–O–C	+4.8
	C–C	+35.2		C–CH$_2$–O–C[c]	+3.9
				C–C	+33.1

[a] Taken from Ref. 131.
[b] Number of fragments.
[c] Total contribution of this fragment.

Later, it was shown by Wu and Cremer[132] that the multipath spin–spin coupling mechanism in (poly)cyclic compounds may lead to spin–spin couplings strongly deviating from their "normal" values. Actually, the multipath-coupling constant may depend on a through-space part, two or more through-bond parts, and the path–path interaction part, where the latter results from the steric exchange repulsion between the bond paths, as exemplified in Table 5.[132]

For example, in cyclopropane, the simplest carbocycle with the dual-pathway coupling $^{1+2}J_{CC}$, the situation is not as obvious as one can assume based on the simple additive dual-pathway model. Wu and Cremer[132] found this interpretation, in spite of its formal vividness, to be highly misleading. According to their results, the one-bond contribution of J_{CC} in cyclopropane is as much as 54.4 Hz, as it actually should be for a carbon–carbon bond with a substantial p-character. Accordingly, summing the through-space (−27.1 Hz) and two-bond (10.1 Hz) contributions leads to a typical value for the *geminal* $^2J_{CC}$ of a strongly strained hydrocarbon ring (−17.1 Hz). The path interaction term is −24.5 Hz reflecting the strong interaction between the carbon–carbon bond orbitals in the three-membered ring. The resulting total J_{CC} of cyclopropane is thus dramatically reduced by both the two-bond and the paths interaction contributions to 12.9 Hz, which is in excellent agreement with the experimental value of 12.4 Hz[133] (see also Ref. 134).

Table 5. Multipath FC contributions to the J_{CC} couplings (in Hz) in cyclopropane, bicyclopentane, norbornane, and norbornene calculated at the J-OC-PSP-CP-DFT level[a]

Contribution				
I,j	1,2	1,3	1,4	1,4
One-bond	54.39			
Two-bond	10.08	−4.44	−2.46	−3.04
Three-bond			7.52	7.62[b]; 6.94[c]
Paths int.	−24.48	−10.21	−0.04	0.55
T-S	−27.08	−2.58	−4.49	−4.88
Total	12.91	−26.11	7.60	7.20
Exp.	12.4[d]	(−)25.16[e]	7.38[e]	

[a]Calculated values taken from Ref. 132.
[b]Aliphatic.
[c]Olefinic.
[d]Taken from Ref. 133.
[e]Taken from Ref. 381.

Further support of the multipath coupling mechanism and better understanding of the spin–spin coupling transmission mechanisms in (poly)cyclic molecules could be gained from the development of the idea of spin–spin coupling density surface formulated very recently by Soncini and Lazzeretti[135] and, independently, by Malkina and Malkin.[50] Indeed, spin–spin coupling density introduced as a second-rank tensor[4,136] being integrated over the three-dimensional (3D) real space gives the nuclear spin–spin coupling tensor components and should provide direct insight into the spin–spin coupling transmission routes incorporating chemical bonds which build up additive increments. This was explicitly illustrated by Malkina and Malkin,[50] who showed on several illustrative examples how 3D coupling pathways could be directly visualized by using the real space functions in calculations of either "coupling energy density" or "coupling electron deformation density," which allow unprecedented insight into the nature of the individual coupling pathways.
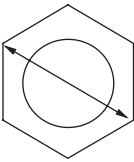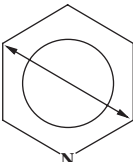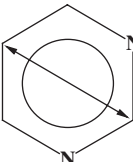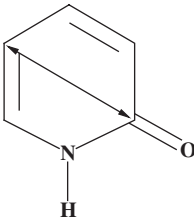
However, in a most recent publication by Soncini and Lazzeretti,[137] the very idea of the multipath-coupling mechanism regarding the J_{CC} in cyclic systems was subjected to criticism based on the *ab initio* calculations of the maps of the electronic current density induced by the permanent magnetic dipole moment of ^{13}C nuclei for three saturated hydrocarbons: ethane, cyclopropane, and bicyclobutane. Indeed, the plots of the spin–spin coupling density that are directly connected to the title density maps by a geometry-dependent scaling provided a visual representation of the coupling mechanism explicitly excluding the possibility of significant multipath effects. Within this model, the marked difference between the three J_{CC} coupling constants in ethane,

cyclopropane, and bicyclobutane can be rationalized solely in terms of the hybridization character of the chemical bond through which the coupling is transmitted.

An interesting example of the multipath additivity was discussed recently when analyzing the transmission mechanism of the FC term of the $^4J(C_4,F)$ coupling constant in 1-F-cubane. As commented in Section 2.4, this FC interaction is transmitted through the cubane cage by the σ-hyperconjugative interactions between edge-cube bonds and $(C_1–F)^*$ and $(C_4–H)^*$ antibonding orbitals. Since this compound has a threefold symmetry axis, there are a total of six equivalent hyperconjugative interactions. Therefore, in this unique compound, the $^4J(C_4,F)$ coupling is transmitted through six equivalent coupling pathways, and this is the reason why this coupling as well as similar couplings in 1-F-4-X-cubanes, are so unusually large[66] (see Section 2.4).

In unsaturated compounds, a few interesting examples of a dual-pathway transmission were discussed recently. These few examples, which include experimental and theoretical values of $^3J_{CC}$ in benzene, pyridine, pyrimidine, and (1 H)2-pyridone could help in understanding at least a few factors, which define the efficiency of each coupling pathway. For instance, the presence of a nitrogen atom seems to increase the efficiency of each coupling pathway by about 4 Hz, which is probably due to the presence of its nonbonding electron pair. Indeed, the protonation of (1 H)-2-pyridone decreases notably its efficiency of the coupling pathway including nitrogen. This effect is so notorious that the two $^3J_{CC}$ *intra*-ring couplings, $^4J_{C_2,C_5}$ and $^4J_{C_3C_6}$, are considered to be the adequate probes to detect experimentally the preferential tautomeric forms in the compounds of this type. Calculated values given in Table 6 were obtained at the DFT-B3LYP/6-311G**/EPR-III level, and were taken from Ref. 84 for benzene, pyridine, and pyrimidine, while experimental values were taken from Refs. 138 (benzene), 139 (pyridine), and 84 (pyrimidine). For (1 H)-2-pyridone, both experimental and theoretical values are taken from

Table 6. Comparison of *trans*-ring couplings (in Hz) in benzene, pyridine, pyrimidine and (1 H)-2-pyridone

Exp.	10.01^a	13.95^b	18.2^c	7.4^d
Calc.	10.88^c	15.29^c	20.1^c	7.0^d

[a] Taken from Ref. 138.
[b] Taken from Ref. 139.
[c] Taken from Ref. 84.
[d] Taken from Ref. 140.

Ref. 140, for benzene is also shown the $^3J_{CC}$ coupling calculated by Del Bene and Elguero[141] using the EOM-CCSD approach. Indeed, if dielectric solvent effects are taken into account when calculating these couplings, a better agreement between calculated and measured values is found.

It is to be noted that the examples quoted earlier correspond to the couplings dominated by the FC term. Since it is now known that there are many couplings dominated by the noncontact contributions, an open question is, how far the PSO and SD terms follow a multipath additivity?

3. CALCULATION OF SPIN–SPIN COUPLING CONSTANTS

3.1. Wavefunction-based methods

A vast amount of *ab initio* calculations of coupling constants published during this review period correspond to studies of couplings transmitted through a hydrogen bond. Next to that point, many of these papers where *ab initio*-calculated couplings were reported, were aimed at verifying the performance of the DFT-calculated couplings in a variety of bonding situations (see Section 3.3). Several papers reporting *ab initio* calculation of coupling constants aimed at gaining physical insight into the structure of compounds were also published; in most cases, they are discussed in Section 4. Papers published before May 2003 are not commented here since they were briefly reviewed in Ref. 35; however, for the sake of completeness a few of them are quoted when commenting results published during this review period that are closely related to those published previously.

Del Bene and coworkers published a long series of papers where they applied the EOM-CCSD method in the CI-like approximation,[38–41] using the Aces II suit of programs,[142] to study different aspects of *trans*-hydrogen-bond couplings. Calculation of coupling constants within coupled cluster methods were reviewed a few years ago by Auer and Gauss.[143] Theoretical analysis of intermolecular couplings were reviewed by Pecul and Sadlej,[31] and theoretical analysis of $^{2h}J_{CN}$, $^{2h}J_{NN}$ and $^{2h}J_{FN}$ couplings were reviewed by Del Bene.[11] A few years back Del Bene and Bartlett[61] presented a detailed analysis of $^{2h}J_{NN}$ transmitted through a hydrogen bond of the type N–H⋯N in neutral complexes, and similar couplings in cationic complexes with hydrogen bonds of the type N–H$^+$–N.[144] In both cases, these authors found that such couplings are largely dominated by the FC term, and that calculated values of the *geminal trans*-hydrogen-bond couplings depend monotonically on the N⋯N distance. The plot of $^{2h}J_{NN}$ couplings vs. the N⋯N distance can be used, with good accuracy (about 0.05 Å), to estimate the N⋯N distances from the experimental $^{2h}J_{NN}$ couplings. Interestingly, during the review period, Söntjens *et al.*[62] measured $^{2h}J_{NN}$ couplings in ureidopyrimodinone dimers in solution. Couplings measured in different isomers of one of these dimers allowed them to test the relationship between $^{2h}J_{NN}$ and the N⋯N distance proposed by Del Bene and Bartlett.[61] They calculated the N⋯N distances from the Del Bene *et al.*'s plot and found excellent agreement with the distances derived from the X-ray crystal structures determined in the dimer

of a derivative of ureidopyrimodinone. This agreement was better still when the nonlinearity of the hydrogen bonds was taken into account.

During the review period Del Bene and coworkers continued studying several features of couplings transmitted through a hydrogen bond. For instance, Del Bene and Elguero reported[121] a systematic study of $^{2h}K_{XY}$ couplings in complexes stabilized by the $X \cdots H \cdots Y$ hydrogen bonds, where X and Y are from the series of "organic" elements C, N, O, and F. In that paper they excluded complexes stabilized by the $F \cdots H \cdots F$ hydrogen bonds. One of the important observations was that in all cases, with the exception of $X = F = Y$, $^{2h}K_{XY}$ was positive and determined by the FC term. In this connection, it is important to recall that in the dimer $(HF)_2$, the reduced coupling constant was found to be negative, $^{2h}K_{FF} < 0$.[145] A similar result was also found by Del Bene et $al.$[146] when studying the overall features of the J_{FF} coupling surface with respect to the F–F distance and the orientation of the pair of HF molecules. Calculations of $^{2h}J_{NF}$ couplings corresponding to several neutral complexes stabilized by a "traditional" $F–H \cdots N$ hydrogen bonds were presented in Ref. 147 (for Del Bene's classification of hydrogen bonds, see Ref. 37). Similar calculations of $^{2h}J_{NF}$ couplings in several cationic complexes that are stabilized by a "traditional" $N–H^+ \cdots F$ hydrogen bonds were also reported.[148] The same authors studied one- and two-bond couplings through the hydrogen bond in 2:1 $FH \cdots NH_3$ and $FH \cdots$ collidine,[149] and in 3:1 $FH \cdots NH_3$ and the $FH \cdots$ collidine complexes.[150] These works were inspired by the measurement of the intermolecular couplings in 1:1, 2:1, 3:1, and 2:3 complexes between FH and 2,4,6-trimethylpyridine, carried out by Shenderovich et $al.$[151] (see also references cited therein).

In another paper Del Bene and Elguero[152] reported their study on the dependence of $^1K_{XH}$ couplings on the $X \cdots H$ distance (X = C, N, O, F) in 16 monomers and 64 complexes, where these monomers are proton donors. For monomers with known couplings, a good agreement was found between calculated and experimental values. One of the most important conclusions reported in this paper is that $^1K_{XH}$ decreases when increasing the X–H distance, the effect which is mainly due to the increase of the "proton-shared character"[37] of the respective hydrogen bond. That is to say, it is not simply the X–H distance that influences $^1K_{XH}$ in a complex, since, when increasing that length the proton shared character of the hydrogen bond increases, decreasing concomitantly the electron density on the hydrogen-bonded proton.

Recently, the same authors[153] carried out a systematic study of $^{2h}J_{NN}$ and $^{1h}J_{NH}$ couplings in hydrogen bonds of the type $N–H^+–N$ corresponding to 11 nitrogen bases with experimentally measured proton affinities. It is noteworthy that all $^{2h}J_{NN}$ couplings were positive and decreased when increasing the $N \cdots N$ distance; all $^1K_{NH}$ were positive, while $^{1h}K_{NH}$ were positive for the "traditional" hydrogen bonds, becoming negative as soon as the hydrogen bond showed a sufficient "proton-shared" character (see Ref. 37).

The same authors,[122] applied the EOM-CCSD method to calculate $^{1h}J_{XY}$ coupling constants across hydrogen bonds of the type $X–H \cdots Y$, where Y = N, O, and F. They considered 44 complexes, where they studied the two different types of the one-bond couplings, namely $^1J_{XH}$ and $^{1h}J_{YH}$ in line with the results of the related study.[152] Briefly, they reported that for the traditional hydrogen bonds, the FC

contribution to the reduced $^{1h}K_{YH}$ coupling is negative, regardless of the nature of the X–H donor. This result was discussed in terms of the NMRTWM model to rationalize the sign of the FC contribution to the one-bond couplings, presented by the same authors in a different paper[120] (see Section 2.5). Also, they noted that both $^1K_{XH}$ and $^{1h}K_{HY}$ should undergo a change in their sign along the proton transfer coordinate, and for symmetric hydrogen bonds, both of them should be positive in the equilibrium point. If instead of a symmetric hydrogen bond, a complex is stabilized by a hydrogen bond of the type X–H–Y with a certain "proton-shared" character of the type X–H–Y, then $^1K_{XH}$ and $^{1h}K_{YH}$ are positive.

Several features of J_{FF} couplings in $(HF)_2$ clusters were also studied by Del Bene et al.[146] using the same theoretical approach, EOM-CCSD. It is important to note that $^{2h}J_{FF}$ couplings present features that are notably different from those of other couplings in other complexes. Although for some orientations of the monomers in $(HF)_2$ clusters the PSO term may provide a significant contribution, it is the FC term that defines several features of the J_{FF} surface. Contrary to what was observed for other $^{2h}J_{XY}$ in X$\cdots$H$\cdots$Y hydrogen bonds, where X and Y are from the series of "organic" elements C, N, O, and F with the exception of X$=$Y$=$F, in $^{2h}J_{FF}$ the FC term changes its sign along the F$\cdots$F distance. The most negative value of $^{2h}J_{FF}$ is observed for the F–H$\cdots$H–F configuration; in this case both monomers are not bound. As a result, both the FC and $^{2h}J_{FF}$ are small and negative for the F–H$\cdots$F–H configuration.

For the hydrogen bonds of the type C–H$\cdots$N, Del Bene et al.[154] studied $^{2h}J_{CN}$ couplings in 17 neutral, 3 cationic, and 3 anionic complexes. They found that such couplings are by far dominated by the FC term and, therefore, they equated the FC term with the $^{2h}J_{CN}$ coupling. Although such couplings were found to depend slightly on the hybridization at the C atom, a plot of $^{2h}J_{CN}$ versus the C$\cdots$N distance was obtained based on all complexes considered. This is expected to be useful for estimating the C$\cdots$N distances in complexes where the $^{2h}J_{CN}$ coupling is amenable to measurement. Alkorta et al.[155] applied the EOM-CCSD method to calculate trans-hydrogen-bond couplings in hydrogen bonds of the type N–H$\cdots$O$=$P. The considered molecular systems were $PO_2H_2^-$ as the proton acceptor and urea or two CNH molecules as the N–H proton donors. Based on their previous results,[156] in the present study[155] they considered only FC term to find out that linearity of the hydrogen bond is required for observing a substantial value of $^{3h}J_{NP}$ coupling. This result provides a practical guide to the experimental studies of $^{3h}J_{NP}$ in related systems.

When comparing the performance of the DFT and ab initio methods for calculating trans-hydrogen-bond couplings (see Section 3.3.2), Pecul et al.[157] pointed out that, for small complexes, the convergence of the MCSCF methods[158–160] with the number of active orbitals is slow. As an example, a very large active space was required to bring the MCSCF-calculated intermolecular couplings in $(HF)_2$ into agreement with those obtained by the CCSD method. It is this feature, which makes the MCSCF calculations inapplicable to large molecular systems, at least for the time being.

The large computational requirements demanded by the post-Hartree-Fock calculations of spin–spin couplings prompted some authors to look for the means of

reducing them without affecting seriously the quality of the calculated couplings. One of the ideas consists in employing a Locally Dense Basis Set (LDBS), i.e., of partially enriching the basis set in some neuralgic points of the coupling pathway with special functions. Sanchez *et al.*[161] performed a systematic study of how such partial enrichment can be realized for calculating *vicinal* J_{FF} couplings, both in saturated and unsaturated compounds, without affecting seriously the calculated values at the Second-Order Polarization Propagator Approach (SOPPA)[162–164] level. The LDBSs used in that paper[161] were obtained as different combinations of the following basis sets: (i) cc-pVXZ (X = D, T) and their augmented versions aug-cc-pVXZ,[165–167] (ii) the optimized NMR-J basis sets cc-pVTZ-J and aug-cc-pVTZ-J,[168] and (iii) a minimal basis set of Gaussian functions. That study was carried out in a set of nine model systems of both unsaturated and saturated difluoro compounds. Some recommendations were also made for choosing an LDBS adequate to calculate *vicinal* J_{FF} in related compounds.

Most *ab initio* calculations quoted in Section 4.2 were carried out using LDBSs. Provasi *et al.*[115] calculated long-range $^nJ_{FF}$ couplings in fluorine derivatives of alkanes, conjugated polyenes, conjugated polyynes, and cumulenes within the SOPPA and SOPPA(CCSD) methods using a locally dense basis set. Only SOPPA results were reported therein since the SOPPA(CCSD) calculations provided almost the same numerical data. It is interesting to note that $^nJ_{FF}$ couplings in three of the studied compounds were also calculated by Del Bene *et al.*[169] using the EOM-CCSD method.[38–41] The values of $^nJ_{FF}$ couplings in *trans*-1,2-difluoroethane, *trans*-1,2-difluoroethene, and 1,3-difluorodiyne are compared in Table 7 (SOPPA and EOM-CCSD values are taken from Refs. 115 and 169, respectively).

Table 7. Comparison of calculated and experimental (whenever possible) J_{FF} couplings (in Hz) in *trans*-1,2-difluoroethane (**1a**), *cis*-1,2-difluoroethane (**1b**), *trans*-1,2-difluoroethene (**2**) and 1,3-difluorodiyne (**3**)

Compound	Method	Exp.	DSO	PSO	SD	FC	Total
1a	EOM-CCSD[a]	−30.0[b]	−1.5	−43.6	15.8	−10.8	−40.1
1a	SOPPA[c]	−30.0[b]	−1.52	−39.97	15.02	−9.88	−36.34
1a	SOPPA[d]	−30.0[b]	−1.52	−38.74	14.67	−10.75	−36.35
1a	SOPPA(CCSD)[d]	−30.0[b]	−1.51	35.55	14.26	−10.54	−33.34
1b	EOM-CCSD[a]		0.2	−16.0	8.3	37.0	29.5
1b	SOPPA[d]		0.20	−13.27	9.05	37.00	32.98
1b	SOPPA(CCSD)[d]		0.20	−12.80	8.67	35.76	31.84
2	EOM-CCSD[a]	−124.8[e]	−1.7	−139.9	15.9	−11.9	−137.6
2	SOPPA[c]	−124.8[e]	−1.76	−141.39	23.14	−9.51	−129.5
3	EOM-CCSD[a]		−1.7	−56.7	24.4	8.7	−25.3
3	SOPPA[c]		−1.74	−73.68	24.11	7.63	−43.67

[a]Taken from Ref. 169.
[b]Taken from Ref. 231.
[c]Taken from Ref. 115. The total SOPPA value reported in Ref. 227 is –36.68 Hz.
[d]Taken from Ref. 231.
[e]Taken from Ref. 230.

Important discrepancies are observed between EOM-CCSD and SOPPA values. Only for *trans*-1,2-difluoroethene the experimental value is known from three different studies: $-132.70\,\mathrm{Hz}$,[170] $-133.79\,\mathrm{Hz}$,[171] and $-132.43\,\mathrm{Hz}$.[172] Some differences between the SOPPA and EOM-CCSD couplings may originate in the different geometries used for their calculations, though it should not be the dominant factor. In *trans*-1,2-difluoethane and 1,3-difluoro-diyne the largest discrepancies are observed for the PSO term followed by the FC term while in *trans*-1,2-difluoroethene the largest difference originates in the SD term, followed by the FC and the PSO terms.

The idea of using a partially enriched basis set for calculating coupling constants is nowadays frequently employed not only in the wavefunction but also in the DFT-based coupling calculations, especially when dealing with polyatomic compounds which require very large computational resources. A case in point is, for instance, the study on the structural dependence of $^2J_{WW}$ couplings reported by Bagno and Bonchio[173] in tungsten polyoxometalates. In fact, they verified that it is possible to perform a coupling calculation on a complete polyoxometalate structure, using a relatively low level except for the W–O–W fragment being investigated.

The BH molecule was chosen by Auer et al.[174] to compare the performance of various coupled-cluster methods for the treatment of the electron correlation effects on calculated coupling constants. It was found that using the frozen-core approximation in unrelaxed coupled cluster calculations of couplings could lead to erroneous results due to the complete neglect of the core–orbital relaxation effects. It was also observed that, when sufficiently large basis sets are used and all electrons are correlated, both the CCSD[38–41] and CC3[143] methods could provide very accurate values of spin–spin couplings.

MCSCF calculations carried out by Bryce et al.[175] show that in phosphine oxides the anisotropy of the $^1J_{PO}$ tensor is larger (in absolute value) than its isotropic value. The latter is dominated by the FC followed by an important PSO contribution. The former is dominated by the FC/SD cross-term.

3.2. DFT-based methods

During the 1990s, several attempts to calculate coupling constants within the DFT framework were reported, first of all those of Malkin et al.[176,177] and Dickson and Ziegler,[178] see reviews[35,179] for details. Most other attempts were restricted to only part of the four Ramsey coupling contributions, mainly the FC term. In most cases, the Finite Perturbation Theory (FPT), of Pople et al.,[180,181] either in the single or the double perturbation version, was used as the perturbative approach in the calculation of the FC term. In the approach by Malkin et al.'s[176,177] the PSO and DSO terms were also taken into account. The PSO term was calculated using a special version of the sum over states (SOS) approach while the DSO term, as it is usual, was calculated as a first-order quantity.

Few years later, following different lines, Sychrovský et al.[182] presented the analytical formulation of the Couple Perturbed (CP-DFT) approach and Helgaker et al.[183] developed the analytical linear response theory within the DFT approach.

Readers interested in details of these approaches are specially referred to the respective original papers. At present, the superiority of the CP-DFT over the FPT-DFT perturbative approach is beyond question.[63] However, and this point must be specially emphasized, when adequate precautions are taken,[184] the FPT and CP calculations yield the same numerical results. It is important to note that, although in several papers it is claimed that all four Ramsey terms are calculated within the CP-DFT approach, in fact only the three second-order terms, FC, PSO, and SD, are calculated within this approach while the DSO term is calculated as a first-order quantity, i.e., as an expectation value over the ground electronic state.

Since the computational requirements of the coupling constant calculations within the DFT framework are much lighter that those of the post-Hartree-Fock calculations, one of the main concerns observed in the literature during this review period was to verify the reliability of such calculations. Commented in Section 3.3 are several works where the performance of the DFT coupling calculations are compared with the high-level *ab initio* results. Another two points of concern were how much the DFT-calculated couplings depend both on the chosen functional and the basis set, and these are considered in the next two subsections.

3.2.1. *Dependence of calculated couplings on the chosen functional*

The dependence of spin–spin couplings calculated at the DFT level on the chosen functional was studied in several papers. For instance, the advantages of the hybrid B3LYP functional were pointed out by Sychrovský et al.,[182] who presented the analytic formulation of the coupled-perturbed DFT approach and used it for the calculation of coupling constants; and Helgaker et al.,[183] who calculated the coupling constant second-order terms as the linear response functions of the respective operators. Shortly afterwards, Lantto et al.[185] compared the performance of the LDA, BLYP,[186] and B3LYP[82,83] functionals to calculate parts of the **J** second-rank tensor, i.e., the diagonal and symmetric off-diagonal terms. They compared their calculated values with both MCSCF calculations, either taken from the literature or obtained from *ad hoc* calculations, and experimental data. A special care was taken of using the same geometries as well as the same basis sets in both types of calculations. The performance of the studied functionals[185] improved along the series LDA→BLYP→ B3LYP. It was found[185] that in most cases, the errors of DFT-calculated coupling constants arised from a failure to describe the frequently dominant FC term. It was also observed that the PSO term is quite sensitive to the choice of the functional. These effects in some cases could lead to a fortuitous agreement of the total values with experiment, which is due to the error cancellation between the FC and PSO terms.

Tuttle et al.[63] studied the comparative performance of the B3LYP and B3PW91 functionals in the calculation of the *trans*-hydrogen-bond couplings in ubiquitin and concluded that results obtained with the former were obviously in a better agreement with the experimental data.

An exhaustive study of how calculated coupling constants depend on the chosen functional was carried out by Maximoff et al.[187] They selected a set of 96 experimental $^1J_{CH}$ couplings with different hybridizations at the C atom from the

literature, and 20 different funcionals were used to calculate the corresponding couplings with the aug-cc-pVTZ-J basis set[168] in this series of compounds optimized at the PBE0/6-31+G(2df,p) level. The aug-cc-pVTZ-J basis set was chosen following the results reported by the same team on the convergence of the DFT-calculated couplings with the basis set size.[188] The performance of 20 chosen funcionals in reproducing the experimental $^1J_{CH}$ couplings was statistically analyzed considering the mean error, the mean absolute error, the standard deviation, and the minimum and maximum deviations as merit parameters, all of them referred to the experimental values corrected for the Zero Point Vibration (ZPV). It is interesting to point out that these results[187] do not support the statement frequently found in the literature that hybrid functionals, especially B3LYP (see, e.g., Refs. 183 and 185), show a better performance in the calculations of $^1J_{CH}$ couplings than those of the GGA type.

Recently, Keal *et al.*[189] verified that, although the PBE functional performs better for calculating $^1J_{CH}$ couplings than other functionals, as reported by Maximoff *et al.*,[187] this assertion does not hold for couplings involving N, O, and F atoms in simple molecules. And what is more, the PBE functional performed notably worse than B3LYP in this case; besides it was found that the B97-2 (Ref. 190) and B-97-3 (Ref. 191) semiempirical functionals provided very good results for the couplings involving N, O, and F atoms.

The performance of the hybrid B3LYP functional for calculating coupling constants in several hydrocarbons together with pyrrole, furan, and thiophene was studied by Lutnæs *et al.*[192] An extensive basis set investigation was carried out considering three series of correlation-consistent basis sets that allow a correct description of the electron correlation effects, namely, cc-pVXZ, cc-pCVXZ[165–167] and the latter with decontracted all s-functions and augmented with *n* tight s-functions, dubbed as cc-pCVXZsun. For example, in ethylene calculated coupling constants converged for the basis set cc-pCV5Zsu5. However, this basis set is too demanding for routine calculations, and computational demands can be reduced by using a smaller and adequately chosen basis set, like Huzinaga's H-IV[193,194] augmented with five tight s-functions, H-IVsu5. The latter was used for calculating the FC term while the NC contributions were calculated with the original H-IV basis set. On the whole, the DFT-B3LYP-calculated couplings are somewhat overvalued in about 10%, and they suggest that the B3LYP functional could be less reliable for small coupling constants.[192]

Keal *et al.*[195] compared DFT-calculated couplings with the following functionals: the Dirac-VWN local density approximation (LDA), and those of Becke-Lee-Yang-Parr of the generalized gradient approximation (GGA), BLYP, and the hybrid B3LYP,[82] with KT_1 and KT_2 functionals.[196] The last two funcionals are linear combinations of the Dirac local density exchange, VWN, with local correlation.[197] All these calculations were carried out with the Huzinaga-III basis set,[193] augmented with three tight s-functions and employing spherical harmonic basis functions.

Hansen *et al.*[198] reported a few experimental couplings in [^{15}N]formamide, measured in CCl_4, in comparison with the corresponding DFT values in order to analyze the performance of three hybrid functionals, B3LYP,[82,83] B1LYP,[199,200] and

MPW1PW91[201] with the 3-21G, 6-31G, 6-31 + G*, and 6-311 + +G** basis sets, both in their standard form, and with decontracted s-functions. It was observed that all three hybrid density functionals gave similar results with the decontracted basis sets converging much faster than in their standard contracted forms.

3.2.2. *Dependence of calculated couplings on the chosen basis sets*

Long before the review period, Helgaker *et al.*[202] studied in detail the convergence of the MCSCF-calculated couplings with the extension of the basis set in HF and H_2O. In this study, they found a systematic way to increase the size of the correlation-consistent basis sets by decontracting the s-functions and increasing the number of tight s-functions. During the review period, Peralta *et al.*[188] carried out a similar basis set study at the DFT level using the B3LYP functional and taking into account all four Ramsey terms, FC, SD, PSO, and DSO, with the Gaussian 03 package of programs.[203] The first three were calculated using the CP-DFT method, while the latter, as usual, was found as an average value of the DSO operator on the electronic ground state. They chose a set of five small molecules, HF, H_2O, CH_4, C_2H_4, and CH_3F, to be able to use large basis sets, as required for this type of studies. The correlation-consistent basis sets of Dunning *et al.*,[165–167] cc-pVXZ (X = D, T, Q, 5, 6) and cc-pCVXZ (X = D, T, Q, 5)-sd + t with fully decontracted s-functions and additional tight s-functions were used. The different convergence properties (with the basis set size) of the FC and of the PSO and SD terms was observed, and it led the authors to suggest a way for saving computing time by employing a large basis set for the FC term and a much smaller one for the NC contributions. Another important observation is that the DFT-calculated couplings were almost converged with the triple-ζ basis set while the MCSCF–calculated couplings required the inclusion of the higher angular-momentum functions for correlation purposes.[202] Another important conclusion of that study[188] is that the DFT-B3LYP/ aug-ccpVTZ-J-calculated couplings[168] are close to the basis-set-converged values, being thus an excellent alternative for calculating couplings in large molecules. However, other triple-ζ basis sets, the Sadlej-J,[204] the EPR-III,[205] and the IGLO-III,[206] also showed a good performance in this series. It should also be noted that the aug-cc-pVTZ-J basis set supports only H, C, N, O, F, and only one-third row element, S.

Very recently, Deng *et al.*[207] presented a systematic way to modify standard basis sets for calculating the FC term of coupling constants. This approach is based on extending a basis set like, for instance, aug-cc-pVTZ by systematically adding s- and d-functions. Different progressions of functions were taken into account to be added for atoms belonging to the different rows of the periodic table. The s-functions to be added had even tempered exponents starting from the tightest s-function in the original basis set. For atoms up to the second row, the adequate ratio of 3 for the successive exponents was appropriate, while for the third-row atoms a ratio of 2 was recommended. For the noncontact contributions, the unmodified contracted basis set was used throughout.

The behavior of the DFT-calculated coupling constants with the basis set employed in their calculation[207] was also analyzed in several other papers. Thus, Lutnæs

et al.[192] studied the performance of the hybrid B3LYP functional for calculating coupling constants in 10 rigid hydrocarbons, and carried out an extensive basis set investigation on acetylene (see Section 3.2.1) looking for a basis set that yielded calculated couplings close to the basis set limit. The performance of the three series of the correlation-consistent basis sets, cc-pVXZ, cc-pCVXZ, and cc-pCVXZsun, was investigated. With the first two, no smooth convergence was observed with increasing X $=$ D, T, Q, 5, and 6. However, they achieved a better convergence of the FC term by uncontracting the original s-functions together with adding tight s-functions to the cc-pCV5Z basis set to give cc-pCV5Zsu5. This conclusion is consistent with the results reported in Ref. 188, and like the authors of that paper, Lutnæs *et al.*[192] looked for a smaller basis set with a performance similar to cc-pCV5Zsu5. Finally, the Huzinaga-type H-IVsu5 basis set was chosen for calculating the FC term and the unmodified H-IV was recommended for calculating the noncontact contributions.

Salvador and Dannenberg[208] studied the basis set dependence of the $^{1h}J_{OH}$, $^{2h}J_{CH}$, $^{2h}J_{NO}$, $^{3h}J_{HH}$, $^{3h}J_{NH}$, and $^{4h}J_{HH}$ *trans*-hydrogen-bond couplings in the amide dimers used as peptide models. Calculations were carried out at the CP-DFT level employing the B3LYP functional. This study included 15 basis sets taken from three different "families," namely, 6-31G, D95, and cc-pVXZ, and different levels of basis set completeness were chosen within each family to evaluate their influence on the four Ramsey coupling terms. One point, not directly connected with the basis set size that is interesting to stress is following: long-range *trans*-hydrogen-bond J_{HH} couplings in the formamide dimer are, in several cases, dominated by the DSO contribution, and its sign follows the trend described above for this term (see Section 2.5).

It should be recalled that the first experimental long-range *trans*-hydrogen-bond $^{nh}J_{HH}$ couplings reported in the literature were $^{4h}J_{FH_{Me}}$ in *N*-methyl-*ortho*-fluoro-benzamide.[33] Results of Salvador and Dannenberg[208] could indicate that these long-range couplings are indeed dominated by the DSO term. On the other hand, according to the comments made in Section 2.4 about the pathways for transmitting the FC term, such long-range couplings could only have a substantial FC contribution if the intramolecular F$\cdots$H–N hydrogen bond would have a high degree of covalency given by the interactions of type $LP(F) \rightarrow \sigma^*_{N-H}$. Certainly, this is not the case expected for this type of hydrogen bond.[209]

Jokisaari and Autschbach[210] compared the basis set dependence of both $^{1}J_{CSe}$ and $^{1}J_{SeSe}$ isotropic couplings together with the anisotropy of the respective coupling tensors in carbon diselenide at the ZORA-DFT-BP level. Almost similar sensitivities to the basis set were observed for both types of couplings. The flexibility of the basis sets, together with the relative importance of the different contributions to the isotropic couplings, was also discussed therewith.

3.2.3. *Dispersive interactions*

It is commonly accepted that basically, the DFT approaches cannot describe correctly dispersion interactions[211] and therefore, a question immediately arises whether the DFT level is reliable for the calculation of spin–spin coupling constants in molecular systems where such interactions are relevant, for instance, for defining their

stability. Bagno *et al.* addressed this point in a series of papers,[212–214] and their results were subsequently reviewed.[215] In the latter review paper, the DFT results were critically compared with high-level *ab initio* coupling calculations in a series of van der Waals complexes. In particular, considered therewith were the coupling constants transmitted through the C–H···π interaction, which is known to play an important role in organic and biological chemistry.[216] The authors of the latter publication discussed the methane–ethylene and methane–acetylene complexes stabilized by C–H···π interactions. Their equilibrium positions were calculated at the MP2/cc-pVTZ level, and corrected by the corresponding Basis Set Superposition Error (BSSE). Through-space J_{CH} couplings were calculated both at the DFT-VWN/IGLO-III and the SOPPA/aug-cc-pVDZsu1 levels,[162] the former by using the DeMon-NMR program.[177,217] It was observed that around the intermolecular equilibrium distance *ab initio* and DFT-calculated couplings were very close to each other. These results suggest that, although the DFT approaches cannot describe correctly the energy associated with the dispersion interactions, the through-space transmission of couplings between moieties separated by van der Waals distances is correctly described at the DFT level, provided adequate basis sets are used. At this point, it is important to recall that the overlap of the electronic clouds of two proximate atoms is efficient for the through-space transmittion of the FC term regardless of how well the energy associated with these interactions is reproduced. It should be noted that the optimized geometries of such complexes were obtained at the MP2/cc-pVTZ level.

However, it is important to remark that Cybulski *et al.*[218] calculated at the CCSD and DFT-B3LYP levels the $^{1h}J_{HH}$ and $^{3h}J_{LiH}$ intermolecular coupling constants in the dihydrogen-bonded complex LiH···H_2. This is considered to be a weak complex, bonded mainly by the dispersion interactions. The plots of both types of couplings, calculated both at the DFT and CCSD levels with the aug-cc-pVTZsu1 basis set, as a function of the intermolecular distance are quite similar, however, the DFT curve is vertically displaced, with both couplings larger in absolute value than the corresponding CCSD values. According to Cybulski *et al.*,[218] such difference between the CCSD- and DFT-calculated couplings originates in the incorrect description of the dispersion interactions in the latter approach.

Bagno *et al.*[219] calculated both at *ab initio* and DFT levels the through-space spin–spin couplings J_{CH} and J_{HH} in the CH/π bonded van der Waals dimers involving acetylene. Within the regions where the intermolecular interactions are stabilizing J_{HH} couplings were found to be pretty small (less than 0.1 Hz). In the acetylene–methane complex, J_{CH} was also very small, whereas in the acetylene–benzene complex and in the acetylene dimer it showed a relatively large dependence on the tilt angle from the T-shaped arrangement, for which the smallest values were calculated, to a parallel slipped arrangement where J_{CH} was *ca.* 0.5 Hz, which is encouragingly amenable to the experimental observation.

Bagno and Saielli[215] also considered several van der Waals complexes of the type xenon–methane, xenon—benzene, and xenon with a silicate residue, and calculated couplings involving ^{129}Xe within the DFT framework using the Zeroth-Order Regular Approximation (ZORA)[220–223] with the TZ2p basis set implying the ADF software code.[224] In order to verify how well the theoretical approach used

reproduces coupling constants involving [129]Xe, these authors[215] calculated also couplings involving [129]Xe in several xenon covalent molecules. Intermolecular couplings were calculated at the relativistic ZORA/TZ2p level of theory (calculations were run with the ADF software code[224]). For example, in the complex $Xe \cdots CH_4$ with the intermolecular distance of 3.9 Å Bagno and Saielli calculated $J_{XeH} = 3$ Hz. In this case the ZORA-DFT-calculated values could not be compared with the corresponding *ab initio* results.

3.2.4. *Electron correlation effects*

Auer *et al.*[174] investigated the performance of various coupled-cluster methods in comparison with the full configuration interaction (FCI), calculations for treating the electron-correlation effects on calculated coupling constants. Owing to the high-computational requirements of the last method, all calculations were carried out in a molecular system with very few electrons, BH, to evaluate the FC, SD, PSO, and DSO coupling terms at the HF-SCF, CCSD, CC3, CCSDT, and FCI levels of theory using the cc-pVDZsu1 basis set. The convergence of the four isotropic terms of $^1J_{BH}$ in BH calculated at the CCSD level with the basis set size was also studied in the series of cc-pVXZsu1 and cc-pCVXZsun (X = D, T, Q, 5, and n = 1, 2, 3). Assuming the additivity of the electron-correlation and basis set effects, the value of $^1J_{BH} = 50.67$ Hz in BH was estimated.

An interesting example of the electron-rich molecules is the set of three small compounds, ClF_3, PF_3, and PF_5. It is expected that in compounds of this type dynamic electron correlation effects on calculated coupling constants should be very important. Jaszuński[225] applied the CCSD method to calculate coupling constants in these three molecules, using the Aces II package of programs.[142] Unfortunately, in this series very few coupling constants can be observed experimentally. For the known values, like the $^1J_{PF}$ coupling in PF_3, Jaszuński's results are in reasonably good agreement with experiment, and this observation led the author to consider calculated couplings, like $^1J_{PFeq}$ and $^1J_{PFax}$ in PF_5, to be quite accurate. Also, Jaszuński highlights the fact that spin–spin couplings in compounds with so many nonbonding electron pairs are expected to be reproduced very badly by the DFT calculations.

3.3. Comparison between DFT- and *ab initio*-calculated coupling constants

One of the points addressed in many papers is this: how reliable are the DFT-calculated coupling constants? Here is reviewed a selection of papers where a comparison of *ab initio* and DFT-calculated coupling constants is performed.

For example, the DFT-B3LYP calculations of the contributions to the diagonal and symmetric off-diagonal parts of the indirect coupling tensor in a series of compounds were compared with MCSCF calculations and, whenever possible, with experimental values reported by Lantto *et al.*[185] In general, it was observed that for the J_{CC}, J_{CH}, and J_{HH} tensors, the accuracy obtained within the DFT-B3LYP framework is similar to that of the MCSCF calculations. It was also found that for

the isotropic as well as the anisotropic contributions to the couplings involving either N or Si, the DFT-B3LYP calculations provide quantitatively correct values. However, for the coupling tensors involving fluorine some problems were observed, as it also happens for the corresponding isotropic couplings.[217,218]

According to Lantto *et al.*,[185] poor results obtained for the $\mathbf{J}_{FF}$ tensors originate in an inadequate description of the spin density at the F nuclei, which gives problems for calculating the FC contribution. However, the accuracy of the DFT-B3LYP results for the $^n\mathbf{J}_{FC}$ tensors (with the exception for $n = 1$) in *para*-difluorobenzene is almost just the same as that of the MCSCF calculations (see also Section 3.6). Obviously, for $n = 1$, the DFT-calculated tensor, $^n\mathbf{J}_{FC}$ is not satisfactory, with the anisotropic part of this coupling, $\Delta^1\mathbf{J}_{FC}$, reproduced more accurately than the isotropic coupling contribution, $^1\mathbf{J}_{FC}$.

3.3.1. *Conformational dependence of coupling constants*

Ratajczyk *et al.*[226] examined glycolaldehyde as a model compound to compare the conformational dependence of its coupling constants calculated with the DFT-B3LYP and coupled-cluster singles-and-doubles (CCSD) methods for selected conformers. Both the optimized geometry and the potential energy surface were calculated at the frozen-core second-order Møller-Plesset, MP2, level using the basis sets aug-cc-pVDZ and aug-cc-pVTZ, while the coupling constant surfaces were calculated with the H-II, H-III, and H-IIIsu3[206,202] basis sets. The latter was derived from the original Huzinaga's H-III basis set,[193] decontracted and augmented with three tight s-functions with the exponents forming a geometric progression. In general, the DFT-calculated couplings are in good agreement with those calculated by the CCSD method and with experimental results. One of the main conclusions of this study[226] is that the DFT-calculated couplings are adequate for studying the conformational dependence of spin–spin couplings. However, they observed larger differences between the DFT- and CCSD-calculated $^1J_{CO}$ and $^1J_{OH}$ couplings, i.e., for couplings involving oxygen. This is in agreement with the common observation that the DFT-calculated couplings are less reliable when they involve at least one electron-rich atom. One of the most conspicuous cases is that of couplings involving fluorine atoms; however, several exceptions to this comment are known (see Section 3.6).

Glycolaldehyde
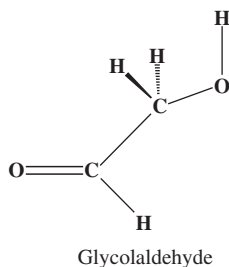
San Fabián and Westra Hoekzema[227] studied the angular dependence of *vicinal* $^3J_{FF}$ couplings using 1,2-difluoroethane as a model compound. They compared the performance of two different *ab initio* methods, MCSCF in the Complete Active

Space (CAS), and Restricted Active Space (RAS),[228] and SOPPA, with one based on the DFT framework with the BLYP functional, calculating the $^3J_{FF}$ couplings in 1,2-difluoroethane for different F-C-C-F dihedral angles using the Dalton software[229] and the ADF code.[224] The MCSCF calculations corresponded to the RAS SCF type,[228] while the functional chosen was the BLYP. Calculated couplings were compared with the experimental values for the *gauche* conformation of 1,2-difluoroethane and for some other conformations observed in the fluorinated derivatives of norbornane, the latter used for the additional source of the experimental $^3J_{FF}$ couplings. Experimental value of $^3J_{FF}$ in *trans*-1,2-difluoroethene was taken from Ref. 230. The $^3J_{FF}$ couplings were represented by a truncated Fourier series in the F-C-C-F dihedral angle. The possible existence of a through-space component of the $^3J_{FF}$ couplings was also studied in the same paper[227] by SOPPA and the DFT-ADF methods, using adequate configurations of the $(FH)_2$ dimer as model systems.

Recently, Provasi and Sauer[231] also studied the angular dependence of $^3J_{FF}$ couplings in 1,2-difluoroethane calculating these couplings at the RPA (usually referred to as SCF or CHF), MCRPA, RAS-A and RAS-B, SOPPA and SOPPA(CCSD) levels of theory using the aug-cc-pVTZ-J basis set for F and C and cc-pVTZ for H atoms. They also studied the influence of the optimized geometries at different levels on $^3J_{FF}$ couplings.

It is interesting to compare the values of $^3J_{FF}$ for the *gauche* and *trans* conformations of 1,2-difluoroethane calculated by different authors and measured experimentally. For the former conformation both MCSCF and SOPPA couplings calculated by San Fabián and Westra Hoekzema[227] are −10.2 Hz, while their DFT value is −6.6 Hz, with the *ab initio* values much closer to the experimental one, −10.9 Hz.[232] The DFT calculated coupling is somewhat underestimated (in absolute value), and it must be compared with the DFT result of −8.2 Hz reported in the same compound by Kurtkaya *et al.*[233] about 2 years earlier. Provasi and Sauer[231] reported for this conformation optimized at the MP4/6-311G(d,p) level the following values: –10.59 Hz with SOPPA and –9.77 Hz with SOPPA(CCSD). The latter is in poorer agreement with the experimental value. For the *trans* conformation of 1,2-difluoroethane, both *ab initio* values obtained in the former paper[227] differ substantially between RAS (−21.5 Hz) and SOPPA (−36.7 Hz), while SOPPA (−36.35 Hz) and SOPPA(CCSD) (−33.34 Hz) results by Provasi and Sauer[231] are in better agreement with each other and with experiment (−30.0 Hz)[232] (see also Table 7). The SOPPA(CCSD) result is closer to the experimental value than that calculated with the EOM-CCSD method.
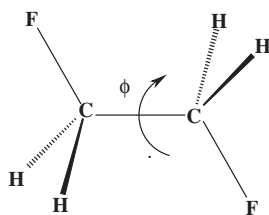
1,2-difluoroethane, $\phi = 180°$

San Fabián and Westra Hoekzema[227] calculated $^3J_{FF} = -79.1$ Hz for this conformation, which is interesting to compare with the DFT value reported by Kurtkaya et al.,[233] -58.4 Hz. Indeed, both DFT couplings are overestimated (in absolute value) with respect to the ab initio results and to experimental values as well. In fact, the DFT-calculated $^3J_{FF}$ couplings for gauche- and trans-1, 2-difluoroethane and for the derivatives of norbornane where substantial substituent effects are expected, do not reproduce the experimental values. However, it was concluded in the former paper[227] that the DFT calculations reproduced correctly the overall substituent trends. It is important to note that similar conclusions were reached at by Barone et al.[234] when comparing the DFT- and ab initio-calculated $^2J_{FF}$ coupling constants in fluorinated derivatives of ethane and oxetane. It was found that experimental substituent effects were correctly described although the experimental $^2J_{FF}$ couplings were reproduced very badly. These observations somewhat support several comments made in Section 3.6.

3.3.2. *Couplings transmitted through a hydrogen bond*

Pecul et al.[157] compared DFT- and ab initio-calculated indirect nuclear spin–spin couplings transmitted through a hydrogen bond in $(NH_3)_2$, $(H_2O)_2$, and $(HF)_2$ complexes together with their charged counterparts, $N_2H_7^+$, $H_5O_2^+$, and FHF^-. The DFT coupling constants calculations were carried out using the linear-response theory approach[183] while ab initio methods used in that paper[157] included CCSD[143] and MCSCF.[158–160] In both cases, geometries were optimized at the frozen-core MP2/aug-cc-pVTZ level, and coupling constants were calculated using the same basis set. It was found that for the X–H···Y hydrogen bonds, $^{1h}J_{XH}$ couplings were almost similar, and even their change in sign when going from neutral to charged complexes was observed with all three methods. However, when increasing the number of LPs on X and Y in the X–H···Y hydrogen bond the DFT-calculated $^{2h}J_{XY}$ couplings notably differ from their ab initio values. In fact, while the DFT-calculated $^{2h}J_{NN}$ couplings in $(NH_3)_2$ and $N_2H_7^+$ were only slightly overestimated, $^{2h}J_{OO}$ in $(H_2O)_2$ was about one-half of the value obtained with the CCSD and MCSCF methods, showing the same problems similar to those found in DFT-calculated intramolecular couplings. This suggests that the DFT and high-level ab initio methods show comparable performance at least in the case of J_{NN} and J_{NH} while it is not so for $^{2h}J_{OO}$ couplings. An important observation made by Pecul et al.[157] is that the CCSD method has very high basis set requirements, since it is necessary to generate a virtual space that could describe correctly a substantial proportion of the dynamical electron correlation effect. Since a problem of this type is not present in the DFT coupling constants calculations, methods based on this framework seem to be the most practical choice for calculating couplings not involving fluorine in large molecular systems (for more comments on the DFT-calculated long-range J_{FF} couplings, see Section 3.6). However, the basis set requirements for describing correctly electron density in the immediate proximity to the coupling nuclei for calculating the FC term imply, including the tight s-functions, are common to all methods.

Unusually, large $^{2h}J_{CO} \approx -10\,Hz$ has been calculated in the NCH$\cdots$OH$_2$ complex at the SOPPA level, and this was accounted for the important contribution of the unoccupied LMO of the C–H$\cdots$O* type to this coupling, as followed from the CLOPPA decomposition of the FC term of $^{2h}J_{CO}$ carried out at the RPA level.[235] More recently, Giribet and Ruiz de Azúa[236] applied the same approach to study several features of D–H$\cdots$A hydrogen bonds by analyzing the $^{1h}K_{AH}$- and $^{2h}K_{AD}$-reduced coupling constants in nine hydrogen-bonded complexes. One of the main points that they intended to rationalize in terms of LMOs is why the absolute value of $^{2h}K_{AD}$ is larger than that of $^{1h}K_{AH}$ In particular, they evaluated the role played by the vacant LMOs localized in the region of the D–H$\cdots$A interaction.

3.3.3. *Couplings transmitted through a dihydrogen bond*

A series of four dihydrogen-bonded complexes LiH$_2\cdots$H$_2$, LiH$\cdots$CH$_4$, LiH$\cdots$C$_2$H$_6$, and LiH$\cdots$C$_2$H$_2$ with LiH playing the role of a proton acceptor were studied by Cybulski *et al.*[218] For comparison purposes, spin–spin coupling constants were calculated at the CCSD and DFT-B3LYP approaches with the aug-cc-pVDZsu1 and aug-cc-pVTZsu1 basis sets using the Aces II[142] and a development version of the Dalton[229] programs, respectively. The first three representatives of this series can be classified as weak van der Waals complexes bound predominantly by the dispersion interactions (see Section 3.2.3). Special attention was paid to the decomposition of the interaction energy into different contributions. The LiH$\cdots$C$_2$H$_2$ interaction energy is notably larger than in other complexes being dominated by the electrostatic and induction contributions, and its total value is close to that in conventional hydrogen bonds. $^{1h}J_{HH}$ couplings are relatively small and negative and they do not correlate with the interaction energy. This is evident when considering that the largest (in absolute value) coupling is –0.95 Hz for the weakest complex, LiH$\cdots$H$_2$, while for the strongest complex, Li$\cdots$C$_2$H$_2$, this coupling is $-0.37\,Hz$. It should be noted that in all four complexes, the DSO and PSO contributions play important roles. As expected from the considerations presented in Section 2.5, in all four complexes, the DSO term of $^{1h}J_{HH}$ is positive. On the other hand, the $^{2h}J_{HX}$ couplings involving the LiH proton and the hydrogen or carbon nucleus of the atom playing the role of a proton donor correlate with the interaction energy only when reduced coupling constants are considered. It is important to note that the DFT-B3LYP-calculated interaction energy is described correctly for LiH$\cdots$H$_2$ complex. For the remaining complexes considered in Ref. 218, the dispersion interactions are not correctly described. Intermolecular DFT-calculated couplings are only of qualitative accuracy if compared with the corresponding CCSD results.

3.3.4. *Vibrational corrections to calculated couplings*

When calculating coupling constants, nuclear motions must be taken into consideration to account for the intermolecular dynamic effects. Experimentally, such dynamic effects on coupling constants are manifested both through the temperature

and through the isotope effects. Intermolecular dynamic effects were highlighted in several works where coupling constants were measured in gas phase. Just for the sake of brevity, only the case of J_{CH} couplings in [^{13}C]benzene is quoted.[237] In general, the study of the effect of nuclear motions on calculated couplings is computationally very demanding since basically, accurate *ab initio* methods cannot be applied to compounds with 10 or more atoms. For this reason, during the last few years there was an important interest in the performance of the DFT-based methods for calculating vibrational corrections that are not too much demanding of computational resources.

Ruden *et al.*[238] performed a detailed comparison of vibrational corrections to coupling constants calculated within the DFT framework and those obtained with an *ab initio* MCSCF method. It was found that the DFT-calculated vibrational corrections in a selected set of several small molecules were in good agreement with those calculated previously in the same set of molecules using wavefunction-based methods. Based on this result, the vibrationally averaged coupling constants were also calculated within the DFT framework in benzene, a molecule that would demand too much computational resources if attempted to perform such calculations using any *ab initio* method. They used these results to calculate empirical values of couplings corresponding to their equilibrium geometries, and suggested that to test any theoretical approach, results should be compared with those empirical equilibrium constants instead of the corresponding experimental values.

In a subsequent paper, Ruden *et al.*[239] presented a systematic comparison of the performance of three *ab initio* methods, CCSD, SOPPA, and MCSCF, together with the DFT-B3LYP approach in the calculation of rovibrational corrections to coupling constants in allene, cyclopropane, cyclopropene, and cyclobutane. It was observed that vibrational corrections to the studied couplings were typically of the same order of magnitude as the difference between their theoretical and experimental values. Rovibrational corrections to coupling constants were approximated as the ZPV contributions since the available results on temperature effects suggested that they changed only by approximately 10% with temperatures ranging from 0 to 300 K. Thus, the "empirical equilibrium constants" were evaluated by subtracting the DFT-B3LYP-calculated ZPV contributions from the corresponding experimental values. It should be remembered that the computational requirements for calculating the ZPV corrections within the DFT-B3LYP method are much lighter than those of any of the *ab initio* methods considered in that paper.[239] In allene, they found a poorer performance of the RASSCF and SOPPA methods than that of the CCSD approach that is notably more important for small couplings. On the other hand, the DFT performance is similar to that of CCSD for small couplings and similar to that of the SOPPA method for larger couplings in allene. For the strained cyclic compounds, cyclopropane and cyclopropene, it was observed[239] that the quality of the DFT-B3LYP results is comparable to that of the best *ab initio* methods, SOPPA and CCSD. For this reason, the DFT-B3LYP ZPV corrections to J_{CH} and J_{CC} couplings were calculated in cyclobutane and cyclobutene, compounds that are too large to obtain such corrections within the post-Hartree-Fock methods.

However, a point that was not properly addressed so far is how much the nuclear motion effects on coupling constants are dependent on the medium dielectric solvent effects?

3.3.5. *Calculation of solvent effects*

Pecul and Ruud[240] carried out a detailed comparison between DFT-B3LYP and *ab initio* CASSCF-calculated solvent effects on coupling constants. To this end, these authors extended these methods used for calculating coupling constants by including the dielectric continuum effects as given by the Polarizable Continuum Model (PCM) of Tomasi and coworkers.[241–243] This required the modification of the Dalton suite of programs[229] by implementing the PCM model for the singlet and triplet linear response functions used to calculate spin–spin couplings at the DFT and MCSCF levels. They took acetylene as a model system since in this molecule there are experimental values of couplings measured in different solvents.[244] Solvent effects were also calculated within the "supermolecular approach" to study the effects of formation of molecular complexes of acetylene with water, acetone, acetonitrile, and benzene.

The fully analytical implementation of the PCM model for the calculation of solvent effects on indirect spin–spin coupling constants have been applied by Ruud *et al.*[245] in the study of the solvent effects on the coupling constants in benzene. However, the noticeable solvent effects were found only for the one-bond couplings $^1J_{CH}$ and $^1J_{CC}$ in quite good agreement with experiment when the molecular geometry was allowed to relax in the solvent. For the longer range coupling constants, the solvent effects were too small to be considered accurate, and for these coupling constants, agreement with experiment was only fair. These results[245] did not support the use of the extrapolation schemes to estimate coupling constants in gas phase from the solvent effects observed in solution, as frequently used in the literature.

The PCM results by Pecul and Ruud[240] were also compared with previous *ab initio* results obtained by Pecul and Sadlej,[246] where a spherical cavity was used to describe the solvent; the authors observed that the PCM model was an important improvement when compared with the spherical cavity approach. The DFT-PCM solvent effects on $^1J_{CH}$ and $^1J_{CC}$ couplings in acetylene were in very good agreement with experimental values, especially for highly polar solvents. Similar effects on $^2J_{CH}$ couplings were of the wrong sign both within the DFT-PCM and CASSCF-PCM calculations, which might, in the authors'opinion, originate in some specific interactions. It is interesting to compare Pecul and Sadlej's result for $^2J_{CH}$ in acetylene[240] with the solvent effect known experimentally on $^2J_{CH}$ in acetaldehyde, especially in view that this experimental trend was adequately reproduced with the DFT-B3LYP-PCM calculations, although the strong experimental solvent effect could not be reproduced quantitatively, probably due to specific interactions between acetaldehyde and solvent.[247]

A good agreement between *ab initio* and DFT-PCM solvent effects on coupling constants found by Pecul and Ruud[240] prompted several studies of J_{CC} and J_{CH} couplings in heteroaromatic compounds. One of those studies dealing with the substituent effects on the *keto-enol* tautomerism is based on the analysis of coupling
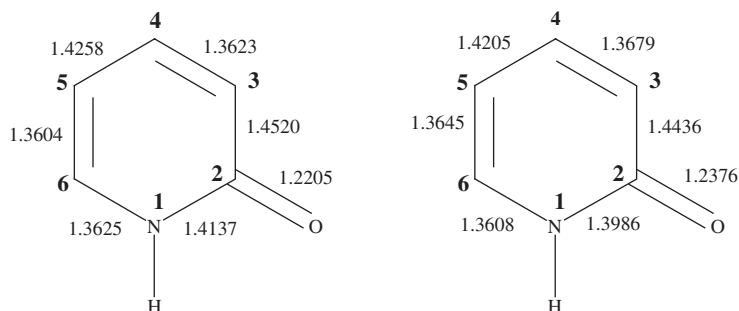
Fig. 2. Solvent effect on the geometry of the (1H)-2-pyridone tautomer as optimized at the DFT-B3LYP/6-311G** level (all distances are given in Å).

Table 8. Dielectric solvent effect on total calculated $^1J_{CC}$ couplings (in Hz) in (1 H)-2-pyridone[a]

Medium	$^1J_{C_2C_3}$	$^1J_{C_3C_4}$	$^1J_{C_4C_5}$	$^1J_{C_5C_6}$
$\varepsilon = 1$	70.6	61.7	52.9	69.7
$\varepsilon = 46.7$	68.8	59.6	51.4	66.3
Exp.[b]	67.0	58.2	51.8	65.6

[a]Experimental as well as theoretical values are taken from Ref. 140.
[b]Solutions in DMSO.

constants in the derivatives of 2-hydroxypyridine.[140] Although not directly related with the calculation of spin–spin coupling constants, it is worth comparing here the solvent effect on the optimized geometry of the (1 H)-2-pyridone tautomer considering an isolated molecule ($\varepsilon = 1$), and an infinitely dilute DMSO solution ($\varepsilon = 46.7$) (as shown in Fig. 2). Observing the lengthening of the carbonyl double bond and the alternating lengthening and shortening of the C–C ring bonds, this result shows that the solvent dielectric effect calculated at this level enhances slightly the conjugative $\pi \rightarrow \pi^*$ effect involving the carbonyl double bond. This result contrasts with the known fact that the solvent effect on the negative hyperconjugative interactions produces a slight inhibition when increasing the solvent dielectric constant.[248,249] Compared in Table 8 are the $^1J_{CC}$ couplings in (1 H)-2-pyridone for $\varepsilon = 1$ and $\varepsilon = 46.7$ calculated at the DFT-B3LYP/6-311G**/EPR-III level using the PCM-DFT optimized geometries. It is important to note that related experimental measurements required using high concentrations and therefore the $\varepsilon = 46.7$ samples could not represent quantitatively the polarity of the solution. Observing the data displayed in Table 8, it is evident that the inclusion of the solvent effect on both the geometry optimization (i.e., letting the geometry to relax in solvent) and the calculation of coupling constants improves the agreement between theoretical and experimental couplings. The largest calculated solvent effect amounts to -3.4 Hz for the $^1J_{C_5C_6}$ coupling while for all other three couplings it is close to -2 Hz.

Taurian *et al.*[250] observed nearly the same solvent effects calculated for $\varepsilon = 1$ and 46.7 of slightly less than 2 Hz (in absolute value) for all ring $^1J_{CC}$ couplings in the three positional isomers of pyridinecarboxaldehyde. All couplings calculated in the isolated molecules were larger than those including solvent effects. It is noteworthy that the agreement between calculated and experimental values improved when solvent effects on calculated couplings were taken into account. Another noteworthy point is that in all cases, solvent effects on $^1J_{CC}$ couplings showed a saturation trend for ε slightly larger than 10.

A point, which is worth stressing here, is that solvent effects could be quite different for the same type of coupling, e.g., $^2J_{CH}$, in different compounds, depending mainly on the type of the intramolecular interactions that affect that coupling. Therefore, when considering solvent effects on coupling constants, it is important to note that there is experimental as well as theoretical evidence that, for a given type of coupling, the amplitude of dielectric solvent effects strongly depends on those interactions. Among many intramolecular interactions, very important in determining the dielectric solvent effects, are the negative hiperconjugative interactions and electrostatic proximity effects as illustrated by $^2J_{XH}$ (X=C, N) in acetaldehyde and formamide.

$$ O{=\!=\!=}C_c \big\langle \begin{matrix} CH_3 \\ H_f \end{matrix} \qquad O{=\!=\!=}C_c \big\langle \begin{matrix} NH_2 \\ H_f \end{matrix} $$

<center>Acetaldehyde   Formamide</center>
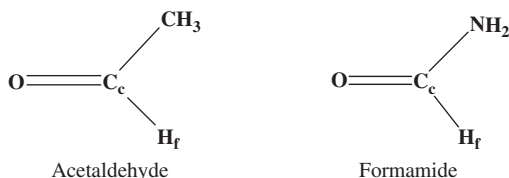
Experimental values of $^2J_{C_{Me}H_f}$ couplings in acetaldehyde are 29.74 and 26.25 Hz in gas phase and in the DMSO solution, respectively,[251] while those of $^2J_{^{15}NH_f}$ in formamide are -20.14 and -15.30 Hz.[252] It is known that the main factor defining these unusually large two-bond couplings is a very large FC term that is due to the strong negative hyperconjugative interactions that take place in the carbonyl group, i.e., $LP(O_p) \rightarrow \sigma^*_{C_c-}C_{Me}$ and $LP(O_p) \rightarrow \sigma^*_{C_c-}C_{H_f}$ in acetaldehyde, and $LP(O_p) \rightarrow \sigma^*_{C_c-}N$ and $LP(O_p) \rightarrow \sigma^*_{C_c-}C_{H_f}$ in formamide.[35] Accordingly, the large solvent effects quoted above originate in the partial inhibition of a negative hyperconjugative interaction that takes place when observations are carried out in a polar solvent.[248,249]

Considering $^1J_{CH}$ couplings, it is important to take into account that they are notably affected by the electrostatic as well as hyperconjugative interactions[47] (for the latter, see Section 2.3). An interesting paper published recently by Sigalov *et al.*[253] presents a rather detailed study of the intramolecular C_{Ar}–H$\cdots$O hydrogen bonds; these authors discuss the influence of such interactions on the chemical shifts of the donor C atom, the chemical shift of the proton involved in that hydrogen bond, and the value of the $^1J_{C_{Ar}H}$ coupling. To their surprise, no definite trends in the aromatic ^{13}C chemical shifts and the one-bond couplings were found. Probably, this last point is indicative of an interaction involving some charge transfer effect that compensates the electrostatic effect on the $^1J_{C_{Ar}H}$ coupling (see Section 2.3).

Table 9. Solvent effects on total $^1J_{C_2,H_2}$ and $^1J_{C_6,H_6}$ coupling constants (in Hz) in benzaldehyde (**1**) and phenol (**2**) calculated at the DFT-B3LYP/EPR-III level[a]

Compound	ε	$^1J_{C_2,H_2}$	$^1J_{C_6,H_6}$	ΔJ^b
1	1	168.4	160.8	7.6
	46.7	167.7	165.2	2.5
	$\Delta\varepsilon^c$	−0.7	4.4	
2	1	158.4	165.2	−6.8
	46.7	163.1	164.4	−1.3
	$\Delta\varepsilon$	4.7	−0.8	

[a] Taken from Ref. 254.
[b] $\Delta J = {}^1J_{C_2,H_2} - {}^1J_{C_6,H_6}$.
[c] Solvent effect given by the difference $^1J_{CH}(\varepsilon = 46.7) - {}^1J_{CH}\ (\varepsilon = 1)$.

The sensitivity of $^1J_{CH}$ couplings to electrostatic effects makes this type of couplings to be an interesting probe to study conformations.[35,47] Effects of this type were also discussed by Ratajczyk *et al.*[226] when comparing the performance of the DFT-B3LYP and CCSD methods for studying the conformational dependence of coupling constants in glycolaldehyde. Recently,[254] electrostatic interactions as well as their solvent effects were studied on $^1J_{CH}$ couplings in benzene derivatives. Thus, in benzaldehyde and phenol (see numeration of atoms below), it can be expected that differences in $^1J_{C_2,H_2}$ and $^1J_{C_6,H_6}$ couplings originate mainly in the proximity interactions between the side-chain and the C_2–H_2 and C_6–H_6 aromatic bonds. It is known that the proximity of the carbonyl oxygen atom to the C_2–H_2 bond in benzaldehyde, and the proximity of the two-coordinated oxygen atom to the C_6–H_6 bond in phenol, yield an increase in $^1J_{C_2,H_2}$ and $^1J_{C_6,H_6}$, respectively. On the other hand, the proximity of a C–H bond *ortho* to the side-chain hydrogen atom in both compounds yields a decrease in the corresponding aromatic $^1J_{CH}$ coupling. For numerical data in benzaldehyde and phenol, see Table 9.

Benzaldehyde   Phenol
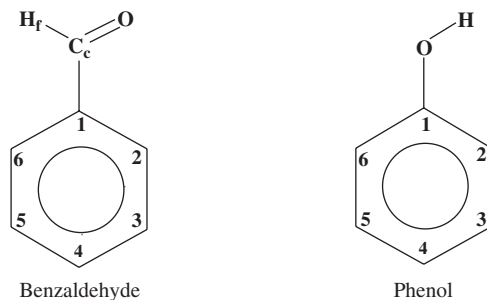
On the other hand, the difference between $^1J_{C_2,H_2}$ and $^1J_{C_6,H_6}$ in both compounds originates mainly in the proximity effects commented above. It is observed that the DFT-calculated solvent effects show opposite signs for these two couplings, and

when increasing ε, the difference between $^1J_{C_2,H_2}$ and $^1J_{C_6,H_6}$ is notably decreased. This result is compatible with a shielding of the electrostatic effect when a polar solvent is considered. These results call for some caution when intending to consider that in all $^1J_{CH}$ aromatic couplings solvent effects are the same as in benzene.

In complexes $[(NC)_5Pt–Tl(CN_n)]^{n-}$ $(n = 0–3)$ and $[(NC)_5Pt–Tl–Pt(CN)_5]^{3-}$ it is demonstrated that by the application of the increasingly accurate computational models, both the huge $J_{Pt,Tl}$ for complex $(NC)_5Pt–Tl$, as well as the whole experimental trend along the series are entirely due to the solvent effects. Both an approximate inclusion of the bulk solvent effects by means of a continuum model and the direct coordination prove to be crucial.[255] Ziegler and Autschbach gave a brief account of the effects on coupling constants involving metals due to coordination with solvent molecules in a review paper[256] on theoretical methods in the studies of inorganic reaction mechanisms.

Jokisaari and Autschbach[210] expected notably smaller solvent effects on the $^1J_{CSe}$ and $^1J_{SeSe}$ tensors in carbon diselenide than those in the heavy metal complexes, and, apparently, solvent effects notably less influence the coupling anisotropy than the isotropic coupling constant.

Thus it follows that spin–spin coupling constants are solvent-dependent. Solvent effects might be negligible in most cases, but they are always present, to a more or less extent, in the experimental values of spin–spin couplings. Molecular interactions are responsible for the variations of coupling constants, and this effect is certainly smaller for gases than for liquids. It is gaseous data that are used for the verification of the high-level *ab initio* calculations performed for isolated molecules. Measurements in the gas phase certainly give better approximation than any other experiments in liquids. However, intermolecular interactions and intramolecular nuclear motions are obviously present in the gas phase and they influence experimental results, as recently reviewed by Jackowski[257] (see also Section 3.3.4).

3.4. Decomposition of coupling constants into orbital contributions

The transmission of the indirect spin–spin coupling constants through the electronic system of both molecules and molecular complexes attracted much interest since the early times of high-resolution NMR spectroscopy. Early references on this subject can be found in the introduction of the Gräfenstein and Cremer's paper,[258] where they presented a new approach to deconvolute the four Ramsey terms into the LMOs contributions. This approach was based on the COLOGNE program[259] developed by Cremer and coworkers using the analytical formulation of the coupled perturbed-DFT, CP-DFT or CP-KS calculation of the Ramsey's second-order terms,[182] together with its computational implementation. This approach was dubbed as J-**OC**-PSP, decomposition of J into orbital contributions using orbital currents and partial spin polarization,[258] and it was presented at two different levels, J-**OC**-PSP1[260] and J-**OC**-PSP2.[261] Within the former, the deconvolution includes only one- and two-orbital contributions, each of them having different physical meaning. Within the latter, a difference is made between active, passive,

and frozen orbitals, allowing the possibility of, e.g., discriminating between through-bond and through-space transmitted contributions, and, in unsaturated compounds, into FC coupling contributions transmitted through the σ-framework or through the π-electronic system. The J-**OC**-PSP approach (in any of its two levels) can be used to study transmission mechanisms of coupling constants within the wavefunction or within the DFT formalisms. In a series of papers, Cremer and coworkers applied this approach to study some interesting problems arising when couplings are calculated within the CP-KS approximation. Here, a brief description of some of these problems is presented.

The problem of the transmission mechanisms of $^1J_{XH}$ couplings in hydrides of the type XH_n was addressed by Wu *et al.*[260] in the same paper where they presented the J-**OC**-PSP1 approach. Thus, in the series of 12 selected hydrides XH_n ($n = 1-4$), X = C, Si, Ge, N, P, As, O, S, Se, F, Cl, Br, it was observed that for $^1J_{XH}$ couplings the main contributions arise from the FC and PSO terms, while the SD and DSO contributions were negligible. It is important to note that, although Wu *et al.*[260] used a notation similar to that employed when analyzing $^1J_{XH}$ couplings within the CLOPPA method,[80] they are used with a different meaning and therefore, a direct comparison of the different orbital contributions obtained with the CLOPPA and the J-**OC**-PSP1 approaches cannot be made; however, some results are qualitatively similar.

The J-**OC**-PSP method can provide interesting insight into the coupling mechanisms present in a *trans*-hydrogen-bond coupling, and Tuttle *et al.*[262] carried out a study of this type to analyze the nature of the hydrogen bond in proteins analyzing $^{2h}J_{ON}$ and $^{3h}J_{CN}$ in the N–H⋯O = C moiety. Gräfenstein *et al.*[263,264] were interested in studying the π character of a C–C bond, and to this end, they made a detailed study on how the PSO and DSO terms could be used for this purpose. In a subsequent paper,[265] they reported the analysis of the SD term of the $^1J_{CC}$ couplings in terms of the orbital contributions, spin polarization, and spin-dipole energy density distribution. From that analysis, they arrived at the conclusion that the SD term is a sensitive "antenna" for detecting the π-character of a bond. In a separate paper, Cremer *et al.*[134] performed the J-**OC**-PSP decomposition of all four Ramsey terms contributing to a coupling constant to study how far the $^1J_{CC}$ coupling is good as a descriptor of the nature of the C–C bond. They arrived at a conclusion that if the FC term is considered separately from the other three Ramsey terms, then it is possible to achieve a semiquantitative description of the character of the C–C bond.

Both the J-**OC**-PSP1 and J-**OC**-PSP2 methods were also employed to study the mechanisms that define the through-space transmission of J_{FF} couplings.[266] It is important to recall that using the second approach, contributions can be determined by freezing selected orbitals during the calculation of a coupling constant which is equivalent to the suppression of the interaction of that orbital with both the coupling nuclei and with other orbitals. *Peri*-difluoronaphthalene and the FH dimer taken in different configurations were used as model compounds in that study. What is most interesting is a very large σ-framework contribution of –19.5 Hz calculated within the J-**OC**-PSP2 approach for J_{FF} in *peri*-difluoronaphthalene.

Gräfenstein et al.[267] studied the π-transmission coupling mechanism in four model polyenes, namely, ethylene, 1,3-butadiene, 1,3,5-hexatriene, and 1,3,5, 7-octatetraene. It was observed that orbitals involved in the π-electronic coupling mechanism, as expected, play a passive role in transmitting the FC term. It was also found that the π-transmitted components of $^nJ_{CC}$ and $^nJ_{CH}$ couplings are notably smaller than those predicted many years ago by INDO calculations,[52] the latter are affected by the minimal basis set used at the semiempirical level. This is much less pronounced in the π-transmission of the FC term of $^nJ_{HH}$ couplings, and therefore a better agreement between values reported by Gräfenstein et al.[267] and those calculated within the semiempirical INDO approach is observed.

The J-**OC**-PSP method was also applied by Gräfenstein et al.[268] to study several aspects of the electronic structure in several model molecular systems. As an example, the case of the FH molecule was considered in detail, where the four Ramsey terms were decomposed into orbital contributions and then described by their spin densities and orbital current densities.

3.5. DFT calculations of coupling constants in large systems

Watson et al.[269] reported DFT calculations of coupling constants in large molecular systems, valinomycin and hexapeptide, containing more than 100 atoms. One of the important conclusions of this study is that the long-range couplings are dominated by the PSO and DSO terms (see Section 3.2.2 for similar comments on long-range through hydrogen-bond couplings). The distance-dependence of different contributions to coupling constants was also discussed, pointing out that the FC term decays exponentially; the SD contribution decreases inversely proportional to the cube of the distance separating the coupling nuclei; and the sum of the PSO and DSO terms (which in many cases are of opposite sign) decreases inversely proportional to the cube of the distance (for considering the sign of the DSO term, see Section 2.5). More examples of the DFT calculations of coupling constants in large systems of biomolecular origin are given in Section 4.2.6.

3.6. DFT calculations of coupling constants involving either oxygen or fluorine atoms

In the middle of 1990s, Malkin et al.[217] and Dickson and Ziegler,[178] using their original DFT-implementations, observed that calculated coupling constants involving fluorine atoms did not reproduce correctly the experimental values. It was assumed that the problem originated in the electron-rich valence shell of fluorine. Since then, many examples and comments were found in the current literature and, at first, it led to think that calculation of couplings involving any LP bearing atom was doomed to fail when they were calculated within the DFT framework. However, nowadays it is well known (see Section 3.3) that many couplings involving some LP bearing atoms are correctly reproduced by the DFT calculations. Several illustrative examples of problematic as well as nonproblematic cases are quoted further. The selection given below is by no means exhaustive.

Ratajczyk *et al.*[226] studied the DFT conformational dependence of couplings in glycolaldehyde, and for selected conformations, they compared such values with those obtained with the CCSD method (see Section 3.3.1), and concluded that DFT is suitable for the calculation of the $^1J_{CO}$ couplings. However, they found notable differences between the DFT- and CCSD-calculated values of $^1J_{OH}$ couplings, and they pointed out that to a larger extent, DFT-calculated couplings involving fluorine are less reliable than couplings involving H, C, and N atoms. They stressed that this is in agreement with the general observation that DFT is less reliable for calculations of spin–spin coupling constants of electron-rich atoms.

Similarly, Ruden *et al.*[238] when comparing vibrational corrections to coupling constants calculations with the DFT-B3LYP, MCSCF, and SOPPA methods, observed that their DFT results failed badly when considering couplings involving fluorine atoms. Difficulties for calculating $^1J_{FH}$ and $^1J_{CO}$ couplings within the DFT framework in FH and CO were reported by Keal *et al.*[195] Some difficult cases of J_{FF} couplings were found by Fruchier *et al.*[270] in fluorine derivatives of cyclotriphosphazenes. Pecul *et al.*[157] compared the performance of the DFT-B3LYP calculations of *trans* X–H···Y hydrogen bond couplings with the respective *ab initio* results, using the MCSCF and CCSD methods, and they observed that the DFT description of $^{1h}J_{YH}$ and $^{2h}J_{XY}$ couplings deteriorated when increasing the number of the LPs that bear the atoms containing the coupling nuclei. Del Bene and coworkers[146,169] also considered that the DFT-B3LYP calculations of coupling constants did not reproduce J_{FF} couplings in a number of cases.

Bryce *et al.*[175] compared ZORA-DFT and MCSCF calculations of both the isotropic $^1J_{PO}$ coupling and its anisotropy, Δ^1J_{PO}, in phosphine oxides using different basis sets and different levels of theory. For the anisotropy, both MSC-SCF- and DFT-yielded values around -300 Hz, which is within the experimental range estimated in the same paper. On the other hand, the DFT overestimation (compared with both experimental and MCSCF results) of the isotropic part, $^1J_{PO}$, arises from an overestimate of the ZORA combined FC + SD contributions. It is important to note that Lantto *et al.*[185] observed that in general within the DFT framework, the anisotropy part of the J_{CF} coupling tensors is described better than the corresponding isotropic part. According to Lantto *et al.*,[185] this happens since the FC contribution is small at fluorine compared with carbon, leading to a small error in the calculation of the FC/SD cross-term.

When comparing the general performance of the DFT- and wavefunction-based methods, Ruden *et al.*[238] concluded that the best-calculated couplings available in the literature for small molecular systems containing only light atoms were those obtained with the RASSCF method. They observed also that SOPPA- and DFT-B3LYP-calculated couplings in small molecular systems are of similar quality, with the exception of molecules containing fluorine where DFT fails badly. On the other hand, they considered that the quality of spin–spin couplings obtained within the coupled-cluster theory is difficult to assess due to its basis set deficiencies.

San Fabián and Westra Hoekzema[227] compared MCSCF, SOPPA, and DFT calculations of the dihedral angular dependence of $^3J_{FF}$ couplings in 1,2-*trans*-difluoethane and found a notably poorer performance for DFT when comparing results with the available experimental couplings. It seems that the failure of the DFT approaches to describe correctly calculated couplings, involving nuclei corresponding to the electron-rich atoms, originates in the DFT inability to describe correctly the dynamic electron correlation effects, which are very important for an adequate description of coupling constants (see Section 3.2.4).

However, the assertion about the general failure of the DFT approaches used for calculating coupling constants involving fluorine and/or oxygen atoms (more generally, halogen and/or chalcogen atoms) should be taken with some caution. In fact, a critical revision of papers published in the current literature containing DFT-calculated couplings involving atoms bearing two or three nonbonding electron pairs shows a good number of them reporting DFT-calculated couplings in fair agreement with the respective experimental values. A few of them are quoted as follows, and several rather speculative hypotheses are formulated but their actual validity should be assessed more carefully.

In a set of fluorinated pyridines (2,6-difluoropyridine, 2,4,6-trifluoropyiridine, pentafluoropyridine, and 2-bromohexafluoroquinoline), Barone et al.[271] calculated all $^nJ_{FF}$ couplings within the DFT-B3LYP approach. In pentafluoropyridine, these authors tested five different basis sets and in all cases took into account the four Ramsey terms. As an example, calculated J_{FF} couplings in pentafluoropyridine are compared with their experimental values in Table 10. Spin–spin couplings were calculated using the cc-pVTZ basis set on the C and N atoms and the aug-cc-pVTZ-J basis set for F atoms while the corresponding experimental values were taken from Refs. 272, 273. The most significant difference between theory and experiment was observed for $^5J_{F_2,F_5}$ (33.7 *vs.* 26.3 Hz). A very good agreement between calculated and experimental values for all other couplings is surprising considering that most of these couplings show important contributions from the FC, the SD,

Table 10. Comparison between calculated and experimental values of J_{FF} coupling constants (in Hz) in pentafluoropyridine[a]

$^nJ_{F_iF_j}$	DSO	PSO	SD	FC	Total	Exp.[b]
$^3J_{F_2F_3}$	0.1	−17.1	13.7	−16.2	−19.5	−20.3
$^3J_{F_3F_4}$	0.1	−24.2	11.5	−4.3	−16.8	−18.1
$^4J_{F_2F_4}$	−1.1	13.4	3.1	−2.0	13.3	13.7
$^4J_{F_2F_6}$	−1.1	−1.2	−5.3	−9.1	−16.6	−15.0
$^4J_{F_3F_5}$	−1.1	5.0	−1.2	−5.4	−2.7	0.0
$^5J_{F_2F_5}$	−1.1	8.8	19.3	6.7	33.7	26.3

[a]Geometries were optimized at the DFT-B3LYP/6-311G** level. Coupling constants were calculated with the same functional with the basis sets cc-pVTZ on C and N, and aug-cc-pVTZ-J for F atoms. Calculated couplings are taken from Ref. 271.
[b]Taken from Refs. 272 and 273.

and the PSO contributions, which in several cases are very different for different couplings.

Pentafluoropyridine
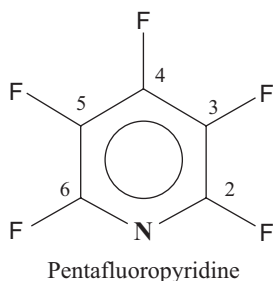
In the analogous derivatives of 1,8-*peri*-difluoronaphthalene, the performance of DFT-B3LYP for the calculation of J_{FF} couplings dominated by a "through-space" contribution is also good,[274] as can be appreciated in Fig. 3, where experimental J_{FF} couplings are taken from Ref. 275. When comparing compounds (b) and (c), it is observed that in the latter the d_{FF} distance is longer while the corresponding J_{FF} is larger. This trend is counterintuitive for a coupling constant largely dominated by a through-space mechanism. The rationalization of such a behavior is mainly based on the important PSO contribution (18.5 Hz) in compound (c) as compared to the markedly smaller PSO contribution (4.6 Hz) in compound (b).

Why this term is so different in these two compounds? There are some intuitive reasons to believe that the PSO term is more efficiently transmitted through-space in (c) than in (b). This can be understood easily resorting to a qualitative analysis of the PSO operator, Eq. (2c). In fact, according to the CLOPPA approach,[80] the PSO term can be splitted into a sum of LMO contributions, each depending on two occupied and two vacant LMOs. Because the PSO Hamiltonian involves the rotation operator, $(\mathbf{r}_{kA} \times \nabla_k)$, the CLOPPA contributions are significant when at least these two conditions are satisfied: (i) there is a substantial overlap between an occupied LMO rotated by $90°$ and a vacant LMO localized at the site of a chemical bond; (ii) there is an adequate energy gap between such two LMOs, the larger this gap, the smaller the corresponding PSO term.

According to this qualitative description of the PSO operator, it is evident that, at least at first glance, in compounds (a)–(c) depicted in Fig. 3, the relative orientations of the C–F bonds are adequate for a through-space transmission of the PSO term corresponding to the J_{FF} couplings. In fact, condition (i) is satisfied since the rotation operator applied to both the in-plane LPs of very high p-character (p-LP) and to that of π-symmetry (π-LP) yields important overlaps with the corresponding σ^*_{C-F} antibond. Therefore, changes in the PSO contribution from compound (b) to compound (c) should differ mainly in the energy gaps between the p-LP and the σ^*_{C-F} antibond, and that of the π-LP and the same the σ^*_{C-F} antibond. In the case under consideration no considerable change in both the p- and the π-LP orbitals can be envisaged. On the other hand, it can be expected that the short $C_4{=}C_5$ bridge introduces a strong distortion of the C_1–F and C_8–F bonds. As commented above,
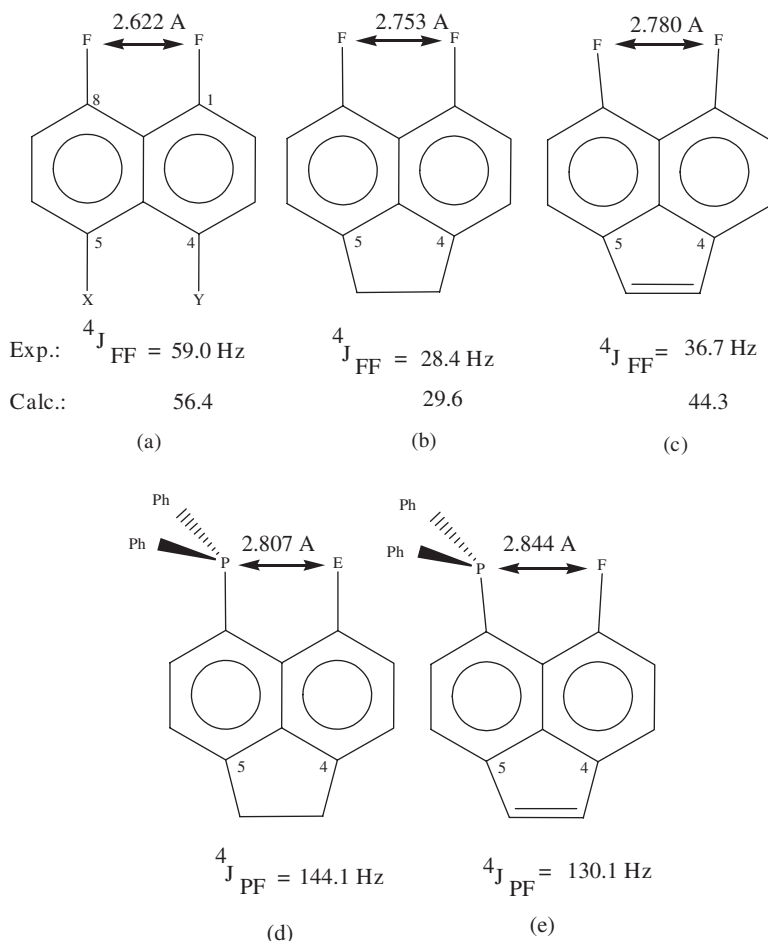
Fig. 3. Interatomic distances and spin–spin couplings involving fluorine in the derivatives of 1,8-*peri*-difluoronaphthalene (a)–(c) and heteroanalogs (d)–(e). The d_{FF} distances are given in Å and correspond to the DFT-B3LYP/6-311G** optimized geometries.

strong distortions of bond angles make the corresponding bonds to be very good electron donors or, equivalently, decrease the energy gap between the p-LP and the σ^*_{C-F} antibond in (c) as compared to (b), favoring the transmission of the PSO term.

Since considerations made above, about the behavior of the PSO term, are based on qualitative considerations, it is reasonable to look for the experimental evidence supporting such a simplified model. In fact, this can be found in the same Mallory et al.'s paper.[275] Compounds (d) and (e) are analogs to (b) and (c) shown above (Fig. 3). The only difference is that one fluorine atom is replaced by the PPh$_2$ group. At the bottom of Fig. 3, the d_{PF} distances taken from Mallory et al.[275] are shown together with the experimental J_{PF} couplings. In these two compounds, the anomalous behavior found in (b) and (c) is not observed, as expected that the J_{PF}

coupling is dominated by far by a through-space mechanism for transmitting only the FC term and not the PSO contribution. Indeed, it is quite expected that this coupling decreases when increasing the d_{PF} distance, which suggests that the PSO term is much smaller than the corresponding FC contribution. Indeed, it is obvious that condition (i) mentioned above still holds, i.e., the rotation operator applied to the P LP yields an important overlap with the σ_{C-P}^* antibond. When considering the energy gap between the P LP and the σ_{C-P}^* antibonding orbital, it should be noted that the percentage of s-character of the P LP is very high[276] and therefore, the LMO representing the P LP is very deep in energy, which indicates that the PSO term of J_{PF} is insignificant. This is a nice evidence that the qualitative model used to rationalize the trend observed in compounds (b) and (c) behaves correctly (Fig. 3).

When San Fabián and Westra Hoekzema[227] compared the performance of the DFT approach with the MCSCF and SOPPA calculations for evaluating the dihedral angular dependence of $^3J_{FF}$ couplings using 1,2-difluoroethane as a model compound, they found that for a *cis*-conformation its value is quite close to the experimental one (taken from a fluorinated derivative of norbornene), *cis*-$^3J_{FF} = +16.1\,Hz$.[277] On the other hand, for *trans*-1,2-difluoroethane, the DFT-calculated *trans*-$^3J_{FF}$ is negative, as it should be, but its absolute value is notably overestimated as commented in Section 3.3.1. It should also be noted that in *cis*-1,2-difluoroethene the DFT-calculated $^3J_{FF}$ ($-16.0\,Hz$ at the DFT/aug-cc-pVTZ level)[234] is close to its experimental value, $-18.7\,Hz$.[170] These last observations suggest that the dynamic electron correlation effects that are assumed to cause the failure of the DFT calculations of couplings involving fluorine atoms are much less significant for *cis*-$^3J_{FF}$ than for *trans*-$^3J_{FF}$ couplings. This could be the reason why the experimental $^3J_{FF}$ couplings in pentafluoropyridine (Table 10) are very well reproduced. However, it should be recalled that in tetrafluoroethylene, *cis*-$^3J_{FF} = 91.5\,Hz$[234] (calculated at the DFT/aug-cc-pVTZ level), while the experimental value is $74.567\,Hz$.[278] This seems to indicate that the strong level of substitution in tetrafluoroethene would increase the importance of the dynamic electron correlation effect on the DFT-calculated couplings.

A very good description of the calculated *peri*-$^4J_{FF}$ couplings transmitted "though-space"[274] suggests that dynamic electron correlation effects should not be of too much relevance in this case. Accordingly, DFT-B3LYP level can account for them in a reasonable form provided an adequate basis set is used. It is known that the main coupling pathway of these couplings is the direct overlap of the non-bonding electron pairs of the two proximate fluorine atoms in *peri* orientation to each other. This seems to indicate that either the failure or the success of the DFT calculations of spin–spin couplings involving fluorine and/or oxygen atoms depend mainly on the coupling pathways connecting the coupling nuclei.

This assertion is also supported by the recently published $^4J_{CF}$ and $^5J_{CF}$ couplings in 1-F-4-X-cubanes (where the α-atom of the X group is ^{13}C) calculated at the DFT/EPR-III level that are in excellent agreement with their experimental values.[66] This study allowed to explain why these couplings are so particularly large: the FC is transmitted due to the existence of six σ-hyperconjugative interactions that are

Table 11. Long-range $^5J_{C\alpha,F}$ coupling constants (in Hz) in 1-F-4-X-cubanes calculated at the DFT/EPR-III level[a]

X	DSO	PSO	SD	FC	Total	Exp.
CH$_2$OH	−0.26	0.42	0.07	6.45	6.69	6.84
CH$_3$	−0.28	0.48	0.07	6.64	6.91	7.01
CO$_2$H	−0.22	0.35	0.11	6.89	7.13	7.21
CN	−0.24	0.47	0.14	7.79	8.15	8.40
COCl	−0.21	0.53	0.13	9.43	9.88	9.77

[a]Experimental as well as theoretical values taken from Ref. 66.

equivalent in the compounds of this series having a threefold symmetry axis, like their parent compound, 1-fluorocubane. It is noteworthy that the noncontact terms of $^5J_{CF}$ of these compounds are more sensitive to substitution than the dominant FC contribution. The SD term changes from 0.07 Hz (X$=$CH$_3$) to 0.14 Hz (X$=$CN); PSO from 0.35 Hz (X$=$CO$_2$H) to 0.53 Hz (X$=$COCl); DSO from –0.28 Hz (X$=$CH$_3$) to –0.21 Hz (X $=$ COCl)[66] (Table 11).

Thus, it follows that some coupling pathways do not require a detailed description of the dynamic electron correlation effects to be well reproduced by the DFT-based methods. In this case the description of the σ-hyperconjugative interactions would not require calculations that recover most of the dynamic electron correlation effects. On the other hand, it would also be possible to get an *a priori* estimation if a given DFT coupling calculation can be expected to be reliable.

As mentioned above, several couplings involving ^{17}O were also reported as wrongly reproduced by the DFT calculations, as compared to the high-level *ab initio* results. The amount of the available experimental couplings involving ^{17}O is scarce, and for this reason, it is not very easy to make a direct comparison between the experimental and DFT-calculated couplings. Wrackmeyer[279] calculated several $^1J_{CO}$ and a few other couplings involving oxygen at the DFT-B3LYP/6-311$+$G(d,p) level in good agreement with experiment. For example, calculated $^1J_{CO}$ couplings in CO$_2$ and CO are $+17.1$ and $+17.2$ Hz, respectively, that compare favorably with the experimental values of 16.1 and 16.4 Hz (taken from Ref. 280). This very good agreement between the experimental and DFT-calculated $^1J_{CO}$ couplings in CO$_2$ and CO is in line with the observations made by Ratajczyk *et al.*[226] on this type of couplings when comparing *ab initio* and DFT-calculated couplings in glycolaldehyde.

However, in acetone, the discrepancy is much larger between calculated, $+32.1$ Hz, and experimental, 22 Hz, values (taken from Ref. 281). When looking at these values it should be recalled that the ^{17}O magnetogyric ratio is negative. In the same paper,[279] Wrackmeyer highlighted a good agreement between the calculated and experimental values of $^2J_{OH}$ couplings in methyl formate. It is interesting to note that in this compound one of these couplings corresponds to a *geminal* one through a carbonyl group. As commented above, spin–spin couplings of this type are unusually large and by far dominated by the FC term.

Large values of $^2J_{OH}$ across carbonyl function originate mainly in the very strong negative hyperconjugative interactions that take place within the carbonyl group. In the case of methyl formate these interactions are of the $LP(O_p) \rightarrow \sigma^*_{C_C-H_f}$ and $LP(O_p) \rightarrow \sigma^*_{C_C-O}$ types, where $LP(O_p)$ stands for the in-plane carbonyl oxygen LP of pure p-character; C_C is the carbonyl C atom; H_f is the formyl proton, and O stands for the dicoordinated oxygen atom. The coupling pathway for the FC term of this coupling is mainly determined by these two hyperconjugative interactions. For this coupling, Wrackmeyer[279] reported a DFT-calculated value of -39.5 Hz, which is almost equal, within the experimental error, to the measured value of $ca.$ 38 Hz.[282] This result seems to support the assumption made above that couplings mainly transmitted through the hyperconjugative interactions are not much affected by the dynamic electron correlation effects, and therefore, they can be reasonably predicted by the DFT calculations.

Methyl formate
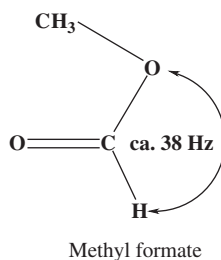
In the current literature, there are some few experimental couplings involving oxygen, ^{17}O, due to its low isotopic natural abundance and nuclear electric quadrupole moment. Therefore, it is interesting to comment here on the DFT calculations of coupling constants involving any of the chalcogen atoms where they are expected to meet similar problems. However, couplings involving ^{33}S, the isotope that has also electric quadrupolar moment, are similarly scarce as those involving ^{17}O because, although its natural abundance is a bit higher, its sensitivity is much lower. Couplings involving ^{77}Se and ^{125}Te nuclei are much better for being considered owing to their 1/2 spin, their larger natural isotopic abundances, as well as larger sensitivities. However, couplings involving the ^{77}Se isotopic species could provide better information on the DFT performance since relativistic effects are expected to be more significant for couplings involving ^{125}Te than for those involving ^{77}Se.

Wrackmeyer[283] calculated at the nonrelativistic DFT-B3LYP/6-311 + G(d,p) level $^nJ_{SeSe}$ ($n = 1, 2, 3$) in several compounds. Calculated couplings, whenever possible, were compared with their corresponding experimental values; however, available experimental values are scarce enough to prevent a reliable conclusion about the DFT performance for this type of couplings. For this reason, only few calculated couplings reported by Wrackmeyer[283] are commented here, intending to get insight into the DFT performance when calculating couplings involving chalcogen atoms.

However, in the same paper[283] Wrackmeyer observed rather large deviations between calculated and experimental values of ^{77}Se chemical shifts, and ascribed

these differences to the deficiencies of the DFT-B3LYP/6-311 + G(d,p) approach to describe correctly the electron correlation effects. It follows that one of the best agreements between calculated and experimental J_{SeSe} values corresponds to the cis-$^3J_{SeSe}$ in tetraselenafulvalene with the total calculated coupling, $+98.8$ Hz (FC = $+92.7$ Hz, SD = -0.6 Hz, and PSO = $+6.6$ Hz), as compared to the experimental value in dimethyltetraselenafulvalene, 90.7 Hz.[284] In the latter paper, Johannsen and Eggert also reported experimental cis-$^3J_{SeSe}$ = 96.5 Hz in cis-1, 2-bis(methylseleno)-1-phenylethylene, a value similar to that measured in dimethyltetrafulvalene. An IPPP analysis carried out on cis-1,2-bis(methylseleno)ethylene revealed that the large cis-$^3J_{SeSe}$ coupling is dominated by the FC term, and its coupling pathway is determined by the overlap of the in-plane non-bonding electron pair of both Se atoms,[285] which means that this transmission mechanism corresponds to what is usually referred to as "couplings transmitted through space."

cis-Dimethyltetraselenafulvalene   cis-1,2-Bis(methylseleno)-1-phenylethylene
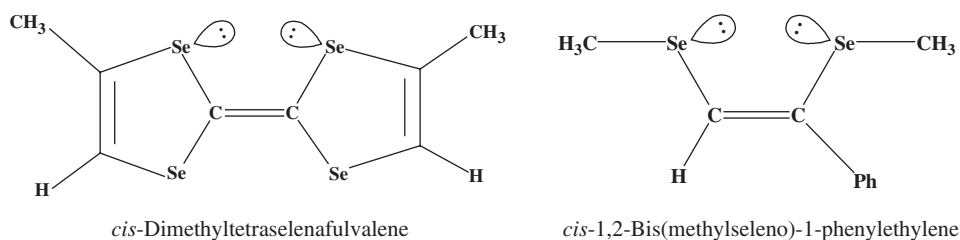
   This result seems to reinforce the working hypothesis (see above) that it is not correct to generalize the idea that the DFT calculations of coupling constants, involving either halogen or chalcogen atoms, are doomed to fail. For certain coupling pathways reasonable values could be calculated within the DFT framework while for some others could not. According to the assertions made above, spin–spin couplings corresponding to the pathways with the through-space transmission by the overlap of the nonbonding electron pairs, and, on the other hand, mainly transmitted by either negative- or σ-hyperconjugative interactions, can be predicted rather well by the DFT calculations, provided adequate basis sets are employed. As stated above, the idea behind this conclusion is that the interactions defining such coupling pathways would not require some fine details of the dynamic electron correlation effects to be adequately reproduced.

   The isotropic values and the anisotropy of the $^1J_{XF}$ (X = F, Si, Ge, Sn, P, As, Sb, Bi, S, Se, Te, Pt, and Nb) coupling tensors in a variety of compounds including, among others, PF_3, SiF_4, PF_5, and a series of groups 14 and 15 hexafluoride anions, were calculated within the ZORA-DFT approach by Feindel and Wasylishen.[286] They observed that, although this approximation is effective for the qualitative reproduction of the experimental trends and signs of the isotropic $^1J_{XY}$ couplings, in many cases, calculated couplings deviate notably from their measured values. For instance, experimental value of $^1J_{SiF}$ = $+172$ Hz in SiF_4,[287] while its ZORA-DFT-calculated value is $+419.9$ Hz (!) However, it is noteworthy that the absolute value of the anisotropy of most $^1J_{XF}$ coupling tensors considered in the Feindel and

Wasylishen's paper[286] is of the same order of magnitude as the corresponding calculated isotropic $^1J_{XF}$ coupling. It should also be noted that these authors reported the calculated relativistic spin-orbit contribution $(FC + SD) \times PSO$ (we use here the Feindel and Wasylishen's notation). Thus, for $^1J_{TeF}$ coupling in TeF_6, the total calculated isotropic coupling, 2,611.0 Hz, includes an $(FC + SD)xPSO$ contribution of -254.8 Hz while the corresponding experimental coupling is $^1J_{TeF} = 3,736$ Hz.[288]

Very recently, Keal et al.[189] demonstrated that in a few small compounds spin–spin couplings involving either O or F atoms are better reproduced by the B97-2 and B97-3 semiempirical functionals. However, these preliminary results are not confident enough to establish that all known DFT problems associated with the calculation of the coupling constants involving electron-rich atoms in their valence shell could be eliminated simply by choosing the given functionals.

3.7. Relativistic effects

During the review period, the analysis of relativistic effects on coupling constants has increased notably both within the wavefunction and DFT frameworks. The first implementation and application of the analytical density functional response theory was used by Oprea et al.[289] to evaluate the spin-orbit corrections to calculate $^2J_{HH}$ couplings in XH_2 (X = O, S, Se, Te) and XH_4 (C, Si, Ge, Sn, Pb). They applied the quadratic response theory formalism developed previously.[290] For the chalcogen series, they calculated the SO/FC and SO/SD corrections including the one- and two-electron terms, and compared results obtained both within the wavefunction and DFT formalisms. For the XH_4 series, they found negligible values of the SO/SD both for the one- and two-electron terms. It is interesting to note that the total spin-orbit correction for the $^2J_{HH}$ coupling in TeH_2 is about 10 times as large as that found for SnH_4. From an empirical point of view, similar effects were observed in the ^{13}C chemical shifts when carbon is bonded to the heavy atom, the "heavy atom effect."[291]

One of the crucial questions explicitly unanswered so far is from which atom onward in the Periodic Table relativistic effects become significant? For instance, Forgeron et al.[292] studied the $^1J_{PP}$ tensor as well as its isotropic value, $^1J_{PP}$, in a variety of molecular systems with $Z \leq 24$, including cis-MeP$=$PMe, trans-RP $=$ PR (R = H, Me), H_2P–PH_2, and H_2P–PF_2 using the ZORA-DFT approach. They found that the isotropic part of the $^1J_{PP}$ tensor is dominated in all cases by the FC term if both P atoms are bonded by a formal single bond, while for a formal multiple bond the PSO term could be at least of equal importance as the FC term. They compared ZORA-DFT values with those of the nonrelativistic calculations, and in all cases, observed differences were less than 10%, which means that relativistic effects in this series were not very important.

Wrackmeyer et al.[293] performed the DFT-B3LYP/6-311 + G(d,p) calculations of $^1J_{FeC}$ and $^2J_{FeH}$ couplings in ferrocenes and cyclopentadienyliron complexes together with their experimental measurements, including several determinations of

signs. For instance, in ferrocene, the experimental $^1J_{FeC}$ = 4.8 Hz, while the calculated value is + 5.0 Hz (FC = + 2.6 Hz, SD = + 0.3 Hz, and PSO = + 2.1 Hz; the DSO term was neglected); in the cyclopentadienyl iron complex, the experimental (calculated) values are as folows: $^1J_{FeC}$(Cp) = 2.3 Hz (+ 2.4 Hz); $^1J_{FeC}$(CO) = 27.8 Hz (+ 27.4 Hz); $^1J_{FeC}$(CCH) = 19.5 Hz (+ 18.7 Hz), and $^2J_{FeC}$(CCH) = 3.0 Hz (+ 2.8 Hz). In view of the very good agreement between the calculated and experimental values, relativistic corrections to these couplings seem to be next to negligible. However, some caution should be taken when intending to extrapolate this observation to other couplings involving Fe since, for instance, in these ferrocenes, the atoms containing coupling nuclei are not covalently bonded. So far, it is not well known what are the transmission mechanisms of the relativistic contributions to the coupling constants involving Fe and other metals.
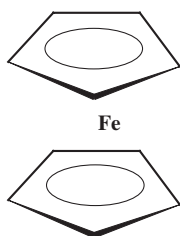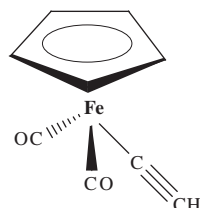
Ferrocene   Cyclopentadienyliron complex

Filatov and Cremer[294] presented a new approach to calculate coupling constants, including relativistic effects using the infinite-order regular approximation with modified metric (IORAmm),[295,296] and compared their approach with that of Autschbach and Ziegler,[297] the latter based on the ZORA approximation. For instance, one of the notable diffrences is that the Autschbach and Ziegler's approach is based on the numeric integration for calculating the Hamiltonian matrix elements, while Filatov and Cremer's approach does not employ numeric integration for calculating relativistic corrections to the molecular Hamiltonian and can be employed with both pure and hybrid exchange functionals being valid both within the wavefunction and DFT frameworks. However, a minor point of this approach is that it does not include spin-orbit interactions. The IORAmm results for the $^1K_{XH}$-reduced couplings in hydrides XH_4 (X = C, Si, Ge, Sn, Pb) and $^1K_{XC}$ (X = Pb, Cd, Hg) in $Pb(CH_3)_3H$, $Pb(CH_3)_4$, $Cd(CH_3)_2$, $Hg(CH_3)_2$, $Hg(CH_3)Cl$, $Hg(CH_3)Br$, $Hg(CH_3)I$, $Hg(CN)_2$ calculated using different functionals were also compared with the nonrelativistic CP-DFT calculations.[294]

Recently, Melo et al.[298] implemented the relativistic calculation of coupling constants using the Douglas-Kroll-Hess (DKH1 and DKH2) approximation[299–302] for decoupling the large and small components of the Dirac Hamiltonian. This implementation was carried out in a Gaussian 03[203] development version, and it is adequate to be applied within both the Hartree-Fock and the DFT frameworks. Calculations were carried out in the series of four hydrides, XH_4 (X=C, Si, Ge,

Sn), using the generalized Kohn-Sham and the generalized Hartree-Fock approaches. The latter was used to compare uncorrelated relativistic calculations with those obtained by Enevoldsen et al.[27] using a four-component random phase approximation. They also analyzed the basis set requirements for calculating coupling constants within the DKH approximation. Relativistic DFT-DKH2 calculations including the spin-orbit correction were carried out using three different functionals, PBE, PBEh, and B3LYP. Such results were also compared with the corresponding experimental $^1J_{XH}$ couplings, and it was observed that for all cases, with the exception of CH_4, the DFT-B3LYP values were the closest to the experimental values.

Bagno et al.[303] recently calculated the $^1J_{SnH}$ coupling in SnH_4 at the BP-ZORA/TZ2P level of theory using the ADF software;[224] this calculated coupling ($-1,549.47$ Hz[303]) can be compared with the DKH2 result including the spin-orbit correction ($-1,922.6$ Hz[298]) as well as with its experimental values ($-1,933.3$ Hz[304] or $-1,930$ Hz[305]). It is obvious that substantial difference between the values of $^1J_{SnH}$ in SnH_4 calculated at the BP-ZORA/TZ2P and DKH2 levels amounting to 374 Hz (!) could hardly be ascribed to the slightly different geometries used in those calculations but rather originates in the different level of approximations implemented in these two methods.

Many more examples showing the significance of the relativistic effects in the calculation of spin–spin couplings involving heavy nuclei are discussed further on in Sections 4.1.3 and 4.1.4.

4. COMPUTATIONAL RESULTS – AN ILLUSTRATIVE COMPILATION AND A PRACTICAL GUIDE

Computational results dealing with the *ab initio* and DFT calculations of the different coupling constants in several representative examples are compiled and briefly discussed in this section just to show some illustrative structural trends and their practical applications. By no means the authors of this review intended to cover all amount of data appeared during the review period dealing with the theoretical calculations of spin–spin couplings in a wide variety of chemical species.

4.1. Inorganic compounds

4.1.1. *Benchmark di- and triatomics*

A number of papers were focused on a proving ground of six first- and second-row benchmark di- and triatomics, HD, HF, CO, N_2, H_2O, and HCN, to evaluate the merits and shortcomings of different theoretical approaches currently used to calculate spin–spin couplings, mainly those exploiting the MCSCF,[202,306–310] CCSD,[143] and SOPPA[164,311] wavefunction methods together with the DFT-based computational schemes.[182–184,188,238] Some representative results extracted from

Table 12. Total coupling constants (in Hz) in the benchmark di- and triatomic molecules calculated by different methods in comparison with experiment

Compd.	J_{XY}	CHF[a]	B3LYP[a]	MCSCF[a]	CCSD[b]	CC3[b]	SOPPA[c]	SOPPA(CCSD)[c]	Exp.
HD	J_{HD}	47.3	42.6	36.9			43.93	41.17	42.94[d]
HF	J_{HF}	632.7	419.5	517.7	521.57	521.50	539.52	529.43	500 ± 20[e]
CO	J_{CO}	−5.0	19.5	16.1	15.67	15.30	20.41	18.60	16.4[e]
N_2	J_{NN}	−15.0	1.6	0.8	1.81	1.77	2.67	2.06	1.8[e]
H_2O	J_{OH}	−97.1	−71.8	−74.5	−78.85	−78.52	−82.42	−80.60	−80.6[e]
HCN	J_{CH}		283.5[f]	258.9[f]	245.78	242.12			267.3[e]
	J_{CN}	−119.7	−17.2	−19.8	−18.19	−17.90			−18.5[e]

[a]Taken from Ref. 183.
[b]Taken from Ref. 143.
[c]Taken from Ref. 164.
[d]Cited in Ref. 164.
[e]Cited in Ref. 143.
[f]Taken from Ref. 238.

those studies are compiled in Table 12. For example, CCSD, CCSD(T), and CC3 results are taken from Ref. 143; HF-SCF, MCSCF, and DFT-B3LYP results, together with the experimental data cited therein, from Refs. 183 and 238; while SOPPA and SOPPA(CCSD) results are retrieved from Ref. 164.

Apparently, the obvious unreliability of the HF-SCF results to reproduce experiment (which is most illustrative in the case of J_{CN} in HCN) is not surprising. It is well known and well documented (see, e.g., review 3 and references given therein) that ignoring correlation effects dramatically overestimates FC contribution of spin–spin coupling constant. It is noteworthy that the DFT-B3LYP method essentially underestimates J_{HF} in HF while the wavefunction-based methods perform much better (see Section 3.6).

Many authors[164,183,188,202,238,306,307] focused their efforts on the study of the basis set effect upon the accuracy of J_{XY} calculations in this series (see also Section 3.2.2). For example, in the MCSCF study of J_{HF} in the most popular HF molecule by Åstrand et al.,[306] it was found that the basis set convergence was particularly slow. The uncontracted ANO and the aug-cc-pCV5Z basis sets gave the same result to within a few Herz. However, the addition of diffuse functions to the ANO basis changed this coupling by several Herz. As expected, the largest basis set effects were found for the FC term, although substantial changes were also observed for the PSO and SD contributions. The contraction of the ANO basis resulted in the dramatic changes in the FC term, which was related to the sensitivity of the FC term to the electron distribution at the coupling nuclei. To investigate the FC term in more detail, basis functions with large negative exponents were added to the primitive ANO basis, forming a geometric series. To converge the coupling constant to within a few tenths of a Herz, an extension of the primitive ANO basis set with three s-functions at the fluorine atom and five s-functions at the hydrogen atom was required. The effect of these extra s-functions was, as large as 22.6 Hz (!). Both the uncontracted ANO basis

and the aug-cc-pCV5Z basis were therefore more than 20 Hz off the estimated basis set limit, a change that was about as large as the experimental error.

In much the same way, in the concurrent MCSCF study of the basis set convergence in the J_{HF} calculations in HF, San Fabian et al.[307] also found that the FC contribution was greatly influenced by the basis set and electron correlation effects. Apparently, accurate FC contributions must be obtained with the large basis sets including tight s-functions and contracted specifically (or fully decontracted). The noncontact contributions and especially the PSO term (which is very important in the HF molecule) are also affected by the basis set quality.

4.1.2. Small molecules and ions

In addition to the six first- and second-row di- and triatomics, HD, HF, CO, N_2, H_2O, and HCN, discussed in the preceding section, a number of J_{XY} in small light inorganic molecules (including up to the third-row elements) were investigated at different levels of theory. Among those are NH_3,[182–184,188,238,310] CH_4,[164,182,183,188,238,310] HCl,[310,312] H_2S,[309,310] F_2, Cl_2, ClF, SiH_4, PH_3,[310] LiH, LiF, NaF, and ClF,[312] ClF_3, PF_3, and PF_5[225] (the latter three are discussed in Section 3.2.4). Basic results of these studies are very much the same with those reached at in the series of the title di- and triatomics. Namely, the correlation effects are vital, relativistic and rovibrational effects are small in most cases, basis sets used in the calculations of J_{XY} should be large, uncontracted, and flexible in both the inner and the outer parts and should be augmented with tight s-functions accounting for the correlation effects of inner electrons, which is crucial for the FC contribution. However, no improvements of the basis sets could account for the electron correlation effects, which should be treated at the appropriate level of theory.

The absolute values of $^1J_{SiH}$ couplings in the series SiH_nCl_{4-n} ($n = 1$–4) were studied both experimentally (in THF-d_8) and theoretically by Thorshaug et al.[313] $|^1J_{SiH}|$ increases with n, the number of chlorine atoms bonded to Si. These authors observed that the Cl substituent effects were different from those measured in cyclohexane-d_{12} solutions, trend that, according to their DFT calculations, originate in the formation of complexes between solute and solvent molecules.

Wrackmeyer[314] reported the CP-DFT-B3LYP calculations of the FC, PSO, and SD terms of $^1J_{PC}$ couplings in a set of 12 λ^3-phosphaalkynes, and presented an interesting comparison of each component with $^1J_{^{14}N^{13}C}$ calculated in the corresponding nitriles. In both series of compounds, total calculated couplings are in good agreement with the respective experimental couplings. The SD and PSO terms are notably more important for the phosphaalkynes than for the nitriles. In the former compounds the FC terms are negative, while in the latter they are positive. This change in sign was predicted years ago applying the CLOPPA approach,[80] and it was ascribed mainly to the larger s-character of the nonbonding electron pair of the P atom as compared to N.

$$X-C\equiv\!\!\equiv P \qquad\qquad X-C\equiv\!\!\equiv N$$

phosphaalkynes   nitriles
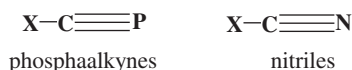
Sauer *et al.*[315,316] performed SOPPA and SOPPA(CCSD) calculations of J_{XH} (X = B, N, O) and $^2J_{HH}$ in four small-charged systems, BH_4^-, NH_4^+, OH^-, and H_3O^+. The effects of nuclear motion were investigated by calculating state effective average values. It was found that strong inversional dependence of $^1J_{OH}$ and $^2J_{HH}$ in H_3O^+ resulted in the pronounced and nonmonotonic variation of the average values with the vibrational state. This was in particular the case for the *geminal* coupling constant $^2J_{HH}$. The effects of nuclear motion in H_3O^+ were thus quite different from what was observed for H_2O and OH^-. It was also found that in H_3O^+ both coupling constants, $^1J_{OH}$ and $^2J_{HH}$, were geometry dependent and thus the vibrational effects were larger than for the nuclear magnetic shielding constants. A linear temperature dependence of J_{OH} was observed for OH^- with almost the same coefficient as in H_2O, whereas the temperature effects in H_3O^+ were found to be quite nonlinear and much larger than those in the neutral H_2O molecule.

4.1.3. *Molecules with heavy atoms*

Enevoldsen *et al.*[26] performed fully relativistic four-component RPA calculations of the indirect one-bond spin–spin coupling constants $^1J_{MH}$ in the group IV tetrahydrides MH_4 (M = C, Si, Ge, Sn, Pb) and also $Pb(CH_3)_3H$ using the uncontracted Dunning's correlation-consistent basis sets augmented with polarization and tight s-functions. Large relativistic effects were found not only for the couplings *involving* the heavy atom itself but also for the *geminal* proton–proton couplings *through* the heavy atom (see also Section 3.7). Even for silane, a compound with a third row atom, the relativistic increase in $^1J_{SiH}$ is as large as *ca.* 10%. Accordingly, in GeH_4 a relativistic increase in $^1J_{GeH}$ is 12%, while for $^1J_{PbH}$ in PbH_4 the effect is as large as 156% (at uncorrelated level). Large relativistic effects on the one-bond couplings involving heavy atoms in this series were found mainly due to the scalar relativistic factors rather than spin–orbit corrections.

A very detailed study of $^1J_{MH}$ (M = Si, Pb) and corresponding $^2J_{HH}$ in silane, SiH_4, and plumbane, PbH_4, was also performed by Sauer and colleagues[317,318] at the correlated nonrelativistic SOPPA(CCSD) level using very large basis sets. In silane,[317] a total of 78 different geometries corresponding to 133 distinct points on the $^1J_{SiH}$ surface and 177 distinct points on the $^2J_{HH}$ surface were calculated. The results were fitted to fourth order in Taylor series expansions and presented to second order in the coordinates. Both couplings, $^1J_{SiH}$ and $^2J_{HH}$, were found to be sensitive to geometry changes over a wide range of temperatures. For $^1J_{SiH}$, both stretching and bending contribute to the nuclear motion effects with the former being considerably larger. The rovibrationally averaged calculated value of $^1J_{SiH} = -199.9$ Hz at 298 K is in an excellent agreement with the experimental value of -201.3 (± 0.4) Hz measured in the same work.[317]

In plumbane,[318] $^1J_{PbH}$ and $^2J_{HH}$ were calculated at the RPA and correlated SOPPA, SOPPA(CCSD), CAS, and RAS levels. Correlation does not change the importance of the individual contributions, although the FC term is reduced by about 20%, thus resulting in the substantially reduced total values of $^1J_{PbH}$ calculated at one of the correlated levels (*ca.* 1,400 Hz) as compared to the RPA results

(*ca.* 1,600 Hz). The marked difference between SOPPA and SOPPA(CCSD) results (1,444 and 1,368 Hz, respectively) is unexpectedly large and seems to be the result of the nonrelativistic level applied to the heavy atom system. The spin-orbit correction, here approximated by the one-electron part of the FC/OP cross-term, is the second most important contribution to the $^1J_{PbH}$ coupling and amounts to 10% of the FC term at the relativistic RPA level. However, total scalar relativistic effects cannot be estimated from these results without a four-component relativistic linear-response calculation, as presented elsewhere.[26]

Spin–spin coupling **J**-tensors in the interhalogen diatomics, F_2, Cl_2, Br_2, I_2, ClF, BrF, IF, ClBr, ClI, and BrI, have been calculated by Bryce *et al.*[319] at the ZORA-DFT level accounting for the spin-orbit relativistic corrections. It was found that the magnitudes of the isotropic coupling constants together with their anisotropies increased linearly with the product of the atomic numbers of the coupling nuclei. The relative importance of the various coupling mechanisms was found to be approximately constant for all of the compounds, with the PSO term being the dominant and contributing, *ca.* 70–80% to the total values of the isotropic coupling constants. This result clearly emphasizes some caveats of interpreting the **J**-tensors. The importance of the spin–orbit relativistic correction increases with the atomic number, and essentially improves the calculated value of the isotropic coupling constants above and beyond the scalar relativistic values that strongly emphasizes the necessity of the spin–orbit relativistic corrections for the calculations of **J**-tensors involving heavy nuclei.

In a previous study, Autschbach and Ziegler[320] performed the ZORA-DFT calculations of spin–spin couplings and their anisotropies for some plumbanes, PbH_4, $PbMe_2H_2$, and $PbMe_3H$, interhalogen diatomics, XF (X═Cl, Br, I), and thallium halides, TlX (X═F, Cl, Br, I). One-bond coupling constants for plumbanes including spin–orbit coupling were found to be in a better agreement with experiment than the scalar relativistic ones, since the strong scalar relativistic increase of the generalized FC contribution was partially canceled by the spin-orbit corrections, while in the XF series, the spin-dipole term contributed largely to the coupling constants and spin-orbit effects were essential for the J_{TlX} couplings. All coupling constants involving heavy atoms were found to be very sensitive to relativistic effects in this series. The sign and order of magnitude of the individual terms in the coupling constant of ClF were in good agreement with the correlated *ab initio* results.[320] Spin-orbit effects were essential to obtain reasonable coupling constants J_{TlX} for the TlX (X═F, Cl, Br, I) systems. Basically, results by Autschbach and Ziegler[320] showed that scalar relativistic calculations may lead to completely wrong values of spin–spin couplings in cases where heavy elements are involved and both the FC and the PSO contributions are already large at the nonrelativistic limit.

Varga *et al.*[321] performed the four-component calculations of the potential energy curves in the series of the heavy closed-shell diatomic molecules, Cu_2, Ag_2, Au_2, Tl_2, Pb_2, Bi_2, and Pt_2, in the framework of the relativistic DFT using local- and gradient-corrected density functional schemes. Spin–spin couplings have not been calculated in this study, although the four-component calculations of the potential energy curves revealed the importance of the relativistic effects in this series.

Not only does the spin-orbit coupling split the single-particle energies but the radial parts of the large and small components of the four spinors also showed an increasingly different radial and angular behavior, which in turn influences the other wave functions due to the self-consistent effects. Apparently, these effects are to be taken into account in the calculations of any second-order properties like spin–spin couplings in this series and related heavy diatomics.

Åstrand et al.[322] performed a systematic study of solvent effects on $^1J_{SeH}$ and $^2J_{HH}$ in hydrogen selenide (H_2Se), by modeling the surroundings as a continuous dielectric medium for a number of solvents. The introduction of a dielectric medium improved the agreement with experiment for the $^2J_{HH}$ coupling constant, whereas it got worse in the case of $^1J_{SeH}$. However, in the latter discouraging case, this may be an artifact caused by the neglect of the relativistic effects being of crucial importance for couplings involving heavy atoms.

The anisotropies of the $\mathbf{J}_{CSe}$ and $\mathbf{J}_{SeSe}$ spin–spin coupling tensors in carbon diselenide (CSe_2) were derived from the ZORA-DFT calculations and from NMR experiments performed in liquid crystalline solutions.[210] The computed coupling tensor anisotropies appeared to be ca. 20% larger than the respective experimental ones derived from their NMR measurements. However, the deviation between the computed and experimental results for the ratio $\Delta\mathbf{J}_{CSe}/\mathbf{J}_{CSe}$ was less than 4%.

Autschbach et al.[323] reported their ZORA-DFT results for the $^1J_{HgHg}$ couplings in Hg_2Cl_2, $Hg_2(CN)_2$, Hg_2^{2+} and Hg_3^{2+}. It was demonstrated that even subtle effects on the Hg–Hg bond due to the environment of the metal–metal fragments could result in drastic changes of $^1J_{HgHg}$. It was found that two effects had to be considered when analyzing the magnitude of $^1J_{HgHg}$: (i) coordination, i.e., the formation of more or less strong bond between the metal atoms and surrounding ligands, solvent molecules, or counterions, and (ii) polarization of the metal–metal fragment due to different coordinating ligands. Both effects tend to reduce $^1J_{HgHg}$ in Hg_2^{2+}. For Hg_3^{2+}, it was shown that surrounding solvent molecules decrease both $^1J_{HgHg}$ considerably, through a preferred coordination of the terminal mercuries.

Again, Autschbach and Ziegler[324] reported relativistically and nonrelativistically computed $^1J_{HgC}$ spin–spin coupling constants for the unsolvated HgMeX (X = Me, Cl, Br, I) and $Hg(CN)_2$. It was demonstrated that solvent effects on $^1J_{HgC}$ could be very substantial. The DFT computations of a number of solvated species yielded reasonable agreement with experimental data obtained from solution. It was shown that charge donation by the solvent to the coordinated heavy atom played an important role for the large increase of the FC contribution to $^1J_{HgC}$. Spin-orbit effects as well as the influence of the spin–dipole term turned out to be rather small as compared to the scalar relativistic and solvent effects on the FC contribution.

Bagno and Bonchio[173] studied at the ZORA-DFT level the structural dependence of $^2J_{WW}$ couplings in polyoxotungstenates. Bagno et al.,[303] using also the ZORA-DFT level, calculated coupling constants in stannane, tetramethylstannane, methyltin halides $Me_{4-n}SnX_n$ (X = Cl, Br, I; n = 1−3), tin halides and some stannyl cations. Coupling constants between tin and halogen nuclei, $^1J_{SnX}$, were reasonably well reproduced, and contributions from the relativistic spin-orbit effects were quite evident. On the other hand, for J_{SnC} and J_{SnH} couplings in alkylstannanes, the

chosen approach shows a somewhat poor performance, resulting in significant deviations from the experimental values.

Forgeron et al.[325] studied $^1J_{129_{XeF}}$ coupling constant in xenon difluoride. Experimentally, they obtained the isotropic value of $^1J_{129_{XeF}} = (-5{,}560 \pm 50)$ Hz and the anisotropy of the corresponding tensor, $\Delta^1J_{129_{XeF}} = +2{,}370$ Hz with an error of ± 1.8 KHz from the solid-sate spectrum. According to the earlier ZORA-DFT calculations, $^1J_{129_{XeF}} = -6{,}030$ Hz and $\Delta^1J_{129_{XeF}} = +4{,}048$ Hz,[326] and $^1J_{129_{XeF}} = -5{,}958$ Hz.[214]

4.1.4. Inorganic and metal complexes

One of the first and most comprehensive DFT study of spin–spin couplings involving heavy metal nuclei in the metal complexes was that of Khandogin and Ziegler[327] who reported their extensive DFT calculations of the one-bond metal-ligand spin–spin coupling constants in 3d-, 4d-, and 5d-transition-metal complexes, namely $^1J_{MC}$ (M = V, Fe, Co, Nb, Mo, Rh, W) in the transition-metal carbonyls, $V(CO)_6^-$, $Fe(CO)_5$, $Co(CO)_4^-$, $Nb(CO)_6^-$, $Mo(CO)_6$, $Rh(CO)_4^-$, $W(CO)_6$; $^1J_{MO}$ (M = V, Cr, Mn, Mo, Tc) in the transition-metal oxo complexes, VO_4^{3-} CrO_4^{2-} MnO_4^-, MoO_4^{2-} TcO_4^-, and $^1J_{MF}$ (M = Sc, Ti, V, Nb, W) in the transition-metal hexafluoro complexes, ScF_6^{3-} TiF_6^{2-} VF_6^-, NbF_6^-, WF_6. Calculated coupling constants for the 3d complexes were in good agreement with experiment whereas theoretical estimates for the 4d- and 5d complexes were consistently smaller than the experimental values, especially without the inclusion of relativistic effects. Based on the MO analysis,[65] it was shown that the dominant FC coupling contribution was a valence property with the core orbitals playing only a minor role. Through a similar MO analysis, it was concluded that the LP orbitals hardly contributed to the PSO coupling term (see also Section 3.6). Coupling constants calculated by a nonrelativistic approach were too small for the 4d- and especially 5d-transition-metal complexes. The inclusion of relativistic effects brought the calculated values into better agreement with available experiment by increasing the coupling constants from 20% for the 4d complexes to 50% for the 5d complexes.

Later, Autschbach, Ziegler, and coworkers[255,328–330] reported the ZORA-DFT results for the metal–ligand and metal–metal couplings in a number of metal complexes, including platinum–thallium cyanides,[255,328] dinuclear platinum carbonyls and chlorides,[329] and platinum ammine and phosphine complexes together with some main group element hydrides, cyanides, and alkyl complexes.[330]

In platinum–thallium cyanides $[(NC)_5Pt–Tl(CN_n)]^{n-}$ (n = 0−3) and $[(NC)_5Pt–Tl–Pt(CN)_5]^{3-}$ it was demonstrated that the whole experimental trend of J_{PtTl} were due to the solvent effects. In particular, the combination of relativistic effects and a solvent-induced positive shift of the couplings explains why $^1J_{PtTl}$ is so large and why $^2J_{TlC} > {}^1J_{TlC}$ as observed experimentally[255,328] (see also Section 3.3.5).

In dinuclear platinum complexes $[Pt_2(CO)_6]^{2+}$ and $[Pt_2(CO)_2Cl_4]^{2-}$ experimental trends of $^1J_{PtPt}$ are well reproduced by the ZORA-DFT calculations and can be explained based on the nature of the ligands coordinated to the Pt–Pt fragment. The changes of $^1J_{PtPt}$ are caused by the interplay between the influence of different

ligands on the Pt–Pt bond, and relativistic effects on the metal–metal and metal–ligand bonds. In particular, σ-interaction with the CO ligands in axial position is responsible for the reduction of $^1J_{PtPt}$. Owing to the more pronounced σ-bonding capability of Pt in the relativistic case, the expected large magnitude of the FC contribution to $^1J_{PtPt}$ is compensated by the increasing σ-interaction with the axial CO ligands. Thus, it follows that the $^1J_{PtPt}$ coupling constant for a bare metal–metal fragment is reduced upon the coordination of this fragment in case of a strong platinum–ligand σ-interaction.[329]

In platinum ammine and phosphine complexes $[Pt(NH_3)_4]^{2+}$, $Pt(PF_3)_4$, *cis* and *trans* $PtCl_2(NH_3)_2$, $PtCl_2(PMe_3)_2$, $PtH_2(PMe_3)_2$, and $PtCl_4(PEt_3)_2$, although the metal–ligand bond distance and angles influence the magnitude of $^1J_{PtP}$ and $^1J_{PtN}$, the major factor that gives rise to the difference between the *cis* and *trans* configuration is of electronic nature. This can be attributed to the change in the overlap population between the metal s- and ligand σ-orbitals under the influence of a *trans* ligand, which is caused by the polarization of the antibonding virtual orbital on the occupied trans σ-bonds. The relativistic correction of the s-orbital value at the heavy nucleus platinum in the evaluation of the FC contribution gives significant improvement. It is also able to satisfactorily describe the bulk of the relativistic increase for couplings to platinum, $^1J_{PtP}$ and $^1J_{PtN}$, and reproduce the experimental trends in different ligand environment due to the relativistic effects which are accounted for the s-orbital contraction, together with the predominant relativistic effect on the contact-type nuclear spin–spin interactions.[330]

In the early DFT study, Hush[331] examined the behavior of J_{HD} coupling in the closed-shell "eighteen electron" molecular hydrogen complexes of the type $[Os(II)(NH_3)_4L(\eta^2-H_2)]$ for a wide range of *trans*-ligands L and established an essentially identical linear relationship between the J_{HD} spin–spin coupling and the corresponding internuclear separation r_{HH}. The same trend was also observed experimentally for a series of related complexes of Fe, Cr, Ru, and Os, also containing a variety of ligands. At this point it is important to recall that the difference between the dihydrogen and dihydride complexes is based only on the H–H (or H–D) distance (see Section 2.3). For distances ranging from 0.8 to 1.0 Å, i.e., not much longer than the bondlength in an isolated H_2 molecule, the complex is referred to as a dihydrogen complex. On the other hand, for the H–H distance longer than *ca.* 1.5 Å, the complex is referred to as a dihydride one.[332] Recently, Gelabert *et al.*[333] classified this type of complexes according to the position of the main minimum on the potential energy surface. If this position corresponds to the H–H distance within the "dihydrogen" region, then it is called a "compressed dihydride" complex. If it falls within the dihydride region, then it is called an "elongated" or "stretched" dihydrogen complex.[334] It is noteworthy that compressed and elongated dihydrogen complexes show a different temperature dependence of their $^1J_{HD}$ couplings.

In order to study from a theoretical point of view the temperature dependence of the J_{HD} coupling for the compressed dihydride complex $[Cp^*Ir(dmpm)H_2]^{2+}$, where dmpm stands for bis(dimethylphosphino)methane, Gelabert *et al.*[335] calculated at the DFT-B3LYP level a complete 2D surface of the J_{HD} coupling as a function of the geometry of the Ir–H_2 moiety. These results were used to calculate

both the vibrational averaged value and the temperature dependence of $^1J_{HD}$ reproducing almost quantitatively experimental temperature dependence of that coupling. Mort and Autschbach[336] studied both the ZPV correction and the temperature dependence of J_{HD} couplings in six transition metal hydride and dihydrogen complexes.

Le Guennic et al.[337] performed ZORA-DFT calculations of $^1J_{HD}$ couplings in dihydrogen and dihydride complexes containing heavy metal atoms. They analyzed the role of the geometry, relativistic spin-orbit contributions, and gradient corrections in the functional exchange–correlation kernel. The latter yielded an overestimation of $^1J_{HH}$ in the H_2 molecule by ca. 30%. As a result, for complexes with short H–D distances, a similar overestimation is observed. On the other hand, these factors are very important for longer H–D distances, and they should be taken into account to describe correctly the $^1J_{HD}$ sign in complexes with the longest H–D distances. It is important to stress that several J_{HD} couplings with small absolute values (0–1 Hz) are negative (see also Ref. 338). Le Gennic et al.[337] also discussed the importance of the geometry optimization for obtaining reasonable coupling constants at the ZORA-DFT level. For short H–D distances the FC term of $^1J_{HD}$ dominates, while for longer distances all four coupling contributions can be important. With respect to the relativistic spin–orbit contribution in the heavy metal complexes, this correction is required to obtain the correct magnitudes of small $^1J_{HD}$ couplings. However, vibrational corrections should be included as well.[337]

Dubberley et al.[339] performed the DFT calculations of J_{SiH} in a series of silylhydrido complexes of thallium, $Cp(ArN)Ta(PMe_3)(H)(SiR_3)$, with the nonclassical M–H···Si–X interligand hypervalent interactions. A correlation between the magnitude of J_{SiH} values and the identity of the substituent X opposite to that in silane σ-complexes was observed. Thus, the increase in J_{SiH} was not paralleled by the strengthening of the interligand interaction. Other factors, such as increase of the through-two-bond Si–Ta–H magnetic interactions due to the increase in silicon 3 s character in the Ta–Si bond, should be considered to account for this behavior. A reverse correlation between the number of the electron-withdrawing substituents at silicon and the silicon hydride coupling constants in the transition metal silyl hydride complexes was established. Contrarily to expectation, it was shown that increase in the magnitude of J_{SiH} does not necessarily correspond to a stronger bonding interaction between ligands.

Bryce and Wasylishen[340] examined the structure of silver cyanide, AgCN, by the solid-state multinuclear NMR spectroscopy and related ZORA-DFT calculations of δ_C and $^1J_{AgC}$ tensors that provided the evidence for the linearity of the polymeric $(-Ag-CN-)_n$ chains. It was shown that $30 \pm 10\%$ of the silver sites were disordered, i.e., either –NC–Ag–CN– or –CN–Ag–NC–, and $70 \pm 10\%$ of the silver sites were ordered, i.e., –NC–Ag–NC–. Effective dipolar coupling data extracted from the ^{13}C NMR spectra of stationary samples allowed an upper limit of 1.194 Å to be placed on the carbon–nitrogen internuclear distance, r_{CN}. After incorporation of the effects of the anisotropy of the indirect nuclear spin–spin coupling and motional averaging on the NMR-derived distance, a corrected value of $r_{CN} = (1.16 \pm 0.03)$ Å was obtained.

Relativistic ZORA-DFT calculations of the one-bond metal–ligand couplings in the complexes containing ^{183}W, ^{195}Pt, ^{199}Hg, and ^{207}Pb by Autschbach and Ziegler[297] showed that scalar relativistic calculations were able to reproduce the major parts of the relativistic effects on coupling constants, which could be even larger in magnitude than the respective total nonrelativistic values. The spatial origin of the regular approximate relativistic analog of the FC contribution, which is usually responsible for the strong relativistic increase of the couplings, was analyzed in this paper, and it was shown that relativistic effects could be described by the relativistic increase of the valence orbital density in the very vicinity of the heavy nucleus.

Bagno and Bonchio[341] performed ZORA-DFT spin–orbit calculations of different spin–spin couplings involving ^{99}Ru nucleus in four ruthenium complexes, in reasonably good agreement with experiment, namely, $^1J_{RuC} = -43.5\,Hz$ in $[Ru(CN)_6]^{4-}$ (Exp.: (−)44.8 Hz[342]), $^1J_{RuO} = 41.9\,Hz$ in $[Ru(H_2O)_6]^{2+}$ (No experiment available), $^1J_{RuSn} = 690\,Hz$ in $[Ru(SnCl_3)_5Cl]^{4-}$ (Exp.: 846 Hz[342]), and $^1J_{RuO} = 12.1\,Hz$ in RuO_4 (Exp.: 23.4 Hz[342]). Whereas the $^1J_{RuC}$ in $[Ru(CN)_6]^{4-}$ is reproduced to within 3%, the accuracy of $^1J_{RuO}$ in RuO_4 and $^1J_{RuSn}$ in $[Ru(SnCl_3)_5Cl]^{4-}$ is substantially worse. This result seems to indicate that the coupling involving the electron-rich atom, oxygen, is not well accounted for within the DFT framework (see Section 3.6). No general conclusions about the reliability of the ZORA-DFT spin-orbit calculations of spin–spin couplings involving ^{99}Ru nucleus could be achieved at this stage besides the encouraging one that, at least, the correct order of magnitude could be achieved at the level chosen by Bagno and Bonchio.[341]

One cannot but mention the early comprehensive DFT study by Onak *et al.*[343] of one-bond, *geminal*, *vicinal* and *longer range* $^nJ_{BH}$ and $^nJ_{CH}$ ($n = 1-4$) coupling in a series of 25 representative polyhedral carboranes and boron hydrides. The calculated results (only the FC contribution was taken into account) were in good agreement with the solution experimental data for a wide range of $^nJ_{BH}$ and $^nJ_{CH}$ The largest disparities were observed for the one-bond $^1J_{BH}$ and $^1J_{CH}$ couplings larger than 120 Hz. These were underestimated on average by about 5%, a value close to that expected from the effects of the nuclear motion averaging. The accurate prediction of a number of $^nJ_{BH}$ and $^nJ_{CH}$ in polyhedral boron compounds proved to be extremely helpful in their NMR spectral analyses that have essential experimental difficulties connected with the occurrence of numerous chemically equivalent but magnetically nonequivalent boron nuclei in the carborane frameworks.

Wrackmeyer[344] calculated at the DFT-B3LYP/6-311+G(d,p) level of theory $^1J_{CH}$, $^1J_{BH}$, J_{CC}, and J_{CB} couplings in cyclic C_4H_2 and C_4H_4 molecules containing carbene centers and in their boron analoga. It is important to note that several of the J_{CC} couplings considered are dominated by the noncontact SD and PSO terms (which is very unusual for the J_{CC} couplings). Wrackmeyer and Berndt[345] calculated, at the same level, $^1J_{CB}$, and $^1J_{SiC}$ in 1,2-diborane-3-ylidene, a compound with a unique bonding situation, and in other related model compounds. For the first time they reported a calculated negative $^1J_{CB}$ coupling. Also at the same level of theory, Wrackmeyer[346] calculated $^nJ_{BH}$ and $^nJ_{BB}$ couplings in 17 neutral and anionic boron hydrides. In most of the cases, where a comparison with experimental data

was possible, a good agreement between calculated and measured couplings was found.

Wrackmeyer and Schanz[347] studied both experimentally and theoretically the deprotonation and the complexation of hexaethyl-2,4-dicarba-*nido*-hexaborane. The geometries of some of the carboranes, borates, and iron complexes were optimized within the DFT-B3LYP approach, and several relevant couplings, $^1J_{CH}$, $^1J_{BH}$, $^1J_{FeH}$, and $^1J_{FeB}$, were calculated at the same level of theory. These couplings were discussed in terms of their structural trends.

Wrackmeyer[348] has also calculated within the DFT-B3LYP approach the $^1J_{BH}$, $^1J_{CH}$, $^1J_{BB}$, $^1J_{CB}$, and $^1J_{CC}$ couplings in five-, six-, and seven-vertex dicarboranes, monocarboborane anions, and boranes dianions with the *closo* structures. In general, calculated couplings were in good agreement with the available experimental values. Also, Bakardjiev *et al.*[349] isolated several *nido*-di- and triphosphacarboranes and performed $^1J_{PC}$, $^1J_{PP}$, and $^2J_{P(C)H}$ coupling calculations at the DFT-B3LYP/6-311 + G(d,p) level for three 11-vertex *nido* compounds, 7,8,9-P$_2$CB$_8$H$_{10}$, 7,8,9,10-P$_3$CB$_7$H$_8$, and [7,8,9-P2CB8H9]$^-$, in reasonable agreement with the experimental values reported in the same paper. Recently, Del Bene *et al.*[350] reported the calculations of F and Li substituent effects on $^1J_{NB}$ couplings in a series of substituted borazines.

4.2. Organic compounds

4.2.1. *Benchmark calculations and illustrative examples*

Spin–spin couplings of different types calculated at different levels of theory in four benchmark hydrocarbons with the sp^3, sp^2, and sp hybridizations of carbon atoms, methane, ethylene, allene, and acetylene, are compiled in Table 13. These data are extracted from Refs. 183, 238, and 239, and all original references (including both theoretical and experimental) can be found therein, except for the ultrahigh-accuracy experimental data for acetylene in dilute gaseous solution measured by Jackowski *et al.*[244] The wavefunction-based methods give much better results for $^1J_{CC}$ and $^1J_{CH}$ in acetylene as compared to DFT, while both levels of theory are of the same reliability for the rest of couplings in the benchmark series. On the other hand, the uncorrelated HF-SCF level is absolutely inappropriate for the calculation of spin–spin couplings. This is particularly true for the molecules with the HF-ground state wavefunction affected either by instability or quasi-instability of the nonsinglet type.[3] When this condition, frequently found in unsaturated compounds, is present, both the FC and SD contributions calculated at the CP-SCF level (usually known as CHF, which is also equivalent to the RPA approximation) lack any physical meaning. However, it is important to note that for compounds not affected by the instability or quasi-instability of their HF-ground state, many experimental trends can be qualitatively reproduced when couplings are calculated at the RPA level.

Pecul and Helgaker[351] performed a systematic comparison of the DFT and *ab initio* MCSCF and CCSD results of the calculation of the spin–spin couplings

Table 13. Coupling constants (in Hz) in the benchmark hydrocarbons calculated by different methods in comparison with experiment[a]

Molecule	$^nJ_{XY}$	B3LYP	CAS	RAS	CCSD	SOPPA (CCSD)	Exp.
CH$_4$	$^1J_{CH}$	132.2	116.7	121.9		122.3	120.9
	$^2J_{HH}$	−13.3	−13.2	−13.6		−14.0	−12.0
	$^1J_{CC}$	72.4	75.7	69.5	70.1	70.1	67.5
	$^1J_{CH}$	166.7	155.7	154.0	153.2	157.2	156.3
H$_2$C=CH$_2$	$^2J_{CH}$	−1.5	−5.8	−3.0	−3.0	−3.1	−2.4
	$^2J_{HH}$	3.8	−2.4	1.3	0.4	1.0	2.4
	$^3J_{HH}(c)$	13.0	12.4	11.6	11.6	17.8	11.7
	$^3J_{HH}(t)$	20.0	18.4	18.5	17.8	24.7	19.0
	$^1J_{CC}$	108.8		116.5	102.9	107.5[b]	98.7
	$^1J_{CH}$	175.4		178.2	161.3	174.1[b]	167.8
H$_2$C=C=CH$_2$	$^2J_{CH}$	−3.4		−13.2	−4.9	−8.4[b]	−3.9
	$^3J_{CH}$	7.7		13.3	7.3	10.1[b]	7.7
	$^4J_{HH}$	−9.1		−14.4	−8.5	−11.5[b]	−7.1
HC≡CH	$^1J_{CC}$	204.9	187.7	182.6	166.2	190.0	174.78[c,d]
	$^1J_{CH}$	274.0	238.5	241.4	226.7	254.9	247.56[c,e]
	$^2J_{CH}$	55.9	47.0	49.2	43.2	51.7	50.14[c,e]
	$^3J_{HH}$	11.0	12.1	12.6	7.6	11.3	9.62[c,e]

[a]Calculated couplings are taken from Refs. 183, 238, and 239 together with their experimental values cited therein (if not cited otherwise).
[b]Calculated at the SOPPA level.
[c]Taken from Ref. 244.
[d]±0.02 Hz.
[e]±0.05 Hz.

involving the ^{1}H, ^{13}C, ^{15}N, and ^{17}O nuclei in three benchmark molecules – ethane, methanol, and methylamine, – so as to benchmark the performance of the DFT framework against high-level *ab initio* methods and experimental data. For each molecule, the Karplus curve has been evaluated at the three computational levels. The comparisons with the *ab initio* methods indicated that DFT reproduced the $^1J_{CH}$, $^1J_{CC}$, and $^1J_{NH}$ one-bond couplings well but was less accurate for $^1J_{CN}$, $^1J_{OH}$, and $^1J_{CO}$. While DFT performed well for the *geminal* couplings $^2J_{HH}$ and $^2J_{CH}$, it tended to overestimate the *vicinal* $^3J_{HH}$ couplings. In particular, the analysis of the Karplus-type dependence of $^3J_{HH}$ on the dihedral angle showed that the overestimation of the CCSD values by the DFT ones were *ca.* 15–20% for all three molecules. For most couplings, the discrepancies between the DFT, MCSCF, and CCSD results originated in the dominant FC terms; in some cases relatively large differences were also found for the PSO contributions.

Kawahara *et al.*[352] performed a systematic study on the relationship between *trans*-hydrogen-bond couplings and the hydrogen bond strength. Their coupling calculations included only the FC term and were performed at the

DFT-B3LYP/6-311 + G** level of theory where the FPT was used as the perturbation scheme, while the orbital interactions involved in hydrogen bonds were calculated within the NBO approach.

Del Bene et al.[123] calculated $^1J_{XY}$ in a set of 18 molecules of the type $H_mX–YH_n$ with X, Y = C, N, or P, including ethane, ethylene, acetylene, methylamine, methanimine, hydrogen cyanide, methyl phosphine, methylene phosphine, methylidene phosphine, hydrazine, E-diazene, dinitrogen, phosphinous amide, E-phosphinimine, phosphorous, diphosphine, E-diphosphene, and molecular phosphorus. The respective geometries were optimized within the MP2 approximation, and coupling constants were calculated by the EOM-CCSD method. One of the points considered in that paper was the sign of the reduced $^1K_{XY}$ couplings (see Section 2.5). It is interesting to observe that the predictions of signs of the one-bond couplings given at such high level of ab initio calculations are in line with the trends predicted semiquantitatively by the CLOPPA approach at the semiempirical INDO level.[80]

Cybulski et al.[353] used both the SOPPA as well as DFT-B3LYP approaches to study spin–spin couplings in water clusters of different sizes $(H_2O)_n$, $n = 2−6$, 12, and 17. They carried out a careful search for the possibly smallest and most flexible basis set, and performed a detailed analysis of the effects of complex formation on the different coupling constants.

Holzer et al.[354] studied the possibility of using the geminal $^2J_{C_4,H_{3(5)}}$ constants of the pyrazole ring as a probe to diagnose the tautomerism in pyrazolones. Their experimental measurements of $^2J_{CH}$ were accompanied with the CP-DFT-B3LYP calculations in 11 compounds showing that $^2J_{C_4,H_3}$ couplings have a positive sign and that the adjacent LP makes an important contribution (see also Section 2.3). In a subsequent paper, Claramunt et al.[355] studied different coupling constants in a set of eight N-R-pyrazole derivatives. The total CP-DFT-B3LYP calculated couplings in N-phenylpyrazole and other pyrazole derivatives were obtained with four different basis sets, namely 6-311 + +G**, 6-311G, 6-311G**, and cc-pVTZ. They employed the first of these four basis sets to perform coupling calculations in the other pyrazole derivatives and found a very good agreement between experimental and calculated couplings with the exception of $^1J_{CC}$, although calculated values correlated linearly with the corresponding experimental values.

The concept of the resonance-assisted hydrogen bonds was investigated by Alkorta et al.[356,357] calculating both the $^{2h}J_{NN}$ and $^{2h}J_{OO}$ couplings through hydrogen bonds of the type $X···H···X$ (X = N, O) and the corresponding proton chemical shifts. Trans-hydrogen-bond couplings were calculated with the CCSD method, and the latter were calculated at the MP2 level. Alkorta et al.[356,357] did not find any evidence of the influence of the heteroconjugated interactions involving either the proton-donor or the proton-acceptor atoms on any of the trans-hydrogen-bond couplings or chemical shifts of such systems. Such NMR descriptors have values that are only a consequence of the σ-skeleton framework but not of the π-electronic system. Indeed, it follows that the electronic effects on the trans-hydrogen-bond couplings and chemical shifts are transmitted within the σ-skeleton framework being unaffected by changes in the π-electronic system.

When studying conformational transitions of calixphyrin derivatives, Bernárková et al.[358] measured unusual J_{HH} couplings in the pyrrolyl moiety of calixphyrins, which they assigned to the $^4J_{H_NH_3}$ type. To confirm this assignment, they performed the CP-DFT-BPW91/6-31G** calculations of the corresponding $^3J_{H_3H_4}$ and $^4J_{H_1H_3}$ couplings. Experimental values of the former were ca. 4.2 Hz, those of the latter were ca. 3.0 Hz. Calculated couplings correctly reproduced this trend. Several different factors are to be considered to account for the coupling trends in this case. In accord with the multipath coupling mechanism (see Section 2.6), $^4J_{H1H3}$ coupling possesses the four− and five−bond contributions; both of them could have a π-transmitted component, which tend to cancel each other since they must be of opposite sign and similar absolute values. The σ−four-bond coupling pathway corresponds to a W arrangement which favors the σ-transmission of the FC term. On the other hand, the σ–five-bond coupling pathway is expected to be very inefficient in transmitting the FC term.
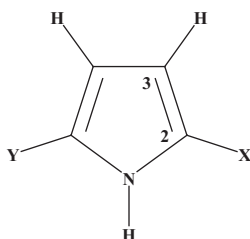
The pyrrolyl moiety of calixphyrins studied by Bernárková et al. [358]

Tähtinen et al.,[359] when performing a conformational analysis of saturated *trans*-fused 1,3,2-benzoxazaphosphinine 2-oxides, studied the performance of DFT, within the ADF software,[224] to calculate $^3J_{PH}$ and $^4J_{PH}$ couplings. It was found that the SD contribution to these couplings is negligible, while the PSO and DSO contributions almost cancel each other. They observed that calculated couplings correlate well with the corresponding experimental values including the FC term of $^3J_{PH}$ couplings in three methyl derivatives of 2-bis(2-chloroethyl)amino-*trans*-octahydro-2H-1,3,2-benzoxazaphosphinine 2-oxide. For these last calculations, they used the Gaussian 98 suite of programs restricted to the FPT-DFT perturbative approach.

Fruchier et al.[270] calculated at the DFT-B3LYP/6-311G** level of theory several couplings involving at least one P atom in cyclotriphosphazenes, although they concentrated mainly on $^2J_{PP}$ couplings in reasonable agreement with experimental values. In the same series, for coupling constants involving at least one fluorine atom, they found a notably worse agreement between experimental and calculated values providing one more example where, apparently, DFT calculations fail to account for couplings involving fluorine (see Section 3.6).

Bagno et al.[360] determined both experimentally and theoretically chemical shifts and J_{HH} and J_{CH} couplings in the following set of organic molecules: furane, *o*-dichlorobenzene, *o*-chlorobromobenzene, 2,3-dichlorophenol, 2,4-dichlorophenol,

2,5-dichlorophenol, 3,4-dichlorophenol, cyclohexane, and *n*-butyl chloride. For the point of view of this review paper, only $^nJ_{CH}$ and $^nJ_{HH}$ couplings will be considered. Although experimental conditions are described, a very important point was omitted, i.e., the solvent used to prepare samples, since, as commented in Section 3.3.5, it could be very important to take it into account for $^1J_{CH}$ couplings. DFT calculations of coupling constants were carried out with two different programs, namely the DeMon-NMR[177,217] and the Gaussian 98. Unfortunately in a study of this type (including unsaturated compounds), they have not taken into account the four Ramsey terms. Within the former program, the SD term is not calculated, and within the latter, only the FC term is calculated using the FPT-DFT approach (see Section 3.2).

The four Ramsey terms of $^1J_{CC}$ couplings in benzene and pyridine calculated at the DFT-B3LYP/EPR-III level[84] are compared in Table 14 with the respective experimental values, taken from Refs. 138, 361, and 362 and Ref. 363, respectively. These calculations were carried out for isolated molecules; in other, it was observed that aromatic $^1J_{CC}$ calculated values considering a polar solution were by *ca.* 1–2 Hz smaller than those for isolated molecules. Therefore, results displayed in Table 14 are considered to be in excellent agreement with the experimental values, which means that the overestimation of $^1J_{CC}$ couplings in aromatic compounds seems to be mainly introduced by the dielectric solvent effects. The PSO and SD terms are of opposite sign, the former being more important. As expected, the smaller contribution comes from the DSO term. In agreement with the respective experimental values, the two $^1J_{CC}$ couplings in pyridine are only slightly smaller than the $^1J_{CC}$ coupling in benzene. The slightly smaller $^1J_{C_2C_3}$ coupling in pyridine than $^1J_{CC}$ in benzene seems to be defined by three competing effects, namely, (i) the *anti*-periplanar orientation of the N LP, (ii) the larger absolute values of the "other-bond contributions" corresponding to the N–C_2 and C_2–H bonds, and (iii) the inductive effect of the nitrogen atom. The latter should increase the FC term of the $^1J_{C_2C_3}$ coupling, while the former two should noticeably decrease it (see Sections 2.3 and 4.2.4).

Table 14. The comparison between calculated (at the DFT-B3LYP//6-311G**/EPR-III level) and experimental $^1J_{CC}$ couplings (in Hz) in benzene (**1**) and pyridine (**2**)[a]

Coupling term	(1)	(2)	
	$^1J_{CC}$	$^1J_{C_2C_3}$	$^1J_{C_3C_4}$
FC	63.73	62.00	61.93
SD	1.30	1.34	1.24
PSO	−7.19	−7.32	−7.31
DSO	0.22	0.24	0.22
Total	57.07	56.26	56.08
Exp.	55.95[b]	54.3[c]	53.7[c]

[a]Calculated values taken from Ref. 84.
[b]Taken from Ref. 138. Other experimental values are, 55.88 Hz (Ref. 361) and 55.87 Hz (Ref. 362).
[c]Taken from Ref. 363.

Kamiénska-Trela and coworkers[364] (see also references cited therein) continued studying the dramatic fluorine and lithium substituent effects on $^1J_{CC}$ couplings by measuring and performing DFT calculations in 2- and 3-fluorosubstituted derivatives of thiophene, pyrrole, and furan.[365] Unfortunately, in these unsaturated compounds, they only considered the FC, PSO, and DSO terms. However, it is expected that the SD term (in absolute value) should be notably more important than the DSO term. However, their calculations reflected correctly the observed trends of $^1J_{CC}$ couplings involving any of the carbon atoms placed α to the F atom.

The good accuracy achieved at present for calculating high-resolution NMR parameters within the DFT framework prompted several researchers to predict the general aspect that the NMR spectrum of a given organic compound should show. For instance, Bassarello et al.[366] calculated the proton and carbon chemical shifts together with all homo- and heteronuclear coupling constants of ethyl ether of the exo-2-norbornanecarbamic acid to predict the 2D ^1H-^1H COSY, 2D ^1H-^{13}C HSQC, and 2D ^1H-^{13}C HMBC spectra of this compound in fairly good agreement with experiment. Plaza et al.[367] used a combination of the experimental ^1H and ^{13}C NMR spectra with the DFT calculations of the ^1H and ^{13}C chemical shifts and J_{HH} couplings, including all four Ramsey terms of several natural pregnane glycoside products to study their structural and conformational behavior. Bifulco et al.[368] presented an approach which relies on the DFT-calculated J_{HH} and J_{CH} coupling constants used for the assignment of the relative configurations of the chiral organic compounds, which is most important for the carbon frameworks containing several adjacent stereogenic centers.

During the review period, some interesting considerations on the Karplus equation were published. For instance, Provasi et al.[369] analyzed, within the CLOPPA approach,[80] the dihedral angle dependence of the FC term contribution to vicinal couplings taking into account several types of coupling nuclei. From their analysis, they reached a conclusion that the electronic mechanism underlying the Karplus equation is hyperconjugation. However, it is important to recall that Provasi et al.[369] used this term in a somewhat generalized form; they even coined the expressions "first and second kind hyperconjugations," the former corresponding to the commonly known hyperconjugative interactions, while the latter is related to the probability amplitude that two electrons be delocalized simultaneously from two occupied to two vacant MOs (see Section 2.4).

The influence of the chain elongation in polyacetylene derivatives on the Karplues-type relationships of $^nJ_{HH}$ was studied by Alkorta and Elguero.[370] Only the FC contribution calculated at the FPT-DFT level was considered in line with the results known from the literature that in many cases the SD contribution to J_{HH} coupling is negligible while the PSO and DSO terms almost cancel each other. However, as commented above, the last assertion is valid in several cases but this is not a general rule. The FC term of the coupling pathway of the long-range J_{HH} couplings in the dimethyl derivative of polyacetylene is defined by the hyperconjugative interactions between the methyl C–H bonds with the conjugating π-electronic system. Alkorta and Elguero[370] obtained $^nJ_{HH}$ couplings for n up to 15, fitting the resulting angular dependence to the Karplus-type curves. It was

observed that the maxima of $^{n}J_{HH}$ angular curves decrease with n when increasing the length of the unsaturated chain.
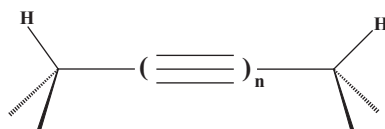
Dimethyl derivative of polyacetylene

Alkorta and Elguero[371] have also compared the $^{3}J_{HH}$ Karplus-type curves in ethane, methylamine, and methanol with the dihedral dependences of $^{4h}J_{HH}$ couplings through the hydrogen bond in complexes $[H_3N\cdots H\cdots NH_3]^{+}$ (both under conditions of proton-shared hydrogen bonds and common hydrogen bonds) $[HOH\cdots NH_3]$ and $[HOH\cdots OH_2]$. They observed that $^{4h}J_{HH}$ couplings followed closely a Karplus-type relationship with the respective amplitudes notably smaller than those in a "normal" $^{3}J_{HH}$ Karplus curve.

Díez et al.[372] calculated at the DFT-B3LYP level many $^{3}J_{HH}$ coupling constants in a series of selected molecules with optimized geometries looking to develop a practical procedure for predicting their reliable values. This led the authors to develop a procedure to predict $^{3}J_{HH}$ couplings, which provides an alternative to the empirically extended Karplus equations (see Ref. 372 and references cited therein), commonly used in structural and conformational studies. Doubtless, this procedure is rather more complicated and expensive than the use of the known empirical equations; however, it provides more precise predictions of $^{3}J_{HH}$ and can be safely applied to the highly strained molecules where empirical Karplus-type equations meet with failure. What is more, this procedure enables to obtain more precise empirically extended Karplus equations than those frequently used by many authors and is valid to calculate torsional contributions from the large amplitude vibrations.[372]

Galasso et al.[373] investigated some structural aspects of 11 oxo-derivatives of sparteine and complemented their study with the DFT-B3LYP calculation of $^{1}J_{CH}$, $^{2}J_{HH}$, and $^{3}J_{HH}$ couplings in this series. The following two points of this study should be highlighted: (i) a very good agreement between the calculated and measured $^{2}J_{HeqHax}$ couplings in the sparteine lactams was obtained; (ii) calculated $^{1}J_{CH}$ couplings corresponding to the lactamic unit reproduce correctly the "normal" Perlin effect[74] observed experimentally in that unit by the same authors, i.e., $^{1}J_{CHeq} > {}^{1}J_{CHax}$. The authors[373] found that their DFT-B3LYP calculations also reproduced correctly the $^{1}J_{CH}$ couplings corresponding to the C–H$_{\alpha}$ bonds in the parent sparteine, and a similar good performance of DFT-B3LYP was also observed in cyclohexane, where the experimental difference between $^{1}J_{CHeq}$ and $^{1}J_{CHax}$ was quantitatively reproduced.

De Luca et al.[374] presented an interesting study of the cooperative nature of the internal rotational motions in the enriched $^{13}C_2$-acetophenone. A set of 19 direct (dipolar) spin–spin couplings were measured in a liquid-crystalline solvent in combination with the DFT-B3LYP calculation of the different components of the

J_{C_8,C_9} indirect coupling tensor necessary to evaluate the corresponding dipolar coupling.
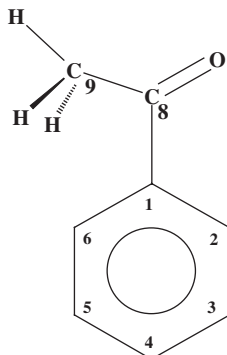
Acetophenone

The use of $^1J_{CC}$ and $^3J_{CC}$ couplings as potential probes to detect the *keto-enol* tautomerism in 3-OH-, 3-NO$_2$-, 5-Cl-, 6-Cl-, 6-NH$_2$-, and 6-CH$_3$-2-hydroxypyridines was studied both experimentally and theoretically by de Kowalewski et al.[140] The PCM-DFT calculations were carried out using $\varepsilon = 1$ and $\varepsilon = 46.7$, and in all cases, the more polar solvent shifted the tautomeric equilibrium towards the *keto* form. However, in spite of this trend, the preferential tautomer of 6-Cl-2-hydroxypyridine is the *enol* form, even for $\varepsilon = 46.7$. Two different types of J$_{CC}$ couplings, namely, $^1J_{C_5C_6}$ and the *trans*-ring $^3J_{CC}$, were found to be adequate probes to detect the preferential tautomeric forms in this series (see also Section 2.6).

Jimeno et al.[375] analyzed 73 unique spin–spin coupling constants J$_{HH}$, J$_{CC}$, J$_{CH}$, J$_{NH}$, and J$_{NC}$ of different types for the 10 species of the 2 series X(CH$_3$)$_n$H$_{4-n}$, where the central atom X is ^{13}C or ^{15}N$^+$, calculated at both the DFT-B3LYP and EOM-CCSD levels in comparison with experiment to reveal structural trends and computational difficulties.

Sýkora et al.[376] performed a systematic study of J$_{SiC}$ in *para*-substituted silylated phenols, both experimentally and theoretically, the latter at the DFT-B3LYP level. The experimental results were in reasonable agreement with theoretical calculations. In agreement with the data reported in the literature for couplings between other nuclei, the two-bond and three-bond couplings were of similar magnitudes but of opposite signs, which is of prime importance for spectral assignments in this series and related compounds. However, calculations were performed using the Gaussian 03 program package,[203] and it was noted by the authors[376] that in the revision Rev C.02 of June 12, 2004, the sign of J$_{SiC}$ arising from the negative magnetogyric ratio of silicon is neglected, a caution that should be taken into account by those using that revision of the Gaussian suite of programs to avoid misleading results.

Very recently, Del Bene and Elguero[377] reported the results of the EOM-CCSD calculations of $^nJ_{CC}$ $^nJ_{NC}$, and $^nJ_{PC}$ ($n = 1$–3) coupling constants, including all four coupling terms in benzene, pyridine, and phosphinine together with the protonated

forms of the latter two, pyridinium and phosphininium. One of the most interesting findings of this study is that the introduction of either N or P heteroatoms into the aromatic ring changes not only the magnitudes of the corresponding coupling constants, J_{XC}, but also the signs and magnitudes of the corresponding reduced coupling constants, K_{XC}. It was also found that protonation of the heteroatoms produced dramatic changes in coupling constants and, by removing the LP of electrons from the σ-electron framework, led to the same signs for the corresponding reduced coupling constants in benzene, pyridinium, and phosphininium. However, $^{n}J_{CC}$ couplings were found to be rather insensitive to either the presence of the heteroatoms or protonation.
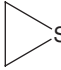
4.2.2. Carbo- and heterocycles

Ruden et al.[239] performed a comparitive MCSCF, SOPPA, CCSD, and DFT-B3LYP benchmark calculations of J_{CC}, J_{CH}, and J_{HH} in cyclopropane and cyclopropene. In general, the effects of electron correlation were underestimated by the MCSCF, somewhat better described within SOPPA, and well described by the CCSD methods. Moreover, even though the molecules studied in that paper were rather small (allowing authors to use a fairly large RASSCF space), the description of the dynamic electron correlation effects was incomplete in RASSCF theory, leading to an uneven quality of the calculated coupling constants. By contrast, this problem does not arise in the SOPPA and CCSD approaches, where the inclusion of the electron correlation is carried out in the full orbital space. The quality of the DFT-B3LYP results was comparable to that of the best *ab initio* methods, SOPPA and CCSD.

The J_{CC} spin–spin coupling constants calculated by Krivdin et al.[378,379] in monoheterocyclopropanes and monoheterocyclobutanes using SOPPA are compiled in Table 15. In the first paper,[378] the carbon–carbon coupling constants in cyclopropane, aziridine, and oxirane have been investigated at the RPA, SOPPA, and DFT-B3LYP levels. The SOPPA and DFT results were in a very good agreement with each other and with the experimental values, whereas calculations at the RPA level of theory strongly overestimated their experimental values. Significant differences in the basis set dependence of the calculated J_{CC} obtained with either wavefunction methods, RPA and SOPPA, or the density functional method, DFT-B3LYP, were observed. The SOPPA results depended much stronger on the quality of the basis set than the results of the DFT-B3LYP calculations. The medium size core-valence basis sets cc-pCVTZ and even cc-pCVDZ were found to perform quite well at the SOPPA level. In the second paper,[379] the basis set quality was examined in the reliability of the SOPPA calculations of J_{CC} in the series of five monoheterocyclopropanes and five monoheterocyclobutanes. At the SOPPA level, even the double zeta quality of the basis set was enough to account for the structural trends of J_{CC} couplings in the studied series of monoheterocycloalkanes with strong steric strain effects, provided the basis sets were augmented with core s-functions of Woon and Dunning[167] describing the inner electronic correlation.

Sauer and Krivdin[380] performed a systematic study of J_{CC} couplings in the series of six monocycloalkanes at the SOPPA and SOPPA(CCSD) levels. One-bond

Table 15. J_{CC} couplings (in Hz) of monoheterocycloalkanes calculated at the SOPPA level[a]

Compd.	DSO	PSO	SD	FC	Total	Exp.
⟶NH	0.16	−0.51	−0.29	22.55	21.91	21.0
⟶O	0.18	−0.52	−0.42	28.48	27.72	28.0
⟶SiH$_2$	0.18	−0.01	0.34	11.02	11.53	
⟶PH	0.19	−1.56	−0.02	25.42	24.04	
⟶S	0.20	−1.85	−0.06	28.62	26.91	
◇NH	0.20	0.83	1.14	28.66	30.83	
◇O	0.21	0.97	1.21	28.22	30.60	29.54
◇SiH$_2$	0.20	0.95	1.21	26.47	28.83	24.6
◇PH	0.21	0.64	1.13	30.22	32.20	
◇S	0.22	1.05	1.30	30.80	33.37	31.52

[a]All values are taken from Refs. 378 and 379.

couplings rapidly increase with the ring size being *ca.* 12 Hz in cyclopropane, *ca.* 28 Hz in cyclobutane, and *ca.* 33–35 Hz in the larger size monocycloalkanes; the latter are typical for the ordinary carbon–carbon bonds in the strain-free aliphatics. Apparently, unusually small J_{CC} in cyclopropane and, to a lesser extent, in cyclobutane are mainly due to the ring strain and, as a result, decreased s-characters of their endocyclic bonds, in line with the very recent results of Soncini and Lazzertetti,[137] see Section 2.6. Wu and Cremer[132] also show that measured and calculated J_{CC} coupling constants of pseudorotating cyclopentane are the averages over its pseudorotational motion, where each individual coupling of a conformation passed in the pseudorotation is the sum of the different path contributions.

As follows from the former study,[380] *geminal* $^2J_{CC}$ couplings span from –2 Hz to –11 Hz. However, the typical range of $^2J_{CC}$ is $-(2-3)$ Hz for the monocycloalkanes, where the *geminal* route is the principal coupling path. Large negative "double-*geminal*"

coupling constant $J_{CC} \approx -11$ Hz, calculated in bent cyclobutane, is mainly due to the dual-*geminal*-path coupling mechanism with the possible negative contribution of the through-space interaction involving the diagonal coupling carbons. It follows that the hyperconjugative interactions, discussed in Section 2.3, provide the main effect upon the values of *geminal* couplings in this series: hyperconjugative interactions *from* the coupling pathway result in a negative increase, while those *to* the coupling pathway yield a positive contribution to the FC term of $^2J_{CC}$ couplings.

Vicinal couplings are *ca.* $+2$ Hz in cyclohexane and are next to zero (<0.2 Hz) in larger monocycloalkanes, which is due to the Karplus dependence of $^3J_{CC}$. Indeed, calculated dihedral angles of the coupling paths are, accordingly, $\varphi = 54.4°$ in cyclobutane, $85.7°$ in cyclopentane and $100.2°$ in cyclohexane, which corresponds roughly to the *gauche* arrangement of the coupling carbons in the former and to the *orthogonal* orientation in the latter, both adopted in their preferential conformations.

In very good agreement with experiment and with the DVM, one-bond, *geminal* and *vicinal* alicyclic J_{CC} alternate in sign, as illustrated for cyclohexane (given in parentheses are the experimental couplings measured by Roznyatovski *et al.*[361]):

33.97 (33.10) Hz	-2.93 (-2.12) Hz	+2.03 (+2.05) Hz
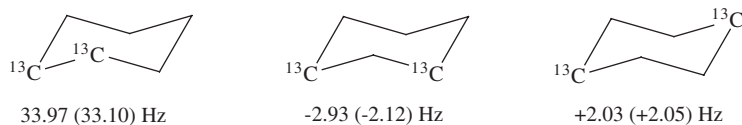
Calculated and experimental J_{CC} couplings in cyclohexane

Longer range J_{CC} spin–spin couplings in cyclooctane and larger monocycloalkanes involving four-bond coupling paths are very small, leaving less than 0.1 Hz (in absolute value) per each four-bond contribution (which means that the four-bond contributions to the *geminal* couplings in the six-membered rings are negligibly small as well), in good agreement with the experimental estimations by Della *et al.*[124] and in line with the known structural trends of the long-range J_{CC} couplings.[381]

One of the interesting aspects of spin–spin coupling constants in the five-membered rings is their pseudorotational averaging. In the recent and the most comprehensive publication by Wu and Cremer,[132] it was shown that measured and calculated J_{CC} couplings of pseudorotating cyclopentane are the averages over its pseudorotational motion where each individual coupling of a conformation passed in the pseudorotation is the sum of the different path contributions. Indeed, the molecule of cyclopentane can be represented as a free pseudorotating five-membered ring; each conformation of cyclopentane in its pseudorotational movement can be described by two parameters, namely, the pseudorotational phase angle and, on the other hand, the puckering amplitude, which both can be calculated from the five momentary endocyclic torsion angles of the ring and related to NMR spin–spin coupling constants which can be expressed as a function of the puckering coordinates.[382]

Zubkov and Chertkov[383] used *vicinal* proton–proton couplings to evaluate the continuous potential of pseudorotation for *trans*-1,2-dichloro- and *trans*-1, 2-dibromocyclopentane describing a fast low-barrier pseudorotation in terms of

the continuous distribution of conformations. In the same line, Karplus relationships for all 26 possible spin–spin coupling constants of the pseudorotating tetrahydrofuran were derived by Wu and Cremer[384] by expanding J_{XY} as a function of the puckering amplitude and the pseudorotational phase angle providing spin–spin couplings as suitable descriptors for the conformation of tetrahydrofuran in solution.

Ramalho and Bühl,[385] when studying the structure and dynamics of 5-nitro-imidazole derivatives, calculated its coupling constants at the DFT-B3LYP/EPR-II level of theory. One unexpected conclusion of their work is the authors' statement that small long-range couplings in unsaturated compounds cannot be described correctly with the DFT-B3LYP approach since they could not reproduce correctly the trend of the $^3J_{NH}$ and $^4J_{NH}$ couplings. However, along this review several papers were commented that do not substantiate such a statement as a general one. It seems most likely that this is a special condition for the particular couplings considered by Ramalho and Bühl.[385]

Pihlaja et al.[386] calculated $^3J_{HH}$ couplings at the DFT-B3LYP/cc-pVTZ/6-31G(d,p) level of theory to study the conformational equilibria in trans-4′, 7-dihydroxyisoflavan-4-ol and trans-isofravan-4-ol.

Very recently, conformational study of 2-(2-pyrrolyl)pyridine and 2,6-di(2-pyrrolyl)pyridine was performed by Rusakov et al.[387] on the basis of the experimental measurements and SOPPA calculations of $^1J_{CC}$, $^1J_{CH}$, and $^1J_{NH}$ spin–spin couplings showing marked stereochemical behavior upon the internal rotation around the pyrrole–pyridine interheterocyclic bonds. Both compounds were established to adopt predominant s-cis conformations with no noticeable out-of-plane deviations.

4.2.3. Polycycloalkanes and heteroanalogs

Dodziuk et al.[388] have studied both experimentally and theoretically J_{CH} and J_{CC} coupling constants in cis- and trans-decalins. Calculations were performed within the DFT-B3LYP approach, using the CP-DFT methodology as implemented in the Dalton program.[229] The complexity of the spectra of both conformers prevented the experimental determination of several couplings and therefore most comparisons between calculated and measured values were based on $^1J_{CC}$ couplings involving nonequivalent carbon atoms together with $^1J_{CH}$ coupling constants. In general, a good agreement between calculated and measured couplings was observed. The authors[388] discuss possible reasons for the small, observed discrepancies.

A large number of polycycloalkanes, including spiroalkanes,[389,390] bicycloalkanes,[391] bridged bicycloalkanes,[390,392] propellanes,[390,393] bicyclobutane-containing polycycloalkanes,[394] polyhedranes,[395] and cage polycycloalkanes[396] have been investigated at the SOPPA level by Krivdin with a special focus upon the structural behavior of their J_{CC} couplings. As a result of these studies, many unknown couplings were predicted with high reliability filling many experimental gaps, and this provided a good reference dataset and a practical guide to the structural elucidation of saturated polycarbocycles by means of J_{CC} coupling constants.[397] Established structural trends of J_{CC} are briefly summarized below for the representative series.

4.2.3.1. Spiroalkanes. The typical ranges of the calculated one-bond carbon–carbon couplings involving the *spiro* carbon in the series of spiroalkanes ($n = 1$–4) are given below. The most obvious trend is that the one-bond J_{CC} couplimgs of this type in spiroalkanes are substantially increased as compared to those in related monocycloalkanes. This is due to the steric strain on the *spiro* carbons. This effect is most pronounced when the second ring (i.e., the ring adjacent to that containing both coupling carbons) is cyclopropane ($n = 1$) provides considerable steric strain, and is almost negligible when the second ring bears no steric strain, such as cyclohexane ($n = 4$), see below.

(14.3 - 22.1) Hz   (30.0 - 37.0) Hz   (33.3 - 42.3) Hz   (34.2 - 42.6) Hz

J_{CC} couplings involving the *spiro* carbon in spiroalkanes
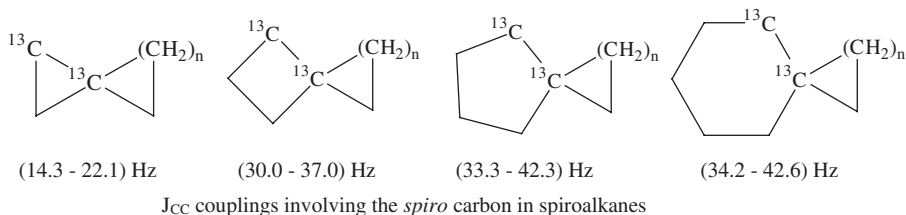
Interring *geminal* $^2J_{CC}$ across *spiro* carbon are almost always negative falling into the range of *ca.* $-(0.5$–$2.5)$ Hz markedly increasing in absolute value with the bond angle at the *spiro* carbon, in line with the known structural trends of $^2J_{CC}$ in the open-chain aliphatics[381] originated mainly in the hyperconjugative interactions, see Section 2.3. The noted bond angle dependence of $^2J_{CC}$ is almost solely due to the dominant FC contribution. On the other hand, intraring *geminal* couplings across *spiro* carbon depend primarily on the ring size, as shown below:

+(10.2 - 12.7) Hz   –(7.3 - 8.9) Hz   +(4.1- 5.2) Hz   –(0.3 - 1.7) Hz

Intraring J_{CC} couplings in spiroalkanes
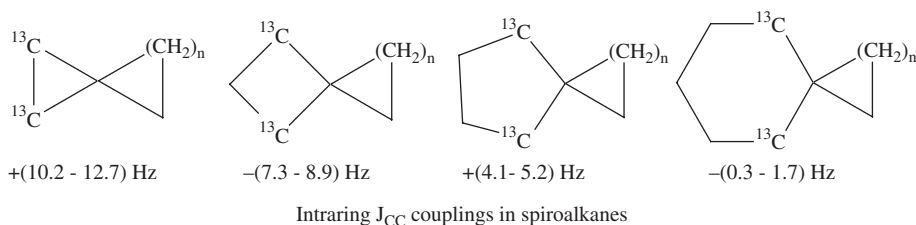
There seems to be a rather good agreement between those couplings in spiroalkanes and monocycloalkanes except for the cyclopentane ring where $^2J_{CC}$ are considerably larger in spiroalkanes. Actually, they are the dual-pathway couplings containing one *geminal* pathway across the *spiro* carbon rather than the genuine *geminal* couplings. On the other hand, in the cyclopentane ring, there are two coupling pathways – *geminal* and *cis-vicinal*, and the observed difference could be explained by either increased *vicinal* pathway (positive) or decreased *geminal* pathway (negative) in the cyclopentane ring of spiroalkanes as compared to the parent cyclopentane.

4.2.3.2. Bicycloalkanes.[391] One-bond carbon–carbon coupling constants in bicycloalkanes range from 25 Hz to 36 Hz falling into two groups: the "cyclobutane-type" (*ca.* 25–29 Hz), and the "larger cycle-type" (*ca.* 31–36 Hz) couplings with the

gap of at least 2 Hz, which makes them obviously distinguishable. Long-range mul-
tipath bridgehead–bridgehead couplings are nearly additive (within *ca.* 2–3 Hz) giv-
ing rise to the following coupling increments (given in parentheses are those derived
by Della *et al.*[124] on pure empirical grounds). In this context, it is also interesting to
compare the empirical three-bond coupling increment, 4.3 Hz, with the dual-path
$^3J_{CC}$ coupling in benzene,[138] 10.01 Hz (calculated values: FC = 8.47 Hz;
SD = 1.86 Hz; PSO = 0.54 Hz; DSO = −0.01 Hz; total: 10.87 Hz; Ref. 84) (Table 6).
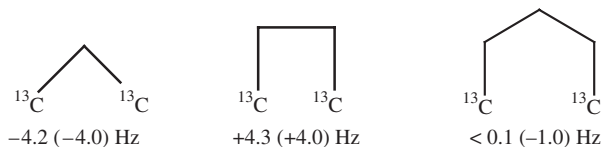
Additive increments of J_{CC} couplings in bicycloalkanes

The only exception is provided by bicyclo[1.1.1]pentane, which demonstrates a
dramatic nonadditivity of *ca.* −15 Hz for the bridgehead–bridgehead J_{CC} coupling
as shown below (given in parenthesis are the nonadditivities found as the deviations
of total calculated J_{CC} values from those derived from the additive increments given
above):
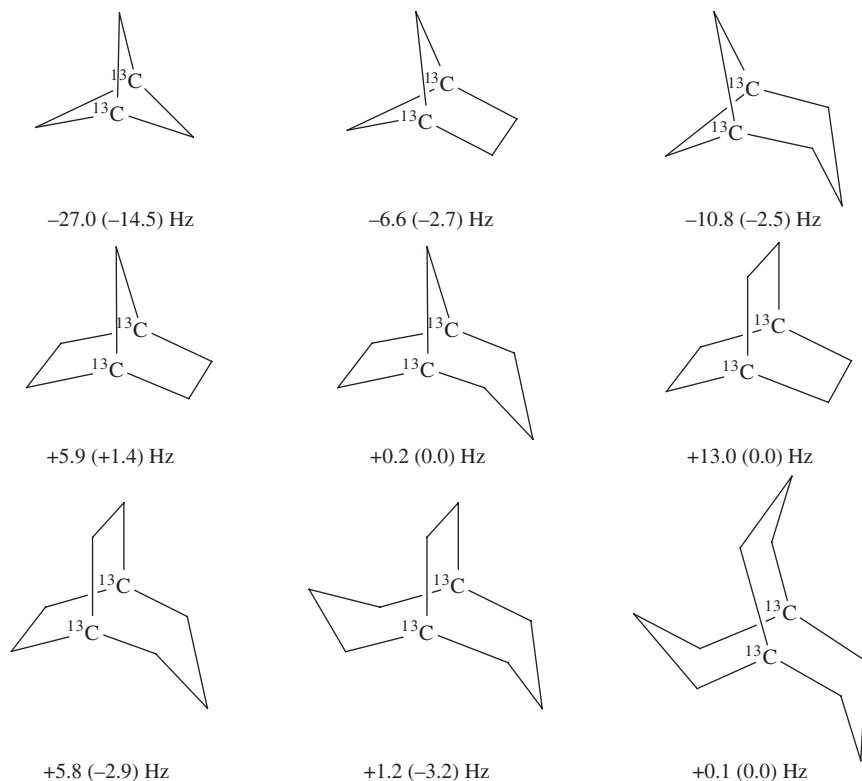
Bridgehead -bridgehead J_{CC} couplings and their non-additivities in bicycloalkanes

The dramatic nonadditivity of J_{CC} in bicyclo[1.1.1]pentane should be attributed to the well-known through-space nonbonded interactions at bridgeheads ("rear lobes effect") reported by Barfield et al.[398] and later by Contreras et al.[127] It is these nonbonded interactions that provide additional and effective nonbonding coupling path for the bridgehead carbons in the bicyclo[1.1.1]pentane framework.

4.2.3.3. Bridged bicycloalkanes.[390,392]   Obviously, the most fascinating representative of this family is its ancestor, bicyclo[1.1.0]butane. Apart from the pure theoretical and chemical reactivity arguments, a good deal of evidence of its singularity has been gained from the investigation of its J_{CC} couplings. The most intriguing fact about carbon–carbon coupling in the bicyclobutane skeleton is, of course, the negative sign of J_{CC} between chemically bonded bridgehead carbons, which reflects the unique nature of the bridgehead–bridgehead bond in bicyclobutane providing almost pure p-character. The negative sign of the bridgehead–bridgehead J_{CC} was theoretically predicted by Newton and Schulman[399] and confirmed experimentally several years later by Pomerantz et al.[400] and, independently, by Finkelmeier and Lüttke.[401]

Historically, early semiempirical calculations tended to underestimate the value of this unique coupling giving only –(2–8) Hz, while later *ab initio* calculations by Galasso,[402] Sekino and Bartlett,[403] and Carmichael[404] noticeably improved this result giving the value of *ca.* –(8–13) Hz. However, only very recent MCSCF study by Jaszunski et al.[405] and the SOPPA calculations by Krivdin[390] resulted in the values of *ca.* –15 Hz, which were much closer to the experimental reference, −17.49 Hz.[401] It is noteworthy that large negative value of the bridgehead–bridgehead $^1J_{CC}$ coupling in bicyclo[1.1.0]butane is almost solely due to the negative FC contribution that in itself is very unusual (and seems to be the only example) of the coupling constant between chemically bonded carbons.

In the rest of the bridged bicycloalkanes, the calculated bridgehead–bridgehead J_{CC} couplings are positive markedly increasing with increasing the ring size (and decreasing the ring strain) as illustrated below:

Bridgehead-bridgehead J_{CC} couplings in bridged bicycloalkanes
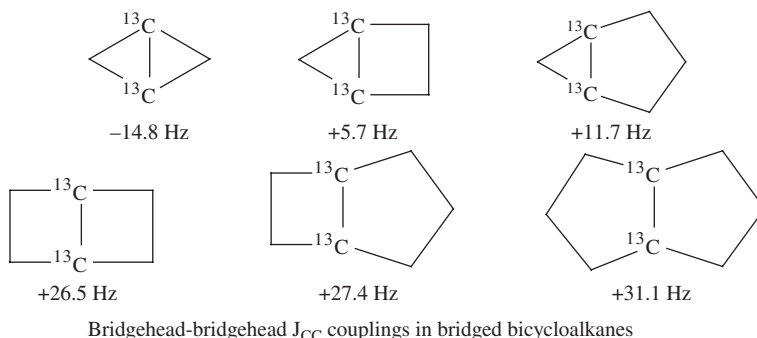
Typical ranges of the formally one-bond J_{CC} couplings, excluding those between bridgeheads, are 15–22 Hz in the cyclopropane, 30–38 Hz in the cyclobutane, and 33–42 Hz in the cyclopentane units. These values are somewhat larger than

corresponding experimental $^1J_{CC}$ couplings in the parent monocycles: 12.4 Hz in cyclopropane,[133] 28.4 Hz in cyclobutane,[406] and 32.6 Hz in cyclopentane.[407] This trend is due to the increased s-character of the corresponding carbon hybrids at bridgeheads forming the bridgehead–nonbridgehead bonds reflecting the degree of steric strain. This trend is demonstrated most clearly in the case of the adjacent cyclopropane rings, and the whole tendency is evident from the following calculated J_{CC} couplings:

Bridgehead-non-bridgehead J_{CC} couplings in bridged bicycloalkanes
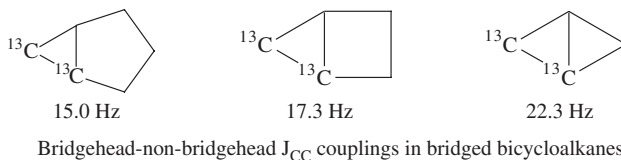
There are two types of the intraring long-range J_{CC} couplings in the bridged bicycloalkanes, namely $^{2+2}J_{CC}$ in the cyclobutane ring and $^{2+3}J_{CC}$ in the cyclopentane moiety. Couplings of the first type vary from -8.9 Hz to -11.0 Hz, in a good agreement with the experimental value of $(-)8.1$ Hz in cyclobutane.[406] The values of the second type of couplings, $^{2+3}J_{CC}$, are rather small and span from -1.2 Hz to $+1.3$ Hz, which is possibly due to the fact that negative *geminal* and positive *vicinal* increments almost compensate each other. On the other hand, interring long-range J_{CC} couplings are rather small (as a rule, <2 Hz in absolute value), alternate in sign and are almost solely dominated by the FC contribution. Basically, it is difficult to derive any obvious structural trends in this case due to the fact that formally identical coupling pathways in different bridged bicycloalkanes have different geometries, strongly depending upon their ring size that makes any comparison to be rather ambiguous.

4.2.3.4. Propellanes.[390,393]   Since the first historical synthesis of [1.1.1]propellane by Wiberg and Walker[408] in 1982, it has been permanently the object of the theoretical discussions, first of all, due to the mystifying nature of its bridgehead–bridgehead "bond-phantom." Apparently, bridgehead–bridgehead coupling constant in propellane is one of the most difficult physical quantities to calculate being a challenge to the modern theoretical methods. The most annoying uncertainty regarding this coupling is still remaining in whether it is *ca.* 18–20 Hz, according to the CCSD calculations by Pecul *et al.*,[409] the DFT-B3LYP data by Peralta (cited as private communication in Ref. 393) and the SOPPA results by Krivdin,[393] or is it almost zero (1.6 Hz) as was predicted by Galasso[402] based on his early EOM calculations, and measured experimentally (0.5 Hz) by Werner *et al.*[410] in alkyl derivatives of propellane, see Table 16. In our opinion, this striking agreement of the early EOM data with experiment (which, in view of the addressed results, claims for a thorough verification), in contrast to the more reliable theoretical methods like SOPPA, CCSD, and DFT, may appear to be fortuitous due to a possible compensation of errors. In any case, further experimental as well as theoretical investigations of this mystifying coupling constant seem to be highly warranted.

Table 16. Bridgehead–bridgehead J_{CC} coupling (in Hz) in [1.1.1]propellane calculated by different methods in comparison with experiment

Method	DSO	PSO	SD	FC	Total
SCF	0.17	−0.92	8.93	119.47	127.65[a]
MCSCF				39.45	42.93[b]
CCSD				18.36	21.84[b]
B3LYP	0.16	0.50	2.73	16.97	19.37[c]
SOPPA	0.17	−0.27	1.99	15.56	17.46[a]
EOM	−0.32	0.18	0.21	1.52	1.59[d]
Exp.					0.5[e]

[a]Taken from Refs. 390 and 393.
[b]Taken from Ref. 409.
[c]Cited as private communication of J. E. Peralta in Ref. 393.
[d]Taken from Ref. 402.
[e]Measured in alkylsubstituted derivatives (Ref. 410).

Unfortunately, there is a lack of experimental data on J_{CC} couplings between bridgeheads in the series of the larger propellanes. On the other hand, some theoretical results do exist, basically, those arising from the recent SOPPA results[390,393] and the early EOM calculations by Galasso[402] (the latter are given in parentheses):

17.5 (1.6) Hz   5.5 (−1.8) Hz   9.7 (10.0) Hz

34.0 (31.8) Hz   30.2 Hz   31.7 Hz
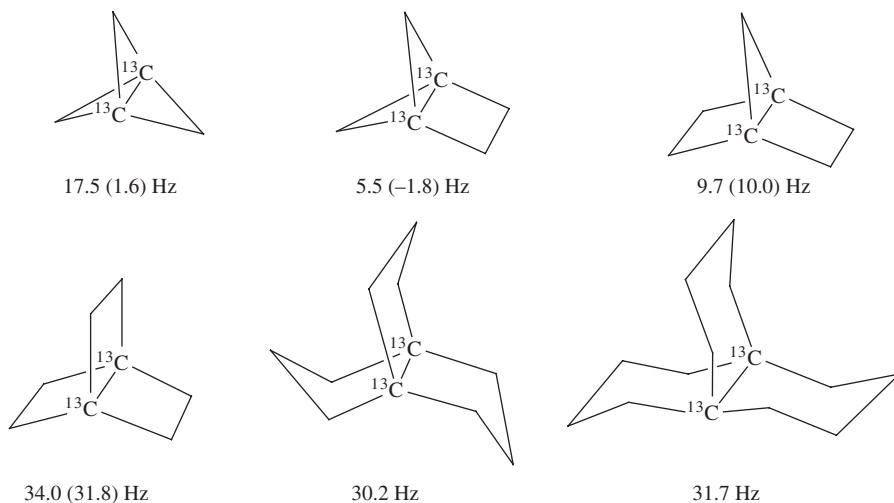
Bridgehead-bridgehead J_{CC} couplings in propellanes

The values of J_{CC} couplings calculated at the EOM and SOPPA levels are in a good agreement with each other for [2.2.1]- and [2.2.2]propellanes, while they are strikingly different for [2.1.1]- and [1.1.1]propellanes. It is obvious that in the most difficult cases, which undoubtedly present the two latter compounds, the reliability of any *ab initio* method depends primarily upon the level of theory describing the

effects of electronic correlation. On the other hand, the most evident reason of this disagreement is a poor quality of the basis sets used in the cited EOM calculations.[402] It is well known that standard basis sets (and especially those of double zeta quality) including no tight and/or core functions, which are traditionally used for the geometry optimizations and calculations of energies and the first-order molecular properties, are absolutely inappropriate for the calculations of spin–spin coupling constants.

In the series of propellanes, a marked decrease of the bridgehead–bridgehead coupling should be accounted for the decrease of the s-character of their bridgehead–bridgehead bonds. Accordingly, on going from [2.1.1]propellane to [1.1.1]propellane, one should expect further decreasing of the bridgehead $^1J_{CC}$ couplings becoming at least as large (and negative) as that in bicyclo[1.1.0]butane, -17.49 Hz.[401] However, nothing of this kind takes place: this $^1J_{CC}$ coupling in [1.1.1]propellane changes in the opposite direction and becomes even larger (and positive!), and this provides the most unexpected trend that is not yet rationalized at present.

Interring long-range J_{CC} couplings alternate in sign and, depending on the multipath coupling routes, span from -2 Hz to $+7$ Hz, while intraring long-range J_{CC} couplings in the monocyclic units of propellanes are pretty close to the experimental long-range J_{CC} in the corresponding monocycloalkanes. Both intraring and interring long-range couplings obviously follow the multipath coupling mechanism schemes. For example, successive removal of the positive *vicinal* coupling paths results in the markedly increased negative values of the total J_{CC} coupling arising basically from the two negative *geminal* increments, *ca.* -6 Hz each:

Coupling path: 2+2+3+3   Coupling path: 2+2+3   Coupling path: 2+2
      –5.1 Hz   –8.7 Hz   –13.1 Hz

Multipath intraring J_{CC} couplings in propellanes
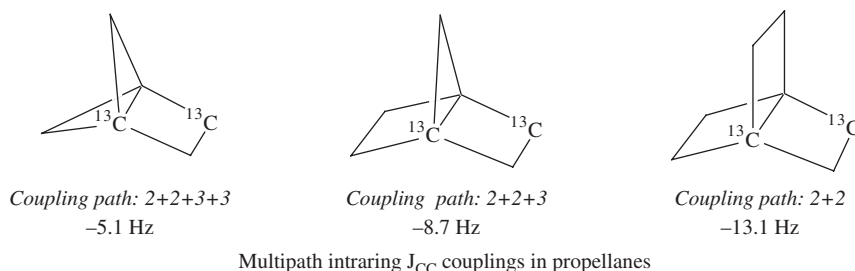
4.2.3.5. Bicyclobutane-containing polycycloalkanes.[394]   As mentioned earlier, steric strain of the bicyclobutane framework results in the most unusual hybridization of its bridgehead carbons which, in turn, gives rise to the dramatically reduced s-characters of the bridgehead–bridgehead carbon–carbon bond and the unusual (negative) value of the corresponding one-bond J_{CC} coupling in bicyclobutane. In the series of the bicyclobutane-containing polycycloalkanes, two chemically nonbonded carbons of the bicyclobutane moiety at bridgeheads are linked by different carbocyclic bridges giving rise to the different steric shrinkage of the two condensed cyclopropane rings resulting in the quite different hybridization effects throughout the series which has a pronounced effect on the J_{CC} couplings.

Among the bicyclobutane-containing polycycloalkanes studied in Ref. 394, experimental measurement of the bridgehead–bridgehead J_{CC} coupling has been performed only for octabisvalene by Trupp *et al.*[411] Although the sign of the measured $J_{CC} = (-)13.6\,Hz$[411] between bridgehead carbons of the bicyclobutane moiety in octabisvalene was not determined experimentally, it could be safely adopted as negative based on the early EOM calculations by Galasso[412] and the recent SOPPA results[394] together with the explicit analogy with the parent bicyclobutane.[401]

Numerical value of the bridgehead–bridgehead J_{CC} coupling calculated by Galasso[412] for octabisvalene $(-11.9\,Hz)$ agrees well with the experiment $(-13.6\,Hz)$[411] and the SOPPA calculations $(-14.3\,Hz)$.[394] However, Galasso's EOM value of this coupling in the parent bicyclobutane $(-9.4\,Hz)$[402] is obviously underestimated, if compared with the most reliable experimental data by Finkelmeier and Lüttke $(-17.49\,Hz)$.[401] What is the reason of this marked discrepancy? Obviously, the crucial point of any nonempirical calculation of spin–spin coupling constants is the portion of electronic correlation taken into account by the applied method together with the quality of the basis set. EOM method by Galasso[412] accounts for only *1p-1h* (particle-hole) operators, which means that in fact, electron correlation effects are not included (in the presence of a perturbation these operators do not describe real correlation corrections), which means that the pure EOM approach is not a consistent second-order theory.

The most interesting trend of J_{CC} couplings calculated at the SOPPA level observed in the series of the bicyclobutane-containing polycycloalkanes[394] is the marked decrease in absolute value of the negative J_{CC} coupling between bridgehead carbons with the increase of the puckering angle in the bicyclobutane moiety, as illustrated below (given in parenthesis are the corresponding puckering angles of the bicyclobutane units):

$-16.1\,Hz\,(55.9°)$ $-14.6\,Hz\,(59.4°)$ $-9.5\,Hz\,(69.5°)$ $-1.1\,Hz\,(86.1°)$
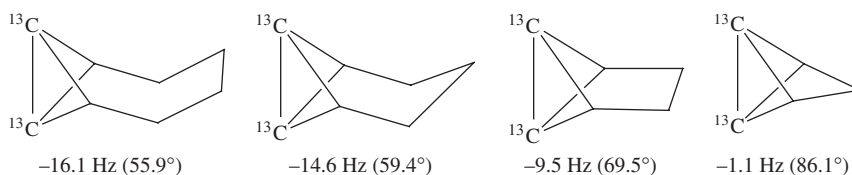
J_{CC} couplings and puckering angles in the bicyclobutane moiety
of the bicyclobutane-containing polycycloalkanes

As a result of this trend, the almost zero J_{CC} coupling in tricyclopentane was predicted,[394] which should be accounted for the strong steric shrinkage of the bicyclobutane moiety by the methylenic bridge. This is probably the main reason why this mystifying coupling has not been measured in the derivatives of tricyclopentane so far.

Long-range J_{CC} couplings of the bicyclobutane-containing polycycloalkanes alternate in sign and range from $-18\,Hz$ to $+5\,Hz$. It is obvious that rationalization of the behavior of these couplings can be based on the ideas of the multipath-coupling mechanism. For example, positive values of the J_{CC} couplings in the

compounds shown below could be associated with the *vicinal* coupling path presented only in two species, while remarkably large and negative J_{CC} couplings in tricyclopentane is mainly due to the three *geminal* paths and substantial through-space negative contribution involving spatially proximate carbons at bridge-heads:

+ 4.7 Hz   +2.4 Hz   −18.1 Hz
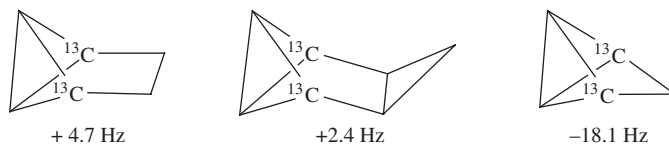
Bridgehead-bridgehead J_{CC} couplings in the bicyclobutane-containing polycycloalkanes

4.2.3.6. Polyhedranes and cage polycycloalkanes.[395,396]   One-bond J_{CC} couplings of cage polycycloalkanes fall into range of *ca.* 11–13 Hz for the cyclopropane units and *ca.* 30–40 Hz for the four-, five-, and six-membered moieties which comprise the polycarbocyclic frameworks. Available experimental data are very scarce but are in a good accordance with the recent SOPPA results.[395,396] Total values of the one-bond J_{CC} couplings are almost solely governed by the dominant FC contribution. Noncontact contributions are essentially negligible in most cases.

Only rough estimation of the experimental J_{CC} couplings in tetrahedrane of *ca.* 9 Hz could be derived from the corresponding tetra-*tert*-butyltetrahedrane data reported by Loerzer et al.[413] According to the SOPPA calculations,[395] this unique coupling is positive which is accounted for the marked increase of the J_{CC} coupling between bridgehead carbons with the increase of the puckering angle in the bicyclobutane moiety,[394] as discussed earlier.

Both one-bond J_{CC} couplings of prismane are positive. However, the one be-longing to the cyclopropane moiety is markedly smaller (12.7 Hz) and is very close to that in the parent cyclopropane (12.4 Hz),[133] while the one involving the two adjacent cyclobutane units is dramatically larger (42.2 Hz). This is consistent with the increased $^1J_{CC}$ coupling in the parent cyclobutane as compared to cyclopropane. Accordingly, the calculated multipath two-bond coupling of the cyclobutane type $J_{CC} \approx -6$ Hz is close to that measured in cyclobutane (−8.1 Hz):[406]

+12.7 Hz   +42.2 Hz   -6.1 Hz
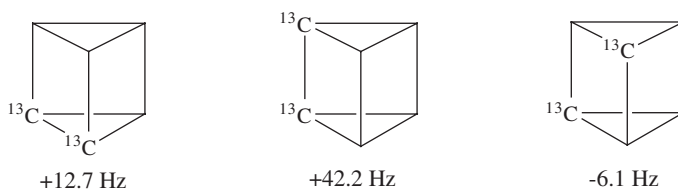
Multipath J_{CC} couplings in prismane

Flat-faced cubane, pentaprismane, and hexaprismane possess almost no pecu-liarities in terms of their J_{CC} couplings.[396] One-bond couplings (each involving

carbons of the cyclobutane unit) fall into range *ca.* 30–32 Hz, which is close to J_{CC} in the parent cyclobutane; multipath cyclobutane-type couplings are negative (*ca.* −12 Hz), while the "multi-*vicinal*" couplings are positive and remarkably large (of up to +18 Hz), mainly due to the fact that these couplings are transmitted through six equivalent pathways, as shown very recently by Contreras *et al.*[66]

+31.7 Hz   -11.5 Hz   +17.8 Hz
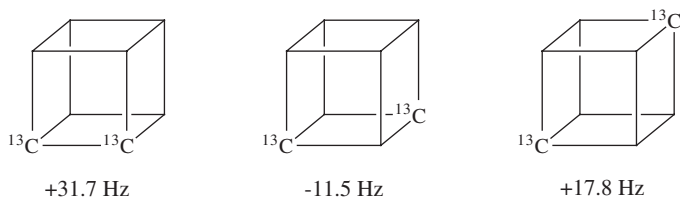
Multipath J_{CC} couplings in cubane

One-bond, *geminal* and *vicinal* J_{CC} in adamantane and diamantane calculated at the SOPPA level are very close to those in the chair cyclohexane which suggests that both carbocages are essentially steric-strain-free, as illustrated below for adamantane (given in parentheses are the corresponding couplings in cyclohexane calculated within the same method and basis set):

32.3 Hz (34.0 Hz)   -2.9 Hz (-2.9 Hz)   1.5 Hz (2.0 Hz)
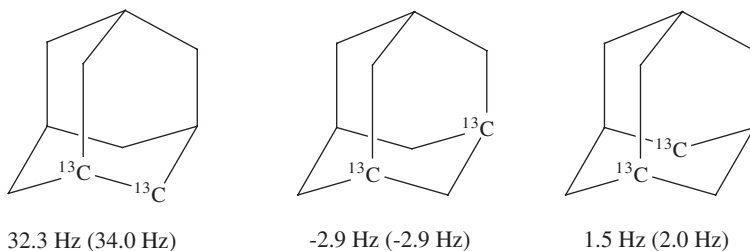
Intraring J_{CC} couplings of the cyclohexane moiety in adamantane

Galasso[414] performed the DFT-B3LYP calculations on a variety of $^{n}J_{PX}$ couplings in a series of phosphatrane compounds, obtaining a series of very interesting couplings. Since calculations performed in a couple of cases were dominated by the FC contribution, Galasso's study was constricted to this term. Whenever possible, calculated couplings were compared with the corresponding experimental values, and in general, a good agreement between them was observed. The only exception was $^{1}J_{PB}$ where an important underestimation was observed. According to Galasso, this discrepancy originates both in the important role played by the electron correlation effects in this coupling, and in the low flexibility of the basis set employed (see Section 3.6). Very interesting and markedly large $^{4}J_{PNax}$ values were calculated for several of these compounds. It should be noted that such sizeable couplings originate in the following two effects: (i) the coupling nuclei are connected by the three equivalent coupling pathways (see Section 2.6); (ii) it is expected that there are

strong negative- and σ-hyperconjugative interactions along each pathway, as commented above for 1-F-4-X-cubanes[66] (see Section 2.4).

E = NH, NMe, O   E = NH, NMe, O; Z = H⁺, O, S, CH₃⁺, BH₃

Phosphatranes studied by Galasso [414]
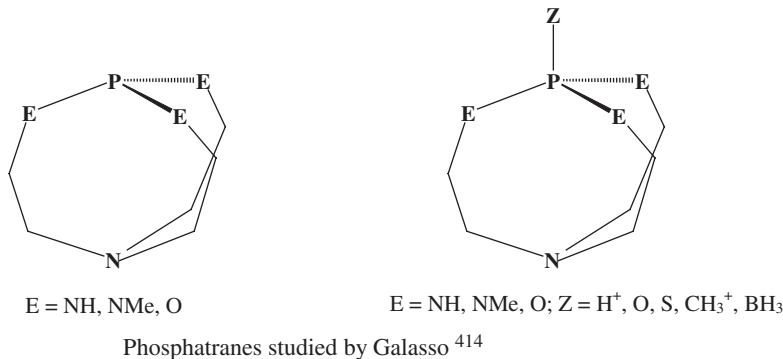
4.2.4. *Azomethines and azocompounds*

The interest in azomethines is originated in their remarkable chemical properties. It is common knowledge that certain types of these compounds are widely used in the preparation of different heterocyclic systems and serve as the useful ligands in the synthesis of the metal coordinative compounds. Many chemical transformations and rearrangements involving azomethines occur stereoselectively, which makes the problem of the configurational assignment at the $C{=}N$ bond to be of crucial importance. In this connection, early extensive experimental studies of the $^1J_{CC}$ coupling constants in oximes and their derivatives provided a new guide in the configurational assignment of azomethines based on the stereospecificity of these couplings toward the orientation of the nitrogen LP.[415] Indeed, the difference between J_{cis} and J_{trans} amounts to *ca.* 20% of their total values and the same holds for the $^1J_{CH}$ couplings involving the α-imino carbon:

Notations of J_{cis} and J_{trans} in azomethines

The nature of this interesting effect providing the marked difference between J_{cis} and J_{trans} could be accounted for the three different contributions, namely those of (i) the nitrogen LP, (ii) the carbon–carbon bonds containing coupling carbons, and (iii) the carbon inner core orbitals.[416] The first one relates to the direct nitrogen LP participation in the transmission of spin–spin coupling giving a positive contribution to J_{cis} and a negative one to J_{trans} (primary LPE). On the other hand, the second and the third contributions originate mainly in the charge transfer from the nitrogen LP to the antibonding orbital of the adjacent carbon–carbon (or carbon–hydrogen) bond in *trans* orientation to the nitrogen LP as explained in

detail by Cuevas and Juaristi.[417] This charge transfer interaction, very similar to anomeric effect, results in the substantial lengthening of the *transoid* carbon–carbon bond and hence in the negative contribution to J_{trans} (secondary LPE). It is the cooperation of these different intramolecular interactions, which gives rise to the primary and secondary LPEs upon the one-bond J_{CC} and J_{CH} couplings involving the α-imino carbon of azomethines and that results in a dramatic difference between J_{cis} and J_{trans} used for the configurational assignment at the C=N bond.

Thus, calculation of J_{CC} and J_{CH} couplings in azomethines provides a rewarding goal and a challenging task to reproduce experimental trends dealing with the orientational LPE. In a number of the recent publications by Krivdin and co-workers,[418–423] J_{CC} and J_{CH} couplings were calculated at the SOPPA and SOPPA(CCSD) levels in very good agreement with experiment in a number of different azomethines involving the open-chain aliphatic and alicyclic oximes,[418,419] aminosulfonylamidines,[420] azomethines of the α,β-unsaturated aldehydes,[421] all-enylthioimidates,[422] and methylglyoxal bisdimethylhydrazones.[423]

What is most remarkable in the latter example, methylglyoxal bisdimethylhydrazone, is a presence of the two azomethine functions, each providing the nitrogen lone-pair effects (LPE) upon the values of $^1J_{CC}$ and $^1J_{CH}$ couplings – a positive contribution to J_{cis} (+LPE) and the negative one to J_{trans} (–LPE) of the adjacent either C–C or C–H bond as shown below:
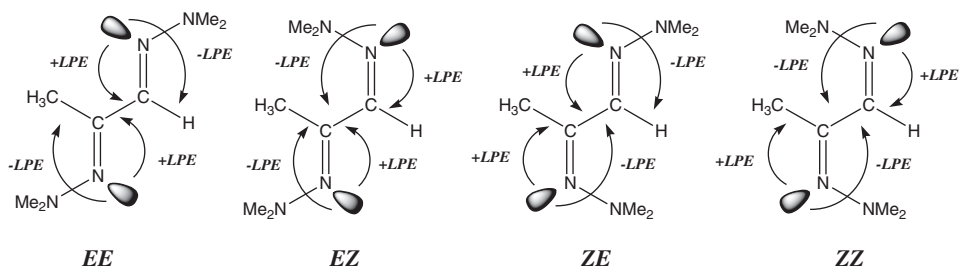
The lone-pair effects on $^1J_{CC}$ and $^1J_{CH}$ in methylglyoxal bisdimethylhydrazone

Comparison of the calculated total values of $^1J_{CC}$ and $^1J_{CH}$ couplings in all four possible isomers of methylglyoxal bisdimethylhydrazone (Table 17) demonstrates the marked stereochemical dependence of these couplings upon the orientation of the LPs of both nitrogen atoms in the different isomers in accord with the additive arguments. Indeed, $^1J_{C_1C_2}$ coupling in *EE* and *EZ* are *ca.* 39–42 Hz (–LPE), while they are *ca.* 50–53 Hz in *ZE* and *ZZ* (+LPE). On the other hand, $^1J_{C_2C_3}$ coupling in *ZZ* are *ca.* 52 Hz (–2LPE), *ca.* 75 Hz in *EE* (+2LPE) and *ca.* 57–64 Hz in *EZ* and *ZE* (–LPE of one azomethine nitrogen and +LPE of the other). In much the same manner, $^1J_{C_3H}$ in *EE* and *ZE* are *ca.* 162–166 Hz (–LPE), while they are *ca.* 171–178 Hz in *EZ* and *ZZ* (+LPE). Established manifestation of the LPE in the values of $^1J_{C_1C_2}$, $^1J_{C_2C_3}$, and $^1J_{C_3H}$ of the four different isomers of methylglyoxal bisdimethylhydrazone leaves no doubt that the major isomer is *EE* and the minor *ZE*, both adopting predominant s-*trans* conformations. The most encouraging

Table 17. $^1J_{C_iC_j}$ and $^1J_{C_iH_j}$ couplings (in Hz) of methylglyoxal bisdimethylhydrazone calculated at the SOPPA(CCSD) level and compared with experimental values whenever possible[a]

Isomer	$^1J_{X_iY_j}$	Conformation	DSO	PSO	SD	FC	Total	Exp.
EE	$^1J_{C_1C_2}$	s-cis	0.3	−1.2	0.7	41.9	41.7	41.5
		s-trans	0.3	−1.3	0.7	42.1	41.8	
	$^1J_{C_2C_3}$	s-cis	0.3	−1.7	0.9	5.3	74.8	75.3
		s-trans	0.3	−2.1	0.9	75.4	74.5	
	$^1J_{C_3H}$	s-cis	1.2	0.1	0.1	152.7	154.1	
		s-trans	1.2	−0.2	0.1	161.0	162.1	162.7
EZ	$^1J_{C_1C_2}$	s-cis	0.3	−1.1	0.7	40.9	40.8	
		s-trans	0.3	−1.3	0.7	39.6	39.3	
	$^1J_{C_2C_3}$	s-cis	0.3	−1.8	0.9	62.9	62.3	
		s-trans	0.3	−1.3	0.9	57.4	57.3	
	$^1J_{C_3H}$	s-cis	1.1	0.2	0.1	168.4	169.8	
		s−trans	1.1	−0.4	0.1	177.8	178.6	
ZE	$^1J_{C_1C_2}$	s-cis	0.3	−0.9	0.7	51.0	51.1	
		s-trans	0.3	−1.1	0.7	50.3	50.2	50.3
	$^1J_{C_2C_3}$	s-cis	0.3	−1.9	0.9	64.6	63.9	64.8
		s-trans	0.3	−2.0	0.9	65.1	64.3	
	$^1J_{C_3H}$	s-cis	1.2	0.1	0.1	152.6	154.0	
		s-trans	1.3	−0.2	0.1	165.2	166.4	166.8
ZZ	$^1J_{C_1C_2}$	s-cis	0.3	−0.8	0.7	52.8	53.0	
		s-trans	0.3	−0.9	0.7	51.7	51.8	
	$^1J_{C_2C_3}$	s-cis	0.3	−1.8	0.9	52.3	51.7	
		s-trans	0.3	−1.2	0.9	44.5	44.5	
	$^1J_{C_3H}$	s-cis	1.1	0.0	0.1	170.2	171.4	
		s-trans	1.1	−0.5	0.1	170.7	171.4	

[a]All values are taken from Ref. 423.

result of this study[423] is that experimental differences between J_{cis} and J_{trans} for both $^1J_{CC}$ and $^1J_{CH}$ couplings, induced by the nitrogen LPEs of the two azomethine functions in methylglyoxal bisdimethylhydrazones, are large and essentially additive and are very well reproduced in the SOPPA(CCSD) calculations, which provides a straightforward guide to the configurational assignment at the C=N bond and conformational analysis in the related systems based on the experimental measurements and theoretical calculations of their $^1J_{CC}$ and/or $^1J_{CH}$ couplings.

In line with these results,[418–423] Provasi *et al.*[424] reported a systematic SOPPA(CCSD) study of the orientational nitrogen LPE upon the different spin–spin couplings in two simplest azomethines – methanimine and ethanimine,
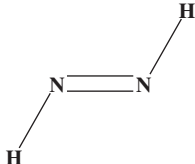
H_2C=NH and CH_3CH=NH, together with the corresponding oximes, H_2C=NOH and CH_3CH=NOH. It was found that the LP contribution is always more positive for the *synperiplanar* rather than the *antiperiplanar* couplings, independent of the number of bonds which separate the coupling nuclei, in good agreement with experiment. The stereoelectronic effects of the nitrogen LP on the one-bond couplings were significantly reduced by the OH and CH_3 substituents, whereas the corresponding differences between *geminal* coupling constants were increased.

A similar oxygen LP orientational effect on $^1J_{CC}$ couplings was reported many years ago.[425] When studying the tautomeric behavior of the 2-hydroxypyridine derivatives, the influence on $^1J_{CC}$ couplings of the O–H conformation in 3-hydroxypyridine was analyzed.[140] Calculations as well as spectroscopic results showed that by far the preferential tautomeric form of this compound was the *enol* form with the preferential conformation **A** when the O–H bond is eclipsing the C_2–C_3 bond. For both conformations, **A** and **B**, coupling constants were calculated at the DFT-B3LYP/6-311G**/EPR-III level of approximation. In both cases, the 5 Hz difference between these two couplings originates in the FC term (with the exception of the difference between the values of 63.6 Hz and 63.5 Hz, which originates also in the slightly different PSO terms).

A   **B**
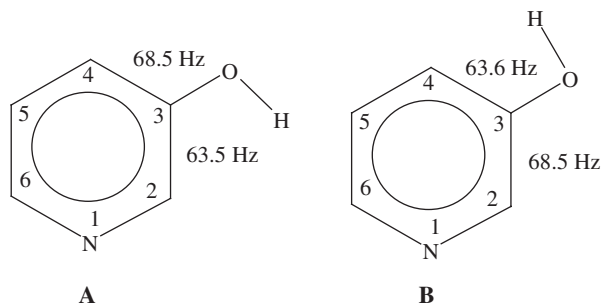
Wrackmeyer and Köhler[426] carried out calculations of coupling constants of different types in a series of azocompounds and some aminonitrenes. Although for many calculated couplings reported in that paper there are no experimental values to compare with, for the few couplings where such comparison is possible, a reasonable agreement is observed. Many of the couplings reported in that paper show interesting features; a few of them are as follows. In all cases $^1J_{NN}$ couplings across the N=N bond are negative and are dominated by the noncontact PSO and SD contributions, which are negative, as it is also the FC term. However, in pyridazine, which is not classified as an azocompound, $^1J_{NN}$ is negative, but it is dominated by the FC term. For the *trans* and *cis*-configurations of H–N = N–H, the four Ramsey terms of the $^3J_{HH}$ couplings are compared in Table 18. It is observed that the FC term is only slightly larger for the *trans* than for the *cis*-configuration, while the DSO term of the former is large and negative, as expected (see Section 2.5). On the other hand, the large value of the total calculated $^3J_{HH}$ for the *cis*-configuration is in agreement with the trend depicted in Table 6 for the $^3J_{CC}$ couplings in benzene and other six-membered heteroaromatic compounds.

Table 18. Comparison of the calculated four Ramsey terms for *vicinal* J_{HH} couplings (in Hz) for the *trans*- and *cis*-configurations of H–N = N–H[a]

Coupling term		
	trans-$^3J_{HH}$	*cis*-$^3J_{HH}$
FC	42.9	41.6
SD	0.6	0.0
PSO	2.9	−0.7
DSO	−5.5	−0.4
Total	40.9	40.5

[a]Values taken from Ref. 426.

4.2.5. *Fullerenes*

As an illustration of the insight into the nature of chemical bonding that can be gained through the calculation of spin–spin couplings, we will consider the classical example of fullerenes. Since the historical discovery of C_{60} fullerene[427] and the first NMR evidence of the chemical equivalence of its all sixty carbons,[428] the first theoretical prediction of all 23 possible J_{CC} couplings of the fullerene C_{60} ''buckyball'' has been performed in the pioneering paper by Jaszunsky *et al.*[429] at the DFT-B3LYP Kohn-Sham level using the Huzinaga basis set [9s5p1d/5s4p1d][194] with the polarization functions suggested by van Wüllen.[430] The C_{60} ball is built from 12 nonadjacent equilateral pentagons. Between two selected pentagons in antipode locations, there are two concentric shells, each containing five nonadjacent pentagons, symmetrically located about the axis connecting the reference pentagon and its antipode. Within each pentagon, there are two distinct coupling constants. Next, there are nine distinct coupling constants between the reference pentagon and the carbon nuclei in the first concentric shell, and likewise, nine couplings with the carbon nuclei in the second shell. Finally, there are three distinct couplings between the reference pentagon and its antipode, giving a total of 23 distinct coupling constants in C_{60} compiled in Table 19. The one-bond couplings within a single pentagon and between neighboring pentagons were calculated as 62 Hz and 77 Hz, respectively. It is noteworthy that both couplings and especially the latter are substantially larger than that in benzene (55.87 Hz).[362] This seems to suggest that the hexagonal bonds in fullerene possess essentially higher s-character than the carbon–carbon bond in benzene. The *geminal* couplings are *ca.* 7 Hz within one pentagon and *ca.* 1 Hz between neighboring pentagons. Except for the *vicinal* couplings, which are *ca.* 4 Hz, the long-range couplings are 1 Hz or smaller. Again, there is a striking difference of $^2J_{CC}$ and $^3J_{CC}$ couplings in fullerene and benzene

Table 19. J_{CC} spin–spin coupling constants of fullerene C_{60} calculated at the DFT-B3LYP level[a]

Pentagon	Number of intervening bonds	Coupling path[b]	$^nJ_{CC}$
Self	1	p	61.63
	2	pp	6.94
First shell	1	h	77.35 (55.87)[c]
	2	ph	1.00 (−2.49)
	3	php-*cis*	4.27 (10.11)
	3	php-*trans*	3.83
	3	pph	3.81
	4	pphp *cis*	−0.99
	4	pphp-*trans*	0.43
	5	pphpp-*cis*	0.52
	5	pphpp-*trans*	−0.07
Second shell	4	*hpph*	0.27
	5	hpphp-*cis*	0.55
	5	hpphp-*trans*	0.21
	6	phpphp-*cis*	−0.34
	6	phpphp-*trans*	0.30
	6	hpphpp	0.15
	7	phpphpp-*cis*	0.34
	7	phpphpp-*trans*	−0.28
	8	pphpphpp	0.33
Antipode	7	hpphpph	−0.08
	8	phpphpph	0.27
	9	pphpphpph	−0.27

[a]All couplings are in Hz. Calculated values are taken from Ref. 429.
[b]The shortest coupling paths are considered; "p" stands for the pentagon bond while "h" stands for the hexagon bond.
[c]Given in parentheses are the related J_{CC} experimental values in benzene, taken from Ref. 362.

(cf. Table 19) that indicates how different the nature of the carbon–carbon bonds forming the frameworks of these two classical π-systems is. To the best of our knowledge, no experimental J_{CC} couplings in C_{60} were reported so far. The reason for this is very clear: the NMR spectrum of C_{60} consists only of a single line, which demonstrates that all the 60 carbon atoms are equivalent.

Shortly after Jaszunsky *et al.*'s paper[429] appeared, Peralta *et al.*[431] reported the DFT calculation of all $^nJ_{CC}$ couplings in C_{70}. The spectrum of this fullerene consists of 5 lines showing that only 5 out of the 70 carbon atoms are nonequivalent.[428] Johnson *et al.*[432] reported a 2D spectrum of this compound. The connectivity of the nonequivalent carbon atoms was established, and four different $^1J_{CC}$ couplings were measured. Shown below are the transversal and longitudinal views of C_{70} possessing D_{5h} symmetry. The geometry of C_{70} was optimized at the DFT-B3LYP/cc-pVDZ level, and all four Ramsey contributions to couplings were calculated using three different basis sets and two different functionals, BLYP and B3LYP, comparing the experimental results with calculated values. The best values were

Table 20. Comparison between calculated and experimental $^1J_{CC}$ couplings (in Hz) in C_{70}[a]

$^1J_{CiCj}$	FC	SD	PSO	DSO	Total	Exp.[b]
$^1J_{1,11}$	73.6	1.5	−7.1	0.4	68.4	68
$^1J_{11,36}$	58.6	0.7	−4.7	0.4	55.0	55
$^1J_{36,56}$	58.1	0.7	−4.5	0.4	54.7	55
$^1J_{56,66}$	65.7	1.0	−6.0	0.4	61.1	62

[a]Calculated values are taken from Ref. 431.
[b]Experimental values are taken from Ref. 432.

obtained at the B3LYP/cc-pCVDZ-sd level, being 1,680 the total number of basis functions used in this calculation. In the transversal view, it is easy to observe five nonequivalent carbons, e.g., C_1, C_{11}, C_{36}, C_{56}, and C_{66}. Couplings involving non-equivalent carbon atoms are compared with experimental values in Table 20, where the different Ramsey contributions are displayed.
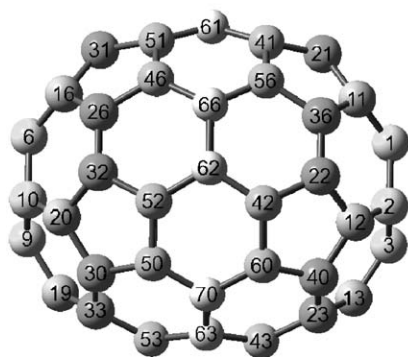
Transversal view of C_{70}
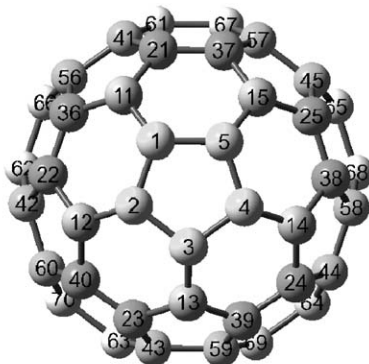
Longitudinal view of C_{70}

The calculation gives eight $^1J_{CC}$ couplings but, since experiments were observed, only four of them, i.e., those involving two equivalent atoms were not observed; Table 20 shows only those four couplings. The agreement between calculated and experimental couplings is surprisingly good, and, therefore, other calculated couplings were considered reliable enough to analyze them in order to gain further insight into the electronic structure of this remarkable compound.

A few comments should be made to highlight the similarities and differences of the C_{60} and C_{70} structures. In both compounds, all pentagon rings are not adjacent and, while in C_{60} all pentagons are equilateral, in C_{70}, the only equilateral is both in the apical positions, e.g., C_1-C_2-C_3-C_4-C_5. The sequence of carbon atoms C_{61}, C_{66}, C_{62}, C_{70}, C_{63} defines the symmetry plane of this D_{5h} symmetry compound. The sequence of carbon atoms C_{21}, C_{41}, C_{56}, C_{36} and its specular image are known as the "borders of the belt."[431] Here, $^1J_{CC}$ couplings along these borders follow the sequence of 59.7, 54.7, and 65.7 Hz that is typical of a conjugated C–C bonds, and

Table 21.   Calculated $^1J_{CC}$ couplings in C_{60} and $C_{60}^{(6-)}$ (in Hz)

Compd.	$^1J_{CiCj}$	FC	SD	PSO	DSO	Total
C_{60}	$^1J_{1,2}{}^a$	73.6	1.6	−7.2	0.4	68.5
	$^1J_{1,13}{}^a$	58.8	0.7	−4.6	0.4	55.3
	$^1J_{1,2}{}^b$	82.2	0.4	−5.7	0.4	77.3
	$^1J_{1,13}{}^b$	64.6	0.3	−3.7	0.4	61.6
$C_{60}^{(6-)}$	$^1J_{1,2}{}^a$	62.5	0.3	−5.2	0.4	58.0
	$^1J_{1,13}{}^a$	57.1	0.8	−5.2	0.4	53.1
Benzene^a	$^1J_{CC}$	61.5	1.3	−6.7	0.4	56.3^c

^{a}Taken from Ref. 433.
^{b}Taken from Ref. 429.
^{c}Experimental value 55.8 Hz taken from Ref. 362.

this is supported also by the trend of their respective SD and PSO contributions. This observation suggests that diamagnetic currents of opposite sense are circulating along these borders. It is remarkable to note that this observation allows an adequate rationalization of the large difference on the nuclear magnetic shielding constants for apical and for carbon atoms belonging to the symmetry plane.

All two-bond J_{CC} couplings in C_{70} fall into two well-separated groups, namely, those with coupling pathway containing two pentagon bonds, and those containing only one pentagon bond, and, on the other hand, those containing two hexagon bonds. The former are in the range of 6–7 Hz, and are mainly contributed from the one two-bond and one three-bond pathways and, therefore, they can be designed as $^{2+3}J_{CC}$ couplings while the latter two *geminal* $^2J_{CC}$ couplings are only of about 1 Hz.

The excellent results obtained for $^1J_{CC}$ couplings in C_{70} suggested that similar calculations could also be carried out both in C_{60} and in C_{60}^{6-} by the same group.[433] The respective $^1J_{CC}$ couplings are compared with those in benzene and those reported in Ref. 429 for C_{60} in Table 21. The discrepancy between both calculations of $^1J_{CC}$ couplings in C_{60} is noteworthy.
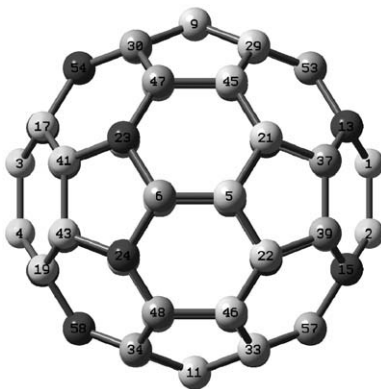
Fullerene C_{60}

Table 22. Comparison between the FC term of long-range $^nJ_{Ci,Cj}$ couplings (in Hz) in C_{70} for pathways along the belt border and transversal to it[a]

n	Belt border		Transversal	
9	$J_{C_{53},C_{61}}$	+0.24	J_{C_{10},C_1}	−0.05
8	$J_{C_{63},C_{61}}$	−0.20	J_{C_{20},C_1}	+0.04
7	$J_{C_{63},C_{41}}$	+0.21	J_{C_{32},C_1}	−0.02

[a]Taken from Ref. 433.

The assertion that in C_{70} the belt borders behave like a conjugating C–C bond sequence suggests that the FC term of the long-range $^nJ_{CC}$ ($n>4$) couplings along the borders of the "belt" should follow the known trends of the π-transmitted contribution. These follow the alternating sign rule, $(-1)^{n+1}$, and show the low-decreasing rate of their absolute values with n, the number of bonds separating the coupling nuclei.[433] It must be recalled that for $n>4$, the σ-transmitted component usually is notably smaller than that transmitted through the π-electronic system. Since the adjacent bonds transversal to the symmetry plane, e.g., C–C_s–C (where C_s belongs to the symmetry plane) are equal, they cannot form part of a conjugating C–C sequence. For this reason, it can be expected that the longer range $^nJ_{CC}$ couplings ($n>4$) providing pathways across the symmetry plane should be notably smaller (in absolute value) than similar couplings transmitted along any border of the belt. Table 22 shows the examples $n=7, 8, 9$, for a coupling pathway along the belt border and for a coupling pathway transversal to the belt. It is noteworthy that longer range couplings for transversal pathways do not hold the sign rule since, for these couplings with small absolute values, the small contributions from the pathways of different parities are not negligible.

The excellent agreement between calculated and measured values for the $^1J_{CC}$ couplings in C_{70} found by Peralta et al.[431] prompted a very interesting attempt by Anklin and Alemany[434] to measure $^nJ_{CC}$ ($n>1$) in C_{70}. With advanced techniques, they were able not only to increase the accuracy commonly achieved for measuring the $^1J_{CC}$ couplings but were also able to measure several longer range couplings. It is very encouraging that the small difference[431] between calculated $^1J_{11,36} = 55.0$ Hz and $^1J_{36,56} = 54.7$ Hz is in a nice agreement with the new experimental values of Anklin and Alemany,[434] see Table 23.

Recently Barone et al.[435] studied five boron nitride hollow octahedral cages using density functional theory (DFT) and calculated several $^1J_{14N,11B}$ couplings, after testing their approach, DFT-B3LYP/cc-PVTZ, by calculating the $^1J_{14N,11B} = 22.6$ Hz coupling in N-N′-N″-tris(trimethylsylil)borazine, and comparing it with its experimental value, 23.0 ± 0.5 Hz.[436]

4.2.6. Carbohydrates and biopolymers

A large number of papers appeared recently dealing with the theoretical studies, mainly at the DFT level, of stereochemical behavior of different spin–spin couplings

Table 23. Comparison of $^1J_{CC}$ couplings (in Hz) calculated in C_{70} with new experimental values

$^1J_{CiCj}$	Old Exp.[a]	New Exp.[b]	Calc.[c]
$^1J_{1,11}$	68	68.77 or 68.69	68.4
$^1J_{11,36}$	55	55.64 or 55.65	55.0
$^1J_{36,56}$	55	55.35 or 55.45	54.7
$^1J_{56,66}$	62	61.74 or 61.83	61.1

[a]Experimental values taken from Ref. 432.
[b]Experimental values taken from Ref. 434. $^1J_{CC}$ values from each half of the quartet are given.
[c]Calculated values taken from Ref. 431.

in carbohydrates, peptides, proteins, nucleic acids, and other biopolymers claiming for a specialist comprehensive review. Only very few illustrative examples from the wide scope of basic results in this area are touched upon in this section just to drop some hints on what can be gained from these studies.

Tähtinen et al.[437] studied the solution-state conformations of various cis-fused 7a(8a)-methyl octa(hexa)hydrocyclopenta[d][1,3]oxazine and [3,1]oxazine derivatives complementing their previous study.[438] In the former paper,[437] they reported the FPT-DFT study of the FC terms, including geometry optimizations using the Gaussian 98 suite of programs, while for three structures, they also used the DeMon-NMR program[176,217] to calculate the FC, PSO, and DSO terms, and found a good agreement between the calculated and experimental $^3J_{HH}$ couplings.

González-Outeiriño et al.[439] studied the structure and conformational behavior of sulfonium salt glycosidase inhibitors in solution. They measured and calculated $^3J_{HH}$ and $^3J_{CH}$ couplings. Using a combination of calculated couplings and the determination of NOE data, they were able to get a complete picture of the conformational properties of this complex system.

The COLOGNE 99 program[259] was used by Sychrovský et al.[440] to calculate couplings within the CP-DFT-B3LYP approach. Calculated couplings were used to distinguish between the specific direct and the water-mediated binding of the divalent metal cations, Mg^{2+} and Zn^{2+}, to a guanine base. Indeed, the intermolecular couplings $^1J_{XO_6}$ and $^1J_{XN_7}$ ($X = Mg^{2+}, Zn^{2+}$) provide perspective means to unambiguously assign the specific inner-shell binding motif of the hydrated cation. These couplings approach zero when the binding of the cation is water mediated.

Thibaudeau et al.,[441] performed a systematic study of the C–C and C–O bond conformations of the saccharide hydroxymethyl groups. They measured $^1J_{CH}$, $^2J_{CH}$, and $^3J_{CH}$ couplings in methyl α- and β-pyranosides of D-glucose and D-galactose enriched with the ^{13}C isotope at the C_4, C_5, and C_6 positions and performed detailed DFT calculations determining the hypersurfaces of several $^nJ_{HH}$ $^nJ_{CH}$, and $^nJ_{CC}$ ($n = 1$–3) spin–spin couplings. Coupling constants were calculated with the FPT-DFT methodology considering only the FC term by using a modified version of the Gaussian 98 suite of programs, reported previously.[442] Coupling constant calculations performed in conformationally constrained systems were compared with

their corresponding experimental values and almost quantitative agreement between the calculated and measured couplings was observed. Stereochemical behavior of $^1J_{CC}$ couplings with respect to the rotational conformations of the hydroxymethyl groups in monosaccharides[443] together with the configuration of the anomeric center in pyranoses,[444] furanoses,[445] and septanoses[446] were also studied recently at the FPT-INDO level.

Klepach et al.,[447] using the same theoretical methodology commented above,[441] studied the stereochemical dependence of $^2J_{CH}$ couplings corresponding to the C–C–H coupling pathway in order to use them as probes to determine the ϕ-glycosidic torsion angle in oligosaccharides. The aldopyranosyl ring involving the C_2 and H_1 atoms in the coupling pathway of the $^2J_{CH}$ coupling was used as a model system. It was found that $^2J_{CCH}$ values were influenced by the C–O torsion angles at both carbon atoms of the coupling pathway, but the effect was greater at the carbon bearing the coupling proton (see also Section 2.3).

Zhu et al.[448] applied the same methodology for calculating J_{CH} and J_{CC} couplings in the model N-acetylated aldopyranosides. Besides, they prepared 2-acetamido-2-deoxy-D-[1-13C]aldohexopyranosides to compare the OH and $NHCOCH_3$ substituent effects at C_2 on the J_{CH} and J_{CC} couplings under study. The DFT-calculated $^1J_{CH}$ and $^1J_{CC}$ couplings were significantly affected by the exocyclic C–O torsions, whereas $^3J_{CH}$ and $^3J_{CC}$ appeared much less influenced.

Based on the DFT approach, Houseknecht et al.[449] obtained the improved Karplus equations for $^3J_{C_1,H_4}$ coupling in aldopentofuranosides accounting for the effect of anomeric stereochemistry to exploit new potentialities in the conformational analysis of aldopentofuranose residues, especially those containing any substituent at the anomeric center.

Bouř et al.[450] studied several furanose derivatives with restricted conformational flexibility in order to assess the performance of the DFT framework for studying saccharides. The conformationally restricted compounds were prepared making furanose models containing the polar and strained oxirane, thiirane, and aziridine rings that virtually freeze the furanose ring. The details of synthesis and the X-ray experiments are given elsewhere (see references in Ref. 450), while all NMR data are reported in the commented paper.[450] Coupling constants were calculated within the CP-DFT-B3LYP approximation, and all four Ramsey contributions were considered, using the COLOGNE program.[259] Convergence of the calculated couplings with the size of the basis set was considered in this paper including seven basis sets, 4-31G, 6-31G**, 6-311G**, IGLO-II, aug-cc-pVDZ, and IGLO-III. As it can be expected from the known facts about the influence of the hyperconjugative interactions on couplings in small strained rings (see Section 2.3), conventional Karplus equations are not adequate for this type of compounds. In general, a good agreement between the calculated and measured couplings was obtained, while the observed differences were rationalized as originating either in the shortcomings of the DFT approach or in the neglecting of the vibrational effects.

Cordier et al.[451] performed the direct observation of $^{3h}J_{C_αC'}$ couplings through the hydrogen bond in the β-sheets of proteins, i.e., with a coupling pathway of the type $C_α$–$H_α$···O=C. This corresponds to a bifurcated hydrogen bond which takes

place between the carbonyl oxygen atom and both hydrogens, H_α and H_N. The absolute value of this experimental coupling is close to 0.3 Hz, in reasonable agreement with the calculated FPT-DFT couplings, which included only the FC term. In the previous detailed study of the structural dependence of the interresidue $^{3h}J_{NC'}$ scalar couplings in α-helices and β-sheets in proteins, Barfield[452] found that the magnitude of these couplings is explicitly dependent on the local geometry of the hydrogen bond, in particular, the H···O internuclear separation, the C=O···H angle and the N–C=O···H dihedral angle.

There has been a considerable interest in establishing the effect of conformational averaging on measured physical properties associated with a distribution over an ensemble of microscopic states of proteins. Molecular dynamics simulations of proteins have demonstrated that it is possible to obtain ensemble averages compatible with a particular microscopic state from the trajectory of a single molecule. Following these principles, Markwick *et al.*[453] combined molecular dynamics simulation with the FPT-DFT calculations to obtain the FC contributions to $^{3h}J_{NC'}$ scalar couplings in the SMN Tudor domain, a 55-residue β-barrel-shaped protein with the well-defined X-Ray and NMR structures. Calculated couplings were in good agreement with experiment showing marked stereochemical dependence upon the local molecular geometry in the peptide backbone and opening new guides in the stereochemical studies of proteins and related biomolecular research.

ACKNOWLEDGEMENTS

REFERENCES

1. J. Kowalewski, *Prog. NMR Spectrosc.*, 1977, **11**, 1.
2. J. Kowalewski, *Ann. Repts. NMR Spectrosc.*, 1982, **12**, 81.
3. T. Helgaker, M. Jaszuński and K. Ruud, *Chem. Rev.*, 1999, **99**, 293.
4. J. Vaara, J. Jokisaari, R. E. Wasylishen and D. L. Bryce, *Prog. NMR Spectrosc.*, 2002, **41**, 233.
5. T. Helgaker and M. Pecul, *Calculation of NMR and EPR Parameters. Theory and Applications,* Wiley-VCH, Weinheim, 2004, 101.
6. T. A. Ruden and K. Rudd, *Calculation of NMR and EPR Parameters. Theory and Applications*, Wiley-VCH, Weinheim, 2004, 153.
7. I. Ciofini, *Calculation of NMR and EPR Parameters. Theory and Applications*, Wiley-VCH, Weinheim, 2004, 191.
8. J. Autschbach, & T. Ziegler, *Encyclopedia of Nuclear Magnetic Resonance,* Vol. 9, John Wiley & Sons, Chichester, 306.
9. J. Autschbach, T. Ziegler, *Calculation of NMR and EPR Parameters. Theory and Applications,* 2004, Wiley-VCH, Weinheim, 249.
10. O. L. Malkina, *Calculation of NMR and EPR Parameters. Theory and Applications,* Wiley-VCH, Weinheim, 2004, 307.

11. D. A. Case, *Calculation of NMR and EPR Parameters. Theory and Applications,* Wiley-VCH, Weinheim, 2004, 341.
12. J. E. Del Bene, *Calculation of NMR and EPR Parameters. Theory and Applications,* Wiley-VCH, Weinheim, 2004, 353.
13. M. Bühl, Calculation of NMR and EPR Parameters. Theory and Applications, Wiley-VCH, Weinheim, 2004, 421.
14. R. E. Wasylishen, Calculation of NMR and EPR Parameters. Theory and Applications, Wiley-VCH, Weinheim, 2004, 433.
15. J. Autschbach, *Principles and Applications of Density Functional Theory in Inorganic Chemistry I*, Vol. 112, Springer, Heidelberg, 2004 1.
16. J. Vaara, P. Manninen, P. Lantto, *Calculation of NMR and EPR Parameters. Theory and Applications,* Wiley-VCH, Weinheim, 2004, 209.
17. S. P. A. Sauer and M. J. Packer, *Computational Molecular Spectroscopy*, Wiley, London, 2000 221.
18. T. Helgaker, P. Jørgensen and J. Olsen, *Molecular Electronic Structure Theory*, John Wiley & Sons, Ltd, Chichester, West Sussex, England, 2000.
19. M. Kaupp, M. Bühl and V. G. Malkin, *Calculation of NMR and EPR Parameters. Theory and Applications*, in: M. Kaupp, M. Bühl and V. G. Malkin, eds., Wiley-VCH, Weinheim, 2004.
20. N. F. Ramsey, *Phys. Rev.*, 1953, **91**, 303.
21. S. P. A. Sauer, *J. Chem. Phys.*, 1993, **98**, 9220.
22. J. Linderberg and Y. Őhrn, *Propagators in Quantum Chemistry*, Academic Press, London, 1973.
23. J. Olsen and P. Jørgensen, *J. Chem. Phys.*, 1985, **82**, 3235.
24. D. L. Bryce and R. E. Wasylishen, *Acc. Chem. Res.*, 2003, **36**, 327.
25. G. A. Aucar and J. Oddershede, *Int. J. Quantum Chem.*, 1993, **47**, 425.
26. L. Visscher, T. Enevoldsen, T. Saue, H. J. A. Jensen and J. Oddershede, *J. Comput. Chem.*, 1999, **20**, 1262.
27. T. Enevoldsen, L. Visscher, T. Saue, H. J. A. Jensen and J. Oddershede, *J. Chem. Phys.*, 2000, **112**, 3493.
28. I. Alkorta and J. Elguero, *Int. J. Mol. Sci.*, 2003, **4**, 64.
29. A. J. Dingley, F. Cordier and S. Grzesiek, *Concepts Magn. Reson.*, 2001, **13**, 103.
30. S. Grzesiek, F. Cordier and A. J. Dingley, *Methods Enzymol*, 2001, **338**, 111.
31. M. Pecul and J. Sadlej, in *Computational Chemistry: Reviews of Current Trends*, Vol. 8, World Scientific, Singapore, 2003, 131.
32. A. V. Afonin, Z. V. Stepanova, V. K. Voronov and A. V. Vashchenko, *Khim. Geterotsikl. Soedin.*, 1987, 1422.
33. I. D. Rae, J. Weigold, R. H. Contreras and R. R. Biekofsky, *Magn. Reson. Chem.*, 1993, **31**, 836.
34. A. J. Dingley and S. Grzesiek, *J. Am. Chem. Soc.*, 1998, **120**, 8293.
35. R. H. Contreras, V. Barone, J. C. Facelli and J. E. Peralta, *Ann. Repts. NMR Spectrosc.*, 2003, **51**, 167.
36. J. E. Del Bene, *J. Phys. Chem. A*, 2004, **108**, 6820.
37. J. E. Del Bene, S. A. Perera and R. Bartlett, *J. Am. Chem. Soc.*, 2000, **122**, 3560.
38. S. A. Perera, H. Sekino and R. J. Bartlett, *J. Chem. Phys.*, 1994, **101**, 2186.
39. S. A. Perera and R. J. Bartlett, *J. Am. Chem. Soc.*, 1996, **118**, 7849.
40. S. A. Perera and R. J. Bartlett, *J. Am. Chem. Soc.*, 1995, **117**, 8476.
41. S. A. Perera, M. Nooijen and R. J. Bartlett, *J. Chem. Phys.*, 1996, **104**, 3290.
42. M. Pecul, *J. Chem. Phys.*, 2000, **113**, 10835.
43. S. J. Grabowski, W. A. Sokalski and J. Leszczynski, *J. Phys. Chem. A*, 2006, **110**, 4772.
44. R. F. W. Bader, *Atoms in Molecules: A Quantum Theory*, Oxford University Press, Oxford, 1990.
45. W. A. Sokalski, S. Roszak and K. Pecul, *Chem. Phys. Lett.*, 1988, **153**, 153.
46. D. B. DuPré, *J. Phys. Chem. A*, 2005, **109**, 622.
47. R. H. Contreras and J. E. Peralta, *Prog. NMR Spectrosc.*, 2000, **37**, 321.
48. A. R. Engelmann and R. H. Contreras, *Int. J. Quantum Chem.*, 1983, **23**, 1033.
49. A. C. Diz, R. H. Contreras, M. A. Natiello and H. O. Gavarini, *J. Comp. Chem.*, 1985, **6**, 647.
50. O. L. Malkina and V. G. Malkin, *Angew. Chem. Int. Ed.*, 2003, **42**, 4335.

51. M. Kaupp, A. Patrakov, R. Reviakine and O. L. Malkina, *Chem. Eur. J.*, 2005, **11**, 2773.
52. R. H. Contreras, M. A. Natiello and G. E. Scuseria, *Magn. Reson. Rev.*, 1985, **9**, 239.
53. J. -C. Hierso, A. Fihri, V. V. Ivanov, B. Hanquet, N. Pirio, B. Donnadieu, B. Robière, R. Amardiel and P. Meunier, *J. Am. Chem. Soc.*, 2004, **126**, 11077.
54. I. Alkorta and J. Elguero, *Struct. Chem.*, 2004, **15**, 117.
55. R. W. F. Bader, *J. Phys. Chem. A*, 1998, **102**, 7314.
56. M. Iwaoka, T. Katsuda, H. Komatsu and S. Tomoda, *J. Org. Chem.*, 2005, **70**, 321.
57. P. F. Provasi, G. A. Aucar, M. Sanchez, I. Alkorta, J. Elguero and S. P. A. Sauer, *J. Phys. Chem. A*, 2005, **109**, 6555.
58. A. Asensio, N. Kobko and J. J. Dannenberg, *J. Phys. Chem. A*, 2003, **107**, 6441.
59. P. Salvador, N. Kobko, R. Wieczorek and J. J. Dannenberg, *J. Am. Chem. Soc.*, 2004, **126**, 14190.
60. N. Juranic, M. C. Moncrieffe, V. A. Likic, F. G. Pendergast and S. Macura, *J. Am. Chem. Soc.*, 2002, **124**, 14221.
61. J. E. Del Bene and R. J. Bartlett, *J. Am. Chem. Soc.*, 2000, **122**, 10480.
62. S. H. M. Söntjens, M. H. P. van Genderen and R. P. Sijbesma, *J. Org. Chem.*, 2003, **68**, 9070.
63. T. Tuttle, E. Kraka, A. Wu and D. Cremer, *J. Am. Chem. Soc.*, 2004, **126**, 5093.
64. J. E. Del Bene, J. Elguero, I. Alkorta, O. Mó and M. Yañez, *J. Phys. Chem. A*, 2005, **109**, 2350.
65. A. E. Reed and F. Weinhold, *J. Chem. Phys.*, 1983, **78**, 4066.
66. R. H. Contreras, A. L. Esteban, E. Díez, N. J. Head and E. W. Della, *Mol. Phys.*, 2006, **104**, 485.
67. M. Barfield, in *Encyclopedia of Nuclear Magnetic Resonance*, Wiley, Chichester, 1996, 2520.
68. J. A. Pople and A. A. Bothner-By, *J. Chem. Phys.*, 1965, **42**, 1339.
69. M. L. Munzarová and V. Sklenář, *J. Am. Chem. Soc.*, 2002, **124**, 10666.
70. M. L. Munzarová and V. Sklenář, *J. Am. Chem. Soc.*, 2003, **125**, 3649.
71. E. Kleinpeter, A. Koch and K. Pihlaja, *Tetrahedron*, 2005, **61**, 7349.
72. J. E. Anderson, J. Cai, A. G. Davies, *J. Chem Soc., Perkin Trans.*, 1997, 2633.
73. R. Notario, M. V. Roux, G. Cuevas, J. Cárdenas, V. Leyva and E. Juaristi, *J. Phys. Chem. A*, 2006, **110**, 7703.
74. A. S. Perlin and B. Casu, *Tetrahedron Lett.*, 1969, 292.
75. K. Martínez-Mayorga, E. Juaristi and G. Cuevas, *J. Org. Chem.*, 2004, **69**, 7266.
76. G. Cuevas, K. Martínez-Mayorga, M. C. Fernández-Alonso, J. Jiménez-Barbero, C. L. Perrin, E. Juaristi and N. López-Mora, *Angew. Chem. Int. Ed.*, 2005, **44**, 2360.
77. A. E. Reed and P. v. R. Schleyer, *J. Am. Chem. Soc.*, 1990, **112**, 1434.
78. N. C. Maiti, Y. Zhu, I. Carmichael, A. S. Serianni and V. E. Anderson, *J. Org. Chem.*, 2006, **71**, 2878.
79. R. H. Contreras, A. L. Esteban, E. Díez, E. W. Della, I. J. Lochert, F. P. dos Santos and C. F. Tormena, *J. Phys. Chem. A*, 2006, **110**, 4266.
80. R. H. Contreras, M. C. Ruiz de Azúa, C. G. Giribet, G. A. Aucar and R. Lobayan de Bonczok, *J. Mol. Struct. (Theochem)*, 1993, **284**, 249.
81. B. Wrackmeyer and O. L. Tok, *Z. Nasturforsch.*, 2005, **60b**, 259.
82. A. D. Becke, *J. Chem. Phys.*, 1993, **98**, 5648.
83. C. T. Lee, W. T. Yang and R. G. Parr, *Phys. Rev. B*, 1988, **37**, 785.
84. D. G. de Kowalewski, E. Díez, A. L. Esteban, V. Barone, J. E. Peralta and R. H. Contreras, *Magn. Reson. Chem.*, 2004, **42**, 938.
85. W. Scherer and G. S. McGrady, *Angew. Chem. Int. Ed.*, 2004, **43**, 1782.
86. D. L. Lichtenberger, *Organometallics*, 2003, **22**, 1599.
87. X. Solans-Monfort, E. Clot, C. Copéret and O. Eisenstein, *Organometallics*, 2005, **24**, 1586.
88. X. Solans-Monfort and O. Eisenstein, *Polyhedron*, 2006, **25**, 339.
89. J. Autschbach, *Struct. Bond.*, 2004, **112**, 1.
90. C. Mahaim, P. A. Corrupt and P. Vogel, *Helv. Chim. Acta*, 1985, **68**, 2182.
91. M. Barfield and D. M. Grant, *J. Am. Chem. Soc.*, 1963, **85**, 1899.
92. P.E. Hansen, *The Chemistry of Double-Bonded Functional Groups*, Wiley, New York, 1989, 321
93. C. F. Tormena, R. Rittner, R. H. Contreras and J. E. Peralta, *J. Phys. Chem. A*, 2004, **108**, 7762.
94. D. D. Elleman and S. L. Manatt, *J. Mol. Spectrosc.*, 1962, **9**, 477.

95. P. E. Hansen, *Prog. NMR Spectrosc.*, 1981, **14**, 175.

96. V. Barone, J. E. Peralta and R. H. Contreras, *Encyclopedia of Computational Chemistry* (Electronic version), John Wiley & Sons, DOI 10.1002/0470845015.cu0020 (May 15, 2004).

97. A. L. Esteban, M. P. Galache, F. Mora, E. Díez, J. Casanueva, J. San Fabián, V. Barone, J. E. Peralta and R. H. Contreras, *J. Phys. Chem. A*, 2001, **105**, 5298.

98. A. Soncini and P. Lazzeretti, *Chem. Phys. Lett.*, 2005, **409**, 177.

99. N. Castillo, C. F. Matta and R. J. Boyd, *J. Chem. Inf. Model.*, 2005, **45**, 354.

100. A. Soncini and P. Lazzeretti, *J. Chem. Phys.*, 2003, **119**, 1343.

101. R. F. W. Bader and M. E. Stephens, *J. Am. Chem. Soc.*, 1975, **97**, 7391.

102. M. Barfield and B. Chakrabarti, *Chem. Rev.*, 1969, **69**, 757.

103. R. H. Contreras and J. C. Facelli, *Ann. Repts. NMR Spectrosc.*, 1993, **27**, 255.

104. Y. G. Gakh, A. A. Gakh and A. M. Gronenborn, *Magn. Reson. Chem.*, 2000, **38**, 551.

105. E. W. Della, I. J. Lochert, J. E. Peralta and R. H. Contreras, *Magn. Reson. Chem.*, 2000, **38**, 395.

106. E. W. Della and N. J. Head, *J. Org. Chem.*, 1995, **60**, 5303.

107. E. W. Della, E. Corsaris and P. T. Hine, *J. Am. Chem. Soc.*, 1981, **103**, 4131.

108. R. H. Contreras, E. Díez, A. L. Esteban, E. W. Della and I. J. Lochert, *J. Arg. Chem. Soc.*, (in press).

109. W. Adcock and A. R. Krstic, *Magn. Reson. Chem.*, 2000, **38**, 115.

110. M. Barfield, E. W. Della, P. E. Pigou and S. R. Walter, *J. Am. Chem. Soc.*, 1982, **104**, 3549.

111. K. B. Wiberg and D. S. Connor, *J. Am. Chem. Soc.*, 1966, **88**, 4437.

112. G. A. Olah, J. G. Shih, V. V. Krishnamurthy and B. P. Singh, *J. Am. Chem. Soc.*, 1984, **106**, 4492.

113. W. Adcock, H. Gangodawila, G. B. Kok, V. S. Iyer, W. Kitching, G. M. Drew and D. Young, *Organometallics*, 1987, **6**, 156.

114. W. Adcock and A. R. Krstic, *Magn. Reson. Chem.*, 1997, **35**, 663.

115. P. F. Provasi, G. A. Aucar and S. P. A. Sauer, *J. Phys. Chem. A*, 2004, **108**, 5393.

116. R. M. Lynden-Bell and R. K. Harris, *Nuclear Magnetic Resonance Spectroscopy*, Appleton Century Crofts, New York, 1969.

117. W. S. Lee and J. M. Schulman, *J. Chem. Phys.*, 1979, **70**, 1530.

118. J. E. Pérez, F. S. Ortiz, R. H. Contreras, C. G. Giribet and M. C. Ruiz de Azúa, *J. Mol. Struct. (Theochem)*, 1990, **210**, 193.

119. H. Cibulski, M. Pecul, T. Helgaker and M. Jaszuński, *J. Phys. Chem. A*, 2005, **109**, 4162.

120. J. E. Del Bene and J. Elguero, *Chem. Phys. Lett.*, 2003, **382**, 100.

121. J. E. Del Bene and J. Elguero, *Magn. Reson. Chem.*, 2004, **42**, 421.

122. J. E. Del Bene and J. Elguero, *J. Phys. Chem. A*, 2004, **108**, 11762.

123. J. E. Del Bene, J. Elguero and I. Alkorta, *J. Phys. Chem. A*, 2004, **108**, 3662.

124. E. W. Della, P. E. Pigou, D. K. Taylor, L. B. Krivdin and R. H. Contreras, *Aust. J. Chem.*, 1993, **46**, 63.

125. M. Stöcker, *Org. Magn. Reson.*, 1982, **20**, 175.

126. M. Klessinger and J. -H. Cho, *Angew. Chem. Int. Ed. Engl.*, 1982, **21**, 764.

127. G. A. Aucar, V. Zunino, M. B. Ferraro, C. G. Giribet, M. C. Ruiz de Azua and R. H. Contreras, *J. Mol. Struct. (Theochem)*, 1990, **205**, 63.

128. G. A. Aucar, M. C. Ruiz de Azua, C. G. Giribet and R. H. Contreras, *J. Mol. Struct. (Theochem)*, 1990, **205**, 79.

129. A. R. Engelmann, M. A. Natiello, G. E. Scuseria and R. H. Contreras, *Comp. Phys. Commun.*, 1986, **39**, 409.

130. R. H. Contreras, C. G. Giribet, M. C. Ruiz de Azua, C. N. Cavasotto, G. A. Aucar and L. B. Krivdin, *J. Mol. Struct. (Theochem)*, 1990, **210**, 175.

131. L. B. Krivdin and T. A. Kuznetsova, *Russ. J. Org. Chem.*, 2003, **39**, 698 [Engl. Transl. of *Zh. Org. Khim.*, 2003, **39**, 744].

132. A. Wu and D. Cremer, *Phys. Chem. Chem. Phys.*, 2003, **5**, 4541.

133. J. Wardeiner, W. Lüttke, R. Bergholz and R. Machinek, *Angew. Chem. Int. Ed. Engl.*, 1982, **21**, 872.

134. D. Cremer, E. Kraka, A. Wu and W. Lüttke, *Chem. Phys. Chem.*, 2004, **5**, 349.

135. A. Soncini and P. Lazzeretti, *J. Chem. Phys.*, 2003, **118**, 7165.

136. R.E. Wasylishen, *Encyclopedia of Nuclear Magnetic Resonance*, John Wiley & Sons, Chichester, 1996, 1685.
137. A. Soncini and P. Lazzeretti, *Chem. Phys. Chem.*, 2006, **7**, 679.
138. V. Wray, L. Ernst, T. Lund and H. J. Jakobsen, *J. Magn. Reson.*, 1980, **40**, 55.
139. K. Kamienska-Trela, L. Kania, P. Bernatoicz, M. Bechcicka, L. Kacsmarek and J. Wójcik, *Spectrochim. Acta A*, 2000, **56**, 2079.
140. D. G. de Kowalewski, R. H. Contreras, E. Díez and A. L. Esteban, *Mol. Phys.*, 2004, **102**, 2607.
141. J. E. Del Bene and J. Elguero, *Magn. Reson. Chem.*, 2006, **44**, 784.
142. J. F. Stanton, J. Gauss, J. D. Watts, M. Nooijen, N. Oliphant. S. A. Perera, P. G. Szalay, W. J. Lauderdale, A. R. Gwalney, S. Beck, A. Balkova, D. E. Bernholdt, K.-K. Baeck, P. Tozyczko, H. Sekino, C. Huber and R. J. Bartlett, *Aces II*. Quantum Theory Project, University of Flodrida.
143. A. A. Auer and J. Gauss, *J. Chem. Phys.*, 2001, **115**, 1619.
144. J. E. Del Bene, S. A. Perera and R. J. Bartlett, *Magn. Reson. Chem.*, 2001, **39**, S109.
145. J. E. Del Bene, M. J. T. Jordan, S. A. Perera and R. J. Bartlett, *J. Chem. Phys. A*, 2001, **105**, 8399.
146. J. E. Del Bene, J. Elguero, I. Alkorta, M. Yáñez and O. Mó, *J. Chem. Phys.*, 2004, **120**, 3237.
147. J. E. Del Bene, S. A. Perera, R. J. Bartlett, M. Yañez, O. Mó, J. Elguero and I. Alkorta, *J. Phys. Chem. A*, 2003, **107**, 3121.
148. J. E. del Bene, S. A. Perera, R. J. Bartlett, M. Yañez, O. Mó, J. Elguero and I. Alkorta, *J. Phys. Chem. A*, 2003, **107**, 3126.
149. J. E. Del Bene and J. Elguero, *J. Phys. Chem. A*, 2005, **109**, 10769.
150. J. E. Del Bene and J. Elguero, *J. Phys. Chem. A*, 2006, **110**, 1128.
151. I. G. Shenderovich, P. M. Tolstoy, N. S. Golubev, S. N. Smirnov, G. S. Denisov and H.-H. Limbach, *J. Am. Chem. Soc.*, 2003, **125**, 11710.
152. J. E. Del Bene and J. Elguero, *J. Am. Chem. Soc.*, 2004, **126**, 15624.
153. J. E. Del Bene and J. Elguero, *J. Phys. Chem. A*, 2006, **110**, 7496.
154. J. E. Del Bene, S. A. Perera, R. J. Bartlett, M. Yañez, O. Mó, J. Elguero and I. Alkorta, *J. Phys. Chem. A*, 2003, **107**, 3222.
155. I. Alkorta, J. Elguero and J. E. Del Bene, *Chem. Phys. Lett.*, 2005, **412**, 97.
156. J. E. Del Bene, S. A. Perera, R. J. Bartlett, J. Elguero, I. Alkorta, C. López-Leonardo, M. Alajarín and D. Bautista, *J. Am. Chem. Soc.*, 2002, **124**, 6393.
157. M. Pecul, J. Sadlej and T. Helgaker, *Chem. Phys. Lett.*, 2003, **372**, 476.
158. P. Jørgensen, H. Jensen and J. Olsen, *J. Chem. Phys.*, 1988, **89**, 3654.
159. J. Olsen, D. L. Yeager and P. Jørgensen, *J. Chem. Phys.*, 1989, **91**, 381.
160. O. Vahtras, H. Ågren, P. Jørgensen, H. J. A. Jensen, S. B. Padkjær and T. Helgaker, *J. Chem. Phys.*, 1992, **96**, 6120.
161. M. Sanchez, P. F. Provasi, G. A. Aucar and S. P. A. Sauer, *Adv. Quant. Chem.*, 2005, **48**, 161.
162. E. S. Nielsen, P. Jorgensen and J. Oddershede, *J. Chem. Phys.*, 1980, **73**, 6238.
163. J. Geertsen and J. Oddershede, *Chem. Phys.*, 1984, **90**, 301.
164. T. Enevoldsen, J. Oddershede and S. P. A. Sauer, *Theor. Chim. Acta*, 1998, **100**, 275.
165. T. H. Dunning Jr., *J. Chem. Phys.*, 1989, **90**, 1007.
166. R. A. Kendall, T. H. Dunning Jr. and R. J. Harrison, *J. Chem. Phys.*, 1992, **96**, 6796.
167. D. E. Woon and T. H. Dunning Jr., *J. Chem. Phys.*, 1993, **98**, 1358.
168. P. F. Provasi, G. A. Aucar and S. P. A. Sauer, *J. Chem. Phys.*, 2001, **115**, 1324.
169. J. E. Del Bene, I. Alkorta and J. Elguero, *Z. Phys. Chem.*, 2003, **217**, 1565.
170. Y. Kanazawa, J. D. Baldeschwieler and N. C. Craig, *J. Mol. Spectrosc.*, 1965, **16**, 325.
171. A. M. Ihrig and S. L. Smith, *J. Am. Chem. Soc.*, 1972, **94**, 34.
172. G. J. den Otter and C. McLean, *Chem. Phys.*, 1974, **3**, 119.
173. A. Bagno and M. Bonchio, *Angew. Chem. Int. Ed.*, 2005, **44**, 2023.
174. A. A. Auer, J. Gauss and M. Pecul, *Chem. Phys. Lett.*, 2003, **368**, 172.
175. D. L. Bryce, K. Eichele and R. E. Wasylishen, *Inorg. Chem.*, 2003, **42**, 5085.
176. V. G. Malkin, O. L. Malkina and D. R. Salahub, *Chem. Phys. Lett.*, 1994, **221**, 91.
177. V.G. Malkin, O.L. Malkina, L.A. Eriksson, D.R. Salahub, *Modern Density Functional Theory: A Tool for Chemistry*, Elsevier, Amsterdam, **2**, 1995.

178. R. M. Dickson and T. Ziegler, *J. Phys. Chem.*, 1996, **100**, 5286.
179. R. H. Contreras, J. E. Peralta, C. G. Giribet, M. C. Ruiz de Azúa and J. C. Facelli, *Ann. Repts. NMR Spectrosc.*, 2000, **41**, 55.
180. J. A. Pople, J. W. McIver and N. S. Ostlund, *J. Chem. Phys.*, 1968, **49**, 2960.
181. J. A. Pople, J. W. McIver and N. S. Ostlund, *J. Chem. Phys.*, 1968, **49**, 2970.
182. V. Sychrovský, J. Gräfenstein and D. Cremer, *J. Chem. Phys.*, 2000, **113**, 3530.
183. T. Helgaker, M. Watson and N. C. Handy, *J. Chem. Phys.*, 2000, **113**, 9402.
184. J. E. Peralta, M. C. Ruiz de Azúa and R. H. Contreras, *Theor. Chem. Acc.*, 2000, **105**, 165.
185. P. Lantto, J. Vaara and T. Helgaker, *J. Chem. Phys.*, 2002, **117**, 5998.
186. A. D. Becke, *Phys. Rev. A*, 1988, **38**, 3098.
187. S. N. Maximoff, J. E. Peralta, V. Barone and G. E. Scuseria, *J. Chem. Theory Comput.*, 2005, **1**, 541.
188. J. E. Peralta, G. E. Scuseria, J. R. Cheeseman and M. J. Frisch, *Chem. Phys. Lett.*, 2003, **375**, 452.
189. T. W. Keal, T. Helgaker, P. Salek and D. J. Tozer, *Chem. Phys. Lett.*, 2006, **425**, 163.
190. P. J. Wilson, T. J. Bradley and D. J. Tozer, *J. Chem. Phys.*, 2001, **115**, 9233.
191. T. W. Keal and D. J. Tozer, *J. Chem. Phys.*, 2005, **123**, 121103.
192. O. B. Lutnæs, T. A. Ruden and T. Helgaker, *Magn. Reson. Chem.*, 2004, **42**, S117.
193. S. J. Huzinaga, *J. Chem. Phys.*, 1965, **42**, 1293.
194. S. J. Huzinaga, *Approxcimate Atomic* Functions, Technical report, University of Alberta, Edmonton, 1971.
195. T. W. Keal, D. J. Tozer and T. Helgaker, *Chem. Phys. Lett.*, 2004, **391**, 374.
196. T. W. Keal and D. J. Tozer, *J. Chem. Phys.*, 2003, **119**, 3015.
197. S. J. Vosko, L. Wilk and M. Nusair, *Can. J. Phys.*, 1980, **58**, 1200.
198. M. J. Hansen, M. A. Wendt, F. Weinhold and T. C. Farrar, *Mol. Phys.*, 2002, **100**, 2807.
199. A. D. Becke, *J. Chem. Phys.*, 1996, **104**, 1040.
200. C. Adamo and V. Barone, *Chem. Phys. Lett.*, 1997, **274**, 242.
201. C. Adamo and V. Barone, *J. Chem. Phys.*, 1998, **108**, 664.
202. T. Helgaker, M. Jaszuński, K. Ruud and A. Górska, *Theor. Chem. Acc.*, 1998, **99**, 175.
203. M. J. Frisch, G. W. Trucks, H. B. Schlegel, G. E. Scuseria, M. A. Robb, J. R. Cheeseman, J. A. Montgomery, Jr., T. Vreven, K. N. Kudin, J. C. Burant, J. M. Millam, S. S. Iyengar, J. Tomasi, V. Barone, B. Mennucci, M. Cossi, G. Scalmani, N. Rega, G. A. Petersson, H. Nakatsuji, M. Hada, M. Ehara, K. Toyota, R. Fukuda, J. Hasegawa, M. Ishida, T. Nakajima, Y. Honda, O. Kitao, H. Nakai, M. Klene, X. Li, J. E. Knox, H. P. Hratchian, J. B. Cross, C. Adamo, J. Jaramillo, R. Gomperts, R. E. Stratmann, O. Yazyev, A. J. Austin, R. Cammi, C. Pomelli, J. W. Ochterski, P. Y. Ayala, K. Morokuma, G. A. Voth, P. Salvador, J. J. Dannenberg, V. G. Zakrzewski, S. Dapprich, A. D. Daniels, M. C. Strain, O. Farkas, D. K. Malick, A. D. Rabuck, K. Raghavachari, J. B. Foresman, J. V. Ortiz, Q. Cui, A. G. Baboul, S. Clifford, J. Cioslowski, B. B. Stefanov, G. Liu, A. Liashenko, P. Piskorz, I. Komaromi, R. L. Martin, D. J. Fox, T. Keith, M. A. Al-Laham, C. Y. Peng, A. Nanayakkara, M. Challacombe, P. M. W. Gill, B. Johnson, W. Chen, M. W. Wong, C. Gonzalez and J. A. Pople, *Gaussian 03, Revision B.02*, Gaussian, Inc., Pittsburgh, PA, 2003.
204. A. J. Sadlej, *Collec. Czech. Chem. Commun.*, 1988, **53**, 1995.
205. V. Barone, *J. Chem. Phys.*, 1994, **101**, 6834.
206. M. Schindler and W. Kutzelnigg, *J. Chem. Phys.*, 1982, **76**, 1919.
207. W. Deng, J. R. Cheeseman and M. J. Frisch, *J. Chem. Theor. Comput.*, 2006, **2**, 1028.
208. P. Salvador and J. J. Dannenberg, *J. Phys. Chem. B*, 2004, **108**, 15370.
209. G. R. Desiraju and T. Steiner, *The Weak Hydrogen bond in Structural Chemistry and Biology*, Oxford University Press, New York, 1999, p. 202.
210. J. Jokisaari and J. Autschbach, *Phys. Chem. Chem. Phys.*, 2003, **5**, 4551.
211. M. Kamiya, T. Tsuneda and K. Hirao, *J. Chem. Phys.*, 2002, **117**, 6010.
212. A. Bagno, G. Saielli and G. Scorrano, *Angew. Chem. Int. Ed.*, 2001, **40**, 2532.
213. A. Bagno, G. Saielli and G. Scorrano, *Chem. Eur. J.*, 2002, **8**, 2047.
214. A. Bagno and G. Saielli, *Chem. Eur. J.*, 2002, **9**, 1486.
215. A. Bagno and G. Saielli, *J. Phys. Org. Chem.*, 2004, **17**, 945.

216. M. Nishio, M. Hirota and Y. Umezaua, *The CH–π Interanction, Evidence, Nature and Consequences*, Wiley-VCH, New York, 1998.
217. O. L. Malkina, D. R. Salahub and V. G. Malkin, *J. Chem. Phys.*, 1996, **105**, 8793.
218. H. Cybulski, M. Pecul, J. Sadlej and T. Helgaker, *J. Chem. Phys.*, 2003, **119**, 5094.
219. A. Bagno, G. Casella, G. Saielli and G. Scorrano, *Int. J. Mol. Sci.*, 2003, **4**, 193.
220. C. Chang, M. Pelissier and P. Durand, *Phys. Scr.*, 1986, **34**, 394.
221. E. van Lenthe, E. Baerends and J. G. Snijders, *J. Chem. Phys.*, 1993, **99**, 4597.
222. E. van Lenthe, E. Baerends and J. G. Snijders, *J. Chem. Phys.*, 1994, **101**, 9783.
223. E. van Lenthe, R. van Leeuwen, E. Baerends and J. G. Snijders, *Int. J. Quantum Chem.*, 1996, **57**, 281.
224. E. J. Baerends, J. Autschbach and A. Berces, *ADF 2002.01*, SCM, Theoretical Chemistry, Vrije Universiteit, Amsterdam, 2002 (see http://www.scm.com; last accessed: December 2006).
225. M. Jaszuński, *Chem. Phys. Lett.*, 2004, **385**, 122.
226. T. Ratajczyk, M. Pecul, J. Sadlej and T. Helgaker, *J. Phys. Chem. A*, 2004, **108**, 2758.
227. J. San Fabián and A. J. A. W. Hoekzema, *J. Chem. Phys.*, 2004, **121**, 6268.
228. J. Olsen, B. O. Roos, P. Jorgensen and H. J. A. Jensen, *J. Comput. Phys.*, 1988, **89**, 2185.
229. T. Helgaker, H. J. A. Jensen, P. Jorgensen, J. Olsen, K. Ruud, H. Ågren, A. A. Auer, K. L. Bak, V. Bakken, O. Christiansen, S. Coriani, P. Dahle, E. K. Dalskov, T. Enevoldsen, B. Fernandez, C. Hättig, K. Hald, A. Halkier, H. Heiberg, H. Hettema, D. Jonsson, S. Kirpekar, R. Kobayashi, H. Koch, K. V. Mikkelsen, P. Norman, M. J. Packer, T. B. Pedersen, T. A. Ruden, A. Sanchez, T. Saue, S. P. A. Sauer, B. Schimmelpfenning, K. O. Sylverster-Hvid, P. R. Taylor and O. Vahtras, *Dalton, an Ab Initio Electronic Structure Program, Release 1.2*, 2001 (see http://www.kemi.uio.no/software/dalton/dalton.hmtl; last accessed: March 2005).
230. E. F. Mooney and P. H. Winson, *Ann. Rev. NMR Spectrosc.*, Vol. 1, Academic Press, New York, 1968, 251.
231. P. F. Provasi and S. P. A. Sauer, *J. Chem. Theory Comput.*, 2006, **2**, 1019.
232. R. J. Abraham and R. H. Kemp, *J. Chem. Soc. B*, 1971, 1240.
233. S. Kurtkaya, V. Barone, J. E. Peralta, R. H. Contreras and J. P. Snyder, *J. Am. Chem. Soc.*, 2002, **124**, 9702.
234. V. Barone, P. F. Provasi, J. E. Peralta, J. P. Snyder, S. P. A. Sauer and R. H. Contreras, *J. Phys. Chem. A*, 2003, **107**, 4748.
235. C. G. Giribet, M. C. Ruiz de Azua, C. V. Vizioli and C. N. Cavasotto, *Int. J. Mol. Sci.*, 2003, **4**, 203.
236. C. G. Giribet and M. C. Ruiz de Azúa, *J. Phys. Chem. A*, 2005, **109**, 11980.
237. K. Jackowski, E. Maciaga and M. Wilczek, *J. Mol. Struct.*, 2005, **744–747**, 101.
238. T. A. Ruden, O. B. Lutnæs, T. Helgaker and K. Ruud, *J. Chem. Phys.*, 2003, **118**, 9572.
239. T. A. Ruden, T. Helgaker and M. Jaszuński, *Chem. Phys.*, 2004, **296**, 53.
240. M. Pecul and K. Ruud, *Magn. Reson. Chem.*, 2004, **42**, S128.
241. S. Miertuš, E. Scrocco and J. Tomasi, *J. Chem. Phys.*, 1981, **55**, 117.
242. J. Tomasi and R. Cammi, *J. Comp. Chem.*, 1995, **16**, 1449.
243. B. Menucci, E. Cancés and J. Tomasi, *J. Phys. Chem. B*, 1997, **101**, 10506.
244. K. Jackowski, M. Wilczek, M. Pecul and J. Sadlej, *J. Phys. Chem. A*, 2000, **104**, 5955.
245. K. Ruud, L. Frediani, R. Cammi and B. Mennucci, *Int. J. Mol. Sci.*, 2003, **4**, 119.
246. M. Pecul and J. Sadlej, *Chem. Phys.*, 1998, **234**, 111.
247. D. Zaccari, V. Barone, J. E. Peralta, R. H. Contreras, O. E. Taurian, E. Díez and A. Esteban, *Int. J. Mol. Sci.*, 2003, **4**, 93.
248. E. L. Eliel and G. A. Giza, *J. Org. Chem.*, 1968, **33**, 3754.
249. R. U. Lemieux, A. A. Pavia, J. C. Marti and K. A. Watanabe, *Can. J. Chem.*, 1969, **47**, 4427.
250. O. E. Taurian, D. G. De Kowalewski, J. E. Pérez and R. H. Contreras, *J. Mol. Struct.*, 2005, **754**, 1.
251. I. Ando, Y. Inoue, S. Watanabe, Y. Sakamoto and G. A. Webb, *J. Mol. Liquids*, 1984, **27**, 179.
252. A. N. Taha and N. S. True, *J. Phys. Chem. A*, 2000, **104**, 2985.
253. M. Sigalov, A. Vashchenko and V. Khodorkovsky, *J. Org. Chem.*, 2005, **70**, 92.
254. O. E. Taurian, R. H. Contreras and D. G. de Kowalewski, *J. Arg. Chem. Soc.* (in press).
255. J. Autschbach and B. Le Guennic, *J. Am. Chem. Soc.*, 2003, **125**, 13585.

256. T. Ziegler and J. Autschbach, *Chem. Rev.*, 2005, **105**, 2695.
257. K. Jackowski, *Int. J. Mol. Sci.*, 2003, **4**, 135.
258. J. Gräfenstein and D. Cremer, *Magn. Reson. Chem.*, 2004, **42**, S138.
259. E. Kraka, J. Gräfensterin, J. Gauss, F. Reichel, L. Olsson, Z. Konkoli and D. Cremer, *Programa Package COLOGNE 99*, Göteborg University, Göteborg, 1999.
260. A. Wu, J. Gräfenstein and D. Cremer, *J. Phys. Chem. A*, 2003, **107**, 7043.
261. J. Gräfenstein, T. Tuttle and D. Cremer, *J. Chem. Phys.*, 2004, **120**, 9952.
262. T. Tuttle, J. Gräfenstein, A. Wu, E. Kraka and D. Cremer, *J. Phys. Chem. B*, 2005, **108**, 1115.
263. J. Gräfenstein and D. Cremer, *Chem. Phys. Lett.*, 2004, **383**, 332.
264. J. Gräfenstein, E. Kraka and D. Cremer, *J. Phys. Chem. A*, 2004, **108**, 4520.
265. J. Gräfenstein and D. Cremer, *Chem. Phys. Lett.*, 2004, **387**, 415.
266. T. Tuttle, J. Gräfenstein and D. Cremer, *Chem. Phys. Lett.*, 2004, **394**, 5.
267. J. Gräfenstein, T. Tuttle and D. Cremer, *Phys. Chem. Chem. Phys.*, 2005, **7**, 452.
268. J. Gräfenstein, T. Tuttle and D. Cremer, *J. Phys. Chem. A*, 2005, **109**, 2325.
269. M. A. Watson, P. Sałek, P. Macak, M. Jaszuński and T. Helgaker, *Chem Eur. J.*, 2004, **10**, 4627.
270. A. Fruchier, V. Vicente, I. Alkorta and J. Elguero, *Magn. Reson. Chem.*, 2005, **43**, 471.
271. V. Barone, J. E. Peralta, R. H. Contreras and J. P. Snyder, *J. Phys. Chem. A*, 2002, **106**, 5607.
272. J. W. Emsley and L. Phillips, *J. Chem. Soc. B*, 1969, **X**, 434.
273. V. Barboiu, J. W. Emsley and J. C. Lindon, *Chem. Soc., Faraday Trans. 2*, 1972, **68**, 241.
274. J. E. Peralta, V. Barone, R. H. Contreras, D. Zaccari and J. P. Snyder, *J. Am. Chem. Soc.*, 2001, **123**, 9162.
275. F. D. Mallory, C. W. Mallory, K. E. Butler, M. B. Lewis, A. Q. Xia, E. D. Luzik Jr., L. E. Fredenburgh, M. N. Ramanjulu, Q. N. Van, M. N. Francl, D. A. Freed, C. C. Wray, C. Hann, M. Nerz-Stormes, P. J. Caroll and L. E. Chirlian, *J. Am. Chem. Soc.*, 2000, **122**, 4108.
276. G. A. Aucar and R. H. Contreras, *J. Magn. Reson.*, 1991, **93**, 413.
277. A. M. Ihrig and S. L. Smith, *J. Am. Chem. Soc.*, 1970, **92**, 759.
278. J. H. Kühn-Velten, G. Hägele, W. Fuss, P. Hering and M. M. Ivanenko, *Magn. Reson. Chem.*, 2002, **40**, 77.
279. B. Wrackmeyer, *Z. Naturforsch.*, 2004, **59b**, 286.
280. R. E. Wasylishen, J. O. Friedrich, S. Mooibroek and J. B. Macdonald, *J. Chem. Phys.*, 1985, **83**, 548.
281. M. Broze and Z. Luz, *J. Phys. Chem.*, 1969, **83**, 1600.
282. D. G. de Kowalewski, V. J. Kowalewski, R. H. Contreras, E. Díez and A. L. Esteban, *Magn. Reson. Chem.*, 1998, **36**, 336.
283. B. Wrackmeyer, *Struct. Chem.*, 2005, **16**, 67.
284. I. Johannsen and H. Eggert, *J. Am. Chem. Soc.*, 1984, **106**, 1240.
285. R. H. Contreras, H. O. Gavarini and M. A. Natiello, *J. Comput. Chem.*, 1987, **8**, 265.
286. K. W. Feindel and R. E. Wasylishen, *Magn. Reson. Chem.*, 2004, **42**, S158.
287. S. Brownstein, *Can. J. Chem.*, 1980, **58**, 1407.
288. T. Birchall, R. D. Myers, H. de Waard and G. Schrobilgen, *Inorg. Chem.*, 1982, **21**, 1068.
289. C. I. Oprea, Z. Rinkevicius, O. Vahtras and H. Ågren, *J. Chem. Phys.*, 2005, **123**, 014101.
290. I. Tunell, Z. Rinkevicius, O. Vahtras, P. Salek, T. Helgaker and H. Ågren, *J. Chem. Phys.*, 2003, **119**, 11024.
291. V. Barone, J. E. Peralta and R. H. Contreras, *J. Comput. Chem.*, 2001, **22**, 1615.
292. M. A. Forgeron, M. Gee and R. E. Wasylishen, *J. Phys. Chem. A*, 2005, **108**, 4895.
293. B. Wrackmeyer, O. L. Tok and A. A. Koridze, *Magn. Reson. Chem.*, 2004, **42**, 750.
294. M. Filatov and D. Cremer, *J. Chem Phys.*, 2004, **120**, 11407.
295. M. Filatov, *Chem. Phys. Lett.*, 2002, **365**, 222.
296. M. Filatov and D. Cremer, *J. Chem. Phys.*, 2003, **118**, 6741.
297. J. Autschbach and T. Ziegler, *J. Chem. Phys.*, 2000, **113**, 936.
298. J. I. Melo, M. C. Ruiz de Azúa, J. E. Peralta and G. E. Scuseria, *J. Chem. Phys.*, 2005, **123**, 204112.
299. M. Douglas and N. M. Kroll, *Ann. Phys.*, 1974, **82**, 89.
300. B. A. Hess, *Phys. Rev.*, 1985, **32**, 756.

301. B. A. Hess, *Phys. Rev.*, 1986, **33**, 3742.
302. A. Wolf, M. Reiher and B. A. Hess, *J. Chem. Phys.*, 2002, **117**, 9215.
303. A. Bagno, G. Casella and G. Saielli, *J. Chem. Theory Comput.*, 2006, **2**, 37.
304. H. Dreeskamp, *Z. Naturforsch.*, 1964, **19**, 139.
305. C. Schumann and H. Dreeskamp, *J. Magn. Reson.*, 1970, **3**, 204.
306. P. -O. Åstrand, K. Ruud, K. V. Mikkelsen and T. Helgaker, *J. Chem. Phys.*, 1999, **110**, 9463.
307. J. San Fabián, J. Casanueva, E. San Fabián and J. Guilleme, *J. Chem. Phys.*, 2000, **112**, 4143.
308. J. Casanueva, J. San Fabián, E. Dez and A. L. Esteban, *J. Mol. Struct.*, 2001, **565–566**, 449.
309. K. V. Mikkelsen, K. Ruud and T. Helgaker, *J. Comp. Chem.*, 1999, **20**, 1281.
310. P. Lanto and J. Vaara, *J. Chem. Phys.*, 2001, **114**, 5482.
311. R. D. Wigglesworth, W. T. Raynes, S. P. A. Sauer and J. Oddershede, *Mol. Phys.*, 1990, **94**, 851.
312. D. L. Bryce and R. E. Wasylishen, *J. Am. Chem. Soc.*, 2000, **122**, 3197.
313. K. Thorshaug, O. Swang, I. M. Dahl and A. Olafsen, *J. Phys. Chem. A*, 2006, **110**, 9801.
314. B. Wrackmeyer, *Z. Nasturforsch.*, 2003, **58b**, 1041.
315. S. P. A. Sauer and W. T. Raynes, *J. Chem. Phys.*, 2000, **113**, 3121.
316. S. P. A. Sauer, C. K. Møller, H. Koch, I. Paidarová and V. Špirko, *Chem. Phys.*, 1998, **238**, 385.
317. S. P. A. Sauer, W. T. Raynes and R. A. Nicholls, *J. Chem. Phys.*, 2001, **115**, 5994.
318. S. Kirpekar and S. P. A. Sauer, *Theor. Chem. Acc.*, 1999, **103**, 146.
319. D. L. Bryce, R. E. Wasylishen, J. Autschbach and T. Ziegler, *J. Am. Chem. Soc.*, 2002, **124**, 4894.
320. J. Autschbach and T. Ziegler, *J. Chem. Phys.*, 2000, **113**, 9410.
321. S. Varga, B. Fricke, H. Nakamatsu, T. Mukoyama, J. Anton, D. Geschke, A. Heitmann, E. Engel and T. Baştuğ, *J. Chem. Phys.*, 2000, **112**, 3499.
322. P. -O. Åstrand, K. V. Mikkelsen, P. Jørgensen, K. Ruud and T. Helgaker, *J. Chem. Phys.*, 1998, **108**, 2528.
323. J. Autschbach, C. D. Igna and T. Ziegler, *J. Am. Chem. Soc.*, 2003, **125**, 4937.
324. J. Autschbach and T. Ziegler, *J. Am. Chem. Soc.*, 2001, **123**, 3341.
325. M. A. M. Forgeron, R. E. Wasylishen and G. H. Penner, *J. Phys. Chem. A*, 2004, **108**, 4751.
326. D. L. Bryce and R. E. Wasylishen, *Inorg. Chem.*, 2002, **41**, 3091.
327. J. Khandogin and T. Ziegler, *Spectrochim. Acta Part A*, 1999, **55**, 607.
328. J. Autschbach and T. Ziegler, *J. Am. Chem. Soc.*, 2001, **123**, 5320.
329. J. Autschbach, C. D. Igna and T. Ziegler, *J. Am. Chem. Soc.*, 2003, **125**, 1028.
330. J. Khandogin and T. Ziegler, *J. Phys. Chem. A*, 2000, **104**, 113.
331. N. S. Hush, *J. Am. Chem. Soc.*, 1997, **119**, 1717.
332. G. S. McGRady and G. Guilera, *Chem. Soc. Rev.*, 2003, **32**, 383.
333. R. Gelabert, M. Moreno, J. M. Lluch, A. Lledós, V. Pons and D. M. Heinekey, *J. Am. Chem. Soc.*, 2004, **126**, 8813.
334. D. M. Heinekey, A. Lledós and J. M. Lluch, *Chem. Soc. Rev.*, 2004, **33**, 175.
335. R. Gelabert, M. Moreno, J. M. Lluch, A. Lledos and D. M. Heinekey, *J. Am. Chem. Soc.*, 2005, **127**, 5632.
336. B. C. Mort and J. Autschbach, *J. Am. Chem. Soc.*, 2006, **128**, 10060.
337. B. Le Guennic, S. Patchkovskii and J. Autschbach, *J. Chem. Theory Comput.*, 2005, **1**, 601.
338. D. G. Gusev, *J. Am. Chem. Soc.*, 2004, **126**, 14249.
339. S. R. Dubberley, S. K. Ignatov, N. H. Rees, A. G. Razuvaev, P. Mountford and G. I. Nikonov, *J. Am. Chem. Soc.*, 2003, **125**, 642.
340. D. L. Bryce and R. E. Wasylishen, *Inorg. Chem.*, 2002, **41**, 4131.
341. A. Bagno and M. Bonchio, *Magn. Reson. Chem.*, 2004, **42**, S79.
342. C. Brevard and P. Granger, *Inorg. Chem.*, 1983, **22**, 532.
343. T. Onak, J. Jaballas and M. Barfield, *J. Am. Chem. Soc.*, 1999, **121**, 2850.
344. B. Wrackmeyer, *Z. Nasturforsch.*, 2004, **59b**, 37.
345. B. Wrackmeyer and A. Berndt, *Magn. Reson. Chem.*, 2004, **42**, 490.
346. B. Wrackmeyer, *Z. Nasturforsch.*, 2004, **59b**, 1192.
347. B. Wrackmeyer and H. -J. Schanz, *Z. Naturforsch.*, 2004, **59b**, 685.
348. B. Wrackmeyer, *Z. Nasturforsch.*, 2005, **60b**, 955.

349. M. Bakardjiev, J. Holub, B. Štibr, D. Hnyk and B. Wrackmeyer, *Inorg. Chem.*, 2005, **44**, 5826.
350. J. E. Del Bene, J. Elguero, I. Alkorta, M. Yánez and O. Mó, *J. Phys. Chem. A*, 2006, **110**, 9959.
351. M. Pecul and T. Helgaker, *Int. J. Mol. Sci.*, 2003, **4**, 143.
352. S. -I. Kawahara, C. Kojima, K. Taira and T. Uchimaru, *Helv. Chim. Acta*, 2003, **86**, 3265.
353. H. Cybulski, M. Pecul and J. Sadlej, *Chem. Phys.*, 2006, **326**, 431.
354. W. Holzer, C. Kautsch, C. C. Lagger, R. M. Claramunt, M. Pérez-Torralba, I. Alkorta and J. Elguero, *Tetrahedron*, 2004, **60**, 6791.
355. R. M. Claramunt, D. Sanz, I. Alkorta and J. Elguero, *Magn. Reson. Chem.*, 2005, **43**, 985.
356. I. Alkorta, J. Elguero, O. Mó, M. Yáñez and J. E. Del Bene, *Mol. Phys.*, 2004, **102**, 2563.
357. I. Alkorta, J. Elguero, O. Mó, M. Yáñez and J. E. Del Bene, *Chem. Phys. Lett.*, 2005, **411**, 411.
358. M. Bernárková, H. Dvořáková, B. Andrioletti, V. Král and P. Bouř, *J. Phys. Chem. A*, 2005, **109**, 5518.
359. P. Tähtinen, A. Bagno, A. Koch and K. Pihlaja, *Eur. J. Org. Chem.*, 2004, 4921.
360. A. Bagno, F. Rastrelli and G. Saielli, *J. Phys. Chem. A*, 2003, **107**, 9964.
361. V. A. Roznyatovsky, N. M. Sergeyev and V. A. Chertkov, *Magn. Reson. Chem.*, 1991, **29**, 304.
362. J. Kaski, J. Vaara and J. Jokisaari, *J. Am. Chem. Soc.*, 1996, **118**, 8879.
363. A. Yu. Denisov, W. I. Mamatiuk and O. P. Skurko, *Khim. Geterotsikl. Soedin.*, 1985, 1383.
364. A. Dabrowski, K. Kamieńska-Trela and J. Wójcik, *Spectrochim. Acta A*, 1999, **56**, 91.
365. E. Dvornikova, M. Bechcicka, K. Kamieńska-Trela and A. Krówczyński, *J. Fluorine Chem.*, 2003, **124**, 159.
366. C. Bassarello, P. Cimino, L. Gomez-Paloma, R. Riccio and G. Bifulco, *Tetrahedron*, 2003, **59**, 9555.
367. A. Plaza, S. Piacente, A. Perrone, A. Hamed, C. Pizza and G. Bifulco, *Tetrahedron*, 2004, **60**, 12201.
368. G. Bifulco, C. Bassarello, R. Riccio and L. Gomez-Paloma, *Org. Lett.*, 2004, **6**, 1025.
369. P. F. Provasi, C. A. Gómez and G. A. Aucar, *J. Phys. Chem. A*, 2004, **108**, 6231.
370. I. Alkorta and J. Elguero, *Org. Biomol. Chem.*, 2003, **1**, 585.
371. I. Alkorta and J. Elguero, *Theor. Chem. Acc.*, 2004, **111**, 31.
372. E. Díez, J. Casanueva, J. San Fabián, A. Esteban, M. P. Galache, V. Barone, J. E. Peralta and R. H. Contreras, *Mol. Phys.*, 2005, **103**, 1307.
373. V. Galasso, F. Asaro, F. Berti, I. Habuš, B. Kovač and C. de Risi, *Chem. Phys.*, 2004, **301**, 33.
374. G. De Luca, M. Longeri, G. Pileio and P. Lantto, *Chem. Phys. Chem.*, 2005, **6**, 2086.
375. M. -L. Jimeno, I. Alkorta, J. Elguero and J. E. Del Bene, *Magn. Reson. Chem.*, 2006, **44**, 698.
376. J. Sýkora, V. Blechta, V. Sychrovský, J. Hetflejš, S. Šabata, L. Soukupová and J. Schraml, *Magn. Reson. Chem.*, 2006, **44**, 669.
377. J. E. Del Bene and J. Elguero, *Magn. Reson. Chem.*, 2006, **44**, 784.
378. L. B. Krivdin, S. P. A. Sauer, J. E. Peralta and R. H. Contreras, *Magn. Reson. Chem.*, 2002, **40**, 187.
379. L. B. Krivdin and T.A. Kuznetsova, *Russ. J. Org. Chem*. 2003, **39**, 1618 [Engl. Transl. of *Zh. Org. Khim.*, 2003, **39**, 1688].
380. S. P. A. Sauer and L. B. Krivdin, *Magn. Reson. Chem.*, 2004, **42**, 671.
381. L. B. Krivdin and E. W. Della, *Prog. NMR Spectrosc.*, 1991, **23**, 301.
382. A. Wu, D. Cremer, A. A. Auer and J. Gauss, *J. Phys. Chem. A*, 2002, **106**, 657.
383. S. V. Zubkov and V. A. Chertkov, *Int. J. Mol. Sci.*, 2003, **4**, 107.
384. A. Wu and D. Cremer, *Int. J. Mol. Sci.*, 2003, **4**, 158.
385. T. C. Ramalho and M. Bühl, *Magn. Reson. Chem.*, 2005, **43**, 139.
386. K. Pihlaja, P. Tähtinen, K. D. Klika, T. Jokela, A. Salakka and K. Wähälä, *J. Org. Chem.*, 2003, **68**, 6864.
387. Yu. Yu. Rusakov, L. B. Krivdin, E. Yu. Schmidt, A. I. Mikhaleva and B. A. Trofimov, *Magn. Reson. Chem.*, 2006, **44**, 692.
388. H. Dodziuk, M. Jaszunski and W. Schiff, *Magn. Reson Chem.*, 2005, **43**, 639.
389. L. B. Krivdin, *Magn. Reson. Chem.*, 2004, **42**, 500.
390. L. B. Krivdin, *Magn. Reson. Chem.*, 2003, **41**, 91.
391. L. B. Krivdin, *Magn. Reson. Chem.*, 2003, **41**, 417.
392. L. B. Krivdin, *Magn. Reson. Chem.*, 2003, **41**, 885.
393. L. B. Krivdin, *Magn. Reson. Chem.*, 2004, **42**, 1.

394. L. B. Krivdin, *Magn. Reson. Chem.*, 2004, **42**, S168.

395. L. B. Krivdin, *Magn. Reson. Chem.*, 2003, **41**, 157.

396. L. B. Krivdin, *Magn. Reson. Chem.*, 2004, **42**, 919.

397. L. B. Krivdin, *Magn. Reson. Chem.*, 2005, **43**, 101.

398. M. Barfield, E. W. Della and P. E. Pigou, *J. Am. Chem. Soc.*, 1984, **106**, 5051.

399. M. D. Newton and J. M. Schulman, *J. Am. Chem. Soc.*, 1972, **94**, 767.

400. M. Pomerantz, R. Fink and G. A. Gray, *J. Am. Chem. Soc.*, 1976, **98**, 291.

401. H. Finkelmeier and W. Lüttke, *J. Am. Chem. Soc.*, 1978, **100**, 6261.

402. V. Galasso, *Chem. Phys. Lett.*, 1994, **230**, 387.

403. H. Sekino and R. J. Bartlett, *Chem. Phys. Lett.*, 1994, **225**, 486.

404. I. Carmichael, *J. Phys. Chem.*, 1993, **97**, 1789.

405. M. Jaszunski, G. Dolgonos and H. Dodziuk, *Theor. Chem. Acc.*, 2002, **108**, 240.

406. M. Stöcker and M. Klessinger, *Org. Magn. Reson.*, 1979, **12**, 107.

407. F. J. Weigert and J. D. Roberts, *J. Am. Chem. Soc.*, 1972, **94**, 6021.

408. K. B. Wiberg and F. H. Walker, *J. Am. Chem. Soc.*, 1982, **104**, 5239.

409. M. Pecul, H. Dodziuk, M. Jaszunski, O. Lukin and J. Leszczynski, *Phys. Chem. Chem. Phys.*, 2001, **3**, 1986.

410. M. Werner, D. S. Stephenson and G. Szeimies, *Liebigs Ann. Org. Bioorg. Chem.*, 1996, **11**, 1705.

411. B. Trupp, D. R. Handreck, H. P. Böhm, L. Knothe, H. Fritz and H. Prinzbach, *Chem. Ber.*, 1991, **124**, 1757.

412. V. Galasso, *Int. J. Quant. Chem.*, 1996, **57**, 587.

413. T. Loerzer, R. Machinek, W. Lüttke, L. H. Franz, K. D. Malsch and G. Maier, *Angew. Chem.*, 1983, **95**, 914.

414. V. Galasso, *J. Phys. Chem. A*, 2004, **108**, 4497.

415. L. B. Krivdin, G. A. Kalabin, R. N. Nesterenko and B. A. Trofimov, *Tetrahedron Lett.*, 1984, **25**, 4817.

416. V. Barone, J. E. Peralta, R. H. Contreras, A. V. Sosnin and L. B. Krivdin, *Magn. Reson. Chem.*, 2001, **39**, 600.

417. G. Cuevas and E. Juaristi, *J. Am. Chem. Soc.*, 2002, **124**, 13088.

418. L. B. Krivdin, N. A. Scherbina and N. V. Istomina, *Magn. Reson. Chem.*, 2005, **43**, 435.

419. N. A. Scherbina, N. V. Istomina and L. B. Krivdin, *Russ. J. Org. Chem.*, 2005, **41**, 1103 [Engl. Transl. of *Zh. Org. Khim.*, 2005, **41**, 1127].

420. L. B. Krivdin, L. I. Larina, K. A. Chernyshev and I. B. Rozentsveig, *Magn. Reson. Chem.*, 2005, **43**, 937.

421. L. B. Krivdin, L. I. Larina, K. A. Chernyshev and A. Yu. Rulev, *Magn. Reson. Chem.*, 2006, **44**, 178.

422. L. B. Krivdin and N. A. Nedolya, *Tetrahedron Lett.*, 2005, **46**, 7367.

423. L. B. Krivdin, L. I. Larina, K. A. Chernyshev and N. A. Keiko, *Austr. J. Chem.*, 2006, **59**, 211.

424. P. F. Provasi, G. A. Aucar and S. P. A. Sauer, *Int. J. Mol. Sci.*, 2003, **4**, 231.

425. L. B. Krivdin and G. A. Kalabin, *Prog. NMR Spectrosc.*, 1989, **21**, 293.

426. B. Wrackmeyer and C. Köhler, *Heteroatom. Chem.*, 2005, **16**, 84.

427. H. W. Kroto, J. R. Heath, S. C. O'Brien, R. F. Curl and R. E Smalley, *Nature*, 1985, **318**, 162.

428. R. Taylor, J. P. Hare, A. K. Absulsada and H. W. Kroto, *J. Chem. Soc., Chem. Commun.*, 1990, 1423.

429. M. Jaszunski, K. Ruud and T. Helgaker, *Mol. Phys.*, 2003, **101**, 1997.

430. C. van Wüllen, Die Berechnung Magnetischer Eigenschaften unter Berücksichtung der Elektronkorrelation: Die Multikonfigurations-Verallgemeinerung der IGLO-Methode, Ph.D. thesis, Ruhr-Universität Bochum, Germany, 1992.

431. J. E. Peralta, V. Barone, G. E. Scuseria and R. H. Contreras, *J. Am. Chem. Soc.*, 2004, **126**, 7428.

432. R. D. Johnson, G. Meijer, J. R. Salem and D. S. Bethune, *J. Am. Chem. Soc.*, 1991, **113**, 3619.

433. R. H. Contreras, J. E. Peralta, V. Barone and G. E. Scuseria, *Adv. Quant. Chem.*, 2005, **48**, 127.

434. C. Anklin and L. B. Alemany, *Magn. Reson. Chem.*, 2006, **44**, 230.

435. V. Barone, A. Koller and G. E. Scuseria, *J. Phys. Chem. A.*, 2006, **110**, 10844.

436. B. Wrackmeyer, B. Schwarze, D. M. Durran and G. A. Webb, *Magn. Reson. Chem.*, 1995, **33**, 557.
437. P. Tähtinen, A. Bagno, K. D. Klika and K. Pihlaja, *J. Am. Chem. Soc.*, 2003, **125**, 4609.
438. P. Tähtinen, J. Sinkkonen, K. D. Klika, V. Nieminen, G. Stájer, Z. Szakonyi, F. Fülöp and K. Pihlaja, *Chirality*, 2002, **14**, 187.
439. J. González-Outeiriño, J. Glushka, A. Siriwardena and R. J. Woods, *J. Am. Chem. Soc.*, 2004, **126**, 6866.
440. V. Sychrovský, J. Šponer and P. Hobza, *J. Am. Chem. Soc.*, 2004, **126**, 663.
441. C. Thibaudeau, R. Stenutz, B. Hertz, T. Klepach, S. Zhao, Q. Wu, I. Carmichael and A. S. Serianni, *J. Am. Chem. Soc.*, 2004, **126**, 15668.
442. F. Cloran, I. Carmichael and A. S. Serianni, *J. Am. Chem. Soc.*, 1999, **121**, 9843.
443. V. A. Danilova, N. V. Istomina and L. B. Krivdin, *Russ. J. Org. Chem.*, 2004, **40**, 1194 [Engl. Transl. of *Zh. Org. Khim.*, 2004, **40**, 1241].
444. V. A. Danilova and L. B. Krivdin, *Russ. J. Org. Chem.*, 2003, **39**, 663 [Engl. Transl. of *Zh. Org. Khim.*, 2003, **39**, 708].
445. V. A. Danilova and L. B. Krivdin, *Russ. J. Org. Chem.*, 2003, **39**, 1764 [Engl. Transl. of *Zh. Org. Khim.*, 2003, **39**, 1836].
446. V. A. Danilova and L. B. Krivdin, *Russ. J. Org. Chem.*, 2004, **40**, 57 [Engl. Transl. of *Zh. Org. Khim.*, 2004, **40**, 66].
447. T. E. Klepach, I. Carmichael and A. Serianni, *J. Am. Chem. Soc.*, 2005, **127**, 9781.
448. Y. Zhu, Q. Pan, C. Thibaudeau, S. Zhao, I. Carmichael and A. S. Serianni, *J. Org. Chem.*, 2006, **71**, 466.
449. J. B. Houseknecht, T. L. Lowary and C. M. Hadad, *J. Phys. Chem. A*, 2003, **107**, 372.
450. P. Bouř, I. Raich, J. Kaminský, R. Hrbal, J. Čejka and V. Sychrovský, *J. Phys. Chem. A*, 2004, **108**, 6365.
451. F. Cordier, M. Barfield and S. Grzesiek, *J. Am. Chem. Soc.*, 2003, **125**, 15750.
452. M. Barfield, *J. Am. Chem. Soc.*, 2002, **124**, 4158.
453. P. R. L. Markwick, R. Sprangers and M. Sattler, *J. Am. Chem. Soc.*, 2003, **125**, 644.

Solid-State NMR Studies on Semicrystalline Polymers

QUN CHEN[1] AND HIROMICHI KUROSU[2]

[1]*Physics Department and Shanghai Key Laboratory for Functional Magnetic Resonance Imaging, East China Normal University, Shanghai 200062, P.R. China*
[2]*Department of Human Life and Environment, Nara Women's University, Kitauoya-Nishimachi, Nara 630-8506, Japan*

In this review, we summarize recent works on semicrystalline polymers as studied by solid-state NMR, with the emphasis on demonstrating the potential of NMR techniques in characterizing the phase structures, chain conformation, intermolecular interactions as well as chain dynamics of semicrystalline polymers.

1. INTRODUCTION

Semicrystalline polymers, including polyethylene (PE) and polypropylene (PP), are a large group of polymer material with great industrial importance. To probe their structures at different levels and to establish the structure–property relationship for them, and on the basis of this to improve their macro properties in utilization, have lasted to be the key research topics for polymer physics for many years. Solid-state nuclear magnetic resonance (NMR) has been known to be one of the most powerful techniques for studying bulk structures of semicrystalline polymers, owing to its capabilities of reflecting conformational, packing and morphologic structures and its sensitivity to specific interactions and chain dynamics at different levels. Solid-state NMR has been employed to investigate the bulk structures of semicrystalline polymers for more than 40 years, which has led to a huge amount of literature. Through reviewing papers published in recent years, we found that it is still an active area of research. By employing some recently developed NMR techniques and by carrying out more systematic studies, application of solid-state NMR spectroscopy has kept on providing new insights to bulk structures of semicrystalline polymers either traditional or with novel physical and chemical structures. In this review, we try to summarize some recent works on semicrystalline polymers by

solid-state NMR, with the emphasis on demonstrating the potential of NMR techniques in characterizing the phase structures, chain conformation, intermolecular interactions as well as chain dynamics of semicrystalline polymers.

2. POLYETHYLENE AND ETHYLENE COPOLYMERS

The phase structure of a series of ethylene–vinyl acetate (EVA) copolymers (Table 1) has been investigated by solid-state wide-line ^{1}H NMR and solid-state high-resolution ^{13}C NMR spectroscopy.[1]

The ^{13}C cross-polarization magic-angle spinning (CP-MAS) NMR spectrum of EVA28 acquired at room temperature is depicted in Fig. 1 with the details of peak assignment. Two small peaks at ~169 and 70 ppm are attributed to the carbonyl group and CH group, respectively. Peaks corresponding to methylene carbons in various sequences all appear in the region between 20 and 40 ppm. Two overlapping peaks at 32.4 and 33.4 ppm for the crystalline region can be observed in Fig. 1. As is known, the peak at 32.4 ppm can be attributed to the orthorhombic crystals, whereas the other peak at 33.4 ppm can be assigned to the monoclinic crystals. ^{13}C CP-MAS NMR spectra of five EVA samples are illustrated in Fig. 2. The

Table 1.   Characteristics of EVA samples

Samples							
	EVA05	EVA09	EVA12	EVA14	EVA18	EVA28	EVA40
VA content (mol%)	1.7	3.1	4.3	5.0	6.7	11.2	17.8
Index of melt	3	7	9	3	7	150	50
Degree of crystallinity	72.45	68.62	60.62	63.70	61.50	30.13	6.39
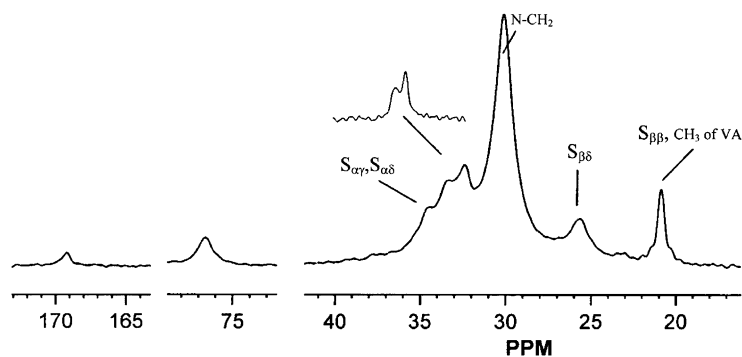
Fig. 1.   ^{13}C CP-MAS NMR spectrum of EVA28. S is used to represent the CH_2 group, whereas the Greek characters are used to indicate the position of the CH_2 group relative to the nearest CH group. The upper part of the figure corresponds to a partially decayed spectrum containing only the crystalline signals acquired with Torchia's pulse sequence. [*Source:* Q. J. Zhang *et al.*, 2002]
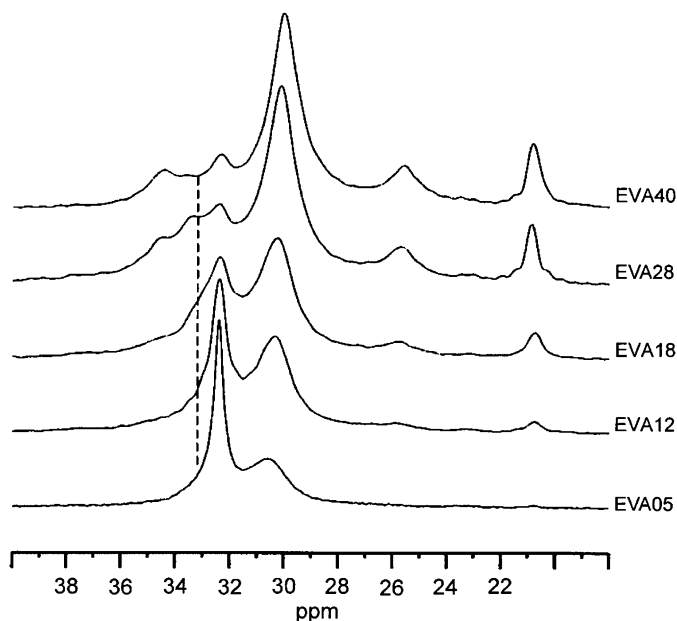
Fig. 2. ^{13}C CP-MAS NMR spectra of five EVA samples. The dashed line indicates the monoclinic crystalline signal. [*Source:* Q. J. Zhang *et al.*, 2002]

chemical shift of the monoclinic signals is marked by a dashed line. The result of peak decomposition on the decayed spectrum of EVA28 is given as an example in Fig. 3. The resulting relaxation curves of the crystalline region are portrayed in Fig. 4. For EVA05, EVA12, and EVA18, because of the low content of the monoclinic crystals, analyzing the relaxation of monoclinic crystal alone will not give any credible results. Therefore, the intensity of the crystals of these five samples shown in Fig. 4 contains the contribution of both monoclinic and orthorhombic crystals. All relaxation curves need to be fitted with two components, that is, two ^{13}C NMR spin–lattice relaxation times (T_1) exist in the crystalline regions of all five samples. The component with longer ^{13}C T_1 was attributed to the internal part of the crystalline region, whereas the component with shorter ^{13}C T_1 to the mobile crystalline component located between the noncrystalline (NC) region and the internal part of the crystalline region. As shown in Fig. 5, the content of the mobile crystalline component relative to the internal part of the crystalline region increased with the VA content, showing that the ^{13}C NMR spin–lattice relaxation behavior is closely related to the crystalline structure of the copolymers.

The sequence distribution and crystalline structure of a series of EVA copolymers (Table 2) with different VA contents were investigated with high-resolution NMR spectroscopy.[2] It was found that most of the VA segments are isolated in the main chain, though three kinds of sequence distributions (VA–VA head to tail, VA–E–VA head to tail, and VA–E–E–VA head to tail) exist in the EVA copolymers with higher VA content (EVA18, EVA28, and EVA40). Furthermore, two
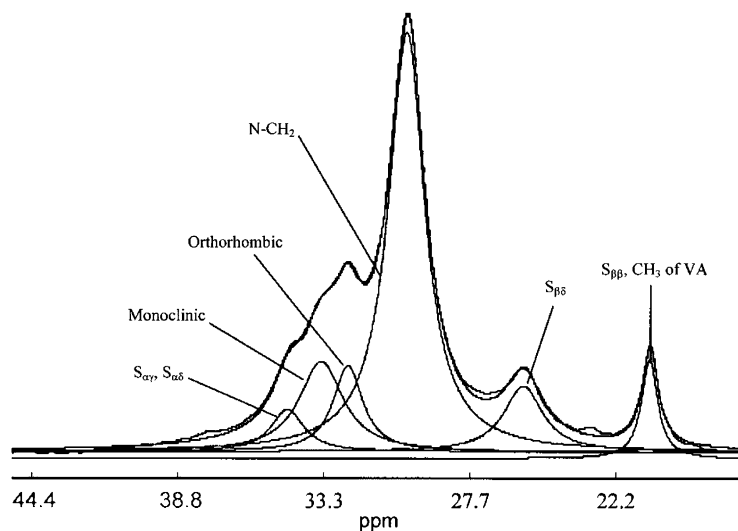
Fig. 3. Results of peak decomposition on a partially decayed spectrum of EVA28 acquired by Torchia's pulse sequence. [*Source:* Q. J. Zhang *et al.*, 2002]
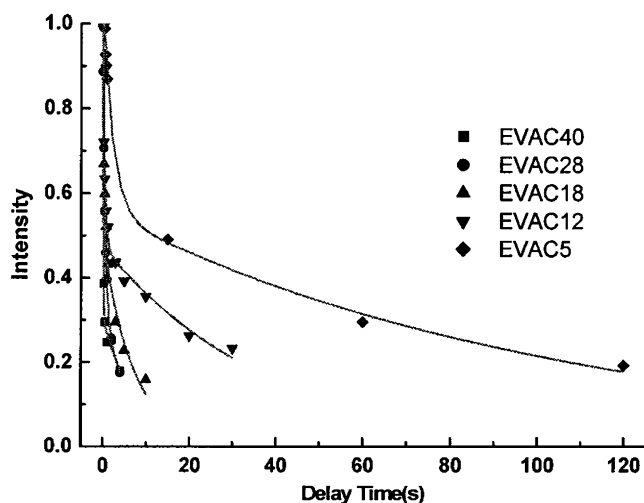
Fig. 4. ^{13}C NMR T_1 relaxation curves of the crystalline signals of five EVA samples, where the real lines represent the fitting results of each relaxation curve. [*Source:* Q. J. Zhang *et al.*, 2002]

kinds of alkyl-branching signals were detected in the high-temperature solution ^{13}C NMR spectra of EVA copolymers. The length of alkyl branches decreases with increasing ethylene segments content. The *n*-butyl branch exists in EVA copolymers with lower VA content (EVA9, EVA14, EVA18), and the *n*-hexyl branch exists in EVA copolymers with higher VA content (EVA28, EVA40). Solid-state ^{13}C NMR
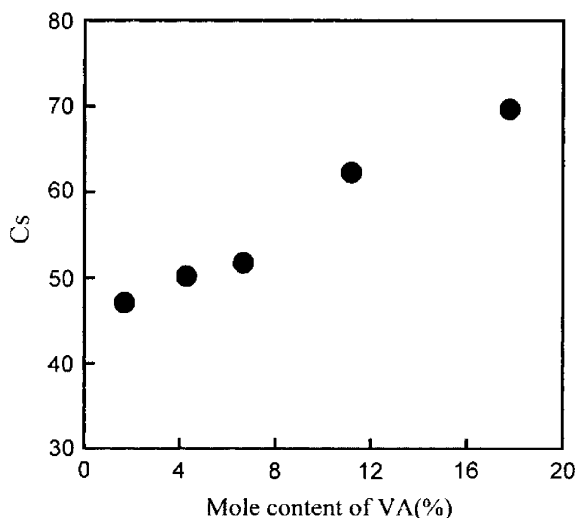
Fig. 5. Variation of the content of the shorter T_1 component in the crystalline region (Cs) with the VA content. [*Source:* Q. J. Zhang *et al.*, 2002]

Table 2. Basic properties of EVA copolymers

Sample code	Comonomer		d (g/cm^3)	T_m (°C)	T_c (°C)	MI (g/10 min)
	wt%	mol%				
EVA9	9	3.3	0.932	98	88	2
EVA14	14	5.0	0.935	88	72	2
EVA18	18	6.7	0.940	84	69	3
EVA28	28	11.2	0.955	65	52	150
EVA40	40	17.8	0.980	49	30	50

spectra of EVA copolymers are shown in Fig. 6. The peak fitting of these spectra indicated that only orthorhombic phase exists in the crystalline region of the EVA copolymers with lower VA content. For the EVA copolymers with higher VA content, however, besides the occurrence of orthorhombic crystalline phase, monoclinic phase was also detected. Fig. 7 shows the crystallinity and monoclinic/orthorhombic ratio of EVA under different crystallization conditions as a function of VA content. This shows that monoclinic phase, as a metastable state, is mainly affected by VA content as well as the thermal treating history.

High-resolution solid-state ^{13}C NMR spectra of undrawn and drawn (ethylene–vinyl alcohol, EVOH) copolymers and their ^{13}C T_1 were measured, in order to elucidate the structure and dynamics of EVOH in the drawn state.[3] Fig. 8 shows the results of the computer lineshape analysis of the CH CP-MAS resonance line for the drawn EVOH. Chemical shift, half-height width and relative peak intensity of each decomposed component observed by CP-MAS and pulse saturation transfer (PST)/
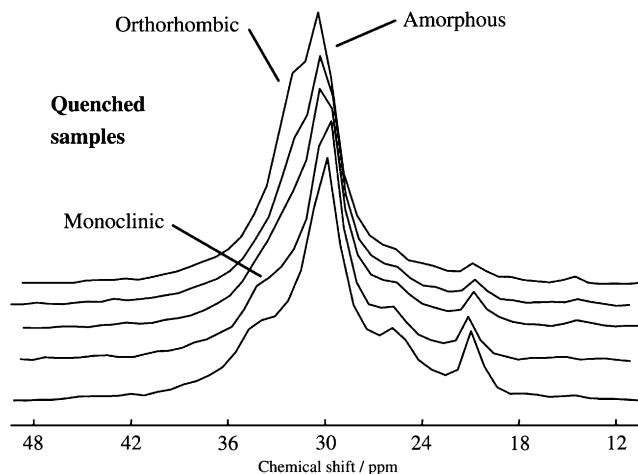
Fig. 6. ^{13}C CP-MAS NMR spectra of EVA copolymers by quenching treatment. From top to bottom: EVA9, EVA14, EVA18, EVA28, and EVA40. [*Source:* Z. Q. Su *et al.*, 2004]
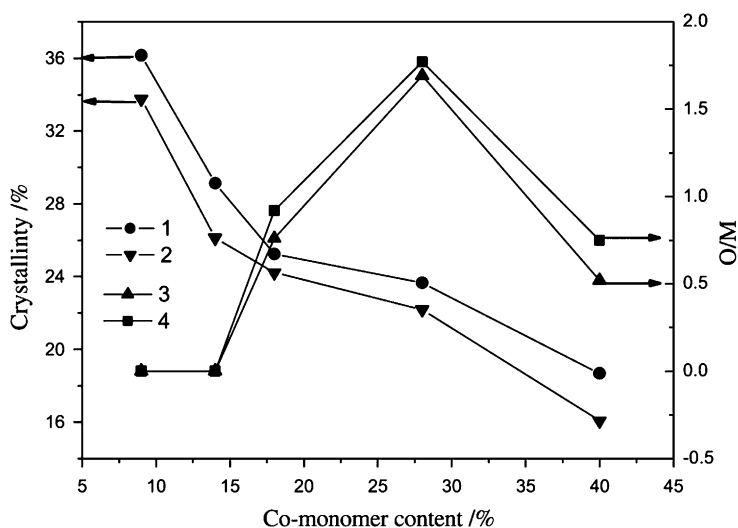
Fig. 7. Crystallinity and M/O ratio of EVA under different crystallization conditions as a function of VA content: (1) crystallinity of air-cooled samples; (2) crystallinity of quenched samples; (3) M/O ratio of air-cooled samples; (4) M/O ratio of quenched samples. [*Source:* Z. Q. Su *et al.*, 2004]

MAS are listed in Tables 3 and 4, respectively. Three peaks of the CH carbon are named peaks I, II, and III from downfield.

For immobile component observed by CP-MAS, the half-height widths of all peaks are almost constant between drawn and undrawn EVOH. This shows that the order structure of immobile component did not change by drawing sample. On the
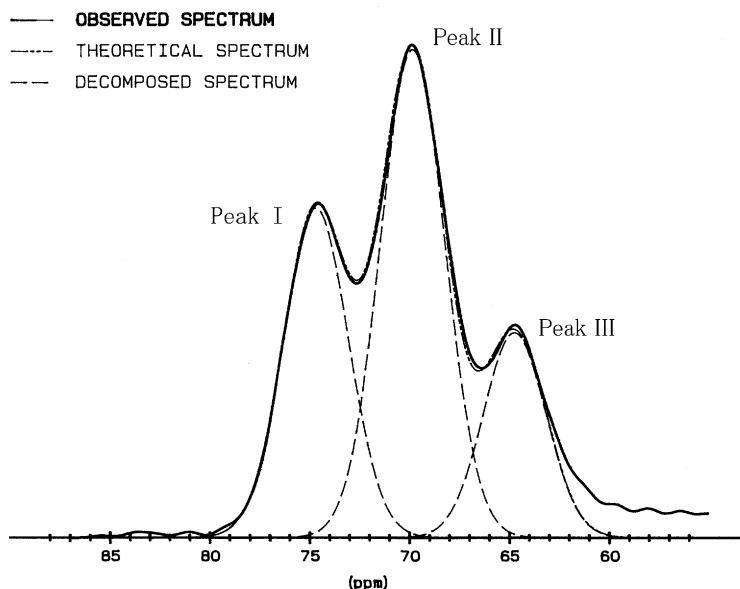
Fig. 8. Lineshape analysis for the CH carbon of CP-MAS resonance line measured for drawn EVOH sample. The broken line indicates the decomposed curves of the components. [*Source:* H. Kurosu *et al.*, 2002]

Table 3. Observed ^{13}C CP-MAS NMR chemical shifts, half-height widths and relative peak intensities of undrawn and drawn EVOH in the solid state

Peak	Undrawn			Drawn[a]		
	δ[b]	$\delta_{1/2}$[c]	Peak intensity[d]	δ[b]	$\delta_{1/2}$[c]	Peak intensity[d]
I	75.2	3.9	30.5	74.7	3.8	32.5
II	70.2	3.8	49.1	69.8	3.8	47.9
III	64.8	3.7	20.4	64.8	3.7	19.6

[a]Draw ratio: × 10.
[b]Chemical shift (ppm from TMS).
[c]Half-height width (ppm).
[d]In percent.

other hand, the half-height widths of peaks I, II and III of drawn EVOH observed by PST/MAS were decreased as compared with those of undrawn EVOH as shown in Table 4. This means that the order structure of mobile component for drawn EVOH improved as compared with that of undrawn EVOH. Table 3 shows that the chemical shifts of peaks I and II move upfield and that of peak III remain constant by drawing the sample. It is known that a formation of hydrogen bond makes downfield shift of ∼6 ppm and the chemical shift depends on the length of hydrogen bond. Therefore, it can be considered that the upfield shift of peaks I and II of CH

Table 4. Observed ^{13}C PST/MAS NMR chemical shifts, half-height widths and relative peak intensities of undrawn and drawn EVOH in the solid state

Peak	Undrawn			Drawn[a]		
	δ[b]	$\delta_{1/2}$[c]	Peak intensity[d]	δ[b]	$\delta_{1/2}$[c]	Peak intensity[d]
I	73.8	4.8	33.1	73.5	4.0	33.0
II	69.5	3.8	40.0	69.1	3.7	44.2
III	65.3	5.2	26.9	64.5	4.5	22.8

[a]Draw ratio: $\times 10$.
[b]Chemical shift (ppm from TMS).
[c]Half-height width (ppm).
[d]In percent.

carbon shows the increase in the interchain hydrogen bond length by drawing the sample. If the hydrogen bond length is increased, the restriction of molecular motion of the carbons of peaks I and II will be decreased. In order to elucidate dynamics of EVOH samples, ^{13}C T_1 of undrawn and drawn EVOH samples were measured using Tochia pulse sequence. The T_1 values of the long T_1 component of peaks I and II of undrawn EVOH are 39.2 and 29.0 s, while those of drawn EVOH are 28.4 and 22.1 s. The long ^{13}C T_1 values of peaks I and II of drawn EVOH were decreased as compared with those of undrawn EVOH. This means that the molecular motion of the carbons of peaks I and II were increased by drawing. It can be considered that the interchain hydrogen bond length is increased by drawing and then the mobility of carbons of peaks I and II is increased because of decrease in restriction of molecular motion by the interchain hydrogen bond. Further, this means that not only formation of the intrachain hydrogen bond but also that of the interchain hydrogen bond are contributed to the peaks I and II.

The crystalline structures of ethylene–dimethylaminoethyl methacrylate (EDAM) copolymers, which were either melt-quenched (mq) or isothermally crystallized (iso), were studied by solid-state high-resolution ^{13}C NMR spectroscopy.[4] Fig. 9 shows the change of monoclinic/orthorhombic (M/O) ratio against DAM molar content of three series of samples, that are mq, iso, and solution-precipitated (sp), respectively. From this figure, it is clear that, no matter what the sample preparation process is, M/O values always increase, almost linearly, with the increase of the DAM molar contents. This shows that for semicrystalline copolymers, not only the crystallinity but also the structures of the crystalline region are influenced by comonomer content, or in other words, by chain structure of the copolymer. Fig. 10 shows the stacked plot of ^{13}C CP-MAS spectra of ethylene segments of solution-precipitated EDAM with DAM content of 10.7 mol% at different temperatures. The signal of monoclinic crystals disappeared completely at 80°C, while the orthorhombic signal was still clearly visible at 90°C. The thinner the lamella is, the lower will be the melting temperature, and thus, the lower melting temperature of the monoclinic crystals obviously indicates that the average lamellar thickness of the monoclinic crystals is smaller than that of the orthorhombic crystals.
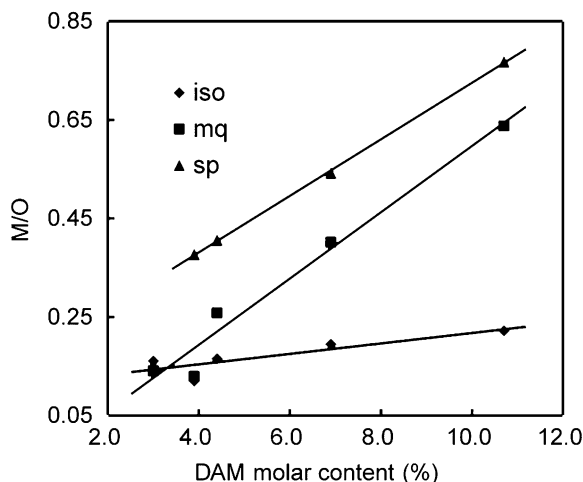
Fig. 9. Plot of M/O vs. DAM content for sp, mq, and iso samples. [*Source:* W. X. Lin *et al.*, 2002]

The solid-state NMR and wide-angle X-ray scattering (WAXS) studies of ethylene–butene (EB) and ethylene–octene (EO) copolymers are carried out.[5] Monoclinic crystallites are found to exist in significant quantity in ethylene copolymers with high comonomer content and bulky side groups. They have a lower melting point and are less favored to form during slow cooling, but are significantly enhanced under fast cooling conditions. On the other hand, the crystallization into the orthorhombic form is favored during slow cooling. It is proposed that the monoclinic structures of ethylene copolymers and deformed linear PE share the same mechanism: the crystalline–amorphous interface is a crucial contribution to the stability of the monoclinic phase. Shear, fast cooling and bulky comonomer increase the contribution of the interface to the free energy, thus favoring the monoclinic form.

A dipolar filter pulse sequence combined with CP-MAS is applied to characterize the phase distribution, morphology and spin diffusion within a high-density polyethylene (HDPE) sample.[6] A new method to obtain quantitative ^{13}C NMR by combining CP-MAS and spin-diffusion NMR is presented. Fig. 11 shows the generalized pulse sequence used in this work and was composed of a "dipolar filter" and a spin-diffusion window prior to CP. The "dipolar filter" refocused the dipolar coupling and chemical shift of the mobile protons while the rigid phase signal was depleted due to its much stronger dipolar–dipolar coupling. In order to probe the spin–spin relaxation time (T_2) of the protons after spin diffusion, a variable delay time was inserted between the spin-diffusion window and the CP part of the pulse sequence (Fig. 11b). Fig. 12 depicts a typical ^{13}C NMR spectrum of the HDPE sample obtained by this technique and a series of ^{13}C NMR spectra as a function of diffusion time t_m as obtained by the pulse sequence shown in Fig. 11a. As can be seen in Fig. 12, three functions (two Gaussians and one Lorentzian) were needed to fit the observed spectra and are assigned to amorphous phase (31.2 ppm),
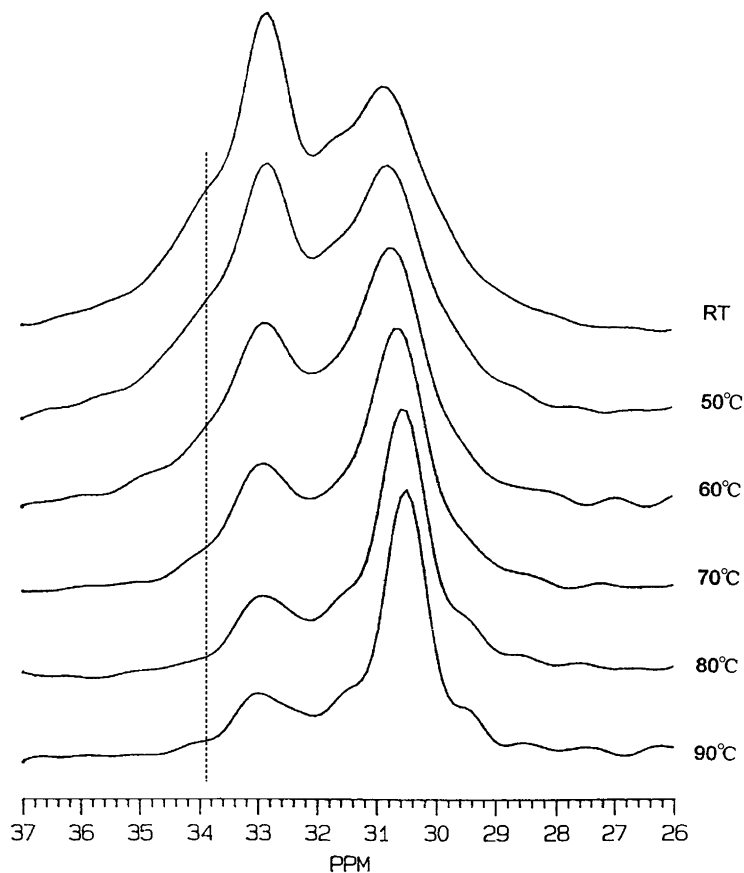
Fig. 10. Variable-temperature stacked plot of the ^{13}C CP-MAS spectra of ethylene segments of sp EDAM samples from room temperature to 90°C, where the dashed line indicates the signal of monoclinic crystals. [*Source:* W. X. Lin *et al.*, 2002]
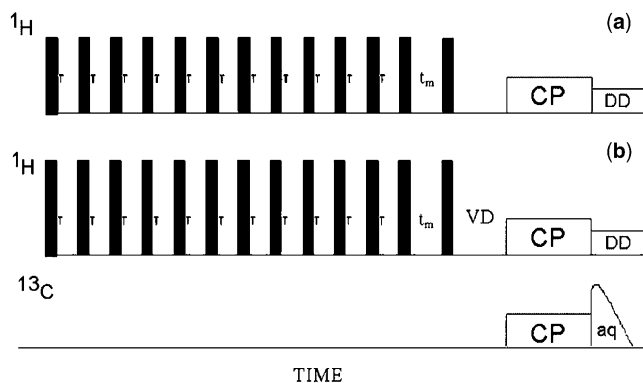
Fig. 11. Illustration of the pulse sequences. [*Source:* L. L. Zhang *et al.*, 2005]
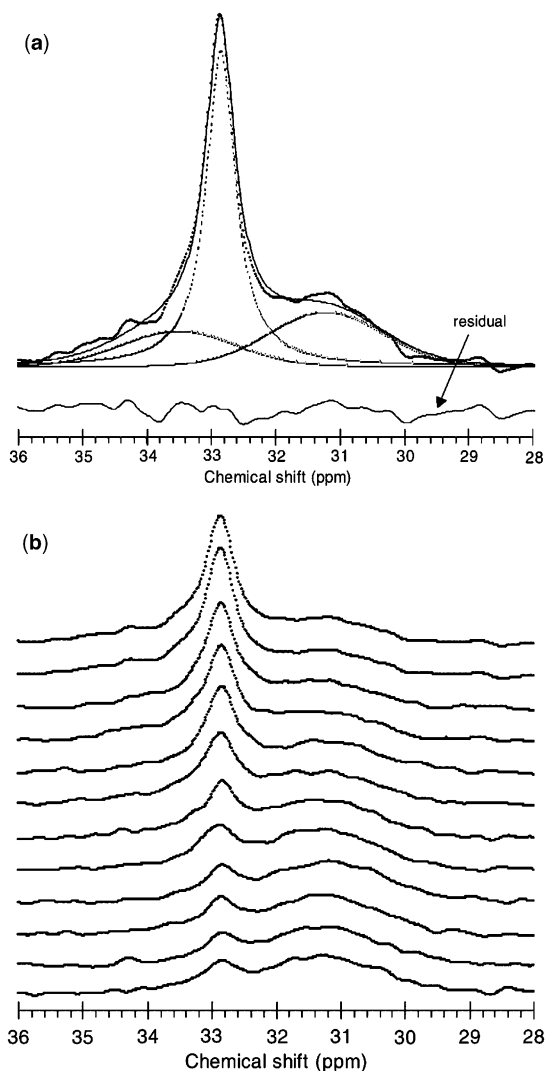
Fig. 12. (a) Typical ^{13}C NMR spectrum of the high-density polyethylene (HDPE) sample obtained by applying the pulse sequence described in the original literature. The spectrum reveals three resonance peaks: C1 (32.98 ppm), C2 (32.32 ppm) and A (30.69 ppm). (b) A series of ^{13}C NMR spectra as a function of diffusion time t_m (0.025, 0.05, 0.1, 0.4, 1, 2, 5, 8, 10, 15, and 25 ms) as obtained by the pulse sequence shown in Fig. 11a. [*Source:* L. L. Zhang *et al.*, 2005]

orthorhombic phase I combined with intermediate phase (32.9 ppm) and orthorhombic phase II (33.5 ppm). Table 5 summarizes the overview of the phase characteristics within the HDPE sample.

This table shows that the two regions C1 and C2A have rather similar properties regarding molecular mobility (M_2(H)), spin diffusion (D), and domain size (≈ 5 Å).

Table 5.   Overview of the phase characteristics within the high-density polyethylene (HDPE) sample

Parameter	Phase			
	Crystalline	Intermediate		Amorphous
Phase notation	C2B	C1	C2A	A
Structure	Orthorhombic I	Orthorhombic II		
Dimension (Å)	65	3–8	5	50
$M_2(H) \times 10^{-10}$ (s^{-2})	4.45	2.6	2.2	0.45
T_2 (ms)	6.9	8.8	9.5	24
δ (ppm)	32.9	33.5		31.2
^{13}C intensity (%)	50	5	5	40
$D \times 10^{16}$ (m^2/s)	6.0	4.6	4.2	1.9

Both regions reveal physical properties having values between those of the pure crystalline region and the pure amorphous region. Of particular importance is the fact that the shape of the spin-diffusion curves of regions C1 and C2A are different, suggesting that C1 is more crystalline-like, e.g., representing an extension of the crystalline region, C2B. Likewise, the C2A region is more amorphous-like, e.g., representing an extension of the amorphous region, A. The structures of the two regions are somewhat different as revealed by their different chemical shifts. Based on this information, we conclude that two regions C1 and C2A constitute an intermediate phase.

In short, when moving from the amorphous region "A" (where the chains have more free volume, more flexibility and less influence from the tie points) into the region "C2A", a transition occurs from a disordered to a more ordered structure as confirmed by the change in proton second moment ($M_2(H)$) and spin diffusivity. As one approaches the crystalline-like region C1, constraints build up from folding and entanglements and segments tend to lose their freedom to explore all of conformational space, and some chains are trapped in a stressed state. However, the motional characteristics remain nearly the same (no change in 2, moment) when moving from region C2A to C1. Some structural changes occur, as revealed by the change in chemical shift. The C1 phase attains a more loosely orthorhombic structure in which the methylene groups appear in a different motional state containing defects in the orthorhombic structure. As one moves further into the crystalline region "C2B", a transition occurs in which segments rearrange into a more ordered, orthorhombic crystalline structure. The transition is verified by the observed change in chemical shift, spin diffusivity and proton second moment.

Preparative temperature rising elution fractionation (TREF) in conjunction with NMR can provide us with a wealth of information and insight into the microstructure of ethylene-co-1–butene (LLDPE(C4)) and ethylene-co-1–hexene (LLDPE(C6)).[7] LLDPE(C4) and LLDPE(C6) had very similar densities, MFIs, comonomer contents (mol%) and percentage crystallinity; however, distinct differences were observed in the physical properties of these two polymers. LLDPE(C6)

could be fractionated into five fractions, while only four significant fractions were obtained for LLDPE(C4). Although the amount of crystallinity was the same for both polymers, the type of crystallinity differed significantly. It is believed that the higher degree of clustering in LLDPE(C6) inhibits crystallization more and thereby increases the number of tie molecules in the polymer, making it a stronger product. Hence, higher impact strength is observed for LLDPE(C6) over LLDPE(C4). This was further substantiated by the coarser spherulitic structure of LLDPE(C6) observed in the scanning electron microscopy (SEM) micrographs. This, in addition to the fact that LLDPE(C6) contains a higher amount of linear chains that can crystallize at higher temperatures, thereby forming larger crystals, explains the poor optical properties of the material. The results from triad sequence distributions, relaxation studies, crystallization, and melting behavior all point to LLDPE(C6) having a more heterogeneous distribution of short chain branches along the backbone than LLDPE(C4) which in turn has significant effects on the observed properties.

The structure and dynamics of several components, particularly those of the oriented noncrystalline components, present in highly drawn PE samples were studied by solid-state ^{13}C NMR spectroscopy.[8] The analyses of the ^{13}C T_1 and ^{13}C T_2 have revealed that at least three components with different T_1^C and T_2^C values, which correspond to the crystalline, less mobile noncrystalline and rubbery amorphous components, exist for these materials, as in the case of isothermally crystallized samples. However, another component with a mass fraction of 0.13–0.18 exists which has a ^{13}C chemical shift very close to that of the orthorhombic crystalline phase but has an extremely small T_1^C Since this component is believed to have the all-*trans* conformation, it is termed fast all-*trans*. Each longitudinal relaxation decay curve of the resonance line at 33.0 ppm is found to be composed of four components that have different T_1^C values, while the transverse relaxation decay of the NC component is composed of two components having different T_2^C values as depicted in Figs. 13 and 14. The drawing appears to mainly affect the T_1^C values in a manner such that these values increase with the draw ratio. The fully relaxed spectra have been resolved into seven or eight components as shown in Fig. 15. In addition to the six resonance lines that are generally observed in the isotropic samples as one monoclinic, three orthorhombic, and two noncrystalline components, two additional peaks are found to exist 0.3 and 0.5 ppm downfield from the orthorhombic resonance line. By examining the broad half-width, small T_1^C value, and narrow chemical shift anisotropy (CSA) of the former peak as well as by comparing the mass fractions with the degree of crystallinity determined by X-ray diffractometry, the former peak is assigned to the NC component with the all-*trans* conformation that probably exists as taut-tie molecules. It is suggested that the lack of lateral order may allow those chains to undergo rapid random jump or diffusional rotation around the chain axis. Moreover, it can be assumed that each chain may be subjected to rapid fluctuation with fairly large amplitudes around the torsional potential minimum in each C–C bond as deduced from the narrow CSA. Additional experiments also confirmed that these fast all-*trans* chains are aligned in
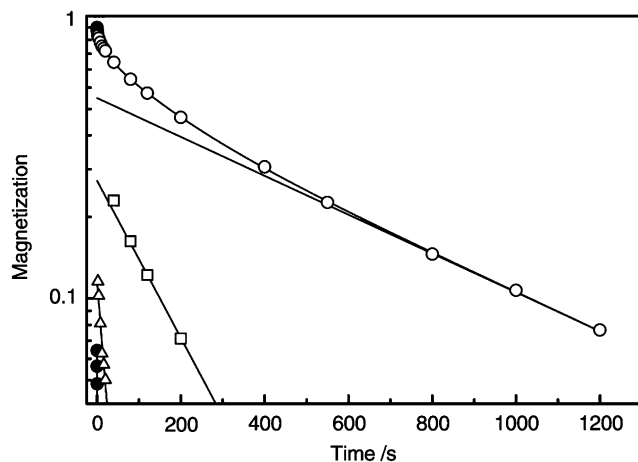
Fig. 13. ^{13}C spin–lattice relaxation behavior of the resonance line at 33.00 ppm for drawn PE sample (draw ratio: 16), which was obtained by the CPT1 pulse sequence. The peak intensities indicated by circles are plotted against the delay time for the relaxation. [*Source:* N. Chaiyut *et al.*, 2006]
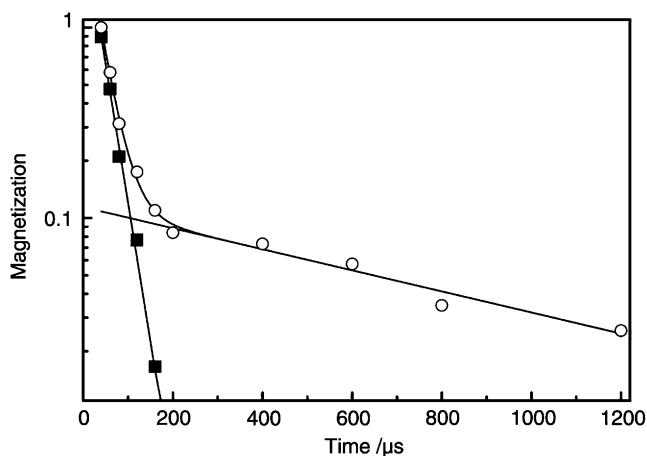
Fig. 14. ^{13}C Spin–spin relaxation behavior of the resonance line at 31.50 ppm for drawn PE sample (draw ratio: 16), which was obtained by the solid-state ^{13}C spin–echo pulse sequence. The peak intensities indicated by circles are plotted against the delay time for the relaxation. [*Source:* N. Chaiyut *et al.*, 2006]

the draw direction and that rapid motion occurs around their chain axis. The results of the component that appears 0.5 ppm downfield from the orthorhombic reso-nance line suggest that the component can be considered to be a cluster or a group of chains that have the all-*trans* conformation. At room temperature, they appear downfield due to packing. As a result of increased motion at higher temperatures,
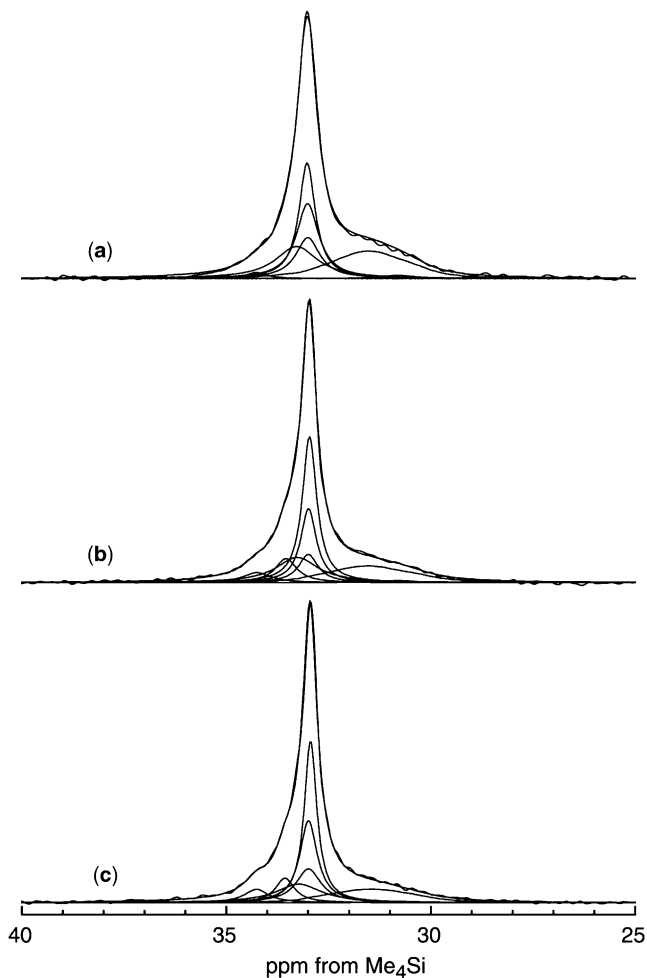
Fig. 15. Fully relaxed DD/MAS ^{13}C NMR spectra measured for drawn high-density PE by the 90° single-pulse sequence with recycle delay times longer than five times of the longest T_1^{C} value for the respective samples: (a) draw ratio: 9 times, (b) draw ratio: 12 times, and (c) draw ratio: 16 times. [*Source:* N. Chaiyut *et al.*, 2006]

they may dissociate themselves and behave in the same manner as isolated chains having the all-*trans* conformation and, namely, as the fast all-*trans* component.

The relationship between the morphology and the mechanical properties of ethylene–methyl methacrylate (EMMA) films with different MMA contents (EMMA-I with 3.0 mol%, EMMA-II with 6.5 mol%, and EMMA-III with 14.6 mol%) were investigated as a function of temperature by using polarized light scattering, X-ray diffraction, and ^{13}C solid-state NMR.[9] X-ray diffraction measurement revealed that the crystallites within EMMA films are much smaller than those within branched PE (G201) film and that the crystallinity is much lower. Furthermore, the number of

crystallites drastically decreased as temperature increased. This indicates the presence of unstable crystallites with a disordered lattice. On the other hand, the intensity distribution from the amorphous phase showed the first and second scattering maxima, indicating that the ethylene sequences in the amorphous phase have an ordered arrangement rather than a random orientation. ^{13}C NMR measurements revealed that the overall decay curves for the orthorhombic crystals and the amorphous phase could be classified into two components, i.e., a slow decay curve and a rapid decay curve, indicating the existence of two kinds of T_1^C The shorter T_1^C value for the orthorhombic crystal was shorter than the longer T_1^C value of the amorphous component, indicating crystallites with unstable lattice formation. These results were in good agreement with those estimated by X-ray. The EMMA (EMMA-III) film with a maximum draw ratio of 10 times at room temperature provided a reversible change of stress–strain curves when the specimen was stretched.

A proton NMR method, based on simple Bloch-decay spectra in the solid state, is presented that enables one to follow, with excellent sensitivity superior to differential scanning calorimetry (DSC), structural changes associated with aging in semicrystalline polymers whose T_g is well below the aging temperature.[10] The method is demonstrated for two representative isotactic polypropylene (iPP) samples, a Ziegler–Natta product and a metallocene product. Starting with samples that had been melt crystallized at a cooling rate of $1^\circ C/min$ and then aged at ambient temperature for long periods of time, subsequent mild heating cycles between ambient temperature and temperatures below $90^\circ C$ were applied. Such heating cycles remained more than $70^\circ C$ below the major crystalline melting temperature for iPP. Aging at $20^\circ C$ was monitored by NMR over aging times, $6\,min < t_{age} < 4$ days, following those heating cycles as shown in Fig. 16. It was shown that changes in the Bloch-decay spectra, corresponding to a lower limit of 2–3% of the mass of iPP being transformed from mobile to rigid components, accompanied the aging process over the 4-day period. Moreover, the time dependence was linear in $\log(t_{age})$. It was further shown that the population of those NC stems with the highest mobility was most strongly reduced by aging; this observation does not, however, unambiguously establish that these same chains were the actual stems participating in the newly formed structures. The aging process was also shown to be reversible in the sense that the structures formed could be completely destroyed by repeating the mild heating cycle. Attention was paid to the definition of crystallinity, and an operational definition of crystallinity for the NMR measurements was based on the component with a long ($> 150\,ms$) value of T_{1xz}, the relaxation along the quantization axis of the toggling frame in a multiple pulse (MP) experiment. The complementary NC component, by this definition, includes not only the motionally averaged protons seen in the Bloch-decay spectrum but also certain protons with more hindered motions which, by Bloch-decay criteria, appear rigid. Approximately 75% of the NC protons transformed by aging are converted to "crystalline" protons, using the T_{1xz} definition; hence, the structural changes in aging seem to be dominated by crystallization, which we are comfortable to call secondary crystallization. A quick assay of the longitudinal proton relaxation, T_1^H, was also made during aging. Aside from some changes originating from oxygen losses during
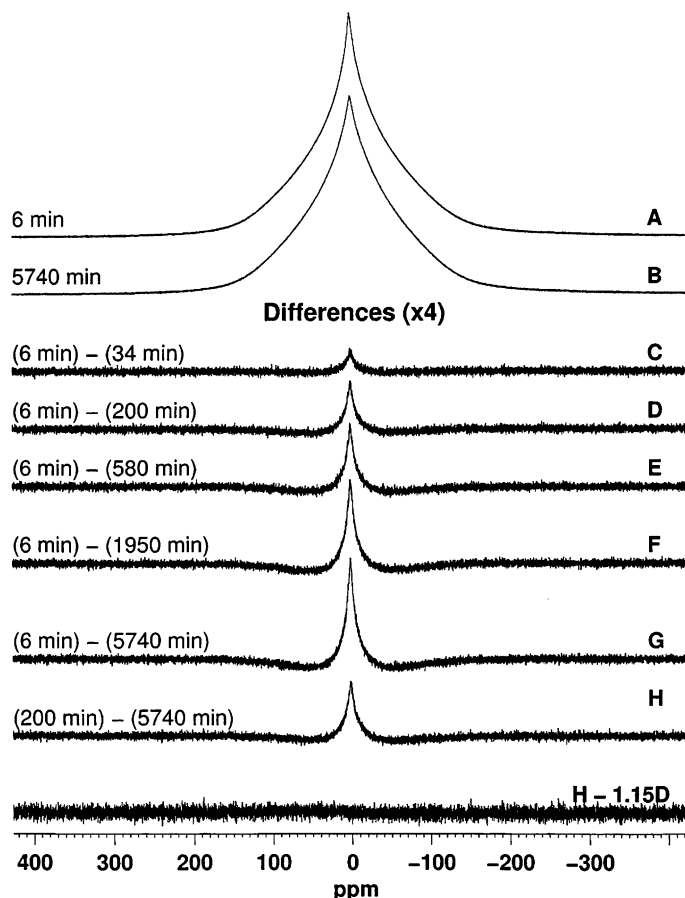
Fig. 16. Bloch-decay spectra and difference spectra associated with a 4-day aging period for iPP-1. A, B: full spectra for $t_{age} = 6$ min and 4 days, respectively. C–H: vertically amplified ($\times 4$), zero-integral difference spectra involving spectra at the two indicated t_{age} values. Spectrum G = A − B. The lower spectrum is the indicated "difference of difference" spectrum illustrating that, within experimental error, the lineshape changes over the first half of the aging-induced conversion are identical to those in the second half. [*Source:* D. L. Vander-Hart *et al.*, 2003]

heating, T_1^H was found to be independent of aging time, and implications are pursued. Without making firm conclusions, observations are noted that may have relevance to the morphological location of secondary crystallites and to the factors that influence the amount of material available for such crystallization. The extent of secondary crystallization in the metallocene iPP is only modestly smaller than in the Ziegler–Natta iPP, although the metallocene iPP has a lower stereo-regiodefect concentration, a narrower polydispersity and no expected "amorphous fraction". It is speculated that significant secondary crystallization would also characterize a defect-free iPP with low polydispersity.

3. SOME OTHER SEMICRYSTALLINE POLYMERS

Elongation-induced crystallization and its related structural changes for polymer elastomer are subjects of extensive studies. Solid-state NMR has been turned out to be a powerful way of probing both crystalline and amorphous structural changes of polymeric elastomer induced by stretching. Comparing with other *in situ* techniques like X-ray diffraction, solid-state NMR, due to its higher resolution, provides the potential of monitoring the behavior of individual groups and therefore is especially suitable for studying multi-component samples. Kameda and Asakura[11] recently reported a static ^{13}C NMR study on natural rubber (NR) by using a home-built device which allows uniaxially stretching elastomeric sample inside the magnet. Due to the high mobility nature of NR, high-resolution spectrum of the amorphous region can be attained without using of MAS. Strain-induced crystallization was found to occur at 200% strain, as indicated by the appearance of broad signals in the corresponding ^{13}C CP spectra. Because ^{13}C chemical shifts of the amorphous signals exhibit no apparent changes with increasing stretching ratio, it was concluded that the mobility of the amorphous region disrupted the molecular chain orientation and the amorphous chains remained unoriented under uniaxial deformation. Moreover, the authors reported an interesting phenomenon that the mobility of the amorphous region of NR varies with the increase of time, after the sample being stretched to a certain ratio. As shown in Fig. 17, in the variable contact time experiments, the build-up curves of the ^{13}C amorphous signals with increasing CP contact time are markedly different for the sample in the period of
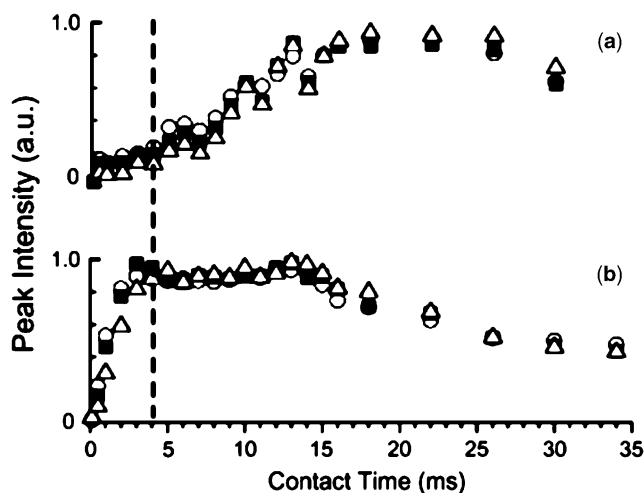
Fig. 17. Contact time-dependent peak intensities of the aliphatic carbons of 31.9 ppm ($\bigcirc$), 26.1 ppm ($\blacksquare$) and 22.9 ppm ($\triangle$), for natural rubber, at elapsed time from 0 to 20 min (a), and from 60 to 80 min (b) immediately after stopping the deformation at 30% strain. The dotted line represents a contact time of 4 ms. The number of scans for obtaining each plot was 16 times. [*Source:* T. Kameda *et al.*, 2003]

0–20 min after stretching and for sample in the period of 60–80 min, indicating that the mobility of the amorphous varies with time. ^{1}H spin–lattice relaxation time in the rotating frame ($T_{1\rho}$) became shorter with the increase of time after stretching, which in turn provides the evidence that the mobility increases first and then gradually decreases with time.

Contrary to the above work, Lin *et al.*[12] developed a simple device which allows the elastomeric sample being stretched inside the MAS rotor. With the application of such a device, a series of MAS based high-resolution solid-state ^{13}C NMR experiments were performed on stretched NR samples for the first time. As depicted by the ^{13}C CP-MAS spectra shown in Fig. 18, crystalline signals appeared upon stretching as shoulders on the upfield side of the corresponding signals and their intensities increased with the stretching ratio. The crystalline signals are much better resolved, compared with that obtained by Kameda and Asakura without using MAS. ^{13}C T_1 as well as ^{1}H T_2 of the individual signals were determined. The aforementioned upfield shoulders exhibit longer ^{13}C T_1 and shorter ^{1}H T_2, compared with their low-field counterparts, demonstrating that they are corresponding to the crystalline structure. Through quantitative ^{13}C dipolar decoupling (DD)/MAS studies, it was shown that strain-induced crystallization occurs when the draw ratio reaches ∼2.0 and the maximum crystallinity of the NR samples is ∼20% upon stretching. This result agrees well with that of Kameda's work. Furthermore, by comparing the ^{13}C CP-MAS spectrum of the unstretched NR sample with that of the stretched NR sample, straightforward evidence was given that there exists a small amount of crystalline structure in the unstretched NR sample at room temperature.
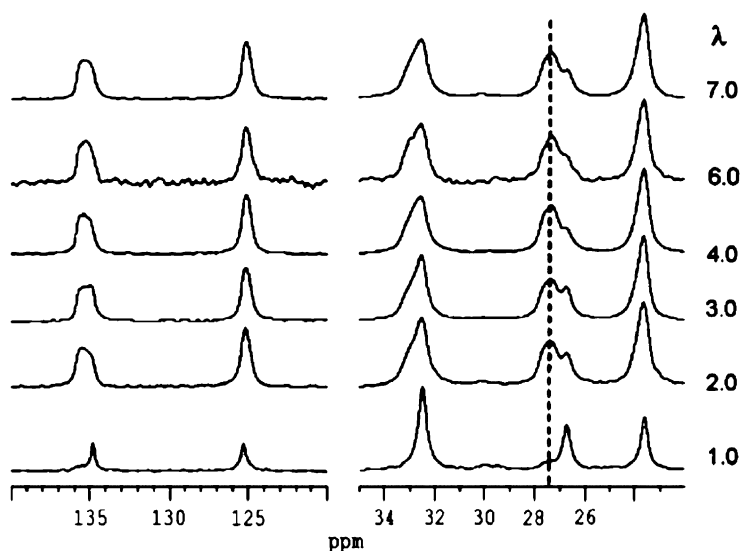
Fig. 18. ^{13}C CP-MAS spectra of NR sample with different draw ratios (λ); where the dashed line denotes the crystalline signals of the δ methylene carbon. [*Source:* W. X. Lin *et al.*, 2004]
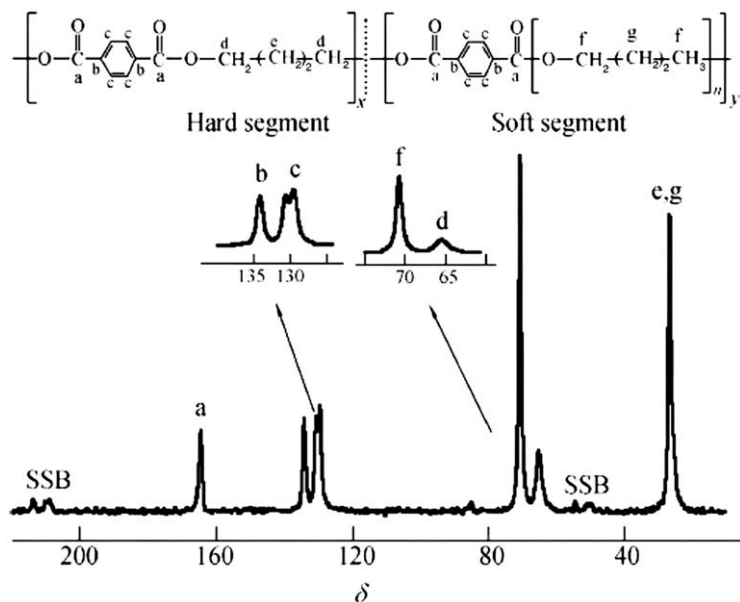
Fig. 19. ^{13}C CP-MAS spectrum of the unstretched 4GT-PTMO2000 and its assignments, where SSB denotes the signal of spinning side band. [*Source:* W. X. Lin *et al.*, 2004]

The above methodology was further employed by Lin *et al.*[13] to study the strain-induced crystallization of a poly(ether–ester) sample (Fig. 19). The phase structure of the poly(ether–ester) sample is rather complicated compared with that of NR, due to the fact that the hard segment is partially crystallized and the poly(tetra-methylene oxide) (PTMO) soft segment is only partially miscible with the amorphous hard segment. Furthermore, strain-induced crystallization of the PTMO soft segment was found to occur at a draw ratio of 2.0 and its crystallinity increases with the draw ratio, as indicated by the dashed line in Fig. 20. From Table 6, it can be found that at relatively higher draw ratio, the crystalline signal of PTMO also exhibits two ^{13}C T_1 values, similar to the behavior of ethylene copolymers afore-mentioned. The value of the longer ^{13}C T_1 increases with draw ratio, indicating perhaps the lamellar thickness of the PTMO crystallites increasing with increase in draw ratio. The molecular motion at higher frequency of the amorphous PTMO was found to be almost independent of the draw ratio. Through ^1H T_2 measurements, it was demonstrated that the strain-induced crystallization mainly happens in the "pure" PTMO region.

Poly(vinyl alcohol) (PVA) is a semicrystalline polymer. However, when it is blended with poly(acrylic acid) (PAA), the crystalline structure of PVA can be completely destroyed due to the interpolymer hydrogen bonding formed between the hydroxyl group of PVA and the carboxyl group of PAA, when the molar ratio of acrylic acid in the blend exceeds a certain value. It was found by solid-state high-resolution ^{13}C NMR and wide-angle X-ray diffraction (WAXD) studies that
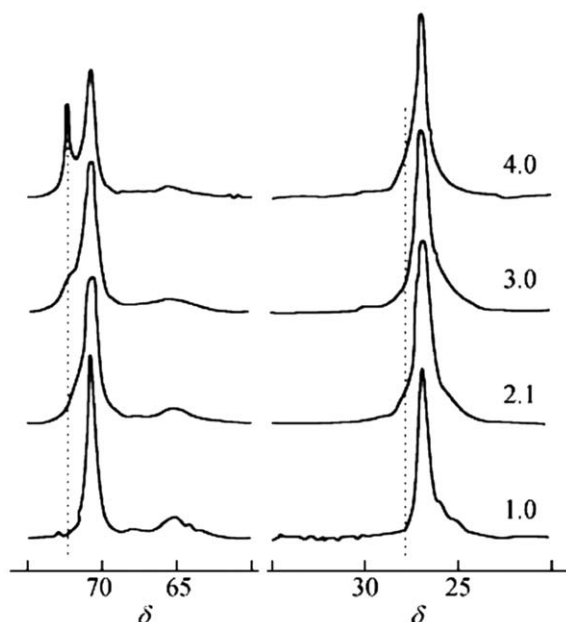
Fig. 20. ^{13}C CP-MAS spectra of 4GT-PTMO2000 with different draw ratios. [*Source:* W. X. Lin *et al.*, 2005]

Table 6. ^{13}C T_1 values of PTMO segment for 4GT-PTMO2000 sample with different draw ratios

λ	T_1 (s)		
	Crystalline		Amorphous
1.0	–	–	0.25
2.1	4.3	–	0.27
3.0	28.5	0.84	0.27
4.0	114.6	0.69	0.27

elongation on such a blend sample can lead to elongation-induced phase separation of the polymer pair and subsequently lead to the "re-crystallization" of PVA.[14] As is shown in Fig. 21, for sample I with PAA content in monomer molar of 0.21, the relative intensities of three methine carbon peaks of vinyl alcohol vary apparently with the draw ratio and become very close to that of the pure PVA sample at the largest draw ratio, indicating that the interpolymer hydrogen bonding formed between the hydroxyl group and the carboxyl group gradually break and in the meantime more intrapolymer hydrogen bonds are formed between the hydroxyl groups as the draw ratio increases. However on the other hand, no apparent changes in the relative intensities of the methine peaks was observed in the ^{13}C CP-MAS spectra of sample II with PAA content in monomer molar of 0.53.
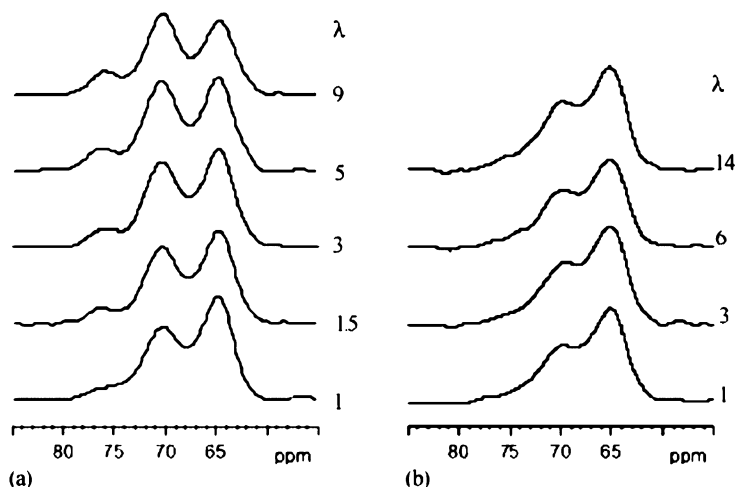
Fig. 21. ^{13}C CP-MAS spectra of the methine carbon of PVA: (a) sample I; (b) sample II with different draw ratios (λ). [*Source:* Q. Chen *et al.*, 2002]

Such results agree well with that of the WAXD studies. For sample I, with the increase of draw ratio, the crystallinity of PVA increased markedly, while for sample II, no such change was observed. ^{1}H $T_{1\rho}$ measurements manifest that when elongated, sample I gradually becomes phase separated, while PVA and PAA keep miscible even at the largest draw ratio.

Recently, Tonelli *et al.* reported a series of works on reorganized polymers with unique morphological and conformational structures.[15,16] The polymer samples were produced from polymer/cyclodextrin inclusion complexes, by removing cyclodextrin (CD) with appropriate solvent. The polymers were believed to stack with less entanglement compared to their counterparts processed by normal methods and take the conformation similar to that polymer chains take inside the narrow channels formed by CD host. Some novel properties were observed for these reorganized polymers. For example, bulk poly(ethylene terephthalate) (PET) processed from PET-γ-CD inclusion complex,[16] comparing with the as-received PET, is found to be readily crystallizable and lack glass transition. Fig. 22 shows the ^{13}C CP-MAS signals of the carbonyl and methylene carbons of three PET samples processed through different ways. From the spectra, the difference in chemical shift is apparent. The signals of the as-received PET appear at the lower field side; that of the PET coalesced from PEI-γ-CD inclusion complex at the upper field side and that of the precipitated PET in-between. Such difference in chemical shift is a direct reflection of difference in conformation. The authors concluded that the coalesced PET has predominantly t –CH$_2$–CH$_2$– bonds, as-received PET predominantly $g \pm$ –CH$_2$–CH$_2$– bonds, and the precipitated PET sample seems to have ~30% $g \pm$ and 70% t –CH$_2$–CH$_2$– bonds.

Porbeni *et al.* presented a work on the morphology and dynamics of poly(ε-caprolactone)-b-poly(L-lactide) (PCL-b-PLLA) diblock copolymer and its inclusion
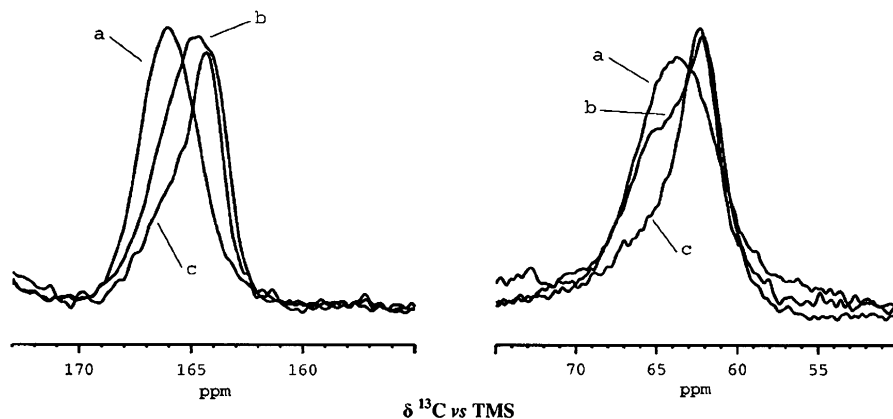
Fig. 22. Methylene carbon (∼60–65 ppm) and carbonyl carbon (∼163–168 ppm) resonance peaks for PET: (a) as-received; (b) precipitated; and (c) coalesced from PET-γ-CD inclusion complex. [*Source:* M. Wei *et al.*, 2002]

complex with α-CD by ^{13}C CP-MAS NMR spectroscopy.[17] Under appropriate conditions, α-CD threads simultaneously both the PCL and PLLA segments, forming inclusion complex. In the inclusion complex, the polymer chain is isolated from other polymer chains by the channel formed by the host CDs, providing the possibility of studying the inherent characteristics of isolated polymer chain and evaluating the cooperative interactions occurring between chains in the bulk polymer, through comparing the behavior of polymer chains inside the inclusion complex with that in the bulk state.

By comparing the ^{13}C CP-MAS spectra of PCL-b-PLAA inclusion complex with that of the bulk copolymer sample, the differences in chemical shifts of the corresponding signals were found to be less than 1 ppm. It was therefore deduced that PCL-b-PLAA chains, either in the inclusion complex or in the bulk state, take all-*trans*, planar zigzag conformation. As was stated by the authors, ^{13}C NMR chemical-shift change can be attributed to the crystal packing effect when $\Delta\delta \sim 1$–2 ppm and to conformational change when $\Delta\delta$ is over 4 ppm.

For PCL-b-PLLA in bulk state, two [13]C T_1 values were observed for all carbons, confirming the semicrystalline structure of the copolymer. Longer [13]C T_1 was attributed to the crystalline region, while the shorter one to the amorphous region. On the other hand, for inclusion complex, single exponential decay was observed for all carbons of the copolymer. The obtained T_1 values are much shorter, indicating much faster motion for isolated copolymer chains in comparison with the bulk copolymer. Such a result suggests that motion in the megahertz frequency region is strongly influenced by the tight packing of polymer chains in the bulk state, or in other words, intermolecular interactions dominate the megahertz frequency dynamics of the polymer chains in the bulk.

Block copolymer of poly(butylenes terephthalate) and PTMO (PBT-*block*-PTMO) is a kind of thermoplastic elastomers (TPE) with extensive research interests.

The mechanical properties of the material are found to be largely dependent on the phase structures, i.e., the crystallinity of PBT and PTMO, the crystal size and perfection, and the fraction of the mixed PBT/PTMO phase. ^{1}H wide-line, ^{2}H as well as ^{1}H 2D double-quantum back-to-back (DQ BABA) spectroscopes based on fast MAS were employed to study the phase composition of a serial of PBT-*block*-PTMO with different segmental length and content.[18] It was shown that there are three different phases coexisting at 40°C in the PBT-*block*-PTMO samples, i.e., a crystalline PBT, a PBT/PTMO mixed phase, and a PTMO-rich phase. The ^{1}H 2D DQ BABA experiment shows a close proximity of the aromatic protons from PBT and OCH$_2$ protons of PTMO, indicating molecular scale mixing of PBT and PTMO blocks in the PBT/PTMO phase.

The detailed phase composition and the crystallinity of PBT block of the copolymers were determined by the ^{1}H T_2 relaxation experiment, a relative traditional method which has been widely used in characterizing the phase structure of semicrystalline polymers. It is worth to note that different techniques discriminate the crystalline phase from the amorphous one on the basis of different characteristics, such as the enthalpy of melting (DSC), long-range periodicity (WAXD), bond vibrations (vibrational spectroscopy), the specific volume (density analysis) and conformation (^{13}C solid-state high-resolution NMR), leading to different values of crystallinity. ^{1}H T_2 relaxation experiments discriminate different phases by their different mobility and therefore should be performed at temperatures well above T_g, yielding distinct differences in chain mobility in the crystalline and amorphous phases. For block copolymers, the ^{1}H free induction decay (FID) signal which was measured by employing a solid-echo pulse sequence, was found to comprise two decaying components with different ^{1}H T_2 values. The component with shorter ^{1}H T_2 (T_2^s) is attributed to the rigid domain, while the component with longer ^{1}H T_2 (1^1) to the soft domain. Through performing the least-squares of the FID signal using a linear combination of Gaussian (rigid phases) and stretched exponential (soft domains) functions (Eq. 1), the ^{1}H T_2 values of both components and the ^{1}H contents of the corresponding components ($A(0)^s$ and $A(0)^l$) can be attained.

$$A(t) = A(0)^s \, \exp\left[-\left(\frac{t}{T_2^s}\right)^2\right] + A(0)^l \, \exp\left[-\left(\frac{t}{T_2^l}\right)^\alpha\right] \qquad (1)$$

For copolymer samples, the rigid domains are formed by crystalline PBT segment and PBT chain portions at the crystal–amorphous PBT interface with restricted mobility, whereas soft domains are composed of PBT/PTMO mixed phase and PTMO-rich phase. Fig. 23A and 23B show ^{1}H T_2^s, T_2^l and the ^{1}H content in the rigid phase of the copolymers and PBT homopolymer at different temperatures. The behaviors of the copolymer and PBT homopolymer are apparently different. While the ^{1}H T_2 decay FID of the copolymers always consists of two components in the temperature range of study, the PBT homopolymer exhibits only one ^{1}H T_2 at temperatures lower than 100°C, the dynamic glass-transition temperature of the sample. The hydrogen content of the rigid phase of PBT homopolymer reaches a
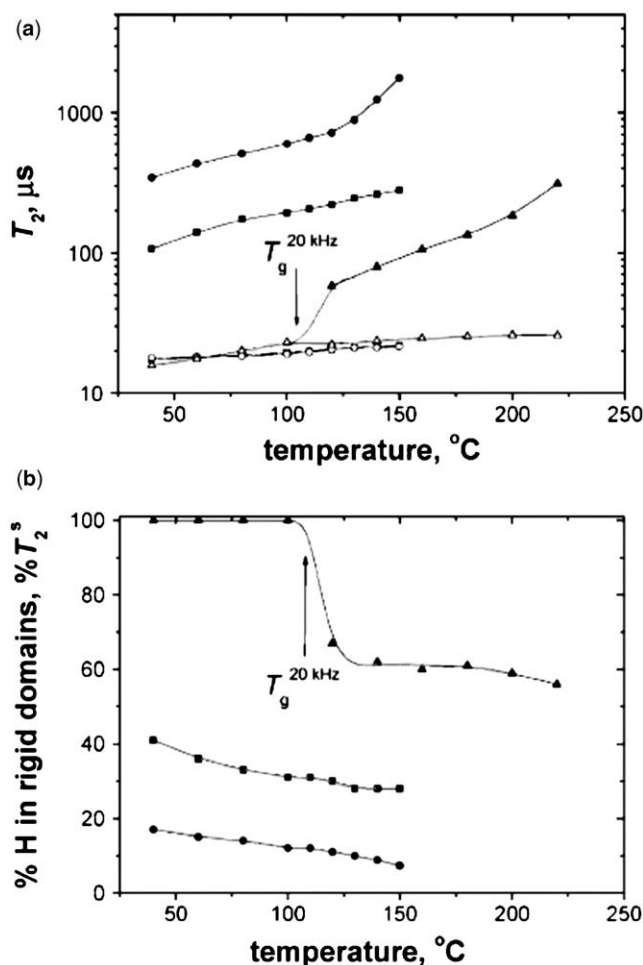
Fig. 23.   Temperature dependence of the T_2 relaxation time for the hard (open points T_2^s relaxation) and the soft (filled points, T_2^l relaxation) fractions of the PBT homopolymer (triangles), sample A1000/35 (squares), and sample A1000/60 (spheres) (a) and the content of hydrogen in the rigid phase of these samples, $\%T_2$ (b). The arrow denotes the dynamic glass-transition temperature for the PBT homopolymer at a frequency of $\sim$20 kHz. [*Source:* V. M. Litvinov *et al.*, 2003]

constant value of $\sim$60% when temperature is over 130°C, which suggests that the chain mobility in rigid and soft domains differ significantly at this temperature. Meanwhile, for copolymer samples, the hydrogen content of the rigid phase decreases gradually with increasing temperature, in a wide range of temperature, and approaches zero at the melting temperature, indicating the existence of a wide range of melting temperatures due to the distribution of crystal sizes and perfection. The comparison of the crystallinities of the homopolymer and copolymers were based

on the data acquired at $130°C$, because it is not possible to determine the crystallinity accurately of PBT homopolymer by ^1H T_2 measurement lower than such a temperature. The above results demonstrate again that when studying phase structure of polymers by NMR relaxation measurements, variable-temperature experiment is important, if not necessary, for getting reliable results. It is also worth to note that the crystallinity determined by ^1H T_2 measurement is apparently higher than that determined by WAXD and DSC, due to the fact that some small and imperfect crystals might be omitted by the latter two methods. Therefore, as stated by the authors, the combined use of different techniques is required for better understanding of the phase structure of polymers.

When employing solid-state high-resolution NMR to study the phase structure of semicrystalline polymers, to discriminate signals originated from different phase components is always a necessary step. A recent study by Hucher *et al.*[19] on the poly(vinylidene fluoride) (PVF_2) gives a good example of how to separate signals from different phase structures. PVF_2 is known to have three different types of crystalline structures, namely the α form with antiparallel packed chains and a distorted TG^+TG^- conformation, the β form with all-*trans* zigzag planar conformation, and the γ form with $T_3G^+T_3G^-$ conformation, respectively. Three PVF_2 samples comprising of α (sample 1), α + β (sample 2), and α + γ (sample 3) polymorphs were studied by both ^{19}F and ^{13}C NMR spectroscopy. To discriminate the crystalline signals from the amorphous one, ^{19}F $T_{1\rho}$ filter and ^1H T_2 filter were used to selectively remove the amorphous and crystalline signals from the spectrum. ^{19}F MAS spectra of sample 1 acquired with high-power ^1H dipolar decoupling and ultra-fast MAS (30 kHz) shown in Fig. 24 manifest clearly the spectral characteristics of the α crystal and that of the amorphous domain.

Fig. 25 shows the ^{19}F MAS spectra of the crystalline components in samples 2 and 3, by using a ^{19}F $T_{1\rho}$ filter of 40 ms. As mentioned earlier, Fig. 25a comprises the contribution of both α and β polymorphs, while Fig. 25a′ of α and γ polymorphs. To separate the signals from different crystal forms, a SELDOM pulse train was employed for selectively excitation. Appropriate use of such a pulse train can lead to the disappearance of all the signals from spectrum except those located near the carrier frequency and those to which the selected magnetization can migrate by ^{19}F spin diffusion. Fig. 24(b, b′) shows the selectively excited signals of α polymorph in samples 2 and 3, by using a SELDOM pulse train with the carrier frequency located at the position of the low-field signal of α form. Subtraction of spectra b and b′ from spectra a and a′ lead to separated signals of β and γ polymorphs. As depicted in Fig. 25(c, c′), there is only a single peak in the spectrum of β polymorph, giving immediately evidence of the all-*trans* conformation in the β form. Meanwhile, four peaks in the spectrum of γ polymorph also support the $T_3G^+T_3G^-$ conformation of γ form.

^{13}C CP-MAS spectrum was acquired through ^{19}F–^{13}C cross-polarization and with simultaneous ^{19}F and ^1H dipolar decoupling. A spin-locking of 40 ms which acted as $T_{1\rho}$ filter was added at the ^{19}F channel before CP contact time, in order to eliminate the amorphous signals from the spectrum. The obtained spectra for three samples are shown in Fig. 26. This suggests that the α and β forms are represented
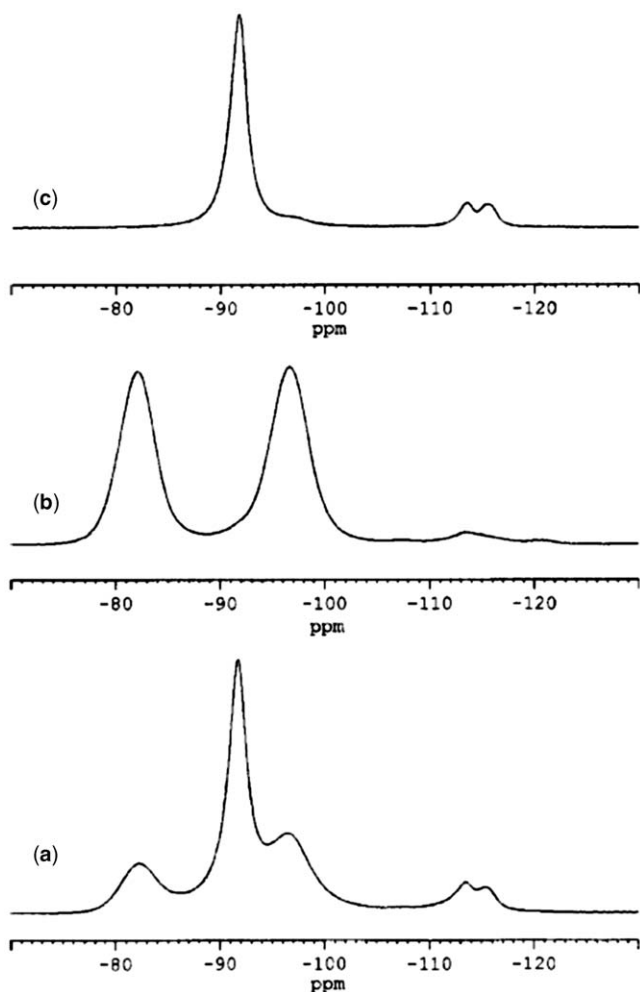
Fig. 24. ^{19}F-{^{1}H} MAS NMR spectra of sample 1 having the crystalline phase present in the α form only. (a) Total spectrum. (b) Spectrum of the crystalline component recorded by using the $T_{1\rho}$(^{19}F) filter (spin-lock period of 40 ms). (c) Spectrum of the amorphous component recorded by using the T_2(^{19}F) filter τ–π–τ ($\tau = 40$ μs). For better visualization, all spectra are shown with the same intensity. [*Source:* C. Hucher *et al.*, 2005]

by single peak at 43.0 and 42.1 ppm, while the γ form exhibits two peaks resonating at 41.3 and 44.5 ppm.

It is known that there exist reverse monomeric units in PVF$_2$, leading to H–H and T–T defects in the polymer chains which have been shown to have significant influence on the macroscopic properties of the material. To identify the location of chain defects, i.e., to check if the chain defects could enter the crystalline region and what the partition ratio of defects between the crystalline and amorphous regions is,
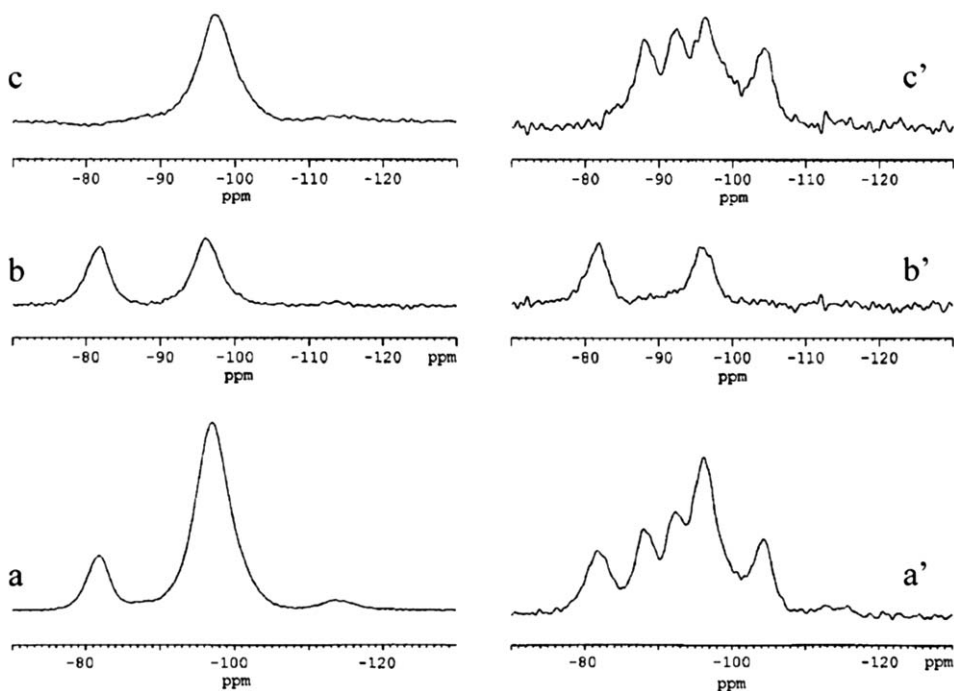
Fig. 25. (a, a′) ^{19}F-{^1H} MAS NMR spectra of crystalline components in samples 2 and 3 having mixed polymorphs. Both spectra have been recorded after using the $T_{1\rho}(^{19}F)$ filter (SL = 40 ms). (b, b′) Selectively excited resonance signals of the α polymorph by an additional application of a SELDOM pulse train. (c, c′) Separated resonance signals of β and γ polymorphs, respectively, obtained by corresponding spectral subtraction. [*Source:* C. Hucher *et al.*, 2005]

is an important application of solid-state NMR to semicrystalline polymer studies. The ^{19}F $T_{1\rho}$ measurements showed that the majority of the reverse units are located in the mobile amorphous part, and a significant portion of them is located in the interface region. The α polymorph contains a negligible percentage of reverse units, while 5% and 9% of the reverse units are included in β and γ polymorphs. Such a conclusion is unambiguously supported by a ^{19}F spin-diffusion experiment. As depicted in Fig. 27, the defect signals resonating at the higher field side of the spectra were selectively excited by a SELDOM pulse train and with the increase of spin-diffusion time, signal corresponding to the β form gradually increases, while the characteristic signal peak of α polymorph at the lower field side was not observed even in spectrum at longest spin-diffusion time.

Vanhaecht *et al.*[20] studied the cocrystallization of linear and cycloaliphatic residues in a series of copolyamides of 12.6/12.1,4–cyclohexane dicarboxylic acid (12.6/12.1,4–CHDA) by WAXD and NMR. Through monitoring ^1H $T_{1\rho}$ relaxation-dependent ^{13}C CP-MAS spectra, ^1H $T_{1\rho}$ values of the individual groups were measured on two samples with comparable 1,4–CHDA contents, but with different
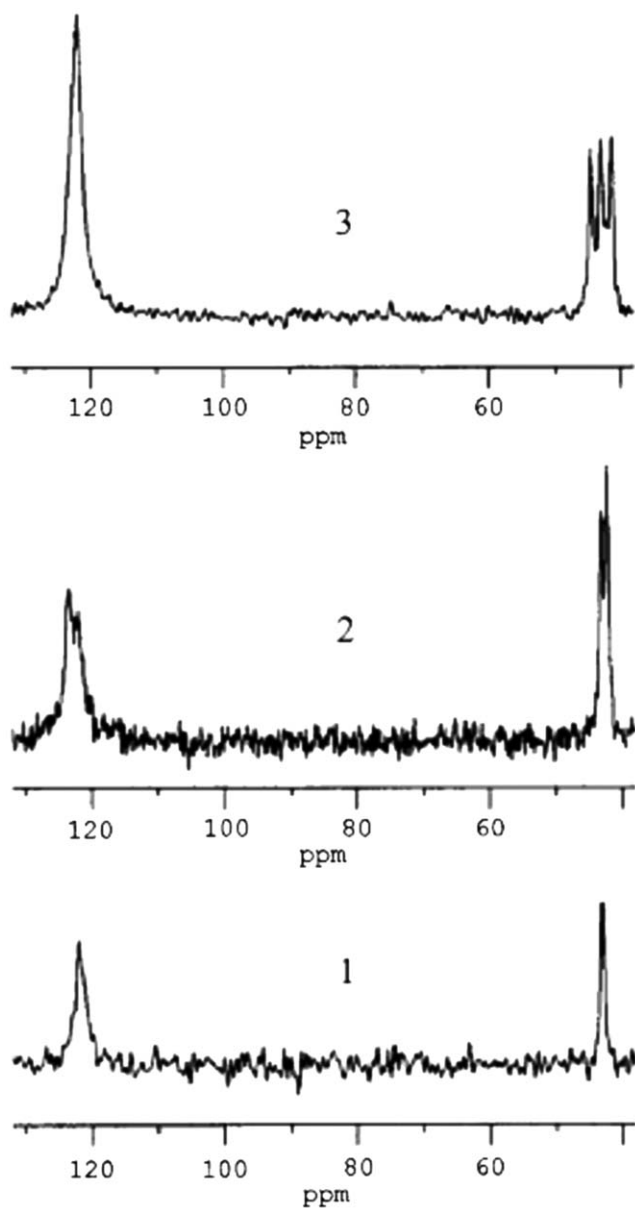
Fig. 26. Double decoupled ^{13}C CP-MAS spectra of crystalline components in samples containing α (1), α and β (2), and α and γ (3) polymorphs recorded by using the $T_{1\rho}(^{19}F)$ filter (spin-lock period of 40 ms). MAS: 10 kHz, contact time: 3 ms. [*Source:* C. Hucher *et al.*, 2005]
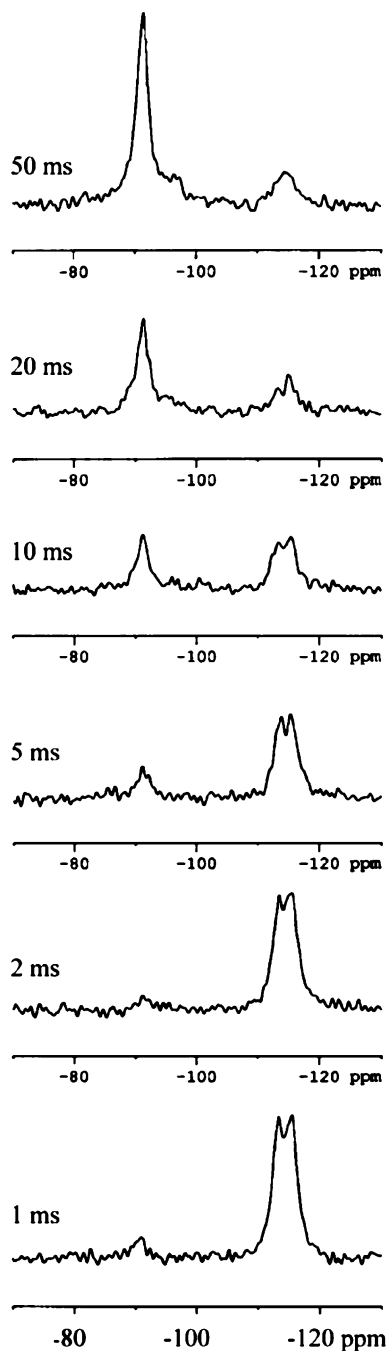
Fig. 27. ^{19}F spectra of PVF$_2$ sample 2 with mixed α and β polymorphs recorded for different times of spin-diffusion flow of fluorine magnetization from selectively excited reverse units to the main units. SELDOM pulse train has been used to prepare the initial gradient of magnetization. All spectra have been recorded using high-power proton decoupling and magic-angle spinning at a frequency of 30 kHz. [*Source:* C. Hucher *et al.*, 2005]

cis/*trans* configuration ratios (80/20, 15/85) of 1,4–CHDA. It was found that: (1) the crystalline signals exhibits longer ^{1}H $T_{1\rho}$ than that of the amorphous ones; (2) ^{1}H $T_{1\rho}$ of 1,4–CHDA residue in *trans*-rich copolyamide sample is similar to that of the adipic residues and is in between the values of the crystalline and amorphous signals; (3) ^{1}H $T_{1\rho}$ of 1,4–CHDA residue in the *cis*-rich copolyamide sample is comparable to that of the amorphous signals and is apparently shorter than that of the crystalline signals. The above experimental observations support directly the conclusion that the *trans* isomers can readily cocrystallize with the adipic acid residues, whereas the *cis* isomers are excluded by the crystalline phase. Similar strategy was applied to investigate a series of copolyamides containing *trans* or *cis* isomers of 1,4–diaminocyclohexane (1,4–DACH), namely 4.14/1,4–DACH14.[21] The *trans* isomer is found to be present in both the crystalline and amorphous regions, while the *cis* isomer is mainly, if not completely, present in the amorphous region.

Poly(ethylene oxide) (PEO) is a semicrystalline polymer that has been subjected to extensive studies. The research interests arise not only from its application importance, but also from the fact that PEO can serve as a model sample for studying the polymer crystallization, molecular motions as well as intermolecular interactions. The phase structure of PEO can be readily tailored by adding a second polymer or small molecules which can form intermolecular interaction with the ether oxygen of PEO. The interaction between fullerene (C_{60}) and PEO in their complex was recently studied by solid-state ^{13}C NMR.[22] Fig. 28a–d show the ^{13}C CP-MAS spectra of a series of PEO/C_{60} complex samples with different O/C molar ratios of PEO to C_{60}. From the figure, it can be found that in contrast to the spectrum of physically mixed sample (Fig. 28d), samples prepared by lyophilization exhibit strong C_{60} signal around 143 ppm in their ^{13}C CP-MAS spectra. Moreover, the relative intensity of C_{60} increases with increasing C_{60} content in the complexes. Since the C_{60} molecules have no directly bonded protons, the C_{60} signal in the spectra must arise from the intermolecular CP happened between the ^{13}Cs of C_{60} and the protons of neighboring PEOs. It is known the efficiency of ^{1}H–^{13}C polarization transfer depends on the strength of static dipolar interaction between ^{1}H and ^{13}C spins, which is partly determined by the ^{1}H–^{13}C internuclear distance. Effective intermolecular CP transfer can occur only when the ^{1}H–^{13}C distance is less than 5 Å. Apparently, the appearance of C_{60} signal with marked intensity in these ^{13}C CP-MAS spectra of PEO/C_{60} complexes demonstrates that C_{60}s are well dispersed in PEO matrix. The driving force for such a good dispersion of C_{60} molecules in PEO matrix is attributed to the n–p donor–acceptor interactions between the n-orbital of the PEO ether oxygen and the π-system of C_{60}.

As can be observed from Fig. 28a–d, the ^{13}C CP-MAS signal of PEO consists of two components, a broad and a narrow one corresponding to the crystalline and amorphous regions, respectively. It is also known that the ^{1}H $T_{1\rho}$ of the crystalline region of PEO is much shorter than that of the amorphous region. For this, short CP contact time is needed for observing crystalline signal in ^{13}C CP-MAS spectrum of PEO, otherwise the crystalline signal will diminish due to the fast ^{1}H $T_{1\rho}$ relaxation during the period of contact time. As is shown in Fig. 28e acquired with the contact time of 5 ms, the broad component of PEO signal disappeared almost
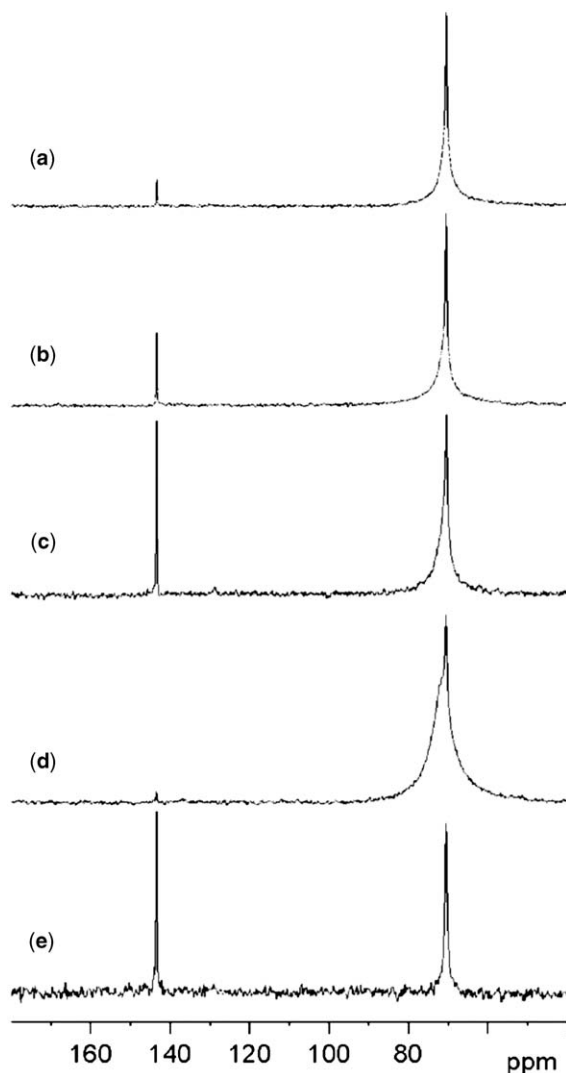
Fig. 28. The ^{13}C CP-MAS spectra of freeze-dried samples [25:1] (a), [5:1] (b), [1:1] (c), [1:1] (e) and the physical mixture sample [1:1] (d). For spectra a–d, the contact time of CP was set to be 1 ms, while for spectrum e, the contact time was set to be 5 ms. [*Source:* M. J. Li *et al.*, 2003]

completely, due to the fact that ^{1}H $T_{1\rho}$ of the crystalline region is much shorter than 5 ms. Interestingly, like the amorphous component, the signal of C_{60} in the spectrum is rarely influenced by the long contact time, indicating that C_{60}s are dispersed in the amorphous region of PEO.

Through comparing ^{13}C static CP/DD spectra of PEO/C_{60} complex and pure C_{60} samples, it was found that the linewidth of the C_{60} signal in complex is much broader

than that of pure C_{60} sample. Such a result suggests that isotropic rotation of C_{60} is inhibited to some extent in the complex sample, due to the intermolecular interaction aforementioned. ^1H T_2 was obtained through monitoring the signal of C_{60} in the complex. This T_2, which actually reflects the mobility of PEO chains around C_{60}, was much shorter than that of the amorphous region of PEO, indicating that PEO chains around C_{60}s are fastened by C_{60}s due to intermolecular interactions.

The interpolymer interaction of PEO with poly(methacrylic acid) (PMAA) was also studied recently by solid-state high-resolution ^{13}C NMR spectroscopy, with the emphasis on the PEO molecular weight effect on forming complex.[23] As is known, PEO and PMAA can form interpolymer complex with 1:1 molar ratios of MAA:EO in their aqueous solution. The ^{13}C CP-MAS spectra demonstrated apparently that the crystalline phase of PEO is completely destroyed in the complex. The results of ^1H T_2 and ^{13}C T_1 measurements indicate that the chain mobility of both PEO and PMAA are greatly restricted by intermolecular hydrogen bonding interactions. Interestingly, as shown in Table 7, ^1H T_2 of PEO in the complexes increases with increasing PEO molecular weight. Meanwhile, ^{13}C T_1 of PEO in the complexes was found to be the longest when molecular weight of PEO is the smallest. From these results, conclusions can be drawn as: (1) The bulk structures of the complexes are dependent on the molecular weight of PEO; (2) The fraction of "free" PEO segments without forming hydrogen bonds with PMAA increases with increasing PEO molecular weight, as reflected by their relatively higher mobility.

Molecular motion of polymers is known to deeply affect the macroscopic properties of these materials. The situation is same with semicrystalline polymers. To understand the relationship between structure and molecular dynamics is of special importance for polymer materials. Recently, McElheny *et al.* employed several kinds of solid-state NMR techniques to study dynamics of a series of semicrystalline aromatic polyamides.[24] The so-called two-dimensional separate-local-field MAS (2D SLF MAS) NMR, which is capable of revealing the dynamics of each site in a molecule as sideband spectra, shows that for all the polyamide samples the dynamic behavior of aromatic ring over a wide range of temperatures, can be well described by a static and π-flipping ring model. During their work, the authors rediscovered that ^{13}C $T_{1\rho}$ relaxation behavior cannot be safely interpreted in terms of molecular motion, although it was sometimes used as a measure of molecular

Table 7. ^1H T_2 values of PMAA and PMAA/PEO complex samples, where 1.5 K, 4 K, 10 K and 5 M correspond to the molecular weight of PEO, respectively

Samples	^1H T_2 values (μs)	
	Carboxyl group	PEO
PMAA	16.2	
Complex 1.5 K	10.3	10.8
Complex 4 K	13.0	19.5
Complex 10 K	11.5	20.7
Complex 5 M	13.8	21.8

dynamics in the range of several tens of kHz. They demonstrated that even crystalline L-alanine, a small molecule with simple crystalline structure, exhibits biexponential decay in its ^{13}C $T_{1\rho}$ relaxation. By applying an off-resonance Lee–Goldberg (LG) decoupling field on proton channel during the spin-locking time of ^{13}C to achieve ^{1}H–^{1}H decoupling, they demonstrated again that not only the molecular motions, but also the ^{1}H–^{1}H spin-diffusion processes, via their field fluctuations, can contribute to the ^{13}C $T_{1\rho}$ relaxation.

   ^{13}C T_1 is a parameter reflecting molecular motions at MHz region and is of special importance for semicrystalline polymer studies, due to its sensitivity to the packing and conformational structures. By using a modified Torchia pulse sequence, Alamo et al. recently proposed a CP-based method, which can be applied to selectively measure the ^{13}C T_1 of the NC region of semicrystalline polymers.[25] They demonstrated that by using CP, the method has higher sensitivity compared with the conventional saturation or inversion recovery method. The idea of modifying Torchia pulse sequence had been used to selectively measure the NC ^{13}C CP-MAS spectra of cross-linked PE.[26] Through studying several PP samples with different configuration structures and with different degrees of crystallinity, Alamo et al. concluded that ^{13}C T_1 of the NC region of PP is insensitive to the phase and configuration structures. They also found that when ^{13}C T_1 of a specific chemical site is shorter than ^{1}H T_1 of the sample, the corresponding ^{13}C T_1 recovery curve will become nonexponential, due to the influence of the transient nuclear Overhauser effect (NOE). The contribution of the transient NOE to the recovery curve was successfully modeled by a double exponential function derived from Solomon equation. ^{13}C T_1, the value of NOE factor as well as the ^{1}H–^{13}C cross-relaxation time (T_{1CH}) were then obtained from computer fitting. They also demonstrated that by adding a $90°$ pulse train on ^{1}H channel during the T_1 relaxation window of the modified Torchia pulse sequence to saturate ^{1}H magnetization, the contribution of transient NOE to ^{13}C T_1 relaxation can be removed, leading to a perfect exponential recovery curve.

   As a bacterially synthesized semicrystalline polymer, poly(3–hydroxybutyrate) (PHB) has attracted much research interests for its biodegradability and biocompatibility. However, its industrial application is still limited, owing to its intrinsic brittleness and narrow processing window. Bio-synthesized poly(3–hydroxybutyrate-co-3–hydroxyvalerate) (PHBV) copolymers, on the other hand, show enhanced properties as reduced brittleness and enhanced flexibility compared with PHB and has been used as a biodegradable substitute of polyolefin thermoplastics. The origin for the property differences between PHB and PHBVs is apparently worth investigating. Chen et al.[27] studied the mobility of the NC regions of PHB and three PHBV copolymer samples with different molar contents of 3–hydroxyvalerate (HV) by employing variable-temperature ^{1}H wide-line and ^{13}C solid-state high-resolution NMR spectroscopy. Quantitative ^{13}C DD/MAS measurements demonstrated that the degrees of crystallinity of these four samples are close to each other. The ^{1}H wide-line spectra of four samples, through spectrum deconvolution, were found to comprise three components with different linewidth and lineshape at temperatures ranging from 298 to 358 K. The component C1 which exhibits Gaussian lineshape and largest half-width was attributed to the crystalline region, while the component

C3 with Lorentzian lineshape and smallest linewidth to "mobile" amorphous. The component C2 with Lorentzian lineshape and linewidth in between C1 and C3 was assigned to "rigid" amorphous. The mobility of C2 was quite low as inspected at NMR time scale. While the content of C1 showed only slight difference among PHB and three PHBV samples, the content of C2 decreased evidently with increase of HV comonomer unit, in accordance with the decreasing order of brittleness of the four samples. Such a result strongly indicates that the brittleness of the samples is largely associated with the existence of the "rigid" amorphous region. The properties improvement of PHBV over PHB can be partly attributed to the fact that the amorphous of PHBV is softer compared with that of PHB. For all four samples, the content of C3 gradually increased with increasing temperature, at the expense of the C2 component.

REFERENCES

1. Q. J. Zhang, W. X. Lin, G. Yang and Q. Chen, *J. Polym. Sci. Polym. Phys.*, 2002, **40**, 2199.
2. Z. Q. Su, Y. Zhao, Y. Z. Xu, X. Q. Zhang, S. N. Zhu, D. J. Wang, J. G. Wu, C. C. Han and D. F. Xu, *Polymer*, 2004, **45**, 3693.
3. H. Kurosu, K. Fukushima, M. Matsuo, I. Ando and S. Amiya, *J. Mol. Struct.*, 2002, **602–603**, 233.
4. W. X. Lin, Q. J. Zhang, G. Yang and Q. Chen, *J. Mol. Struct.*, 2002, **602–603**, 185.
5. W. G. Hu and E. B. Sirota, *Macromolecules*, 2003, **36**, 5144.
6. L. L. Zhang, Q. Chen and E. W. Hansen, *Macromol. Chem. Phys.*, 2005, **206**, 246.
7. H. J. Assumption, J. P. Vermeulen, W. L. Jarrett, L. J. Mathias and A. J. van Reenen, *Polymer*, 2006, **47**, 67.
8. N. Chaiyut, T. Amornsakchai, H. Kaji and F. Horii, *Polymer*, 2006, **47**, 2470.
9. L. Ma, Y. Bin, Y. Sakai, Q. Chen, H. Kurosu and M. Matsuo, *Macromolecules*, 2001, **34**, 4802.
10. D. L. VanderHart and C. R. Snyder, *Macromolecules*, 2003, **36**, 4813.
11. T. Kameda and T. Asakura, *Polymer*, 2003, **44**, 7539.
12. W. X. Lin, M. H. Bian, G. Yang and Q. Chen, *Polymer*, 2004, **45**, 4939.
13. W. X. Lin, L. L. Zhang, H. P. Zhang and Q. Chen, *Acta Polym. Sin.*, 2005, **3**, 432.
14. Q. Chen, H. Kurosu, L. Ma and M. Matsuo, *Polymer*, 2002, **43**, 1203.
15. M. Wei, W. Davis, B. Urban, Y. Q. Song, F. E. Porbeni, X. W. Wang, J. L. White, C. M. Balik, C. C. Rusa, J. Fox and A. E. Tonelli, *Macromolecules*, 2002, **35**, 8039.
16. M. Wei, T. A. Bullions, C. C. Rusa, X. W. Wang and A. E. Tonelli, *J. Polym. Sci. Polym. Phys. Ed.*, 2004, **42**, 386.
17. F. E. Porbeni, I. D. Shin, X. T. Shuai, X. W. Wang, J. L. White, X. Jia and A. E. Tonelli, *J. Polym. Sci. Polym. Phys. Ed.*, 2005, **43**, 2086.
18. V. M. Litvinov, M. Bertmer, L. Gasper, D. E. Demco and B. Blümich, *Macromolecules*, 2003, **36**, 7598.
19. C. Hucher, F. Beaume, R. P. Eustache and P. Tekely, *Macromolecules*, 2005, **38**, 1789.
20. B. Vanhaecht, R. Willem, M. Biesemans, B. Goderis, M. Basiura, P. C. M. M. Magusin, I. Dolbnya and C. E. Koning, *Macromolecules*, 2004, **37**, 421.
21. B. Vanhaecht, B. Goderis, P. C. M. M. Magusin, B. Mezari, I. Dolbnya and C. E. Koning, *Macromolecules*, 2005, **38**, 6048.
22. M. J. Li and Q. Chen, *Polymer*, 2003, **44**, 2793.
23. H. P. Zhao, W. X. Lin, G. Yang and Q. Chen, *Eur. Polym. J.*, 2005, **41**, 2354.
24. D. McElhenya, V. Frydmanb and L. Frydman, *Solid State NMR*, 2006, **29**, 132.
25. R. G. Alamo, J. A. Blanco, I. Carrilero and R. Fu, *Polymer*, 2002, **43**, 185.
26. J. Sohma, Q. Chen, Y. Wang and X. Wu, *Radiat. Phys. Chem.*, 1991, **37**, 47.
27. Y. Chen, G. Yang and Q. Chen, *Polymer*, 2002, **43**, 2095.

Selective NMR Excitations in Chiral Analysis

JONATHAN FARJON, LATIFA ZIANI, LAETITIA BEGUIN,
DENIS MERLET AND JACQUES COURTIEU

Laboratoire de RMN en milieu orienté, Université Paris-Sud 11, ICMMO, UMR CNRS 8182, Bat. 410, 91405 Orsay cedex, France

NMR spectroscopy using chiral liquid crystals as solvents is a powerful tool to visualize enantiomers. Using these oriented solvents, recent NMR studies with selective excitation have proven their effectiveness at simplifying enantiomeric visualization and enantiomeric excess determination through ^1H or ^{13}C spectra. In this review we present different straightforward and robust selective techniques dedicated to the spectral analysis of enantiomers dissolved in such chiral-oriented solvents.

1. INTRODUCTION

The development of new methodologies to determine enantiomeric purity is still of great interest because the different techniques commonly in use are not general.[1–3] For this purpose, one of the latest methods that has been developed uses a chiral liquid crystal as the NMR solvent. The best results so far have been obtained using lyotropic liquid crystals composed of synthetic homopolypeptides dissolved in various organic cosolvents.[4] The most commonly used polypeptide is the Poly-γ-Benzyl-L-Glutamate, PBLG, which can be dissolved in organic solvents such as $CHCl_3$, CH_2Cl_2, DMF, THF….[5–7] Due to anisotropic solute–solvent interactions, solutes dissolved in liquid crystal solvent are partially oriented. Consequently, the order-sensitive NMR interactions are not averaged to zero, namely the chemical shift anisotropies (CSA), the anisotropic part of the direct spin–spin couplings, i.e. the residual dipolar couplings (RDC) together with the anisotropic part of the indirect couplings if any, and the quadrupolar splittings for nuclei with spin $I>1/2$. Furthermore, enantiomers dissolved in a chiral liquid crystal solvent are not ordered to the same extent because of the chirality of the orientating field.[8–10]

Thus they may be differentiated on their NMR spectrum through one of the anisotropic interactions. This methodology has been successfully applied to a wide range of chiral compounds with different kinds of chirality.[5–7,11–18] Various nuclei such as the ^{2}H, ^{13}C, ^{19}F..., may be used to observe the enantiomeric NMR differentiation.[6,7,12,19–23] However, very few studies have been successfully realized using ^{1}H or ^{1}H coupled ^{13}C NMR due to the fact that the spectra obtained are most often overcrowded and not resolved. This is a pity because ^{1}H is the most sensitive nucleus and the best as far as quantitativity is concerned.

One way to simplify such spectra is to let only one coupling evolve in the indirect dimension, t_1, of a 2D NMR experiment. Selective excitations can be used to reach this goal. Special care must be taken to use quantitative experiments in order to be able to measure accurately enantiomeric excesses. In the following we present different 2D NMR experiments on chiral liquid crystal solutions that use selective refocusing excitations and which may lead to the measurement of the enantiomeric purity.

2. SELECTIVE HOMONUCLEAR REFOCUSING EXPERIMENTS: SERF AND SERFph

The proton NMR spectrum of a molecule dissolved in a liquid crystal solvent is sensitive to both the proton chemical shifts and the total spin–spin couplings. The chemical shift is the sum of the isotropic and the anisotropic parts of the chemical shift. The latter interaction is often negligible for protons, particularly in a weakly oriented medium such as the PBLG phase. Consequently, no enantiodifferentiation can be observed on this basis. The total coupling, T_{ij}, can be written as $T_{ij} = J_{ij} + 2D_{ij}$ where J_{ij} is the isotropic part of the scalar coupling and D_{ij} the anisotropy of the total spin–spin coupling. D_{ij} is the sum of two contributions: the purely anisotropic residual dipole–dipole coupling, D'ij, and the anisotropic part of the scalar coupling, ΔJ_{ij}. Most generally this latter contribution can be neglected when dealing with couplings involving protons. This approximation may have important consequences when dealing with molecular topology. But as far as enantiodifferentiation is concerned, this approximation is of no concern because the two contributions behave identically with the molecular ordering. So in the following we will not pay attention to this problem and, following the common conventions, we will call D_{ij} the residual dipolar coupling even if it may have a nondipolar contribution.

The differential ordering effect of enantiomers dissolved in chiral liquid crystals should produce different values of T_{ij} between nuclei in each enantiomer because contribution of D_{ij} to T_{ij} should be different. For example, the proton spectrum of a racemic mixture of $(\pm)$–1,2 dibromopropane is shown in Fig. 1.

In this spectrum, we can distinguish the different protons based on the chemical shifts, but the coupling hyperfine structure is overcrowded and not enough resolved to reveal that the enantiomers are discriminated. First, this is due to the numerous ^{1}H–^{1}H long-range dipolar couplings which are present even in such small
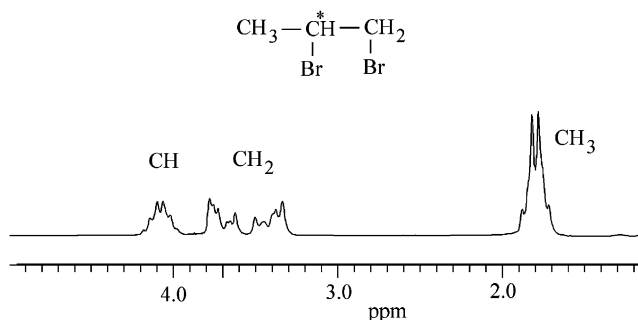
Fig. 1.   400 MHz 1D ^{1}H spectrum of the racemic mixture of dibromopropane dissolved in PBLG/CDCl$_3$ solvent.
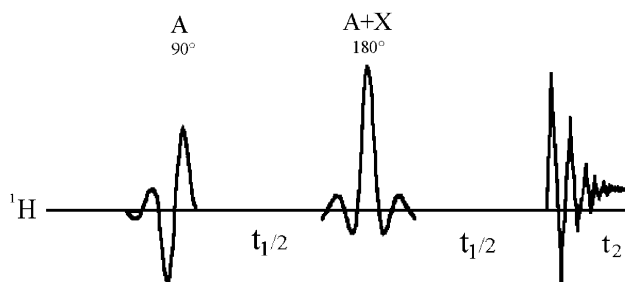
Fig. 2.   Pulse scheme of the SERF 2D experiment.

molecules, and second we are actually observing the mixture of two molecules with hopefully different spectra and this makes the total spectrum still more confused.

One way to simplify such a spectrum is to select one coupling between a pair of nuclei. To reach such a goal, Facke and Berger used exclusively selective pulses in the well-known J-resolved 2D spectroscopy.[24] This experiment was named SERF for SElective ReFocusing.[25] The pulse sequence is shown in Fig. 2.

The first selective pulse excites nucleus A to be observed during t_2. The selective 180° pulses are applied simultaneously on the A and X nuclei. During t_1 evolution, the chemical shift of nucleus A is refocused and all the couplings of A with the surrounding protons are refocused except the coupling between nuclei A and X. First applied in isotropic media, this sequence was used by Farjon et $al.$ to chiral compounds dissolved in chiral liquid crystal solvents.[26] Fig. 3 shows the 2D SERF spectrum of the dibromopropane solute where all the selective pulses are applied on the methyl nuclei.[26]

In the F$_1$ dimension we can distinguish clearly two superimposed triplets. As the two selective pulses are applied on the methyl signal, only the dipolar couplings between the methyl protons are evolving during t_1 thus giving rise to a dipolar triplet in ordered media. Furthermore, we can clearly see one dipolar triplet for each enantiomer which was not possible on the unresolved 1D ^{1}H spectrum. It is now
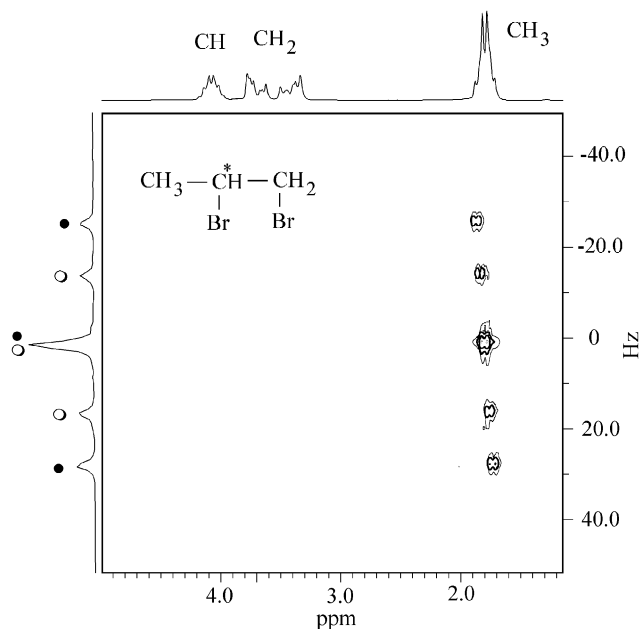
Fig. 3.   400 MHz 2D SERF spectrum of the racemic mixture of dibromopropane dissolved in PBLG/CDCl$_3$ solvent. Open and black circles correspond to the R or S enantiomers.

clear that the dipolar couplings in the enantiomers are strongly different and they can be measured with a high precision. Note that the selective pulse shapes used are an EBURP-2 and a REBURP for the 90° and 180° pulse, respectively.[27,28] But whatever the shapes of the selective pulses are, the results remain unchanged if the necessary selectivity is achieved.

The advantage to use the selective J-resolved 2D experiment is that this experiment is quantitative. Thus by integration it is possible to determine any enantiomeric excess. This is the case for the 1,2-propylene carbonate molecule below. The SERF experiment is shown in Fig. 4 where all the selective pulses have been realized on the methyl protons.

Again we can see clearly two triplets, one for each enantiomer. By integration of the different signals we can evaluate the enantiomeric excess to be 24%, compared to the 18% prepared. This prepared enantiomeric excess is determined by weighing the exact mass of each pure enantiomer which is introduced in the sample tube.

It is a limitation of this experiment to be obliged to work with non-Lorentzian lineshapes. Indeed the FID equation for an AX spin system is:

$$S(t_1, t_2) = \exp[i\pi T_{AX}t_1]\exp[-i(2\pi v_A + \pi T_{AX})t_2]$$
$$+ \exp[-i\pi T_{AX}t_1]\exp[-i(2\pi v_A - \pi T_{AX})t_2] \qquad (1)$$

After double Fourier transform, the signal phase is a so-called phase twist, thus the above spectra are presented in the magnitude mode. Even if different
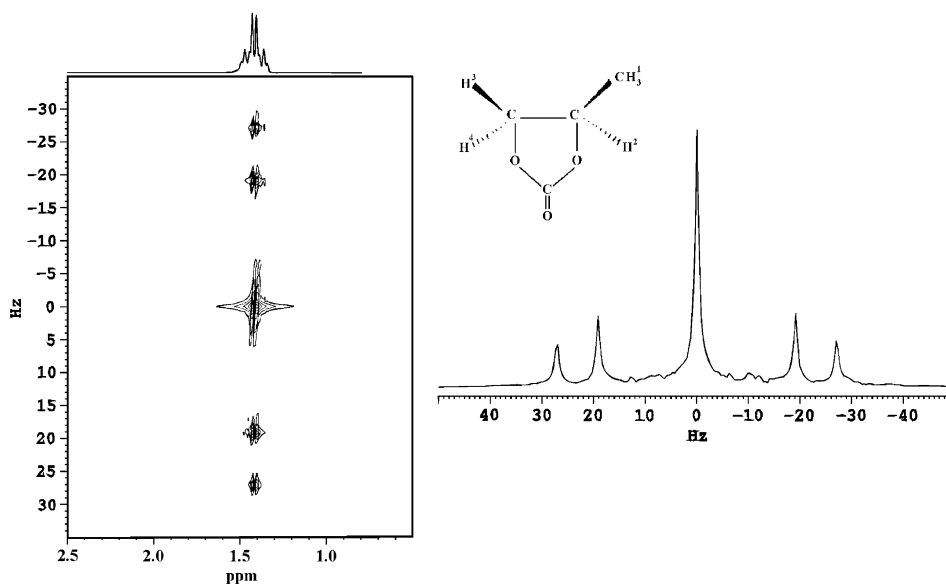
Fig. 4.   400 MHz ^{1}H SERF on the methyl of the 1,2-propylene carbonate dissolved in PBLG/CDCl$_3$ solvent.
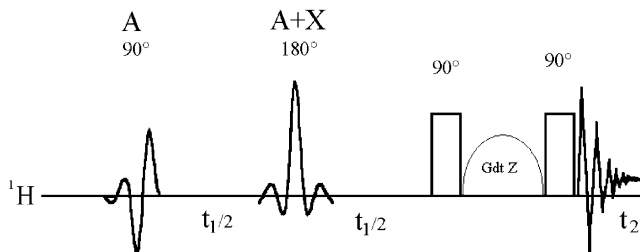
Fig. 5.   Pulse scheme of the phased SERFph 2D experiment.

methodologies exist to treat this kind of signal, it is always important to develop new pulse sequences which could provide pure absorption signals to improve line-shape and integration.[29] In this context, the SERFph sequence has been proposed recently and the pulse sequence is presented in Fig. 5.[30]

At the end of the SERF pulse sequence a gradient z-filter is added to eliminate the antiphase part evolving during t_1. In this case the FID equation becomes:

$$S(t_1, t_2) = \frac{1}{2}\cos[\pi T_{AX}t_1]\{\exp[-i(2\pi v_A + \pi T_{AX})t_2]$$
$$+ \exp[-i(2\pi v_A - \pi T_{AX})t_2]\} \qquad (2)$$
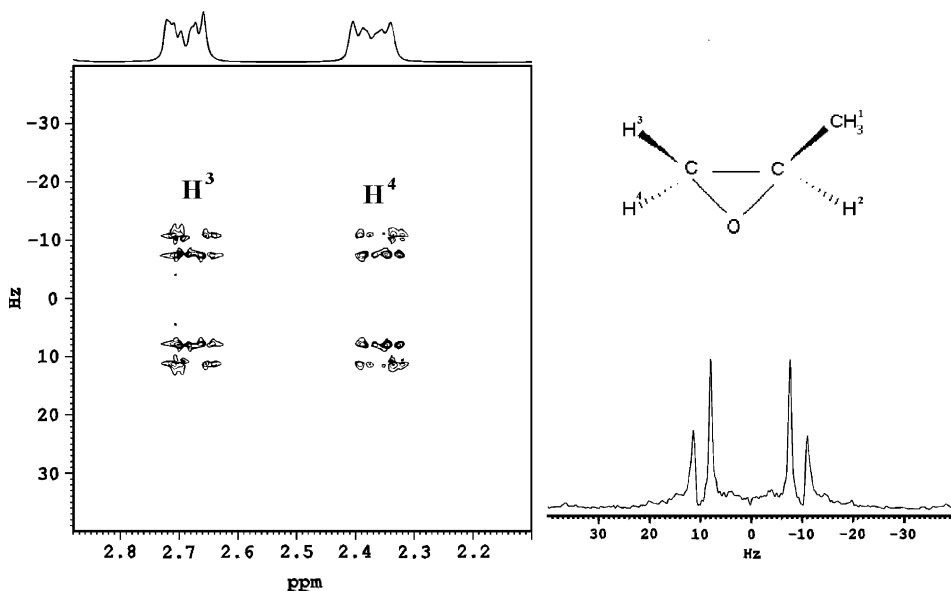
Fig. 6.   400 MHz ^{1}H SERFph on the methylene of the *S* enantiomeric enriched mixture of the propylene oxide dissolved in PBLG/CDCl$_3$ solvent.

After double Fourier transformation such a spectrum can now be phased. Fig. 6 shows the spectrum of propylene oxide where the different selective pulses have been applied to the protons of the CH$_2$ methylene group.

We can see clearly two dipolar doublets one for each enantiomer and due to the quantitativity of the experiment we can determinate by integration the enantiomeric excess, which was measured to be 19%, compared to the 21% prepared.

3. COMBINATION OF VARIABLE ANGLE SAMPLE SPINNING AND SERF OR SERFph EXPERIMENTS

The use of selective excitations is limited because it requires to have proton signals well separated from others. This is not always possible due to either large dipolar couplings or numerous couplings. It will happen frequently for large molecules or when the order parameters of the solute are large. A recent study reports combination of variable angle sample spinning (VASS) techniques and selective excitation in chiral liquid solvent to overcome this limitation.[30] The variable sample spinning technique allows decreasing the magnitude of the dipolar coupling as needed and at the same time to increase the spectrum resolution.[31,32] This was applied in the case of the propylene oxide solute in PBLG/CDCl$_3$ chiral solvent. In Fig. 7 are presented the 1D ^{1}H spectra with and without rotation of the sample at 40° to the magnetic field with a spinning speed of 660 Hz.
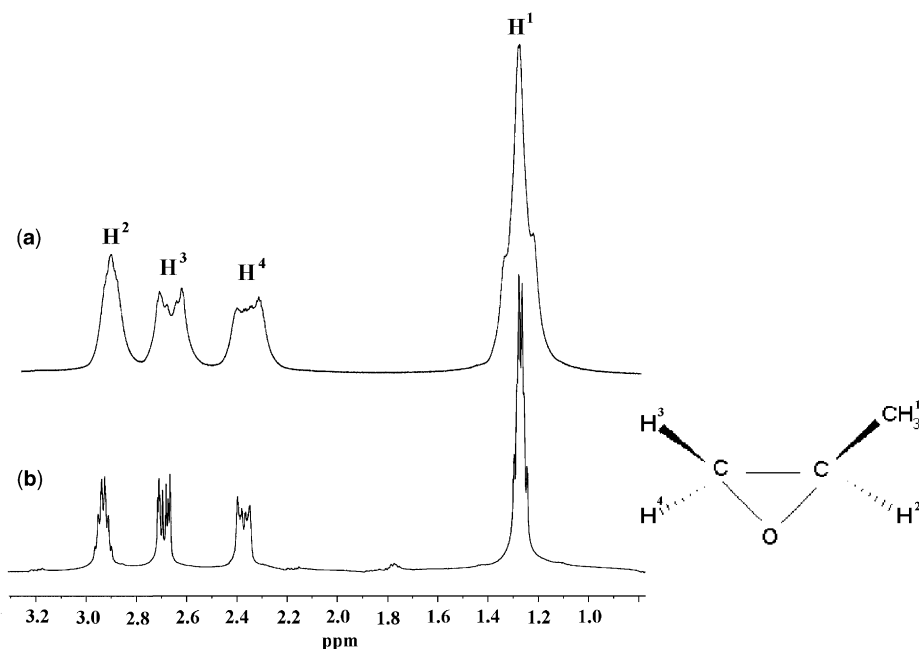
Fig. 7. 400 MHz ^{1}H NMR spectrum of an enantiomeric mixture of propylene oxide dissolved in PBLG/CDCl$_3$ solvent. (a) static sample; (b) sample rotating at an angle of 40° to B$_0$.

Note the increase in the spectrum resolution but even if the quality of the spectrum is better, no conclusion on the enantiomeric differentiation can be drawn. Nevertheless, in this case the different chemical shifts are well resolved. Thus, SERFph experiments on all the sites can now be realized which were not possible on the static sample. The experiment has been done on the methine resonances to let evolve only the methyl–methine coupling. The spectrum is presented in Fig. 8.

The F_1 projection displays two quartets, one for each enantiomer. Again, by integration it has been demonstrated that the enantiomeric excess can be determined accurately within 3%.[30] Note that the coupling T_{12} can be accurately measured on the projection and that this coupling is different for the enantiomers.

4. HETERONUCLEAR SELECTIVE REFOCUSING, HetSERF, EXPERIMENTS

The same methodology has been extended to carbon 13 spectra to benefit from the chemical shift dispersion of this nucleus and because the ^{1}H coupled carbon-13 spectra in chiral liquid crystal is usually not resolved for the same reason as for protons. The pulse sequence is a heteronuclear J-resolved experiment where the
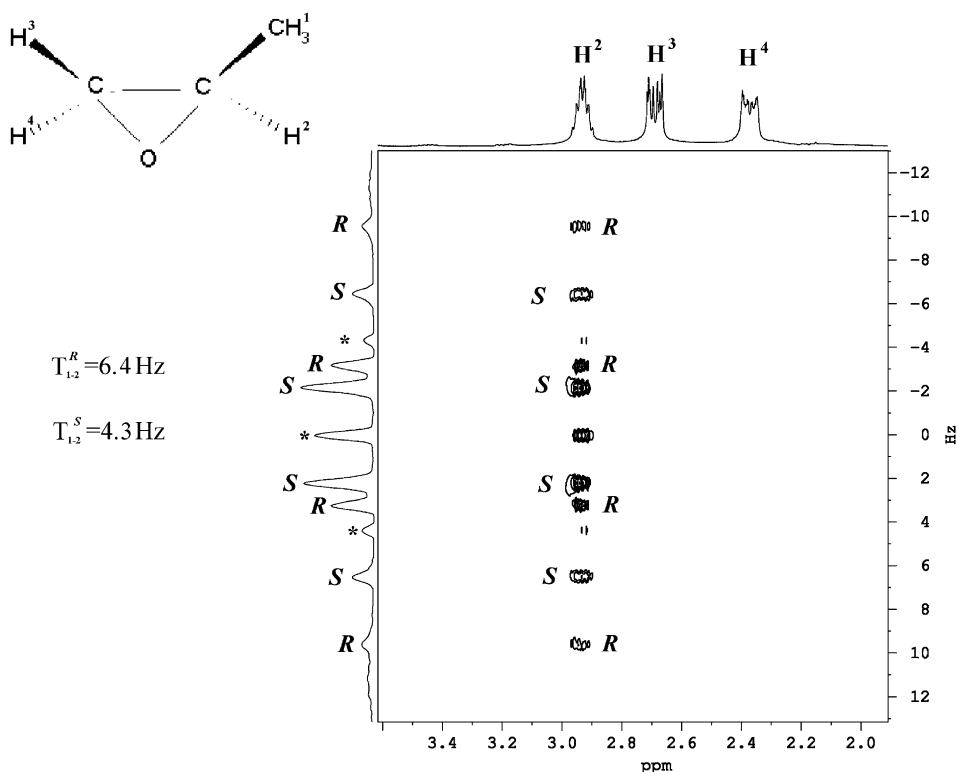
Fig. 8. 400 MHz ^{1}H SERFph spectrum of the propylene oxide in the PBLG/CDCl$_3$ solvent. The sample was spinning at 660 Hz around an axis tilted at 40° to B$_0$.

180° proton pulse is selective as presented in Fig. 9. The spectra obtained can be phased using the quadrature sequential acquisition mode.

Using this pulse sequence, all the NMR interactions are refocused during t_1 except the heteronuclear coupling between the carbons and the selectively excited proton. As for the SERFph pulse sequence, this experiment is also quantitative and it is appropriate for enantiomeric excess measurements. Farjon *et al.* have applied this pulse sequence using a chiral liquid crystal solvent.[33] In Fig. 10 is presented the HetSERF spectrum on a racemic mixture of 1,2-dibromopropane dissolved in PBLG/CDCl$_3$ phase and where the selective 180° pulse was applied on the methyl protons.

The F_1 projection of the different carbons exhibits two quartets for the C$_A$ and C$_B$ carbon, one for each enantiomer, but we observe a single quartet on C$_C$. This HetSERF experiment in chiral liquid crystal solvent allows for measuring the various ^{13}C–H heteronuclear couplings thus increasing the possibilities to visualize the differentiation of enantiomers on the spectrum. Thus not only the single-bond heteronuclear dipolar couplings can be measured but also the long-range heteronuclear dipolar couplings. This methodology has been applied to visualize
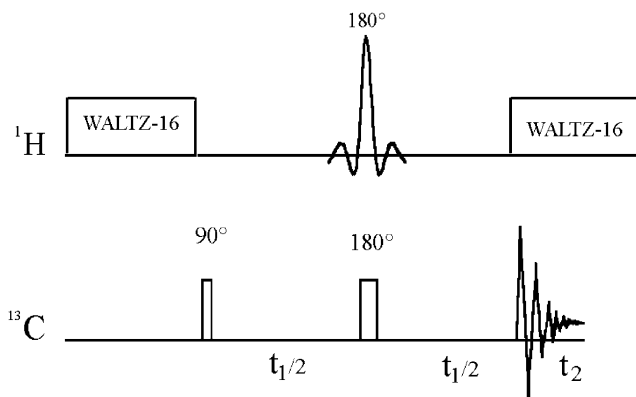
Fig. 9. Basic pulse scheme of the 2D experiment. The selective 180° proton pulse is a REBURP shape pulse. The protons are decoupled using the classical WALTZ-16 sequence.
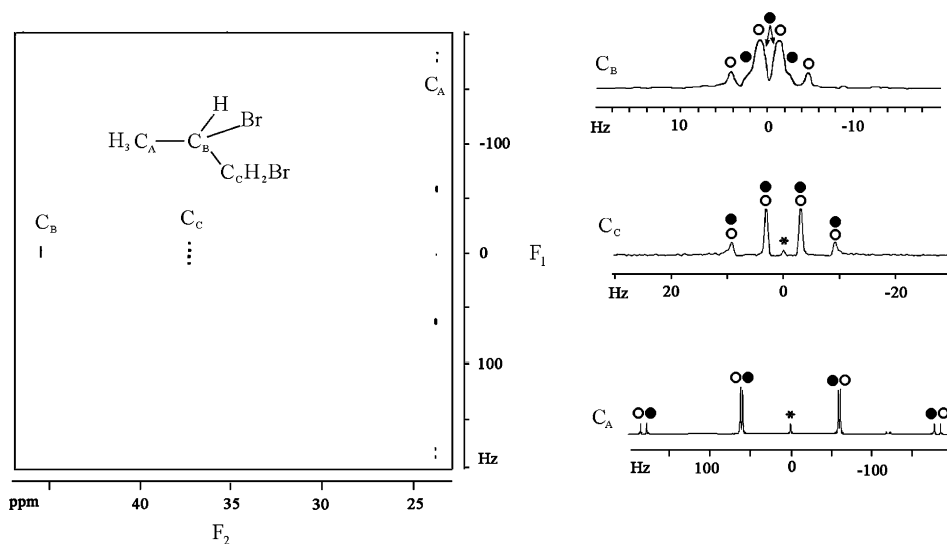
Fig. 10. 100 MHz ^{13}C HetSERF experiment on 1,2-dibromopropane in PBLG/CDCl$_3$ phase. Open and black circle correspond to R or S enantiomers.

enantiomeric differentiation in the case of (η^6-Arene) chromium tricarbonyl, organo-metallic complexes exhibiting planar chirality.[34]

To demonstrate the quantitativity of the experiment, a HetSERF on an S enantiomeric enriched mixture of 2-chloro-propanoic acids dissolved in PBLG/CDCl$_3$ phase is shown in Fig. 11. The selected proton was the methine proton.

In this case, the projections of the various carbons should be one doublet for each enantiomer. We can clearly see on the projections at C$_A$ and C$_B$ carbons two
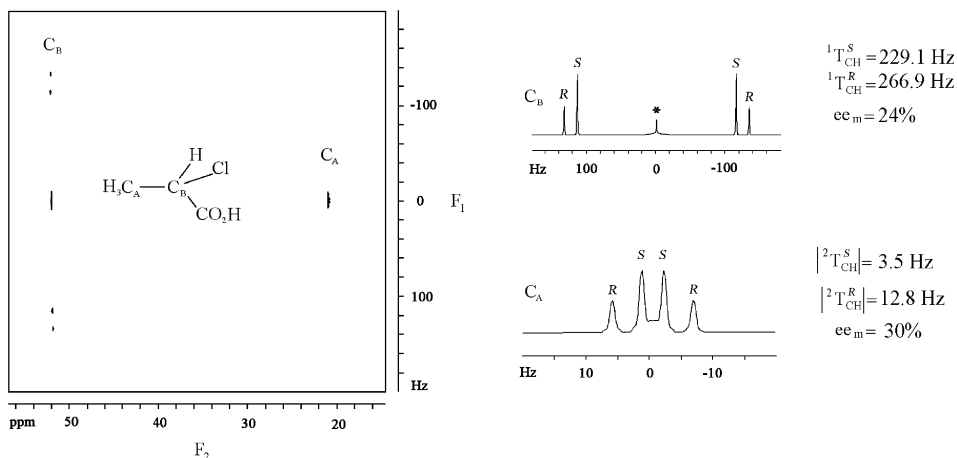
Fig. 11. 100 MHz ^{13}C HetSERF spectrum of S enantiomeric enriched mixture of 2-chloro-propanoic acids dissolved in PBLG/CDCl$_3$ phase.

doublets with different intensities. Thus on these sites the differentiation of the enantiomers can be visualized and enantiomeric excess determined at 24 and 30% respectively compared to the 26% prepared.[33]

5. CONCLUSION

The NMR spectroscopy of chiral liquid crystal solutions is a powerful tool for enantiomeric visualization through the order-sensitive anisotropic NMR interactions. 1D proton and ^{1}H coupled ^{13}C spectra are usually not sufficiently resolved in this medium to exhibit an enantiomeric differentiation. Then the use of selective pulses allows for simplifying the spectra. One way is to let only one coupling to evolve during the t_1 evolution period of a 2D experiment. This can be achieved using homonuclear selective J-resolved experiments, SERFph, for proton spectra or heteronuclear selective J-resolved experiments, HetSERF, for carbon-13 spectra. It has been shown that SERFph is a very powerful tool to determine quickly and accurately enantiomeric excess in these anisotropic solvents. For the carbon-13 spectra the HetSERF experiments have the advantages to give the possibility to visualize the enantiomeric differentiation not only through one coupling but also on the different couplings between the various carbons of the compound and the selectively excited proton. These techniques increase the possibilities to see an enantiodifferentiation and to measure enantiomeric excess.

REFERENCES

1. D. Parker, *Chem. Rev.*, 1991, **91**, 1441.
2. R. Rothchild, *Enantiomer*, 2000, **5**, 457.

3. T. J. Wenzel and J. D. Wilcox, *Chirality*, 2003, **15**, 256.
4. C. Aroulanda, M. Sarfati, J. Courtieu and P. Lesot, *Enantiomer*, 2001, **6**, 1.
5. I. Canet, J. Courtieu, A. Loewenstein, A. Meddour and J. M. Pechine, *J. Am. Chem. Soc.*, 1994, **116**, 9652.
6. A. Meddour, I. Canet, A. Loewenstein, J. M. Pechine and J. Courtieu, *J. Am. Chem. Soc.*, 1995, **117**, 6520.
7. A. Meddour, P. Berdagué, A. Hedli, J. Courtieu and P. Lesot, *J. Am. Chem. Soc.*, 1997, **119**, 4502.
8. P. Lesot, Y. Gounelle, D. Merlet, A. Loewenstein and J. Courtieu, *J. Phys. Chem.*, 1995, **99(40)**, 14871.
9. P. Lesot, D. Merlet, J. Courtieu, J. W. Emsley, T. T. Rantala and J. Jokisaari, *J. Phys. Chem.*, 1997, **A 101**, 5719.
10. J. W. Emsley, P. Lesot and D. Merlet, *Phys. Chem. Chem. Phys.*, 2004, **6**, 522.
11. W. Smadja, S. Auffret, P. Berdague, D. Merlet, C. Canlet, J. Courtieu, J. Y. Legros, A. Boutros and J. C. Fiaud, *Chem. Comm.* 1997, **21**.
12. E. Graf, R. Graff, M. W. Hosseini, C. Huguenard and F. Taulelle, *Chem. Comm.*, 1997.
13. P. Chalard, M. Bertrand, I. Canet, V. Thery, R. Remuson and G. Jeminet, *Org. Lett.*, 2000, **2(16)**, 2431.
14. M. Tavasli, J. Courtieu, R. J. M. Goss, A. Meddour and D. O'Hagan, *Chem. Comm.*, 2002.
15. A. Parenty, J. M. Campagne, C. Aroulanda and P. Lesot, *Org. Lett.*, 2002, **4(10)**, 1663.
16. P. Lesot, M. Sarfati and J. Courtieu, *Chem. Eur. J.*, 2003, **9**, 1724.
17. P. Lesot, C. Aroulanda and I. Billault, *Analyt. Chem.*, 2004, **76**, 2827.
18. D. Riegert, J. Collin, A. Meddour, E. Schultz and A. Trifonov, *J. Org. Chem.*, 2006, **71**, 2514.
19. D. Merlet, B. Ancian, J. Courtieu and P. Lesot, *J. Am. Chem. Soc.*, 1999, **121(22)**, 5249.
20. M. Sarfati, P. Lesot, D. Merlet and J. Courtieu, *Chem. Comm.*, 2000, **21**.
21. O. Lafon, P. Lesot, D. Merlet D and J. Courtieu, *J. Magn. Reson.*, 2004, **171(1)**, 135.
22. P. Lesot, D. Merlet, A. Meddour and J. Courtieu, *J. Chem. Soc., Far. Trans.*, 1995, **91(9)**, 1371.
23. P. Lesot, D. Merlet, J. Courtieu and J. W. Emsley, *Liquid Crystals*, 1996, **21(3)**, 427.
24. W. P. Aue, J. Karhan and R. R. Ernst, *J. Chem. Phys.*, 1976, **64**, 4226.
25. T. Fäcke and S. Berger, *J. Magn. Reson.*, 1995, **113**, 114.
26. J. Farjon, D. Merlet, P. Lesot and J. Courtieu, *J. Magn. Reson.*, 2002, **158**, 169.
27. R. Freeman, *Prog. Nucl. Magn. Reson. Spect.*, 1998, **32**, 59.
28. H. Geen and R. Freeman, *J. Magn. Reson.*, 1991, **93**, 93.
29. R. R. Ernst, G. Bodenhausen and A. Wokaun, *Principles of Nuclear Magnetic Resonance in One and Two Dimensions*, Clarendon Press, Oxford, 1987.
30. L. Beguin, J. Courtieu, L. Ziani and D. Merlet, *Mag. Res. Chem.*, 2006, **44**, 1096.
31. J. Courtieu, J. P. Bayle and B. M. Fung, *Prog. Nucl. Magn. Reson. Spect.*, 1994, **26**, 141.
32. J. Courtieu, D. W. Alderman, D. M. Grant and J. P. Bayle, *J. Chem. Phys.*, 1982, **77(2)**, 723.
33. J. Farjon, J. P. Baltaze, P. Lesot, D. Merlet and J. Courtieu, *Mag. Res. Chem.*, 2004, **42**, 594.
34. O. Lafon, P. Lesot, M. Rivard, M. Chavarot, F. Rose-Munch and E. Rose, *Organometallics*, 2005, **24**, 4021.

Index